

1

AGARD

ADVISORY GROUP FOR AEROSPACE RESEARCH & DEVELOPMENT

7 RUE ANCELLE 92200 NEUILLY SUR SEINE FRANCE

AD-A253 005



AGARD REPORT 786

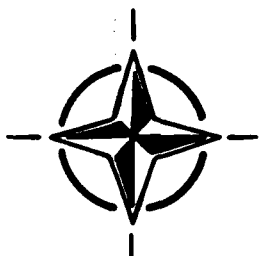
DTIC
SELECTED
JUN 02 1992
S, D

Special Course on Skin Friction Drag Reduction (Réduction de Trainée de Frottement)

The material assembled in this book was prepared under the combined sponsorship of the AGARD Fluid Dynamics Panel, the Consultant and Exchange Programme of AGARD, and the von Kármán Institute (VKI) for Fluid Dynamics. It was presented in an AGARD-FDP-VKI Special Course at the VKI, Rhode-Saint-Genèse, Belgium, 2nd–6th March 1992.

DISTRIBUTION STATEMENT A

Approved for public release
Distribution Unlimited



NORTH ATLANTIC TREATY ORGANIZATION

92-14306



Published March 1992

ribution and Availability on Back Cover

AGARD

ADVISORY GROUP FOR AEROSPACE RESEARCH & DEVELOPMENT

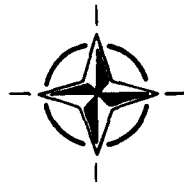
7 RUE ANCELLE 92200 NEUILLY SUR SEINE FRANCE

AGARD REPORT 786

Special Course on Skin Friction Drag Reduction

(Réduction de Traînée de Frottement)

The material assembled in this book was prepared under the combined sponsorship of the AGARD Fluid Dynamics Panel, the Consultant and Exchange Programme of AGARD, and the von Kármán Institute (VKI) for Fluid Dynamics. It was presented in an AGARD-FDP-VKI Special Course at the VKI, Rhode-St-Genèse, Belgium, 2nd–6th March 1992.



North Atlantic Treaty Organization
Organisation du Traité de l'Atlantique Nord

The Mission of AGARD

According to its Charter, the mission of AGARD is to bring together the leading personalities of the NATO nations in the fields of science and technology relating to aerospace for the following purposes:

- Recommending effective ways for the member nations to use their research and development capabilities for the common benefit of the NATO community;
- Providing scientific and technical advice and assistance to the Military Committee in the field of aerospace research and development (with particular regard to its military application);
- Continuously stimulating advances in the aerospace sciences relevant to strengthening the common defence posture;
- Improving the co-operation among member nations in aerospace research and development;
- Exchange of scientific and technical information;
- Providing assistance to member nations for the purpose of increasing their scientific and technical potential;
- Rendering scientific and technical assistance, as requested, to other NATO bodies and to member nations in connection with research and development problems in the aerospace field.

The highest authority within AGARD is the National Delegates Board consisting of officially appointed senior representatives from each member nation. The mission of AGARD is carried out through the Panels which are composed of experts appointed by the National Delegates, the Consultant and Exchange Programme and the Aerospace Applications Studies Programme. The results of AGARD work are reported to the member nations and the NATO Authorities through the AGARD series of publications of which this is one.

Participation in AGARD activities is by invitation only and is normally limited to citizens of the NATO nations.

The content of this publication has been reproduced
directly from material supplied by AGARD or the authors.

Published March 1992
Copyright © AGARD 1992
All Rights Reserved

ISBN 92-835-0661-8



Printed by Specialised Printing Services Limited
40 Chigwell Lane, Loughton, Essex IG10 3TZ

Recent Publications of the Fluid Dynamics Panel

AGARDOGRAPHS (AG)

Design and Testing of High-Performance Parachutes
AGARD AG-319, November 1991

Experimental Techniques in the Field of Low Density Aerodynamics
AGARD AG-318 (E), April 1991

Techniques Expérimentales Liées à l'Aérodynamique à Basse Densité
AGARD AG-318 (FR), April 1990

A Survey of Measurements and Measuring Techniques in Rapidly Distorted Compressible Turbulent Boundary Layers
AGARD AG-315, May 1989

Reynolds Number Effects in Transonic Flows
AGARD AG-303, December 1988

REPORTS (R)

Engineering Methods in Aerodynamics Analysis and Design of Aircraft
AGARD R-783, Special Course Notes, January 1992

Aircraft Dynamics at High Angles of Attack: Experiments and Modelling
AGARD R-776, Special Course Notes, March 1991

Inverse Methods in Airfoil Design for Aeronautical and Turbomachinery Applications
AGARD R-780, Special Course Notes, November 1990

Aerodynamics of Rotorcraft
AGARD R-781, Special Course Notes, November 1990

Three-Dimensional Supersonic/Hypersonic Flows Including Separation
AGARD R-764, Special Course Notes, January 1990



ADVISORY REPORTS (AR)

Air Intakes for High Speed Vehicles
AGARD AR-270, Report of WG 13, September 1991

Appraisal of the Suitability of Turbulence Models in Flow Calculations
AGARD AR-291, Technical Status Review, July 1991

Rotary-Balance Testing for Aircraft Dynamics
AGARD AR-265, Report of WG 11, December 1990

Calculation of 3D Separated Turbulent Flows in Boundary Layer Limit
AGARD AR-255, Report of WG10, May 1990

Adaptive Wind Tunnel Walls: Technology and Applications
AGARD AR-269, Report of WG12, April 1990

Accession For	
NTIS CRA&I <input checked="" type="checkbox"/>	
DTIC TAB <input type="checkbox"/>	
Unannounced <input type="checkbox"/>	
Justification	
By _____	
Distribution/	
Availability Codes	
Distr	Avail and/or Special
A-1	

CONFERENCE PROCEEDINGS (CP)

Effects of Adverse Weather on Aerodynamics
AGARD CP-496, December 1991

Manoeuvring Aerodynamics
AGARD CP-497, November 1991

Vortex Flow Aerodynamics
AGARD CP-494, July 1991

Missile Aerodynamics
AGARD CP-493, October 1990

Aerodynamics of Combat Aircraft Controls and of Ground Effects
AGARD CP-465, April 1990

Computational Methods for Aerodynamic Design (Inverse) and Optimization
AGARD-CP-463, March 1990

Applications of Mesh Generation to Complex 3-D Configurations
AGARD CP-464, March 1990

Fluid Dynamics of Three-Dimensional Turbulent Shear Flows and Transition
AGARD CP-438, April 1989

Validation of Computational Fluid Dynamics
AGARD CP-437, December 1988

Aerodynamic Data Accuracy and Quality: Requirements and Capabilities in Wind Tunnel Testing
AGARD CP-429, July 1988

Aerodynamics of Hypersonic Lifting Vehicles
AGARD CP-428, November 1987

Aerodynamic and Related Hydrodynamic Studies Using Water Facilities
AGARD CP-413, June 1987

Applications of Computational Fluid Dynamics in Aeronautics
AGARD CP-412, November 1986

Store Airframe Aerodynamics
AGARD CP-389, August 1986

Unsteady Aerodynamics — Fundamentals and Applications to Aircraft Dynamics
AGARD CP-386, November 1985

Aerodynamics and Acoustics of Propellers
AGARD CP-366, February 1985

Improvement of Aerodynamic Performance through Boundary Layer Control and High Lift Systems
AGARD CP-365, August 1984

Wind Tunnels and Testing Techniques
AGARD CP-348, February 1984

Aerodynamics of Vortical Type Flows in Three Dimensions
AGARD CP-342, July 1983

Missile Aerodynamics
AGARD CP-336, February 1983

Prediction of Aerodynamic Loads on Rotorcraft
AGARD CP-334, September 1982

Wall Interference in Wind Tunnels
AGARD CP-335, September 1982

Fluid Dynamics of Jets with Applications to V/STOL
AGARD CP-308, January 1982

Aerodynamics of Power Plant Installation
AGARD CP-301, September 1981

Computation of Viscous-Inviscid Interactions
AGARD CP-291, February 1981

Subsonic/Transonic Configuration Aerodynamics
AGARD CP-285, September 1980

Turbulent Boundary Layers Experiments, Theory and Modelling
AGARD CP-271, January 1980

Aerodynamic Characteristics of Controls
AGARD CP-262, September 1979

High Angle of Attack Aerodynamics
AGARD CP-247, January 1979

Foreword

Technology aimed at providing aircraft with the lowest possible drag continues to be the key to the design and operation of the economically successful commercial and general aviation aircraft. To this end, technology programmes focused on reducing aircraft drag have been underway for some time now and are continuing to produce noteworthy results. Many of these previous results have been reported in two FDP/VKI Special Courses held in 1977 and 1985.

The present course will review recent progress in the field of skin friction drag reduction for transport aircraft. After an introduction on its technology, the course will focus on the two aspects of drag reduction: maintaining laminar flow by controlling transition and manipulating the turbulence structure in boundary layers. The use of riblets, LEBU, polymers, additives, etc., will also be discussed.

To better understand the techniques used to reduce the skin friction drag, the basic phenomena involved in transition and turbulence will also be reviewed.

Specific topics planned for the course include:

- Boundary Layer Control for Laminar Flow
 - Natural, Suction or Hybrid
 - Numerical Approaches, including Crossflow and Leading Edge Effects
 - Recent Experimental Results, New Developments and Experience
- Recent Developments with Turbulence Manipulators
 - Riblets and Large Eddy Breakup Devices
 - Recent Experimental Results and Basic Turbulence Studies

Avant-Propos

Les techniques destinées à réduire la trainée des avions restent une clé pour aboutir à une conception d'appareils économiquement et commercialement viables. Pour atteindre ce but, des programmes technologiques orientés vers ces problèmes de réduction de trainée ont été renforcés depuis plusieurs années et ils conduisent à des résultats très prometteurs. L'état de l'art en la matière a déjà fait l'objet de deux séries de cours "FDP/VKI Special Courses" en 1977 et 1985.

Le programme proposé pour ce cours comporte une revue des progrès réalisés dans le domaine de la réduction de frottement des avions de transport. Après une introduction sur l'enjeu industriel que représentent ces questions, le cours sera axé sur deux aspects de la réduction de trainée de frottement: le maintien de l'écoulement laminaire par contrôle de la transition d'une part et la manipulation de la structure de la turbulence dans les couches limites d'autre part. L'utilisation des riblets, LEBU, polymères ou autres additifs sera également discutée.

Pour bien comprendre les techniques mises en œuvre ou imaginées pour réduire la trainée de frottement, les mécanismes de base de la transition laminaire-turbulent et de la turbulence seront d'abord rappelés.

De façon plus précise le cours comprendra les thèmes suivants:

- Maintien du régime laminaire:
 - Laminarité naturelle, par aspiration ou contrôle hybride
 - Prévision de la transition y compris par instabilité transversale et effets de bord d'attaque
 - Résultats expérimentaux récents, nouveaux développements
- Manipulation de la turbulence
 - Riblets et LEBU (Large Eddy Break-Up Devices)
 - Résultats expérimentaux récents
 - Etudes de base sur la turbulence (approches expérimentales et numériques)

Jean Cousteix
Special Course Director

Special Course Staff

Special Course Director: Dr J. Cousteix
Chef du Département d'Aérothermodynamique
ONERA-CERT
2 Avenue E. Belin — BP 4025
31055 Toulouse Cedex
France

LECTURERS

Dr D. Arnal
Dept. d'Aérothermodynamique
ONERA-CERT
2 Avenue E. Belin — BP 4025
31055 Toulouse Cedex
France

Mr E. Coustols
Dept. d'Aérothermodynamique
ONERA-CERT
2 Avenue E. Belin — BP 4025
31055 Toulouse Cedex
France

Mr J.P. Robert
Airbus Industrie
1 Rond Point Maurice Bellonte
31707 Blagnac Cedex
France

Dr M. Savill
Department of Engineering
University of Cambridge
Trumpington Street
Cambridge CB2 1PZ
United Kingdom

Prof. R.F. Blackwelder
Dept. of Aerospace Engineering
U. of Southern California
University Park
Los Angeles, CA 90089-1191
United States

Dr D.M. Bushnell
Ass. Chief Fluid Dynamics Div.
Mail Stop 197
NASA Langley Research Center
Hampton, VA 23665-5225
United States

Dr J. Kim
Chief, Turbulence Physics Section
Mail Stop 202A-1
NASA Ames Research Center
Moffett Field, CA 94035-1000
United States

Professor W.S. Saric
Mechanical and Aerospace Eng. Arizona State
University
Tempe, AZ 85287-6106
United States

LOCAL COORDINATOR

Professor M. Carbonaro
von Kármán Institute for Fluid Dynamics
Chaussée de Waterloo, 72
1640 Rhode-St-Genèse
Belgium

PANEL EXECUTIVE

Dr W. Goodrich

Mail from Europe:
AGARD—OTAN
Attn: FDP Executive
7, rue Ancelle
92200 Neuilly-sur-Seine
France

Mail from US and Canada:
AGARD—NATO
Attn: FDP Executive
Unit 21551
APO AE 09777
Tel: 33 (1) 47 38 57 75
Telex: 610176 (France)
Telefax: 33 (1) 47 38 57 99

Contents

	Page
Recent Publications of the Fluid Dynamics Panel	iii
Foreword/Avant-Propos	v
Special Course Staff	vi
	Reference
Basic Concepts on Boundary Layers by J. Cousteix	1
Drag Reduction: An Industrial Challenge by J.P. Robert	2
Aircraft Drag Reduction by D.M. Bushnell	3
Laminar-Turbulent Transition: Fundamentals by W.S. Saric	4
Boundary Layer Transition: Prediction, Application to Drag Reduction by D. Arnal	5
The Eddy Structures in Bounded Shear Flows by R.F. Blackwelder	6
Study of Turbulence Structure through Numerical Simulations: The Perspective of Drag Reduction by J. Kim	7
Turbulent Skin-Friction Drag Reduction by Active and Passive Means by E. Coustols and A.M. Savill	8

COMPONENT PART NOTICE

THIS PAPER IS A COMPONENT PART OF THE FOLLOWING COMPILATION REPORT:

TITLE: Special Course on Skin Friction Drag Reduction Held in Rhode-Saint-Genese, Belgium on 2-6 March 1992 (Reduction de Trainee de Frottement)

TO ORDER THE COMPLETE COMPILATION REPORT, USE AD-A253 005

THE COMPONENT PART IS PROVIDED HERE TO ALLOW USERS ACCESS TO INDIVIDUALLY AUTHORED SECTIONS OF PROCEEDING, ANNALS, SYMPOSIA, ETC. HOWEVER, THE COMPONENT SHOULD BE CONSIDERED WITHIN THE CONTEXT OF THE OVERALL COMPILATION REPORT AND NOT AS A STAND-ALONE TECHNICAL REPORT.

THE FOLLOWING COMPONENT PART NUMBERS COMprise THE COMPILATION REPORT:

AD#: PO06 964 thru AD#: PO06 972

AD#: _____ AD#: _____

AD#: _____ AD#: _____

DTIC
SELECTED
JUL 08 1992
S B D

DISTRIBUTION STATEMENT A
Approved for public release
Distribution Unlimited

Accession For	
NTIS GRA&I <input checked="" type="checkbox"/>	
DTIC TAB <input type="checkbox"/>	
Unannounced <input type="checkbox"/>	
Justification _____	
By _____	
Distribution/ _____	
Availability Codes- _____	
Dist	Avail and/or Special
A-1	2.1



92-17806



Basic Concepts on Boundary Layers

Jean COUSTEIX

Office National d'Etudes et de Recherches Aérospatiales (ONERA)
 Centre d'Etudes et de Recherches de Toulouse
 2, Avenue Edouard Belin
 31 055 TOULOUSE CEDEX - FRANCE

1 SUMMARY

Since man has been trying to fly, a war against drag has been engaged. At the present time, drag reduction is an industrial challenge in Aeronautics which justifies the efforts devoted to this topic. One facet of these efforts deals with the skin-friction drag reduction. Two directions are followed. The first one is the manipulation of turbulent boundary layers. By altering the formation of turbulence or by modifying its characteristics it is hoped to decrease the turbulent skin-friction. The second direction concerns the action on laminar-turbulent transition. By delaying the occurrence of the turbulent regime enormous skin-friction reductions are possible.

This Lecture Series on *Skin-Friction Drag Reduction* is aimed at giving an overview of the state of the art on the various means which are being studied to obtain significant gains. It is believed that the improvements in this field are based on a better knowledge of the basic phenomena (transition and turbulence) we want to play with in the boundary layer. Thus a few lectures are devoted to describe these fundamental materials and the present paper reminds the useful concepts on boundary layers which are needed to approach the more specialized questions.

2 INTRODUCTION

The drag of an aircraft is produced by the pressure forces and the friction forces which act on the surface of the body. On a commercial transport transonic aircraft about 45% of the drag is due to the skin friction of the wings, fuselage, fin, etc.

The skin friction is a direct effect of viscosity which has also indirect effects on the pressure drag. Let us take the simple example of a two-dimensional airfoil in incompressible flow. In inviscid fluid, the drag is null. In viscous fluid, the Joukovsky condition at the trailing no longer applies and a pressure drag is induced. It is the presence of the boundary layer and the wake which produce this additional drag. Very often the drag is decomposed into an induced drag (induced by the lift), viscous drag, wave drag, interference drag, etc. This is simply another decomposition which can be useful to analyse the various

sources of drag and to separate various physical phenomena.

Here we are particularly interested in the skin friction reduction. Indeed it is a very challenging and valuable topic as the skin friction drag represents a significant part of the total drag of the aircraft. In order to act on the skin friction it is useful to keep in mind that there are mainly two categories of boundary layers: the laminar boundary layer and the turbulent boundary layer. Now it is known that the skin friction is much higher in turbulent regime. Therefore the procedures which aim at reducing the skin friction drag are divided into two main classes. In the first class we have the procedures which try to delay the laminar-turbulent transition in order to favour the laminar flow. This is a very fascinating idea because the expected gain on the total drag of a transonic aircraft can be in the order of 10-15% if the flow over the wings and the fin is laminarized. It is not a new idea but its application is now possible with the technological progress that has been made to solve the practical problems. In the second class we have the procedures which aim at reducing the turbulent skin friction. An example is the use of riblets. The expected drag reduction is not as large as with laminar flow technology but they can be applied on large surfaces like a fuselage where it seems highly difficult to obtain a laminar flow. Even with smaller skin friction reduction, the total drag can be reduced by a significant amount.

Whatever the means employed to reduce the drag, a good basic knowledge of the involved physical phenomena is needed to try to develop the most efficient techniques. This reasoning led to the following organization of the present Lecture Series:

1. J.P. Robert from Airbus Industrie will talk about the industrial challenge that represents the possibility of reducing the drag of an aircraft. Indeed, Airbus Industrie undertook several research programs on this topic.
2. D.M. Bushnell from NASA Langley will give an overview of the possible means which can be developed to reduce the drag of an aircraft. The drag can be reduced not only by acting on the skin friction but also on the other sources of drag.

3. The next lectures are devoted to the problem of laminar-turbulent transition which is an essential ingredient if one wishes to laminarize the flow. W.S.Saric (Arizona State University) will start with the description of the fundamental mechanisms causing the transition from a laminar to a turbulent flow. D.Arnal (ONERA-CERT Toulouse) will continue with the practical means which are employed to predict transition and talk about applications of laminar flow technology.
4. The last part of this lecture series is devoted to the turbulent skin friction reduction. At first, R.F.Blackwelder (University of Southern California) and J.Kim (NASA Ames) will describe the turbulence structure in boundary layers as known from experiments and from numerical simulations. They will also discuss the implications on skin friction drag reduction. Finally, A.M.Savill (University of Cambridge) and E.Coustols (ONERA-CERT Toulouse) will discuss the numerous techniques which have been studied to reduce the turbulent skin friction.

Before going into the description of physical phenomena in transitional and turbulent boundary layers and of the techniques used to act on them, the present paper is aimed at reminding the elementary notions on viscosity, on turbulence and on boundary layers. Indeed these preliminaries are the basis of studies on techniques devoted to skin friction drag reduction.

3 EFFECTS OF VISCOSITY

In classical Aerodynamics, the fluid is regarded as a continuum. There is no discontinuity inside the fluid and at the interface between the fluid and a solid surface. As a consequence the no slip condition at a wall is applied. In other words, at a body surface the tangential velocities of the flow and of the wall are equal. The velocities normal to the wall are not necessarily equal because suction or blowing can occur through the wall. Another consequence is the existence of tangential forces. On a given volume of fluid, the forces can be tangential to the bounding surface. The pressure force is normal to the bounding surface but there are other forces (viscous forces) which can be normal and tangential.

These effects are associated with a property of the fluid known as the *viscosity*. At a molecular scale, the viscous effects are explained by the random motion of molecules which exchange momentum through their collisions. The statistical average of these exchanges shows the existence of a macroscopic stress when the flow is sheared. In the case of a simple shear $\frac{du}{dy}$ the viscous stress is given by:

$$\tau = \mu \frac{du}{dy}$$

where μ is called the dynamic viscosity of the fluid. This is a property of the fluid which exists even when the fluid is at rest. For air, the viscosity is given by the Sutherland law:

$$\mu = \mu_0 \sqrt{\frac{T}{T_0} \frac{1 + S/T_0}{1 + S/T}}$$

with $\mu_0 = 1.711 \cdot 10^{-5}$ Pl, $S = 110.4$ K, $T_0 = 273$ K.

This formula shows that the viscosity of air depends only on temperature; once again the viscosity is a property of the fluid. It is interesting to notice that the viscosity of air decreases when the temperature decreases. For water it is the contrary; the viscosity decreases when the temperature increases.

At a macroscopic scale, the effects of viscosity are experienced when the fluid is in motion. A simple example is the impulsive start of an infinite flat plate in a fluid initially at rest; for $t < 0$ the velocity of the plate is zero; for $t \geq 0$ the velocity of the plate is $u_w = cst$. The solution of this problem is:

$$\frac{u}{u_w} = \frac{2}{\sqrt{\pi}} \int_{\eta}^{\infty} e^{-\eta^2} d\eta ; \eta = \frac{y}{2(\nu t)^{1/2}}$$

From this solution a conventional viscous layer thickness δ can be defined. For example δ is the distance from the wall where the velocity is equal to 1% of the plate velocity. This gives:

$$\delta = 3.64(\nu t)^{1/2}$$

At time $t = 0$, the thickness of the viscous layer is zero and increases with time. The motion of the plate propagates in the fluid by diffusion, a mechanism which is entirely similar to heat diffusion (for heat diffusion the thermal conductivity has a similar role as viscosity for momentum diffusion). A diffusion velocity is defined as $d\delta/dt$ and varies like $(\nu/t)^{1/2}$. A characteristic viscous time can also be defined:

$$t_v = \frac{\delta^2}{\nu}$$

where t_v is the time needed for the viscous effects to propagate over a distance δ .

In a newtonian fluid (a good approximation for air), the viscous stress tensor and the heat flux in a general flow are given by:

$$\tau_{ij} = 2\mu \left(S_{ij} - \frac{\delta_{ij}}{3} S_{kk} \right) + \kappa S_{kk} \delta_{ij} \quad (1)$$

$$\phi_i = -\lambda \frac{\partial T}{\partial x_i} \quad (2)$$

In the above equations, the quantity δ_{ij} represents the Kronecker symbol. The bulk viscosity κ is generally assumed to be zero. The quantity S_{ij} is the strain tensor defined as the symmetric part of the velocity gradient tensor:

$$S_{ij} = \frac{1}{2} \left(\frac{\partial u_i}{\partial x_j} + \frac{\partial u_j}{\partial x_i} \right) \quad (3)$$

With the above assumptions the governing equations, namely the *Navier-Stokes equations*, are obtained:

$$\rho \frac{du_i}{dt} = -\frac{\partial p}{\partial x_i} + \frac{\partial \tau_{ij}}{\partial x_j} \quad (4a)$$

$$\rho \frac{dh}{dt} = \frac{dp}{dt} - \frac{\partial \phi_i}{\partial x_i} + \varphi_D \quad (4b)$$

with:

$$\varphi_D = \tau_{ij} S_{ij}$$

and the total derivative, $\frac{d\bullet}{dt}$, is defined as:

$$\frac{d\bullet}{dt} = \frac{\partial \bullet}{\partial t} + u_j \frac{\partial \bullet}{\partial x_j}$$

The energy equation can also be written for the total enthalpy h_i :

$$\rho \frac{dh_i}{dt} = \frac{\partial p}{\partial t} + \frac{\partial}{\partial x_i} (u_i \tau_{ij} - \phi_i) ; h_i = h + \frac{u_i u_i}{2} \quad (5)$$

In the energy equation (4b) φ_D is the dissipation function which represents a transformation of mechanical energy into heat due to the deformation work of the viscous stresses. This can be shown by writing down the equation for the kinetic energy $k = (u_i u_i)/2$ which is obtained by multiplying the momentum equation by u_i :

$$\rho \frac{dk}{dt} = p \frac{\partial u_i}{\partial x_i} + \frac{\partial}{\partial x_i} (u_i \tau_{ij} - p u_i \delta_{ij}) - \varphi_D \quad (6)$$

As φ_D appears with opposite signs in the heat equation and in the kinetic energy equation, it is clear that φ_D represents an exchange between both forms of energy. In addition, the second law of thermodynamics shows that $\mu \geq 0$ (and $\lambda \geq 0$). The kinetic energy therefore decreases because of the dissipation.

4 LAMINAR BOUNDARY LAYERS

General information can be found in references [18] or [66] for example.

4.1 Boundary layer concept

A possible interpretation of the Reynolds number is that it represents the ratio of the order of magnitude of inertia forces to viscous forces in the flow. In Aerodynamics, the Reynolds number is much larger than unity. For example, the Reynolds number based on the chord length of the wing of an Airbus A320 in flight is around $35 \cdot 10^6$. A simple application of the above interpretation of the Reynolds number leads to the conclusion that viscous effects are negligible. This would mean that the flow could be considered as inviscid. This is at variance with experimental evidence. In particular the no slip condition at the

wall can not be applied in inviscid flow. In fact, at high Reynolds number the flow behaves as an inviscid flow almost everywhere but this is not true near the solid boundaries where a boundary layer forms.

The boundary layer can be defined as a region of the flow where the viscous effects have the same order of magnitude as the inertia effects. Outside of the boundary layer (and of the wake which forms from the confluence of boundary layers) the flow can be considered as inviscid.

Let us consider the two-dimensional flow around an airfoil in incompressible fluid at a large Reynolds number. The flow is assumed laminar. The analysis of this flow is based on the existence of two length scales. One is the chord length L of the airfoil; the second scale is the boundary layer thickness δ . Applying the definition of the boundary layer and comparing the orders of magnitude of the viscous and inertia forces gives the order of magnitude of the boundary layer thickness:

$$\frac{\delta}{L} = \mathcal{R}_L^{-1/2} \quad (7)$$

with:

$$\mathcal{R}_L = \frac{U_0 L}{\nu}$$

where \mathcal{R}_L is the Reynolds number based on the chord length of the airfoil and on the velocity U_0 which is a reference velocity representative of the free-stream velocity.

An alternate interesting definition of the boundary layer is to say that the viscous time has the same order of magnitude as the convection time. Indeed this definition gives $\delta^2/\nu = L/U_0$. This result is strictly equivalent to the first definition.

Formula (7) shows that the dimensionless boundary layer thickness decreases when the Reynolds number increases. The boundary layer theory applies better at very large Reynolds number. This theory can be analyzed by using the technique of matched asymptotic expansions in which the small parameter is $\epsilon = \mathcal{R}_L^{-1/2}$ [78].

Formula (7) also shows that the Reynolds number characteristic of the boundary layer $\mathcal{R}_\delta = U_0 \delta / \nu$ is small compared to \mathcal{R}_L : $\mathcal{R}_\delta / \mathcal{R}_L = \mathcal{R}_L^{-1/2}$ so that the viscous effects are significant in the boundary layer. In fact whatever the value of the Reynolds number is the viscosity plays a role somewhere in the flow. When \mathcal{R}_L is of order unity the flow is viscous everywhere (in a domain of the size of the airfoil). When \mathcal{R}_L is much larger than unity a new structure forms—the boundary layer—in such a way that its characteristic Reynolds number is relatively low and viscous effects are present in this boundary layer. However, if \mathcal{R}_L is very large, \mathcal{R}_δ can also be very large but a new phenomenon occurs: the formation of turbulence. In turbulent flow, the characteristic Reynolds number of the smallest turbulent structures is of order unity; the viscosity plays its role in these structures. The viscosity is a singular

parameter in the sense that the structure of the flow adapts to the value of the Reynolds number in such a way that there is always a region of the flow where viscous effects are significant.

A consequence of equation (7) is that the velocity normal to the wall is small compared to the longitudinal velocity. This can be shown from the continuity equation:

$$\frac{\partial u}{\partial x} + \frac{\partial v}{\partial y} = 0$$

The analysis of order of magnitude shows that the first term is of order U_0/L because the longitudinal characteristic length is L . Now the characteristic length normal to the wall is δ . Then to obtain a non trivial continuity equation the velocity v has an order of magnitude such that:

$$\frac{v}{U_0} = \mathcal{R}_L^{-1/2}$$

In the same way it can be shown that the longitudinal diffusion is much smaller than the diffusion normal to the wall.

4.2 Boundary layer equations

The hypothesis of a large Reynolds number simplifies the Navier-Stokes equations. The boundary layer equations can be obtained from an order of magnitude analysis. They can also be obtained from the method of matched asymptotic expansions. In fact, the hypothesis of a large Reynolds number leads to a double approximation. In the boundary layer or in the wake, the boundary layer approximation holds. In the other regions of the flow, the inviscid flow approximation holds (the Euler equations are also an approximation of Navier-Stokes equations).

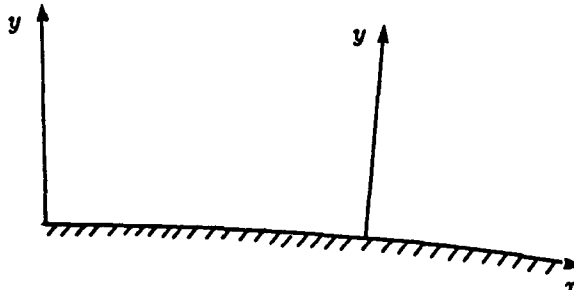


Figure 1: Boundary layer axis system.

The equations are written in an axis system tied to the wall (figure 1). The x -axis is along the wall and the y -axis is normal to the wall. It is assumed that the boundary layer thickness is much smaller than the curvature radius of the body. For a two-dimensional compressible flow the boundary layer equations read:

$$\frac{\partial \rho}{\partial t} + \frac{\partial \rho u}{\partial x} + \frac{\partial \rho v}{\partial y} = 0 \quad (8)$$

$$\rho \frac{du}{dt} = -\frac{\partial p}{\partial x} + \frac{\partial \tau}{\partial y} \quad (9)$$

$$0 = \frac{\partial p}{\partial y} \quad (10)$$

$$\rho \frac{dh_i}{dt} = \frac{\partial p}{\partial t} + \frac{\partial}{\partial y} (u\tau - \phi) \quad (11)$$

with:

$$\tau = \mu \frac{\partial u}{\partial y}$$

$$\phi = -\lambda \frac{\partial T}{\partial y}$$

and h_i is the total enthalpy. With the boundary layer assumption, the total enthalpy is related to the static enthalpy by:

$$h_i = h + \frac{u^2}{2}$$

The boundary layer equations are completed with the state law:

$$\frac{p}{\rho} = RT$$

where R is the constant of the gas considered.

Another form of the energy equation is:

$$\rho \frac{dh_i}{dt} = \frac{\partial p}{\partial t} + \frac{\partial}{\partial y} \left(\mu \frac{\partial h_i}{\partial y} \right) + \frac{\partial}{\partial y} \left(\left(\frac{1}{\rho} - 1 \right) \mu \frac{\partial h}{\partial y} \right) \quad (13)$$

In this equation, ρ is the Prandtl number: $\rho = \mu C_p / \lambda$ (C_p is the specific heat at constant pressure).

The boundary layer equations contain diffusion terms of momentum and heat only in the y -direction. The static pressure is constant in the boundary layer thickness along a normal to the wall.

The system of boundary layer equations is *parabolic*. A perturbation placed in a point of the boundary layer propagates along the normal to the wall and along the streamlines in the downstream direction.

Let us examine now how to proceed to calculate the flow around an airfoil for example.

According to the method of matched asymptotic expansions the standard calculation of the flow around a body proceeds step by step. The first step consists of calculating the inviscid flow around the real body. This calculation gives characteristics of the inviscid flow at the wall which are used as boundary conditions for the boundary layer calculation. A third step consists of correcting the inviscid flow as discussed in subsection 4.3. The domain of calculation of the boundary layer is defined as in figure 2. This is an open domain limited by the wall, a normal to the wall and a boundary BC placed above the boundary layer thickness.

At the wall the boundary conditions are:

1. $u = 0$.
2. $v = 0$ if the wall is impermeable or $v = v_w$ if a suction or a blowing is applied through the wall.
3. $T = T_w$ if the wall temperature is prescribed or $\phi = \phi_w$ if the wall heat flux is prescribed.

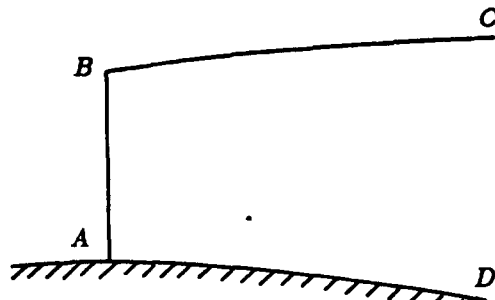


Figure 2: Boundary layer calculation domain.

At the outer edge of the boundary layer the boundary conditions are:

1. $u = u_e$
2. $T = T_e$

where u_e and T_e are obtained from the inviscid flow calculation at the wall. In steady flow, the total enthalpy in the inviscid flow is generally a constant everywhere and the pressure is a function of the outer velocity:

$$\rho_e u_e \frac{\partial u_e}{\partial x} = - \frac{\partial p}{\partial x}$$

Along the normal to the wall AB initial conditions are prescribed: the velocity and the temperature profiles are generally obtained from self-similarity solutions (see subsection 4.4).

The process given above to calculate the boundary layer is valid as long as the flow does not separate. When separation occurs, the boundary layer equations can still be used but a strong interaction with the inviscid flow exists and other techniques [42] are needed to solve the complete problem: boundary layer equations, inviscid flow equations, interaction law.

4.3 Boundary layer characteristics

The solution of the boundary layer equations gives the velocity profiles $u(y)$ and the temperature profiles $T(y)$ along the wall for all abscissae x . From these results, a few important characteristics are deduced.

The wall shear stress is:

$$\tau_w = \left(\mu \frac{\partial u}{\partial y} \right)_{y=0}$$

From integration along the wall the skin friction drag is calculated. Very often the wall shear stress is non-dimensionalized to form the skin friction coefficient:

$$C_f = \frac{\tau_w}{\frac{1}{2} \rho_e u_e^2}$$

where ρ_e and u_e are the values of density and velocity at the outer edge of the boundary layer taken at the same abscissa as the wall shear stress.

The wall heat flux is:

$$\phi_w = - \left(\lambda \frac{\partial T}{\partial y} \right)_{y=0}$$

The heat flux coefficient is often defined as:

$$C_h = \frac{\phi_w}{\rho_e u_e (h_w - h_{aw})}$$

where h_w is the wall enthalpy and h_{aw} is the recovery enthalpy which is defined as the wall temperature when the wall heat flux is zero (adiabatic wall).

Boundary layer thicknesses are also defined. The displacement thickness δ_1 and the momentum thickness θ are given by:

$$\delta_1 = \int_0^\infty \left(1 - \frac{\rho u}{\rho_e u_e} \right) dy \quad (14a)$$

$$\theta = \int_0^\infty \frac{\rho u}{\rho_e u_e} \left(1 - \frac{u}{u_e} \right) dy \quad (14b)$$

The ratio δ_1/θ is called the shape parameter:

$$H = \frac{\delta_1}{\theta}$$

The displacement thickness plays an important role in the theory of boundary layer because it characterizes the displacement effect of the boundary layer on the inviscid flow. This is shown by calculating the mass flow in the boundary layer:

$$q = \int_0^\delta \rho u dy$$

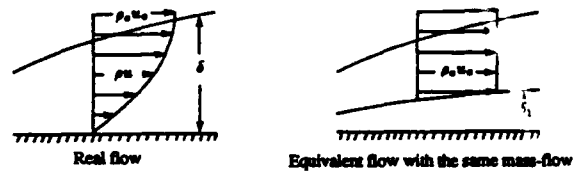


Figure 3: Displacement effect of boundary layer.

Now, we would like to construct an equivalent fictitious inviscid flow (figure 3). By construction, the mass flow through the boundary layer edge is the same in the real flow and in the fictitious flow and the equivalence of both flows is based on the equality of mass flow between the wall and the edge of the boundary layer. Then the thickness δ_1 is defined as:

$$q = \int_{\delta_1}^\delta \rho_e u_e dy = \int_0^\delta \rho u dy$$

and equation (14a) is obtained.

Then the calculation of the flow around an airfoil involves the following sequence of operations:

1. a first inviscid flow calculation around the real body is performed,
2. from the results of this calculation the boundary layer is calculated,
3. the body surface is displaced in the normal direction over a distance equal to the displacement thickness and a new inviscid flow calculation is performed around the so-obtained fictitious body.

Sometimes the procedure is iterated but in principle it is not necessary.

Instead of using the concept of displacement thickness it is also possible to use the concept of *transpiration velocity*. Using similar arguments as for the displacement thickness, it is shown that the normal wall velocity (transpiration velocity) to apply to the inviscid flow in order to construct an equivalent inviscid fictitious flow is (figure 4):

$$\frac{v_w}{u_e} = \frac{1}{\rho_e u_e} \frac{d}{dx} (\rho_e u_e \delta_1)$$

For numerical purposes, the concept of a transpiration velocity is interesting because only the wall boundary condition is modified.

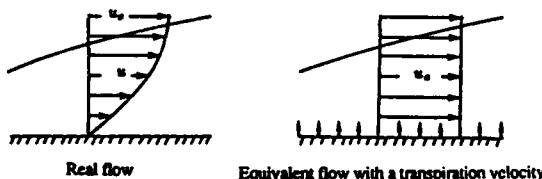


Figure 4: Equivalent wall transpiration velocity.

4.4 Self-similar solutions

The boundary layer equations can be solved numerically for any type of boundary conditions but it is interesting to study particular solutions which are representative of many practical situations and which illustrate the influence of the pressure gradient.

In incompressible laminar flow, these solutions are obtained for an external velocity distribution given by:

$$u_e = k x^m$$

In inviscid flow theory, this is the flow around a wedge (figure 5) with an angle $\pi\beta = \pi 2m/(m+1)$.

It can be shown that the solution is self-similar meaning that the velocity profiles at two stations are deduced one from the other by an affinity rule. A reduced transverse coordinate is used:

$$\eta = y \sqrt{\frac{m+1}{2} \frac{u_e}{\nu x}}$$

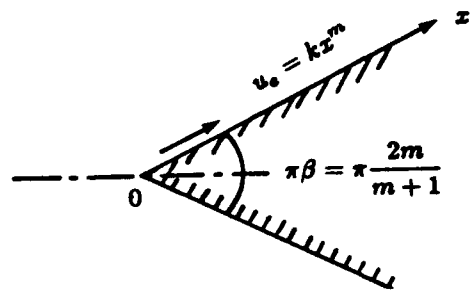


Figure 5: Flow around a wedge.

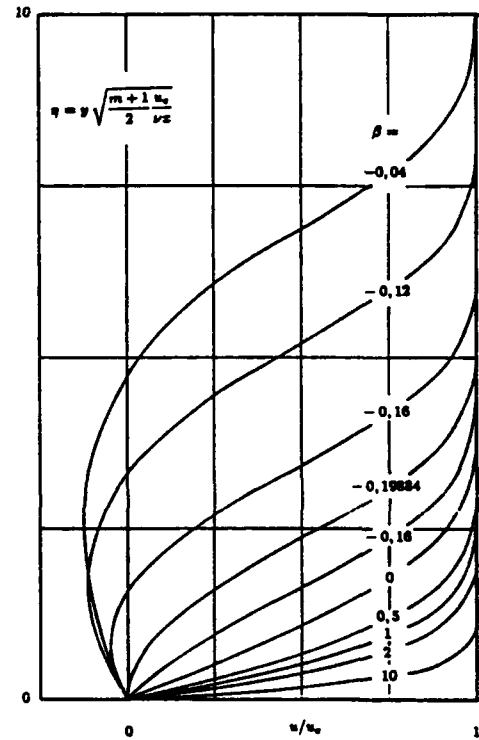


Figure 6: Falkner-Skan self-similarity solutions [15].

The self-similarity law expresses that the reduced velocity profile u/u_e is a function of the single variable η :

$$\frac{u}{u_e} = f'(\eta)$$

The boundary layer equations become:

$$f''' + f f'' + \beta (1 - f'^2) = 0 \quad (15)$$

This is the *Falkner-Skan equation* [27]. The primes indicate a derivative with respect to η and f is a reduced stream function ($f = \int_0^\eta f' d\eta$). The quantity β represents a pressure gradient parameter which is related to the exponent m by:

$$\beta = \frac{2m}{m+1}$$

The Falkner-Skan equation can be solved numerically for a given value of β . These solutions result

in a family of velocity profiles which depend on the pressure gradient parameter. Figure (6) shows the velocity profiles from which the effect of pressure gradient is evidenced. In particular, it is noticed that with a positive pressure gradient ($\beta < 0$) the velocity profiles exhibit an inflection point. It will be shown that this feature favours instabilities and transition of the laminar boundary layer (see subsection 7.2). For negative values of β , Stewartson [72] demonstrated the existence of a double solution; one of them has negative velocities near the wall. The limiting value $\beta = -0.19884$ corresponds to incipient separation because the slope at the wall is zero.

4.5 Kinetic energy balance

With the boundary layer assumption, the kinetic energy is:

$$k = \frac{u^2}{2}$$

and the kinetic energy equation becomes:

$$\rho \frac{dk}{dt} + u \frac{\partial p}{\partial x} + \mu \left(\frac{\partial u}{\partial y} \right)^2 - \mu \frac{\partial^2}{\partial y^2} \left(\frac{u^2}{2} \right) = 0$$

In this equation the first term represents the convection of kinetic energy, the second term is the work performed by the pressure, the third term is the dissipation, and the fourth term is the diffusion by viscosity

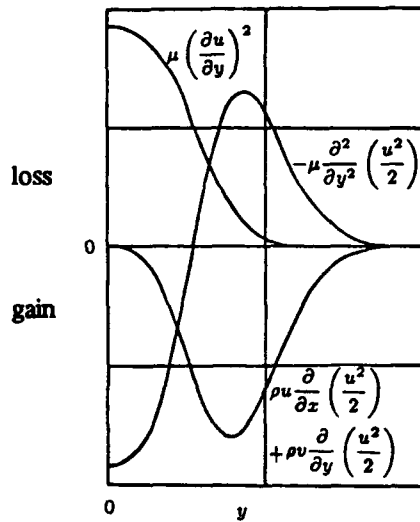


Figure 7: Balance of kinetic energy in flat plate boundary layer.

Figure 7 shows the balance of energy for the flat plate solution (Blasius solution [6]: $\beta = 0$). Conventionally, the losses of kinetic energy are represented with a positive sign. The integral of the diffusion term through the boundary layer thickness is zero; this term's contribution is to transfer energy (without destruction or creation) from the external part

of the boundary layer towards the wall. Near the wall, the kinetic energy is completely transformed into heat by dissipation. When there is a positive pressure gradient, its contribution is to decrease the kinetic energy, in particular near the wall and this favours the onset of separation.

4.6 Compressible boundary layers

Compressibility effects occur when the Mach number increases or when the differences of temperature in the flow are large. In the latter case, the thermodynamic properties of the fluid vary significantly and depend on the temperature distribution in the boundary layer. The momentum and energy equations are coupled. In transonic or low supersonic flow, the variations of temperature in the boundary layer are rather small if the wall is adiabatic. The effects on the velocity profiles are not very large (figure 8) but the stability properties of the laminar boundary layer are strongly affected by the value of the Mach number.

Figure 9 shows the general behaviour of temperature profiles in different circumstances. First, let us examine the case of an adiabatic wall. If the wall is not radiating this means that the wall heat flux is zero. The wall temperature is called the recovery temperature. The recovery factor is defined as:

$$r = \frac{T_{aw} - T_e}{T_{i_e} - T_e}$$

When the Prandtl number is equal to unity, a simple solution to the steady state energy equation is $h_i = cst = h_{i_e}$ (see equation 13) and the value of the recovery factor is 1. For air, the value of the Prandtl number is not unity and the recovery factor is slightly smaller than 1. For a flat plate flow, the recovery factor is given with a good accuracy by $r = \mathcal{P}^{1/2}$; for air flow, the value of the recovery factor is $r = 0.85$ ($\mathcal{P} = 0.725$).

For a non-zero wall heat flux, the wall is cold (hot) if the wall temperature is lower (greater) than the recovery temperature. For a steady flat plate flow, the energy equation has a simple solution when the Prandtl number is unity and the wall temperature is uniform. This is the *Crocco solution* which is a linear relationship between the total enthalpy and the velocity:

$$h_i = h_w + (h_{i_e} - h_w) \frac{u}{u_e}$$

For air, this solution is a rather good approximation. However, the shape of the relationship between the total enthalpy and the velocity is strongly affected by the pressure gradient. Figure 10 gives an idea of the effect of the pressure gradient on this relationship; these results have been obtained from the Cohen-Reshotko similarity solutions with a Prandtl number equal to unity [16].

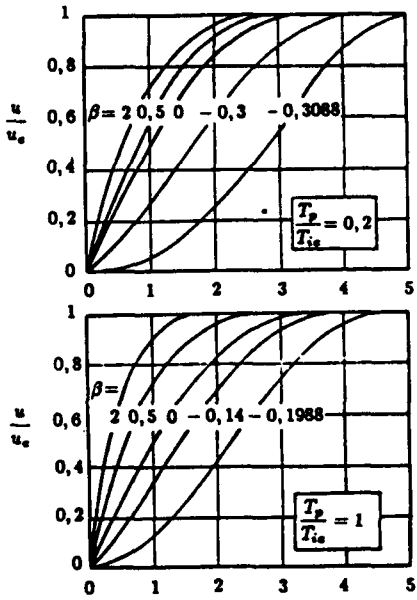


Figure 8: Compressible boundary layer with pressure gradient (from Cohen-Reshotko solutions [16]).

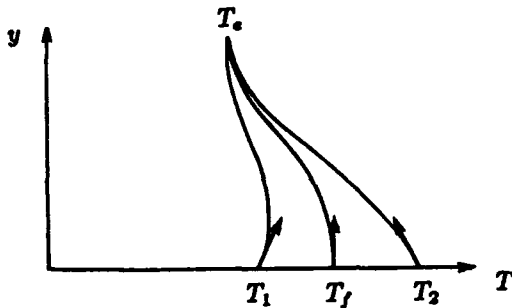


Figure 9: General behaviour of temperature profiles.
 $T = T_{aw}$: adiabatic wall.
 $T_1 > T_{aw}$: cold wall.
 $T_2 < T_{aw}$: hot wall.

4.7 Three-dimensional boundary layers

On a swept wing or on a fuselage, the boundary layer is no longer two-dimensional. In the boundary layer there is a *crossflow* which modifies considerably the stability properties of the boundary layer.

Let us consider an initially two-dimensional boundary layer which is influenced by the application of a crosswise pressure gradient (figure 11). In the outer inviscid flow, the streamlines bend in such a way that there is an equilibrium between the centrifugal force and the crosswise pressure force: the crosswise pressure force is directed towards the inner side of streamlines curvature. In the boundary layer the pressure derivative normal to the wall $\frac{\partial p}{\partial y}$ is zero and therefore the crosswise pressure force is constant within the boundary layer. Compared with the ex-

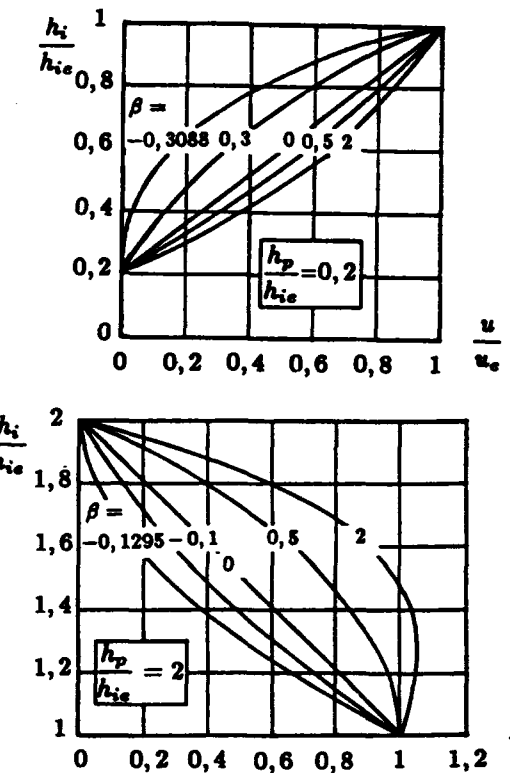


Figure 10: Enthalpy-velocity relationship in boundary layer with pressure gradient (from Cohen-Reshotko solutions [16]).

ternal flow the velocity is smaller in the boundary layer; therefore the inertia is smaller and the fluid particles tend to move towards the inner side of the curvature of the external streamlines. When the external streamlines have an inflection point, the crossflow reverses but reversal does not occur at the same time in the whole boundary layer. The crossflow reverses near the wall at first because the inertia is smaller in this region and S-shaped crossflow velocity profiles can be observed (figure 12).

For the study of transition on a swept wing, the flow near the leading edge is of special importance. On a swept leading edge (figure 13) there is no stagnation point and the inviscid velocity along the attachment line is non-zero. In incompressible flow, the laminar boundary layer equations for an infinite swept wing are:

$$\frac{\partial u}{\partial x} + \frac{\partial v}{\partial y} = 0 \quad (16a)$$

$$u \frac{\partial u}{\partial x} + v \frac{\partial u}{\partial y} = U_1 \frac{\partial U_1}{\partial x} + \nu \frac{\partial^2 u}{\partial y^2} \quad (16b)$$

$$u \frac{\partial w}{\partial x} + v \frac{\partial w}{\partial y} = \nu \frac{\partial^2 w}{\partial y^2} \quad (16c)$$

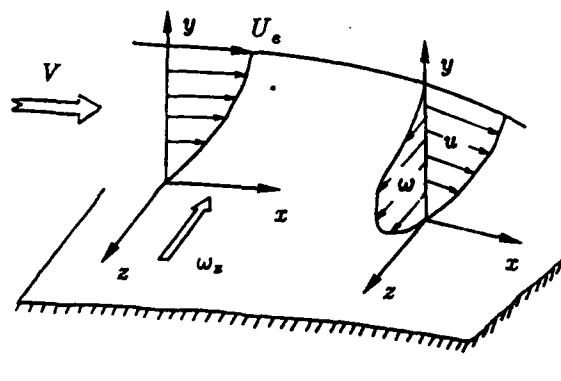


Figure 11: Crossflow in a three-dimensional boundary layer.

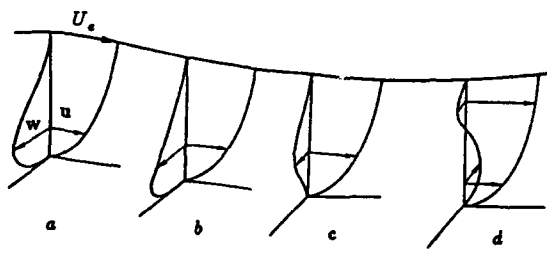


Figure 12: S-shaped crossflow velocity profiles.

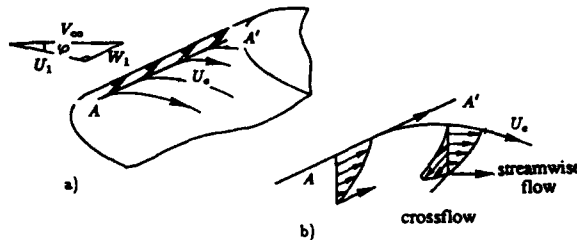


Figure 13: Flow near the attachment line of a swept leading edge.

In these equations, the coordinate z is normal to the leading edge and y is normal to the wall. The coordinate z does not appear in the equations because the hypothesis of infinite swept wing eliminates the dependence of any function with respect to the spanwise direction. The components of the inviscid flow velocity along x and z are U_1 and W_1 . Let us remind that W_1 is constant on an infinite swept wing.

Along the attachment line, the solution of the boundary layer equations is obtained under the form:

$$\frac{u}{U_1} = f'(\eta) ; \frac{w}{W_1} = g'(\eta)$$

with:

$$\eta = y \left(\frac{k}{\nu} \right)^{1/2} ; k = \left(\frac{dU_1}{dx} \right)_{z=0}$$

The boundary layer equations become:

$$\begin{aligned} f''' + ff'' + 1 - f'^2 &= 0 \\ g''' + fg'' &= 0 \end{aligned}$$

with:

$$f = \int_0^y f' d\eta$$

The solution of these equations gives the following results:

$$\begin{aligned} \frac{W_1 \delta_1}{\nu} &= 1.026 \bar{R} \\ \frac{W_1 \theta}{\nu} &= 0.404 \bar{R} \\ H &= \frac{\delta_1}{\theta} = 2.54 \end{aligned}$$

with

$$\bar{R} = \frac{W_1}{\nu} \left[\frac{\nu}{\left(\frac{dU_1}{dx} \right)_{z=0}} \right]^{1/2} \quad (17)$$

and:

$$\begin{aligned} \delta_1 &= \int_0^\infty \left(1 - \frac{w}{W_1} \right) dy \\ \theta &= \int_0^\infty \frac{w}{W_1} \left(1 - \frac{w}{W_1} \right) dy \end{aligned}$$

5 TURBULENT FLOWS

General descriptions of this field are given in textbooks [19], [30], [36], [43], [73], [74]. This section presents very briefly a few basic elements.

In nearly all practical cases, the laminar regime is not stable and the flow becomes turbulent. Turbulence is due to *non linearities* of the convection terms in the Navier-Stokes equations. In fully turbulent flow at large Reynolds number, the velocity fluctuations cover a large spectrum of wave numbers and of frequencies. A global picture of turbulence is given as follows. In a shear flow, there is an interaction

between turbulence and the mean flow. The latter generates large turbulent structures. If the Reynolds number of the mean flow is large the Reynolds number associated with the large structures is also large. A cascade process takes place in which smaller and smaller structures are created. A class of structures is fed by slightly larger structures. At the beginning of this process, the characteristic Reynolds number of the structures is large so that the process is practically non viscous. For small enough structures the characteristic Reynolds number is of order unity and all the energy is converted into heat by dissipation and no smaller structures can be formed. This means that the spectrum of energy is limited at high frequency (small wave number). *Dissipation* is an essential characteristic of turbulent flows. Here again we see that viscosity acts whatever the value of the Reynolds number is. At large Reynolds number, there is an *adaptation* of the flow which leads to a range of turbulent structures in such a way that viscosity is effective in dissipating energy at the scale of the smaller structures.

If the Reynolds number is not too large, the range of wave numbers involved in the turbulent fluctuations is also not too large and *direct numerical simulations* are possible. These calculations consist of solving numerically the three-dimensional unsteady Navier-Stokes equations. No other modelling than the expression of the viscous shear stress (and the heat flux) is introduced in the equations. These simulations are not free of numerical difficulties but they provide very useful information on turbulence. For example, the instantaneous pressure field which is practically impossible to obtain experimentally can be obtained with these simulations. They help us better understand turbulence and provide us with results which can be used to improve the turbulence models necessary to solve the Reynolds equations (averaged Navier-Stokes equations). The direct numerical simulations are also very useful for the understanding of the laminar-turbulent transition mechanisms. If the Reynolds number is very large, direct numerical simulations are no longer possible because the range of wave numbers increases and the size of memory needed to solve the equations becomes prohibitively large. To overcome this difficulty, *large eddy simulation* techniques are employed. The idea is to filter (with a low-pass filter) the turbulent field and the Navier-Stokes equations. The larger structures are calculated with the filtered equations (which are unsteady and three-dimensional) and the interaction between the filtered and non-filtered fields is modelled; the underlying assumption is that if the cut-off is at a sufficiently high wave number the behaviour of the interaction is universal in the sense that it is not influenced by conditions of development of the flow. The large eddy simulations are also very useful to better understand turbulence. However, they are also restricted in Reynolds numbers because of the limited capacity

of computers. For practical calculations (engineering calculations), a more drastic operation is performed. The flow is decomposed into a statistical averaged component and a turbulent part. The same operation is performed on the Navier-Stokes equations to obtain the *Reynolds equations*.

5.1 Effects of turbulence

The practical effects of turbulence are most often analyzed by defining a mean flow. Any instantaneous quantity is decomposed as:

$$f = F + f'$$

where F is the statistical average of f and f' is the turbulent fluctuation the mean value of which is zero.

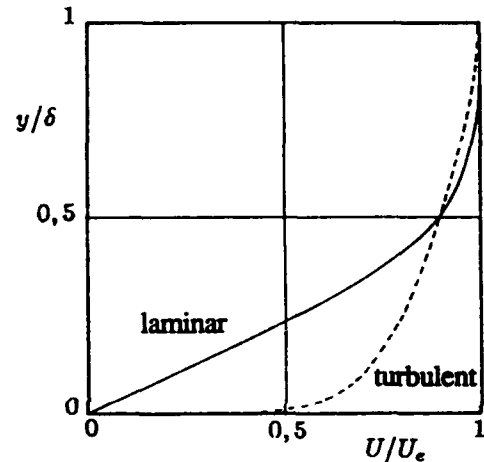


Figure 14: Velocity profiles in laminar and turbulent flat plate boundary layers.

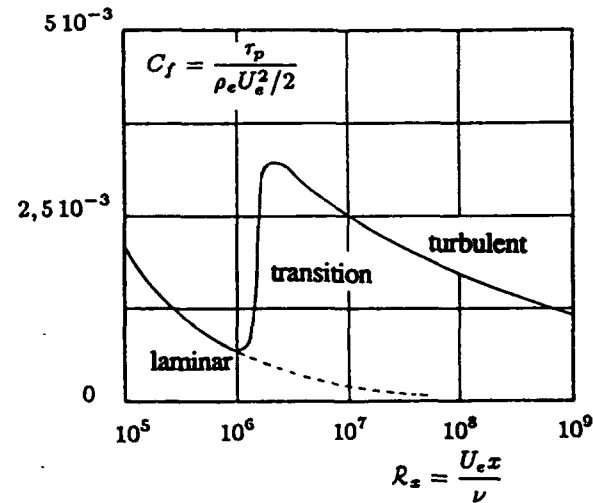


Figure 15: Evolution of skin-friction along a flat plate.

One of the most obvious effects of turbulence is to improve the mixing in the flow. This means that dis-

tant parts of the flow with very different properties (velocity, temperature) are brought closer together because of the turbulent motion of the flow. On the average, the flow is therefore more uniform in a turbulent regime than in laminar regime; in laminar flow the uniformization of the flow is performed only through diffusion by viscosity which is a very slow process. Figure 14 shows the comparison of the velocity profiles in laminar and in turbulent flat plate boundary layers. In the core of the flow, the differences of velocity are much smaller in the turbulent case as explained above. A consequence is that the slope at the wall is larger in turbulent flow (the no slip condition at the wall holds in turbulent flow). *The skin friction is therefore much higher in the turbulent boundary layer.* A typical example is shown on figure 15 with the evolution of the skin friction coefficient along a flat plate as a function of the Reynolds number based on the distance from the leading edge. In laminar flow, the skin friction decreases according to the Blasius law. Through the transition region there is a strong increase of C_f , and in the turbulent region the skin friction coefficient decreases slowly (compared to the laminar case). Such a result is qualitatively the same for an airfoil. The skin friction drag of an airfoil being a very significant part of the total drag it is obviously very profitable to delay transition in order to reduce the drag. Several means are discussed in this lecture Series (airfoil shaping, wall suction, etc...).

In the turbulent boundary layer, the kinetic energy is much higher than in the laminar boundary layer. Thus, *the turbulent boundary layer sustains larger adverse pressure gradient without separation.* On an airfoil, rather large positive pressure gradients are needed to create the lift but separation is generally not desired because the drag increases and the lift decreases as a result; in addition, separation is a source of unsteadiness.

The results described above on the effects of turbulence on the drag of the flat plate have to be interpreted with care because their extension to any type of body is not straightforward. Let us consider the evolution of the drag of the circular cylinder as a function of the Reynolds number (figure 16). This evolution is strongly related to the modification of the flow structure when the Reynolds number changes. It is an illustration of the adaptation of the flow in order that viscosity plays its role. At very low Reynolds number (10^{-2}), the flow, called a creeping flow, is symmetrical without separation. At a Reynolds number of order 20, the flow is laminar and steady but a symmetrical separation is present. At a higher Reynolds number (100), the flow is still laminar but no longer steady. The wake is unstable and vortices are formed: the so-called Kármán street is observed. Increasing again the Reynolds number (10^4), the wake becomes turbulent while the boundary layer stays laminar, and separation occurs in the laminar flow regime: this is the subcritical regime.

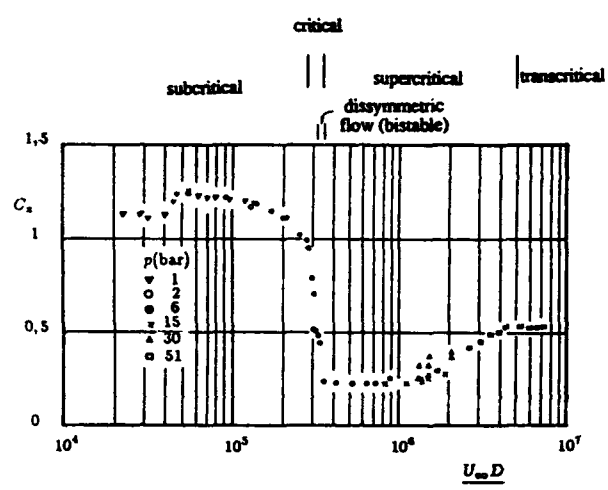


Figure 16: Drag coefficient of a circular cylinder (from Schewe [65]).

$C_d = T / (\frac{1}{2} \rho_\infty U_\infty^2 D)$; T =Drag force per span unit; D =cylinder diameter.

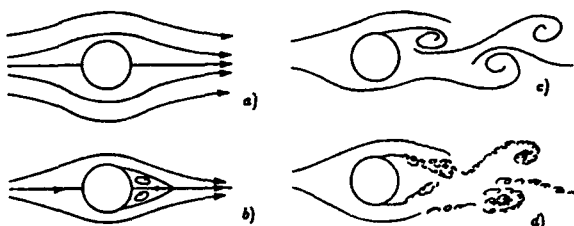


Figure 17: Flow around a circular cylinder.
a) $\mathcal{R}_D = 10^{-2}$ b) $\mathcal{R}_D = 20$ c) $\mathcal{R}_D = 100$ d) $\mathcal{R}_D = 10^4$

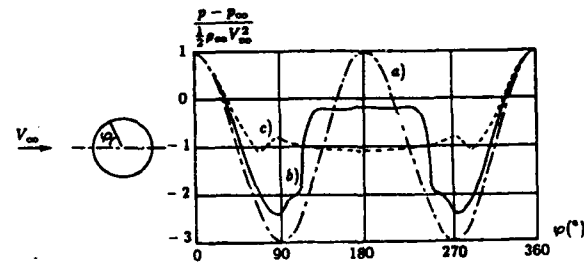


Figure 18: Pressure distribution on a circular cylinder. a) inviscid flow b) supercritical regime c) subcritical regime

In the critical regime, there is a strong decrease of the drag caused by a change of the flow structure. In the supercritical regime, separation occurs in the turbulent flow region and hence later than in the subcritical regime. For the inviscid outer flow the shape of the equivalent body is modified and the pressure distribution is also modified (figures 17 and 18). For a circular cylinder which is a very thick body, the pressure drag represents a much larger percentage of the total drag than for an airfoil. The decrease of the drag in the critical regime is due to the variation of the pressure drag. Here it appears that the laminar-turbulent transition decreases the drag by delaying the separation. At higher Reynolds numbers in the supercritical regime, the drag starts increasing again because transition occurs earlier on the cylinder and consequently the skin friction drag increases. In the transcritical regime, the movement of transition towards the leading edge is not very large and the drag decreases slowly due to the Reynolds number effect. As in the case of the flat plate, the skin friction coefficient in turbulent flow decreases when the Reynolds number increases.

Turbulent flows have other very important properties. The turbulent fluctuations are three-dimensional. A two-dimensional turbulent flow signifies that the mean flow is two-dimensional but the velocity fluctuations are three-dimensional. Sometimes turbulence is studied in two dimensions but the properties are very different from three-dimensional turbulence. The *Navier-Stokes equations are valid for describing all the scales of the turbulent motion*. Indeed even the length scale of the smallest structures and the associated characteristic time are very different from the molecular scales so that the turbulent field appears as a continuum. *Vorticity and dissipation* are also very important features of turbulent flows [73]. The dynamics of vorticity plays an essential role in the cascade process by which smaller and smaller structures are created and dissipation (which is related to small scale vorticity) is the final result of the action of viscosity. Another feature of turbulent flows is their *unpredictable character* [43]. This means that if a small perturbation is introduced somewhere in the flow the whole field is affected after a certain time. It should be noticed that this feature does not prevent us from trying to calculate a particular realization of a turbulent flow and from defining a mean flow which has a statistical meaning.

5.2 Reynolds average equations

In incompressible flow, any instantaneous quantity is decomposed in a mean value and a turbulent fluctuation. A statistical average is used to define the mean values:

$$u_i = \langle u_i \rangle + u'_i$$

$$p = \langle p \rangle + p'$$

From this definition the mean value of a fluctuation is zero:

$$\langle u'_i \rangle = 0$$

$$\langle p' \rangle = 0$$

The usual properties of random variables hold:

$$\langle a + b \rangle = \langle a \rangle + \langle b \rangle$$

$$\langle \langle a \rangle b \rangle = \langle a \rangle \langle b \rangle$$

$$\langle \frac{\partial a}{\partial t} \rangle = \frac{\partial \langle a \rangle}{\partial t}$$

$$\langle \frac{\partial a}{\partial x_i} \rangle = \frac{\partial \langle a \rangle}{\partial x_i}$$

$$\langle \int a dx_i dt \rangle = \int \langle a \rangle dx_i dt$$

The equations for the mean flow are obtained by taking the statistical average of the continuity equation and of the Navier-Stokes equations. In incompressible flow, the Reynolds equations are:

$$\frac{\partial U_i}{\partial x_i} = 0 \quad (18)$$

$$\rho \frac{DU_i}{Dt} = - \frac{\partial P}{\partial x_i} + \frac{\partial}{\partial x_j} \left(2\mu S_{ij} - \rho \langle u'_i u'_j \rangle \right) \quad (19)$$

with

$$\frac{D \bullet}{Dt} = \rho \frac{\partial \bullet}{\partial t} + \rho U_j \frac{\partial \bullet}{\partial x_j}$$

$$S_{ij} = \frac{1}{2} \left(\frac{\partial U_i}{\partial x_j} + \frac{\partial U_j}{\partial x_i} \right)$$

In the above equations the symbol $\langle \bullet \rangle$ has been omitted when no confusion is possible and capital letters are used to note an average quantity:

$$U_i = \langle u_i \rangle$$

$$P = \langle p \rangle$$

The system of mean flow equations (18) and (19) is not closed: there are more unknowns than equations. The main variables are the velocity components U_i and the pressure P but the momentum equations contain additional unknowns: the velocity correlations $-\rho \langle u'_i u'_j \rangle$ which are called the *Reynolds stresses*. There are six additional unknowns because the correlations form a symmetrical tensor: $\langle u'_i u'_j \rangle = \langle u'_j u'_i \rangle$. The equations and hypotheses developed to close the Reynolds equations system are called the *closure assumptions*.

The origin of the Reynolds stresses lies in the non linearity of the convection terms of the momentum equations. The instantaneous momentum equation can be written under the vectorial form:

$$\int_D \rho \frac{\partial \vec{v}}{\partial t} d\tau + \int_S \rho \vec{v} (\vec{v} \vec{n}) d\sigma = \int_S \vec{t} d\sigma \quad (20)$$

where the components of the vector \vec{t} are:

$$t_i = (-p \delta_{i\ell} + 2\mu s_{i\ell}) n_\ell$$

$$s_{i\ell} = \frac{1}{2} \left(\frac{\partial u_i}{\partial x_\ell} + \frac{\partial u_\ell}{\partial x_i} \right)$$

and n_ℓ are the components of the outer normal \vec{n} to the surface S bounding the volume \mathcal{D} .

Taking the average of (20) we get:

$$\int_{\mathcal{D}} \rho \frac{\partial \bar{V}}{\partial t} d\tau + \int_S \rho \bar{V} (\bar{V} \vec{n}) d\sigma + \int_S \rho \bar{v}^i (\bar{v}^i \vec{n}) d\sigma = \int_S \bar{T} d\sigma \quad (21)$$

The i -component of the turbulent term in equation (21) is:

$$\int_S \rho \langle u_i' u_i' \rangle n_\ell d\sigma$$

This expression shows that the Reynolds stresses are due to fluctuations of the flux of momentum. The Reynolds stresses can be grouped with the right member of equation (21) where it is associated with the viscous stresses as this is done in equation (19). From the momentum theorem, the Reynolds stresses are interpreted as apparent turbulent stresses having the same modulus but the opposite direction as the flux of momentum. The analogy between the viscous and turbulent stresses is unfortunate because *viscosity is a property of the fluid whereas turbulence is a property of the flow*. Viscosity exists even if the fluid is at rest whereas turbulence disappears when there is no velocity gradient in the flow. This does not mean that the turbulent motion is independent of viscosity since the viscous dissipation is an essential feature of turbulent flow.

5.3 Kinetic energy equations

The mean value of the kinetic energy of the instantaneous flow is decomposed into the kinetic energy K of the mean flow and the kinetic energy k of the turbulent motion:

$$\frac{\langle u_i' u_i' \rangle}{2} = K + k$$

with:

$$K = \frac{U_i U_i}{2}$$

$$k = \langle \frac{u_i' u_i'}{2} \rangle$$

The mean kinetic energy equation is obtained by multiplying equation (19) by U_i :

$$\rho \frac{DK}{Dt} = -T_{i\ell} S_{i\ell} + \frac{\partial T_{i\ell} U_i}{\partial x_\ell} \quad (22)$$

where $T_{i\ell}$ represents the total stress composed of the pressure, the viscous stress and the turbulent stress:

$$T_{i\ell} = -P \delta_{i\ell} + 2\mu S_{i\ell} - \rho \langle u_i' u_\ell' \rangle$$

In equation (22) the first term on the right hand side is the deformation work of the total stress which is made of three terms:

1. The pressure work $P \delta_{i\ell} S_{i\ell} = P S_{ii}$ which is zero in incompressible flow because of the continuity equation.

2. The work of the viscous stresses: $-2\mu S_{i\ell} S_{i\ell}$. This term is always negative and represents the viscous dissipation of the mean kinetic energy.

3. The work of the turbulent shear stress: $\rho \langle u_i' u_\ell' \rangle S_{i\ell}$. It will be seen that this term represents an exchange of kinetic energy between the mean motion and the turbulent motion.

The second term on the right hand side of equation (22) is a diffusion term. When integrated over a volume \mathcal{D} , we obtain the flux of $T_{i\ell} U_i$ through the surface S bounding \mathcal{D} :

$$\int_{\mathcal{D}} \frac{\partial T_{i\ell} U_i}{\partial x_\ell} d\tau = \int_S T_{i\ell} U_i n_\ell d\sigma$$

The quantity $T_{i\ell} U_i$ is either constant or zero if the bounding surface is at infinity or a wall. Generally, the contribution of the diffusion term is to move energy from one place to another in the volume without creating or destroying energy.

The equation for the turbulent energy k is obtained from the difference between the equation for $\langle u_i' u_i' \rangle / 2$ and equation (22) :

$$\rho \frac{Dk}{Dt} = -\rho \langle u_i' u_\ell' \rangle S_{i\ell} - 2\mu \langle s'_{i\ell} s'_{i\ell} \rangle + \frac{\partial \Gamma_\ell}{\partial x_\ell} \quad (23)$$

where $s'_{i\ell}$ represents the fluctuation of the rate of strain tensor:

$$s'_{i\ell} = \frac{1}{2} \left(\frac{\partial u_i'}{\partial x_\ell} + \frac{\partial u_\ell'}{\partial x_i} \right)$$

The flux of diffusion Γ_ℓ contains contributions from viscosity and from the fluctuations of pressure and velocity:

$$\Gamma_\ell = -\langle p' u_\ell' \rangle + 2\mu \langle u_i' s'_{i\ell} \rangle - \rho \frac{\langle u_i' u_\ell' u_\ell' \rangle}{2}$$

By comparing equations (22) and (23) for K and k , we find that the term $-\rho \langle u_i' u_\ell' \rangle S_{i\ell}$ is in both equations but with an opposite sign: the deformation work of the Reynolds stresses represents an exchange of energy between the mean and turbulent motions. Generally, energy is taken from the mean flow to feed the turbulent flow ($-\rho \langle u_i' u_\ell' \rangle S_{i\ell} > 0$). However there can be particular regions where the turbulent flow feeds back the mean flow.

In equation (23) the term:

$$\rho \epsilon = 2\mu \langle s'_{i\ell} s'_{i\ell} \rangle$$

represents the dissipation of turbulent kinetic energy due to the work of the fluctuations of the viscous stresses.

5.4 Reynolds stress equations

The Reynolds stress equations are obtained from the Navier-Stokes equations. First the u'_i -equation is formed by subtracting the average momentum equation from the instantaneous momentum equation; the u'_i -equation is multiplied by u'_j ; a similar equation is obtained by multiplying the u'_j -equation by u'_i ; the sum of the two equations is an equation for $u'_i u'_j$; this equation is averaged to get the $\langle u'_i u'_j \rangle$ -equation:

$$\frac{D \langle u'_i u'_j \rangle}{Dt} = P_{ij} - D_{ij} + \Phi_{ij} + \frac{\partial J_{ij\ell}}{\partial x_\ell} \quad (24)$$

with:

$$P_{ij} = - \left(\langle u'_i u'_\ell \rangle \frac{\partial U_j}{\partial x_\ell} + \langle u'_j u'_\ell \rangle \frac{\partial U_i}{\partial x_\ell} \right)$$

$$D_{ij} = 2\nu \left\langle \frac{\partial u'_i}{\partial x_\ell} \frac{\partial u'_j}{\partial x_\ell} \right\rangle$$

$$\Phi_{ij} = \left\langle \frac{p'}{\rho} \left(\frac{\partial u'_i}{\partial x_j} + \frac{\partial u'_j}{\partial x_i} \right) \right\rangle$$

$$J_{ij\ell} = - \langle u'_i u'_j u'_\ell \rangle - \left\langle \frac{p'}{\rho} (u'_i \delta_{j\ell} + u'_j \delta_{i\ell}) \right\rangle + \nu \frac{\partial \langle u'_i u'_j \rangle}{\partial x_\ell}$$

The meaning of the various terms of the Reynolds stress equations is:

- P_{ij} contain products of Reynolds stresses with velocity gradient components, but it is not exactly a work of Reynolds stresses as in the kinetic energy equation.
- D_{ij} is a destruction term due to the action of viscosity.
- The pressure-velocity correlation Φ_{ij} has no equivalent in the kinetic energy equation because its contraction is zero due to the continuity equation. The contribution of this term is an exchange between $\langle u'^2 \rangle$, $\langle v'^2 \rangle$, $\langle w'^2 \rangle$ without modifying their sum. This term is called redistribution term.
- $J_{ij\ell}$ represents a flux of diffusion due to viscosity and to the fluctuations of velocity and pressure.

5.5 Notion of scales

Viscous scales have already been introduced. Let us recall that the viscous time t_V is the time needed for viscosity to transport information by diffusion over a certain distance d :

$$t_V = d^2 / \nu$$

A convection time scale t_C is also defined as the time needed to transport information over a distance D with a characteristic velocity V :

$$t_C = D / V$$

In turbulent flows two classes of structures play an important role: the energetic structures and the dissipative structures. They are characterized by length, velocity and time scales:

- energetic structures: ℓ, u, θ
- dissipative structures: η, v, τ .



Figure 19: Turbulence in the sky in Toulouse.

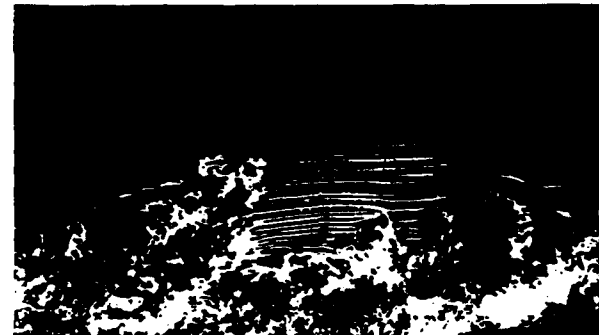


Figure 20: Boundary layer visualization from Corke, Guézennec and Nagib [17].

An appreciation of the length scale of large structures is given by the observation of the smoke issuing from the mouth of a chimney or by any smoke visualization of turbulent flows (figures 19 and 20).

A more precise definition can be obtained from the measurement of the energy spectrum of velocity fluctuations or from two-point correlations. The velocities are measured at the same time but at two different points A and B :

$$\bar{r}_{ij} = \frac{\langle (u'_i)_A (u'_j)_B \rangle}{(\langle u'^2 \rangle_A \langle u'^2 \rangle_B)^{1/2}}$$

where A and B are the two measurement points.

Such measurements show that the correlation extends over a finite length (figure 21). The turbulent

der of magnitude the dimensional analysis gives:

$$\varepsilon = \frac{u^3}{\ell} \quad (26)$$

In an equivalent manner this hypothesis can be interpreted as a unique time scale hypothesis which says that the characteristic time of dissipation t_D is of the same order as the characteristic time of large structures. The time needed to dissipate an amount u^2 of kinetic energy is:

$$t_D = \frac{u^2}{\varepsilon}$$

Equating this characteristic time to the large scale time θ gives the relationship (26).

This hypothesis is supported by experimental results. A first result is given by the flow in a tube with a rough wall. Experiments show that the pressure drop coefficient is independent of the Reynolds number. Now the pressure drop coefficient is directly proportional to the mean value of dissipation (the mean value is taken here on a cross section). This leads to a paradox because the dissipation is independent of the Reynolds number and it must be kept in mind that dissipation is due to viscosity. The paradox is solved by saying that the dissipation rate is nearly equal to the transfer of energy from the large structures to the dissipative structures and the transfer of energy is mainly governed by the characteristics of large structures which are non viscous. The dimensional analysis gives relationship (26). Another result is the approximate balance of turbulent kinetic energy in a turbulent boundary layer:

$$-(u'v') \frac{\partial U}{\partial y} = \varepsilon$$

It is further assumed that the exchange of energy between the mean flow and the turbulent flow is possible only if their time scale have the same order of magnitude:

$$\frac{\partial U}{\partial y} = \frac{u}{\ell}$$

In addition the experimental results show that the correlation between u' and v' is good. Thus we have $-(u'v') = u^2$. The combination of these results gives equation (26).

The relationship between the large and small scales is obtained by using equation (26) in formulae (25). We obtain:

$$\frac{\eta}{\ell} = R_\ell^{-3/4}; \frac{u}{\ell} = R_\ell^{-1/4}; \frac{\tau}{\theta} = R_\ell^{-1/2} \quad (27)$$

where R_ℓ is the characteristic Reynolds number of large structures:

$$R_\ell = \frac{u\ell}{\nu}$$

The above relationship shows that the gap between the large and small structures increases as the Reynolds number increases. When the Reynolds

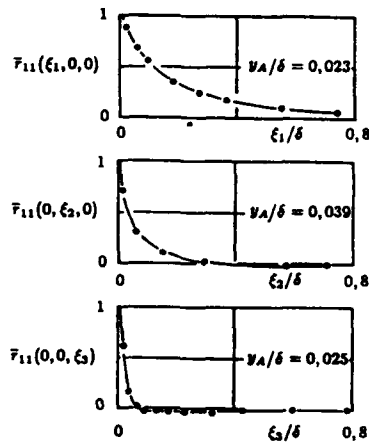


Figure 21: Spatial correlations in two points in a boundary layer (from Grant [33]).

motion is organized although the velocity signal at a given point has an apparent random behaviour. An integral scale in the x_1 -direction is defined as:

$$\Lambda_1 = \int_0^\infty r_{11}(\xi_1, 0, 0) d\xi_1$$

A velocity scale of energetic structures is easier to define. The scale u can be taken as the square root of the kinetic energy.

A turbulent time scale can be defined from the measurement of a frequency spectrum of energy (the characteristic time corresponds for example to the peak of spectral density) or from the measurement of a time correlation.

The scales of length, velocity and time are related by: $\theta = \ell / u$.

The dissipative scales are evaluated by using the rate of dissipation ε . The characteristic Reynolds number of these structures is of order unity since viscosity is effective in dissipating energy at their scale. From this we obtain the Kolmogorov scales of dissipative structures:

$$\tau = \left(\frac{\nu}{\varepsilon} \right)^{1/2}; u = (\nu \varepsilon)^{1/4}; \eta = \frac{\nu^{3/4}}{\varepsilon^{1/4}} \quad (25)$$

A relationship between the large scales and the small scales is obtained by assuming that the rate of dissipation is entirely determined by the characteristics of the large structures. This hypothesis is based on the idea that the rate of dissipation is nearly equal to the flux of energy from the large to the small structures. Now this flux is due to a non viscous process—the vortex stretching—which takes place at a range of scales characterized by a large Reynolds number. Therefore it seems reasonable to assume that the rate of dissipation depends on large scales. In terms of or-

number is large, the small structures are independent of the large structures; they have a universal behaviour. An example of application of this result is given in figure 22. The spectra of energy made dimensionless with the Kolmogorov scales are independent of the Reynolds number in the range of high wave numbers. In figure (22), the Reynolds number \mathcal{R}_λ is formed with the Taylor microscale λ defined for an isotropic turbulence as:

$$\epsilon = 15\nu \frac{\langle u'^2 \rangle}{\lambda^2}$$

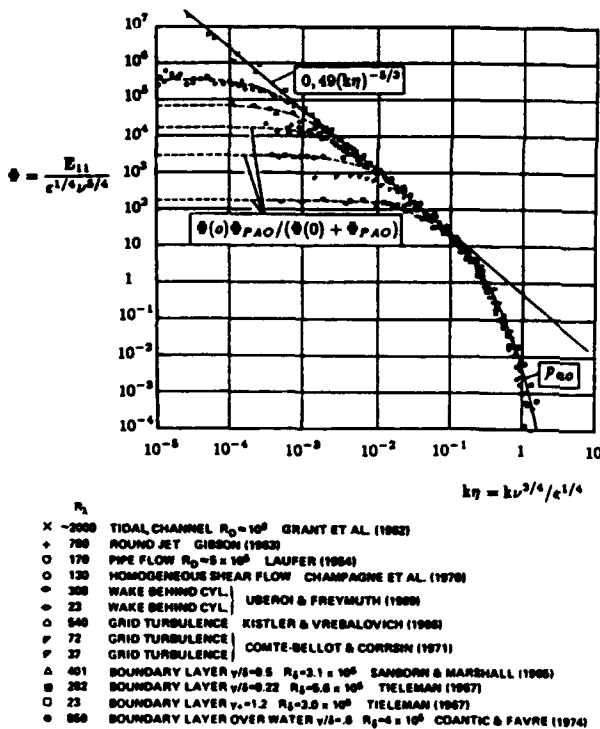


Figure 22: Spectral energy density of longitudinal velocity in Kolmogorov scales (from Chapman [13])

The independency of small structures is also used in large eddy simulation methods to assume that the interaction between filtered and unfiltered fields is universal.

These ideas also lead to the hypothesis of local isotropy of small structures. This hypothesis is very often used to model the destruction term in the Reynolds equation as an isotropic tensor since the responsible structures belong to the dissipative range:

$$D_{ij} = 2\nu \left\langle \frac{\partial u'_i}{\partial x_\ell} \frac{\partial u'_j}{\partial x_\ell} \right\rangle = A \delta_{ij} \quad (28)$$

Now we have:

$$\epsilon' = \nu \left\langle \frac{\partial u'_i}{\partial x_\ell} \frac{\partial u'_i}{\partial x_\ell} \right\rangle = \epsilon - \nu \frac{\partial^2 \langle u'_i u'_\ell \rangle}{\partial x_i \partial x_\ell}$$

At large Reynolds number it is shown that the difference between ϵ' and ϵ is negligible. Then by contraction of equation (28) we obtain:

$$A = \frac{2}{3} \epsilon$$

and:

$$D_{ij} = \frac{2}{3} \epsilon \delta_{ij} \quad (29)$$

6 TURBULENT BOUNDARY LAYERS

Details on turbulent boundary layers can be found in references [12], [19], [30], [66].

6.1 Boundary layer equations

In incompressible flow, statistical averages are used to define mean quantities. In compressible flow there are many other possible choices. Very often mass weighted averages (Favre averages [30]) are used. All the flow characteristics but the pressure and the density are averaged using the mass weighted averages. Using a tilde ($\tilde{\cdot}$) for the mean values we have:

$$\begin{aligned} \tilde{\rho} &= \langle \rho \rangle \\ \tilde{\rho} &= \langle \rho \rangle \\ \tilde{u}_i &= \langle \rho u_i \rangle / \langle \rho \rangle \\ \tilde{T}_i &= \langle \rho T \rangle / \langle \rho \rangle \\ \text{etc} \dots \end{aligned}$$

However, for not very large Mach numbers ($M_\infty < 5$), a first approximation is to make no difference between statistical averages and mass weighted averages. This assumption will be used here.

In a two-dimensional flow, the boundary layer hypotheses lead to the following set of equations:

$$\frac{\partial \rho}{\partial t} + \frac{\partial \rho U}{\partial x} + \frac{\partial \rho V}{\partial y} = 0 \quad (30a)$$

$$\rho \frac{\partial U}{\partial t} + \rho U \frac{\partial U}{\partial x} + \rho V \frac{\partial U}{\partial y} = - \frac{\partial P}{\partial x} + \frac{\partial \tau}{\partial y} \quad (30b)$$

$$\frac{\partial P}{\partial y} = 0 \quad (30c)$$

$$\rho \frac{\partial h_i}{\partial t} + \rho U \frac{\partial h_i}{\partial x} + \rho V \frac{\partial h_i}{\partial y} = \frac{\partial P}{\partial t} + \frac{\partial}{\partial y} (U \tau - \phi) \quad (30d)$$

with:

$$\tau = \mu \frac{\partial U}{\partial y} - \rho \langle u' v' \rangle$$

$$\phi = -\lambda \frac{\partial T}{\partial y} + \rho \langle v' h' \rangle$$

These equations are completed with the state law:

$$P = \rho R T$$

In the above equations the mean value sign has been omitted when no confusion is possible.

Formally, equations (30a) to (30d) are the same as in laminar flow. Obviously the expressions of the total stress and of the total heat flux are not the same since they include the turbulent contribution. However, the boundary conditions are the same and the global boundary layer equations are also the same.

The wall shear stress and the wall heat flux are defined by the same expressions as in laminar flow:

$$\tau_w = \left(\mu \frac{\partial U}{\partial y} \right)_{y=0}$$

$$\phi_w = \left(-\lambda \frac{\partial T}{\partial y} \right)_{y=0}$$

6.2 Experimental results

Measurements of shear stress and normal stresses in a turbulent flat plate boundary layer are presented in figures 23 and 24. The reference velocity in the dimensionless normal stresses is the external velocity and the level of turbulence is about 5 to 10%. In fact, the local turbulence level near the wall is higher; if the normal stresses are reduced by the local velocity the turbulence level near the wall is of order 20 to 30%.

Figure 23 shows that the turbulent shear stress is much higher than the viscous stress in a large part of the boundary layer, where the flow is fully turbulent. Near the wall, the turbulent shear stress decreases simply because the wall imposes the no slip condition (which applies even to the instantaneous velocity). In addition the turbulence Reynolds number is low near the wall and the turbulence properties are probably affected. Even very close to the wall the velocity fluctuations are not small; at the wall itself the turbulence level $(u'^2)^{1/2}/U$ is in the order of 30%. Thus near the wall the flow is not laminar even if the viscous stress is higher than the turbulent stress.

Figure 25 gives the ratio $-(u'v')/k$ (k is the turbulent kinetic energy) measured in boundary layers with and without pressure gradient. In a large part of the boundary layer this ratio is nearly constant and around 0.3. This result is often used implicitly or explicitly in turbulence modelling.

The turbulent boundary layer is further analyzed with the equations of kinetic energy for the mean flow and the turbulent flow. In steady flow, the mean flow energy equation is:

$$\underbrace{\rho U \frac{\partial K}{\partial x} + \rho V \frac{\partial K}{\partial y}}_A - \underbrace{\rho (u'v') \frac{\partial U}{\partial y}}_B + \underbrace{\mu \left(\frac{\partial U}{\partial y} \right)^2}_C$$

$$+ \underbrace{\frac{\partial}{\partial y} (\rho (u'v') U)}_D - \underbrace{\frac{\partial}{\partial y} \left(\mu \frac{\partial K}{\partial y} \right)}_E + \underbrace{U \frac{dP}{dx}}_F = 0$$

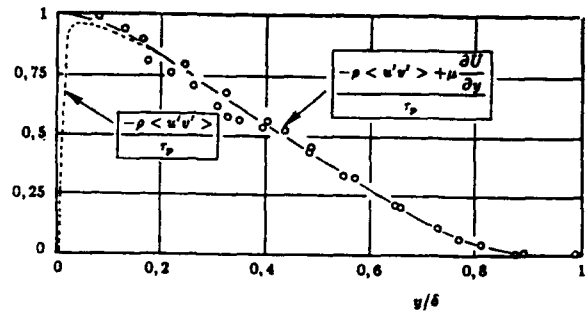


Figure 23: Shear stress in a turbulent boundary layer (from Favre and Gaviglio [28]).

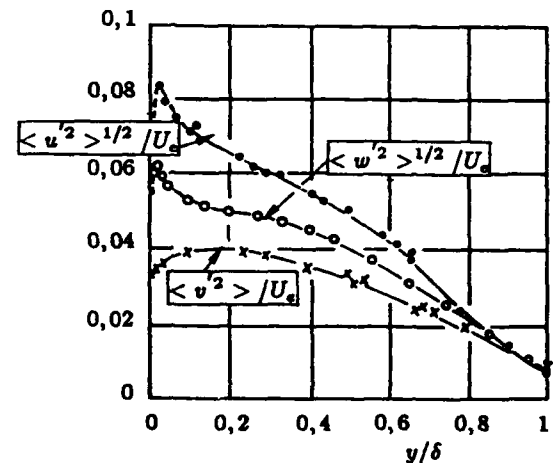


Figure 24: Reynolds stresses in a turbulent boundary layer (from Klebanoff [38]).

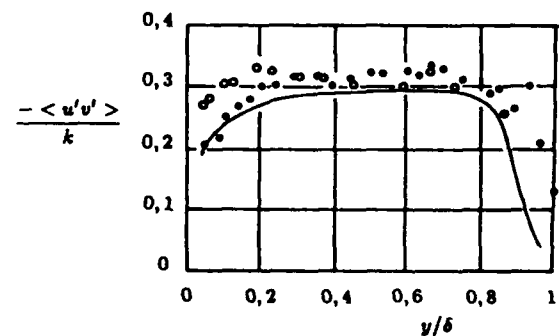


Figure 25: Ratio $-(u'v')/k$.
— Flat plate (Klebanoff [38])
○ boundary layer with moderate positive pressure gradient ($H=1.59$) [4]
● boundary layer with strong adverse pressure gradient ($H=2.13$) [4]

In this equation all the terms have been brought together in the same member and are given in figure 26 for a flat plate boundary layer. Conventionally, an energy loss is represented as a positive quantity. Let us recall the meaning of the various terms:

- Term *A* is due to convection. Integrated over a fixed volume this term represents the outflux through the bounding surface.
- Terms *B* and *C* are the deformation work of the turbulent shear stress and of the viscous stress. Term *B* also represents an exchange of energy between the mean flow and the turbulent flow.
- Terms *D* and *E* are diffusion terms due to turbulence and viscosity.
- Term *F* is the work of pressure. This term is zero for a flat plate flow.

As $\langle u'v' \rangle$ is negative in the boundary layer, term *B* represents a loss of mean kinetic energy which is used to feed the turbulent motion. This is not always the case. For example, in a boundary layer perturbed by a wall jet parallel to the wall, there is a maximum velocity in the boundary layer but there is no reason for the turbulent shear stress to be zero at the same point. There is therefore a small region where turbulence feeds energy back to the mean flow.

Term *C*—viscous dissipation—is significant only near the wall. Figure 27 gives a more detailed view of the balance of energy very close to the wall. At the wall itself, there is a strict equilibrium between the viscous dissipation and the viscous diffusion.

The diffusion terms (*D* and *E*) have a null global contribution because their integral through the boundary layer thickness is zero. These terms contribute to transfer energy from one place to another without creation or destruction. The experimental results show that the turbulent diffusion tends to transport energy from a high energy region towards a low energy region leading to the same global result as viscous effects but in a much more efficient manner.

Using the boundary layer hypotheses the turbulent kinetic energy equation reads:

$$\underbrace{\rho U \frac{\partial k}{\partial x} + \rho V \frac{\partial k}{\partial y}}_a + \underbrace{\rho \langle u'v' \rangle \frac{\partial U}{\partial y}}_b + \underbrace{\rho \epsilon'}_c - \underbrace{\frac{\partial}{\partial y} \left(-\rho \left\langle \frac{u'^2 + v'^2 + w'^2}{2} v' \right\rangle - \langle p'v' \rangle + \mu \frac{\partial k}{\partial y} \right)}_d = 0$$

In this equation ϵ' is defined as:

$$\epsilon' = \nu \left(\frac{\partial u'}{\partial x} \frac{\partial u'}{\partial x} \right)$$

At large Reynolds numbers, ϵ' is equivalent to the true dissipation and generally the distinction between ϵ' and ϵ is not made.

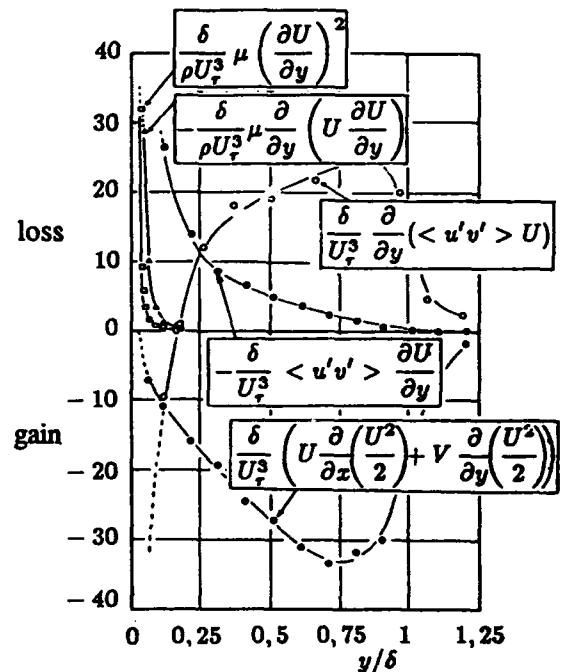


Figure 26: Balance of mean flow kinetic energy. Flat plate (from Favre and Gaviglio [28]).

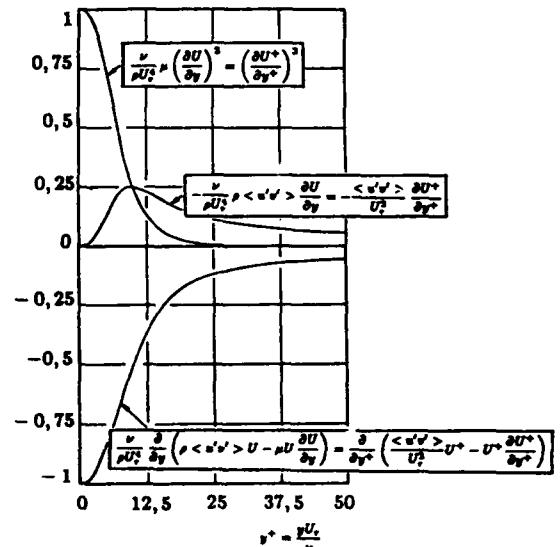


Figure 27: Balance of mean flow kinetic energy near the wall. Flat plate (from Favre and Gaviglio [28]).

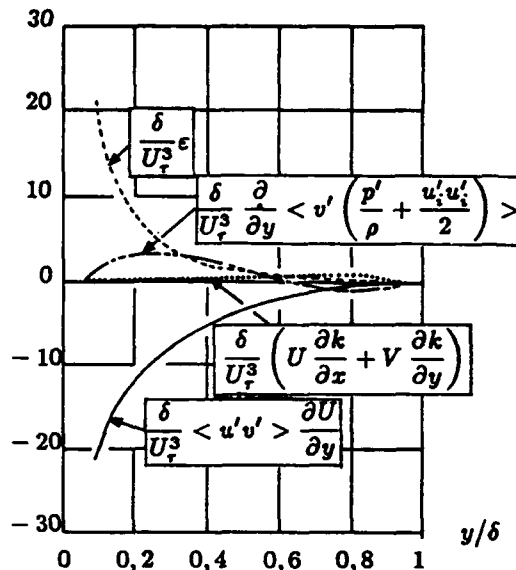


Figure 28: Balance of turbulent kinetic energy. Flat plate (from Townsend [74], measurements from Klebanoff).

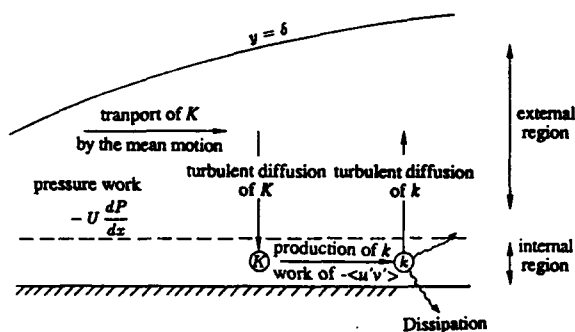


Figure 29: Exchanges of energy in a turbulent boundary layer.

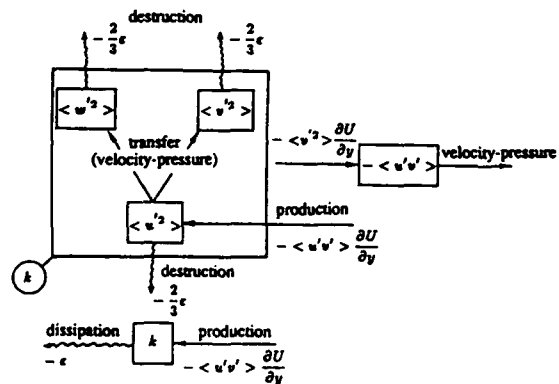


Figure 30: Interdependence of Reynolds stresses.

The meaning of the various terms of the k -equation is:

- Term a is the transport of turbulent kinetic energy by the mean flow.
- Term b is the exchange of energy between the mean flow and the turbulent flow. This term is often called production (of turbulent kinetic energy) because the transfer is generally from the mean flow to the turbulent flow.
- Term c is the dissipation.
- Term d is the diffusion due to velocity and pressure fluctuations and to viscosity.

The experimental results (figure 28) show that to a first approximation there is a balance between the production and dissipation terms which may be written symbolically as:

$$\text{Production} = \text{Dissipation}$$

Figure 28 also shows that the diffusion term contributes to transport turbulent kinetic energy from the near wall region towards the outer region of the boundary layer.

The main mechanisms of production, exchange and dissipation of turbulent kinetic energy are brought together in figure 29 with those pertaining to the mean flow [74]. Energy of mean motion is transported from upstream in the boundary layer by convection along the streamlines. The boundary layer is fed by the external flow through an entrainment mechanism which occurs at the edge of the boundary layer; there the external irrotational flow is transformed into a rotational flow. According to the sign of the pressure gradient, the work performed by pressure contributes to increase or to decrease the boundary layer energy. The mean flow energy is transferred near the wall by turbulent diffusion where a part of this energy is transformed into turbulent kinetic energy through the deformation work of the Reynolds stresses. Most of this turbulent kinetic energy is locally transformed into heat by dissipation and a small part is transferred towards the outer part of the boundary layer by turbulent diffusion.

A more detailed description of the exchanges in a boundary layer is obtained by analyzing the Reynolds stress equations. In the same way as for the turbulent kinetic energy equation, the convection and diffusion terms can be neglected in a first approximation. It is also assumed that the destruction term is modelled with equation (29). Then with the boundary layer hypotheses, the relevant Reynolds stress equations are:

$$-2 \langle u' v' \rangle \frac{\partial U}{\partial y} + 2 \left\langle \frac{p'}{\rho} \frac{\partial u'}{\partial x} \right\rangle - \frac{2}{3} \epsilon = 0 \quad (31a)$$

$$2 \left\langle \frac{p'}{\rho} \frac{\partial u'}{\partial y} \right\rangle - \frac{2}{3} \epsilon = 0 \quad (31b)$$

$$2 \left\langle \frac{p' \partial w'}{\rho \partial z} \right\rangle - \frac{2}{3} \epsilon = 0 \quad (31c)$$

$$-\left\langle v'^2 \right\rangle \frac{\partial U}{\partial y} + \left\langle \frac{p'}{\rho} \left(\frac{\partial u'}{\partial y} + \frac{\partial v'}{\partial x} \right) \right\rangle = 0 \quad (31d)$$

The above equations are respectively for $\langle u'^2 \rangle$, $\langle v'^2 \rangle$, $\langle w'^2 \rangle$, $\langle u'v' \rangle$.

Equations (31a-31c) show that the production of turbulent kinetic energy concerns only the $\langle u'^2 \rangle$ -component.

The dissipation term is negative so that the source of $\langle v'^2 \rangle$ and of $\langle w'^2 \rangle$ is necessarily the velocity-pressure correlation; the role of this term is to redistribute energy among the components $\langle u'^2 \rangle$, $\langle v'^2 \rangle$ and $\langle w'^2 \rangle$.

The production term in the $\langle u'v' \rangle$ -equation is $-\langle v'^2 \rangle \frac{\partial U}{\partial y}$ which is negative in the boundary layer ($\frac{\partial U}{\partial y} > 0$); the correlation $\langle u'v' \rangle$ is negative as confirmed by experiment. This source term is balanced by the velocity-pressure correlation.

Figure 30 shows the scheme of exchanges in the boundary layer as given by equations (31a-31d) and completes figure 29.

6.3 Inner and outer regions of the boundary layer

The experimental results discussed in the preceding sections incline us to consider two regions in the boundary layer. In the outer region, the flow is fully turbulent; the turbulent shear stress is much larger than the viscous stress. In the near wall region, the viscous stress is no longer negligible.

6.3.1 Inner region

At least for a flat plate boundary layer, it is a good approximation to assume that the total shear stress is constant near the wall. The momentum equation reduces to:

$$\tau = -\rho \langle u'v' \rangle + \mu \frac{\partial U}{\partial y} = \tau_w \quad (32)$$

Then it is assumed that the velocity profile $U(y)$ in this region is completely determined by the characteristics of the fluid ρ and μ and by the wall shear stress τ_w :

$$U = U(y, \tau_w, \rho, \mu) \quad (33)$$

This form assumes that the behaviour of the velocity near the wall is independent of the conditions under which the boundary layer develops. In particular it is assumed that the boundary layer thickness δ and the external velocity U_∞ do not play any role in the structure of the near wall boundary layer. Using dimensional analysis and considering the quantities $(U, y, \tau_w, \rho, \mu)$, it is easily shown that it is possible to

form only two dimensionless groups of independent variables, which can be chosen as:

$$U^+ = \frac{U}{U_\tau} ; y^+ = \frac{yU_\tau}{\nu} \quad (34)$$

where U_τ is the friction velocity:

$$U_\tau = \sqrt{\frac{\tau_w}{\rho}}$$

The quantities U^+ and y^+ are called the inner variables or *wall variables*.

Equation (33) then reads:

$$U^+ = f(y^+) \quad (35)$$

From our hypotheses, the function $f(y^+)$ is a "universal" function in the sense that it is independent of the boundary layer thickness, the Reynolds number or the pressure gradient. The function $f(y^+)$ is called the *law of the wall*.

Very close to the wall it is easy to determine explicitly the function f . When $y \rightarrow 0$ equation (32) reduces to:

$$\mu \frac{\partial U}{\partial y} = \tau_w$$

and the velocity profile is:

$$U = \tau_w \frac{y}{\mu}$$

or using the wall variables:

$$U^+ = y^+ \quad (36)$$

This law is valid for $y^+ < 3$.

Now let us examine the behaviour of the law of the wall when y^+ is large ($y^+ \gg 1$) but still inside the domain of the inner region. For such a region, the viscous stress is negligible compared to the turbulent shear stress. The effect of viscosity disappears and relation (33) becomes $U = U(y, \tau_w, \rho)$. A difficulty arises because there is only one dimensionless variable left, U/U_τ , and the conclusion would be $U/U_\tau = \text{cst}$. This is not acceptable because the overlap with the outer region would not be possible and this is at variance with the experimental results. The solution to this problem is obtained by studying the behaviour of $\frac{dU}{dy}$ instead of U . Therefore we study the function:

$$\frac{dU}{dy} = \frac{dU}{dy}(y, \tau_w, \rho) \quad (37)$$

The quantities $\frac{dU}{dy}, y, \tau_w, \rho$ determine only one dimensionless group of independent variables:

$$\frac{dU}{dy} y \tau_w^{-1/2} \rho^{1/2}$$

Relation (37) expresses that this group is a constant. In terms of wall variables we obtain:

$$\frac{dU^+}{dy^+} y^+ = \frac{1}{\chi} \quad (38)$$

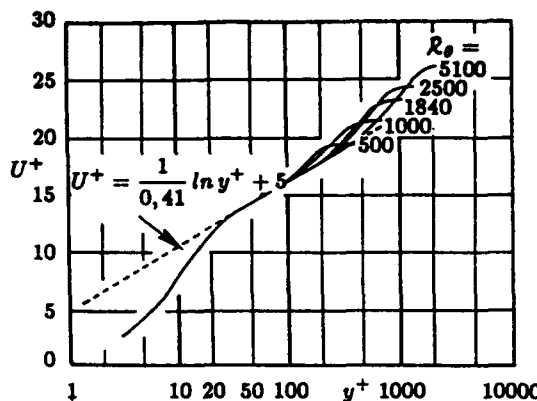


Figure 31: Velocity profiles in wall coordinates. Flat plate boundary layer (from Purtell et al. [57]).

where χ is a constant called the von Kármán constant.

The above relation integrates as:

$$U^+ = \frac{1}{\chi} \ln y^+ + C \quad (39)$$

This logarithmic law pertains to the law of the wall and therefore χ and C should be "universal" constants. Indeed the experimental results confirm this law very well (figure 31). The experimental values of χ and C are: $\chi = 0.41$, $C = 5$. This law of the wall is one of the most important results on turbulent boundary layers and all the turbulence models include it explicitly or implicitly. The logarithmic law applies for $y^+ > 50$. The end of the logarithmic behaviour depends on the Reynolds number; in terms of wall variables the extent of this region increases when the Reynolds number increases (figure 31). The region between the viscous sublayer ($y^+ < 3$) and $y^+ = 50$ is called the buffer layer.

6.3.2 Outer region

In the outer region of the boundary layer, the flow behaviour is entirely governed by its turbulent character. The viscous shear stress is negligible compared with the turbulent shear stress. In this region, the length scale of turbulence is given by the boundary layer thickness and the velocity scale is given by the friction velocity because the order of magnitude of the correlation $-\langle u'v' \rangle$ is U_τ^2 . On the other hand, the mean shear $\frac{\partial U}{\partial y}$ in the boundary layer is at the origin of the turbulent flow. To ensure a good interaction between the mean flow and the large turbulent structures, it is assumed that the time scales of both phenomena should have the same order of magnitude. This means that [51]:

$$\frac{\partial U}{\partial y} = \frac{U_\tau}{\delta} \Phi' \left(\frac{y}{\delta} \right) \quad (40)$$

The function Φ' is of order unity but it is not a universal function because the velocity profile is influenced by the pressure gradient, for example.

Relation (40) is valid for the outer part of the boundary layer and can be integrated up to the edge of the boundary layer to give a velocity defect formulation:

$$\frac{U_e - U}{U_\tau} = \Phi(\eta); \quad \eta = \frac{y}{\delta} \quad (41)$$

with:

$$\Phi = \int_\eta^1 \Phi' d\eta$$

6.3.3 Overlap law

Between the inner and the outer regions there is an intermediate layer which belongs to both regions in order to ensure the overlap between the law of the wall and the velocity defect law. A formal derivation can be done with the method of matched asymptotic expansions [47], [73], [82] which requires that the Reynolds number tends to infinity; then the overlap is possible when simultaneously $y^+ \rightarrow \infty$ and $\eta \rightarrow 0$. In practical cases, the overlap exists at finite Reynolds number, for finite values of y^+ and for non-zero values of η . The overlap requires the simultaneous validity of equations (35) and (41):

$$\frac{U}{U_\tau} = f\left(\frac{yU_\tau}{\nu}\right) \quad (42a)$$

$$\frac{U_e - U}{U_\tau} = \Phi\left(\frac{y}{\delta}\right) \quad (42b)$$

Adding the two above relationships gives:

$$\frac{U_e}{U_\tau} = \Phi\left(\frac{y}{\delta}\right) + f\left(\frac{yU_\tau}{\nu}\right) \quad (43)$$

This relationship is paradoxical because the left hand side does not depend on y whereas the right hand side does. The solution is a logarithmic behaviour [50] of f and Φ which is obtained by equating the expressions of $\frac{dU}{dy}$ calculated from equations (42a) and (42b):

$$\frac{U_\tau^2}{\nu} \frac{df}{dy^+} = - \frac{U_\tau}{\delta} \frac{d\Phi}{d\eta}$$

This gives:

$$y^+ \frac{df}{dy^+} = -\eta \frac{d\Phi}{d\eta}$$

The variables y^+ and η are independent so that the above quantities equal a constant. Therefore the overlap occurs in the logarithmic region:

$$\frac{U}{U_\tau} = \frac{1}{\chi} \ln \frac{yU_\tau}{\nu} + C \quad (44a)$$

$$\frac{U_e - U}{U_\tau} = -\frac{1}{\chi} \ln \frac{y}{\delta} + B \quad (44b)$$

In the above equations C is a universal constant but not B which depends on the pressure gradient.

The simultaneous validity of equations (44a) and (44b) gives a logarithmic skin friction law:

$$\frac{U_e}{U_\tau} = \left(\frac{C_f}{2} \right)^{-1/2} = \frac{1}{\chi} \ln \frac{U_\tau \delta}{\nu} + B + C \quad (45)$$

6.4 Turbulence models

In two-dimensional incompressible steady flow, the turbulent boundary layer equations are:

$$\frac{\partial U}{\partial x} + \frac{\partial V}{\partial y} = 0 \quad (46a)$$

$$\rho U \frac{\partial U}{\partial x} + \rho V \frac{\partial U}{\partial y} = - \frac{dP}{dx} + \frac{\partial}{\partial y} (\tau) \quad (46b)$$

with:

$$\tau = \mu \frac{\partial U}{\partial y} - \rho \langle u' v' \rangle$$

In the standard way used to solve the above equations, the pressure is a given data obtained from the solution of inviscid flow equations. In steady flow, the pressure is related to the outer edge boundary layer velocity by:

$$\frac{dP}{dx} = - \rho_e U_e \frac{dU_e}{dx}$$

and the boundary conditions are:

- $U = U_e$ at the boundary layer edge
- $U = V = 0$ at the wall (impermeable wall)

Let us notice that the above problem is correctly posed if the boundary layer is attached (see subsection 4.2).

The solution of equations (46a) and (46b) needs the adjonction of a turbulence model to express the turbulent shear stress $-\rho \langle u' v' \rangle$, which is an additional unknown (compared with the laminar case).

6.4.1 Mixing length model

It is assumed that the time scale of large structures is of the same order of magnitude as the time scale of the mean shear in the boundary layer:

$$\frac{u}{l} \sim \frac{\partial U}{\partial y}$$

Now the velocity fluctuations u' and v' are well correlated and the correlation $-\langle u' v' \rangle$ is of the same order of magnitude as u^2 .

The mixing length model expresses the turbulent shear stress as:

$$-\rho \langle u' v' \rangle = \rho l^2 \left(\frac{\partial U}{\partial y} \right)^2 \quad (47)$$

The mixing length l is not known and experimental results are used to determine it (figure 32). An analytical expression has been given to represent the experimental distribution of mixing length [49]:

$$\frac{l}{\delta} = 0.085 \tanh \left(\frac{x}{0.085 \delta} \frac{y}{\delta} \right) \quad (48)$$

Near the wall this formulation needs to be corrected to reproduce the effects of near wall and of viscosity on turbulence:

$$-\rho \langle u' v' \rangle = \rho F^2 l^2 \left(\frac{\partial U}{\partial y} \right)^2 \quad (49)$$

Van Driest [77] proposed to express the damping function F as:

$$F = 1 - e^{-y^+/26}$$

Improved formulations of this function have been proposed by many authors (see for example Cebeci-Smith [12]).

The mixing length model gives good results for calculating standard boundary layers but the expression of the mixing length is specific to boundary layers. For calculating a wake or a jet for example other expressions of the mixing length l are adapted. More elaborated turbulence models are needed to calculate complex shear flows.

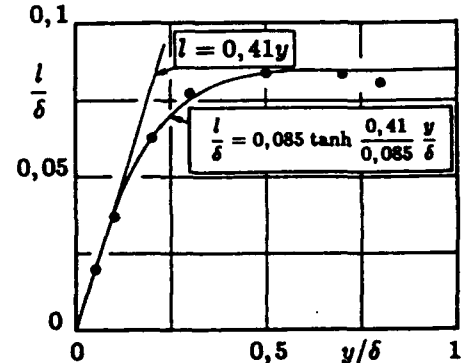


Figure 32: Mixing length distribution. Measurements from Klebanoff [38].

6.4.2 Transport equation models

These models were mainly developed in the seventies [9], [23], [24], [34], [41], [44], [45], [58], [62]; some basic work was made before but the lack of computers handicapped the development of these models.

The basic idea is to try to calculate the turbulence characteristics, in particular the length scale, with the help of transport equations similar to the equation for the turbulent kinetic energy. There are many ways to define the turbulence length scale. One of them is to use the dissipation and its inviscid estimate:

$$\varepsilon = \frac{u^3}{l} \quad \text{or} \quad l = \frac{u^3}{\varepsilon}$$

and the length scale is defined from the dissipation and the turbulent kinetic energy. Replacing this expression of the length in the mixing length model gives:

$$-\langle u' v' \rangle = C_\mu \frac{k^2}{\varepsilon} \frac{\partial U}{\partial y} \quad (50)$$

Joined to the boundary layer equations (46a) and (46b) this expression introduces two new unknowns: the turbulent kinetic energy k and its dissipation rate ε . Exact equations for these quantities are obtained from the Navier-Stokes equations. The k -equation has already been given (equation 23). A similar (and a little more complicated) equation can be obtained for ε . These equations do not form a closed system because many new unknowns appear. Closure assumptions are needed to obtain the turbulence model. The k -equation does not require too much work. Only the diffusion term needs to be modelled; a simple hypothesis of gradient diffusion is generally used. The discussion of the modelling of the ε -equation is out of the scope of this paper. The final result is an equation very similar to the k -equation. The $k - \varepsilon$ model of turbulence is finally obtained as:

$$-\langle u'v' \rangle = C_\mu \frac{k^2}{\varepsilon} \frac{\partial U}{\partial y} \quad (51a)$$

$$\rho \frac{Dk}{Dt} = -\rho \langle u'v' \rangle \frac{\partial U}{\partial y} - \rho \varepsilon + \frac{\partial}{\partial y} \left(\rho \frac{C_\mu}{\sigma_k} \frac{k^2}{\varepsilon} \frac{\partial k}{\partial y} \right) \quad (51b)$$

$$\rho \frac{D\varepsilon}{Dt} = \frac{\varepsilon}{k} \left(-C_{\varepsilon_1} \rho \langle u'v' \rangle \frac{\partial U}{\partial y} - C_{\varepsilon_2} \rho \varepsilon \right) + \frac{\partial}{\partial y} \left(\rho \frac{C_\mu}{\sigma_\varepsilon} \frac{k^2}{\varepsilon} \frac{\partial \varepsilon}{\partial y} \right) \quad (51c)$$

The various constants of the model are determined from applications to reference properties of certain simple flows (logarithmic law of the wall, decay of isotropic turbulence behind a grid, ...). The generally accepted values of these constants are:

$$C_\mu = 0.09, C_{\varepsilon_1} = 1.44, C_{\varepsilon_2} = 1.92, \sigma_k = 1, \sigma_\varepsilon = 1.25$$

As given above, the model is valid for the external part of the boundary layer and does not apply to the near wall region. Several solutions have been proposed to overcome this problem. One of them is to use the above model with boundary conditions not at the wall but in the logarithmic region of the boundary layer (for example at $y^+ = 50$). Then the boundary layer is not calculated near the wall. The boundary conditions are obtained from relationship (39) and assuming:

$$k = \frac{U_r^2}{C_\mu^{1/2}}$$

$$\varepsilon = \frac{U_r^3}{xy}$$

A second solution to calculate the near wall region is to modify the $k - \varepsilon$ model to take into account the effect of the presence of the wall on the turbulence properties and effects of low Reynolds number. The original version of this model was proposed by Jones-Launder [37]. Subsequently, many other versions have been proposed. One of them is from Chien [14]. The dissipation is split into its isotropic

part and its near-wall contribution $2\nu k/y^2$. Damping functions are introduced as functions of y^+ . The model is valid not only near the wall but throughout the boundary layer. It is made of the following equations:

$$-\langle u'v' \rangle = C_\mu f_\mu \frac{k^2}{\varepsilon}$$

$$\rho \frac{Dk}{Dt} = -\rho \langle u'v' \rangle \frac{\partial U}{\partial y} - \rho \varepsilon - 2\mu \frac{k}{y^2}$$

$$+ \frac{\partial}{\partial y} \left[\left(\mu + \frac{\mu_t}{\sigma_k} \right) \frac{\partial k}{\partial y} \right]$$

$$\rho \frac{D\varepsilon}{Dt} = -C_{\varepsilon_1} \frac{\varepsilon}{k} \rho \langle u'v' \rangle \frac{\partial U}{\partial y}$$

$$- \frac{\rho \varepsilon}{k} \left[C_{\varepsilon_2} f_2 \varepsilon + \frac{2\nu k \exp(-C_{\varepsilon_2} y^+)}{y^2} \right]$$

$$+ \frac{\partial}{\partial y} \left[\left(\mu + \frac{\mu_t}{\sigma_\varepsilon} \right) \frac{\partial \varepsilon}{\partial y} \right]$$

$$C_\mu = 0.09; C_{\varepsilon_1} = 1.35; C_{\varepsilon_2} = 1.8; C_{\varepsilon_3} = 0.5; \sigma_k = 1.0; \sigma_\varepsilon = 1.3$$

$$f_2 = 1 - \exp \left(-\frac{R_1^2}{36} \right); R_1 = \frac{k^2}{\nu \varepsilon}$$

$$f_\mu = 1 - \exp(-C_3 y^+); C_3 = 0.0115$$

A third solution to calculate the near wall region is to use a simpler model in this region which is matched to the $k - \varepsilon$ model used for the external part of the boundary layer. For example a mixing length model can be used near the wall. The matching is performed around $y^+ = 50$ and boundary conditions are used at this point for the $k - \varepsilon$ model as:

$$k = \frac{-\langle u'v' \rangle}{C_\mu^{1/2}}$$

$$\varepsilon = C_\mu \frac{k^2}{-\langle u'v' \rangle} \frac{\partial U}{\partial y}$$

In the above relationships the values of $\langle u'v' \rangle$ and $\frac{\partial U}{\partial y}$ are determined at the matching point from the mixing length model.

Such a two-layer model is very efficient. The argument in favor of this model is that the near wall region is generally close to equilibrium and the mixing length is appropriate; in the outer region the situations of non equilibrium are more frequent and it is more convenient to use the $k - \varepsilon$ model. A further improvement of this two-layer model is to replace the mixing length model by a one-equation model—the k -equation. As an example, we can give a model derived from the Norris-Reynolds [53] model:

$$-\rho \langle u'v' \rangle = \mu_t \frac{\partial U}{\partial y}$$

$$\mu_t = C_\mu f_\mu \rho \sqrt{k} L; C_\mu = 0.09$$

$$f_\mu = 1 - \exp \left(-0.0198 \frac{\rho \sqrt{k} y}{\mu_w} \frac{25}{A^+} \right)$$

$$\begin{aligned}
 A^+ &= 25(1 + 30.175p^+) ; \quad p^+ = \frac{\mu_w}{\rho_w^2 U_w^3} \frac{dp}{dx} \\
 L &= 6.086 \min(0.41y, 0.085\delta) \\
 \rho \frac{Dk}{Dt} &= -\rho(u'v') \frac{\partial U}{\partial y} - \rho\epsilon \\
 &\quad + \frac{\partial}{\partial y} \left[(\mu + \mu_t) \frac{\partial k}{\partial y} \right] \\
 \epsilon &= \frac{k^{3/2}}{L} \left(1 + \frac{13.2\mu_w}{\rho_w \sqrt{k} L} \right) \quad (52)
 \end{aligned}$$

The above model is used near the wall and is matched to the $k-\epsilon$ model at a point where f_μ is close to unity (for example $f_\mu = 0.95$). The boundary conditions used for the $k-\epsilon$ model at the matching point are directly the values of k and ϵ calculated from the one-equation model at the same point.

More complicated models than the two-equation model can be used. For example, instead of using the eddy viscosity hypothesis to express the turbulent shear stress a transport equation can be employed and the three components of the turbulent kinetic energy can also be computed from transport equations. For boundary layers, all the transport equations are rarely used but they can be simplified by making assumptions for the convection and diffusion terms; the simplified models are called the algebraic stress models (ASM) [40], [61].

6.5 Compressible boundary layers

Basically, the models described in subsections (6.4.1) and (6.4.2) are derived for incompressible boundary layers. In compressible flow, the Morkovin hypothesis [52] consists of assuming that the turbulent velocity fluctuations behave like in incompressible flow. It is generally admitted that this rule is valid for Mach numbers lower than five. Indeed, with this condition, the turbulent Mach number (the Mach number which characterizes the velocity fluctuations) remains small and the velocity fluctuations are solenoidal. The consequence is that the incompressible turbulence models can be extended in a straightforward manner to calculate boundary layers in compressible flows. The influence of compressibility is present in the models simply by taking the local value of density. In hypersonic flow, the influence of compressibility on turbulence is not clearly identified and reliable models are not yet available. Fortunately, it seems that the compressibility effects are not very strong for boundary layers but this is not the case for mixing layers for which there is a tremendous reduction of the spreading rate due to compressibility [7], [25], [54], [64], [81], [83].

6.6 Three-dimensional boundary layers

A simple hypothesis is very often used to calculate three-dimensional boundary layers. It is assumed that the eddy viscosity is isotropic. For example if

a $k-\epsilon$ model is used the two components of the shear stress are given by:

$$\begin{aligned}
 -\rho(u'v') &= \mu_t \frac{\partial U}{\partial y} \\
 -\rho(w'v') &= \mu_t \frac{\partial W}{\partial y}
 \end{aligned}$$

with:

$$\mu_t = C_\mu \rho \frac{k^2}{\epsilon}$$

The equations for k and ϵ are:

$$\begin{aligned}
 \rho \frac{Dk}{Dt} &= \rho P - \rho\epsilon \\
 &\quad + \frac{\partial}{\partial y} \left(\rho \frac{C_\mu}{\sigma_k} \frac{k^2}{\epsilon} \frac{\partial k}{\partial y} \right) \\
 \rho \frac{D\epsilon}{Dt} &= \frac{\epsilon}{k} (C_\epsilon, \rho P - C_\epsilon, \rho\epsilon) \\
 &\quad + \frac{\partial}{\partial y} \left(\rho \frac{C_\mu}{\sigma_\epsilon} \frac{k^2}{\epsilon} \frac{\partial \epsilon}{\partial y} \right)
 \end{aligned}$$

with:

$$P = -\langle u'v' \rangle \frac{\partial U}{\partial y} - \langle w'v' \rangle \frac{\partial W}{\partial y}$$

This hypothesis is not completely satisfactory because the three-dimensionality induces a non isotropic eddy viscosity [10], [26], [76] and the level of eddy viscosity is reduced. As a first approximation, the above hypothesis is acceptable, but to obtain more refined results, more elaborate models are needed [21]. Up to now, it has not yet been demonstrated that a reliable model is available and a basic experiment has been undertaken in Europe to build a very complete data base for validating and improving turbulence models in three-dimensional boundary layers [20], [75].

6.7 Turbulence structure

Where and how are the Reynolds stresses produced in the boundary layer? How is the external irrotational flow entrained in the boundary layer and transformed into rotational flow? How is the turbulent energy dissipated? etc...

The goal of the studies on turbulence structure is to answer this type of questions.

It is known that the turbulent motion is *not random but organized in coherent structures* which are responsible for the turbulence features. The apparent random aspect of the velocity signal measured by a hot-wire probe is due to the fact that this information is very partial. *Space-time correlations* measured by Favre-Gaviglio-Dumas [29] showed that a turbulence field is strongly organized. Such an organization does not exist in laminar flow and is characteristic of turbulence.

Figure 33 gives an example of a celebrated space-time correlation. The correlation $\bar{r}_{11}(\xi_1, 0, 0, \tau)$ is defined as:

$$\bar{r}_{11} = \frac{\langle u'_A(t)u'_B(t+\tau) \rangle}{(\langle u'^2_A \rangle \langle u'^2_B \rangle)^{1/2}}$$

where the separation between points A and B is $(\xi_1, 0, 0)$. In figure 33, each curve corresponds to a given separation time τ . The displacement of the maximum of each curve enables us to determine a *convection velocity* of turbulent structures. The measurements indicate that the convection velocity is about $0.8U_e$. The maximum of each curve decreases rather slowly. This indicates that the turbulent structures keep their coherence over a long distance. From the figure, it can be estimated that the life time of a structure is at least $20 10^{-3}$ s. Using the convection velocity to transform time in spatial distance, this corresponds to 10 or 15 boundary layer thicknesses whereas the longitudinal extent of a given structure is about 2 or 3 boundary layer thicknesses.

The first difficulty when studying turbulent structures is the definition of the studied objects. A coherent structure is still a very ill defined concept and different definitions have been adopted by investigators. The definition proposed by Robinson [59] is:

"a three-dimensional region of the flow over which at least one fundamental flow variable (velocity component, density, temperature, etc.) exhibits significant correlation with itself or with another variable over a range of space and/or time that is significantly larger than the smallest local scales of the flow."

This problem of definition probably reflects the poor knowledge of the mechanisms and of the dynamical behaviour of turbulence. In fact, the understanding of turbulence is one of the greatest challenges in Physics.

Mainly two classes of structures are recognized—the shear layers and the vortices. The shear layers are mainly found at the interface of upstream high-speed flow and downstream low-speed flow. The vortical structures are responsible for the transport of momentum. The link between these structures is not yet fully understood.

A first idea of events which contribute to the production of the Reynolds shear stress $-\rho(u'v')$ is given by the *quadrants method*. This method consists of measuring and sampling simultaneously the u' - and v' -evolution at a given point. Each sample is represented by a point in the (u', v') -plane. The second quadrant ($u' < 0, v' > 0$) corresponds to an *ejection* (outwards motion) and the fourth quadrant ($u' > 0, v' < 0$) corresponds to a *sweep* (motion towards the wall). Such a simple analysis shows that the Reynolds stress is mainly the result of these ejections and sweeps; the contribution of the first and third quadrants are smaller. Ejections and sweeps are very important events in the near-wall region (around $y^+ = 12$). Indeed the near-wall buffer region is a zone of high turbulence production and dissipation. In this zone, the turbulent activity is characterized by the *bursting process*. A precise definition of bursting is not easily obtained because the meaning of this term is not the same for everybody and it

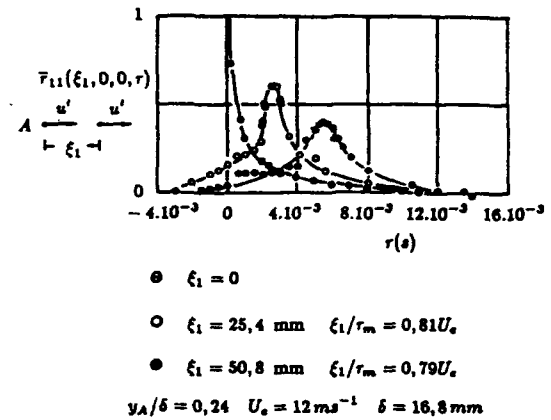


Figure 33: Space-time correlations in a flat plate boundary layer (from Favre, Gaviglio, Dumas [29]).

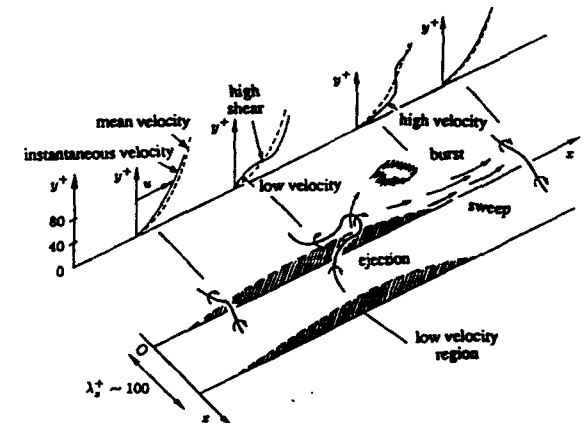


Figure 34: Conceptual model of turbulence production from Hinze [36].

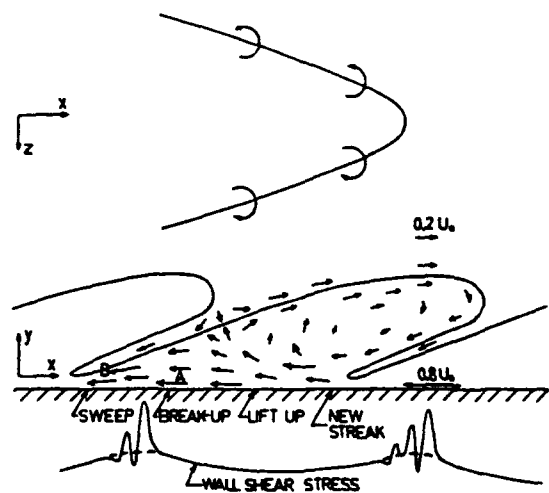


Figure 35: Flow pattern seen by an observer moving at a speed of $0.8U_e$: model proposed by Brown and Thomas [11].

evolved in time. The bursting event is often seen as a violent eruption of fluid outwards associated with the instability of a shear layer.

Conceptual models have been proposed to give a global (idealized) view of the main phenomena involved in a boundary layer. Up to now there is no completely accepted scheme and the interest in this field is renewed by numerical simulations.

As an example, figure 34 shows the model proposed by Hinze [36]. The basic structure is a horse-shoe vortex which lifts low-speed fluid from the near-wall region and produces an unstable shear layer which breaks down in turbulence. After this event, a wallward motion sweeps the near-wall region. Correlatively the deformation of instantaneous velocity profiles is noticed. In particular, the unstable shear layer is associated with an inflection point in the velocity profile. This model emphasizes what happens in a (x, y) plane and does not give a three-dimensional picture of the phenomena. It also concentrates on the near-wall events.

The scheme proposed by Brown and Thomas [11] (figure 35) gives a global average description of the boundary layer motions in a frame of reference moving at a speed $0.8U_\infty$, which is the convection velocity of the large structures. The intermittent region of the boundary layer is made of bulges which are three-dimensional with a length scale equal to the boundary layer thickness. The external irrotational flow is entrained in the boundary layer mainly at the bottom of the indentations of these bulges.

Figure 36 is an example of information given by numerical simulations [60]. This picture illustrates the relationship between low pressure zones (which are vortex cores) and the ejections. Two points are noticeable. First, the figure gives a three-dimensional view of the phenomena. Second, pressure structures are deduced from the numerical simulations. Both elements are hardly obtained experimentally. This does not mean however that experiments are no longer needed. On the contrary, it is necessary to perform more and more detailed experiments to check and validate calculations. The simulations have deficiencies and can produce their own turbulence whereas experiments are real life situations.

A more complete view of the state of the art on turbulence structure is given in this Lecture Series by R. Blackwelder and J. Kim. It is clear that an accurate knowledge of the turbulence mechanisms is needed to understand how the boundary layer can be manipulated to reduce the skin-friction.

7 LAMINAR-TURBULENT TRANSITION

Detailed information on laminar-turbulent transition can be found in textbooks ([66]) or in review articles ([1], [2], [3], [46]).

7.1 Experimental observations

7.1.1 Flat plate boundary layer

The transition of the flat plate boundary layer in a clean environment (low free-stream turbulence level, low roughness of the wall ...) is the most studied case.

The evolution of the mean flow is characterized by a progressive deformation of the velocity profiles (figure 37) which become fuller and fuller. Correlatively, the shape parameter decreases from the Blasius value ($H = 2.591$) to a value dependent on the Reynolds number (for a fully turbulent boundary layer the value $H = 1.4$ is not at all universal and decreases as the Reynolds number increases). In the transition region, the skin-friction coefficient increases rapidly. Consequently, the momentum thickness increases more and more rapidly in the transition region since the slope of the curve $\theta(x)$ is directly related to the skin-friction ($\frac{d\theta}{dx} = \frac{C_f}{2}$). The displacement thickness does not have a monotonic variation due to the combination of the increase of the momentum thickness and the decrease of the shape parameter (figure 38).

Before any substantial effect on the mean flow is visible, the flow becomes unsteady (figure 39). At a certain distance from the leading edge, waves are observed in the boundary layer. These waves are virtually two-dimensional and are called *Tollmien-Schlichting waves*. The linear stability theory describes these waves rather well with the *Orr-Sommerfeld equations*. These waves can be modelled as two-dimensional vortex tubes (figure 40). Downstream, the TS waves become three-dimensional and the vortex tubes are stretched. Due to induced velocities, the downstream part of the vortex tubes (the head) is lifted up whereas the legs go down towards the wall. Compared to the legs, the head is surrounded by higher velocity fluid and the stretching is accentuated. Around the head, a peak and a double peak are observed on the velocity signal (figure 41) and the vorticity intensity increases; there is a strong shear in this region which is very unstable. The next stage is the formation of a turbulent spot; its average contour is shown on figure 42. At this stage the flow is *intermittently turbulent* and the turbulent spots appear randomly in space and time. A turbulent spot is formed of an ensemble of structures which entrain the neighbouring flow. Therefore a turbulent spot grows and eventually the flow is fully turbulent (figure 43). Figure 44 shows the evolution of the energy spectrum of the longitudinal velocity. It is observed that a narrow band of frequencies is first amplified and progressively an increase of the general level of the spectrum is noticed.

7.1.2 Effects of pressure gradients

The global effect of a positive pressure gradient is to trigger transition at a lower Reynolds number than

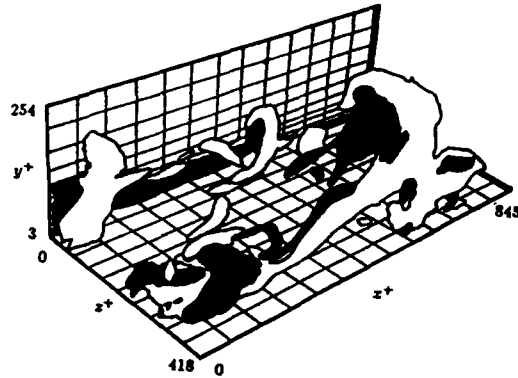


Figure 36: Direct numerical simulation of a flat plate boundary layer from Robinson, Kline and Spalart [60].
in white: low pressure zones
in black: ejections.

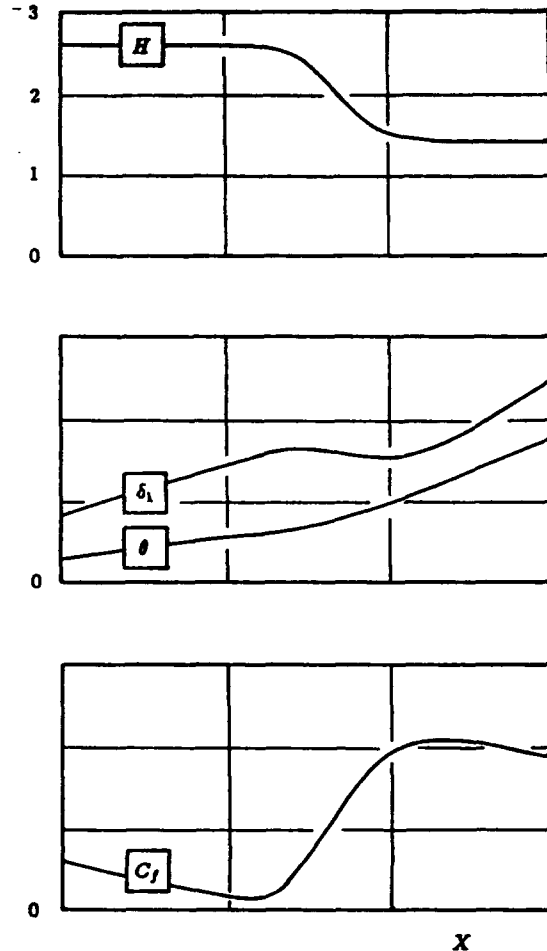


Figure 38: Global boundary layer characteristics in transition

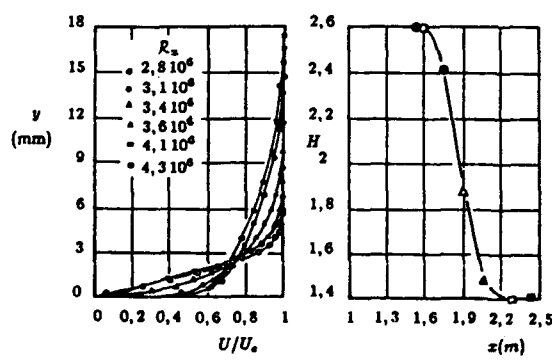


Figure 37: Transition on a flat plate (from Schubauer and Klebanoff [68]).

for the flat plate. If the pressure gradient is strong enough, the laminar boundary layer separates and under certain circumstances the transition which occurs downstream induces the reattachment of a transitional or turbulent boundary layer. This configuration can be observed near the leading edge of airfoils where a separation bubble forms. However, reattachment may not occur and stall can take place.

With a negative pressure gradient, transition can be delayed substantially. This property is used to shape laminar airfoils. It is assumed that the process of transition is the same as in the case of the flat plate but very few data are available to ascertain this hypothesis. Indeed it is difficult to study transition with significant negative pressure gradient because in this case transition occurs at large Reynolds number; very large wind tunnels are needed in which fundamental studies are not easy.

The transition process is affected by strong enough positive pressure gradients. Figure 45 gives such an example. Transition is studied on an airfoil with a pressure distribution given on top of figure 45. The measured velocity profiles and the shape parameter

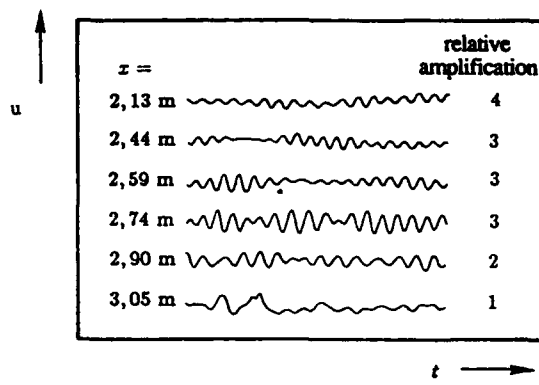


Figure 39: Tollmien-Schlichting waves (from Schubauer and Skramstad [69]).

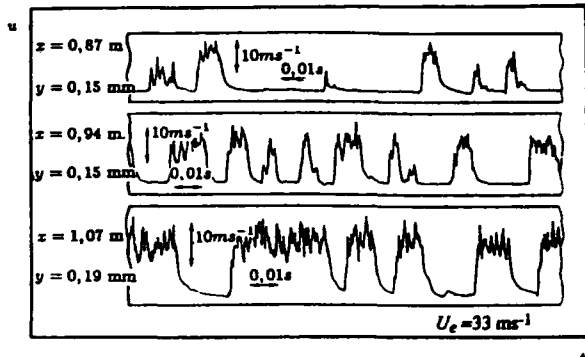


Figure 43: Velocity signal in the intermittent region (from Arnal-Juillen [5]).

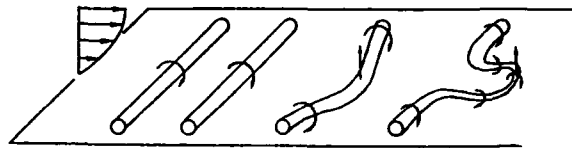


Figure 40: Deformation of vortex tubes.

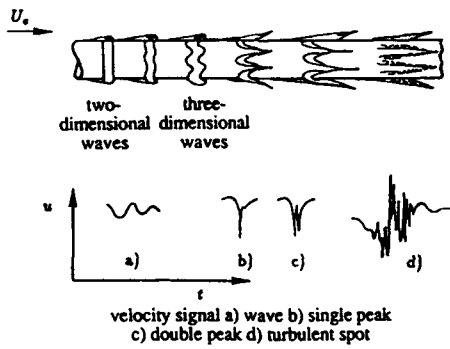


Figure 41: Smoke visualizations (from Knapp, Roache, Mueller [39]).

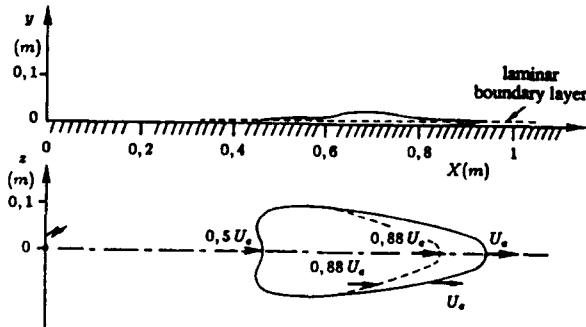


Figure 42: Contours of a turbulent spot (from Schubauer-Klebanoff [88]).

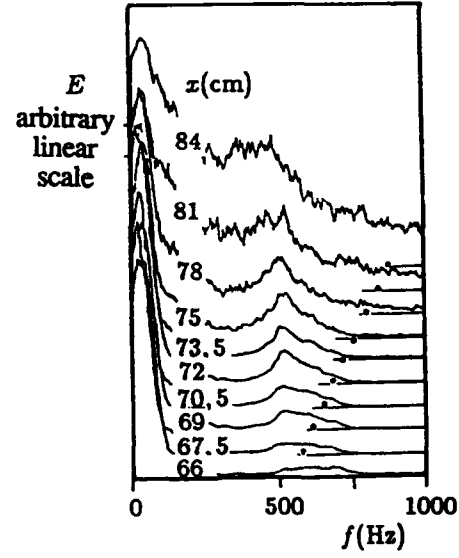


Figure 44: Energy spectra in transition (from Arnal-Juillen [5]).

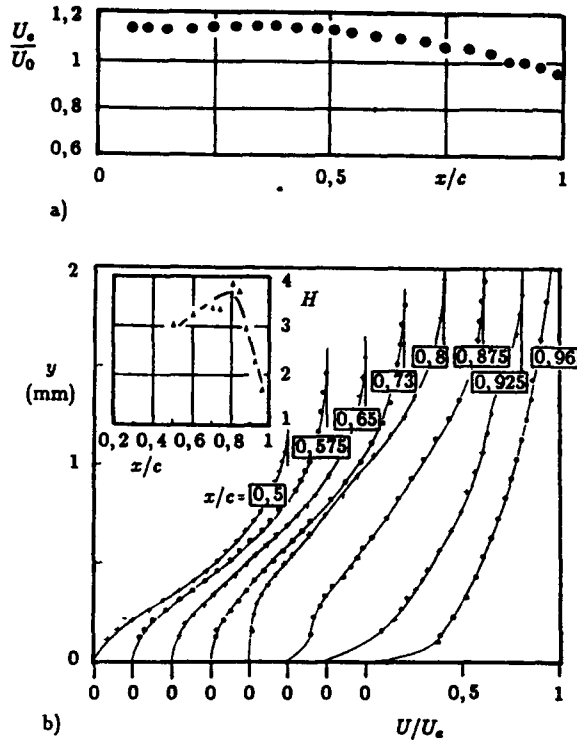


Figure 45: Transition with positive pressure gradient on ONERA D airfoil (from Cousteix-Pailhas [22]).
a) external velocity distribution
b) velocity profiles and shape parameter.

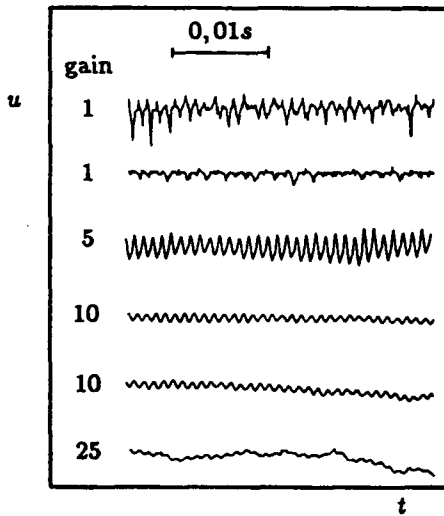


Figure 46: Transition with positive pressure gradient on ONERA D airfoil [22].
Velocity signal ($y=0.5$ mm).

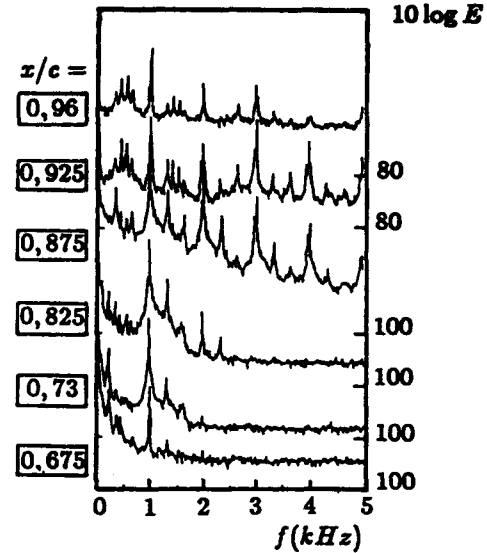


Figure 47: Transition with positive pressure gradient on ONERA D airfoil [22].
Spectral energy density of longitudinal velocity ($y=0.5$ mm).

are also given on this figure. The boundary layer is still laminar in the neighbourhood of the separation zone located around $x/c = 0.8$. Tollmien-Schlichting waves of large amplitude are first observed (figure 46). Downstream the TS waves are perturbed but each wave seems to be deformed in the same manner. The periodic aspect of the velocity signal is observed overall the airfoil. The mean velocity profiles take a turbulent shape but turbulent spots are not observed on the velocity signal. The energy spectrum (figure 47) of the longitudinal velocity shows a narrow peak at the first step ($x/c = 0.675$). Downstream harmonics and subharmonics are formed. Subharmonics are probably the result of the pairing of smaller structures as suggested by visualizations. This type of transition is very different from the standard flat plate and seems closer to the case of transition in a free shear layer.

7.1.3 Effects of other parameters

The Reynolds number and the pressure gradient are not the sole parameters to control transition.

Wall suction, even with small rates, can delay transition in a very spectacular manner and is one of the means studied to design laminar wings. Wall suction has a double effect. First, the boundary layer thickness is reduced and secondly, the stability properties of the boundary layer are improved due to a favourable modification of the shape of velocity profiles. For practical applications, suction is applied through perforated walls. This technique has a limitation. The local flow around each hole being strongly three-dimensional, excessively large suction velocities are likely to trigger transition. A small

amount of suction through perforated plate is therefore favourable (the transition is delayed), but too strong suction rates have negative effects.

The increase of free-stream turbulence level and of noise have generally the effect of triggering transition at lower Reynolds numbers. However, the effect is not so simple because the spectrum also plays a role. The same free-stream turbulence level with a different spectrum can have a different effect on transition. Similarly, the influence of noise depends on its frequency; in particular noise at the frequency of TS waves has a noticeable effect.

Wall roughness is also an important practical parameter. The general effect of wall roughness is to trigger transition at lower Reynolds numbers. Practical criteria are available for certain types of roughness shape and distribution but there is no general rules for all types of roughness.

The curvature of the wall has also an effect on transition. A concave curvature can generate Görtler vortices which give an early transition.

The effects of all these parameters and of others—the effects of compressibility and of three-dimensionality of the flow are of particular importance—are discussed in details in this Lecture Series by W.S.Saric and D.Arnal.

7.2 Linear stability theory

The linear stability theory is now a standard tool for studying transition. This theory describes the first step of instability: the Tollmien-Schlichting waves. The practical importance of this theory is that it is associated to empirical information to construct a transition criterion.

7.2.1 Parallel flow assumption

The stability theory is based on the study of small perturbations superimposed on a basic laminar flow. The purpose of the theory is to tell the conditions under which the perturbations are amplified or damped.

Let us assume that the flow is incompressible and the basic flow is steady. The velocity and pressure are decomposed into a mean part and a perturbation:

$$u_i(x, y, z, t) = U_i(x, y, z) + \tilde{u}_i(x, y, z, t) \quad (53a)$$

$$p(x, y, z, t) = P(x, y, z) + \tilde{p}(x, y, z, t) \quad (53b)$$

All the quantities are reduced by reference quantities: U_0, ρ_0, ν_0, ℓ . The quantities U_0, ρ_0, ν_0 are characteristic of the external flow whereas the length ℓ is characteristic of the boundary layer thickness.

The decomposition (53a-53b) is introduced in the Navier-Stokes equations. It is assumed that the basic flow satisfies the steady Navier-Stokes equations and that the perturbations are small enough for the

quadratic terms to be neglected. The following system is obtained:

$$\frac{\partial \tilde{u}_i}{\partial z_i} = 0 \quad (54a)$$

$$\frac{\partial \tilde{u}_i}{\partial t} + \tilde{u}_j \frac{\partial U_i}{\partial z_j} + U_j \frac{\partial \tilde{u}_i}{\partial z_j} = -\frac{\partial \tilde{p}}{\partial z_i} + \frac{1}{R_\ell} \frac{\partial^2 \tilde{u}_i}{\partial z_i \partial z_i} \quad (54b)$$

where R_ℓ is the reference Reynolds number:

$$R_\ell = \frac{U_0 \ell}{\nu}$$

The boundary conditions for the perturbations are the no-slip condition at the wall and the condition of no perturbation in the external flow. Then the system (54a-54b) has a trivial solution $\tilde{u}_i = 0$ and $\tilde{p} = 0$. The purpose of the stability theory is to determine the non trivial eigensolutions of this system. In the "simplest" theory, a further assumption of parallel flow is introduced. It is assumed that the velocity component normal to the wall V of the basic flow is zero and that the other velocity components U and W are independent of z and z :

$$V = 0 ; U = U(y) ; W = W(y)$$

The following system is obtained:

$$\frac{\partial \tilde{u}}{\partial z} + \frac{\partial \tilde{v}}{\partial y} + \frac{\partial \tilde{w}}{\partial z} = 0 \quad (55a)$$

$$\frac{\partial \tilde{u}}{\partial t} + U \frac{\partial \tilde{u}}{\partial x} + W \frac{\partial \tilde{u}}{\partial z} + \tilde{v} \frac{\partial U}{\partial y} = -\frac{\partial \tilde{p}}{\partial z} + \frac{1}{R_\ell} \frac{\partial^2 \tilde{u}}{\partial z_i \partial z_i} \quad (55b)$$

$$\frac{\partial \tilde{v}}{\partial t} + U \frac{\partial \tilde{v}}{\partial x} + W \frac{\partial \tilde{v}}{\partial z} = -\frac{\partial \tilde{p}}{\partial y} + \frac{1}{R_\ell} \frac{\partial^2 \tilde{v}}{\partial z_i \partial z_i} \quad (55c)$$

$$\frac{\partial \tilde{w}}{\partial t} + U \frac{\partial \tilde{w}}{\partial x} + W \frac{\partial \tilde{w}}{\partial z} + \tilde{v} \frac{\partial W}{\partial y} = -\frac{\partial \tilde{p}}{\partial z} + \frac{1}{R_\ell} \frac{\partial^2 \tilde{w}}{\partial z_i \partial z_i} \quad (55d)$$

7.2.2 Orr-Sommerfeld equation

The eigensolutions of equations (55a-55b-55c-55d) is looked for by using the normal modes form:

$$\left\{ \begin{array}{l} \tilde{u} \\ \tilde{v} \\ \tilde{w} \\ \tilde{p} \end{array} \right\} = \left\{ \begin{array}{l} \hat{u}(y) \\ \hat{v}(y) \\ \hat{w}(y) \\ \hat{p}(y) \end{array} \right\} e^{i(\alpha z + \beta y - \omega t)} \quad (56)$$

where i is the pure imaginary number $i = \sqrt{-1}$. Introducing the normal mode decomposition in equa-

tions (55a-55b-55c-55d) gives:

$$\begin{aligned} i(\alpha U + \beta W - \omega) \hat{u} + \hat{v} D U &= -i \alpha \hat{p} \\ &+ \frac{1}{R} (D^2 - (\alpha^2 + \beta^2)) \hat{u} \end{aligned} \quad (57a)$$

$$\begin{aligned} i(\alpha U + \beta W - \omega) \hat{v} &= -D \hat{p} \\ &+ \frac{1}{R} (D^2 - (\alpha^2 + \beta^2)) \hat{v} \end{aligned} \quad (57b)$$

$$\begin{aligned} i(\alpha U + \beta W - \omega) \hat{w} + \hat{v} D W &= -i \beta \hat{p} \\ &+ \frac{1}{R} (D^2 - (\alpha^2 + \beta^2)) \hat{w} \end{aligned} \quad (57c)$$

$$i(\alpha \hat{u} + \beta \hat{w}) + D \hat{v} = 0 \quad (57d)$$

where D stands for the operator $\frac{\partial}{\partial y}$ (for example $DU = \frac{\partial U}{\partial y}$ and $D^2 \hat{u} = \frac{\partial^2 \hat{u}}{\partial y^2}$).

From the above system, an equation for \hat{v} can be obtained:

$$\begin{aligned} (D^2 - \alpha^2 - \beta^2)^2 \hat{v} - iR [-(\alpha D^2 U + \beta D^2 W) \\ + (\alpha U + \beta W - \omega)(D^2 - \alpha^2 - \beta^2)] \hat{v} = 0 \end{aligned} \quad (58)$$

Generally, the Orr-Sommerfeld equation is given for the study of two-dimensional waves in two-dimensional flow ($\beta = 0$; $W = 0$):

$$(D^2 - \alpha^2)^2 \hat{v} - iR [(\alpha U - \omega)(D^2 - \alpha^2) - \alpha D^2 U] \hat{v} = 0$$

Temporal and spatial theory. The study of the laminar boundary layer stability is performed in two cases:

1. α and β are real numbers, ω is a complex number: this is the temporal theory.
2. α and β are complex numbers, ω is a real number: this is the spatial theory.

In the *temporal theory* the modulus of perturbations amplitude varies in time. We have $\omega = \omega_r + i\omega_i$ and the \hat{u} perturbation for example is:

$$\hat{u} = \hat{u} e^{\omega_r t} e^{i(\alpha x + \beta z - \omega_r t)}$$

In this expression, α and β are the wave-lengths of the perturbation in the x and z direction; ω_r is the pulsation of the perturbation and ω_i is the rate of amplification. If A is the amplitude of the perturbation, we have:

$$\frac{1}{A} \frac{dA}{dt} = \omega_i$$

According to the value of ω_i , the wave is amplified, neutrally stable or damped:

- $\omega_i > 0$: the wave is amplified
- $\omega_i = 0$: the wave is neutrally stable
- $\omega_i < 0$: the wave is damped

The iso-phase lines (for example a line of local maximum amplitude) are orthogonal to the wave number \vec{k} of components (α, β) . The phase velocity is:

$$C = \frac{\omega_r}{(\alpha^2 + \beta^2)^{1/2}}$$

In the *spatial theory*, we have:

$$\begin{aligned} \alpha &= \alpha_r + i\alpha_i \\ \beta &= \beta_r + i\beta_i \end{aligned}$$

The amplification rate is defined with a vector of components $(-\alpha_i, -\beta_i)$.

The iso-phase lines are orthogonal to the wave number \vec{k} of components (α_r, β_r) . The phase velocity is:

$$C = \frac{\omega}{(\alpha_r^2 + \beta_r^2)^{1/2}}$$

The spatial and temporal theory are equivalent for neutrally stable waves. In two-dimensional flows, Gaster [31] showed that both theories are related for small amplification rates by the group velocity. The Gaster relationship has been extended (Mack [46]) to three-dimensional flows as:

$$(-\alpha_i)_g = \frac{\omega_i}{C_g}$$

where $(-\alpha_i)_g$ is the rate of spatial amplification in the direction of the group velocity \vec{C}_g and C_g is the modulus of the real part of \vec{C}_g . In the temporal theory, \vec{C}_g is a vector of components $(\frac{\partial \omega}{\partial \alpha}, \frac{\partial \omega}{\partial \beta})$ and \vec{C}_g is a vector of components $(\frac{\partial \omega_r}{\partial \alpha}, \frac{\partial \omega_r}{\partial \beta})$.

7.2.3 Examples of results. Stability diagrams

Non trivial solutions of the stability equations are obtained for particular combinations of the parameters α , β , ω and R_ℓ . This set of parameters forms the dispersion relation:

$$\Omega(\alpha, \beta, \omega, R_\ell) = 0$$

For each combination of the parameters, the eigenfunctions \hat{u} , \hat{v} , \hat{w} , \hat{p} can be calculated but only up to an arbitrary multiplicative constant, because the stability equations are linear and homogeneous. Any eigenfunction multiplied by a constant is also an eigenfunction of the stability equations.

Let us examine results obtained in two-dimensional flow for two-dimensional waves ($\beta = 0$) by using the spatial theory. To calculate a solution of the Orr-Sommerfeld equation the input data are: i) the velocity profile of the basic flow $U(y)$ —for the flat plate flow this is the Blasius profile, ii) the Reynolds number R_ℓ of the boundary layer under consideration, iii) the frequency of the wave which is analyzed. The result is the value of the wave number α_r and of the amplification coefficient

α_i of the studied wave. By varying the frequency of the wave and the Reynolds number, the complete dispersion relation is determined. Generally, slices of this hypersurface are presented. For example, the iso-amplification coefficient lines are given in a plane with the frequency and the Reynolds number as coordinates: this is a *stability diagram*.

Figure 48 shows such a stability diagram for the flat plate flow. Here, the characteristic Reynolds number is based on the displacement thickness of the boundary layer. This diagram could be completed with the iso-wave number lines but for clarity these lines are not drawn. The plane is separated in two regions by the neutral curve ($\alpha_i^* = 0$). Inside the neutral curve the waves are unstable (amplified) and outside they are stable. The stability diagram shows that below a certain value of the Reynolds number all the waves are stable: this minimum Reynolds number is called the *critical Reynolds number*. For the flat plate flow, the critical Reynolds number is $(R_{\delta_1})_{cr} = 520$ which corresponds to $R_x = 8.8 \cdot 10^4$. This means that for a boundary layer developing in a clean environment (low disturbances), the *transition Reynolds number is higher (and often much higher) than this critical Reynolds number*. Indeed, a common value of the Reynolds number at the onset of transition in wind tunnels is $(R_{\delta_1})_T = 2600$ which corresponds to $R_x = 2.3 \cdot 10^6$. However, with gross disturbances the transition Reynolds number can be lower than the critical Reynolds number; in this case the transition can no longer be studied with the linear stability theory. The stability diagram also shows that for a given Reynolds number only a certain range of waves are unstable. As the Reynolds number increases, the range of amplified frequencies is smaller and smaller. Therefore, viscosity has a destabilizing effect at large Reynolds numbers: the stability is better when viscosity tends to zero.

Figure 49 shows the effect of pressure gradients on the stability diagrams. These results were obtained by solving the Orr-Sommerfeld equation for Falkner-Skan velocity profiles. The neutral curves are given for several basic velocity profiles characterized by the shape parameter. The neutral curve is more opened for positive pressure gradients ($H > 2.59$) and when the Reynolds number tends to infinity the range of unstable frequencies is non-zero: *a positive pressure gradient is destabilizing*. The key feature of the corresponding velocity profile is the presence of an inflection point. If the viscosity is neglected in the Orr-Sommerfeld equation, the Rayleigh equation is obtained:

$$[(\alpha U - \omega)(D^2 - \alpha^2) - \alpha D^2 U] \hat{v} = 0$$

Rayleigh showed that in temporal theory a necessary condition of (non viscous) instability is the existence of an inflection point in the velocity profile. In addition, Tollmien showed that this condition is sufficient for most boundary layer velocity profiles. The solutions of the Orr-Sommerfeld equation

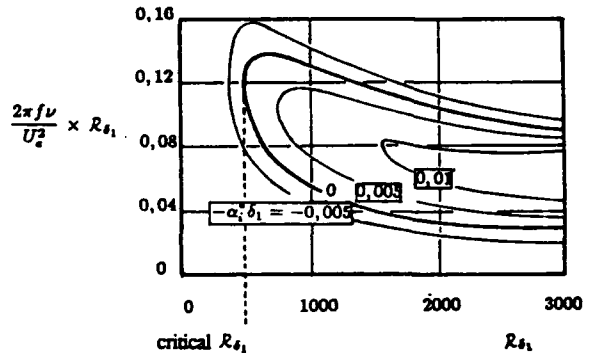


Figure 48: Stability diagram for the flat plate boundary layer. Iso-amplification rate lines (α_i^* is the dimensioned coefficient).

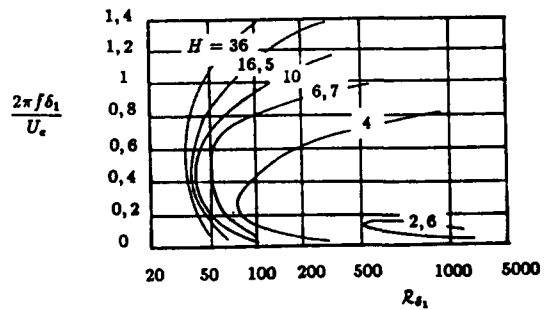


Figure 49: Neutral curves for Falkner-Skan velocity profiles (H is the shape parameter of velocity profiles).

confirm these results and the inflectional instability plays an important role in the stability theory. The stability diagrams (figure 49) show that the critical Reynolds number decreases very much with positive pressure gradient: for the separation velocity profile ($H = 4.029$), we have $(\mathcal{R}_{\delta_1})_{cr} = 67$ whereas for the two-dimensional stagnation point ($H = 2.216$), we have $(\mathcal{R}_{\delta_1})_{cr} = 12490$. Indeed, a negative pressure gradient has a strong stabilizing effect.

7.2.4 Other stability theories

Several theories have been proposed to improve the linear parallel stability theory. For example, the hypothesis of non-parallelism may be discarded (Bouthier [8], Gaster [32], Saric-Nayfeh [63]) by using the technique of multiple scales: a fast scale is used to describe the variations of phase of the waves and a slow scale is used to describe the longitudinal evolution of the amplitude. Other attempts have been proposed to take into account the non-linear effects.

Recently, the method of *parabolic stability equations* has been proposed [35], [71]. This method is very attractive as the effects of non parallelism and non linearity seem to be handled in an efficient way. In this theory, the perturbation of the stream function (in two dimensions) is given in the form:

$$\psi = \Psi(x, y) e^{(\int \alpha(x) dx) - \omega t}$$

Then the stability equation takes the form:

$$[L + L_v] \Psi(x, y) + [M] \frac{\partial \Psi}{\partial x} + [N] \Psi \frac{d\alpha}{dx} = 0$$

where $[L]$ is the Orr-Sommerfeld operator and $[L_v]$, $[M]$ and $[N]$ are other operators introduced by the new decomposition of the perturbation. In particular, $[L_v]$ is associated with the velocity normal to the wall and is zero when the hypothesis of parallel flow is used. Obviously, the stability equation becomes the Orr-Sommerfeld equation when the same hypotheses are introduced.

The main difficulty in this theory is the choice of a hypothesis on $\alpha(x)$ which is needed to solve the stability equation. Several proposals have been studied and the final physical results are not too sensitive to this hypothesis. Comparisons with numerical solutions of the Navier-Stokes equations are very encouraging.

7.3 Prediction of transition

7.3.1 Onset of transition

e^n -method Early transition criteria were based on empirical correlations. As an example, Michel [48] proposed the following criterion:

$$\mathcal{R}_{\delta_T} = 1.535 \mathcal{R}_{\delta_T}^{0.444}$$

where the index T refers to transition location.

To determine the transition with the above criterion, the laminar boundary layer is calculated and gives the evolution $\mathcal{R}_s(\mathcal{R}_x)$. At the origin of the boundary layer, the value of \mathcal{R}_s is lower than the value given by the criterion (for the same value of the Reynolds number \mathcal{R}_x). The onset of transition occurs when the value of \mathcal{R}_s calculated in laminar flow is equal to the value given by the criterion.

At the present time, more elaborated criteria are used. The most popular criterion is the so-called " e^n -method" which was proposed by Van Ingen [79], [80] and Smith and Gamberoni [70]. The principle of this method consists in calculating the total amplification coefficient of a TS wave at a given frequency. This calculation uses the results of stability calculations performed step by step by using the velocity profiles obtained from the laminar boundary layer calculation. If the spatial theory is considered, the total amplification of a wave of given frequency is:

$$\frac{A}{A_0} = e^{\int_{x_0}^x -\alpha_s dx}$$

where x_0 is the location where the wave starts to be amplified (this point is given by the lower branch of the neutral curve).

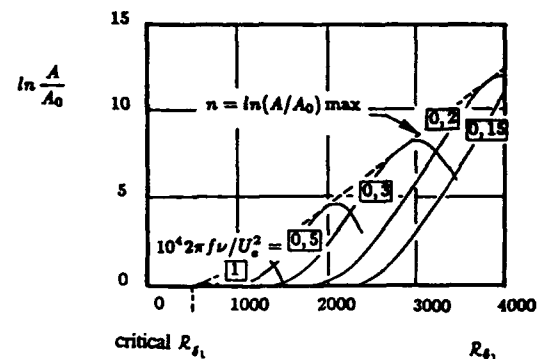


Figure 50: Total amplification curves and their envelope (flat plate boundary layer).

This calculation is performed for all the amplified waves and the factor n is calculated from the envelope of the curves obtained for all these frequencies (figure 50):

$$e^n = \max_f \left(\frac{A}{A_0} \right)$$

Up to this point, all the calculations were performed by using the stability theory. An empirical input is introduced to determine the transition location. As suggested by experimental data, it is assumed that transition occurs when the factor n reaches a critical level n_T . In flight, the critical value is around 10. Mack [46] suggested to take into account the free-stream turbulence by modifying the critical value of

n according to the formula:

$$n_T = -8.43 - 2.4 \ln Tu$$

where the turbulence level Tu is defined as:

$$Tu = \left(\frac{\langle u'^2 \rangle_e + \langle v'^2 \rangle_e + \langle w'^2 \rangle_e}{3U_e^2} \right)^{1/2}$$

The e^n -method is a very efficient engineering tool but it is clear that all the physical processes involved in transition are not included. Real improvements however have not yet been proposed.

The extension of the e^n -method to compressible boundary layers and three-dimensional boundary layers is not straightforward and is discussed by D.Arnal in this Lecture Series.

Data base methods. A practical difficulty with the e^n -method is the computing time necessary to calculate the stability diagrams of the boundary layer. Indeed, the shape of the basic velocity profile varies as the boundary layer develops and it is needed to compute the stability properties at each location.

To reduce the computing time, data base methods have been developed. The principle consists in calculating once and for all the stability diagrams of representative velocity profiles. In incompressible two-dimensional flow, a typical family of velocity profiles is obtained from the Falkner-Skan solutions. These velocity profiles are typical in the sense that even for non-similar flows the shape of velocity profiles is generally well represented by velocity profiles of the Falkner-Skan family. The results of stability calculations performed with the Falkner-Skan solutions are stored in tables or are represented analytically. Essentially, the results of stability calculations are the values of the amplification coefficient for selected frequencies. To be used in the e^n -method, these results are parametrized by suitable parameters which are, for example, the Reynolds number R_s , based on the displacement thickness and the shape parameter H .

7.3.2 Calculation of the transition region

A practical calculation method has been developed by Arnal [3]. The turbulent shear stress is expressed as:

$$-\rho \langle u'v' \rangle = \epsilon \mu_t \frac{\partial U}{\partial y}$$

where the eddy viscosity coefficient is calculated from a mixing length model.

In incompressible flow, the function ϵ is given as a function of the ratio θ/θ_T (figure 51) where θ is the momentum thickness calculated at the current point and θ_T is the momentum thickness calculated at the onset of transition (this point is determined from a transition criterion). The overshoot in the function ϵ has been introduced to reproduce the overshoot

observed experimentally in the evolution of the skin friction.

This method has been extended to supersonic and hypersonic flows by taking into account the lengthening of the transition region. This is done by replacing the parameter $(\theta/\theta_T - 1)$ by $(\theta/\theta_T - 1)/(1 + 0.02M_e^2)$ and the expression of ϵ as a function of this modified parameter remains the same.

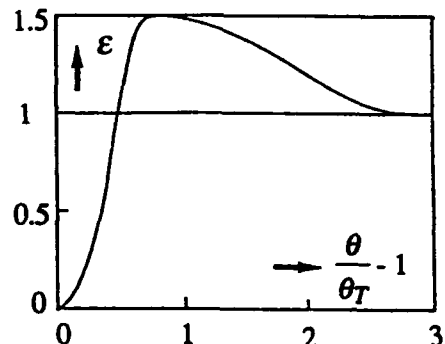


Figure 51: Transition function (from Arnal [3]).

7.4 Three-dimensional effects

Figure 52 shows the location of transition on the lower side of an infinite swept wing as a function of the sweep angle φ for various Reynolds numbers R_{en} , based on the chord length normal to the leading edge. This figure also shows the pressure coefficient reduced by $\cos^2 \varphi$ (for an infinite swept wing this reduced coefficient is independent of the sweep angle).

At low Reynolds numbers, transition is located near the separation point of the laminar boundary layer. At a certain value of the sweep angle, transition moves upstream suddenly near the leading edge. At first glance, this phenomenon is surprising because for higher values of sweep angle, transition occurs in a region of strongly accelerated flow which is known to be very stable in two-dimensional flow. The origin of this transition lies in the amplification of instabilities related to the crossflow which is created in the boundary layer.

This new process of transition is very cumbersome for the design of laminar swept wings. Indeed, these three-dimensional effects must be taken into account very carefully and are extremely sensitive to the sweep angle. It means, in particular, that a good laminar airfoil (in two-dimensional flow) can have very poor laminar properties if it is used with an angle of sweep. An efficient means to delay these types of transition is wall suction through perforated walls.

Another form of transition can occur on a swept wing. The turbulent boundary layer which develops on the fuselage can perturb the boundary layer developing along the leading edge of the wing (see subsection 4.7). Under certain circumstances, the

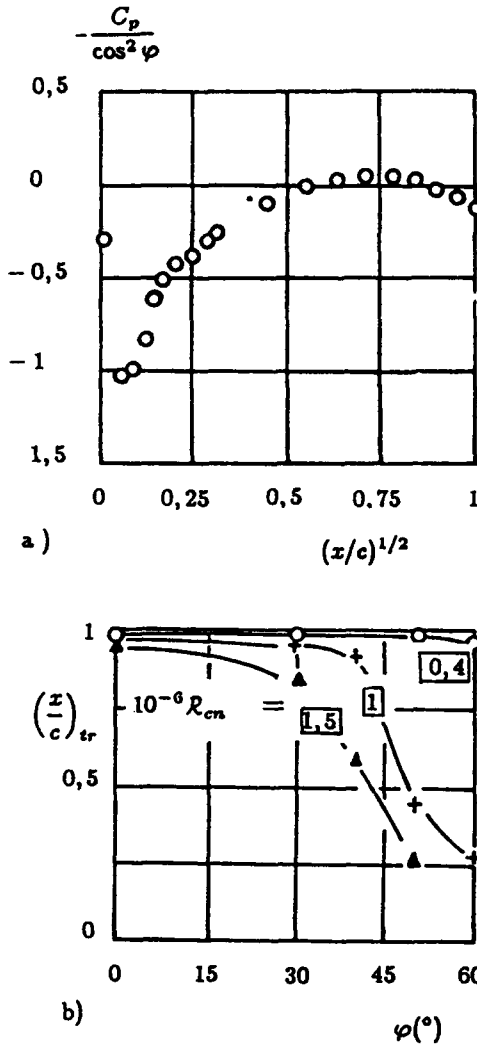


Figure 52: Transition on an infinite swept wing (from Schmitt and Manie [67]).

attachment line boundary layer is turbulent due to the perturbation created by the fuselage boundary layer and the flow on the entire wing can become turbulent. This transition process is called the *leading edge contamination* and occurs if $\bar{R} > 250$ [55] (figure 53), where \bar{R} is defined as:

$$\bar{R} = \frac{W_1}{\nu} \left[\frac{\nu}{\left(\frac{dU_1}{dx} \right)_{x=0}} \right]^{1/2}$$

where x is the coordinate normal to the leading edge and $x = 0$ is the location of the attachment line, U_1 is the component of the inviscid velocity in the x -direction, W_1 is the component of the inviscid velocity along the leading edge.

If the leading edge is a circular cylinder, \bar{R} is given by:

$$\bar{R} = \left[\frac{V_\infty r \tan \varphi \sin \varphi}{\nu} \frac{2}{2} \right]^{1/2}$$

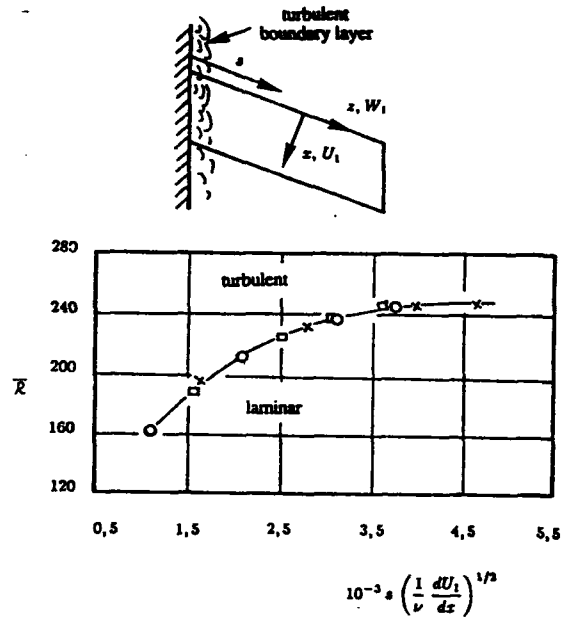


Figure 53: Leading edge contamination (from Poll [56]).

where V_∞ is the free-stream velocity and r is the radius of the cylinder. This formula shows that \bar{R} increases with the sweep angle and with the radius of the leading edge.

Devices such as the Gaster bumps have been proposed to increase the value of \bar{R} for which leading edge contamination occurs. The idea is to create a stagnation point on the bump which is on the leading edge outside the fuselage boundary layer. In this way, a new origin of a laminar boundary layer is created and the contamination is avoided. However, a natural transition can also occur along the leading edge. This means that even if the contamination phenomenon is suppressed, small perturbations can be amplified along the leading edge and transition can take place. Such a natural transition is possible when \bar{R} is larger than about 600.

8 CONCLUSION

A good knowledge of the boundary layer is still today a valuable objective in order to achieve real progress in the design of an aircraft.

Two points deserve to be emphasized.

First, it must be realized that the drag of an airfoil or of a wing must be determined with very good accuracy. A suitable goal would be to know the drag with a relative accuracy of 1%, at least for cruise conditions of a commercial aircraft. To have an idea of the requirements implied by such an accuracy, the flow on a flat plate can be considered. For example, let us assume that the Reynolds number is 10^6 . A variation of transition location corresponding to transition Reynolds numbers of $3 \cdot 10^6$ and $3.5 \cdot 10^6$

represents a variation of the drag of about 5%. With the present knowledges, it seems very difficult to ascertain the location of transition with a better accuracy and therefore the goal of knowing the drag within 1% is not achieved. Moreover, the turbulence models are not accurate enough to calculate the skin-friction with the desired requirements. Another challenge is the prediction of stall. To obtain the stall angle of attack with an accuracy of 1° it is necessary to calculate the boundary layer separation very carefully. Even in incompressible flow, it is a difficult task. In transonic flow, additional complexities are present such as the boundary layer-shock wave interaction.

A second point is to reduce the drag and particularly the skin-friction drag which is a significant part of the total drag of a commercial aircraft. Delaying transition is the most attractive means since reductions in the order of 10 to 15% are expected for a transonic aircraft. The first step to go from a turbulent wing to a first generation laminar wing raises many technological problems, suction for example. However, the transition criteria are not yet completely satisfactory and their link with the physical processes are sometimes questionable. To go beyond, the fundamental knowledge of transition must be improved. For example, the mechanisms of excitation of the laminar boundary layer by the environment need to be understood in a better way. Possibly this progress could improve the control of the laminar boundary layer. The further study of turbulent boundary layers is also interesting. Up to now, the expected reductions are smaller since ripples for example decrease the skin-friction by about 7 or 8%, but these manipulators have been studied in a very empirical manner. It can be hoped that a better understanding of turbulence mechanisms will give new ideas to reduce the turbulent skin-friction drag. The control of separation or of vortical flows are other fields (fundamental and applied) where a good knowledge of turbulence is needed.

To achieve the two objectives given above, fundamental studies on transition and on turbulence are required but engineering tools such as transition criteria or turbulence models are the most useful tools for practical applications. A large gap often exists between these two fields. For example, people who are working on turbulent structures recognition and those who are working on turbulence models seem to belong to two different worlds. A better link between these distinct fields is certainly a valuable research axis for the future.

Acknowledgments

I wish to thank D. Arnal and Y. Maciel for their very detailed reviews of this paper and for the time they spent to do this work.

References

- [1] D. Arnal. Description and prediction of transition in two-dimensional incompressible flow. Report 709, AGARD, 1984. Special Course on Stability and Transition of Laminar Flow.
- [2] D. Arnal. Three-dimensional boundary layers : Laminar-turbulent transition. Report No 741, AGARD, 1986. Special Course on Computation of Three-Dimensional Boundary Layers Including Separation.
- [3] D. Arnal. Laminar-turbulent transition problems in supersonic and hypersonic flow. Report No 761, AGARD, 1988. Special Course on Aerothermodynamics of Hypersonic Vehicles.
- [4] D. Arnal, J. Cousteix, and R. Michel. Couche limite se développant avec gradient de pression positif dans un écoulement turbulent. *La Rech. Aéronaut.*, 1976-1, 1976.
- [5] D. Arnal and J.C. Juillen. Etude expérimentale et théorique de la transition de la couche limite. *La Rech. Aéronaut.*, 1977-2, 1977.
- [6] H. Blasius. Grenzschichten in Flüssigkeiten mit kleiner Reibung. *Z. Math. u. Phys.*, 56:1-37, 1908. English translation in NACA TM 1256.
- [7] J. P. Bonnet. Comparison of computation with experiments - Summary report. In S. J. Kline, B. J. Cantwell, and G. M. Lilley, editors, *Volume III - Comparison of Computation with Experiment, and Computers' Summary Reports*, pages 1408-1410. 1980-81 AFOSR-HTTM-Stanford Conference on Complex Turbulent Flows, 1981.
- [8] M. Bouthier. Stabilité linéaire des écoulements presque parallèles. *Jour. de Mécanique*, 11, 1972.
- [9] P. Bradshaw, D.H. Ferriss, and N.P. Atwell. Calculation of boundary layer development using the turbulent energy equation. *Jour. of Fluid Mech.*, 28:593, 1976.
- [10] P. Bradshaw and N.S. Pontikos. Measurements in the turbulent boundary layer on an infinite swept wing. *Jour. of Fluid Mech.*, 159:105-130, 1985.
- [11] G.L. Brown and A.S.W. Thomas. Large structures in a turbulent boundary layer. *Phys. of Fluids*, 20(10, Part II):S243-S252, 1977.
- [12] T. Cebeci and A.M.O. Smith. *Analysis of Turbulent Boundary Layers*. Academic Press, 1974.
- [13] D.R. Chapman. Computational aerodynamics development and outlook. *AIAA Journal*, 17(12), 1979.

[14] K.Y. Chien. Predictions of channel and boundary layer flows with a low Reynolds number turbulence model. *AIAA Journal*, 20(1):33-38, January 1982.

[15] J.W. Christian, W.L. Hankey, and J.S. Petty. Similar solutions of the attached and separated compressible laminar boundary layer with heat transfer and pressure gradient. Technical Report 70-0023, Aerospace Research Laboratories, 1970.

[16] C.B. Cohen and E. Reshotko. Similar solutions of the attached and separated compressible laminar boundary layer with heat transfer and pressure gradient. Report 1294, NACA, 1956.

[17] C. Corke, Y. Guézennec, and H.M. Nagib. Modification in drag of turbulent boundary layers resulting from manipulation of large scale structures. In G.R. Hough, editor, *Progress in Astronautics and Aeronautics*, volume 72. AIAA, 1980.

[18] J. Cousteix. *Couche Limite Laminaire*. Cepadues-Editions, 1988.

[19] J. Cousteix. *Turbulence et Couche Limite*. Cepadues-Editions, 1989.

[20] J. Cousteix, D. Arnal, B. Aupoix, and C. Gleyzes. Recent studies on transition and turbulence at ONERA-CERT aiaa 91-0332. In *29th Aerospace Sciences Meeting*, Reno, Nevada, January 1991. AIAA.

[21] J. Cousteix, B. Aupoix, and G. Pailhas. Synthèse de résultats théoriques et expérimentaux sur les couches limites et sillages turbulents tridimensionnels. Note Technique 1980-4, ONERA, 1980.

[22] J. Cousteix and G. Pailhas. Etude exploratoire d'un processus de transition laminaire-turbulent au voisinage du décollement d'une couche limite laminaire. *La Rech. Aérosp.*, 1979-3, 1979.

[23] J.B. Daly and F.H. Harlow. Transport equations in turbulence. *Phys. of Fluids*, 13:2634, 1970.

[24] C. du P. Donaldson. A progress report on an attempt to construct an invariant model of turbulent shear flows. CP 93, AGARD, 1971.

[25] J. P. Dussauge and C. Quine. A second-order closure for supersonic turbulent mixing flows - Application to the supersonic mixing. In *The Physics of Compressible Turbulent Mixing*. Princeton University, New Jersey, Lecture Notes in Physics - Springer Verlag, October 1988.

[26] L.F. East. Measurements of the three-dimensional incompressible turbulent boundary layer induced on the surface of a slender delta-wing by the leading-edge vortex. RM 3768, ARC, 1973.

[27] V.M. Falkner and S.W. Skan. Some approximate solutions of the boundary layer equations. Technical Report 1314, ARC RM, 1930.

[28] A. Favre and J. Gaviglio. Turbulence et perturbations dans la couche limite d'une plaque plane. Report 278, AGARD, 1960.

[29] A. Favre, J. Gaviglio, and R. Dumas. Further space-time correlations of velocity in a turbulent boundary layer. *Jour. of Fluid Mech.*, 3:344, 1958.

[30] A. Favre, L.S.G. Kovasznay, R. Dumas, J. Gaviglio, and M. Coantic. *La Turbulence en Mécanique des Fluides*. Gauthier-Villars, 1976.

[31] M. Gaster. A note on the relation between temporally increasing and spatially increasing disturbances in hydrodynamic stability. *Jour. of Fluid Mech.*, 14, 1962.

[32] M. Gaster. On the effect of boundary layer growth in flow stability. *Jour. of Fluid Mech.*, 66, 1974.

[33] H.T. Grant. The large eddies of turbulent motion. *Jour. of Fluid Mech.*, 4:149, 1952.

[34] K. Hanjalić and B.E. Launder. A Reynolds stress model of turbulence and its application to thin shear flows. *Jour. of Fluid Mech.*, 52(Part 4), 1972.

[35] Th. Herbert. Boundary layer transition - Analysis and prediction revisited aiaa 91-0737. In *29th Aerospace Sciences Meeting*, Reno, Nevada, January 1991. AIAA.

[36] J.O. Hinze. *Turbulence*. Mc Graw Hill, 1975.

[37] W.P. Jones and B.E. Launder. The prediction of laminarization with a two-equation model of turbulence. *Int. Jour. of Heat and Mass Transfer*, 15(2), 1972.

[38] P.S. Klebanoff. Characteristics of turbulence in a boundary layer with zero pressure gradient. TM 3178, NACA, 1954.

[39] C.F. Knapp, P.J. Roache, and T.J. Mueller. A combined visual and hot wire anemometer investigation of boundary layer transition. TR 866 CK, UNDAS, 1966.

[40] B.E. Launder. A generalized algebraic stress transport hypothesis. *AIAA Jour.*, 20(3), 1982.

[41] B.E. Launder, G.J. Reece, and W. Rodi. Progress in the development of a Reynolds stress turbulence closure. *Jour. of Fluid Mech.*, 20(3), 1975.

[42] J.C. Le Balleur. Calcul par couplage fort des écoulements visqueux incluant sillages et décollements. *La Recherche Aérospatiale*, 1981-3, 1981.

[43] M. Lesieur. *Turbulence in Fluids. Stochastic and Numerical Modelling*. Martinus Nijhoff, 1987.

[44] J.L. Lumley. Prediction methods for turbulent flows. Introduction. VKI Lecture Series 76, 1975.

[45] J.L. Lumley. Computational modelling of turbulent transport. *Adv. Appl. Res.*, 1978.

[46] L.M. Mack. Boundary layer linear stability theory. Report 709, AGARD, 1984. Special Course on Stability and Transition of Laminar Flow.

[47] G.L. Mellor. The large Reynolds number asymptotic theory of turbulent boundary layers. *Int. J. Eng. Sci.*, 10:851-873, 1972.

[48] R. Michel. Détermination du point de transition et calcul de la traînée des profils d'aile incompressible. Publication 58, ONERA, 1952.

[49] R. Michel, C. Quémard, and R. Durant. Application d'un schéma de longueur de mélange à l'étude des couches limites d'équilibre. Note Technique 154, ONERA, 1969.

[50] C.B. Millikan. A critical discussion of turbulent flow in channels and circular tubes. In *Fifth International Congress on Applied Mechanics, Cambridge, Mass.*, pages 386-392. Wiley, N.Y., 1938.

[51] A.S. Monin and A.M. Yaglom. *Statistical Fluid Mechanics*. MIT Press, 1975.

[52] M.V. Morkovin. Effects of compressibility on turbulent flows. In CNRS, editor, *Mécanique de la turbulence*, 1961. Colloque International CNRS No 108.

[53] L. H. Norris and W. C. Reynolds. Turbulent channel flow with a moving wavy boundary. Report FM-10, Department of Mechanical Engineering Stanford University, Stanford, California, 1975.

[54] D. Papamoschou and A. Roshko. The compressible turbulent shear layer : An experimental study. *Journal of Fluid Mechanics*, 197:453-477, 1988.

[55] W. Pfenninger. Flow phenomena at the leading edge of swept wings. In *Recent Developments in Boundary Layer Research - AGARDograph 97, Part IV*, May 1965.

[56] D.I.A. Poll. Transition description and prediction in three-dimensional flows. Report 709, AGARD, 1984. Special Course on Stability and Transition of Laminar Flow.

[57] R. Purtell, P.S. Klebanoff, and F.T. Buckley. Turbulent boundary layers in incompressible flows. *Phys. of Fluids*, 24(5), 1981.

[58] W.C. Reynolds. Fundamentals of turbulence for turbulence modelling and simulation. Report 755, AGARD, 1987.

[59] S.K. Robinson. Coherent motions in the turbulent boundary layer. *Ann. Rev. Fluid Mech.*, 23:601-639, 1991.

[60] S.K. Robinson, S.J. Kline, and P.R. Spalart. Quasi-coherent structures in the turbulent boundary layer : Part ii. verification and new information from a numerically simulated flat plate boundary layer. Zoran P. Zarić Memorial International Seminar on Near Wall Turbulence, Dubrovnik, 1988.

[61] W. Rodi. *The Prediction of Free Boundary Layers by use of a Two-Equation Model of Turbulence*. PhD thesis, University of London, 1972.

[62] P.G. Saffman and D.C. Wilcox. Turbulence model prediction for turbulent boundary layers. *AIAA Journal*, 12(4), 1972.

[63] W.S. Saric and A.H. Nayfeh. Non parallel stability of boundary layer flows. *Phys. Fluids*, 18, 1975.

[64] S. Sarkar and L. Balakrishnan. Application of Reynolds stress turbulence model to the compressible shear layer. Report 90-18, ICASE, 1990.

[65] G. Schewe. On the force fluctuations acting on a circular cylinder in crossflow from subcritical up to transcritical Reynolds number. *Jour. Fluid Mech.*, 133:265-285, 1983.

[66] H. Schlichting. *Boundary Layer Theory*. McGraw Hill, 1968.

[67] V. Schmitt and F. Manie. Ecoulements subsoniques et transsoniques sur une aile à flèche variable. *La Rech. Aéosp.*, 1979-4, 1979.

[68] G.B. Schubauer and P.S. Klebanoff. Contribution on the mechanics of boundary layer transition. Report 1289, NACA, 1956.

[69] G.B. Schubauer and H.K. Skramstad. Laminar boundary layer oscillations and transition on a flat plate. Report 909, NACA, 1948.

[70] A.M.O. Smith and N. Gamberoni. Transition, pressure gradient and stability theory. Report ES 26 388, Douglas Aircraft Co., El Segundo, Calif., 1956.

- [71] R.E. Spall and M.R. Malik. Görtler vortices in supersonic and hypersonic boundary layers. *Phys. Fluids A*, 1(11):1822-1835, November 1989.
- [72] K. Stewartson. Further solutions of the Falkner-Skan equation. *Proc. Camb. Phil. Soc.*, 50:454-465, 1954.
- [73] H. Tennekes and J.L. Lumley. *A First Course in Turbulence*. MIT Press, 1972.
- [74] A.A. Townsend. *The structure of Turbulent Shear Flows*. Cambridge University Press, 1976.
- [75] B. van den Berg. A european collaborative investigation of the 3d turbulent shear layers of a swept wing. CP 438, AGARD, 1988.
- [76] B. van den Berg, A. Elsenaar, J.P.F. Lindhout, and P. Wesseling. Measurements in an incompressible three-dimensional turbulent boundary layer under infinite swept wing conditions and comparison with theory. *Jour. of Fluid Mech.*, 70:127-149, 1975.
- [77] E.R. van Driest. On turbulent flow near a wall. *Jour. of Aeronaut. Sci.*, 23:1007, 1957.
- [78] M. van Dyke. *Perturbations in Fluid Mechanics*. The Parabolic Press, Stanford, California, 1975.
- [79] J.L. van Ingen. A suggested semi-empirical method for the calculation of the boundary layer transition region. Report UTH-34, Univ. of Technology, Dept. of Aero. Eng., Delft, 1956.
- [80] J.L. van Ingen. Transition, pressure gradient, suction, separation and stability theory. CP 224, AGARD, 1977.
- [81] D. Vandromme and H. Ha Minh. Turbulence modeling for compressible flows. In *Introduction to the Modeling of Turbulence*. VKI Lecture Series 1987-06, May 18-20 1987.
- [82] K.S. Yajnik. Asymptotic theory of turbulent shear flows. *J. Fluid Mech.*, 42 Part 2:411-427, 1970.
- [83] O. Zeman. Dilatation dissipation : The concept and application in modeling compressible mixing layers. *The Physics of Fluids A*, 2(2):178-188, February 1990.

**DRAG REDUCTION: An Industrial Challenge**

by J.P. Robert

Advanced Aerodynamics Manager

AIRBUS INDUSTRIE

1. INTRODUCTION

Over the last few decades and particularly since the 70s, all civil aircraft manufacturers have made great efforts to reduce aircraft drag. The long term aim of this operation is to reduce the specific consumption of aircraft, the potential reduction of over 10 % would represent savings of several million dollars for the airlines (fig. 1). The successive fuel crises (fig. 2) have increased the need for developing new technologies to be applied on the new aircraft; retrofits, however, also have their uses.

Estimating the drag of a transport aircraft through calculation or wind tunnel tests must come as close as possible to the value obtained in flight. Forecast errors to the order of 1 % following wind tunnel/flight transposition lead to technical and financial penalties and entail vast efforts to bring the values obtained during flight down to acceptable levels guaranteed by the aircraft manufacturers to their customer airlines.

The technologies or concepts that could significantly reduce aircraft drag often have a different reduction potential. This reduction must be clearly shown to appear in the high speed tests using large-scale models (~ 1/10 scale). Scale models of this type do not provide the Reynolds numbers corresponding to the flight and this leads to wind tunnel/flight corrections that make it extremely difficult to extrapolate flight results from wind tunnel results. In some cases these corrections may be as high as 20 %.

The various drag sources vary according to the type of aircraft and the type of flight mission.

The different contributions (fig. 3) may be summed up as follows:

- . Induced drag
- . Friction drag
- . Drag due to interference between two elements
- . Wave drag
- . Parasitic drag

92-17807
A standard 1D barcode is positioned below the document number.

The proportion of each drag source may vary according to the type of aircraft, but the source breakdown (fig. 4) clearly shows the proportions of the various sources of drag for subsonic aircraft currently in operation. The two main sources of drag that can account for more than 80 % of total drag are friction and induced drag (fig. 3). Apart from these two important sources of drag, the other contributors such as parasitic, wave and interference drag should not be overlooked and they can frequently be considerably reduced. This paper aims to sum up the main technologies developed in order to reduce the contribution from each source, and particularly from friction drag.

Aircraft manufacturers in association with research organizations invest a great deal of effort in finding and applying new technologies. Although the underlying concept may be easy to demonstrate, the flight test phase which is compulsory for all manufacturers must show a real saving in fuel consumption and this will be taken into account in assessing the aircraft performance. In most cases, the point of view put forward may be taken to be that of any aircraft manufacturer but certain programmes specific to AIRBUS INDUSTRIE will be mentioned and then explained.

2. FRICITION DRAG

There are various methods for reducing an aircraft's friction drag but two are currently getting the particular attention of aircraft manufacturers.

- 1) The transition point on a surface, particularly on an aircraft wing, should be moved as far aft as possible (fig. 5) in order to obtain lower friction coefficient (C_f) (fig. 6) values (in the presence of laminar flow) and by increasing the proportion of surface with laminar flow.
- 2) Modifying the turbulent structures in the boundary layer to significantly reduce the value of the turbulent friction coefficient (C_f).

Friction drag has two important generators, wings and fuselage; these together account for over 80 % of the total friction drag.

So we should carefully consider all the industrial possibilities that could be called on to significantly reduce this friction drag in cruise without penalizing overall aircraft topics such as:

- . Performance (take-off, landing)
- . Weight
- . Cost

- . Maintenance
- . Safety
- . etc...

2.1 Laminarity

Several concepts relating to laminarity are being researched but their application is closely connected to the sweep and Reynolds number of the wings. Transition on such a surface is a function of the instabilities and the contamination encountered and these are of several types:

- . Streamwise instability
- . Cross flow instability
- . Leading edge contamination

Streamwise instability is caused by amplification of the Tollmien Schlichting waves and is responsible for transition when the sweep angle (Φ) is less than 25° (fig. 7).

Cross flow instability has its origin in high cross flow ($\Phi > 25^\circ$), which makes high level Reynolds numbers the first cause of transition. This instability develops around the leading edge, where acceleration is high (fig. 7).

Leading edge contamination is the third cause of transition, and by no means the least. This contamination is due to propagation of disturbance from a fuselage boundary layer (fig. 8). The intensity of such disturbance is closely linked to the sweep angle and the local Reynolds numbers under consideration. It can be assessed using the \bar{R} criterion, $\bar{R} = \left[\frac{U_\infty \cdot r}{\gamma} \frac{b \cdot \sin \Phi}{2} \right]^{\frac{1}{2}}$

The three sources of transition are frequently found together and they prematurely trigger transition near the leading edge. According to the type of aircraft design and flight conditions (Mach, Φ , Re) several methods can be considered in order to move the transition point rearwards. If the sweep angle is less than 17° and this is the case with small or business type aircraft, it is possible to define wings with optimized pressure gradients that help to move the transition point as far aft as possible. This method is called Natural Laminar Flow (NLF) (fig. 9).

If the sweep angle and the Reynolds numbers have high levels as for the current subsonic aircraft (A310, A320, etc.) in order to maintain laminar flow on the wings it is necessary to set

up a suction system over the entire surface area or near the wing profile leading edge. This technique is called "Laminarity Flow Control", that is, "LFC". A combination of the two approaches is Hybrid Laminar Flow Control (HLFC) (fig. 10).

2.1.1 Natural Laminar Flow (NLF)

This is a passive technique that uses optimized pressure gradients to maintain laminar flow over a large part of the wings. To obtain these results, maximum profile thickness must be as far away as possible but we know that such pressure gradients lead to high intensity shocks and high wave drag. In this particular case of natural laminarity, structural weight penalties must be taken into account with the knowledge that for low speed performance of this type of laminar wing design it is not possible to envisage an high lift system (slats or Kruger). The challenge is to design wings maintaining natural laminarity with a high performance level (as, for example, the Mach number). The Mach number effect frequently increases the sweep angle which is contrary to the application of this technology.

The general research taking into account all the constraints due to the introduction of this technology has been performed frequently, especially in Europe. Only **true savings**, including the **effect of the system for cleaning the leading edge required to combat insect contamination, ice formation, and the production costs of such wings will produce tangible benefits where the D.O.C is concerned.**

2.1.2 Laminarity controlled by suction

a) Laminar Flow Control (LFC)

The solution frequently adopted in order to suppress the effects of the cross flow instability concerns suction of the boundary layer. Where LFC technology is concerned, suction makes it possible to maintain laminar flow. **The entire profile, as far as the eventual transition point must have a porous surface, enabling suction.** In this particular case, suction modifies the velocity profile of the boundary layer, which has the effect of significantly reducing the local skin friction coefficient, in some cases it is reduced by more than 10 %. This technique requires a very fine definition of the wing profile. The results obtained depend very much on the state of the surface and on the absence of contamination by insects and dust.

Correct prediction of the transition point during flight is the manufacturers' prime task but the complexity of the suction and cleaning system that has to be integrated into the wing design (wing spar box) is also of concern. The high maintenance costs the airlines have to pay and the energy necessary for the suction system make this technology, developed by

Douglas in the 1970s, unattractive.

b) Hybrid Laminar Flow Control (HLFC)

Hybrid laminar flow control is an ingenious compromise between Natural and Controlled laminarity. This compromise makes it possible to do away with the disadvantages of the two technologies described above. By means of suction in the area between the first 15-20 % of the chord and a favorable pressure gradient as for NLF, the effects of cross flow instabilities are minimized and a natural laminar flow may then develop in the mid-part of the wing profile (fig. 11).

Various stages must first be successfully completed at the pre-project level on a subsonic aircraft flying at a high Mach number (.8 < Mach < .9):

- . determination of the plan form, sweep angle, and wing profile
- . determination of the type of suction (hole or slit)
- . position of transition on the wings
- . acceptable solution, to prevent contamination (ALT)
- . definition of an efficient anti-icing and high lift system
- . effect of propulsion noise

However, such aerodynamic and system constraints should not overshadow the problems relating to the production of such a wing system. The following, in particular, should be borne in mind:

- . manufacturing tolerances
- . roughness compatible with a laminar flow
- . complexity of the suction system

Various programmes are underway in Europe and in the United States, but whatever the position of one programme in relation to the other, the problems existing and the proposed solutions are concordant. To examine this aspect more closely it is necessary to review the problems raised by the development of this particular technology.

Aerodynamics

This section deals with configuration and the definition process (design).

CFD methods must be developed and the transition criteria used in these methods must be validated for high Reynolds numbers (to the order of 30 to $60 \cdot 10^6$). The advantage inherent to these methods is that they will make it possible to considerably reduce the wind tunnel

hours. Once these methods have been validated, a more accurate prediction of transition will be possible and an error of a few percent on transition location (5 %) will have a significant repercussion on total drag. The methods used can only correctly predict the transition point (effect of suction on longitudinal and cross flow instabilities) if the problem of leading edge contamination (ALT) has been solved (fig. 12).

Wind tunnel tests - The Reynolds number effect is far from negligible and it is therefore necessary to use wind tunnels capable of producing a significant Reynolds effect, i.e. highest possible Re.

Currently, many tests are performed on full and 1/2 scale models in the large ONERA wind tunnel at Modane (S1 MA). This wind tunnel is wide enough (dia. 8 m in the test section) to test large wing sections at high speeds. It will be possible to insert a representative suction system in the leading edge of these large scale models. The Reynolds numbers obtained in this type of testing are never representative of the Reynolds numbers obtained in flight. Therefore Airbus Industrie has set up a long term laminarity programme and has suggested calculation codes should be validated on a large scale A320 vertical stabilizer (fig. 13) rather than on a smaller scale wing.

In this case the Reynolds number problem would be solved since the A320 1/2 scale fin model achieves a Reynolds number of 24.10^6 which is exactly that obtained during flight.

Using a cryogenic wind tunnel often makes it possible to obtain Reynolds numbers valid for flight whilst using slightly smaller models. What effect might a pressurized cryogenic wind tunnel have on a thin and perforated surface ? Various problems remain unsolved. There are real difficulties in correctly measuring or comparing aerodynamic loads, stability, fluttering, and the aircraft's real performance. Correct prediction of all these parameters in a wind tunnel is not easy; it should be done in the form of 2 and 3D wind tunnel-flight transpositions and comparisons. Wind tunnel tests must allow determination of the aerodynamic characteristics of a laminar aircraft once it has lost its laminarity.

Flight testing should allow validation of all these results, and numerous flight test hours should prove the merits of laminarity. CFD and wind tunnel results must be validated.

Performance

Obviously, although cruise performance remains the principle objective, low speed and "off design" performance must nevertheless be studied.

Using a perforated leading edge makes it difficult to envisage the use of a slat which is necessary for low speed performance (fig. 14).

There are two possible solutions:

- . a wing with a fixed leading edge but without a high lift system
- . a wing with a fixed leading edge, fitted with a "Kruger" or shield-type system.

In the first case it is not realistic to suggest an aircraft without any lift augmentation system. The increase (30%) in the wing surface area that would make it possible to land with a reasonable V_{app} (~ 70 m/s) is not feasible since there would be a considerable weight and drag penalty.

In the second case, it is necessary to clearly define the function of the system proposed:

- . The "shield" makes it possible to deviate the trajectory of any particles (dust, insects, etc.) on landing or at take-off. It can also contain a cleaning system for cleaning the leading edge with a specific fluid.
- . The Kruger cannot have the same positions as a slat. Performances are different, for example, drag on take-off will be higher. It is doubtful whether it is possible to achieve acceptable CL_{max} levels for landing. The complexity of the various Kruger systems currently in use (variable camber Kruger-VCK ; fixed Kruger) cannot really recommend them since they lead to a decrease of performances and to resistance on the part of users.

Anti-icing system

Anti-icing is a prime concern in the development of a laminar wing system. Currently, the anti-icing systems most commonly used on commercial aircraft function on a basis of very hot air (200 °C) circulating within the slats (fig. 15).

Using a fixed and porous leading edge raises several problems. Possible solutions would be: Blowing hot air through suction holes. Is it possible, however, to envisage a multi-function system (suction and fan-blower) where the suction system must obviously be entirely sealed.

This immediately raises the following questions or remarks:

- Can the system function in two ways, without having to be made far more complex?
- Can the system function correctly at a temperature of 200 °C and over?
- The system must function correctly during all flight phases (climb, descent, cruise).
- Concerning the use of a shield during take-off and landing, the system could be equipped with a special fluid. This system would not work, however, at high speeds and a further system for cruise conditions would have to be developed.
- The use of an integrated anti-icing system has never been envisaged with Kruger.

In general, anti-icing remains an acute problem. Research is underway to define, study and test a new anti-icing system for laminarity application.

The anti-icing problem cannot be shelved and it will be taken into account during the A320 fin flight tests, if possible.

Wing/engine interference

The development of large diameter engines (HBPR) such as the GE90 requires an engine installation system different to that used for a CF6 or PW4000-type engine.

The nacelle could be at the wing level and this could suppress the high lift system in the affected wing section, it would also lead to a different pressure distribution pattern. Insect contamination on the wings could become a very real problem and a special anti-icing and cleaning system would have to be developed for this particular part of the wings.

2.1.3 Conclusions

Development of such laminar flow technology requires a great deal of perseverance (fig. 16). A lot of numbers of flight tests would be necessary before this technology could be introduced to the airlines. The real advantages must be made clear to future users, not only in terms of fuel burn reduction but taking into account problems such as:

- System reliability in order to have minimum breakdown incidents during flight,
- Reduced complexity to ensure minimum maintenance
- Normal operational use without any special attention during take-off or landing in cloudy conditions or in rainy weather.
- Laminarity control during flight, in order to correctly assess the quantities of fuel necessary for the flight.
- The high production costs of such a wing system. For example, to have a laminar upper surface it must not have any roughness greater than 0.1mm.
- Wing reinforcement problems, above each engine, and problems caused by adding performance systems such as strakes, vortex generators, fence, etc.

Finally, the laminar parts of the wing would have to be very clearly defined.

Surely the only possible part of the wing system will be the upper surface. For aerodynamic reasons (contamination due to fuselage boundary layer, high deviation, CL_{max} , etc.) the inboard part of the wing (from the fuselage to the first engine) might be also excluded.

An industrial prototype using the HLFC concept should be rapidly launched by manufacturers. Solving the technical problems and achieving reasonable costs constitute a challenge

for these manufacturers who will have to convince the airworthiness authorities of the feasibility of the project before we convince the airlines.

2.2 Friction drag during turbulence

A further method of significantly reducing friction drag has been studied at length by all the manufacturers. Separate programmes have been launched concerning two different technologies: Ripples and LEBU.

2.2.1 Ripples

In order to modify the sub-layer of a boundary layer, the effect of very fine grooves (fig. 17) (a few microns high) has been tested in wind tunnels. Results showed a significant reduction of between 7 and 8 % (fig. 18), but since the cause is not fully known, riblet studies have remained at the experimental stage.

Airbus Industrie's programme comprises several stages:

- . Transonic pod test in T2 ONERA-Cert
- . Wind tunnel tests on A320 model at S1 (Modane)
- . Flight tests on the A320 A/C 1
- . Industrialization studies

Two parameters are used to define the riblet size: H^+ and S^+ , the value $H/S = 1$ is apparently more productive. In all cases the most optimistic values of H^+ are around $10 < H^+ < 12$ (fig. 19).

The transonic pod tests were performed in the ONERA-CERT T2 cryogenic wind tunnel. The pod was fitted with internal scales. A 3M riblet film was applied to the cylindrical part of the model.

T2 tests confirmed the improved results and showed a reduction in drag even when the riblet direction was different to that of the flow ($\Phi < 20^\circ$) (fig. 20).

The wind tunnel tests on the A320 model (February 1989) showed an identical skin friction reduction at $M = 0.78$. The wind tunnel Reynolds number obtained during the tests was lower than that obtained during flight. A full A320 model was used at a scale of 1/11. With 70 % of the surface covered in riblet film a saving of 1.5 % was noted at cruise Mach number.

The flight tests on the A320 A/C 1 were performed in October 1989. Approximately 75 % of the wetted surface was covered in 3M riblet film. Size (H^+ , S^+) being optimized for cruise flight at $M = 0.78$ but tests at different Mach numbers and C_L were performed (fig. 21). The aircraft was fitted with boundary layer rakes on the fuselage, a wake rake and a moving system for measuring the boundary layer at the forward part of the fuselage during flight.

The numerous measurements during flight were made with and without riblet film. The objective of this programme was to:

- . Assess the real saving in consumption
- . Assess the reduction in local friction drag (C_f)
- . Identify the effect of riblets on buffet onset and on C_L max.

Results obtained during flight indicate an average saving of 1.5 % (fig. 22).

Industrialization - Several problems must be solved before a proposal can be made to the airlines.

- . Visual detection of cracks in the structure and skin,
- . Areas where the film is in contact with skydrol must be accurately defined, the fluid rapidly corrodes both paint and the film.
- . Acceptable installation and removal times must be achieved. Airbus Industrie and 3M has defined a technique that has cut down 3M's first assessment by 10. Concerning removal, aquastripping seems the most suitable technique.
- . Aircraft maintenance frequently involves minor repairs and it will probably be necessary during maintenance to remove a few square metres of film.
- . It is necessary to thoroughly understand the behaviour of the riblet geometry over a 6 year period (fig. 23) which represents the time between repainting aircraft. Tests are currently being performed on the A320 which has not been repainted and cleaned for more than 2 years and still has its riblet film, unaffected.

Conclusions

Although the aerodynamic advantage procured by riblets has been clearly demonstrated, a few problems relating to industrialization still remain to be solved. A programme of industrial assessment is currently underway and should make it possible to conclude on the utility of this technology.

An application of film restricted to the wing upper surface, horizontal stabilizer and the upper

part of the fuselage (i.e. above the windows) would lead to a saving of approximately 1 % in fuel burn on a long haul type aircraft.

2.2.1 LEBU

Large eddy break up (LEBU) depends on small profiles distributed in the boundary layer. These structures act on any large eddies. Studies have been initiated to determine their optimum height (H) in the boundary layer. Results of studies performed at CEAT Poitiers show an optimum with $H/S = 0.8$ (fig. 24).

Results obtained at transonic flow ($M = 0.75$) show a saving of the order of 15 % on the local C_d . This reduction, however, is highly limited over a short distance (30S).

The conclusions drawn from these LEBU studies are not very optimistic taking into account LEBU drag support and the structure necessary. The overall aerodynamic breakdown does not show any significant saving. Installation of these profiles on a fuselage would lead to a lot of problems: flight vibrations and optimization at the various C_L encountered.

4. CONCLUSIONS

Many solutions have been put forward in order to reduce an aircraft overall drag. The potential for reducing drag is real but demonstration of the saving in terms of fuel burn is very difficult.

- . A manufacturer's prime concerns are to correctly predict aircraft drag levels in flight and to examine all possibilities for reducing drag.
- . It should not be forgotten that calculation methods cannot currently predict drag accurately. With atmospheric wind tunnels (such as the Modane S1) results must be corrected in order to predict the (L/D) efficiency of the aircraft when cruising.
- . It is in the manufacturers' interests to promote ideas and check their validity. Research should concentrate on achieving significant reductions in drag (e.g. the HLFC concept). They should take particular care to assess consumption savings and eventual penalties concerning weight, cost, etc. linked to such technologies bearing in mind that in order to convince airlines extra cost of the aircraft must often be recovered during the first or second year of operation.

Among the many difficulties (fig. 25):

- Although results may be shown in 2D tests, transposing them to 3D flow is often uncertain and sometimes impossible today.
- Industrialization of certain concepts often seems highly problematical.
- The overall analysis (e.g. in the case of LEBU) often shows that reduction of the friction coefficient (C_f) implies penalties in other areas such as higher drag (friction drag) or greater weight.

Drag reduction remains a permanent concern for manufacturers whose aim is to offer the best possible product to the airlines.

Effect of laminarity on cost saving

Influence of 1% fuel burn saving

AC type	Range (km)	Flight time (year)	Fuel burn saving 1AC-1 year	Fuel burn saving 20 A320 or 10 A340	Fuel burn saving 15 year	Cost saving %
A320	500	2175	70 L	1400 L	21 000 L	3.5 (1) 7.0 (2)
	2000	802	84 L	1680 L	25 200 L	4.2 (1) 8.4 (2)
A340	3000	657	220 L	2200 L	33 000 L	5.5 (1) 11.0 (2)
	6000	400	310 L	3100 L	46 500 L	7.8 (1) 15.6 (2)

(1) 0.5 %USG
(2) 1.0 %USG

Fig.1

Average world price evolution

Constant 1998 US dollars

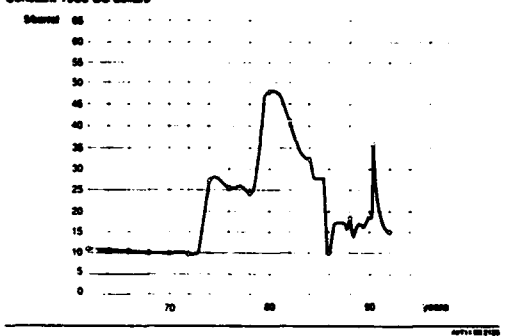


Fig.2

Aircraft drag breakdown

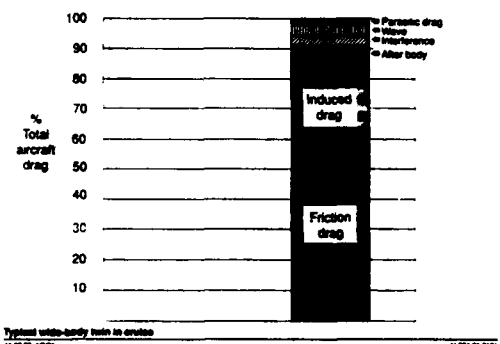


Fig.3

Aircraft skin friction drag breakdown

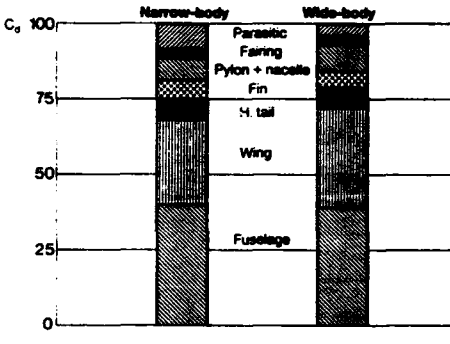


Fig.4

Laminar flow

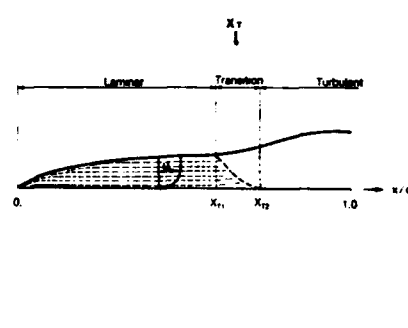


Fig.5

Skin friction coefficient

Turbulent/Laminar

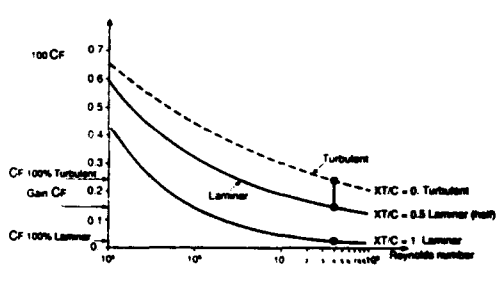


Fig.6

Definition of velocity components on swept wing

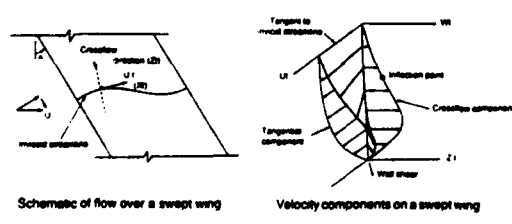


Fig.7

Laminar flow concept

Transition mechanism : problems and solutions

Problem : Fuselage B.L. contaminates the wing L.E.

Solution : Passive device is needed

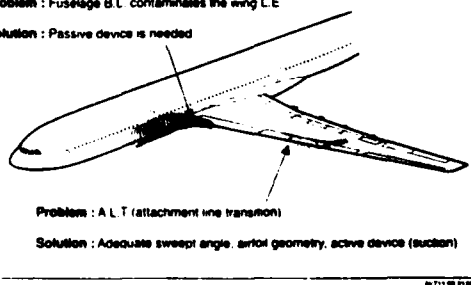


Fig.8

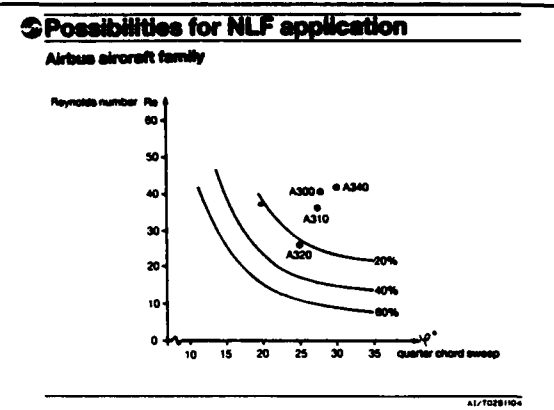


Fig.9

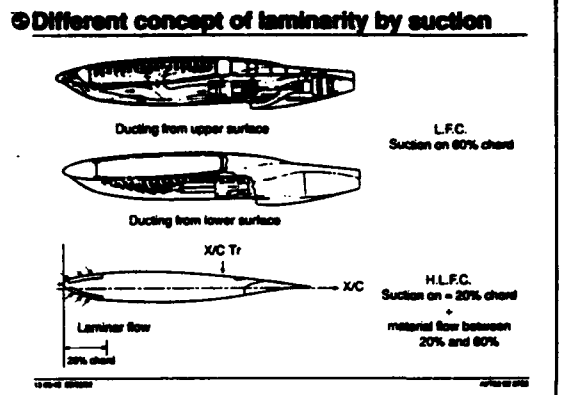


Fig.10

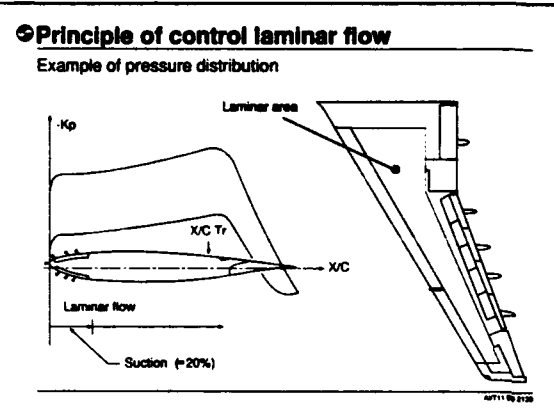


Fig.11

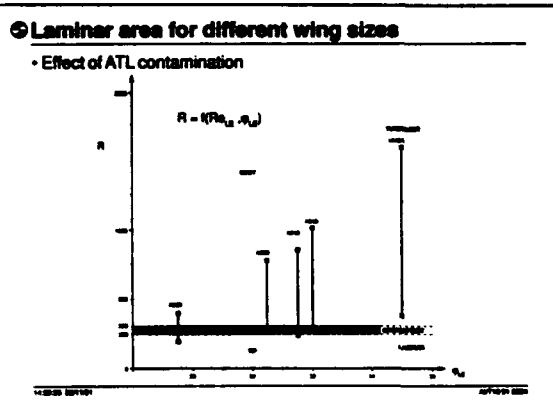


Fig.12

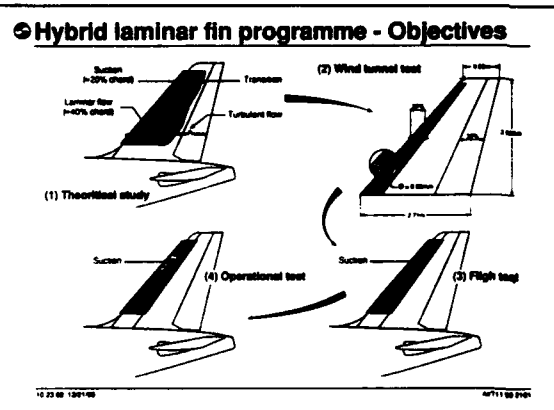


Fig.13

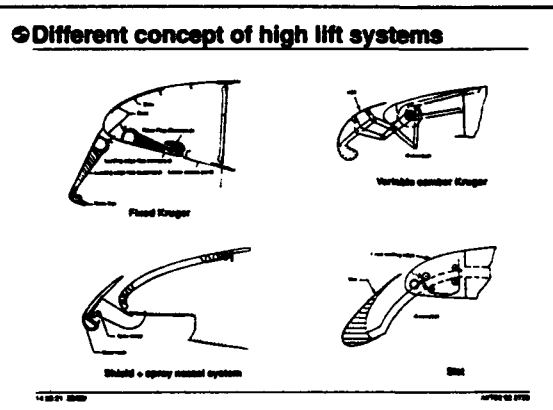


Fig.14

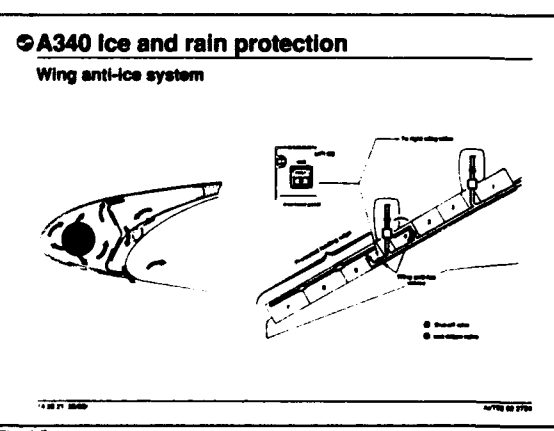


Fig.15

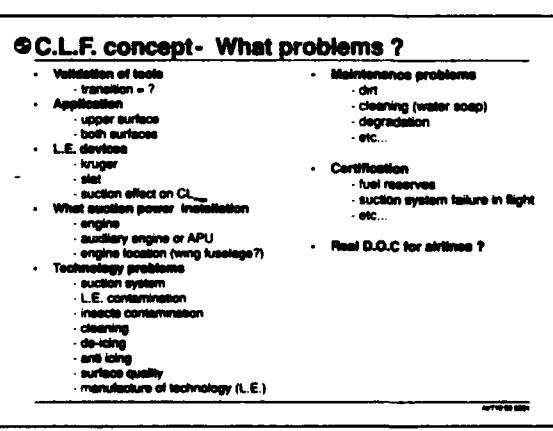


Fig.16

Skin friction drag improvement

What are riblets ?



$$S^* = S \sqrt{\frac{C_f}{2}} \cdot \frac{U_e}{V_e}$$

$$H^* = H \sqrt{\frac{C_f}{2}} \cdot \frac{U_e}{V_e}$$

Riblets consist of a plastic foil with very small grooves, modifying the local skin friction coefficient, (C_f)

The characteristics of riblets are defined by different parameters such as S^* , H^* , groove shape.

Fig.17

Skin friction drag improvement

High speed

Influence of the parameter H^* in transonic flow

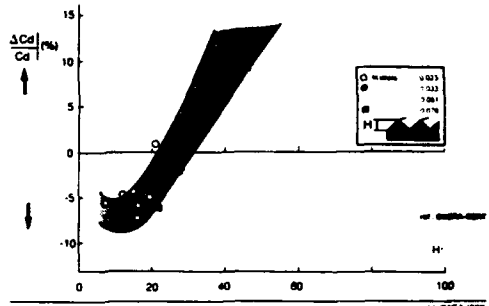


Fig.18

Skin friction drag improvement

High speed

Influence of the yaw angle (ψ) and parameter H^* in transonic flow

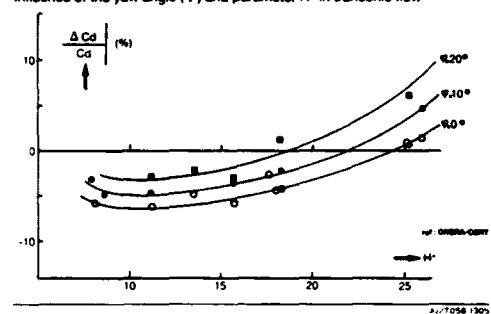


Fig.19

Objective of the TWG1 programme



Skin friction drag improvement

Transonic flow



Fig. 20-21

Riblet flight tests

In October 1989, riblet flight tests took place in Airbus during 2 weeks, in order to achieve the over-all fuel burn reduction and local drag reduction measurements.

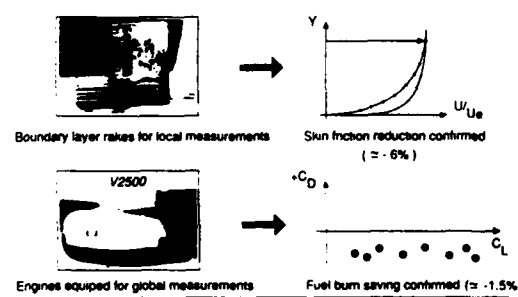


Fig.22

Riblet evaluation on the A320 n° 1

After 1 year in flight on the A320, the aerodynamic and material characteristics of the riblet film have been evaluated directly on the aircraft. For example: geometry and size profile are every 6 months compared with a reference profile.

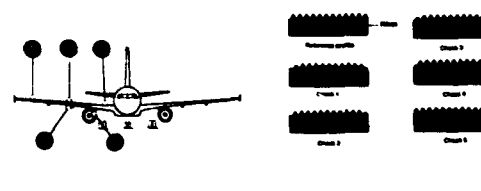


Fig.23

LEBU results in transonic flow

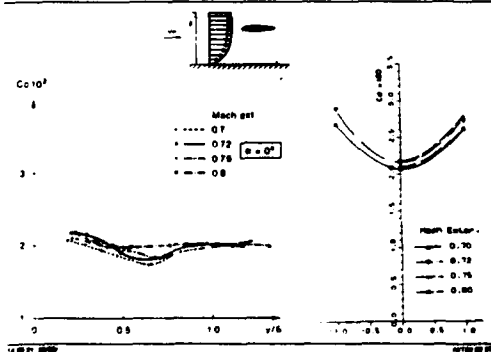


Fig.24

Work stages for technologies application

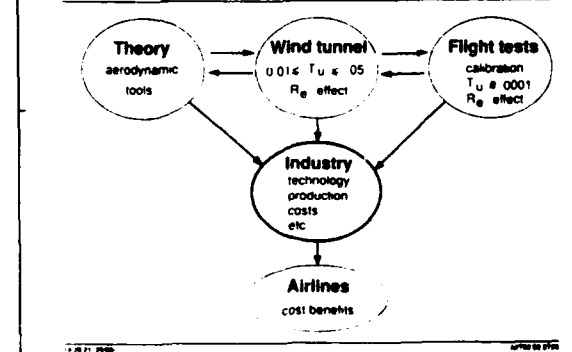


Fig.25



AIRCRAFT DRAG REDUCTION

by

D.M. Bushnell

Fluid Dynamics Division, Mail Stop 191
NASA Langley Research Center
Hampton, VA 23665-5225
United States

92-17808

ABSTRACT

Paper reviews aerodynamic drag reduction for friction, wave and vortex drag associated with supersonic cruise aircraft and suggests approaches and research directions which cover the spectrum from possibly significant to revolutionary. Various synergisms are also included, especially in regard to suction laminar flow control and flow separation control at cruise. The former may also enable improved low-speed, high-lift systems, improved lift-to-drag ratio for subsonic cruise, reduced parasitic viscous drag for favorable interference wave drag reduction approaches, and turbulent skin friction reduction via slot injection. Flow separation control at cruise proffers opportunities for increased leading-edge thrust, increased lift increment from upper surface, increased fuselage lift/camber for wave drag-due-to-lift reduction, improved performance of various favorable interference wave drag reduction schemes, as well as possibly better low-speed, high-schemes and wing cruise performance. More speculative approaches include multi-stage aircraft, thrust vectoring for lift augmentation, as well as trim, and a number of conceptual wave and vortex drag reduction schemes.

INTRODUCTION

For several decades (1920's to 1960's), the development trend of commercial aviation was higher and faster, culminating in the 707 class of conventional takeoff and landing (CTOL) transport (and subsequent derivatives). This extraordinary marriage of the swept wing and jet engines revolutionized long-haul passenger transport and supplanted steam ships, trains, and more recently, even eroded the lower end of the long-haul transport spectrum, buses. The higher and faster trend was abruptly halted in the early '70's by a combination of economic reality and environmental concerns. The next logical step beyond the 707 class aircraft would have been a supersonic transport (SST) or, as they are termed today, a high-speed civil transport (HSCT). Such an aircraft cruises in the Mach number 2 to 3 range and would represent a revolutionary development in long distance transport. An early version of such an aircraft, the Concorde, while a technological marvel for its time, has not proven to be economically viable, and only a small number were produced and operated. Many of the problems associated with SST class aircraft, both economical and environmental, are traceable in a major way to shock waves. These problems include high drag (and associated low lift-to-drag ratio) and sonic boom. The U.S. SST program was canceled in the early '70's in

an era of: (a) general technological antipathy, (b) sharply rising fuel costs, and (c) environmental sensitivity/concern. Since that time the NASA has attempted, through various research programs, to address the technological problems of civilian supersonic flight to maintain the Nation's options in the supersonic arena.^{1,2} Also in this time frame (since the early '70's), there has been renewed military efforts in this arena having been either canceled (XB-70) or, deactivated (B-58, S-71). Conventional supersonic fighter aircraft are capable of supersonic dash, not prolonged supersonic cruise.

Today there is a resurgence of interest in civilian supersonic long-haul aircraft.³ A probable reason for this is the emergence of the Pacific Rim as a major economic entity. The subsonic CTOL flight times associated with passage between some of the major Pacific economic players is on the order of 12 hours or greater, and an HSCT capability is urgently needed to foster improved and continued development of the Pacific area and particularly the U.S. involvement in this economic arena. The Pacific application of an HSCT is more technologically demanding in that longer ranges are required than for many Atlantic flights. Additional technological problems or boundary conditions imposed upon an HSCT for operation in the 1990's and beyond include: (a) ozone depletion and upper atmospheric pollution concerns, (b) sonic boom, (c) sideline noise, and (d) (increasingly) wake vortex hazard. Fortunately, several technologies have developed to a considerable degree since the last large-scale SST studies, including: (a) variable cycle and supersonic through-flow fan^{4,5} engines with higher turbine inlet temperature, (b) lightweight, high-temperature composite materials, and (c) flow control, including automatic load alleviation and laminar flow control. However, even with currently projected technology levels, the development of an economically viable HSCT will be a formidable task. We are not starting from a surfeit of performance, and the available studies indicate the need for both a significant "fare premium" and innovative drag reduction concepts. There exists a clear and pressing need for improved aerodynamic performance, even a 10-percent improvement in L/D would be extremely significant, given the small payload fractions inherent in HSCT design, while a factor of 2 increase in L/D would literally be revolutionary and alter the entire economic viability issue. The historical,⁶ mid-term,^{7,8} and still current⁹ HSCT L/D is on the order of 10 (without the inclusion of many "real vehicle" influences) in excellent agreement with Kucheman's empirical rule

$$\frac{L}{D}_{max} = \frac{4(M+3)}{M} \text{, 10}$$

The Concorde value is on the order of 7. Values greater than 20¹¹ have been recently proffered.

The purpose of the present paper is to review the current status of aerodynamic drag reduction at supersonic speeds and to suggest several approaches and research directions which cover the spectrum from possibly significant to revolutionary. The benefits of sizable drag reductions could also be used to help alleviate several of the environmental as well as economic concerns in that reduced fuel requirements associated with drag reduction results in lower weight, which could provide benefits in terms of reduced: (a) sonic boom, (b) sideline noise, and (c) pollution as well as reduced initial and direct operating costs. Drag reduction is also an enabling technology for an alternative approach to working the ozone and sonic boom problems, flying lower, below the ozone layer and in the near field of the sonic boom to allow tailoring thereof.¹² Obviously, supersonic aircraft drag reduction concepts would also be of interest for possible application in various military arenas such as supercruise fighters, artillery rounds, supersonic cruise missiles, tactical and strategic missiles, and (military/civilian) low-earth-orbit launch vehicles, both airbreathing and non-airbreathing.

The drag breakdown of a typical HSCT design is indicated, for example, in references 13-15. Crudely, assuming no pressure drag associated with flow separation and neglecting trim drag, the drag breakdown is (depending upon detailed design) on the order of 1/3 skin friction, 1/3 wave drag (mostly volume wave drag, but including sizable wave drag-due-to-lift (DDL)), and 1/3 vortex DDL. This classical division of drag sources is followed in the organization of the present report. Thus far, the major drag reduction efforts for HSCT class aircraft have concentrated upon wave drag reduction, and this is still a vital issue. Emerging possibilities in both vortex DDL reduction and friction drag reduction, combined with improved wave drag reduction, may result in the revolutionary factor of 2 increase in L/D mentioned previously. Historically, the search and research for supersonic drag reduction for one component of drag often resulted in increased drag for another component, e.g., the increased surface area (increased skin friction, as well as weight/structure penalties) associated with many favorable interference concepts for wave drag reduction problem from an overall viewpoint using the full arsenal of ancillary penalties to be minimized. Favorable synergisms are even possible in some cases.

Drag reduction is required during both supersonic and subsonic operation. Fuel is approximately one-half of the gross weight,¹⁶ and the weight of the fuel reserves required for landing exigencies during the subsonic flight phase is on the order of the payload. Therefore subsonic drag reduction, especially vortex or DDL reduction on such typically low-aspect-ratio configurations, may have particularly large net benefits. A 1-percent drag decrease corresponds, approximately, to a 5- to 10-

percent increase in passenger payload. Of possibly critical importance and particular interest are drag reduction techniques employing the maturing technologies of: (a) flow control of various types (LFC, flow separation control, vorticity/turbulence control), and (b) nonlinear flow phenomena via CFD. The analyses of references 17 and 18, for example, indicate that major performance improvements are available through exploitation of these areas. "Supersonic aerodynamics has been dominated to a remarkable degree by ideas, theories, targets, and design methodologies that are directed to avoid nonlinear effects . . . more accurate theories consistently predict drags less than those given by linear aerodynamic theory¹⁷ "to obtain the low-drag potential of highly swept wings, leading-edge separation must be avoided."¹⁸ Major future performance improvements for subsonic transports are already predicted to result from various types of flow control devices including passive shock-boundary-layer interaction control, LFC, and variable camber wings.¹⁹

Previous drag reduction summaries for the supersonic case include references 20 and 21. The general thrust of the present discussion is that technology should at least attempt to go beyond the following precepts employed in the development of Concorde class (linear theory) aircraft: (1) disturbances caused in the air should be relatively small, (2) air is able to flow (unaided) around the leading edge, developing local suction forces which decrease drag, and (3) leading-edge flow rolls up into separate (lee-side) vortices to increase lift (for landing/takeoff) for a contiguous body-wing combination.²²

VISCOUS DRAG REDUCTION

Roughness Minimization

Roughness drag per se is not always included in conventional systems studies but was certainly present on all of the supersonic cruise aircraft produced thus far. Roughness at supersonic speeds is particularly worrisome due to the increased element drag caused by element shock wave formation, refs. 23-24). Concomitant with supersonic flight is aerodynamic heating and elevated temperature levels which produce thermal stresses which can be larger than those induced by aerodynamic or mass loading. Design approaches to alleviate these thermal stresses such as tieles, joints, shingles, corrugations, etc., typically result in various types of surface (drag increasing) roughness. Non-smooth aircraft surfaces not only increase drag directly, but are also responsible for promoting early transition; smooth surfaces are an enabling condition for supersonic laminar flow control.²⁵ Fortunately, as in the subsonic LFC case, contemporary materials and fabrication techniques appear to be capable of surfaces of sufficient smoothness to minimize direct roughness drag and delay transition/promote LFC. The lower near-wall density at supersonic speeds usually allows a less stringent physical smoothness criteria than the corresponding subsonic case.

Viscous drag reduction via roughness minimization is both achievable and probably essential for a viable HSCT.

Transition Estimation and Delay

Historically, due to innate surface roughness and the tenuous and incomplete status of transition research, the existence of turbulent flow on HSCT designs was taken as a given. Research over the last 12 years in connection with the Langley subsonic LFC program and, more recently, NASP, has greatly improved the ability to estimate transition location and delay transition via detailed vehicle aerodynamic design. The essential features of this significant improvement in transition estimation capability include: (1) development of advanced linear stability theories (along with utilization of the advancements in flow field CFD), (2) invention and development of high-speed "quiet tunnels," (3) high-quality flight LFC and transition experiments, and (4) the realization (by inference) that the background disturbance levels in both flight and quiet/low-disturbance wind tunnels are similar. These developments have enabled the extension and application of the e^N method into high-speed flows and transition initiated by each of the four major linear instability modes (TS, crossflow, Gortler, and Macks 2nd mode) with a precision (for transition estimation) generally on the order of 20 percent or better in transition Reynolds number/location.²⁶ This compares to a previous uncertainty of an order of magnitude or more. This transition estimation technique parameterizes transition location as a function of the multitudinous variables which affect the mean flow, and in particular the streamwise variation of these parameters, as well as allowing specification of parameter levels required to delay transition. This capability is limited to cases, such as most flight situations, where the background disturbances are low and much of the disturbances amplification leading to transition is linear.

Such a transition estimation capability can be utilized, along with smooth surfaces, to design for transition delay for drag reduction, and thus provide limited "natural laminar flow" over the vehicle nose and other components. The technology can also be applied in conjunction with suction LFC near the wing leading edge to delay transition via the hybrid laminar flow control approach, i.e., depending upon body design, presence/magnitude of crossflow, roughness, etc., significant transition delay and concomitant drag reductions are possible. General guidelines include: (a) avoidance of parameter ranges which produce large disturbance amplification rates such as adverse pressure gradients and bleed (injection), (b) avoidance of instability modes which have large amplification rates such as Gortler and crossflow, and (c) avoidance of "bypasses" such as roughness. As an example, the transition Reynolds number of a "2-D" body is 50 percent greater than the axisymmetric case at high speeds.

Laminar Flow Control

Laminar flow control or LFC is used herein to refer to transition delay via active control as opposed to

transition delay by aerodynamic shaping ("natural" laminar flow). For supersonic aircraft, the usual LFC techniques of choice are suction and wall cooling. The wall cooling approach has been demonstrated by the Russians up to $R_e \sim 34 \times 10^6$ at supersonic speeds,²⁷ but the technique is limited to: (a) nonhypersonic cryogenic-fueled aircraft, and (b) regions of small crossflow as cooling does not significantly damp the crossflow instability.²⁸ Cooling does damp the 1st mode TS waves but actually destabilizes Macks 2nd (hypersonic) modes.²⁹

Supersonic suction LFC (reviewed in refs. 25 and 30) is an extremely powerful technique, particularly for crossflow dominated regions (which are endemic on the typically highly swept HSCT configurations). The net benefits (after allowing for the suction and ducting penalties) are greater than 50 percent of the skin friction drag, and research in the 1960's by W. Pfenninger and his group at Northrop (reviewed in refs. 25 and 30) demonstrated that the technique works (using suction through multiple closely spaced slots) essentially up to the limits of the ground facilities employed, which was on the order of 25 million for swept wings and 50 million for axisymmetric bodies. The success of these tests is remarkable in that they were conducted under the extremely adverse conditions of high unit Reynolds number (stringent smoothness tolerance) and high free-stream noise (radiated nozzle wall turbulent boundary-layer noise, present in all non-quiet supersonic/hypersonic tunnels). Basically, supersonic suction LFC is aerodynamically feasible and the validity of the technique is further bolstered by the long record of successes produced by the Langley subsonic LFC and natural laminar flow control program.³¹ This does not mean that supersonic suction LFC is in hand, considerable research is required such as attachment region and porous/perforated suction surface physics including effective 3-D roughness induced by the discrete suction; laminarization for juncture regions to avoid sizable loss of laminarized area on low-aspect-ratio (supersonic) wings from direct fuselage turbulence contamination; system optimization studies, including minimization of suction drag penalty, the extent to which passive bleed can be used for LFC suction; and supersonic flight suction experiments at appreciable Reynolds number to determine real world maintenance and reliability issues including heated air handling/duct seals, i.e., the known key issues are primarily flight and systems related. Of particular concern are the destabilizing influences of various disturbance fields generated by the (usually turbulent and discretely rough) fuselage and radiated onto the wing LFC surfaces. Even weak waves produced by fuselage joints, etc, would oscillate (and thereby create a dynamic radiated disturbance) due to the fuselage boundary-layer turbulence. Techniques to minimize suction losses include improved slot/hole pressure recovery, passive bleed, and spanwise pressure gradients³² or other approaches to reduce crossflow. Also of concern is the compatibility of LFC with "leading-edge thrust."

What is particularly intriguing concerning

supersonic LFC are the large potential benefits, not only for drag directly but also reduced radiation equilibrium surface temperature³³ and the resizing benefits for sonic boom reduction and possible synergisms with other drag reduction techniques including: (1) reduced skin friction penalty for some favorable interference wave drag reduction and sonic boom reduction approaches (and for strut bracing employed to increase aspect ratio/reduce DDL and increase sweep/reduce wave drag), (2) turbulent skin friction reduction and direct wave drag reduction from boundary-layer thickening/wall wake effects of slot injection of LFC suction air, (3) possible use of LFC suction air for vortex DDL reduction via tip blowing, (4) utilization of LFC suction system and efflux air for high-lift production/separation control for takeoff and landing, and (5) drag reduction during subsonic over-land flight (required by sonic boom restrictions). Various estimates at hypersonic speeds indicate L/D increases of approximately 50 percent for an all-laminar vehicle as compared to an all-turbulent one.³⁴ Wave rider configurations, although having higher wave drag should have less crossflow and, therefore, more direct LFC benefits. Recent estimates for hybrid LFC system on a portion of the wings only indicate on the order of a 10-percent or greater improvement in L/D.³⁵ Extensive application of LFC along with use of strut bracing and multiple bodies could yield L/D increases on the order of 100 percent, see also references 36-38.

Turbulent Drag Reduction

The benefits of lowering the turbulent skin friction drag without resorting to LFC are much less than for the LFC case (10 percent to 15 percent of the friction drag vs. 50 percent to 80 percent), but the techniques are more "robust" than LFC and, in the context of the payload sensitivity of HSCT designs to the level of zero lift drag, are considered worthwhile pursuing particularly as a complement to LFC for "nonlaminarized" body acreage. Reference 39 provides a convenient summary of the various possible approaches for turbulent drag reduction; the present paper considers only those techniques which have application to supersonic flow. The premiere approach is the supersonic application of riblets, small flow aligned grooves in the surface which are now nearly state-of-the-art in subsonic flows following several successful flight experiments.⁴⁰ These grooves are implemented on a vehicle via a lightweight adhesive film. The fundamental mechanism for riblet drag reduction involves utilization of large transverse friction forces near the surface (within and near the groove, forced by the groove presence) to increase the viscous sublayer thickness and provide a slip-flow boundary condition for the wall-turbulence production processes. The benefit is on the order of 8 percent of the turbulent skin friction. The alignment of the grooves is not critical (to within approximately 15°), and their performance does not seem to be degraded by reasonable pressure gradients. Two recent studies of riblets in supersonic flows indicate similar performance as in the subsonic case, decreased turbulence intensity in supersonic wind-tunnel tests,⁴¹ and expected levels of reduced skin friction

from $M = 1.25$ wind-tunnel tests⁴² and unpublished flight experiments up to $M \sim 1.7$ (Dryden-Langley). The presence of a riblet-containing plastic film on the surface also reduces roughness drag via surface smoothing and the necessarily micro-porous film converts, via distributed injection, the usual drag increases associated with pressurized fuselage air leakage into a skin friction reduction. It should be noted that "Reynolds analogy" is increased on the order of 30 percent by riblets and therefore some increase in radiation equilibrium temperature will accompany their utilization.

The second approach of choice for supersonic turbulent skin friction reduction is slot injection, the tangential downstream surface injection of low momentum fluid to reduce the wall shear levels.⁴³⁻⁴⁸ The key to the success of this approach is the provision or availability of a "low-loss" source of injectant. Simply using ram air is much too inefficient. Two possible sources of such low-loss air are LFC suction air and engine bleed air. The former can be used on the wing, downstream of the laminar flow region to both reduce skin friction on the order of 10 percent or greater (depending upon the quantity of air available, e.g., the extent of the laminarized region) and also, due to the resultant boundary-layer thickening, reduce wing trailing-edge shock drag. This latter effect is in contravention to the low-speed case where thicker trailing-edge region boundary layers produce larger pressure or form drag. In the supersonic case, the increased displacement thickness can reduce closure wave drag. Engine bleed air, that is air passively bled from inlets/compressor section to control flow separation, can be applied locally to reduce the external nacelle skin friction drag. The estimated benefit, from reference 48, is on the order of 35 percent of the nacelle friction drag, thereby partially mitigating the effects of the inlet bleed, which can amount to as much as 3 to 5 percent of total airplane drag.

Considerably more speculative, and applicable only in the nose region of locally depending upon the detailed design, is the concept of using the large debilitating influence of convex longitudinal curvature upon wall turbulence to yield a net skin friction reduction.³⁰ Research on this concept, even for the subsonic case, is still in the early stages, but there is evidence that convex longitudinal curvature will appreciably reduce turbulent skin friction, and the effect can last on the order of 50 boundary-layer thicknesses downstream. Whether such an approach can yield a net benefit, considering the possible adverse effects of wave drag remains to be seen. The remaining possibilities for reducing turbulent skin friction are obvious and depend upon the specific design. One such technique is shear size/Reynolds number, due to the well-known reduction of skin friction coefficient with increasing length Reynolds number due to boundary-layer thickening. There is also a favorable influence of increased wall temperature upon skin friction level, produced primarily by the resultant reduction in near-wall air density. This is in contrast to transition delay where wall cooling is required (at supersonic speeds) to reduce drag.

Thus far, the emphasis has been upon reduced skin friction coefficient. What is required is reduced wall shear stress and alternate methods to accomplish this, besides reducing skin friction coefficient, are to reduce wetted area and local dynamic pressure. The former can be accomplished via use of active load alleviation and/or replacement of separate control surfaces by flap systems located on the necessarily elongated lifting surfaces (already incorporated into the Concorde and TU-144), thrust vectoring (enabling use of smaller controls) and planform tailoring/higher C_L values.⁴⁶ These latter can be detrimental to other components of drag tradeoff process. Another (somewhat radical) approach for reduced wetted area is some type of two-stag aircraft either actual (e.g., takeoff requirements met via a stage that separates and flies back⁴⁹) or ersatz such as midair refueling or "ski jumps" on takeoff runways. From reference 49, "the two-stage airplane concept can be described as follows: The first stage of the tandem craft carries the main landing gear, the accelerating engines, and the part of the wing required only for takeoff and acceleration. The second stage has the wing area required only for landing and cruise and an auxiliary landing gear. The fuel required for acceleration is carried entirely by the first stage." Reduced dynamic pressure is provided as a by-product of higher Mach number regions of the flow. Higher local Mach numbers produce not only a dynamic pressure reduction but also a reduced skin friction coefficient level. This again is in contravention to the low-speed case where a higher Mach number increases the skin friction level through increases in U^2 .

An additional viscous drag reduction issue is optimal design of intersection regions to avoid the high local skin friction which can be associated with necklace or horseshoe vortices. Numerical solutions indicate that simple fillets of adequate size can obviate the formation of such highly organized intersection region vortex flows in the supersonic case.⁵⁰

VORTEX DRAG DUE TO LIFT REDUCTION

Classical Approaches

Vortex DDL reduction is particularly critical for HSCT designs in both the cruise and takeoff/landing phases of the flight. Classical linearized theory indicates that elliptic loading, increased aspect ratio (or span) and lower C_L values/reduced weight are the primary means by which vortex drag can be reduced. See reference 51 for a recent review of DDL and the reduction thereof. For the large sweep angles associated with low wave drag supersonic designs increasing aspect ratio/span beyond a certain point becomes inefficient due to increased wetted area/skin friction or oblique wing (especially spanloader) approaches are used. The cranked delta planform is a useful compromise between low and high-speed performance. Even in the variable sweep case, with the wing swept back for cruise, the aspect ratio is still low for high-speed operation; although for lower speeds efficiency is significantly enhanced by unsweeping the wing. The

wetted area problems are addressable via both macro trailing-edge notching (arrow wings) and laminar flow control. The structural problem is possibly addressable via strut bracing¹¹ although detailed supersonic design studies employing the latter are not yet extant (see also refs. 52 and 53). Reducing C_L typically results in a structural penalty and, thus, becomes part of the overall design trades. However, reduced weight via friction and wave drag reduction will synergistically reduce vortex DDL. The effective aspect ratio of supersonic configurations is considerably less than for subsonic CTOL long-haul transports and, therefore, performance may benefit appreciably from various nonclassical approaches to vortex DDL reduction. The application of various techniques other than increased aspect ratio for vortex DDL reduction has not been significantly addressed thus far in high-speed cruise aircraft system studies although some authors considered thrust vectoring for C_L reduction.^{54,55} In the remainder of this section, various approaches which might be tried will be mentioned (see also ref. 56). While some of these approaches can be directly applied, most require considerable further research, even for the subsonic case, and some may not yield any net drag reduction at all. However considering the importance of the problem, many of these possibilities are probably worth at least some further research to determine their applicability and performance in the supersonic case. These devices have associated with them various systems penalties, usually including structural, parasitic drag, or power consumption, and therefore their use, even in the subsonic case, is a function of overall systems design issues. The possible penalties will be different in the supersonic case, and probably aggravated by parasitic wave drag, but a decision as to whether or not to employ them should be based upon at least a cursory design study.

Non-Planar Vortex Sheet Approaches

Relaxing the assumptions of classical linear theory, i.e., closed body, no energy addition, planar vortex sheet, etc., provides alternative DDL reduction possibilities, aside from the usual ones already mentioned. In particular, use of non-planar lifting surfaces, e.g., distributing the lift vertically through various approaches such as upswept tips can provide reductions in DDL.⁵⁷⁻⁵⁹ This approach is related to the winglet case which is discussed in the next section. Besides non-planar tips/non-planar span, there are several interesting "natural" observations (e.g., morphology on Avians or Nektons) which may relate to the DDL reduction problem and in particular to the production of non-planar vortex sheets. The first of these is the swept-back tapered tips seen on many fliers and swimmers. When wings with such tips are placed at incidence, the lift is distributed vertically toward the tip. Also termed sheared tips, research in references 60-64 indicates that there may be a measurable benefit associated with this bionic observation. The other natural observations are still simply just that, observations with the suggestion that DDL mitigation may possibly be involved. These morphologies, which require investigation, include serrated trailing edges, leading-edge bumps, and the curious tip of the shark caudal fin, where a

trailing-edge near-tip cutout has a hinged flap, forming a combined swept back, notched, and winglet-like fin tip arrangement.

Energy/Thrust Extraction from Tip Vortex

The vortex which forms at, and downstream of, the wing tip is due to the upwash from the lower surface high-pressure region and is the cause of vortex DDL. As aspect ratio increases, a smaller percentage of the wing span is influenced by this flow and, as stated previously, the DDL is reduced. A characteristic feature of this vortex formation is flow which is at an angle to the free stream. Devices can therefore be inserted into this flow to produce/recover thrust and/or energy from this tip flow. This (simplistically) is the fundamental rationale behind at least four devices which reduce vortex DDL. These devices can also have an influence upon the vortex formation process itself and, thus, may also directly influence DDL. The devices include tip turbines,⁶⁵⁻⁷³ vortex diffuser vanes,⁷⁴⁻⁷⁶ and tip sails.⁷⁷⁻⁸¹ The vortex diffuser vane is supported by a spar behind the wing tip to allow the tip vortex to concentrate before intercepting it. These devices work quite well, producing, depending upon wing design, on the order of 5- to 15-percent reduction in vortex DDL at subsonic/transonic speeds. Major issues concern structural, etc., penalties, possible use as control devices, and for the high-speed case, associated wave drag and the rather diffuse nature of the vortex formation.

Alteration of Tip Boundary Condition(s)

These DDL reduction techniques are based upon either: (a) eliminating the tips altogether or, (b) adding mass in the tip region. Eliminating the wing tips can be accomplished either via use of "ring wings" or by using joined wings and tails.⁸²⁻⁸⁴ Mass addition at the tip is accomplished either via tip engines,^{68, 85-87} tip blowing,⁸⁸⁻⁹¹ or various types of porous tips. The tip engines and tip blowing result in sizable DDL reduction. The tip blowing is especially intriguing as the required mass flow could possibly be obtained via wing leading-edge ingestion (passive bleed), and the blowing could be used to tailor for the production of, and be modulated to excite, vortent instabilities in the tip vortex at landing/takeoff for amelioration of the "wake vortex hazard" problem. For high speeds unsweeping the wing can evidently reduce vortex drag due to the resulting reduction in "cross-talk" between the upper and lower wing surfaces, but this obviously results in increased wave drag.

WAVE DRAG REDUCTION

As mentioned in the introduction, the formation of, and losses associated with, shock waves at supersonic speeds is probably the major core problem of high-speed civil transport design (apart from the all-pervasive ozone/high-altitude pollution issues). Shock waves cause additional drag due to both volume and lift and are responsible for one of the major impediments to a successful HSCT design--

sonic boom. Therefore, the minimization of wave drag has, historically, been the focus of HSCT drag reduction research. Both volume wave drag reduction and wave DDL reduction are included in this section of the report. It should be noted that the performance of many of these approaches is limited by the "real flow" effects of flow separation control are included herein to allow full advantage to be taken of these various wave drag reduction approaches.

Classical Approaches to Wave Drag Reduction

Several of the zeroth order approaches to supersonic wave drag reduction for supersonic cruise aircraft are extensions, into the supersonic regime, of transonic techniques optimized via linear theory, including wing sweep and area ruling. The literature in this area has a marked continuity, examples include references 93-103. Detailed implementation is different at high speeds in that large sweep angles are required for subsonic (normal Mach number) leading edges. Such wings, however, have the added advantage of distributing the lift vector lengthwise^{92,104} (also, the forward portion of the fuselage is cambered and lift is carried over onto the fuselage) and providing for leading-edge thrust.¹⁰⁵⁻¹⁰⁷ Linear theory is also used to optimize wing twist/camber/warp to minimize DDL.¹⁰⁸⁻¹¹² Strut-braced wings could allow use of both highly swept and extreme arrow configurations to reduce both volume wave drag and wave DDL.¹¹ Other classical approaches include increased effective body length/thin sections (to reduce shock strength) and gradual (even approximations to isentropic) compression,^{113,114} the latter of especial interest for inlets (see Fig. 260 of ref. 115). Simplified theories have been employed to provide various locally optimized solutions using these approaches¹¹⁶ including axisymmetric bodies, the Soviet star bodies,¹¹⁷⁻¹²⁰ and the R. T. Jones skewed wing.¹²¹ More recently, CFD/nonlinear methods have been applied to the supersonic optimization problem.^{17,122-125} Classical nonlinear flow drag reduction techniques include use of nose spikes or "rings" (either physical or shock alteration via forward fluid/particle injection) on blunt-nosed bodies¹²⁶⁻¹³³ and base blunting.¹³⁴ The former is incorporated into the design of the C-4 and D-5 trident missiles and has been further improved via attendant mass addition in the separated flow region formed in the nose region to obviate/alter the separated flow reattachment shock systems/heating.¹³⁵ A blunt base reduces the strength of the base recompression shock¹³⁴ and, as mentioned previously, the favorable influences of base blunting can be mimicked by boundary-layer thickening/displacement thickness effects through, for example slot injection. Also, nose blunting can provide a drag reduction.^{136,137}

As stated previously, many of these classical techniques have been applied over the years^{6,9} to the HSCT/SST design problem with considerable success, producing L/D values of 0(10), some 30 percent greater than existing (Concorde) performance. As discussed subsequently in the present report, these

classical methods can probably be improved upon significantly through the use of flow-separation control.

Wave Drag Reduction via Favorable Interference

There are two fundamental approaches to wave drag reduction: (1) weaken the shock wave initially, during its formation process (or substitute a series of weak shocks for a single stronger one) or (2) utilize the initial shock wave, via reflection/interaction, to create favorable interference, either for body thrust or for lift, or both, i.e., (from ref. 138) "Supersonic wing-body arrangements which, at design Mach number, effectively utilize volume distributions to create lift, lift distributions to cancel volume drag, and wing lateral curvature to minimize sidewash." Favorable interference approaches were recognized early on¹³⁹⁻¹⁴³ and considerable effort, primarily theoretical, was expended in evaluating and optimizing various techniques.

Realizations of favorable interference include: (a) ring wings¹⁴⁴⁻¹⁵³ and various segmented versions, e.g. Parasol wings,^{15,138,154-160} (b) multiple bodies (fuselages and/or control surfaces and fuselages),¹⁶¹⁻¹⁷⁰ and (c) propulsion system interaction.^{112,171-175} For nonlifting bodies, the (nonlifting, i.e., symmetric) ring wing can cancel, in much the same way as a supersonic Busemann bi-plane, the volume wave drag of a body, the expense of increased wetted area/weight, etc. From reference 153, "very significant drag reduction (on the order of 50 percent) can be obtained even with simplified ring wing-body combinations. In addition, beneficial interference effects are only gradually reduced as the Mach number varies from the design Mach number as the angle of attack is increased." For the lifting case, the Parasol type wing is more efficient with the favorable wave interference providing both partial cancellation of the body and/or nacelle volume wave drag and an efficient lifting surface. It may be possible, by using shortened struts, to increase the benefits of Parasol wings via multiple shock reflections.¹⁵

In the multiple body case, wave interactions/favorable interference is used to raise the pressure over the rearward portions of adjacent bodies, providing a "thrust" component to partially cancel the volume wave drag in a similar fashion to the (nonlifting) ring wing. Structural benefits may be appreciable for the multibody case.¹⁶² Favorable propulsion system interactions can be of two types, in one approach, extensively used in SST design, the nacelle flow fields are used as a "multiple body" to provide "thrusting" pressure fields, particularly effective on M wings which are also interesting in and of themselves. In addition, the nacelles can also provide lifting forces on adjacent wing surfaces. The other "favorable interference" propulsion interaction is highly speculative but is now being addressed via contemporary CFD techniques. The basic concept is to reflect body shocks off of the engine exhaust flow back onto the afterbody, i.e., utilize the exhaust flow

as a "multiple body."¹¹⁷ Unfortunately, in many cases there appears to be very little reflection occurring, even if the engines are placed on the body in correct juxtaposition for such a favorable interaction to occur. Studies are underway to determine whether the engine exhaust flow profiles can be altered/tailored to provide for appreciable shock reflection back onto the body.

The application of favorable interference for shock wave drag reduction would be facilitated by: (a) flow separation control (to control extraneous pressure fields induced by shock-boundary layer interactions) and (b) active controls to ensure/maximize optimal wave positioning.¹⁷⁸ From reference 15, the benefits of Parasol-type wings can be on the order of a 20-percent increase in L/D compared to a conventional "optimized" wing. For the propulsion interaction, favorable interference can essentially cancel the nacelle wave drag.

Speculative Wave Drag Reduction Approaches

In addition to the approaches already discussed, there are several other possibilities which could be studied for the wave drag reduction problem. These include: (a) serrated/zig-zag bodies, (b) use of focusing lasers/ions or other beams to increase the effective body length, (c) increase upper surface share of lift, and (d) use of passive bleed. The first of these is suggested in reference 179, but very little follow-up research is available. The fundamental idea is to create a series of very weak shocks and the fundamental problems for a 2-D or axisymmetric realization, are the viscous induced difficulties of (probably unsteady) separated flows and attendant increased wave drag. Possibilities for mitigating the flow separation problems include a 3-D (shingle) design which might be crudely visualized as being similar to a "pinecone" or "artichoke." Such a 3-D geometry, combined with some further flow separation control could possibly lead to an overall benefit (see ref. 80).

Focused and possibly pulsed beams (lasers, etc.) could be studied to attempt to turn the flow ahead of the body, thereby extending the effective body length. The energetics of this approach is probably a major problem, but little is known concerning the effects of such local intense depositions of energy upon flow field development,¹⁸¹⁻¹⁸⁷ and sufficient computational fluid mechanics should be carried out so that the energetics sums can be made.

At supersonic speeds, a significant portion of the lift (more than current practice) could be carried on the upper surface,¹⁸⁸ thereby possibly reducing the wave DDL from the lower surface wave systems. The problem here appears to be upper surface flow separation. (See next section on flow separation control.) "The low pressure side thus emerges as a key consideration in the L/D problem."¹⁹⁰ Another concept, passive bleed, allows a reduction in body flow deflection and, hence, weakens the body shock systems.¹⁹¹ The technique is much studied for

transonic wing application (with possible direct application to "subsonic leading edge," high-speed wings,¹⁹²) especially for mitigation of off-design wave drag and shock-induced separation (see refs. 193 and 194).

SEPARATED FLOW CONTROL

Traditionally, separated flow control, either active (blowing, suction, etc.) or passive (e.g., vortex generators) has been viewed as primarily a local "after the fact" fix to design problems. The conventional view is that separated flow should be avoided as much as possible through mitigation of imposed pressure gradients. This approach (restricting the imposed pressure gradients) has yielded good (but perhaps not optimal) designs, in that the large pressure drag increments associated with separated flow are avoided.

The design restriction that separated flows must be avoided (rather than actively or passively controlled) has, especially in the supersonic case where shock waves can impose tremendous local pressure gradients, perhaps unduly penalized several drag reduction approaches. That is, the anticipation and mitigation of viscous flow effects, i.e., separation, has restricted the extent to which inviscidly-predicted benefits can be realized.^{17,18,92} "Experiment has shown that many of the benefits of leading-edge sweepback are not attained in practice because of separation of the flow over the upper surface of the wing.¹⁹⁵ "Successful configurations have attached flow over the wing upper surface, unsuccessful wings exhibited vortex dominated flow, strong shocks, and large regions of separation."¹⁸ Obvious examples where flow separation control may allow the accrual of greater benefits include: (a) greater leading-edge thrust on subsonic leading-edge wings, (b) increased lift increment from the upper surface,¹⁸⁸ (c) increased fuselage lift and camber (reduced wave DDL), (d) increased favorable wave interference effects from multiple bodies including propulsion modules and displaced wings, and (e) improved isentropic compression surfaces. The fundamental suggestion is straightforward, i.e., incorporate flow separation control into cruise designs to allow accrual of the maximum wave drag reduction benefits available from inviscid considerations. This suggestion includes both supersonic and subsonic operation. In the low-speed case, cruise LFC suction and separated flow control systems could perhaps also be utilized for high lift.

The basic approaches to flow separation control are well known: (1) remove the near-wall low-momentum fluid, (2) add momentum/"energize" the near-wall region, or (3) impose a wall slip layer. Removal of near-wall low-momentum fluid can be accomplished via suction (which can be active or passive (bleed) and either local or distributed) or via boundary-layer "diverters" including, at high speeds, swept shocks. Energizing the near-wall region can involve either adding energy from an external source (e.g., blowing, steady, or pulsing), redirecting energy from the external flow to the wall region (vortex generators, either jets or bodies, augmented turbulence including shock-induced amplification, and even

adding near-wall momentum through increased wall density via surface cooling. Effective wall slip regions can be established using various types of small-scale grooves or moving walls. See references 196-198 for surveys/reviews of flow separation control, particularly in high-speed (shock boundary-layer interaction) flows.

The use of flow separation control for cruise as suggested herein has obvious problems associated with systems penalties for the control technique(s), positioning of the control devices for off- as well as on-design performance and possible interference with smoothness requirements for laminar flow control. In this regard, the use of intelligent walls, which through distributed sensors detect incipient separation may be useful. Considerable synergisms between the various flow control and drag reduction techniques, including flow separation control, are possible as discussed in the next section. Techniques possibly well suited to the high-speed flow separation control problem include passive porous walls¹⁹²⁻¹⁹⁴ and vortex generator jets^{199,200} as well as conventional bleed for high-pressure regions. The high-pressure lines feeding the vortex generator jets could perhaps be used as particularly efficient structural members.²⁰¹

SYNERGISMS AND BENEFITS OF DRAG REDUCTION APPROACHES

The most obvious benefits and synergisms from successful drag reduction approaches occur because of the opportunity to resize the (supersonic cruise) aircraft. In particular, a smaller required fuel load, for an aircraft with such a large fuel fraction and small payload fraction, can have dramatic influences upon other drag components, e.g., smaller size yields smaller wetted area/friction drag, smaller volume diminishes wave drag, and lower weight reduces C_L and, therefore, DDL, etc. Also, and not trivially, reduced weight reduces sonic boom, the size of takeoff gear and sideline noise. Vortex DDL reduction would be especially beneficial for subsonic operation and landing in that required fuel reserves (and their additional weight, which is currently the order of the payload) could be reduced. Wave drag reduction techniques applied to the engine inlets may also increase propulsion efficiency. Use of suction FLC could also provide: (a) suction for flow separation control/high lift during takeoff and landing, with subsequent utilization of suction mass efflux for "vortex generator jets" over aft portion of airfoil to augment/replace flap systems. Alternatively, the efflux could be used to control lee-side vortices or vortex flap systems for vortex lift augmentation or ejected from the wing tips for DDL reduction. Also, suction LFC could provide (b) "low-loss" air for slot injection for skin friction reduction and wave drag reduction, (c) drag reduction during subsonic overland flight (to meet sonic boom restrictions), and (d) reduced wetted surface penalty for struts and other devices employed for favorable interference wave drag reduction and strut-braced wings for drag due-to-lift-reduction and wave drag reduction (higher sweep). At hypersonic speeds, thrust vectoring is highly beneficial for lift production, thereby reducing DDL.

wing size, and weight and friction drag. Thrust vectoring for control can also reduce trim drag. These approaches are evidently not beneficial for subsonic speeds, but their efficiency for the supersonic cruise case should be evaluated.

CONCLUDING REMARKS

Advanced aerodynamics, in particular extensive drag reduction, is an "enabling technology" for a high-speed civil transport. The drag on such a supersonic cruise aircraft is approximately equally split between friction drag, vortex DDL, and wave drag due to both volume and lift. Therefore, drag reduction approaches for all three sources of drag should be considered. Classical drag reduction approaches for high-speed aircraft include increased fineness ratio, area ruling, sweep (subsonic leading edges with leading-edge suction), lift development over the forward fuselage, limited favorable interference, primarily in connection with nacelle placement, and reduced wetted area. Many of these approaches were historically suggested by, and/or optimized via, linear theory.

Developments in nonlinear theory/CFD and flow control allows serious consideration of another stable of approaches including increased performance of various classical methods through active or passive flow separation control at cruise and laminar flow control/riblets/slot injection/active controls for skin friction reduction. In addition, current CFD capability allows drag minimization for juncture regions, etc. Variable geometry could also be employed for variable sweep and camber (mission adaptive wing or cruise flap) as well as for optimal favorable wave interference. Several studies are available which indicate, to first order the levels of performance which can be obtained. The classical drag reduction approaches yield an increase in L/D from the order of 7 (Concorde) to the order of 10. Further increases on the order of 20 percent may be available from favorable interference (e.g., Parasol wings), while extensive LFC and strut-braced wings suggest L/D values on the order of 20,¹¹ a truly revolutionary machine. The present paper includes the entire spectrum of possibilities from ideas which are, as of yet, unevaluated and are included merely as possible suggestions for further research, to techniques which may, if pursued, yield the significant improvements in aerodynamic performance required for a viable HSCT.

The basic approach suggested for maximizing supersonic cruise aircraft drag reduction is to utilize flow control of all types including variable geometry, laminar flow control, vorticity control for viscous and vortex drag (and noise) reduction, and flow separation control, especially for wave drag reduction to allow both full accrual of the benefits suggested by linear theory as well as advantageous application of various nonlinear approaches such as favorable interference via finite strength waves.

In general, we tend to build what we can compute and the Concorde class aircraft are excellent

examples of linearized supersonic theory derived machines. The advent of nonlinear/CFD analyses and flow control may spawn quite different and hopefully better designs. A key to successful HSCT design is minimizing gross weight, which alleviates such key problems as sonic boom, sideline noise, ozone depletion, and economic viability. For HSCT class aircraft, with their large fuel weight fraction, drag reduction provides a highly leveraged approach for gross weight minimization.

REFERENCES

1. Maglieri, D. J.; and Dollyhigh, S. M.: We Have Just Begun to Create Efficient Transport Aircraft. *Astronautics and Aeronautics*, vol. 20, no. 1, Feb. 1982, pp. 26-38.
2. Driver, C.: How Different a Modern SST Would Be. *Aerospace American*, vol. 24, Nov. 1986, pp. 26-29.
3. Harris, R. V., Jr.: On the Threshold - The Outlook for Supersonic and Hypersonic Aircraft. AIAA Paper 89-2071 presented at the 52nd Wright Brothers Lecture.
4. Franciscus, L. C.; and Maidonado, J. J.: Supersonic Through-Flow Fan Engine and Aircraft Mission Performance. NASA TM-102304, also AIAA Paper 89-2139, 1989.
5. Barnhart, P. J.: A Supersonic Through-Flow Fan Engine Airframe Integration Study. AIAA Paper 89-2140, 1989.
6. Baals, D. D.; Robins, A. W.; and Harris, R. V., Jr.: Aerodynamic Design Integration of Supersonic Aircraft. AIAA Paper 68-1018, Oct. 21-24, 1968.
7. Goebel, T. P.; Bonner, E.; and Robinson, D. A.: A Study of Wing Body Blending for an Advanced Supersonic Transport. NASA CP-2108, 1980, pp. 149-169.
8. Roensch, R. L.; and Page, G. S.: Analytical Development of an Improved Supersonic Cruise Aircraft Based on Wind Tunnel Data. NASA CP-2108, 1980, pp. 205-227.
9. Coen, P. G.: The Effect of Advanced Technology on the 2nd-Generation SST. AIAA Paper 86-2672, Oct. 20-22, 1986.
10. Kuchermann, D.: The Aerodynamic Design of Aircraft. Pergamon Press, Oxford, 1978.
11. Pfenninger, W.; and Vemuru, C. S.: Design Aspects of Long Range Supersonic LFC Airplanes with Highly Swept Wings. SAE Technical Paper 88-1397, Oct. 3-6, 1988.
12. Sigalla, A.; Runyan, L. J.; and Kane, E. J.: The Overland Supersonic Transport with Low Sonic Boom - A Feasibility Study. *Acta Astronautica*, vol. 4, Pergamon Press, 1977, pp. 163-179.

13. Kuchermann, D.: Aircraft Shapes and Their Aerodynamics for Flight at Supersonic Speeds. *Adv. in Aero. Science*, vol. 3, 1962, pp. 221-253.
14. Leyman, C. S.; and Markham, T.: Prediction of Supersonic Aircraft Aerodynamic Characteristics. *AGARD-LS-67*, May 1974, pp. 5-1 to 5-52.
15. Kulfan, R. M.: Application of Hypersonic Favorable Aerodynamic Interference Concepts to Supersonic Aircraft. *AIAA Paper 78-1458*, Aug. 21-23, 1978.
16. Gall, Peter D.: Study of an Efficient Long Range Mach 2.7 Supersonic Transport Configuration Concept. *NASA-86414*, July 1985.
17. Mason, W. H.; and DaForno, G.: Opportunities for Supersonic Performance Gains Through Non-Linear Aerodynamics. *AIAA Paper 79-1527*, July 23-25, 1979.
18. Kulfan, R. M.; and Sigalla, A.: Real Flow Limitations in Supersonic Airplane Design. *AIAA Paper 78-147*, Jan. 16-18, 1978.
19. Hilbig, R.; and Szodruch, J.: The Intelligent Wing - Aerodynamic Developments for Future Transport Aircraft. *AIAA Paper 89-0534*, Jan. 9-12, 1989.
20. Hefner, J. N.; and Bushnell, D. M.: An Overview of Concepts for Aircraft Drag Reduction. *AGARD Report 654*, June 1977, pp. 1-1 to 1-30.
21. Jones, Robert T.: Aerodynamic Design for Supersonic Speeds. *Adv. in Aero. Science*, vol. 1, 1959, pp. 34-52.
22. Roe, P. L.: Aerodynamics at Moderate Hypersonic Mach Numbers. *AGARD LS-42*, vol. 1, 1972, pp. 1-1 to 1-8.
23. Gaudet, L.; and Winter, K. G.: Measurements of the Drag of Some Characteristic Aircraft Excrescences Immersed in Turbulent Boundary Layers. *AGARD Conference Proceedings 124*, Aerodynamic Drag, Oct. 1973, pp. 4-1 to 4-12.
24. Czarnecki, K. R.: The Problem of Roughness Drag at Supersonic Speeds. *NASA SP-124*, 1966, pp. 455-468.
25. Bushnell, D. M.; and Malik, M. R.: Supersonic Laminar Flow Control, *NASA CP-2487*, Pt. 3, Research on Natural Laminar Flow and Laminar Flow Control, pp. 923-946.
26. Bushnell, D. M.; and Malik, M. R.: Transition Prediction in External Flows via Linear Stability Theory. *IUTAM Symposium Transsonicum III*, Gottingen, FRG, May 24-27, 1988. (Also *NASP Technical Memorandum 1021*, June 1988.)
27. Kuziminskiy, V. A.: Effect of Cooling of the Wing Surface on the Transition of Laminar Boundary Layer into the Turbulent at Supersonic Speeds of Flow. *Uchenyye Zapiski TSAGI* vol. 12, no. 1, 1981, pp. 1-178.
28. Lekoudis, S.: The Stability of the Boundary Layer on a Swept Wing with Wall Cooling. *AIAA Paper 79-1495*, July 1979.
29. Mack, Leslie M.: Boundary Layer Stability Theory. *AGARD R-709*, June 1984, pp. 3-1 to 3-81.
30. Bushnell, Dennis M.; and Tuttle, Marie, H.: Survey and Bibliography on Attainment of Laminar Flow Control in Air Using Pressure Gradient and Suction, V.I. *NASA RP-1035*, 1979.
31. Hefner, Jerry N.; and Sabo, Frances E.: Research in Natural Laminar Flow and Laminar-Flow Control. *NASA CP-2487*, Parts 1 to 3, 1987.
32. Itoh, N.: Crossflow Instability of 3-D Boundary Layers on a Flat Plate. *IUTAM 3rd Symposium on Laminar-Turbulent Transition*, Toulouse, France, Sept. 11-15, 1989.
33. Poll, D. I. A.; and Bunting, S. R.: An Initial Assessment of the Impact of Boundary Layer Control on SST. *University of Manchester Aeronautical Internal Rep. No. 8802*, 1989.
34. Bowcutt, K. G.; and Anderson, J. D.: Viscous Optimized Hypersonic Waveriders. *AIAA Paper 87-0272*, Jan. 12-15, 1987.
35. Powell, A. G.; and Agrawal, S.; and Lacey T. R.: Feasibility and Benefits of Laminar Flow Control on Supersonic Cruise Airplanes. *NASA CR-181817*, July 1989.
36. Pfenninger, Werner; and Vermuru, C. S.: Suction Laminarization of Highly Swept Supersonic Laminar Flow Control Wings. *AIAA Paper 88-4471*, Sept. 7-9, 1988.
37. Agrawal, S.; Kinard, T. A.; and Powell, A. G.: Supersonic Boundary Layer Stability Analysis with and without Suction on Aircraft Wings. Presented at the 4th Symposium on Numerical and Physical Aspects of Aerodynamic Flows, Long Beach, CA, Jan. 16-19, 1989.
38. Parikh, P. G.; Sullivan, P. P.; Birmingham, E.; and Nagel, A. L.: Stability of 3-D Winged Boundary Layer on a SST Configuration. *AIAA Paper 89-0036*, Jan. 9-12, 1989.
39. Bushnell, D. M.: Turbulent Drag Reduction for External Flows. *AGARD Rep. 723*, Aircraft Drag Prediction and Reduction, July 1985, pp. 5-1 to 5-26.
40. Walsh, M. J.; Sellers, W. L., III; and McGinley, C. B.: Riblet Drag Reduction at

Flight Conditions. AIAA Paper 88-2554, June 6-8, 1988.

41. Robinson, S. K.: Effects of Rilets on Turbulence in a Supersonic Boundary Layer. AIAA Paper 88-2426, June 6-8, 1989.
42. Gaudet, L.: Properties of Rilets at Supersonic Speed. *Applied Scientific Research*, vol. 46, pp. 245-254, 1989.
43. McRee, D. I.; Peterson, J. B., Jr.; and Braslow, A.: Effect of Air Injection through a Porous Surface and through Slots on Turbulent Skin Friction at Mach 3. NASA TND-2427, 1964.
44. Czarnecki, K. R.: Analytical Investigation of Reduction in Turbulent Skin Friction on a Flat Plate by Means of Air Injection through Discrete Slots. NASA TND-2102, 1964.
45. Peterson, J. B., Jr.; McRee, D. I.; Adcock, J. B.; and Braslow, A. L.: Further Investigation of Effect of Air Injection through Slots and Porous Surfaces on Flat Plate Turbulent Skin Friction at Mach 3. NASA TND-3311, 1966.
46. Peterson, J. B., Jr.; and Monta, W. J.: Considerations Regarding Evaluation and Reduction of Supersonic Skin Friction. NASA SP-124, 1966, pp. 437-454.
47. Cary, A. M., Jr.; Bushnell, D. M.; and Hefner, J. N.: Slot Injection for Skin Friction Drag Reduction. AGARD Rep. 654, 1977, pp. 5-1 to 5-11.
48. Sorrells, R. B., III; Czarnecki, K. R.; and Sutshell, L. F.: Drag Reduction Due to Gas Injection through Discrete Slots on a 3-D Wing at Mach 2.01. NASA TND-5307, 1969.
49. Ferri, A.: Goals of Hypersonic Aerodynamics. *Aeronautics and Astronautics*, Oct. 1966, pp. 34-38.
50. Lakshamanan, B.; Tiwari, S. N.; and Hussaini, M. Y.: Control of Supersonic Intersection Flow Fields through Filleting and Sweep. AIAA Paper 88-3534, July 25-29, 1988.
51. Henderson, W. P.; and Holmes, B. J.: Induced Drag-Historical Perspective. Presented at the SAE Aerotech '89 Conference, Anaheim, CA, Sept. 25-28, 1989.
52. Dollyhigh, Samuel, M.; Monta, William J.; and Sangiorgio, Giuliana: Longitudinal Aerodynamic Characteristics at Mach .6 to 2.86 of a Fighter Configuration with Strut Braced Wing. NASA TP-1102, 1977.
53. Krieger, W. B.; and Corlett, William A.: Longitudinal Aerodynamic Characteristics of a Fighter Configuration with Various Wing Structs at Mach 1.6 to 2.0. NASA TM-87662, 1986.
54. Kruse, W. H.: Thrust Deflection for Cruise. *J. of Aircraft*, vol. 4, no. 2, Mar.-Apr. 1967, pp. 162-164.
55. Johnston, P. J.; Cabbage, J. M.; and Weidner, J. P.: Studies of Engine-Airframe Integration on Hypersonic Aircraft. *J. of Aircraft*, vol. 8, no. 7, July 1971, pp. 495-501.
56. DeMeis, Richard: New Tricks for Cutting Drag. *Aerospace America*, 1985, pp. 75-78.
57. Cone, Clarence D., Jr.: The Theory of Induced Lift and Minimum Induced Drag of Nonplanar Lifting Systems. NASA TR-139, 1962.
58. Naik, D. A.; and Ostowair, C.: An Aerodynamic Comparison of Planar and Non-Planar Outboard Wing Planforms. *Proceedings* vol. 1 presented at the 16th ICAS Conference, Jerusalem, Israel, Aug. 28 - Sept. 2, 1988, pp. 468-480.
59. Lundry, J. L.; and Lissaman, P. B. S.: A Numerical Solution for the Minimum Induced Drag of Nonplanar Wings. *J. of Aircraft*, vol. 5, no. 1, Jan.-Feb. 1968, pp. 17-21.
60. van Dam, C. P.: Swept Wing-Tip Shapes for Low-Speed Airplanes. SAE Paper 85AA-9 presented at the 1985 SAE Aerospace Technology Conference and Exposition, Long Beach, CA, Oct. 14-17, 1985.
61. van Dam, C. P.: Induced-Drag Characteristics of Crescent-Moon-Shaped Wings. *J. of Aircraft*, vol. 24, no. 2, Feb. 1987, pp. 115-119.
62. Vijgen, P. M. H. W.; van Dam, C. P.; and Holmes, B. J.: Sheared Wing Tip Aerodynamics: Wing Tunnel and Computational Investigation of Induced Drag Reduction. AIAA Paper 87-2481CP, Aug. 17-19, 1987.
63. Greene, G. C.: Viscous Induced Drag. AIAA Paper 88-2550, June 6-8, 1988.
64. Finch, R.: Wing Tip Design. *Sport Aviation*, Mar. 1984, pp. 40-41.
65. Patterson, J. C., Jr.; and Flechner, S. G.: Exploratory Wind-Tunnel Investigation of a Wing Tip-Mounted Vortex Turbine for Vortex Energy Recovery. NASA TP-2468, June 1985.
66. Lobert, G.: New Drag Reduction Methods for Transport Aircraft. ICAS Paper 84-2.4.3, 1984.
67. Marchman, J. F., III; and Uzel, J. N.: Effect of Several Wing Tip Modifications on a Trailing Vortex. *J. of Aircraft*, vol. 9, Sept. 1972, pp. 684-686.
68. Whitcomb, R. T.: Methods for Reducing Subsonic Drag Due to Lift. AGARD Rep. 654 presented at the Special Course on Concepts for Drag Reduction, June 1977, pp. 2.1 to 2.17.

69. Whitcomb, R. T.: A Design Approach and Selected Wind-Tunnel Results at High Subsonic Speeds for Wing-Tip Mounted Winglets. NASA TND-8260, 1976.

70. Heyson, Harry H.; Riebe, G. D.; and Fulton, C.: Theoretical Parametric Study of the Relative Advantages of Winglets and Wing Tip Extensions. NASA TMX-74003, 1977.

71. KC-135 Winglet Program Review, NASA CP-2211, 1982.

72. Yates, John E.; and Donaldson, C. D.: A Fundamental Study of Drag and an Assessment of Conventional Drag-Due-To-Lift Reduction Devices. NASA CR-4004, Sept. 1986.

73. Kuhlman, J. M.; Liaw, P.; and Cerney, M. J.: Theoretical/Numerical Study of Feasibility of Use of Winglets on Low Aspect Ratio Wings at Subsonic and Transonic Mach Numbers to Reduce Drag. NASA CR-4174, 1988.

74. Hackett, J. E.: Vortex Drag Reduction by Aft-Mounted Diffusing Vanes. ICAS Paper 80-13.4, 1980.

75. Webber, G. W.; and Dansby T.: Wing Tip Devices for Energy Conservation and Other Purposes - Experimental and Analytical Work in Progress at the Lockheed-Georgia Company. Canadian Aeronautics and Space J., vol. 29, no. 2, June 1983, pp. 105-120.

76. Hackett, J. E.: Vortex Diffuser. U. S. Patent 4,190,219, Feb. 26, 1980.

77. Spillman, J. J.: The Use of Wing Tip Sails Reduce Vortex Drag. Aeronautical J., Sept. 1977, pp. 387-395.

78. Boyd, T. M., Jr.: The Effect of Blade To Vanes on Helicopter Rotor Performance. AIAA Paper (DAY/CIN 84-1), Mar. 20, 1984.

79. Spillman, J. J.; and McVitie, A. M.: Wing Tip Sails Which Give Lower Drag at all Normal Flig Speeds. Aeronautical J., Oct. 1984, pp. 362-369.

80. Daxi, Yang: Wing Tip Sails Tested on Y-5 Aircraft. International Aviation, no. 5, May 1988, pp. 2-3.

81. Spillman, J. J.: Wing Tip Sails: Progress Date and Future Developments. Aeronautical J., Dec. 1987, pp. 445-453.

82. Degen, M.; Johnson, A. R.; and Thompson, W. E.: Aerodynamic Characteristics of Ring Wing and Ring Wing-Body Combinations. WADC Technical Report 46-442, March 1957.

83. Letcher, J. S., Jr.: V-Wings and Diamond Ring Wings of Minimum Induced Drag. J. of Aircraft, vol. 9, no. 8, Aug. 1972, pp. 605-607.

84. Gall, Peter D.; and Smith, H. C.: Aerodynamic Characteristics of Biplanes with Winglets. J. of Aircraft, vol. 24, no. 8, Aug. 1987, pp. 518-522.

85. Patterson, J. C., Jr.; and Flechner, S. G.: An Exploratory Wind-Tunnel Investigation of the Wake Effect of a Panel Tip-Mounted Fan-Jet Engine on the Lift-Induced Vortex. NASA TND-5729, May 1970.

86. Patterson, J. C., Jr.; and Bartlett, G. R.: Evaluation of Installed Performance of a Wing-Tip Mounted Pusher Turboprop on a Semi-Span Wing. NASA TP-2739, Aug. 1987.

87. Patterson, J. C.; and Bartlett, G. R.: Effect of a Wing Tip Mounted Pusher Turboprop on the Aerodynamic Characteristics of a Semi-Span Wing. AIAA Paper 85-1347, 1985.

88. Yuan, S. W.; and Bloom, A. M.: Experimental Investigation of Wing-Tip Vortex Abatement. ICAS Paper 74-35, 1974.

89. Wu, J. M.; Vakili, A.; and Chen Z. L.: Wing-Tip Jets Aerodynamic Performance. ICAS Paper 82-5.6.3, 1982.

90. Wu, J. M.; Vakili, A. D.; and Gilliam, F. T.: Aerodynamic Interactions of Wing Tip Flow with Discrete Wing Tip Jets. AIAA Paper 84-2206, Aug. 21-23, 1984.

91. Tavella, D. A.; Wood, N. J.; and Harris, P.: Influence of Tip Blowing on Rectangular Wings. AIAA Paper 85-5001, Oct. 14-16, 1985.

92. Brown, Clinton E.; and McLean, Francis E.: The Problem of Obtaining High Lift Drag Ratios at Supersonic Speeds. J. of Aerospace Sciences, vol. 26, no. 5, May 1959, pp. 298-302.

93. Jones, R. T.: Estimated Lift-Drag Ratios at Supersonic Speed. NACA TN-1350, 1947.

94. Jones, R. T.: Theoretical Determination of the Minimum Drag of Airfoils at Supersonic Speeds. J. of Aeronautical Sciences, vol. 19, no. 12, 1952, pp. 813-822.

95. Whitcomb, Richard T.; and Fischetti, T. L.: Development of a Supersonic Area Rule and an Application to the Design of a Wing-Body Configuration Having High Lift-to-Drag Ratios. NACA RM-L53H31A, 1953.

96. Whitcomb, Richard T.: Some Considerations Regarding the Application of the Supersonic Area Rule to the Design of Airplane Fuselages. NACA RM-L56E23A, 1956.

97. Nielson, J. N.; and Pitts, William C.: General Theory of Wave Drag Reduction for Combinations Employing Quasi-Cylindrical

Bodies with an Application to Swept-Wing and Body Combinations. NACA TN-3722, 1956.

98. Heaslet, M. A.; and Fuller, F. B.: Drag Minimization for Wings and Bodies in Supersonic Flow. NACA Rep. 1385, 1958.

99. Yoshihara, H.; Kainer, J.; and Strand, T.: On Optimum Thin Lifting Surfaces at Supersonic Speeds. vol. 25, no. 8, Aug. 1958, pp. 473-479.

100. Whitcomb, R. T.; and Sevier, J. R., Jr.: A Supersonic Area Rule and an Application to the Design of a Wing-Body Combination with High Lift-Drag Ratios. NASA TR-72, 1960.

101. Das, A.: On Some Basic and New Aspects About the Drag Problem of Wings and Bodies in Supersonic Flows. AGARD CP-124 on Aerodynamic Drag, Oct. 1973, pp. 3-1 to 3-26.

102. Nastase, A.: Optimum-Optimorum Wing-Fuselage Configuration for Supersonic Transport Aircraft of Second Generation. ICAS Paper 86-1.3.6, Sept. 2-12, 1986.

103. Bos, H. J.: Optimum Supersonic Wings with Subsonic Leading Edges. J. of Aircraft, vol. 23, no. 4, Apr. 1986, pp. 326-332.

104. Licher, R. M.: Reduction of Drag Due to Lift in Supersonic Flight by Distributing Lift Along a Fuselage. J. of Aero. Sciences, vol. 23, no. 11, Nov. 1956, pp. 1037-1043.

105. Carlson, H. W.; Mack, R. J.; and Barger, R. L.: Estimation of Attainable Leading Edge Thrust for Wings at Subsonic and Supersonic Speeds. NASA TP-1500, 1979.

106. Carlson, H. W.; and Mack, R. J.: Studies of Leading-Edge Thrust Phenomena. AIAA Paper 80-0325, Jan. 14-16, 1980.

107. Robins, A. W.; Carlson, H. W.; and Mack, R. J.: Supersonic Wings with Significant Leading Edge Thrust at Cruise. NASA TP-1632, 1980.

108. Carmichael, R. L.: The Prospects of Aerodynamic Performance Gains from Wing Camber and Twist and Low Hypersonic Mach Numbers. NASA SP-148, 1967, pp. 79-86.

109. Middleton, W. D.; and Sorrels, R. B.: Off Design Aerodynamic Characteristics at Mach Numbers 1.61 and 2.2 of a Series of Highly Swept Arrow Wings for Mach 2 Employing Various Degrees of Twist and Camber. NASA TND-1630, 1963.

110. Brown, Clinton, E.; McLean, F. E.; and Klunker, E. B.: Theoretical and Experimental Studies of Cambered and Twisted Wings Optimized for Flight at Supersonic Speeds. Adv. in Aero. Science, vol. 3, Pergamon Press, NY, 1961, pp. 415-430.

111. Carlson, H. W.: Pressure Distribution at Mach Number 2.05 on a Series of Highly Swept Arrow Wings Employing Various Degrees of Twist and Camber. NASA TND-1264, 1962.

112. Carlson, H. W.; and McLean, F. E.: Current Methods for Prediction and Minimization of Lift-Induced Drag at Supersonic Speeds. NASA SP-124, 1966, pp. 383-398.

113. Kuchemann, D.: Hypersonic Aircraft and their Aerodynamic Problems. Progress in Aero. Sciences, vol. 6, pp. 271-355.

114. Dulov, V. G.; Shchepanovskiy, V. A.: Deceleration of a Supersonic Flow Behind a Curved Shockwave with Isentropic Pre-Compression. NASA TM-77920. (Translated from Sibirsk. Otd. IZV. Ser. Tekhn. Nauk (USSR), no. 8, June 1977, pp. 72-78.

115. van Dyke, M.: An Album of Fluid Motion. Parabolic Press, Stanford, CA, 1982.

116. Miele, A.: A Theory of Optimum Aerodynamic Shapes. Academic Press, 1965.

117. Ostapenko, N. A.: Conical Bodies with Star-Shaped Section which Possess a Reserve of Static Stability. Fluid Dynamics, vol. 19, no. 6, Nov. - Dec. 1984, pp. 930-938.

118. Folle, M. I.: Wave Drag of Slender Star-Shaped Bodies at Moderate Supersonic Flight Velocities. Fluid Dynamics, vol. 18, no. 5, Sept.-Oct. 1983, pp. 783-788.

119. Shchepanovskaya, G. I.; and Shchepanovskiy, V. A.: Influence of the Shock Layer on the Viscous Drag of Star-Shaped Bodies with Planar Side Panels. J. of Applied Mechanics and Technical Physics, vol. 26, no. 4, July-Aug. 1985, pp. 546-552.

120. Zubin, M. A.; Lapygin, V. I.; and Ostapen, N. A.: Theoretical and Experimental Investigation into the Structure of Supersonic Flow Past Bodies of Star-Shaped Form and Their Aerodynamic Characteristics. Fluid Dynamics, 1982, pp. 355-360.

121. Jones, R. T.: Flying Wing SST for the Pacific. Aerospace America, vol. 24, Nov. 1986, pp. 32-33.

122. Ross, J. M.; Reaser, J. S.; and Bouchard, E. E.: Optimization of a Supersonic Wing by Combining Linear and Euler Methods. SAE Paper 851791, Oct. 14-17, 1985.

123. Pittman, J. L.: Supersonic Aircraft

Optimization. *J. of Aircraft*, vol. 24, no. 12, Dec. 1987, pp. 873-879.

124. Pittman, J. L.: Supersonic Wing Design Using Full Potential Methods. Presented at the Royal Aeronautical Society Symposium "Aerodynamic Design for Supersonic Flight," London, England, Apr. 19, 1988.

125. Pittman, J. L.; and Sinclair, M. J.: Nonlinear Aerodynamic Effects on Bodies in Supersonic Flow. *J. of Aircraft*, vol. 21, no. 10, Oct. 1984, pp. 809-815.

126. Bogdonoff, S. M.; and Vas, I. E.: Preliminary Investigation of Spiked Bodies at Hypersonic Speeds. *J. of the Aero/Space Sciences*, vol. 26, no. 2, Feb. 1959, pp. 65-74.

127. Hinanda, M.; Yamashita, N.; Karashima, K.; Sato, K.; and Honda, M.: Effects of Spikes and Flange-Like Steps as Rocket Drag at Supersonic Speeds. *Adv. in the Astronautical Sciences*, vol. 60 published by American Astronautical Society, AAS Paper 85-682, 1986, pp. 669-677.

128. Karlovskii, V. N.; and Sakharov, V. I.: Numerical Investigation of Supersonic Flow Past Blunt Bodies with Protruding Spikes. *Fluid Dynamics*, vol. 21, no. 3, May-June 1986, pp. 437-445.

129. Reding, J. P.; Guenther, R. A.; and Richter, B. J.: Unsteady Aerodynamic Considerations in the Design of a Drag-Reduction Spike. *J. of Spacecraft and Rockets*, vol. 14, Jan. 1977, pp. 54-60.

130. Mair, W. A.: Experiments on Separation of Boundary Layers on Probes in Front of Blunt-Nosed Bodies in a Supersonic Air Stream. *The Philosophical Magazine*, Ser. 7, vol. 43, no. 342, Jly 1955, pp. 695-716.

131. Maull, D. J.: Hypersonic Flow over Axially Symmetric Spiked Bodies. *J. of Fluid Mechanics*, vol. 8, Pt. 4, Aug. 1960, pp. 584-592.

132. Hunt, G. K.: Supersonic Wind Tunnel Study of Reducing the Drag of a Bluff Body at Incidence by Means of a Spike. *RAE Aero Rep. 2606*, May 1958.

133. Belov, I. A.; Tsymbalov, V. V.; and Lumkin, Iu. P.: Flow Control in a Shock Layer on a Body of Revolution. *NASA TM-77857*. (Translation of "Upravlenie Technnem Vi Udarnom Sloe Tel Vrashchenia," 1982.)

134. Chapman, D. R.: Reduction of Profile Drag at Supersonic Velocities by the Use of Airfoil Sections Having a Blunt Trailing Edge. *NACA TN-3503*, Sept. 1955.

135. Reding, J. P.; and Jecmen, D. M.: An Advanced Aerospike to Minimize Nose Drag. *Lockheed Horizons*, vol. 15, 1984, pp. 46-54.

136. Pugh, P. G.; and Ward, L. C.: A Parametric Study of the Use of Nose Blunting to Reduce the Supersonic Wave Drag of Forebodies. *ARC-CP-1271*, 1974.

137. Furey, R. J.: Minimum Energy Hypersonic Nose and Leading Edge Shapes. *J. of Spacecraft and Rockets*, vol. 9, no. 2, Feb. 1972, pp. 107-115.

138. Boyd, J. A.: Optimal Utilization of Supersonic Favorable Interference to Obtain High Lift-Drag Ratios. *AIAA Paper 65-752*, Nov. 15-18, 1965.

139. Sears, W. R.; and Tan, H. S.: The Aerodynamics of Supersonic Biplanes. *Quarterly of Applied Mathematics*, vol. 9, Apr. 1951, pp. 67-76.

140. Eggers, A. J., Jr.; and Syvertson, C. A.: Aircraft Configurations Developing High Lift-Drag Ratios at High Supersonic Speeds. *NACA RM-A55L05*, 1956.

141. Ferri, A.; and Clarke, J. H.: On the Use of Interfering Flow Fields for the Reduction of Drag at Supersonic Speeds. *J. of Aero. Sciences*, vol. 24, Jan. 1957, pp. 1-18.

142. Graham, E. W.; Ligerstrom, P. A.; Licher, R. M.; and Beane, B. J.: A Theoretical Investigation of the Drag of Generalized Aircraft Configurations in Supersonic Flow. *NACA TM 1421*, 1957.

143. Rossow, V. J.: A Theoretical Study of the Lifting Efficiency at Supersonic Speeds of Wings Utilizing Indirect Lift Induced by Vertical Surfaces. *NACA RM-A55L08*, 1956.

144. Broglio, L.: Theoretical and Experimental Analysis of Cowling Configuration for the Reduction of the Drag on a Body of Revolution with Large Cone Angle. *Scuola Di Ingegneria Aeronautica, Universita Di Roma, STAR Graph 7*, June 1956.

145. Johnson, R. P.: Theoretical Development for Lifting Ring-Body Configurations. *Rand Corp. RM-2260, AD 207751*, Sept. 1958.

146. Browand, F. K.: The Design and Test of a Zero-Wave-Drag Ring-Wing Configuration. *Rand Corp. RM-2638*, June 1960.

147. Morris, O.: Aerodynamic Characteristics in Pitch of Several Ring-Wing-Body Configurations at a Mach Number of 2.2. *NASA TND-1272*, Apr. 1962.

148. Johnson, R. P.: Drag Transformation and Reduction for Bodies of Revolution. *Rand Corp. RM-2107, AD-156008*, 1957.

149. Licher, R. M.: Calculation of the Thickness and Radial Force Distribution for a Ring Wing Having Zero Drag at Supersonic Speeds. Douglas Aircraft Co. Rep. SM-23579, May 1959.

150. Terry, J. E.: Aerodynamic Characteristics of Ring Wings, A Bibliography. U.S. Army Missile Command, Redstone Arsenal RSIC-285, AD-452725, Sept. 1965.

151. Visich, M., Jr.; and Martellucci, A.: Theoretical and Experimental Analysis of a Cowling as a Means of Drag Reduction for an Axisymmetric Center Body. AFOSR RN-58-760, AD-16273, 1958.

152. Erdmann, S. F.; and Zandbergen, P. J.: A Survey of 10 Years of NLR Activities on Ring Wing-Body Configurations (1956-1966), NLR-TR69070U, 1976.

153. Johnson, A. R.; Mead, H. R.; and Scheuing, R. A.: An Experimental Investigation of Simple Symmetric and Unsymmetric Supersonic Ring Wing Configurations Utilizing Beneficial Interference Effects. Grumman Research Dept. Rep. RE-175, May 1964.

154. Gord, P. R.: Development of an Analytical Model for Predicting the First Order Effects of Fuselage-to-Wing Favorable Aerodynamic Interference at $M = 4.5$. AFWAL TR-83-3049, 1983.

155. Morris, O. A.; and Lamb, M.: Aerodynamic Characteristics in Pitch of a Modified Half-Ring-Wing Body Combination and a Swept-Wing-Body Combination at Mach 2.16 to 3.7. NASA TM-1551, 1968.

156. Morris, O. A.; and Mack, R. J.: Aerodynamic Characteristics of a Parasol Wing-Body Combination Utilizing Favorable Lift Interference at Mach Numbers from 3.0 to 4.63. NASA TND-4855, 1968.

157. Erdos, J.: Aeromechanical Applications of Favorable Supersonic Interference, vol. L. GASL-TR-268, AFWAL-TR-82-3020, 1983.

158. Kulfan, R. M.; Yoshihara, H.; Lord, B. J.; and Freibel, G. O.: Application of Supersonic Favorable Aerodynamic Interference to Fighter Type Aircraft. AFFDL-TR-78-33, 1978.

159. Mysliwetz, F.: Supersonic Interference Lift. AIAA J., vol. 1, June 1963, pp. 1432-1434.

160. Beane, B. J.; and Ryan, B. M.: Supersonic Drag Calculations for a Cylindrical Shell Wing of Semi-Circular Cross Section Combined with a Central Body of Revolution. Douglas Aircraft Rep. SM-22627, Oct. 1956.

161. Wood, R. M.; Rose, O. J.; and McMillin, S.: Multi-Body Aircraft: Old Concept - New Application. NASA CP-2398, vol. 11, 1985, pp. 235-249.

162. Wood, R. M.; Miller, D. S.; and Brentner, K. S.: Theoretical and Experimental Investigation of Supersonic Aerodynamic Characteristics of a Twin-Fuselage Concept. NASA TP-2184, 1983.

163. Bauer, S. X. S.; and McMillin, S. N.: Experimental and Theoretical Study of the Effects of Wing Geometry on a Supersonic Multibody Configuration. AIAA Paper 88-2510 presented at the AIAA 6th Applied Aerodynamics Conference, Williamsburg, VA, June 6-8, 1988.

164. Friedman, M. D.; and Cohen, D.: Arrangement of Fusiform Bodies to Reduce the Wave Drag at Supersonic Speeds. NACA Rep. 1236, 1955.

165. Nielsen, J. N.: Arrays for Minimum Wave Drag of Bodies of Revolution. AIAA Paper 85-0449, 1985.

166. Large Payload Capacity SST Concepts - Technical and Economic Feasibility, NASA CR-165934, July 1982.

167. Wood, R. M.; Rose, O. J.; and McMillin, S. N.: Effect of Body Cross-Sectional Shape on the Supersonic Aerodynamics of Multibody Configurations. NASA TP-2587, 1986.

168. McMillin, S. N.; and Wood, R. M.: Planform Effects on the Supersonic Aerodynamics of Multi-body Configurations. NASA TP-02762, 1987.

169. McMillin, S. N.; and Wood, R. M.: Planform Effects for Low-Fineness Ratio Multibody Configurations at Supersonic Speeds. AIAA Paper 86-1799, June 9-11, 1986.

170. Dollyhigh, S. M.; and Coen, P. G.: Advanced Technology and Unconventional Aircraft Concepts. Unconventional Aircraft Concepts, Delft University Press, 1987, pp. 52-71.

171. Squire, L. C.: The Use of Excess Engine Exit Area Over Intake Area to Reduce Zero Lift Drag at High Supersonic Speeds. Aeronautical Quarterly, Aug. 1965, pp. 260-274.

172. Suikat, R.; and Farokhi, S.: Method to Optimize Nacelle Shape in a Supersonic Cruise Aircraft. J. of Aircraft, vol. 25, Aug. 1988, pp. 717-723.

173. Sigalla, A.; and Hallstaff, T. H.: Aerodynamics of Powerplant Installation on Supersonic Aircraft. J. of Aircraft, vol. 4, no. 4, July-Aug. 1967, pp. 273-277.

174. Erdos, J. I.; Ray, R.; and Mandel, M.: Aeromechanical Applications of Favorable

Supersonic INterference. AFWAL-TR-82-3020, vol. 3 and vol. 4, 1983.

175. Nichols, M. R.: Aerodynamics of Airframe-Engine Integration of Supersonic Aircraft. NASA TND-3390, 1966.

176. Robins, A. Warner, and Whitcomb, R. T.: Additional Configuration Approaches. NASA TMX-905, 1963, pp. 277-290.

177. Rethorst, S.; and James, E.: Shock Free Supersonic Aircraft. VRC Rep. 36, ADB06920, Nov. 1982.

178. Wood, R. M.: Multi-Body Aircraft with an All-Movable Center Fuselage Actively Controlling Fuselage Pressure Drag. U.S. Patent 14,735,381, Apr. 1988.

179. Truitt, R. W.: Hypersonic Aerodynamics. Ronald Press, NY, 1959, pp. 110-11.

180. Bumimovich, A. L.; and Dubinskii, A. V.: On a Class of Three-Dimensional Bodies of Minimal Drag at Hypersonic Speeds. Mechanics Bulletin, Moscow State University, vol. 32, no. 3-4, 1977, pp. 54-59.

181. Allen, J. E., Jr.; Anderson, W. R.; and Crosley, D. R.: Optoacoustic Pulses in a Flame. Optic Letters, vol. 1, 1977, pp. 118-120.

182. Fourquette, D. C.; and Long, M. B.: Highly Localized Pressure Perturbations Induced by Laser Absorptive Heating in the Shear Layer of a Gas Jet. Optics Letters, vol. 8, no. 12, 1983, pp. 605-607.

183. Arafaiov, S. I.: Effect of Energy Release in the Shock Layer on Supersonic Flight. Fluid Dynamics, vol. 22, no. 4, Jan. 1988, pp. 645-649.

184. Belokon, V. A.; Rudenko, O. V.; and Khokhlov, R. V.: Aerodynamic Effects of Supersonic Flow Past a Laser Beam. Soviet Physics-Acoustics, vol. 23, July-Aug. 1977, pp. 361-362.

185. Krasnobaev, K. V.: Supersonic Flow Past Weak Sources of Radiation. Fluid Dynamics, vol. 19, no. 4, July-Aug. 1984, pp. 629-632.

186. Georgievskii, P. Yu; and Levin, V. A.: Supersonic Flow About Objects with External Heat - Evolution Sources. Soviet Technical Physics Letters, vol. 14, no. 4, Apr. 1988, pp. 684-687.

187. Kogan, M. N.; Kucherov, A. N.; and Ustinov, M. V.: The Effect of Thermal Self-Action of a Light Beam in a Shear Flow. J. of Engineering Physics, vol. 52, no. 1, Jan. 1987, pp. 39-44.

188. Wood, R. M. and Bauser, S. X. S.: Evaluation of a 3-D Empirically Derived Wing at Supersonic Speeds. AIAA Paper 88-0481, 1988.

189. Pitman, J. L.; and Bonhaus, D. L.; Siclari, M. J.; and Dollyhigh, S. M.: An Euler Analysis of a High Speed Civil Transport Concept at Mach 3. AIAA Paper 89-2174, July 31 - Aug. 2, 1989.

190. Becker, I. V.: Studies of High Lift-Drag Ratio Hypersonic Configurations. Presented at the 4th ICAS Congress, Paris, France, 1964, p. 877-910.

191. Serbanescu, E.; and Savu, G.: Drag Reduction of Perforated Axisymmetric Bodies in Supersonic Flow. J. of Spacecraft and Rockets, vol. 22, no. 6, Nov./Dec. 1985, pp. 663-665.

192. Bauer, S. X. S.; and Hernandez, G.: Reduction of Cross-Flow Shock-Induced Separation with a Porous Cavity at Supersonic Speeds. AIAA Paper 88-2557, 1988.

193. Barnwell, R.; Bushnell, D.; Nagamatsu, H. T.; Bahi, L.; and Ross, J.: Passive Drag Control of Airfoils at Transonic Speeds. U.S. Patent 4,522,360, June 1985.

194. Nagamatsu, H. T.; Trilling, T. W.; and Bossard, J. A.: Passive Drag Reduction to Complete NACA 0012 Airfoil at Transonic Mach Numbers. AIAA Paper 87-1263, 1987.

195. Bertin, J. J.; and Smith, M. L.: Aerodynamics for Engineers. Prentice-Hall, NJ, 1979.

196. Delesy, J. M.: Shockwave/Turbulent Boundary Layer Interaction and its control. Prog. Aerospace Science, vol. 22, 1985, pp. 209-280.

197. Viswanath, P. R.: Shockwave Boundary Layer Interaction and its Control: A Survey of Recent Developments. Sadhana, vol. 12, Pts. 1 and 2, Feb. 1988, pp. 45-104.

198. Chang, P. K.: Control of Flow Separation. Hemisphere Publishing Company, Washington and London, 1976.

199. Grahame, W. E.; and Headley, J. W.: Experimental Investigation of Boundary Layer Control (BLC) Devices at Transonic Speeds. AFFDL-TR-70-22, vol. 1, AD-872970.

200. Johnson, J.; and Nishi, M.: Vortex Generator Jets - A Means for Passive and Active Control of Boundary Layer Separation. AIAA Paper 89-0564, 1989.

201. Compton-Hall, R.: Revolutionizing the Submarine. Jane's Defense Weekly, Aug. 13, 1988, pp. 266-268.



LAMINAR - TURBULENT TRANSITION: FUNDAMENTALS

William S. Saric

Mechanical and Aerospace Engineering
 Arizona State University
 Tempe, AZ 85287-6106 USA

92-17809



SUMMARY

The basic instability mechanisms are discussed from an elementary standpoint considering only boundary layers in external flows. The objective of this report is to provide the basic ideas and results of boundary-layer stability in order that one can understand transition mechanisms, transition control, and transition prediction for aircraft systems. The current state-of-the-art of boundary-layer stability is reviewed and by using recent results, it is shown that a number of unique transition mechanisms exist and each can play a different role in the breakdown to turbulence. The control of the stability and transition characteristics of a particular flow field requires thoroughly understanding the details of these breakdown mechanisms.

TABLE OF CONTENTS

NOMENCLATURE	2
1. INTRODUCTION	3
1.1 The process of transition for boundary layers in external flows	3
1.2 Objectives	3
1.3 Review of literature	3
2. LINEAR STABILITY ANALYSIS	4
2.1 Normal modes and the Orr-Sommerfeld equation	5
2.2 Solution of the Orr-Sommerfeld equation	6
2.3 Temporal and spatial stability: Gaster's transformation	6
2.4 2-D and 3-D disturbances: Squire's transformation	7
3. STREAMWISE INSTABILITIES	8
3.1 Inviscid instability mechanism	8
3.2 Viscous instability mechanism: T-S waves	8
3.3 The Smith-Van Ingen e^N method	9
3.4 Compressibility effects	10
4. CROSSFLOW INSTABILITIES	12
4.1 Stability calculations	13
4.2 Experimental results	14
5. CENTRIFUGAL INSTABILITIES	15
5.1 Stability analysis and computations	16
5.2 Experiments	17
6. ATTACHMENT-LINE INSTABILITIES	17
7. SECONDARY INSTABILITIES LEADING TO TRANSITION	18
7.1 Streamwise secondary instabilities	18
7.2 Crossflow secondary instabilities	19
7.3 Centrifugal secondary instabilities	21
8. RECEPΤIVITY	21
8.1 Acoustic receptivity	22
8.2 Vorticity receptivity	22
9. CONTROL OF INSTABILITIES AND TRANSITION	22
9.1 Laminar Flow Control (LFC)	22
9.2 Active control of transition	23
9.3 Loss of control	23
ACKNOWLEDGEMENTS	24
REFERENCES	24
FIGURES	29

NOMENCLATURE

A	norm of disturbance amplitude	V	basic-state, normal-to-the-wall velocity normalized by U_∞
A_o	amplitude at $R = R_o$, usually Branch I	V_o	blowing or suction velocity at the wall [m/s]
C_p	pressure coefficient	W	basic-state spanwise boundary-layer velocity normalized by U_∞
c	$= c_r + i c_i$: complex wave speed; c_r is phase speed; $i c_i$ is temporal growth rate	W_t	crossflow velocity, [m/s], (perpendicular to U_∞)
c.c.	denotes complex conjugate	$W_{t\max}$	maximum of crossflow velocity [m/s]
D	$= d/dy$	x, y, z	chordwise, normal-to-the-wall, and spanwise coordinates normalized by δ_r
F	$= \omega/R = 2\pi f U_\infty^2$: dimensionless frequency	x^*, y^*, z^*	dimensional coordinates [m]
f	dimensional frequency [hz]	x_t, z_t	coordinates tangent to and perpendicular to the inviscid velocity vector
G	Görtler number, $(\kappa L/\epsilon)^{1/2}$; $G^2 > 0$: concave; $G^2 < 0$: convex	y_s	inflection point (or generalized inflection point)
k	$= k_r + i k_i$: complex wavenumber vector, ($k = \alpha$ for 2-D)	α	$= \alpha_r + i \alpha_i$: chordwise complex wavenumber normalized by δ_r
k_r	(α_r, β_r) wavenumber vector	α_r	$= 2\pi\delta_r/\lambda_x$
k_i	(α_i, β_i) spatial growth-rate vector	β	$= \beta_r + i \beta_i$: spanwise complex wavenumber normalized by δ_r
L	length scale, chord	β_r	$= 2\pi\delta_r/\lambda_z$
M_c	local edge Mach number	δ_r	$= (v x^*/U_\infty)^{1/2}$: boundary-layer reference length, [m], (normalizing length)
M	$= (\alpha U + \beta W - \omega) M_o / (k^2 T)^{1/2}$: relative Mach number	δ^*	displacement thickness [m]
N	$= \ln(A/A_o)$: amplification factor	δ_{10}	largest thickness where $W_t/W_{t\max} = 10\%$ [m]
P	basic-state pressure	ϵ	$= 1/R$: small viscous scale
p'	disturbance-state pressure	η	$= y^*/\delta_r = y$: boundary-layer coordinate
Q	basic-state dependent variable	Θ	$= \int (\alpha dx + \beta dz - \omega dt)$: phase function
q'	disturbance-state dependent variable (i.e. u', v', w' , or p')	θ	momentum thickness [m]
R	$= (R_x)^{1/2} = U_\infty \delta_r / \nu$: boundary-layer Reynolds number	κ	$\kappa(x)$, wall curvature; $\kappa > 0$: concave; $\kappa < 0$: convex
R_o	initial boundary-layer Reynolds number, usually Branch I	Λ	dimensionless spanwise wavelength, $G(2\pi/\beta_r)^{1/2}$, a constant
R_x	$= U_\infty x^*/\nu$: x -Reynolds number or chord Reynolds number	λ_x	chordwise wavelength [m]
R_{cf}	$= W_{t\max} \delta_{10} / \nu$: crossflow Reynolds number	λ_z	spanwise wavelength [m]
T	temperature, normalized with edge temperature	μ	dynamic viscosity [ns/m ²]
U	basic-state chordwise boundary-layer velocity normalized by U_∞	ν	kinematic viscosity [m ² /s]
U_∞	freestream velocity, [m/s], (normalizing velocity)	ρ	density [kg/m ³]
U_t	component parallel to inviscid flow over swept wing [m/s]	ϕ	eigenfunction or the Orr-Sommerfeld equation, $\phi = \phi(y; k, F, R)$
U_{et}	inviscid flow velocity over swept wing [m/s]	ω	$= 2\pi f \delta_r / U_\infty = FR$: dimensionless circular frequency
u', v', w'	disturbance velocity field normalized by U_∞	ξ	slowly varying streamwise coordinate, $\epsilon x^*/L$
$ u' $	rms of u'		

1. INTRODUCTION

These notes on the fundamentals of boundary-layer transition serve as a tutorial on the basic concepts of stability and transition and, as such, are an introduction to the notes on prediction and application to drag reduction (Arnal, 1992). Two AGARD - VKI Special Courses, *Stability and Transition of Laminar Flow* (AGARD Report No. 709, March 1984) and *Aircraft Drag Prediction and Reduction* (AGARD Report No. 723, May 1985), serve as absolute references to the material presented here. During those courses, the written lectures by Arnal (1984), Mack (1984b), Reshotko (1984a,b), Poll (1984b), and Herbert (1984b,c) covered vast amounts of detail on the fundamentals of stability and transition and the lectures by Thomas (1985), Saric (1985a,b), Braslow and Fischer (1985), Bushnell (1985), Poisson-Quinton (1985), Hackett and Sugavanam (1985), Lock (1985), and Stanewsky and Krogmann (1985) covered applications to drag reduction. These reports summarize the activity as of 1985 and therefore, it will not be necessary to present here a detailed research document with complete references but rather it is possible to rely on this considerable collection of information.

1.1 The process of transition for boundary layers in external flows

In fluids, turbulent motion is usually observed rather than laminar motion because the Reynolds-number range of laminar motion is generally limited. The *transition* from laminar to turbulent flow occurs because of an incipient instability of the basic flow field. This instability intimately depends on subtle, and sometimes obscure, details of the flow. The process of transition for *boundary layers in external flows* can be qualitatively described using the following (albeit, oversimplified) scenario.

Disturbances in the freestream, such as sound or vorticity, enter the boundary layer as steady and/or unsteady fluctuations of the basic state. This part of the process is called *receptivity* (Morkovin, 1969) and although it is still not well understood, it provides the vital initial conditions of amplitude, frequency, and phase for the breakdown of laminar flow. Initially these disturbances may be too small to measure and they are observed only after the onset of an instability. A variety of different instabilities can occur independently or together and the appearance of any particular type of instability depends on Reynolds number, wall curvature, sweep, roughness, and initial conditions. The initial growth of these disturbances is described by *linear* stability theory (i.e. linearized, unsteady, Navier-Stokes). This growth is weak, occurs over a viscous length scale, and can be modulated by

pressure gradients, surface mass transfer, temperature gradients, etc. As the amplitude grows, three-dimensional and nonlinear interactions occur in the form of *secondary* instabilities. Disturbance growth is very rapid in this case (now over a convective length scale) and breakdown to turbulence occurs.

Since the linear stability behavior can be calculated, transition prediction schemes are usually based on linear theory. However, since the initial conditions (receptivity) are not generally known, only correlations are possible and, most importantly, these correlations must be between two systems with similar environmental conditions.

At times, the initial instability can be so strong that the growth of linear disturbances is *by-passed* (Morkovin, 1969) and turbulent spots or secondary instabilities occur and the flow quickly becomes turbulent. This phenomenon is not well understood but has been documented in cases of roughness and high freestream turbulence. In this case, transition prediction schemes based on linear theory fail completely.

The *control* of turbulent skin friction has two modes. The first prevents the boundary layer from becoming turbulent by limiting the growth of linear disturbances in order to keep the amplitude below a critical level. This is known as *Laminar Flow Control* and is described below and by Arnal (1992). The second controls the turbulence structure as described by Bushnell (1992), Blackwelder (1992), Savill and Coustols (1992), and Spalart (1992). Control in these cases is limited to passive control. Active feedback control of transition and turbulence is in its infancy.

1.2 Objectives

Aircraft wings are the principal areas of concern with regard to laminar-turbulent transition. The flow over a swept wing is subject to four kinds of instabilities. These are related to the streamwise flow, the crossflow, centrifugal effects, and the attachment-line flow. Since the flight condition is a low-disturbance environment, stability plays an important role in the transition process.

The objective of this report is to provide the basic ideas and results of boundary-layer stability in order that the reader can understand transition mechanisms, transition control, and transition prediction for aircraft systems. The order of topics listed in the Table of Contents outlines the strategy.

1.3 Review of literature

The literature review follows the outline of the process described above and begins with Reshotko (1984a) on

receptivity (i.e. the means by which freestream disturbances enter the boundary layer). In this paper, Reshotko summarizes the recent work in this area and points out the difficulties in understanding the problem. Indeed, the receptivity question and the knowledge of the initial conditions are the key issues regarding a transition prediction scheme. The discussion in Sec.8 will show that this goal is far from being reached.

Mack (1984b) is actually a monograph on boundary-layer stability theory and should be considered required reading for those interested in all aspects of the subject. It covers 58 pages of text with 170 references. In particular, his report updates the three-dimensional (3-D) material in Mack (1969), covering in large part Mack's own contributions to the area. This lecture will rely on Mack(1984b) to some extent since all of the basic details for deriving, analyzing, and solving the stability equations for two-dimensional (2-D) flows, compressible flows, and 3-D flows are given.

The two papers of Herbert (1984b,c) cover the problems of *streamwise* secondary instabilities and nonlinearities i.e. those aspects of the breakdown process that follow the growth of linear disturbances. Two- dimensional waves do not completely represent the breakdown process since the transition process is *always* three-dimensional in bounded shear flows. Herbert describes the efforts in extending the stability analysis into regions of wave interactions that produce higher harmonics, three-dimensionality, subharmonics, and large growth rates--all harbingers of transition to turbulence. Secondary instabilities of *crossflow-dominated* flows are just being investigated. More is said about this in Sec.7.

The paper by Arnal (1984) is an extensive description and review of transition prediction for two-dimensional flows that covers 34 pages of text and over 100 citations. A description of different mechanisms that cause transition such as Tollmien-Schlichting (T-S) waves, Görtler vortices, and turbulent spots is given. The effects that modulate the transition behavior are presented. These include the influence of freestream turbulence, sound, roughness, pressure gradient, suction, and unsteadiness. This paper is of interest to the aircraft systems designer from the standpoint of giving an overall historical perspective of transition phenomena and their anfractuous nature. This work is updated with Arnal (1992).

Poll (1984b) extends the description of the transition territory to 3-D flows. When the basic state is three-dimensional, not only are 3-D disturbances important, but different types of instabilities can occur. Poll concentrates on the problems of leading-edge contamination and crossflow vortices, both of which are of interest to the designer. The history of these problems as well as the recent work on transition

prediction and control schemes are discussed. Additional discussion of 3-D flows is presented below in Sec.4 and Sec.7.

Reshotko (1979; 1984b; 1985) reviews the application of stability and transition information to problems of drag reduction and, in particular, laminar flow control. He discusses some of the laminar flow control issues which are mentioned but not covered in detail in Sec.9. A portion of his work is also devoted to the issues of *viscous simulation*.

Saric (1985a; 1985b) are reviews of stability and control fundamentals that are the basis for the present notes.

2. LINEAR STABILITY ANALYSIS

In this section, the stability analysis of three-dimensional disturbances in an incompressible *parallel* boundary-layer flow, without curvature, is presented. These assumptions are introduced initially to simplify the exposition of basic stability ideas. The *basic-state* velocity vector, $\mathbf{V} = (U, V, W)$, is defined by the following one-dimensional (1-D) flow:

$$U = U(y), \quad V = 0, \quad W = W(y) \quad (1)$$

where U is the chordwise velocity component, W is the spanwise velocity component, and y is the coordinate normal to the wall.

It is, of course, an incongruity to speak of a parallel boundary-layer flow since no such thing can exist except under very special circumstances. However, the parallel-flow assumption is an important first approximation to the actual two-dimensional basic-state problem because the Reynolds number is very large. It is beyond the scope of this lecture to discuss non-parallel stability effects so the reader is referred to Mack (1984b) and Saric (1990) for a summary. In spite of the fact that every year or so, someone makes some heavy weather over non-parallel effects, this is not the most important problem. Likewise, the role of compressibility in subsonic flows is minor and all of the essential physical ideas are represented in the flow of Eq.(1). However, compressibility is indeed important for supersonic flows and this will be discussed in Sec.3.4.

The stability equations are obtained by superposing small disturbances onto the basic state:

$$u^*/U_\infty = U + u'(x,y,z,t) \quad (2a)$$

$$v^*/U_\infty = v'(x,y,z,t) \quad (2b)$$

$$w^*/U_\infty = W + w'(x,y,z,t) \quad (2c)$$

$$p^*/\rho U_\infty^2 = P + p'(x,y,z,t) \quad (2d)$$

where u^* , v^* , w^* , and p^* satisfy the complete dimensional Navier-Stokes equations, $(')$ denotes dimensionless disturbance quantities, and capital letters denote dimensionless basic-state quantities. Equation (2) is substituted into the unsteady Navier-Stokes equations which are made dimensionless by introducing the length scale L . The basic-state velocity components also satisfy the usual Navier-Stokes equations so that the basic-state solution drops out. Thus, equations in terms of the disturbance velocities result. These equations are further simplified by making the approximation that products of disturbance quantities are neglected (i.e. $u' u'_x \ll u'_x$, etc.). This results in the following set of *linear* disturbance equations:

$$u'_x + v'_y + w'_z = 0 \quad (3)$$

$$u'_t + U u'_x + W u'_z + U_y v' + p'_x - \nabla^2 u'/R = 0 \quad (4)$$

$$v'_t + U v'_x + W v'_z + p'_y - \nabla^2 v'/R = 0 \quad (5)$$

$$w'_t + U w'_x + W w'_z + W_y v' + p'_z - \nabla^2 w'/R = 0 \quad (6)$$

where subscripts denote partial differentiation and the Reynolds number is given by $R = U_\infty L / \nu$ for the time being. The question of *stability* is one of whether the solution set of Eqs.(3) – (6) contain disturbances that grow or decay in space (or time).

2.1 Normal modes and the Orr-Sommerfeld equation

The disturbance equations are linear and the coefficients are only functions of y . This suggests a solution in terms of separation of variables using normal modes (i.e. exponential solutions in terms of the independent variables x , z , t) that would reduce Eqs.(3) – (6) to ordinary differential equations. One possible normal mode is the single wave:

$$q'(x,y,z,t) = q(y) \exp[i(\alpha x + \beta z - \omega t)] + \text{c.c.} \quad (7)$$

where c.c. stands for complex conjugate, q' represents any of the disturbance quantities of Eq. (2), α is the chordwise wavenumber, β is the spanwise wavenumber, and ω is the frequency. Here, α and β are, in general, complex and are given by $\alpha = \alpha_r + i\alpha_i$ and $\beta = \beta_r + i\beta_i$ and ω is real. The amplitude function $q(y)$ is complex and q' is real. Equation (7) is strictly valid only for a *parallel flow*.

In a real boundary-layer flow, U , W , and R vary with the chord position, x^* , and thus the problem changes at each location. In practice therefore, the parallel-flow assumption is essentially a local one in that, at each chord location, U and W are re-evaluated and L is

chosen to be the boundary-layer reference length $L = \delta_r = (vx^*/U_\infty)^{1/2}$. In this case, α , β , and R depend on the chordwise position, x^* . Therefore, the use of Eq.(7) is not rigorously correct and the phase function, Θ , must be introduced to define the normal mode as:

$$q'(x,y,z,t) = q(y) \exp(i\Theta) + \text{c.c.} \quad (8)$$

where $\Theta = \Theta(x,z,t)$ and

$$\partial\Theta/\partial x = \alpha \quad (9a)$$

$$\partial\Theta/\partial z = \beta \quad (9b)$$

$$\partial\Theta/\partial t = -\omega \quad (9c)$$

This step produces the zeroth-order approximation (quasi-parallel) and can be rigorously justified using a non-parallel analysis (e.g. Gaster, 1974; Saric and Nayfeh, 1977). Substitution of Eqs.(8) – (9) into Eqs.(3) – (6) gives

$$i\alpha u + i\beta w + Dv = 0 \quad (10)$$

$$i(\alpha U + \beta W - \omega)u + vDU + i\alpha p - (D^2 - k^2)u/R = 0 \quad (11)$$

$$i(\alpha U + \beta W - \omega)v + Dp - (D^2 - k^2)v/R = 0 \quad (12)$$

$$i(\alpha U + \beta W - \omega)w + vDW + i\beta p - (D^2 - k^2)w/R = 0 \quad (13)$$

where $D = d/dy$,

$$k^2 = \alpha^2 + \beta^2 \quad (14)$$

and the usual no-slip boundary condition applies at the wall.

Although Eqs.(10) – (13) look like a 6th-order system of equations, they can be easily combined into a single 4th-order equation called the *Orr-Sommerfeld* equation.

$$D^4\phi - 2k^2D^2\phi + k^4\phi - iR[(\alpha U + \beta W - \omega)(D^2\phi - k^2\phi) - \alpha(D^2U)\phi - \beta(D^2W)\phi] = 0 \quad (15a)$$

where the customary definition of $v = \phi$ is used and the boundary conditions are:

$$\phi(0) = D\phi(0) = 0, \quad \phi(y \rightarrow \infty) \rightarrow 0 \quad (15b)$$

The boundary conditions of $u = w = 0$ at the wall give $D\phi = 0$ [$Dv = 0$ from Eq.(10)] and we have assumed a boundary-layer type flow where the disturbances must die out far from the boundary. When the definition, $kU = \alpha U + \beta W$ is used, Eq.(15) immediately resembles the familiar 2-D form of the Orr-Sommerfeld equation.

Thus, *all* of the 3-D stability characteristics for the class of flows defined by Eq.(1), can be found by solving Eq.(15). This is the subject of sections 3 and 4.

2.2 Solution of the Orr-Sommerfeld equation

Equation (15), represented by the differential operator $\mathcal{L}\phi = 0$ and boundary conditions $\mathcal{B}\phi = 0$, is linear and homogeneous and, as such, forms an eigenvalue problem. Given the basic-state velocities, $U(y)$ and $W(y)$, solutions of Eq.(15) exist for only a specific combination of parameters of the equation such as $\mathcal{F}(\alpha, \beta, \omega, R) = 0$. Thus the eigenvalue problem is expressed as:

$$\mathcal{L}\phi = 0, \quad \mathcal{B}\phi = 0 \quad (15)$$

$$\mathcal{F}(\alpha, \beta, \omega, R) = 0, \text{ for a given } U(y) \text{ and } W(y) \quad (16)$$

2.2.1 Higher modes

In a well-posed eigenvalue problem such as plane Poiseuille flow, Eq.(16) represents an infinite discrete set of eigenvalues and a corresponding infinite discrete set of eigenfunctions. For boundary layers, there is a finite discrete set of eigenvalues and a continuous spectrum. That is to say, for each (β, ω, R) combination, there exists a number of (α_r, α_i) combinations that satisfy Eq.(15). The eigenfunctions are called modes and are superposed to construct an arbitrary disturbance profile. For the incompressible cases we will consider, the least stable mode is called the first mode. For incompressible streamwise instabilities, there is no more than one unstable mode so not much attention is paid to higher modes. For compressible and centrifugal instabilities, more than one mode can be unstable. These concepts are discussed again in sections 3.2, 3.4, and 5.2.

2.2.2 Numerical techniques

Since the Reynolds number is large, Eq.(15) is stiff and care must be taken during its integration. If finite differences or spectral methods are used, accuracy is obtained by the appropriate mesh. With these methods, Eq.(16) is solved as an algebraic matrix problem. If shooting techniques are used, orthonormalization works best and Eq.(16) is an iteration solution with boundary conditions. The algebraic solution has advantages in that all of the eigenvalues are obtained at once. The disadvantage is that it is awkward to obtain the eigenfunctions and to do spatial stability. Finite differences seem to be the most popular these days. An excellent review of current methods of solving the Orr-Sommerfeld equation is given by Malik (1988) who emphasizes finite difference and spectral methods. Mack (1984b) gives a good summary of shooting techniques. An incompressible design code, SALLY (Srokowski and Orszag, 1977), and a compressible

design code COSAL (Malik and Orszag, 1981), are generally available. They use as input, tabulated velocity profiles such as those generated by a Kaups and Cebeci (1977) boundary-layer code.

2.2.3 The adjoint system

It is convenient to define the *adjoint* eigenvalue problem given by:

$$\begin{aligned} \mathcal{L}^* \phi^* &= (D^2 - k^2)^2 \phi^* \\ &- iR[(\alpha U + \beta W - \omega)(D^2 \phi^* - k^2 \phi^*) \\ &+ 2\alpha(DU)\phi^* + 2\beta(DW)D\phi^*] = 0 \end{aligned} \quad (17a)$$

with boundary conditions

$$\mathcal{B}\phi^* = 0: \quad \phi^*(0) = D\phi^*(0) = 0, \quad \phi^*(y \rightarrow \infty) \rightarrow 0 \quad (17b)$$

The adjoint solution will be useful later in the calculation of the group velocity. Since the eigenvalues of Eq.(17) are identical to those of Eq.(15), a check on $\mathcal{F}(\alpha, \beta, \omega, R) = 0$ is possible. Moreover, some eigenvalue iteration schemes seem to converge quicker with Eq.(17) since D^2U is not calculated directly.

2.3 Temporal and spatial stability: Gaster's transformation

For the purposes of discussion, let us consider 2-D disturbances and the 2-D form of the Orr-Sommerfeld equation i.e. $W = 0, \beta = 0, k = \alpha$, given by Eq.(18):

$$(D^2 - \alpha^2)^2 \phi - i\alpha R[(U - \omega/\alpha)(D^2 - \alpha^2) - D^2 U]\phi = 0 \quad (18)$$

2.3.1 Spatial Stability

The local normal mode is given by Eq.(7). With $\alpha = \alpha_r + i\alpha_i$ and ω real, it can be rewritten as

$$q'(x, y, t) = q(y) \exp(-\alpha_r x) \exp[i(\alpha_i x - \omega t)] + \text{c.c.} \quad (19)$$

The *spatial growth rate* is given by $-\alpha_i$ for obvious reasons.

$$\alpha_i < 0 \text{ gives amplified disturbances: } \text{unstable} \quad (20a)$$

$$\alpha_i = 0 \text{ is no change in space: } \text{neutral} \quad (20b)$$

$$\alpha_i > 0 \text{ gives damped disturbances: } \text{stable} \quad (20c)$$

The eigenvalue problem of Eq.(16) is expressed as $\alpha = f(\omega, R)$ where f is a complex map. The phase speed in this case is given by $c = \omega/\alpha_r$. Instead of solving for α , one could specify R and $\alpha_i = 0$ and find α_r and ω .

2.3.2 Temporal stability

In this case, the local normal mode is still given by Eq.(7), except that α is real and positive while ω is complex. It is customary to introduce the complex phase speed, $c = \omega/\alpha = c_r + i\alpha_i$, and write the normal mode as

$$q'(x,y,t) = q(y) \exp[i\alpha(x - ct)] + \text{c.c.} \quad (21a)$$

where one can easily see the wave form of the disturbance. The growth rate can be found by splitting Eq.(21a) into real and imaginary parts.

$$q'(x,y,t) = q(y) \exp(\alpha c_i t) \exp[i\alpha(x - c_r t)] + \text{c.c.} \quad (21b)$$

The *temporal growth rate* is given by αc_i .

$c_i > 0$ gives amplified disturbances: *unstable* (22a)

$c_i = 0$ is no change in time: *neutral* (22b)

$c_i < 0$ gives damped disturbances: *stable* (22c)

The Orr-Sommerfeld equation is identical to Eq.(18) except c replaces ω/α . The eigenvalue problem of Eq.(16) is expressed as $c = f(\alpha, R)$ where f is a complex map. The phase speed is simply c_r in this case. Because the eigenvalue, c , appears linearly in the temporal form of the differential equation, much of the early stability calculations concentrated on this case. However, the spatial theory corresponds more closely to certain physical situations such as boundary layers. With today's advanced computers, one needs a good excuse to do temporal stability in a boundary layer.

2.3.3 Conversion from temporal to spatial

In order to convert from temporal to spatial, one uses the now familiar Gaster transformation (Gaster, 1982). In a region where the disturbance growth rate is small, the weakly-dispersive wave-evolution equation can be written as:

$$\partial \mathcal{A}/\partial t + (d\omega/d\alpha) \partial \mathcal{A}/\partial x + G(\mathcal{A}) = 0 \quad (23)$$

where \mathcal{A} is a complex wave amplitude, G is a complex function that is zero for parallel flow, and $c_g = d\omega/d\alpha$ is the *group velocity*. Since an explicit equation for the *dispersion relationship*, $\omega = \omega(\alpha)$, is not generally known for shear layers, it can be given locally by integration of the eigenfunction and its adjoint:

$$c_g = -\mathcal{M}/\mathcal{N} \quad (24a)$$

$$\mathcal{M} = \int_0^\infty (B_1 D^2 \phi + B_2 \phi) \phi^* dy \quad (24b)$$

$$\mathcal{N} = \int_0^\infty (D^2 \phi - \alpha^2 \phi) \phi^* dy \quad (24c)$$

$$B_1 = U - 4i\alpha/R \quad (24d)$$

$$B_2 = 2\alpha\omega - 2U\alpha^2 - D^2U + 4i\alpha^3/R \quad (24e)$$

For the case of a 2-D wave, the approximate temporal growth rate is the product of the spatial growth rate and the real part of the group velocity. The case of both temporal and spatial growth can apply to a wave packet. For other cases, see Nayfeh and Padhye (1979). The situation for 3-D waves is considered in Sec.4.1.1.

2.4 2-D and 3-D disturbances: Squire's transformation

It is worthwhile to show that the problem of 3-D disturbances is equivalent to a 2-D problem for the case of the 1-D basic states of Eq.(1) and that the minimum critical Reynolds number can be found from a 2-D analysis. The following transformation is introduced into Eqs.(10) – (13):

$$(U, W, u, v, w, p, \alpha, \beta, \omega, R) \rightarrow (U, u, v, p, k, \varpi, R)$$

$$\alpha U = \alpha u + \beta W \quad (25a)$$

$$k u = \alpha u + \beta w, \quad v = v, \quad \alpha p = k p \quad (25b)$$

$$\alpha \varpi = k \omega, \quad k R = \alpha R \quad (25c)$$

The product of α and Eq.(11) is added to the product of β and Eq.(13) and the transformed equations become:

$$i k u + D v = 0 \quad (26)$$

$$i(kU - \varpi)u + vDU + ikp - (D^2 - k^2)u/R = 0 \quad (27)$$

$$i(kU - \varpi)v + Dp - (D^2 - k^2)v/R = 0 \quad (28)$$

If $\beta = 0$ in Eqs.(10) – (13), the result is equations similar in form to Eqs. (26) – (28). Thus, the problem of 3-D disturbances, Eqs.(10) – (13), is equivalent to the 2-D problem. Hence, one needs only to solve the 2-D problem of Eqs.(26) – (28) and supplement it with the transformation of Eq.(25). Moreover, the transformed 3-D problem which is made into the equivalent 2-D problem is associated with a *lower* Reynolds number since $k > \alpha$ and $R < \alpha R/k$ for $\beta \neq 0$. The minimum critical Reynolds number is that Reynolds number below which all disturbances are stable. Since 3-D disturbances are associated with the stability characteristics at a *lower* Reynolds number, 2-D disturbances are more unstable and the minimum critical Reynolds number is given directly by the 2-D

analysis. This is a statement of Squire's theorem.

In other words, Squire's theorem specifically states that insofar as determining the minimum critical Reynolds number, 2-D disturbances are most important. It should be pointed out that Squire's theorem breaks down for compressible flows, nonparallel flows, non-minimum critical Reynolds numbers, and for spatially (instead of temporally growing disturbances (i.e. it is necessary to define a complex Reynolds number). Moreover, we shall find later that although the minimum critical Reynolds number may be important from a fundamental viewpoint, it has nothing to do with the real problem of transition to turbulence. With these caveats, it is easy to see that Squire's theorem should be invoked with caution.

3. STREAMWISE INSTABILITIES

Streamwise instabilities are characterized by streamwise travelling waves that appear in 2-D boundary layers and in the mid-chord region of swept wings.

For tutorial purposes, the disturbance state is restricted to two dimensions with $W = 0$, $\beta = 0$, and $k = \alpha = \alpha_r + i\alpha_i$. This will be sufficient to describe the basic streamwise instability mechanisms.

3.1 Inviscid instability mechanism

In the absence of viscosity, the Orr-Sommerfeld Equation, for temporal stability, reduces to the *Rayleigh* Equation given by:

$$(U - c)(D^2 - \alpha^2)\phi - (D^2U)\phi = 0 \quad (29)$$

It can be shown (Drazin and Reid, 1981) that a necessary condition for an instability of any inviscid shear flow is that (1) D^2U must have a zero in the flow and (2) the extremum of vorticity, DU , associated with $D^2U = 0$, must be a maximum. The first part is the well-known *inflection-point* instability of Rayleigh and the second part is the extension by Fjørtoft. Lin (Drazin and Reid, 1981) showed that this condition is sufficient for bounded shear flows. The instability associated with an inflection point is a streamwise travelling wave called a Rayleigh wave whose wave speed, c_r , is bounded between the maximum and minimum values of the basic-state velocity, i.e. $0 \leq c_r \leq 1$ for a bounded shear layer. The growth rate, $\alpha c_i \leq \max|DU|/2 = O(1)$ in this case.

Since this inviscid instability is strong, the appearance of inflectional profiles usually implies a rapid breakdown to turbulence.

3.2 Viscous instability mechanism: T-S waves

Consideration of a wide class of instability mechanisms can give the general impression that viscosity can only stabilize a flow. A boundary-layer velocity profile is, however, known to exhibit an instability and yet it has no inflection point.

Prandtl first developed the fundamental ideas of a *viscous* instability mechanism and laid the groundwork for the understanding of bounded-shear-layer instabilities. The instability is called viscous because the boundary-layer velocity profile is stable in the inviscid limit and thus, an increase in viscosity (a decrease in Reynolds number) causes the instability to occur. Prandtl's basic idea is that the distribution of the Reynolds' stress through the shear layer is changed by viscosity in such a way as to destabilize the flow. In fact, a general energy analysis shows that the Reynolds' stress is the production term for instabilities (Mack, 1984b).

All of this is contained within the framework of Eq.(15). This mechanism is inappropriately called the *Tollmien-Schlichting* (T-S) instability after two of its very early investigators. The historical development of this work is given in Mack (1984b). It should be mentioned that not all shear-layer instabilities are T-S instabilities. We reserve the *T-S* appellation for the viscous instability.

Equation (15) is linear and homogeneous and forms an eigenvalue problem which consists of determining α (= k) as a function of frequency, ω , Reynolds number, R , and the basic state, $U(y)$. The Reynolds number is usually defined as

$$R = U_\infty \delta_r / v = (R_x)^{1/2} \quad (30)$$

and is used to represent distance along the surface. In general, $\delta_r = (vx^* / U_\infty)^{1/2}$ is the most straightforward reference length to use because of the simple form of Eq.(30) and because the Blasius variable, $\eta = y/\delta_r$, in $2f\eta\eta\eta + ff\eta\eta = 0$, is the same as y in the Orr-Sommerfeld equation. The reader will still find the archaic use of δ^* and θ as reference lengths, so care must be taken in comparing data since, in using these lengths, additional constants must be carried around.

When comparing the solutions of Eq.(15) with experiments, the dimensionless frequency, F , is introduced as

$$F = \omega/R = 2\pi fv/U_\infty^2 \quad (31)$$

where f is the frequency in Hertz and is conserved for single frequency waves. The parameter F is a constant for a given flow condition.

Experiments of naturally occurring transition in low disturbance environments always show 2-D T-S waves as harbingers of the transition process. These are streamwise travelling waves with a phase speed, $0.3 < c_r < 0.4$ whose amplitude and phase vary according to the freestream environment. In order to conduct detailed measurements, controlled (phase-locked) disturbances are introduced into the boundary layer. It is worthwhile to describe such an experiment and in doing so, permit the reader to understand the nature of a T-S wave.

Saric (1990) presents the requirements for conducting a stability experiment. Usually, an experiment designed to observe T-S waves and to verify the 2-D theory is conducted in a low-turbulence wind tunnel ($|u'|/U_\infty = 0.02\% \text{ to } 0.06\%$) on a flat plate with zero pressure gradient (determined from $H = \delta^*/\theta = 2.59$ and not from pressure measurements) where the virtual-leading-edge effect is taken into account by carefully controlled boundary-layer measurements. Disturbances are introduced by means of a 2-D vibrating ribbon using single-frequency, multiple-frequency, step-function, or random inputs (Pupator and Saric, 1989) taking into account finite-span effects (Mack, 1984a). Hot wires measure the $U + u'$ component of velocity in the boundary layer and d-c coupling separates the mean from the fluctuating part. In comparing with the theory, ϕ in Eq.(15) is proportional to the disturbance streamfunction so that u' is proportional to $\partial\phi/\partial y$.

Figure 1 shows the data of the mean flow and disturbance flow measurements from a routine single-frequency experiment (Saric, 1990). These data are compared with the Blasius solution and a solution of the Orr-Sommerfeld equation (15) as shown with the solid lines. In comparing the disturbance measurements (of rms u') and theory (of $|\partial\phi/\partial y|$), both profiles are normalized by their respective maximum values. The agreement between theory and experiment is quite good and illustrates that the 2-D problem is well understood. The fact that the wave amplitude is $1.5\%U_\infty$ while still remaining linear and 2-D is discussed in Sec.7. The disturbance signature of Fig.1 is a recognizable characteristic of T-S waves. The sharp zero and second maximum of $|u'|$ occur because of a 180° phase shift in the region of the critical layer (where $U(y) = c = \omega/\alpha_r$, the phase speed). This shape is quite unlike a turbulence distribution or even a 3-D, T-S wave.

The data of Fig.1 show a first-mode eigenfunction (see Sec.2.2.1) of Eq.(15). The higher modes are highly damped and are gone within a few boundary-layer thicknesses downstream of the disturbance source.

When the measurements of Fig.1 are repeated along a series of chordwise stations, the maximum amplitude varies as shown in the schematic of Fig.2. At constant

frequency, the disturbance amplitude initially decays until the Reynolds number at which the flow first becomes unstable is reached. This point is called the *Branch I* neutral stability point and is given by R_I . The amplitude grows exponentially until the *Branch II* neutral stability point is reached which is given by R_{II} . The locus of R_I and R_{II} points as a function of frequency gives the *neutral stability curve* shown in Fig.3. In order to compare the stability behavior of Fig.2 with theory, Eq.(8) is interpreted locally to have the form of Eq.(7) and is rewritten in the following form:

$$q'(x,y,t) = q(y)[\exp(-\alpha_i x)]\exp[i(\alpha_i x - \omega t)] + \text{c.c.} \quad (32)$$

which shows $-\alpha_i$ as the spatial growth rate. Depending on the sign of this term, the flow is said to be stable or unstable, i.e. if $-\alpha_i > 0$, the disturbances grow exponentially in the streamwise direction and the neutral points are determined by finding the R at which $\alpha_i = 0$. From the eigenvalues of Eq.(15), Fig.3 is $\alpha_i(R, F) = 0$. For $R > 600$ the theory and experiment agree very well for Blasius flow. For $R < 600$ the agreement is not as good because the theory is influenced by nonparallel effects and the experiment is influenced by a number of factors (Saric, 1990). Virtually all problems of practical interest have $R > 1000$ in which case the parallel theory seems quite adequate (Saric and Nayfeh, 1977). The whole theory has also been verified by direct Navier-Stokes simulations. These are reviewed by Spalart (1992).

3.3 The Smith-Van Ingen e^N method

One of the conjectures regarding the prediction of transition is that there exists a critical amplitude of the T-S wave at transition. One means for predicting this is to assume that the exponential growth between Branch I and Branch II (predicted by linear theory) is largely responsible for achieving this critical amplitude. However, the best that linear theory can do is calculate an amplitude ratio, A_{II}/A_I , which is consistently called A/A_o in the literature (the elusive ingredient, A_o , the initial disturbance amplitude, is the soul of the receptivity process described in Sec.8). Nevertheless, the calculation of A/A_o is an important process for many different reasons and the method is described forthwith.

In order to calculate the amplitude ratio (within the quasi-parallel flow approximation) when $\alpha = \alpha(R, F)$, Eq.(8) is used directly. The ratio of the disturbances $q(x,y,t)$ and $q(x_o,y,t)$, at x and x_o , respectively, is proportional to $\exp[i(\Theta(x,y,t) - \Theta(x_o,y,t))]$.

In this case, Eq.(9) is integrated along the stream direction to give:

$$\Theta(x, t) - \Theta(x_0, t) = \int_{x_0}^x \alpha dx - \omega t \quad (33)$$

Since x and R are related through Eq.(30), Eq.(33) can be written as

$$\Theta(R, t) - \Theta(R_0, t) = \int_{R_0}^R 2\alpha dR - \omega t \quad (34)$$

where R_0 is the starting point of the integration. Equation (34) is used in Eq.(8) in order to see how much the disturbance has changed from R_0 to R . The real part of Θ in Eq.(34) is just the phase and does not contribute to amplitude growth. Thus the change in amplitude of the disturbance is carried by the imaginary part of Θ . This is shown in Eq.(35).

$$\exp[i(\Theta - \Theta_0)] + \text{c.c.} =$$

$$\exp\left(-2\alpha_i \int_{R_0}^R dR\right) \left\{ \exp\left[i\left(\int_{R_0}^R 2\alpha_i dR - \omega t\right)\right] + \text{c.c.} \right\} \quad (35)$$

Assume that the disturbances at x and at x_0 each have a norm given by A and A_0 , respectively. This norm could be the maximum amplitude of $|u'|$ or $\int |u'| dy$ (Saric, 1990). In order to determine the relative amplitude ratio, A/A_0 , or as most commonly done, the *amplification factor*, $N = \ln(A/A_0)$, the absolute value of Eq.(35) is used to obtain:

$$N = \ln(A/A_0) = \int_{R_0}^R -2\alpha_i dR \quad (36)$$

where $\alpha_i = \alpha_i(F, R)$, R_0 is the Reynolds number at which the constant-frequency disturbance first becomes unstable (Branch I of the neutral stability curve), and A and A_0 are the disturbance amplitudes at R and R_0 . A typical calculation of Eq.(36) is shown in Fig.4. It illustrates the constant frequency growth of a disturbance and the envelope of maximum N at any R for a Blasius flow.

If the flow is not self similar, integration with respect to x^* may be more convenient. Mack (1984b) suggests:

$$N = \ln(A/A_0) = \int_{x_0}^x - (R_{\infty L} U_e \alpha_i / R) dx \quad (37)$$

where $R_{\infty L} = U_{\infty} L / \nu$, U_e is the local edge velocity normalized with U_{∞} , $R = (U_e x^* / \nu)^{1/2}$ is the local boundary-layer Reynolds number, and all lengths are

made dimensionless with reference length L .

The basic design tool is the correlation of N with transition Reynolds number, R_{Tr} , for a variety of observations. Equation (36) or (37) is integrated with respect to the known basic state. The correlation will produce a number for N (say 9) which is now used to predict R_{Tr} for cases in which experimental data are not available. This is the celebrated e^N method of Smith and Van Ingen (e.g. Arnal, 1984, 1992; Mack 1984b). As a transition prediction device, the e^N method is certainly the most popular technique used today. It works within some error limits *only* if comparisons are made with experiments with identical disturbance environments. Since no account can be made of the initial disturbance amplitude, this method will always be suspect to large errors and should be used with extreme care. When bypasses occur, this method does not work at all. This discussion is continued at the end of Sec.7.

The basic transition *control* technique endeavors to change the physical parameters and flow conditions in order to keep N within reasonable limits which in turn prevents transition. As long as laminar flow is maintained and the disturbances remain linear, this method contains all of the necessary physics to accurately predict disturbance behavior.

Mack (1984b) and Arnal (1984, 1992) give examples of growth-rate and e^N calculations showing the effects of pressure gradients, Mach number, wall temperature, and three dimensionality for a wide variety of flows. However, before using this method, one should be cautioned by Morkovin and Reshotko (1990).

3.4 Compressibility effects

Whereas compressibility does not change the fundamental physics for streamwise instabilities at subsonic Mach numbers, current design projects for supersonic civil transports require the consideration of the role of compressibility. Considerable uncertainty exists in both prediction and control of transition in supersonic flows due to the dearth of reliable experiments. Therefore, this lecture will rely on the ideas of sections 2 and 3 and concentrate on only the basic fundamental differences between subsonic and supersonic streamwise instabilities in order that the reader may understand the topics on transition control in Sec.9 and the prediction methods described by Arnal (1992). All of the details are in Mack (1984b) which is the most complete description of compressible stability that is available anywhere. In fact, the numerical viscous and inviscid results of Mack have long been heralded as the state-of-the-art in both incompressible and compressible stability analysis.

The linear stability analysis of supersonic boundary layers uncovers three major differences between it and the incompressible analysis.

3.4.1 Generalized inflection - point criterion

The extension of the Rayleigh inflection-point criterion to compressible boundary layers has an important change. A sufficient condition for the existence of an instability is

$$D(\rho DU) = 0, \text{ at } y = y_s > y_0 \quad (38)$$

where y_s is called the *generalized inflection point*, y_0 is the point where $U = 1 - 1/M_e$, and M_e is the edge Mach number.

The boundary layer on an adiabatic plate in a compressible flow always has $D(\rho DU) = 0$ somewhere in the flow. Thus, even zero-pressure-gradient flows are subject to inviscid instabilities and these instabilities grow with increasing Mach number. As y_s moves away from the wall with increasing Mach number, the inviscid instability increases. This effect occurs up to a Mach number of approximately 5.0. In contrast to $M = 0$, when viscosity is considered at $M > 1$, it may be stabilizing relative to the dynamic instability. This fact has provided a means to understand the fundamentals of supersonic boundary layers through the inviscid equations.

3.4.2 Multiple acoustic modes: Mack modes

One of the most significant developments in compressible theory comes from Mack, who discovered a new family of solutions to the compressible equations. They can be explained by writing the inviscid stability equation in a form similar to Eq.(29)

$$D^2\psi + D\{\ln[M^2/(1 - M^2)]\}D\psi - k^2(1 - M^2)\psi = 0 \quad (39)$$

where, along with the usual definitions, the following substitutions are made

$$\psi = v/(\alpha U + \beta W - \omega) \quad (40a)$$

$$M = (\alpha U + \beta W - \omega)M_e/(k^2 T)^{1/2} \quad (40b)$$

where $M = M(y)$ is the relative Mach number between the basic-state velocity, $U(y)$, and the propagation speed of a neutral wave.

Obviously, the solutions of Eq.(39) are different depending on whether $M < 1$ or $M > 1$. Recall that $-k^2$ comes from $\partial^2/\partial x^2$ so Eq.(39) can be written as

$$\psi''_{yy} + (1 - M^2)\psi''_{xx} + \mathcal{H}(M, \psi'_y, \psi') = 0 \quad (41)$$

Obviously, when $M < 1$, Eq.(41) is elliptic and the

eigenvalue $\alpha = f(\beta, \omega, R, M)$ is unique as it is in the case of incompressible inviscid theory. When $M > 1$, Eq.(41) is hyperbolic and an infinite discrete set of $\alpha = f(\beta, \omega, R, M)$ can satisfy the boundary conditions. $M = 1$ at $y = y_s$ and y_s is called a *turning point*. The solution of Eq.(39) can be found by using WKB methods. For $y < y_s$, the solutions are oscillatory and for $y > y_s$ they are exponential.

Physically we have a situation where the disturbances propagate at a speed, c_r (normalized with U_e), that is subsonic relative to the edge velocity, U_e , but are supersonic relative to the region near the wall ($y < y_s$). Thus, for an adiabatic flat plate, with $M_e = 3.8$, disturbances with wave speeds, $c_r > 0.5$ are supersonic with respect to the wall region (Morkovin, 1991). At the same phase speed, c_r , a sequence of wavenumbers satisfy the differential equation and boundary conditions. These extra solutions are higher modes and are most unstable as 2-D waves, because it is then that the relative supersonic region is of maximum extent. They have shorter wavelengths than the usual T-S instability waves (first modes) since the wavenumber sequence is approximately $2\alpha_r/\pi = 1, 3, 5, 7, \dots$. They are not T-S waves by character or behavior and it is fitting that they are called *Mack modes* (or Mack waves). They represent sound waves that reflect inviscidly between the solid wall and the relative sonic line in the boundary layer. The Mack modes are discussed again after the discussion of 3-D viscous disturbances.

3.4.3 3-D viscous disturbances

In the supersonic case ($1 < M_e < 10$), Mack completed extensive computations of 3-D stability maps on a flat plate and found many important results (see Mack, 1984b for the details and comparisons with experiment). The earliest results showed that above a Mach number of 1.0, 3-D waves corresponding to the first viscous mode, have a larger amplification factor than the corresponding 2-D disturbance. (The opposite is true for subsonic flows.) As the Mach number is increased above 1, the most unstable wave angle quickly increases to 45° at $M_e = 1.3$, 55° at $M_e = 1.6$, and 60° at $M_e = 2.2$. This phenomenon is due to decreased cross-stream mutual interaction between disturbances and decreased upstream influence both compensated by a lower effective 2-D Mach number. Thus, the convenient assumption of 2-D waves cannot be made in supersonic flows.

Recently, Reed and Balakumar (1990) verified the previous results of Mack, putting to rest a claim that Mack's results are in error. Furthermore, they find the assumption of constant Prandtl number in both the mean-flow and stability calculations to be stabilizing. However, the stability results are insensitive to the

assumptions made in the disturbance equations; rather, the results are governed by the physics contained in the basic state. For example, the inclusion of variable Prandtl number in both the mean-flow and stability calculations was demonstrated to give the same results as variable Prandtl number in the mean-flow and constant Prandtl number in the stability formulation.

The lowest-frequency Mack mode, the so-called second mode, is found to be the dominant instability for Mach number greater than about 4; it is always more unstable than either the 3-D first mode or any of the other higher modes. This is true for both inviscid and viscous problem formulations. An illustration of the viscous calculation is shown in Fig.5. Here, the spatial growth rate of the most-unstable 3-D mode is compared with the growth rate of the 2-D Mack mode. The wave angle of the most unstable 3-D mode is also shown. In addition, Mack observed some unusual behavior associated with the second mode; that is, whereas the first modes are stabilized by cooling in air (as expected), the second mode is actually destabilized. Part of the answer here is that the Mack modes can be destabilized without the presence of a generalized inflection point. It is apparent that the second mode must be understood and controlled with special care.

With regard to the second mode, there is a strong tuning with the boundary-layer thickness, so that the frequency of the most amplified disturbance may be predicted from this flow parameter. In particular, the fluctuation wavelength is approximately twice the boundary-layer thickness. This implies that if the boundary-layer thickness is changed, for example by cooling, a corresponding, predictable change in frequency should be observed.

In related work, the stability of sharp-cone boundary layers at zero angle-of-attack has been investigated by Malik (1984) at supersonic speeds, Gasperas (1987) at Mach 6.8, Mack (1987), and Stuckert and Reed (1991). The consequence of the work of Gasperas has been the recognition that cone results and flat-plate results cannot be accurately related by a similarity transformation. Axisymmetric disturbances in a cone boundary layer are actually more stable than predicted by the approximate analysis. Mack found important differences between the calculated and experimentally determined amplification rates of Stetson et al. (1983). Stuckert and Reed found that the use of disturbance-state variables scaled by the local radius of curvature for a cone minimizes the nonparallel effects introduced by the nonplanar geometry.

Finally, the design computer code COSAL (see Malik and Orszag, 1981; Malik, 1982; Malik et al. 1982) that efficiently computes temporal eigenvalues by finite differences is generally available. It uses the Gaster (1962) transformation to convert the temporal

amplification rate into a spatial one. The code of Chen and Cebeci (1990) is a direct spatial stability code. Both integrate the growth rate along the path defined by the real part of the group velocity.

3.4.3 Summary of compressibility effects

The major changes with compressibility are (1) the existence of a generalized inflection point criterion that is easy to satisfy giving rise to inviscid disturbances, (2) the 3-D nature of the primary instability mode, (3) the existence of unstable 2-D, higher modes that can be more unstable than the primary 3-D unstable modes for $M > 4.5$, and (4) the need for accurate basic-state velocity calculations (including property variations) in the stability analysis. The effects of compressibility on control are discussed in Sec.9.

4. CROSSFLOW INSTABILITIES

Three-dimensional flows offer a rich dessert of instability mechanisms and the 3-D boundary-layer flow over the swept-wing is no exception. This type of flow is susceptible to four types of instabilities that lead to transition. They are leading-edge contamination, streamwise instability, centrifugal instability, and the topic of this section, crossflow instability. Streamwise instability is covered in Sec.3, while centrifugal and leading-edge problems are covered in Sec.5 and Sec.6, respectively.

The focus of this section is on the crossflow instability which occurs in strong pressure gradient regions on a swept wing. In the leading-edge region both the surface and flow streamlines are highly curved. The combination of pressure gradient and wing sweep deflects the inviscid-flow streamlines inboard as shown in the schematic of Fig.6. This mechanism re-occurs in the positive pressure gradient region near the trailing edge. Because of the lower momentum fluid near the wall, this deflection is made larger in the boundary layer, and causes crossflow, i.e. the development of a velocity component inside the boundary layer that is perpendicular to the inviscid-flow velocity vector. This is characteristic of many different 3-D boundary-layer flows and is illustrated in the schematic of Fig.7. The crossflow profile has a maximum velocity somewhere in the middle of the boundary layer, going to zero on the plate surface and at the boundary-layer edge. This profile exhibits an inflection point (a condition which is known to be dynamically unstable) causing so-called crossflow vortex structures to form with their axes aligned near the streamwise direction. These crossflow vortices all rotate in the same direction and resemble a cat's eye structure when viewed along their axis.

A complete description of this instability, the historical development of the research, and a review of current

work is given by Reed and Saric (1989). Summaries of different calculations, given in the reports by Mack (1984b) and Poll (1984b), are also of interest. The work on Navier-Stokes simulations of 3-D flows is reviewed by Kleiser and Zang (1991) and Spalart (1992).

4.1 Stability calculations

In the past ten years considerable progress has been achieved in calculating the stability characteristics of three-dimensional flows. Whereas the swept-wing boundary layer has always been called 3-D, when the parallel flow approximation is used, the basic state is 1-D and is given by Eq.(1). The incompressible stability problem is expressed by Eq.(15) (just as the case of T-S waves) and there is no question that the disturbances are 3-D. When the disturbances propagate at or near the stream direction, they are most likely T-S waves. When they propagate at or near the crossflow direction, they are called crossflow waves or crossflow vortices.

The state-of-the-art transition prediction method still involves linear stability theory coupled with an e^N transition prediction scheme (Mack, 1984b; Poll, 1984b; Chen and Cebeci, 1990; Arnal, 1992). Several computer programs including the SALLY (Srokowski and Orszag, 1977), COSAL (Malik, 1982), and MARIA (Dagenhart, 1981) codes are available to compute crossflow vortex amplification. This work is extended by Chen and Cebeci (1990), who show the value of the saddle-point method in determining the most unstable modes.

4.1.1 Direction of disturbance propagation

With a 3-D disturbance superposed on the velocity field of Eq.(1), one needs to define a number of important directions and the attempt here is to do it as painlessly as possible since the notation is not standardized in the literature. We define the x -axis as the direction of the freestream velocity, U_∞ . All angles are then measured with respect to the x -axis. The following definitions are made.

The basic-state inviscid flow direction, ϕ_e , is

$$\phi_e = \arctan(W_e/U_e) \quad (42a)$$

The angle of the wavenumber vector, $\phi_k = \phi_k(F, R)$, is

$$\phi_k = \arctan(\beta_r/\alpha_r) \quad (42b)$$

The angle of the zero-frequency wavenumber vector, $\phi_{k0} = \phi_{k0}(0, R)$, is

$$\phi_{k0} = \arctan(\beta_{r0}/\alpha_{r0}) \quad (42c)$$

The angle of the growth-rate vector is

$$\phi_{ki} = \arctan(\beta_r/\alpha_i) \quad (42d)$$

The wave angle at which the group velocity ratio is real (found by varying β_r until the imaginary part of $da/d\beta$ = 0) is

$$\phi_g = \arctan(\beta_r/\alpha_{cg \text{ real}}) \quad (42c)$$

None of these angles need be the same in any particular flow configuration and indeed, in general, they are not. In evaluating Eq.(15) for spatial stability for a given basic state velocity, one needs to fix not only ω (or F) and R but also β in order to calculate α . This is no problem for temporal theory since a single growth rate can be defined. However, for the spatial theory, $\alpha = \alpha_r + \alpha_i$ and $\beta = \beta_r + \beta_i$ and only two parts can be calculated [from $\alpha = f(\beta, \omega, R)$] and one part specified. If one makes an assumption regarding the direction of disturbance propagation, the missing piece can be found. All of the angles specified above have been proposed because there has not been a single experiment that has conclusively shown which is correct (more about this later).

The most plausible assumption comes from Cebeci and Stewartson (1980) and Nayfeh (1980a). They assume that the disturbance will propagate along a direction in which the ratio of the group velocities is real.

In 3-D, the equivalent of Eq. (23) is written as

$$\partial A/\partial t + \omega_\alpha \partial A/\partial x + \omega_\beta \partial A/\partial z + G(A) = 0 \quad (43)$$

where

$$c_{gx} = \omega_\alpha = \partial \omega / \partial \alpha, \quad c_{gz} = \omega_\beta = \partial \omega / \partial \beta \quad (44)$$

are the components of the group velocity in the x and z directions respectively.

This makes sense for a very good reason. In general, the ratio of the group velocities, $\omega_\beta/\omega_\alpha = -da/d\beta$, calculated from the 3-D equivalent of Eq.(24) is complex (see Nayfeh, 1980b). When used in Eq.(43), the wave-evolution equation, this equation is elliptic when $da/d\beta$ is complex (an awkward situation for wave propagation).

The criterion for determining the direction of disturbance growth is the (α_r, β_r) combination that makes $da/d\beta$ real. This technique has been recently used with some success by Chen and Cebeci (1990) in a spatial stability analysis. They give a review of the other methods and they show that this is the most amplified wave. This is also a clear method of identifying crossflow waves from T-S waves. Thus, the method of Chen and Cebeci is seen as a useful strategy

in calculating amplification factors of Eq.(37 or 38) where α_i is replaced by k_i and one integrates along the direction of $Imag(d\alpha/d\beta) = 0$.

4.1.2 Travelling and stationary vortices

The crossflow waves that are calculated from Eq.(15) can be amplified in a range extending from zero frequency to some upper cut-off frequency as shown in Fig.8 (there is also weaker amplification for a small range of negative frequencies). Here, $\psi = \varphi_k$ of Eq.(42b). This cut-off frequency is usually below or at the low end of amplified T-S frequencies. Figure 8 clearly shows that a travelling wave is far more amplified than the stationary wave. This is not always observed experimentally where it appears that the stationary vortex is most dominant. This is no fault of the theory and the answer lies within some recent experiments described below.

The calculations of Fig.8 were done with a freestream Mach number near 0.9. This figure also shows the insensitivity of crossflow instabilities to Mach number. Finally, it should be pointed out that a calculation such as Fig.8 exists for a range of wave numbers that are unstable and these include waves that are characterized as streamwise instability.

4.1.3 Curvature effects in crossflow

When addressing geometries such as a swept wing, a rotating disk, or a swept cylinder, Eq.(15) is inadequate because of the influences of body curvature (convex is stabilizing), Coriolis forces (stabilizing), and streamline curvature (?). As this report goes to press, a number of different investigators have recently offered seriously different calculations regarding the effects of curvature on swept wings and swept cylinders. Since this may affect results already in print, it is best that no discussion will be given here until these differences are understood.

4.1.4 Compressibility effects in crossflow instabilities

Balakumar and Reed (1991) examine the crossflow instability characteristic of swept wings. The geometry considered is that of a sharp cone located in a uniform supersonic stream at zero angle of attack and rotating about its axis. They find at all Mach numbers (1.5, 3, 5, 8) that the maximum amplified crossflow is nonstationary with the frequency increasing with Mach number from approximately 5 kHz at $M = 1.5$. They find the inclusion of curvature to be stabilizing for all cases. At $M = 5.0$, for which the 2-D second mode has been observed to dominate the first mode in the flat-plate boundary layer, they find a competition between the crossflow and second mode. Further results show that the most unstable second mode in a 3-D boundary layer is actually oblique whereas the second mode in a

2-D boundary layer is 2-D. Cooling the wall is ineffective in controlling the crossflow instability; a result also seen by Parikh et al. (1989) in limited calculations.

4.1.5 Crossflow Reynolds number

The e^N method is perceived to be too expensive and too non-expert unfriendly for many engineering applications. There is a perceived need to determine correlating parameters, *based purely on basic-state profiles*, that could be easily incorporated into existing basic-state codes and would "accurately" predict transition location for crossflow-dominated problems. Historically (see Reed and Saric, 1989), this led to the development of a *crossflow Reynolds number*, $R_{cf} = W_{max}\delta_{10}/v$ (based on maximum crossflow velocity and the largest boundary-height where the crossflow is 10% of the maximum). Unfortunately, this traditional definition of crossflow Reynolds number does not seem to pass muster. It is poor for incompressible flows and seems to get worse for compressible flows. Reed and Haynes (1990) do an extensive parameter study on rotating cones in a supersonic stream under a variety of wall and stagnation conditions and find the spread on the order of 200%. This leads one to conclude that there are no short cuts to a complete stability analysis.

4.2 Experimental results

Other recent experimental investigations of the crossflow instability problem on swept wings include Saric and Yeates (1985), Bippes and Nitschke-Kowsky (1987), Arnal and Juillen (1987), Muller and Bippes (1988), Kachanov and Tararykin (1990), Bippes (1990, 1991), Arnal et al. (1990), Saric et al. (1989), Dagenhart et al. (1989), Kohama et al. (1991), Takagi et al. (1991). These experiments differ in the arrangements used to simulate the swept-wing boundary layer. The experiments of Saric and Yeates, Bippes et al., and Kachanov and Tararykin use a swept flat plate with separate displacement bodies to generate the three-dimensional boundary layer while the Arnal et al. experiments are conducted on a swept wing. Free-flow boundaries are used on one or both ends of the models for the Arnal et al., Bippes et al. experiments. The Saric and Yeates and the Kachanov and Tararykin experiments employ contoured end liners in a closed test section to simulate infinite swept-wing flow. The Saric et al., Dagenhart et al., Kohama et al. and Takagi et al. were all conducted at Arizona State University (ASU) on a swept wing with contoured end liners that produced an infinite-swept-wing flow.

The experiments of Arnal et al. concentrated on transition measurements of observations of the travelling crossflow disturbances. These are reviewed by Arnal (1992). The experiments of Bippes and co-

workers demonstrated agreement with linear theory with regard to the stability parameters. Moreover, they showed in a wind tunnel with high freestream turbulence ($|u'|$ near 0.4% U_∞) that travelling crossflow waves dominated while in a wind tunnel with low freestream turbulence ($|u'|$ near 0.04% U_∞) stationary crossflow waves dominated. In the latter case, the stationary vortices were seen to be fixed to the plate when the plate was moved in the span direction. The DLR experiments (Bippes, 1990; 1991) continue to provide more detailed comparisons with linear theory, wave-interaction theory (Fischer and Dallmann, 1991), and Navier-Stokes simulations (Meyer and Kleiser, 1991).

Considerable insight to these previous experiments was subsequently gained by the ASU experiments. The basic experiment was designed to generate a purely *crossflow-dominated* transition in a low-turbulence wind tunnel. That is to say, they examined the stability and transition on a model whose pressure gradient is such that the boundary layer is *sub-critical to T-S* waves until 71% chord. The planning and design of the basic experiment is given by Saric et al. (1989). Details of the flow-visualization studies and stationary hot-wire and hot-film measurements that define the *linear-stability* behavior are given in Dagenhart et al. (1989, 1990). In the linear range they observed both stationary and travelling disturbances as one would expect from linear theory, thus verifying the linear theory calculations. However, Kohama et al. (1991) showed that transition is caused by a secondary instability associated with the *stationary* crossflow instability. The travelling crossflow waves were present but played only a passive role in the transition process. This is explained in detail in Sec.7 on secondary instabilities.

Takagi et al. (1991) re-examined the role of surface roughness near the attachment line. In this experiment, crossflow disturbances begin to grow at $x/L = 0.04$ (L is the chord) and our discussion will concentrate on this area. The transition location, x_t/L , was observed to increase with subsequent levels of polishing of the model. The original experiment had a painted model and the peak-to-peak roughness was around 8 to 10 μm . Transition experiments were conducted at a number of different chord Reynolds numbers, R_L . The model surface was then polished to 0.5 μm rms finish and then to a 0.25 μm rms finish. Table 1. is an example from one typical chord Reynolds number.

These results are typical of the whole Reynolds number range. When a 9 μm roughness element was reintroduced at $x_t/L = 0.05$, transition returned to its original upstream location at $x_t/L = 0.40$. The effect seemed to be confined to a small region near the attachment line where crossflow disturbances first begin to be amplified since transition was not influenced by placing roughness much further

downstream.

Table 1. Transition location as a function of roughness height. h is the nominal roughness height in microns, x_t/L is transition location, $N(\omega = 0)$ is the amplification factor for most amplified stationary crossflow wave, and N is amplification factor for the most amplified travelling crossflow wave from Eq.(36). $R_L = 2.7 \times 10^6$

$h [\mu\text{m}]$	x_t/L	$N(\omega = 0)$	N
9	0.40	5.5	7.1
0.5	0.61	8.4	11.0
0.25	0.68	9.2	11.8

It now appears as though crossflow instabilities are dependent on the environment (Muller and Bippes, 1988) and surface conditions (Takagi et al., 1991) to a serious extent. These papers also raise serious questions regarding e^N methods. This is the topic of the receptivity section.

5. CENTRIFUGAL INSTABILITIES

The shear flow over a concave surface is subject to a centrifugal instability whose inviscid mechanism was first given by Rayleigh (Drazin and Reid, 1981). For a circular flow (r, ϕ, z) with basic-state velocity vector, $\mathbf{V} = (U, V, W)$, defined as

$$U = 0, \quad V = V(r), \quad W = 0 \quad (45)$$

this Rayleigh criterion is called the *Rayleigh circulation criterion*. It states that the necessary and sufficient condition for the existence of an inviscid instability is

$$d(\Gamma^2)/dr < 0 \quad \text{anywhere in the flow} \quad (46)$$

where the circulation $\Gamma = rV$.

If in an inviscid flow, $|rV|$ decreases with an increase in r , the flow will be unstable. In a viscous flow, this is only a necessary condition for instability. Taylor (Drazin and Reid, 1981) used this result in his well known work on the stability of a viscous circular Couette flow. In the case of the inner cylinder rotating and the outer cylinder fixed, Eq.(46) is satisfied. This geometry defines the *Taylor* instability and *Taylor vortices*.

When a fully-developed channel flow is curved, the flow along the outer race of the channel is unstable. This is called the *Dean* instability and *Dean vortices* (Drazin and Reid, 1981).

In a boundary-layer flow over a concave surface, the radial direction opposes the velocity gradient. At the center of curvature $rU_\infty = 0$ and at the wall, $r_w U = 0$. Away from the center of curvature, where $U = U_\infty$, rU_∞ increases with r . A maximum must exist and a region where $drU/dr < 0$ must exist. The first application of this idea to boundary layers was presented by Görtler (1941) who showed solutions of the disturbance equations to be in the form of streamwise oriented, counter-rotating vortices. Hence, the viscous instability of boundary-layer flows over concave surfaces bears the name of *Görtler* and the disturbance flow is generally referred to as *Görtler vortices*.

The Görtler instability is an important class of boundary-layer instabilities that should be discussed. It is known that a Görtler instability can cause transition on the wall of a supersonic nozzle (Beckwith et al., 1986). At the same time, recent experiments show that the breakdown to turbulence is typically through a strong secondary instability and it is not clear how to proceed with a transition criterion. Thus, much of what needs to be discussed is in section 7. Moreover, a complete review of the literature and the description of the importance of this physical mechanism to transition are given by Saric (1993).

5.1 Stability analysis and computations

The Görtler instability in a 2-D flow, occurs in the form of steady, streamwise oriented vortices. With weak curvature, they grow weakly in the stream direction. Since there is no $O(1)$ stream variation of the instability due to a travelling wave, it is not possible to separate the weak growth of the boundary layer. This is the heart of the Görtler problem. Therefore, it is important in this case to state the disturbance equations for the Görtler instability including non-parallel effects. By following Floryan and Saric (1982), a small viscous parameter $\epsilon = 1/R = (v/U_\infty L)^{1/2}$ is introduced and the dimensionless coordinates (ξ, y, z) are defined as

$$(\xi, y, z) = (\epsilon x^*/L, y^*/L, z^*/L) \quad (47)$$

with dimensionless basic-state velocity field

$$\mathbf{V} = [U(\xi, y), \epsilon V(\xi, y)] \quad (48)$$

The stability equations are obtained by superposing small disturbances onto the basic state

$$u^*/U_\infty = U(\xi, y) + u(\xi, y)\cos\beta z \quad (49a)$$

$$v^*/U_\infty = \epsilon V(\xi, y) + \epsilon v(\xi, y)\cos\beta z \quad (49b)$$

$$w^*/U_\infty = \epsilon w(\xi, y)\sin\beta z \quad (49c)$$

$$p^*/\rho U_\infty^2 = P + \epsilon^2 p(\xi, y)\cos\beta z \quad (49d)$$

where the dimensionless wave number $\beta = \epsilon L 2\pi/\lambda_z$.

The streamwise disturbance velocity is scaled differently from v and w in order to account for $O(1)$ changes in u^* with $O(\epsilon)$ changes in v^* and w^* because of the convection of streamwise momentum (Floryan and Saric, 1982).

The terms in Eq.(49) are substituted into the Navier-Stokes equations written in curvilinear coordinates. The equations are linearized and terms of higher order than the first in curvature and Reynolds number are disregarded to obtain the disturbance equations

$$u_\xi + v_y + \beta w = 0 \quad (50)$$

$$(Uu)_\xi + Vu_y + U_y v + p_\xi - u_{yy} + \beta^2 u = 0 \quad (51)$$

$$Uv_\xi + V_\xi u + (Vv)_y + 2G^2 Uu + p_y - v_{yy} + \beta^2 v = 0 \quad (52)$$

$$Uw_\xi + Vw_y - \beta p - w_{yy} + \beta^2 w = 0 \quad (53)$$

where the Görtler number is

$$G = (\kappa L/\epsilon)^{1/2} \quad (54)$$

and κ is the dimensional wall curvature. Equations (50) – (53) are the result of the formal limits (Floryan and Saric, 1982):

$$\epsilon \rightarrow 0, \kappa \rightarrow 0, \text{ with } G \text{ fixed} \quad (55)$$

Finally, the boundary conditions are specified as

$$u = v = w = 0 \text{ at } y = 0, y \rightarrow \infty \quad (56)$$

It is easy to see that Eqs.(50) – (53) are not susceptible to a normal-mode solution because the coefficients depend on the stream direction. The equations are parabolic in (ξ, y) and are not separable [historically, everyone used normal modes until Hall (1983)]. Thus, Eq. (56) must be supplemented by initial conditions given as

$$[u(\xi, y), v(\xi, y), w(\xi, y)]$$

$$= [u_o(y), v_o(y), w_o(y)] \text{ at } \xi = x_o \quad (57)$$

Hall (1983) shows that only the numerical integration of the parabolized stability equations is the appropriate method for analyzing the Görtler instability at all wave numbers. A comparison of this idea and the separation-of-variables solution (the *normal-mode* or *eigenvalue* or *local* analysis) is given by Day et al. (1990). They support Hall's conclusions and give guidelines regarding initial conditions and the interpretation of the local analysis.

5.1.1 Wavy walls

It may be worthwhile to describe one type of calculation of Eqs.(50) – (53) that could be useful. Saric and Benmalek (1991) examine the problem of the Görtler instability over wavy walls, i.e. when the wall curvature is periodic and can be convex as well as concave. The problem is solved by the direct integration of the parabolized disturbance equations, Eqs.(50) – (53). In spite of any presumed advantages to the normal-mode solution or a large α solution, it is well known that zero or convex curvature cannot be accounted for by using these methods because the discrete spectrum of eigenvalues does not exist.

This problem is of interest because of stability and transition studies over surfaces which unintentionally may be wavy and because of the *Görtler-Witting* mechanism which is still being discussed (e.g. Lessen and Koh, 1985). The question always arises with wavy walls regarding the nature of stabilization in the convex portion of the wall and whether it is sufficient to overcome the destabilization of the concave region. No *ad hoc* interpretation of the local analysis can address this problem. The basis of the *Görtler-Witting* mechanism, lies in the conjecture that large amplitude T-S waves locally induce concave curvature and hence a Görtler instability.

Saric and Benmalek (1991) show that convex curvature has extraordinary stabilizing influence on the Görtler vortex and they give examples of wavy wall computations where the net result is stabilizing. They conclude that the stabilizing effects of a convex surface make it unlikely that the boundary-layer over a wavy surface is subject to a strong Görtler instability. Moreover, since the *Görtler-Witting* mechanism has concave/convex curvature in the middle of the boundary layer and the maximum source term for the Görtler instability (dU/dy) is at the wall, *Görtler-Witting* is not an important instability.

5.1.2 Swept-wing flows

Hall (1985) has shown that beyond a very small sweep angle, the principal instability on a swept wing with concave curvature is a crossflow instability and not a Görtler instability. This analysis may obviate the need to worry about Görtler problems in swept-wing flows. Experiments are now underway (Peerhossaini, 1991), that may fill in the parameter range and answer this question.

5.2 Experiments

After the recent Görtler vortex workshop (Peerhossaini and Westfreid, 1990) it is clear that the theory is far

ahead of the experiments and that the most important missing ingredient is an experiment in the linear range, with modern diagnostics, in a low disturbance environment, e.g. a modern version of Bippes (1972). The fact that the disturbances are governed by Eqs. (50) – (53) with initial conditions given by Eq. (57) makes it difficult to have two experiments agree unless the initial conditions are controlled. Therefore, there is little in the way of experimental results that have bearing on this section. On the other hand, the experiments of Swearingen and Blackwelder (1987) are described in Sec.7 as an example of a well-conducted experiment concentrating on the secondary instability.

6. ATTACHMENT – LINE INSTABILITIES

The flow along the attachment line of a swept wing, as shown in Fig.9, can either undergo an instability, or be tripped to turbulence with a large roughness, or convect turbulence from the wing root. Whereas the first and second items are instabilities, the third is called *attachment-line contamination*. Should any of these cases be true, the boundary layer on a swept wing will not remain laminar. Nothing much has changed on the fundamentals side since Reed and Saric (1989), so this section paraphrases their comments.

Attachment-line contamination, explained by Pfenniger in 1963, occurs along the leading edge and is caused by disturbances that propagate along the wing as shown in Fig.9. For incompressible flow, Pfenniger (1965) showed that, at sufficiently high Reynolds numbers, turbulent wedges at the front attachment line of a swept wing can spread in the spanwise direction as well as downstream in the chordwise direction when the angle between the local potential-flow velocity vector and the front attachment line is smaller than the half-spread angle of a turbulent wedge.

Pfenniger then established the conditions for the existence of spanwise contamination in the presence of an initially turbulent attachment-line boundary layer ($R_{\theta_{al}} \geq 90$ to 95) and developed methods to reestablish a laminar attachment-line boundary layer. Here, $R_{\theta_{al}} = V_e \theta_{al} / \nu$, where V_e is the spanwise component of the local potential flow velocity and θ_{al} is the local momentum thickness. This should be known as *Pfenniger's criterion*. Applying expressions for the momentum thickness and momentum thickness Reynolds number of an incompressible laminar boundary layer without suction at the front attachment line of a swept wing, it is appropriate to re-define the attachment-line Reynolds number as:

$$R_{\theta_{al}} = 0.404 [U_{\infty} r \sin^2 \Lambda / (1+c) \nu \cos \Lambda]^{1/2} \quad (58)$$

Here the leading-edge region and the front part of the wing have been replaced by an equivalent ellipse of the

same leading-edge radius and Λ is the sweep angle of the attachment line, U_∞ is the undisturbed freestream velocity, r is the wing leading-edge radius measured normal to the leading edge, and e is the thickness ratio of the equivalent ellipse. Subsequent experiments by Carlson and Gregory showed similar results. Pfenninger (1977) reviews all of the old Northrop efforts and British efforts in this area.

Gaster (1967) studied the effect of placing trip wires normal to the attachment line. He defines a length scale h given by

$$h = [v / (dU_e/dx)_{x=0}]^{1/2} \quad (59)$$

where U_e is the edge velocity in the streamwise direction, v is the kinematic viscosity and x is in the chord direction. Gaster found that for large trip wires, $R_{\theta\text{al}} = 104$ at transition. For smaller diameter wires, $R_{\theta\text{al}} = 364 (h/d)^2$ at transition, where d is the wire diameter. This is known as *Gaster's criterion*. Gaster also showed that attachment-line contamination could be prevented by the use of a specially designed bump at the leading edge near the wing root.

Poll (1979) also uses the parameter d/h in an extensive series of experiments on a yawed cylinder. In this geometry, $\theta = 0.404 h$. For the parameter d/h , he determines a maximum ratio of 1.55, below which the wire feeds disturbances along the attachment line until turbulent bursts occur. Above this value, he discovers that the wire introduces turbulent bursts directly at the trip wire. There is a value of d/h equal to 0.8 or less where the wire has no effect on the transition process. Poll (1979) defines a Reynolds number based on the edge velocity V_e parallel to the leading edge and the length scale h mentioned above. Based on this definition he obtains a critical Reynolds number of 250, below which propagation of disturbances along the attachment line does not occur.

The attachment-line flow is susceptible to its own basic instability. Recently, Hall et al. (1984) and Hall and Malik (1986) have attacked this problem with a linear stability solution and both a weakly nonlinear solution and a complete Navier-Stokes simulation. Although they considered only a 2-D instability, they were able to predict and explain the experimental data of Pfenninger and Bacon (see Pfenninger, 1977). Of particular interest is that they were able to explain the absence of upper branch neutral stability modes as being due to a subcritical bifurcation along most of the upper branch. They also hint at the idea that the stabilizing effects of suction predicted from linear theory may not hold here because the suction may lead to a larger band of nonlinear unstable modes. This work is important because it is another illustration of the power of combined analysis and computation dedicated to experimental results. It lays the foundation for more

detailed experimental work and the extension of the theory to three-dimensional disturbances.

There has been a significant amount of work done in applying these ideas to transition prediction and extending the results to compressible flow. These are reviewed by Arnal (1992).

7. SECONDARY INSTABILITIES LEADING TO TRANSITION

There are different possible scenarios for the transition process, but it is generally accepted that transition is the result of the uncontrolled growth of unstable three-dimensional waves. For swept-wing flows, this growth occurs because of the nonlinear interactions of 3-D waves with either of the two basic instabilities discussed in sections 3, 4, and 5 of these notes. Of course, the exact nature of these interactions needs to be defined. The promise of investigating the nature of the breakdown process is that it may be possible to identify a key parameter or disturbance function that can be used for transition prediction or controlled to prevent transition.

7.1 Streamwise secondary instabilities

Secondary instabilities with T-S waves are reviewed in some detail by Herbert (1984b, 1985) and most recently by Corke (1990). The occurrence of three-dimensional phenomena in an otherwise two-dimensional flow is a necessary prerequisite for transition. Such phenomena were observed in detail by Klebanoff et al. (1962) and were attributed to a spanwise differential amplification of T-S waves through corrugations of the boundary layer. The process leads rapidly to spanwise alternating "peaks" and "valleys", i.e., regions of enhanced and reduced wave amplitude, and an associated system of streamwise vortices. The peak-valley structure evolves at a rate much faster than the (viscous) amplification rates of T-S waves. Whereas one can grow T-S waves in the laboratory for meters, once the 3-D structure is established, breakdown occurs on a convective scale in a matter of centimeters. A series of smoke-streakline photographs (Saric and Thomas, 1984) clearly show the rapid sequence of events after the onset of "peak-valley splitting". This represents the path to transition under conditions similar to Klebanoff et al. (1962) and is called a *K-type* breakdown.

Different types of three-dimensional transition phenomena observed (e.g. Kachanov and Levchenko, 1984; Saric and Thomas, 1984; Corke, 1990) are characterized by *staggered* patterns of peaks and valleys and by their occurrence at very low amplitudes of the fundamental T-S wave. This pattern also evolves rapidly into transition. These experiments showed that

the subharmonic of the fundamental wave (a necessary feature of the staggered pattern) was excited in the boundary layer and produced either the resonant wave interaction predicted by Craik (1971), called the *C-type*, or the secondary instability of Herbert (1983), called the *H-type*.

Briefly, the triad resonance can be seen from the quadratic interaction of two harmonic waves. If one has two different 3-D waves (Orr-Sommerfeld modes) like

$$u_1 \exp(i(\alpha x/2 + \beta z - \omega t/2)) \quad (60)$$

$$u_2 \exp(i(\alpha x/2 - \beta z - \omega t/2)) \quad (61)$$

their product would look like

$$u_1 u_2 \exp(i(\alpha x - \omega t)) \quad (62)$$

The fundamental 2-D mode could be written as

$$u_0 \exp(i(\alpha x - \omega t)) \quad (63)$$

Thus, with a weak nonlinearity, Eq.(62) is phase-locked with Eq.(63) and it is possible to transfer energy from the 2-D mode into the 3-D mode. There is only a unique set of (α, β, ω) that satisfy Eqs.(60) - (61) and the question is whether the nonlinearities provide enough detuning to keep the interaction alive (see Zelman and Maslennikova, 1990).

Herbert's theory relies on the linear stability of a basic state made up of a Blasius flow and a T-S wave. Thus, he examines the stability of a system of equations with periodic coefficients. The equation is of the Mathieu type and is solved using Floquet theory. For interacting disturbances, he chooses the so-called Squire modes. These are the solutions of the y -component of disturbance vorticity, $\alpha w - \beta u$, from a second order equation that was discarded when we transformed the sixth-order system, Eqs.(10) - (13), to the fourth-order system, Eq.(15). There is a broad spectrum of these modes that can be phase-locked with the fundamental. This method has had some success.

Complete spectral broadening to turbulence with self-excited subharmonics has been observed in acoustics, convection, and free shear layers and was not identified in boundary layers until the results of Corke (1990) and his team at I.I.T. Corke is able, under controlled conditions, to produce all sorts of subharmonic interactions. This leads one to believe that in low-disturbance environments, the breakdown process is through subharmonic interactions.

Summary of 7.1

The important issue that has come out of the

subharmonic research is that the secondary instability depends not only on disturbance amplitude, but on phase and fetch as well. Fetch means here the distance over which the T-S wave grows in the presence of the 3-D background disturbances. If T-S waves are permitted to grow for long distances at low amplitudes, subharmonic secondary instabilities are initiated at disturbance amplitudes of less than 0.3% U_∞ . If the T-S waves are introduced in the middle of the neutral stability curve instead of at Branch I, the 3-D interaction doesn't occur. On the other hand, if larger amplitudes are introduced, the breakdown occurs as K-type at amplitudes of 1% U_∞ . However, over an even shorter fetch from the disturbance source, large amplitude waves remain 2-D for awhile (This is the 1.5% amplitude of Fig.1). Thus, there no longer exists a "magic" amplitude criterion for breakdown.

Another disappointing aspect of this tremendous effort during the 1980's is that it has revealed the key ingredients for predicting breakdown. The experiments of Corke have provided the storehouse of data with which to compare. However, one needs to know the initial amplitudes of the disturbances inside the boundary layer. It is clear that neither the classical analyses nor the parabolized stability equations nor the Navier-Stokes simulations will get any farther without the initial amplitudes. This brings us to the receptivity questions of Sec.8.

7.2 Crossflow secondary instabilities

During the 1980's crossflow wave interaction theories enjoyed the same growth of activities as the streamwise interactions. These are summarized by Reed and Saric (1989) and Fischer and Dallmann (1991). These theories remain weakly nonlinear theories and provide a modification to the e^N -type calculations. It is worthwhile to discuss a secondary instability that is huge and resists weakly nonlinear theory.

The crossflow experiments of Dagenhart et al. (1990) were conducted in an accelerated boundary layer that was sub-critical to T-S waves. In regions of 20% to 30% percent chord, reasonable agreement was made with linear theory. At a chord Reynolds number of 2.66×10^6 , both stationary and travelling crossflow waves were measured. The maximum amplified crossflow wave was at 150 Hz. At 40% chord, the measurements revealed the data of Figs. (10) - (11). The solid line in the profiles in Figs. (10a) and (11a) are the calculations of an undisturbed 3-D boundary layer. The symbols are the data and note the span position in the caption. These data were taken 3 mm apart. The vertical axis is a laboratory coordinate so the boundary-layer thickness is 3 mm. The rms disturbance profiles of Figs.(10b) and (11b) seem to be orthogonal. This is still a laminar boundary layer and the linear theory, as

part of an e^N method, is using the 1-D profile to make stability calculations in a situation where dU/dz is the same magnitude as dU/dy . The development of this situation can be explained as follows.

Detailed measurements by Kohama et al. (1991) mapped out this scenario. Whereas, the experiments were conducted at a variety of chord Reynolds number, it is instructive to describe the changes in the instability patterns for a particular freestream speed of 25 m/s ($R_L = 2.6 \times 10^6$). In this case transition occurs between 40% and 50% chord depending on the 3-D nature of the breakdown. As measurements were taken in the chord direction from the attachment line to mid-chord the following processes are noted to occur. First, near 5% chord, the onset of the instability has just begun as shown in Fig.(12a). At 20% chord, weak crossflow vortices are observed in the frequency range predicted by linear theory (0 - 180 Hz) and they can be illustrated as shown in Fig.(12b). The naphthalene visualization reveals the periodic spanwise structure of the stationary crossflow vortices. The shaded area in the fourth image of Fig.(12b) shows the displacement of the low-momentum fluid and the third image shows the location of the naphthalene streaks. In areas of higher shear, the naphthalene sublimes faster.

Between 30% and 40% chord, the second harmonic of the fundamental mode is observed (up to 360 Hz) with some distortion of the stationary velocity profiles due to the periodic displacement of low- and high-momentum fluid. This is illustrated in Fig.(12c).

In the neighborhood of 40% chord, large distortions of the stationary profiles occur that include multiple inflection points in the streamwise velocity component. In this region, the high-frequency secondary instability (a band between 3 and 4 kHz) is detected and spatial relations of the process are well documented by coupled use of flow visualization and hot-wire measurement. A schematic of the transition region where the secondary instability is amplified is illustrated in Fig.(12d). Because of the continued roll up of low-momentum fluid, a region of high-momentum fluid is flanked by low-momentum fluid giving rise to multiple inflection points high in the boundary layer. This high-frequency instability is definitely not a T-S wave and it is not any sort of travelling crossflow wave. More than likely, it is an inviscid Rayleigh wave. This has now been put on an analytical footing by Reed and Fuciarelli (1991). They find that the nonlinear distortion of the mean flow, due to the presence of stationary crossflow vortices, causes the strong amplification of the 3.5 kHz waves. They also demonstrate that the stability of a simple superposition of an undistorted basic state and a disturbance state does not account for the observed behavior.

As those two instabilities develop and interact with each other, many other instabilities begin to appear, such as cascades of instabilities spatially and locally in the transition region, and eventually this leads to a fully turbulent state.

So, as far as the 3-D transition is concerned, the energy which drives the boundary-layer into turbulence is produced by the ejection-like motion of the co-rotating stationary crossflow vortices (v' component) near the edge of the boundary-layer. Then this energy is fed to the high-frequency secondary instability and other instabilities occurring inside the vortices. The remarkable thing about this process is that the high-frequency breakdown process is confined to a few millimeters in the span direction. The spanwise scale of the crossflow vortices is same as the boundary layer thickness. The chordwise wavelength of the high-frequency disturbance is also of the same order. Moreover, the spanwise gradients of the mean flow are of the same order as the normal-to-the-wall gradients. Thus, this breakdown may be similar to one of those reported by Swearingen and Blackwelder (1987) for the breakdown of Görtler vortices.

Summary of 7.2

We have learned a great deal about crossflow dominated transition. First, the stationary vortex, in spite of the fact that it is not as highly amplified as the travelling vortex, can cause more of a secondary instability. This secondary instability therefore, plays a more important role than the primary instability in driving the boundary-layer directly to a fully turbulent state.

The second point is with regard to e^N calculations. Since distortion of the basic state occurs relatively early in the transition process, it seems like "straining the gnat ..." to discuss the direction of disturbance growth or the most amplified linear disturbance as part of e^N , when the real issue is a full nonlinear problem. For additional warnings see Morkovin and Reshotko (1990).

The third point is with regard to receptivity. The stationary vortex is strongly influenced by roughness since the flow over roughness in a shear layer is always separated (Saric and Krutkoff, 1990). Thus, the 3-D roughness is a source of streamwise vorticity that feeds the initial amplitude of the stationary crossflow. This may explain the dramatic results of Takagi et al. (1991). Perhaps a zero Reynolds number solution around a 3-D roughness would provide the initial conditions for the crossflow amplitude.

7.3 Centrifugal secondary instabilities

The Görtler vortex flow, because of the slow growth of

the stationary streamwise vortices, produces large distortions in the mean flow. The careful experiments of Swearingen and Blackwelder (1987) and the timely computations of Sabry and Liu (1990) came before the identification of the secondary instability in crossflow. They illustrate the same behavior as the crossflow breakdown and because of the symmetry of the Görtler vortex structure, perhaps something different at the same time.

The upward injection of low-momentum fluid is symmetric because the vortex structure is counter-rotating. It has been described as a mushroom. The spanwise gradient, dU/dz , is the same magnitude as the normal gradient, dU/dy . However, dU/dz changes sign across the axis of the mushroom. This offers the possibility that a two-sided Kelvin-Helmholtz instability (due to $\pm dU/dz$) can occur along with the Rayleigh instability (due to $d^2U/dy^2 = 0$) giving rise to the observations of the sinuous and varicose modes of the oscillating vortex structure. This deserves to be investigated in the crossflow case.

Like the crossflow case, the fact that the stationary vortex pattern quickly changes the mean flow requires one to re-think the linear stability process in this case. Perhaps it is simply not possible to do a linear Görtler experiment beyond what was done by Bippes (1972). If one was designing quiet supersonic nozzles, the Görtler calculations should be conservative.

8. RECEPTIVITY

Receptivity is the first problem in stability and it is the last. It is the first, because it is the initial condition on the disturbance amplitude. It is the last, because we know the least about this aspect of stability and transition and because until a real breakthrough occurs, it is not of use to transition prediction. However, after 20 years of listening to Morkovin urge everyone to address this issue, there is now a broad-based effort in this area and it is the problem of the 1990's. The process of receptivity can be explained qualitatively as follows.

We all know that the origins of turbulent flow and the transition from laminar to turbulent flow are the most important unsolved problems of fluid mechanics and aerodynamics. At the present time, no mathematical model exists that can predict the transition Reynolds number on even a flat plate. One reason for this difficulty is the influence of a variety of agents such as freestream turbulence, surface roughness, sound, etc. whose roles in transition are incompletely understood, yet may trigger transition through a forced response of the flow as a nonlinear oscillator. A second reason, of course, is the poor understanding of the free response of this nonlinear oscillator, i.e., of the fundamental mechanisms which lead initially small disturbances to

transition. Obviously, amplitude and spectral characteristics of the disturbances inside the laminar viscous layer strongly influence which type of transition occurs and the major need in this area is to understand how freestream disturbances are entrained into the boundary layer, i.e., to answer the question of receptivity.

In all of what we discuss, receptivity will refer to the mechanism(s) that cause freestream disturbances to enter the boundary layer and create the initial amplitudes for unstable waves. For simplicity (?), the wave instability is assumed to be of the T-S type. The basic question is therefore how freestream turbulence and acoustic signals enter the boundary layer and ultimately contribute to the growth of unstable T-S waves and how the amplitude within the boundary layer can be determined from a freestream amplitude.

The term *receptivity* first appears in Morkovin (1969). Receptivity refers to the mechanisms that cause environmental disturbances to enter the boundary layer and create the initial amplitudes for the unstable waves. Receptivity has many different paths through which to introduce a disturbance into the boundary layer. They include the interaction of freestream turbulence and acoustical disturbances (sound) with model vibrations, leading-edge curvature, discontinuities in surface curvature, or surface inhomogeneities. Any one or a combination of these may lead to unstable waves in the boundary layer. If the initial amplitudes of the disturbances are small they will tend to excite the linear normal modes of the boundary layer. The normal modes in the case of the present experiment, dealing with a boundary layer developing under the influence of a zero pressure gradient (Blasius boundary layer), are of the T-S type. If the initial amplitudes are large, the T-S waves excite the boundary layer to nonlinear levels, at which point 3-D effects can lead the boundary layer prematurely to transition. These large-amplitude bypass mechanisms will not be discussed in these notes.

Mathematically, the receptivity problem differs from stability. Stability analysis describes the normal modes of disturbances within the boundary layer. These normal modes are determined from the solution of the linearized Navier-Stokes equations with appropriate boundary conditions (i.e. the Orr-Sommerfeld equation). Receptivity differs in the fact that either the equations or the boundary conditions are no longer homogeneous since the boundary layer is being forced by an external disturbance. Therefore, the problem no longer has the form of an eigenvalue problem but rather an initial-value problem. The governing system of equations for the receptivity problem is therefore typically the full Navier-Stokes system with appropriate boundary and initial conditions. Thus, the objective of

any experimental program should address initial conditions for T-S wave generation.

8.1 Acoustic Receptivity

The coupling between the long-wavelength acoustic disturbance and a T-S wave, having wavelengths two orders of magnitude smaller, occurs when the boundary layer is required to adjust locally (Goldstein and Hultgren, 1989). This can occur at four positions on a flat-plate model: the leading edge, the discontinuity in the surface curvature occurring at the flat plate and leading-edge junction, the presence of very strong, localized, pressure gradients, and any surface inhomogeneities.

Aizin and Polyakov (1979) observe the coupling of an acoustical disturbance to the T-S wave due to an extra-thin (10 mm) two-dimensional roughness element (mylar strip). Because of their high-aspect-ratio leading edge (60:1), no T-S waves are observed in the absence of roughness strips. A complete review of the early work is reported by Nishioka and Morkovin (1986) in an overview of experiments in boundary-layer receptivity to unsteady pressure gradients. They provide the translation of Aizin and Polyakov (1979) and offer a critical appraisal of acoustically-driven-transition literature. A more recent review is given by Goldstein and Hultgren (1989).

A goal of any experiment is to follow the criteria established by Nishioka and Morkovin (1986) where they discuss some of the basic difficulties that have occurred in receptivity experiments using freestream acoustical disturbances.

The experimental work of Saric et al. (1991) was motivated by the theoretical work of Kerschen (1989) and Kerschen et al. (1990) who analyze receptivity and the role of 2-D and 3-D roughness by means of a linear triple-deck analysis. One of the more important observations of this experiment is the linearity of the receptivity process with respect to the height of the roughness element. The amplitude of the T-S wave produced by the 2-D roughness increases on a roughly linear basis over the range of 40-120 μm ($y^+ = 0.7 - 2.2$) thus confirming the theory of Kerschen (1989, 1990). Moreover, the experiments seem to confirm the Bodonyi et al. (1989) prediction concerning the onset of nonlinear effects. This work was recently extended to 3-D roughness by Spencer et al. (1991) and with Navier-Stokes simulations of the 2-D sound and elliptical leading edge by Lin et al. (1990).

A recent paper by Kosorygin and Polyakov (1990) has appeared on wave cancellation of T-S waves with 2-D roughness strips. They use a semi-circular leading edge and as a consequence, they have substantial T-S wave generation without roughness. They show the

importance of selective phase interference of differently generated T-S waves. These results have been confirmed and expanded upon by Radeztsky et al. (1991).

8.2 Vortical Receptivity

Vortical disturbances enter the boundary in a manner different than acoustical disturbances. The review of Morkovin (1991) and the recent experimental papers by Kendall (1991) and Parekh et al. (1991) and theoretical papers by Crouch (1991) and Kerschen (1991) will bring the readers up to date. There is an enormous amount of information here, (Kendall has been working on this problem for 10 years) and it is hard in such a short survey to do it justice. Kendall (1991) uses changes in the freestream turbulence level and measures T-S waves and wave packets and finds a strong sensitivity to leading edge radius. In contrast to the acoustic receptivity, he finds the forced response acting along the flat plate in addition to at the leading edge. Moreover, he finds a nonlinear T-S response to changes in the freestream levels.

Parekh et al. (1991) use a convected gust as a source of vorticity to generate T-S waves. Phase-correlated measurements permit identifying leading-edge and forward-facing step contributions. At the present time, no receptivity has been noted in these experiments.

8.3 Summary

Besides the introduction, a short progress report has been given on the current work in this area. The work is important to understand and it is a long way from having an impact on transition prediction.

9. CONTROL OF INSTABILITIES AND TRANSITION

The only purpose of this section is to provide an introduction to the fundamentals of control. The applications are taken up by Arnal (1992).

9.1 Laminar Flow Control (LFC)

The principle behind LFC is to keep the growth of these disturbances within acceptable limits so that 3-D and nonlinear effects do not cause breakdown to turbulence. With this philosophy, one only deals with *linear* disturbances and thus, the difficulties with transition prediction do not directly arise. The manner in which LFC works can be described using the following example of Reshotko (1984b, 1985).

It is well known that the velocity-profile curvature term

in the Orr-Sommerfeld equation, d^2U/dy^2 , is an important driver of the stability behavior. In fact, it is more important than unmeasurable changes in the mean velocity itself. The boundary-layer flow can be made *more stable* by making the curvature term *more negative* near the wall. In the notation of Sec.2, the boundary-layer momentum equation can be evaluated near the wall, as shown in Eq.(64), and used to illustrate the stabilizing effects of different LFC techniques.

$$\begin{aligned} (\rho V_o) \partial U / \partial y + \partial P / \partial x - (\partial \mu / \partial T) (\partial T / \partial y) \partial U / \partial y = \\ = \mu \partial^2 U / \partial y^2, \quad y \rightarrow 0, \quad (64) \end{aligned}$$

Here, ρ is the density, V_o is velocity normal to the wall at the wall (+ for blowing, - for suction), U is the streamwise velocity component, P is the pressure field, μ is the dynamic viscosity, T is the temperature, x is the coordinate in the stream direction, and y is the coordinate perpendicular to the wall.

Equation (64) shows that wall suction ($V_o < 0$), favorable pressure gradient ($\partial P / \partial x < 0$), cooling in air ($\partial \mu / \partial T > 0, \partial T / \partial y > 0$), and heating in water ($\partial \mu / \partial T < 0, \partial T / \partial y < 0$), all tend to stabilize the boundary layer by making the curvature term more negative.

It should be pointed out that these are very sensitive mechanisms and that even *weak* suction or *weak* pressure gradients produce strong effects. For example, a Falkner-Skan pressure gradient of $\beta = +0.1$ (which can be measured by comparing a 6.6% change in the shape factor δ^*/θ with Blasius), increases the minimum critical x -Reynolds number for stability by a factor of 9. At the same time, average suction velocity ratios of $V_o/U_\infty \approx 10^{-3}$ to 10^{-4} are not unusual for LFC applications and can, for example, reduce relative amplitude growth from e^{26} to e^5 at $F = 10 \times 10^{-6}$ (Saric and Nayfeh, 1977). That the system works is evidenced by the fact that the X-21 aircraft achieved laminar flow at chord Reynolds numbers of 27×10^6 with a 20% decrease in overall drag (Pfenninger, 1977).

The eigenvalue problem, Eq.(15) is solved with the appropriate basic state used as input (Reed and Nayfeh, 1986). Justification for using the usual homogeneous boundary conditions on the disturbance velocity (Eq. 15) over the porous sections follows the work of Lekoudis (1978). The experiments (Reed and Saric, 1986) justify all aspects of the theory (Reed and Nayfeh, 1986).

Present designs for supercritical energy-efficient airfoils have LFC systems with a porous region near the leading edge. Generally, suction is applied near the leading edge of a swept wing in order to control leading-edge contamination and crossflow instabilities. Appropriate shaping of the pressure distribution

stabilizes mid-chord instabilities. This arrangement is called a *hybrid* LFC system in that it combines *active* LFC (suction) with *passive* LFC (pressure gradient). Examples of the heating and cooling applications in LFC systems are reviewed by Reshotko (1979, 1984b, 1985).

9.2 Active control of transition

The idea of transition control through active feedback systems is an area that has received considerable recent attention (Liepmann and Noschuck, 1982; Thomas, 1983; Pupator and Saric, 1989). The technique consists of first sensing the amplitude and phase of an unstable disturbance and then introducing an appropriate out-of-phase disturbance that cancels the original disturbance. In spite of some early success, this method is no panacea for the transition problem. Besides the technical problems of the implementation of such a system on an aircraft, the issue of three-dimensional wave cancellation must be addressed. Although Pupator and Saric (1989) successfully canceled random 2-D waves with an active feed-back system, Thomas (1983) showed that, when the 2-D wave is canceled, all of the features of the 3-D disturbances remain to cause transition at yet another location. Some clear advantage over passive systems has yet to be demonstrated for this technique.

9.3 Loss of control

Sometimes an anticipated stabilization works the other way. Just two examples are given to show that one must be careful.

9.3.1 Suction through holes

One possible candidate for a porous surface is perforated titanium with a sub-assembly manifold slot. This has the advantage over surface slots because the skin remains a continuous structural member. An important characteristic of such a surface is that it contributes only a small perpendicular pressure drop when suction is applied and it is generally accepted that it may be necessary to increase the local flow rate and perhaps increase the hole spacing over present designs. This is called the *oversuction* problem.

There are a number of important and *inseparable* stability and transition issues arising from oversuction in holes that are not present when one uses slots. Some of them are: (1) the creation of streamwise vortices at each suction hole as the flow rate increases, (2) the creation of resonant spanwise scales when the hole spacing is changed, (3) the different roles that issues (1)-(2) play with regard to destabilizing C-F vortices or T-S waves or the C-F/T-S interaction. These topics are

discussed below in the light of the fact that there is a dearth of solid experimental data and theoretical models to guide the designer and researcher.

We have already seen with roughness in crossflow, that streamwise vorticity is the major source of three-dimensional disturbances within the boundary layer that cause secondary instabilities leading to transition. The flow over a hole with suction resembles the flow over a finite wing with lift in that a pair of tip vortices are generated. As the suction velocity increases in the hole, the coupling of the local 3-D flow with the streamwise flow intensifies the vortex structure. The key result in the early Northrop work (Pfenninger, 1977) was that an increase in suction velocity destabilized the flow through a basic instability of the vortex structure. The Northrop experiments varied hole spacing, number of holes, freestream velocity, suction velocity, hole diameter, and location of holes. It was observed that a pair of vortices were shed from each holes. For a row of closely spaced holes with an increased suction rate, the trailing vortices of adjacent holes linked together to form horseshoe vortices which grew and then shed downstream followed by the formation of new horseshoe vortices. From the their data, it appears that this *instability of the vortex pattern* occurred in the range $370 < R_D < 720$ with a velocity ratio, r_V , approaching 1. These suction levels are probably a bit high and the experiments relied on qualitative measurements. However, this work is valuable in pointing out the sensitivity of boundary-layer stability to small changes in hole spacing, hole diameter, and flow rate.

In the light of what was discussed on the role of micron-sized roughness in crossflow instabilities, these suction holes could play the role of roughness under some circumstances.

9.3.2 Cooling an air boundary layer

Whereas cooling stabilizes the first-mode supersonic instability, it destabilizes the second mode (Mack, 1984b). In a 3-D flow, cooling also destabilizes the second mode and has only a very weak stabilizing effect on the crossflow wave (Balakumar and Reed, 1991).

ACKNOWLEDGEMENTS

The author prepared these notes while a Professor of Aeronautics and Astronautics at Tohoku University, Sendai, Japan during the 1991/92 Academic Year. He would like to acknowledge the support of Tohoku University and the help and encouragement of Professors Kobayashi, Kohama, and Fukunishi during this time. The author would also like to thank Dr. H. Reed for her helpful comments and suggestions during the course of this work.

REFERENCES

Aizin, L.B. and Polyakov, M.F. 1979. Acoustic generation of Tollmien-Schlichting waves over local unevenness of surface immersed in streams (in Russian). *Preprint 17, ITPM, Akad. Nauk USSR, Siberian Div.* (see Nishioka and Morkovin, 1986).

Arnal D. 1984. Description and prediction of transition in two-dimensional incompressible flow. *AGARD Report No. 709* (Special course on stability and transition of laminar flows) VKI, Brussels.

Arnal D. 1992. Laminar-turbulent transition: prediction, application to drag reduction. *AGARD Report* (Special course on skin friction drag reduction) VKI, Brussels.

Arnal, D. and Jullien, J.C. 1987. Three-dimensional transition studies at ONERA/CERT. *AIAA Paper No. 87-1335*.

Arnal, D., Casalis, G., and Jullien, J.C. 1990. Experimental and theoretical analysis of natural transition on infinite swept wing. *Laminar-Turbulent Transition, Vol III*, eds. D. Arnal and R. Michel, Springer-Verlag.

Arnal, D., Jullien, J.C., and Casalis, G. 1991. The effects of wall suction on laminar-turbulent transition in three-dimensional flow. *Boundary Layer Stability and Transition to Turbulence, FED-Vol. 114*, Eds: D.C. Reda, H.L. Reed, R. Kobayashi, ASME.

Balakumar, P. and Reed, H.L. 1991. Stability of three-dimensional supersonic boundary layers. *Phys. Fluids A*, vol. 3, No. 4, 617.

Beckwith, I.E., Chen, F.J., and Creel, T.R.Jr. 1986. Design requirements for the NASA Langley supersonic low-disturbance wind tunnel. *AIAA Paper No. 86-0763*.

Bippes, H. 1972. Experimentelle untersuchung laminar-turbulenten umschlags an einer parallel angestromten konkaven wand. *Heidelberger Akademie der Wissenschaften, Mathematische-Naturwissenschaftliche Klasse, Sitzungsberichte, NO. 3*, 103.

Bippes, H. 1990. Instability feature appearing on swept wing configurations. *Laminar-Turbulent Transition, Vol III*, eds. D. Arnal and R. Michel, Springer-Verlag.

Bippes, H. 1991. Experiments on transition in three-dimensional accelerated boundary layer flows. *Proc. R.A.S. Boundary Layer Transition and Control*, Cambridge, UK, ISBN 0 903409 86 0.

Bippes, H. and Nitschke-Kowsky, P. 1987. Experimental study of instability modes in a three-dimensional boundary layer. *AIAA Paper*

No. 87-1336.

Blackwelder, R.F. 1992. Turbulence structure in boundary layers. *AGARD Report* (Special course on skin friction drag reduction) VKI, Brussels.

Bodonyi, R.J., Welch, W.J.C., Duck, P.W., and Tadifar, M. 1989. A numerical study of the interaction between unsteady freestream disturbances and localized variations in surface geometry. *J. Fluid Mech.*, vol. 209, 285.

Braslow, A.L. and Fischer, M.C. 1985. Design considerations for application of laminar flow control hardware and systems for transport aircraft. *Proc. AGARD Report No. 723*, (Special course on aircraft drag prediction and reduction), VKI, Belgium.

Bushnell, D.M. 1985. Turbulent drag reduction for external flows. *Proc. AGARD Report No. 723*, (Special course on aircraft drag prediction and reduction), VKI, Belgium.

Bushnell, D.M. 1992. Overview of aircraft drag reduction technology. *AGARD Report* (Special course on skin friction drag reduction) VKI, Brussels.

Bushnell, D.M. and Tuttle, M.H. 1979. Survey and bibliography on attainment of laminar flow control in air using pressure gradient and suction - Volume I. *NASA RP-1035*.

Cebeci, T. and Stewartson, K. 1980. Stability and transition in three-dimensional flows. *AIAA J.*, vol. 18, 398.

Chen, and Cebeci, T. 1990. An evaluation of stability-based methods for transition of three-dimensional flows. *Laminar-Turbulent Transition, Vol III*, eds. D. Arnal and R. Michel, Springer-Verlag.

Corke, T.C. 1990. Effect of controlled resonant interactions and mode detuning on turbulent transition in boundary layers. *Laminar-Turbulent Transition, Vol III*, eds. D. Arnal and R. Michel, Springer-Verlag.

Craik, A.D.D. 1971. Nonlinear resonant instability in boundary layers. *J. Fluid Mech.*, vol. 50, 393.

Crouch, J.D. 1991. Initiation of boundary-layer disturbances by nonlinear mode interactions. *Boundary Layer Stability and Transition to Turbulence, FED-Vol. 114*, Eds: D.C. Reda, H.L. Reed, R. Kobayashi, ASME.

Dagenhart, J.R. 1981. Amplified crossflow disturbances in the laminar boundary layer on swept wings with suction. *NASA TP-1902*.

Dagenhart, J.R., Saric, W.S., Mousseux, M.C., and Stack, J.P. 1989. Crossflow vortex instability and transition on a 45-degree swept wing. *AIAA Paper No. 89-1892*.

Dagenhart, J.R., Saric, W.S., Hoos, J.A., and Mousseux, M.C. 1990. Experiments on swept-wing boundary layers. *Laminar-Turbulent Transition, Vol III*, eds. D. Arnal and R. Michel, Springer-Verlag.

Day, H.P., Herbert, T., and Saric, W.S. 1990. Comparing local and marching analyses of Görtler instability. *AIAA J.*, vol. 28, no. 6, 1010.

Drazin, P.G. and Reid, W.H. 1981. *Hydrodynamic Stability*. Cambridge Univ. Press.

Fischer, T.M. and Dallmann, U. 1991. Primary and secondary stability analysis of a three-dimensional boundary layer flow. *Proc. R.A.S. Boundary Layer Transition and Control*, Cambridge, UK, ISBN 0 903409 86 0.

Floryan, J.M. and Saric, W.S. 1982. Stability of Görtler vortices in boundary layers. *AIAA J.*, vol. 20, no. 3, 316.

Gasperas, G. 1987. The stability of the compressible boundary layer on a sharp cone at zero angle of attack. *AIAA Paper No. 87-0494*.

Gaster, M. 1962. A note on a relation between temporally increasing and spatially increasing disturbances in hydrodynamic stability. *J. Fluid Mech.*, vol. 14, 222.

Gaster, M. 1967. On the flow along swept leading edges. *Aeronaut. Q.*, vol. 18, 788.

Gaster, M. 1974. On the effects of boundary-layer growth on flow stability. *J. Fluid Mech.*, vol. 66, 465.

Görtler, H. 1941. Instabilität laminarer Grenzschichten an konkaven Wänden gegenüber gewissen dreidimensionalen Störungen. *ZAMM*, vol. 21, no. 1, 250.

Goldstein, M.E. and Hultgren, L.S. 1989. Boundary-layer receptivity to long-wave freestream disturbances. *Ann. Rev. Fluid Mech.*, vol. 21, 137.

Hall, P. 1983. The linear development of Görtler vortices in growing boundary layers. *J. Fluid Mech.*, vol. 130, 41.

Hall, P. 1985. The Görtler vortex instability mechanism in three-dimensional boundary layers. *Proc. R. Soc. Lon. Ser. A.*, vol. 406, 93.

Hall, P., Malik, M.R., and Poll, D.I.A. 1984. On the stability of an infinite swept attachment-line boundary layer. *Proc. R. Soc. Lon. Ser. A.*, vol. 395, 229.

Hall, P. and Malik, M.R. 1986. On the instability of an three-dimensional attachment-line boundary layer: weakly nonlinear and numerical approach. *J. Fluid Mech.*, vol. 163, 257.

Hackett, J.E. and Sugavanam, A. 1985. Recent

developments in three-dimensional wake analysis. *Proc. AGARD Report No. 723*, (Special course on aircraft drag prediction and reduction), VKI, Belgium.

Herbert, T. 1984a. Analysis of the subharmonic route to transition in boundary layers. *AIAA Paper No. 84-0009*.

Herbert, T. 1984b. Secondary instability of shear flows. *AGARD Report No. 709* (Special course on stability and transition of laminar flows) VKI, Brussels.

Herbert, T. 1984c. Nonlinear effects in boundary-layer stability. *AGARD Report No. 709* (Special course on stability and transition of laminar flows) VKI, Brussels.

Herbert, T. 1985. Three-dimensional phenomena in the transitional flat-plate boundary layer. *AIAA Paper No. 85-0489*.

Kachanov, Yu.S. and Levchenko, V.Ya. 1984. Resonant interactions of disturbances in transition to turbulence in a boundary layer. *J. Fluid Mech.*, vol. 138, 209.

Kachanov, Yu.S. and Tararykin, O.I. 1990. The experimental investigation of the travelling waves in a three-dimensional boundary layer. *Laminar-Turbulent Transition, Vol III*, eds. D. Arnal and R. Michel, Springer-Verlag.

Kaups, K. and Cebeci, T. 1977. Compressible laminar boundary layers with suction on swept and tapered wings. *J. Aircraft*, vol. 14, 661.

Kendall, J.M. 1991. Studies on laminar boundary-layer receptivity to freestream turbulence near a leading edge. *Boundary Layer Stability and Transition to Turbulence, FED-Vol. 114*, Eds: D.C. Reda, H.L. Reed, R. Kobayashi, ASME.

Kerschen, E.J. 1989. Boundary-layer receptivity. *AIAA Paper No. 89-1109*

Kerschen, E.J. 1990. Boundary-layer receptivity theory. *Appl. Mech. Rev.*, Vol. 43, No. 5, part 2, May 1990.

Kerschen, E.J. 1991. Linear and nonlinear receptivity to vortical freestream disturbances. *Boundary Layer Stability and Transition to Turbulence, FED-Vol. 114*, Eds: D.C. Reda, H.L. Reed, R. Kobayashi, ASME.

Kerschen, E.J., Choudhari, M. and Heinrich, R.A. 1990. Generation of boundary instability waves by acoustic and vortical freestream disturbances. *Laminar-Turbulent Transition vol III*, Eds. D. Arnal and R. Michel, Springer-Verlag.

Klebanoff, P.S., Tidstrom, K.D. and Sargent, L.M. 1962. The three-dimensional nature of boundary-layer instability. *J. Fluid Mech.*, vol. 12, 1.

Kleiser, L. and Zang, T.A. 1991. Numerical simulation of transition in wall-bounded shear flows. *Ann. Rev. Fluid Mech.* vol. 23, 495.

Kosorygin, V. S. and Polyakov, N. F. 1990. Autodestruction of unstable waves in a laminar boundary layer (in Russian)," *Preprint 11-17. ITP. Akad. Nauk USSR, Sib. Otd.*, Novosibirsk.

Lessen, M. and Koh, P.H. 1985. Instability and bursting in the boundary layer," *Laminar-Turbulent Transition, vol II*, Ed. V. V. Kozlov, Springer-Verlag, pp 39-51.

Lin, N., Reed, H. and Saric, W. S. 1990. Leading-edge receptivity: Navier-Stokes computations. *Proc. R.A.S. Boundary Layer Transition and Control*, Cambridge, UK, ISBN 0 903409 86 0.

Lekoudis, S.G. 1978. Stability of boundary layers over permeable surface. *AIAA Paper No. 78-203*.

Liepmann, H.W. and Nosenchuck, D.M. 1982. Active control of laminar-turbulent transition. *J. Fluid Mech.*, vol. 118, 201.

Lock, R.C. 1985. Prediction of the drag of wings at subsonic speeds by viscous/inviscid interaction techniques. *Proc. AGARD Report No. 723*, (Special course on aircraft drag prediction and reduction), VKI, Belgium.

Mack, L.M. 1969. Boundary-layer stability theory. *Jet Propulsion Lab. Rpt. 900-277*, Rev. A.

Mack, L.M. 1984a. Line sources of instability waves in a Blasius boundary layer. *AIAA Paper 84-0168*.

Mack, L.M. 1984b. Boundary-layer linear stability theory. *AGARD Report No. 709* (Special course on stability and transition of laminar flows) VKI, Brussels.

Mack, L.M. 1987. Stability of axisymmetric boundary layers on sharp cones at hypersonic Mach numbers. *AIAA Paper No. 87-1413*.

Malik, M.R. 1982 COSAL - A Black Box Compressible Stability Analysis Code for Transition Prediction in Three-Dimensional Boundary Layers. *NASA CR-165952*.

Malik, M.R. 1988. numerical methods for hypersonic boundary layer stability, *High Technology Corp. Report No. 88-6*.

Malik, M.R. and Orszag, S.A. 1981. Efficient computation of the stability of three-dimensional compressible boundary layers. *AIAA Paper No. 81-1277*.

Malik, M.R., Chuang, S., and Hussaini, M.Y. 1982. Accurate solution of compressible linear stability equations. *ZAMP* vol. 33, 189.

Meyer, F. and Kleiser, L. 1988. *Fluid Dynamics of Three-Dimensional Turbulent Shear Flows and*

Transition, AGARD-CP-438.

Morkovin, M.V. 1969. On the many faces of transition. *Viscous Drag Reduction* ed: C.S. Wells, Plenum.

Morkovin, M.V. 1978. Instability, transition to turbulence and predictability. *AGARDograph No. 236*.

Morkovin, M.V. 1991. Panoramic view of changes in vorticity distribution in transition instabilities and turbulence. *Boundary Layer Stability and Transition to Turbulence, FED-Vol. 114*, Eds: D.C. Reda, H.L. Reed, R. Kobayashi, ASME.

Morkovin, M.V. and Reshotko, E. 1990. Dialogue on progress and issues in stability and transition research. *Laminar-Turbulent Transition, Vol III*, eds. D. Arnal and R. Michel, Springer-Verlag.

Muller, B. and Bippes, H. 1988. *Fluid Dynamics of Three-Dimensional Turbulent Shear Flows and Transition, AGARD-CP-438*.

Nayfeh, A.H. 1980a. Stability of three-dimensional boundary layers. *AIAA J.*, vol. 18, 406.

Nayfeh, A.H. 1980b. Three-dimensional stability of growing boundary layers. *Laminar-Turbulent Transition*, ed: R. Eppler and H. Fasel, Springer.

Nayfeh, A.H. and Padhye, A. 1979. The relation between temporal and spatial stability in three-dimensional flows, *AIAA J.*, vol 17, 1084.

Nishioka, M. and Morkovin, M.V. 1986. Boundary-layer receptivity to unsteady pressure gradients: experiments and overview. *J. Fluid Mech.*, vol. 171, 219.

Parekh, D.E., Pulvin, P., and Wlezien, R.W. 1991. Boundary layer receptivity to convected gusts and sound. *Boundary Layer Stability and Transition to Turbulence, FED-Vol. 114*, Eds: D.C. Reda, H.L. Reed, R. Kobayashi, ASME.

Parikh, P.G., Sullivan, P.P., Birmingham, E., and Nagel, A.L. 1989. Stability of a 3-D wing boundary layer on a SST configuration. *AIAA Paper No. 89-0036*.

Peerhossaini, H. and Westfreid, J.E. 1990. *Proceedings Colloquium on Görler Vortex Flows, EUROMECH 261*, Nantes.

Peerhossaini, H. 1991. *Private Communication*.

Pfenninger, W. 1965. Some results from the X-21 program. Part I. Flow phenomenon at the leading edge of swept wings. *AGARDograph No. 97*.

Pfenninger, W. 1977. Laminar flow control - Laminarization. *AGARD Report No. 654*, (Special Course on Drag Reduction), VKI, Brussels.

Poisson-Quinton, Ph. 1985. Parasitic and interference drag prediction and reduction. *Proc. AGARD Report No. 723*, (Special course on aircraft drag prediction and reduction), VKI, Belgium.

Poll, D.I.A. 1979. Transition in the infinite swept attachment line boundary layer. *Aeronaut. Q.*, vol. 30, 607.

Poll, D.I.A. 1984a. Some observations of the transition process on the windward face of a yawed cylinder. *Cranfield College of Aeronautics Report 8407*.

Poll, D.I.A. 1984b. Transition description and prediction in three-dimensional flows. *AGARD Report No. 709* (Special course on stability and transition of laminar flows) VKI, Brussels.

Pupator, P.T. and Saric, W.S. 1989. Control of random disturbances in a boundary layer. *AIAA Paper No. 89-1007*.

Radeztsky, R.H., Kosorygin, V.S., and Saric, W.S. 1991. Control of T-S waves with freestream sound and 2-D roughness. *Bull. Am. Phys. Soc.*, vol. 36, 2629.

Reed, H.L. and Nayfeh, A.H. 1986. Numerical-perturbation technique for stability of a flat-plate boundary layer with suction. *AIAA J.*, vol. 24, 208.

Reed, H.L. and Balakumar, P. 1990. Compressible boundary-layer stability theory. *Phys. Fluids A*, vol. 2, No. 8, 1341.

Reed, H.L. and Haynes, T.S. 1990. Crossflow instability in supersonic boundary layers. *Bull. Am. Phys. Soc.*, vol. 35, 2322.

Reed, H.L. and Fuciarelli, D.A. 1991. Analysis of high-frequency secondary instabilities in three-dimensional boundary layers. *Bull. Am. Phys. Soc.*, vol. 36, 2630.

Reshotko, E. 1978. Heated boundary layers. *Proc. 12th Symposium on Naval Hydrodynamics*, Nat'l Acad. Sci., Washington, D.C.

Reshotko, E. 1984a. Environment and receptivity. *AGARD Report No. 709* (Special course on stability and transition of laminar flows) VKI, Brussels.

Reshotko, E. 1984b. Laminar flow control - Viscous simulation. *AGARD Report No. 709* (Special course on stability and transition of laminar flows) VKI, Brussels.

Reshotko, E. 1985. Control of boundary-layer transition. *AIAA Paper No. 85-0562*.

Reynolds, G.A. and Saric, W.S. 1986. Experiments on the stability of a flat-plate boundary layer with suction. *AIAA J.* vol. 24, 202.

Robert, J.P. 1992. Drag reduction: and industrial challenge. *AGARD Report* (Special course on skin friction drag reduction) VKI, Brussels.

Sabry, A.S., Yu, X., and Liu, J.T.C. 1990. Secondary instabilities of three-dimensional inflectional velocity profiles resulting from longitudinal vorticity elements in boundary layers. *Laminar-Turbulent Transition, Vol III*, eds. D. Arnal and R. Michel, Springer-Verlag.

Saric, W.S. 1985a. Boundary-Layer Transition: T-S Waves and Crossflow Mechanisms. *Proc. AGARD Report No. 723*, (Special course on aircraft drag prediction and reduction), VKI, Belgium.

Saric, W.S. 1985b. Laminar Flow Control With Suction: Theory and Experiment. *Proc. AGARD Report No. 723*, (Special course on aircraft drag prediction and reduction), VKI, Belgium.

Saric, W.S. 1986. Visualization of different transition mechanisms. *Phys. Fluids*, vol. 29, 2770.

Saric, W.S. 1990. Low-speed experiments: requirements for stability measurements. *Instability and Transition*, vol 1, (eds. M. Y. Houssaini and R. G. Voigt) Springer-Verlag, New York.

Saric, W.S. 1993. Görtler vortices. *Ann. Rev. Fluid Mech.*, vol. 25.

Saric, W.S. and Nayfeh, A.H. 1977. Nonparallel stability of boundary layers with pressure gradients and suction. *AGARD C-P No. 224*, 6.

Saric, W.S. and Thomas, A.S.W. 1984. Experiments on the subharmonic route to transition. *Turbulence and Chaotic Phenomena in Fluids*, ed: T. Tatsumi, North-Holland.

Saric, W.S. and Yeates, L.G. 1985. Experiments on the stability of crossflow vortices in swept-wing flows. *AIAA Paper No. 85-0493*.

Saric, W.S., Dagenhart, J.R., and Mousseux, M.C. 1989. Experiments in swept-wing transition. *Numerical and Physical Aspects of Aerodynamic Flows*, Vol. 4, Ed. T. Cebeci, Springer-Verlag.

Saric, W.S. and Krutckoff, T.K. 1990. Visualization of low-Reynolds-number flow fields around roughness elements," *Bull. Amer. Phys. Soc.*, vol. 35, 2262.

Saric, W.S. and Benmalek, A. 1991. Görtler vortices with periodic curvature. *Boundary Layer Stability and Transition to Turbulence, FED-Vol. 114*, Eds: D.C. Reda, H.L. Reed, R. Kobayashi, ASME.

Saric, W.S., Hoos, J.A., Radeztsky, R.H and Kohama, Y. 1991. Boundary-layer receptivity of sound with roughness. *Boundary Layer Stability and Transition to Turbulence, FED-Vol. 114*, Eds: D.C. Reda, R.L. Reed, R. Kobayashi, ASME.

Savill, M. and Coustols, E. 1992. Turbulent drag reduction techniques: ripples, Lebu, polymers, additives. *AGARD Report* (Special course on skin friction drag reduction) VKI, Brussels.

Spalart, P. 1992. Use of numerical simulation for the study of drag reduction. *AGARD Report* (Special course on skin friction drag reduction) VKI, Brussels.

Spencer, S.A., Saric, W.S., and Radeztsky, R.H. 1991. Boundary-layer receptivity: freestream sound and 3-D roughness. *Bull. Am. Phys. Soc.*, vol. 36, 2618.

Srokowski, A.J. and Orszag, S.A. 1977. Mass flow requirements for LFC wing design. *AIAA Paper No. 77-1222*.

Stenewsky, E. and Krogmann, P. 1985. Transonic drag rise and drag reduction by active/passive boundary layer control. *Proc. AGARD Report No. 723*, (Special course on aircraft drag prediction and reduction), VKI, Belgium.

Stetson, K.F., Thompson, E.R., Donaldson, J.C., and Siler, L.G. 1983. Laminar boundary layer stability experiments on a cone at Mach 8. Part 1: Sharp cone. *AIAA Paper No. 83-1761*.

Stuckert, G.K. and Reed, H.L. 1991. On the linear stability of supersonic cone boundary layers. submitted to *AIAA J.*

Swearingen, J.D. and Blackwelder, R. F. 1987. The growth and breakdown of streamwise vortices in the presence of a wall. *J. Fluid Mech.*, vol. 182, 255.

Takagi, S., Saric, W.S., Radeztsky, R.H., Spencer, S.A., and Orr, D.J. 1991. Effect of sound and micron-sized roughness on crossflow dominated transition. *Bull. Am. Phys. Soc.*, vol. 36, 2630.

Thomas, A.S.W. 1983. The control of boundary-layer transition using a wave superposition principle. *J. Fluid Mech.*, vol. 137, 233.

Thomas, A.S.W. 1985. Aircraft drag reduction technology - A summary. *Proc. AGARD Report No. 723*, (Special course on aircraft drag prediction and reduction), VKI, Belgium.

Zelman, M.B. and Maslennikova, I.I. 1990. Three-dimensional effects in boundary-layer transition: A high Reynolds number weakly nonlinear theory. *Laminar-Turbulent Transition, Vol III*, eds. D. Arnal and R. Michel, Springer-Verlag.

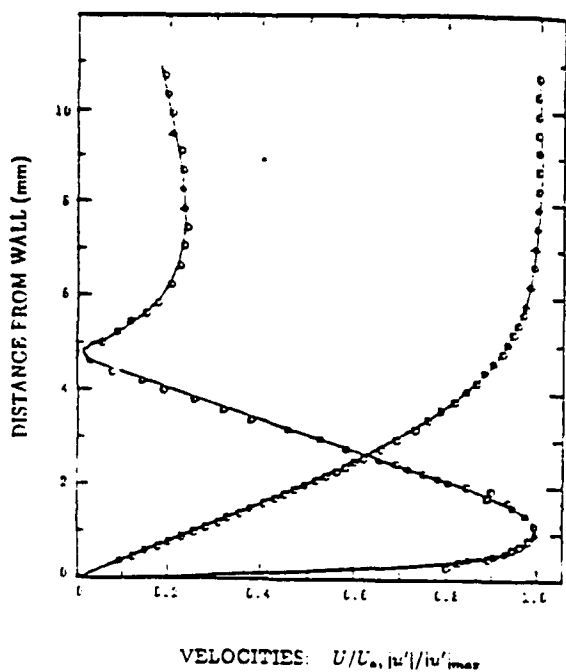


Fig. 1. Mean flow, U/U_∞ , and disturbance flow $|u'|/U_\infty$ velocities as a function of y^* (lab coordinates). Saric (1990).

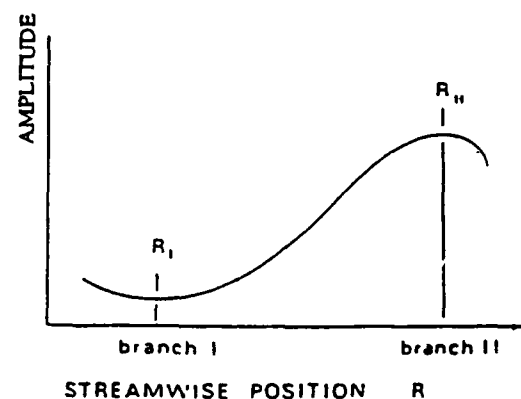


Fig. 2. Schematic of disturbance amplitude change in the stream direction.

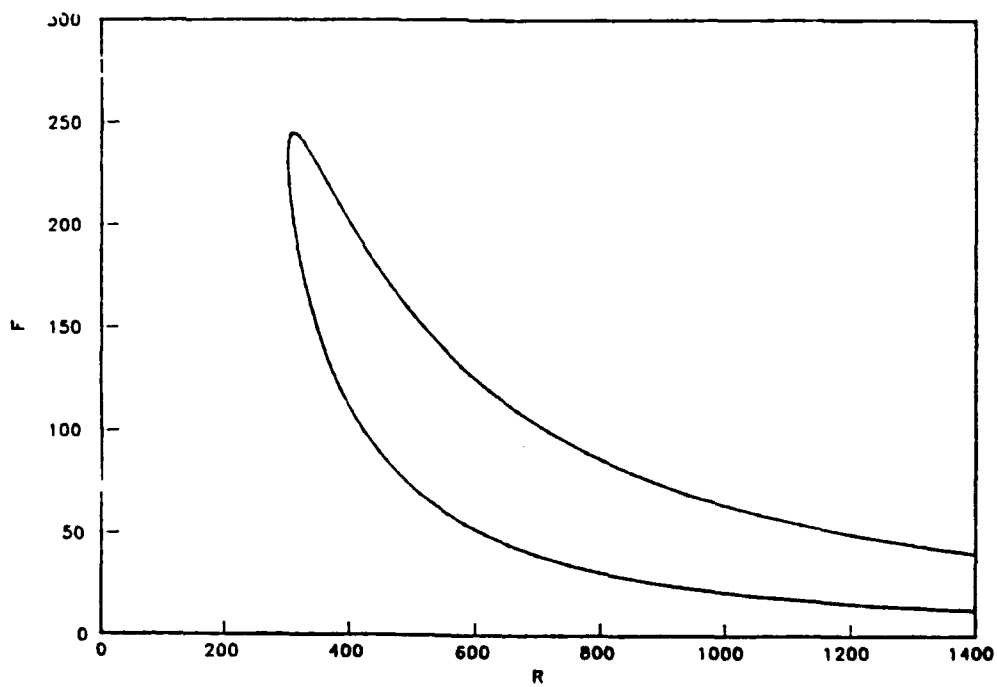


Fig. 3. Neutral stability curve for a Blasius Boundary Layer. Here F is multiplied by 10^6 .

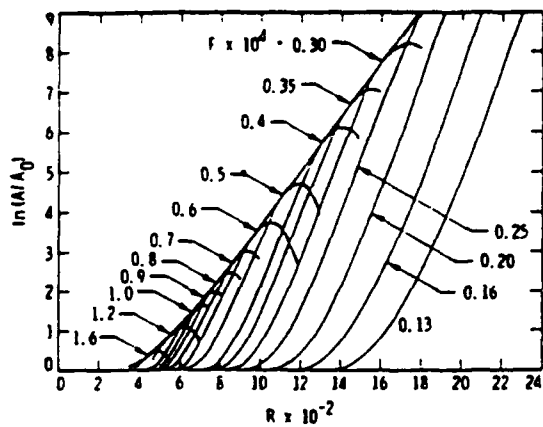


Fig. 4. $\ln(A/A_0)$ as a function of R for 2-D disturbances in a Blasius Boundary Layer. Mack (1984b).

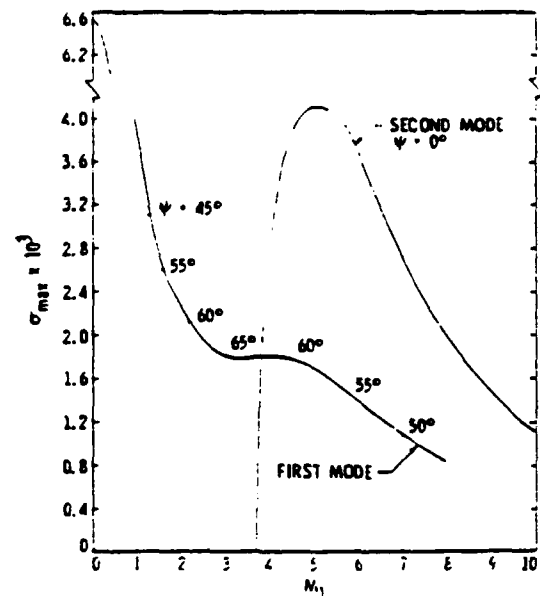


Fig. 5. Effect of Mach number on the maximum spatial amplification rate of first and second mode waves at $R = 1500$. Adiabatic wall, wind-tunnel temperatures. Mack (1984b).

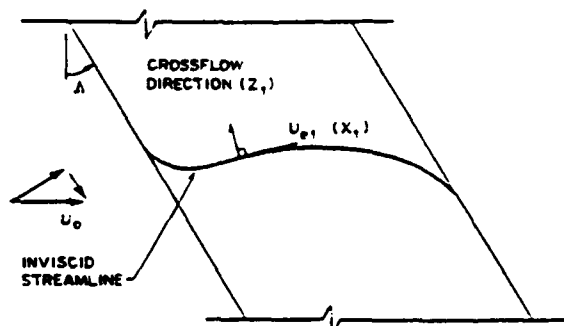


Fig. 6. Schematic of inviscid streamline over a swept wing. Reed and Saric (1989).

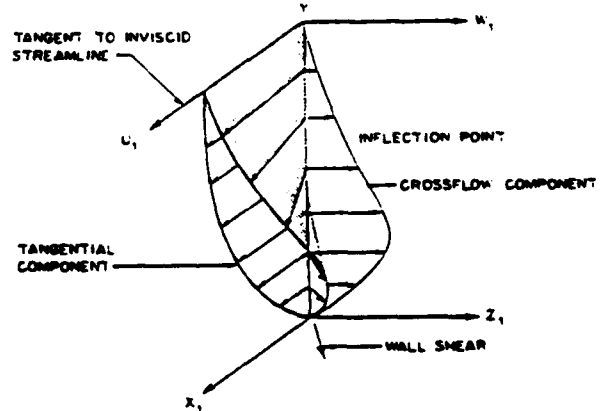


Fig. 7. Schematic of velocity components within a swept-wing boundary layer illustrating the definition of the crossflow velocity. Reed and Saric (1989).

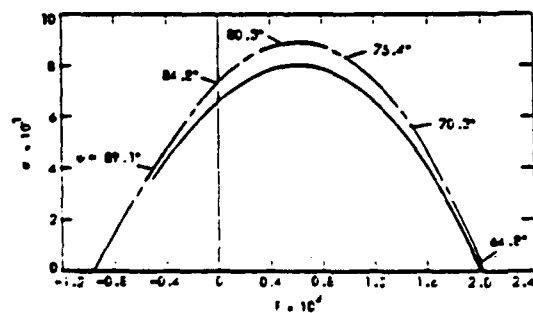


Fig. 8. Unstable frequency range for a 35° swept wing at $R = 301$ and $k = 0.52$; — incompressible theory; — compressible theory. Mack (1984b).

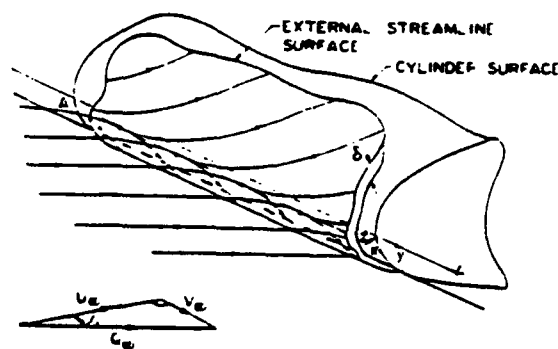


Fig. 9. Schematic of the flow near the leading edge of a swept wing. Poll (1979).

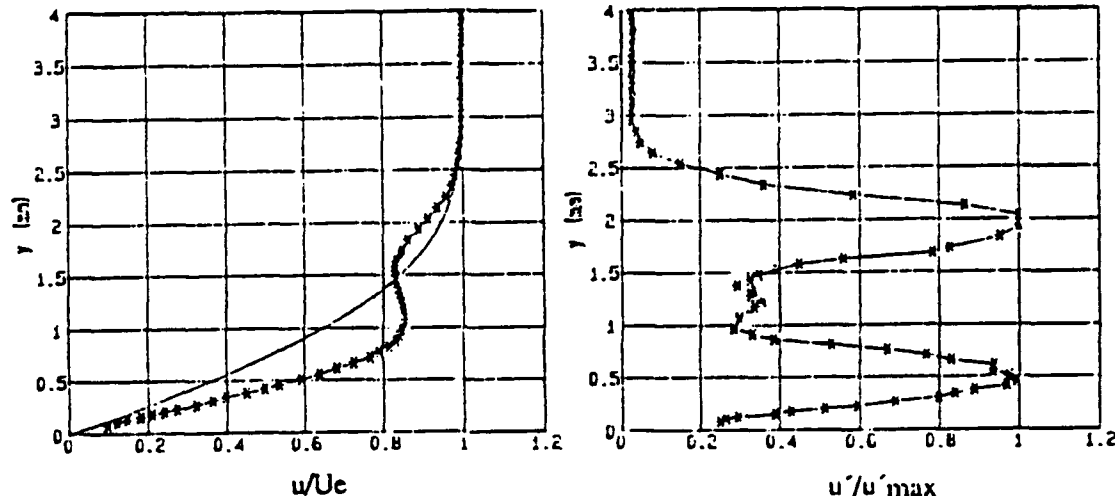


Fig. 10a. Mean velocity profile at $z^* = -0.45$ mm, $x^*/L = 0.4$, and $R_L = 2.66 \times 10^6$. Dagenhart et al. (1990).

Fig. 10b. Disturbance profile band-passed at 150 Hz. Conditions of Fig. 10a.

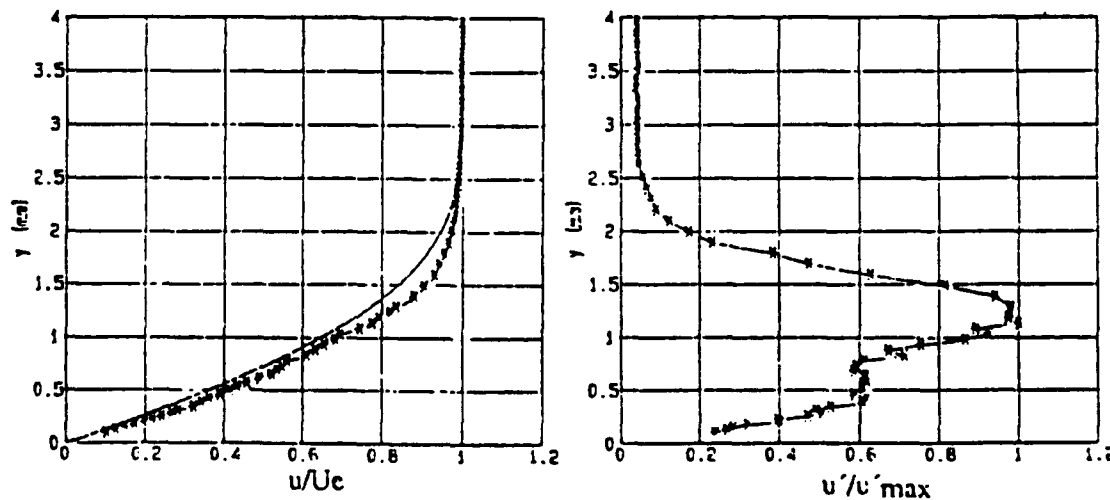


Fig. 11a. Mean velocity profile at $z^* = +2.55$ mm, $x^*/L = 0.4$, and $R_L = 2.66 \times 10^6$. Dagenhart et al. (1990).

Fig. 11b. Disturbance profile band-passed at 150 Hz. Conditions of Fig. 11a.

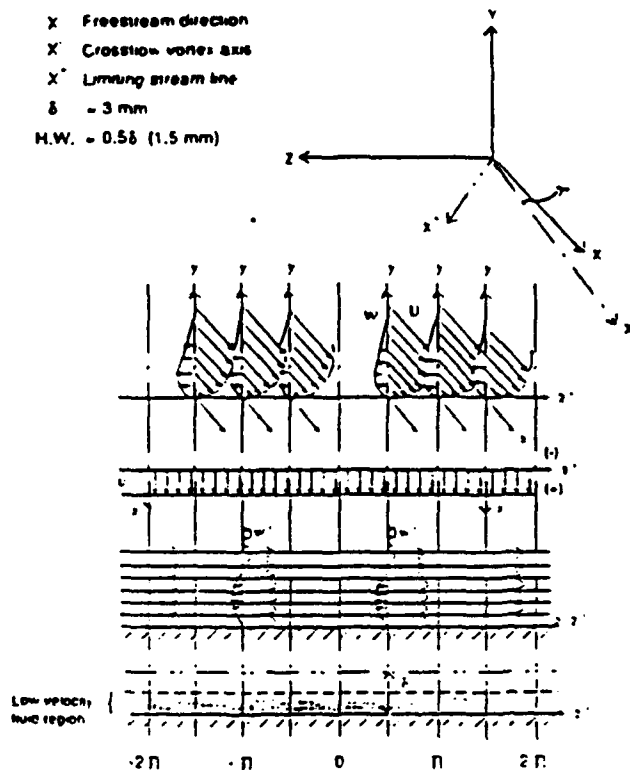


Fig. 12a. Stage 1 development of crossflow vortex structure. Neutral disturbances at $x^*/L = 0.05$. Kohama et al. (1991).

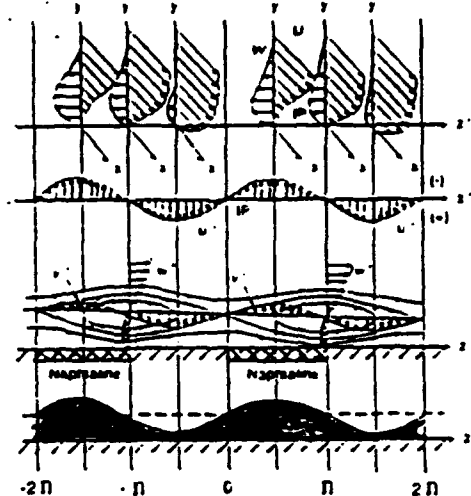


Fig. 12b. Stage 2 development of crossflow vortex structure. Linear disturbances at $x^*/L = 0.2$. Kohama et al. (1991).

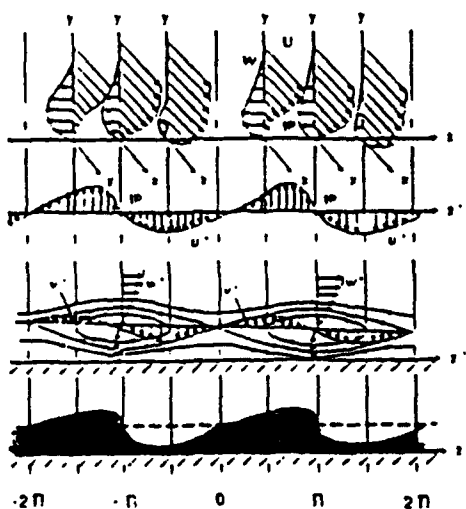


Fig. 12c. Stage 3 development of crossflow vortex structure. Initiation of inflectional profiles at $x^*/L = 0.35$. Kohama et al. (1991).

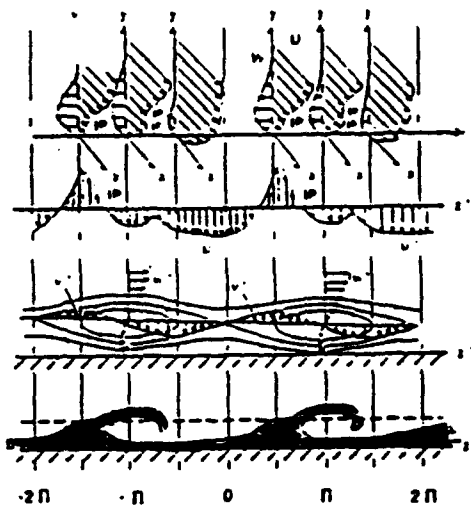


Fig. 12d. Stage 4 development of crossflow vortex structure. Illustration of double inflectional profiles at $x^*/L = 0.4$. Kohama et al. (1991).



**BOUNDARY LAYER TRANSITION :
PREDICTION, APPLICATION TO DRAG REDUCTION**

D. ARNAL

CERT/ONERA

**Department of Aerothermodynamics
2 avenue E. Belin - 31055 TOULOUSE Cedex (FRANCE)**

92-17810



SUMMARY

This paper describes the practical calculation methods which are currently available to predict the transition location in two- and three-dimensional flows. Emphasis is given to the problem of skin friction drag reduction on swept wings at subsonic and transonic speeds. The so-called e^n method, which is deduced from the linear stability theory is widely used in the case of "natural" transition, but simpler techniques (empirical criteria) are useful in more complex situations such as boundary layer tripping or leading edge contamination. The simulation of flight in wind tunnels is also discussed. Wind tunnel/flight correlation includes comparisons between the free stream disturbance environment, the transition Reynolds number and the n factor at transition onset.

CONTENTS

1. INTRODUCTION
2. LINEAR STABILITY THEORY
 - 2.1. Problem formulation
 - 2.2. Some results in two-dimensional flows
 - 2.3. Three-dimensional flows : crossflow instability
 - 2.4. Secondary instability, non linearity, breakdown
3. FREE STREAM DISTURBANCES : WIND TUNNEL / FLIGHT
 - 3.1. Wind tunnel disturbances
 - 3.2. In-flight disturbances
4. TRANSITION PREDICTION ON A SMOOTH WALL
 - 4.1. The e^n method
 - 4.2. Transition criteria
 - 4.3. Data base methods
 - 4.4. First examples of application
 - 4.5. Transition region modelling
5. HOW TO DELAY TRANSITION ?
 - 5.1. Effect of streamwise pressure gradients
 - 5.2. Cooling and heating
 - 5.3. Suction
6. ATTACHMENT LINE AND LEADING EDGE PROBLEMS
 - 6.1. The flow along the attachment line

6.2. "Natural" transition

6.3. Leading edge contamination

6.4. Relaminarisation in a negative pressure gradient

6.5. Concluding remark : the minimum Reynolds number for turbulence

7. OTHER FACTORS AFFECTING TRANSITION IN FLIGHT CONDITIONS

- 7.1. Surface imperfections and vibrations
- 7.2. Environmental factors

8. TRANSITION REYNOLDS NUMBERS AND n FACTORS : WIND TUNNEL/FLIGHT EXPERIMENTS

- 8.1. Direct wind tunnel / flight comparisons
- 8.2. Other flight experiments
- 8.3. n factors in wind tunnels. Discussion

9. CONCLUSION

1. INTRODUCTION

We believe that it is not necessary to remind the importance of skin friction reduction in aerodynamic studies. The essential properties of boundary layer flows are described by Cousteix [1] at the beginning of this Lecture Series, and Robert [2] discusses the industrial challenge of aircraft drag reduction. The different methods for skin friction reduction are reviewed by Bushnell [3]. It has been shown that drag reduction can be obtained either by maintaining laminar flow on the surface or by modifying the structure of the turbulent boundary layer downstream of the transition region. In this paper, attention is focused on the first aspect of the problem, i.e. the control of laminar-turbulent transition by delaying the appearance of the turbulent structures which cause an increase in the skin friction drag.

This objective requires, of course, to have a good knowledge of the transition mechanisms. There are in fact several routes to turbulence, which can be summarized as follows. Let us consider a laminar flow developing along a given body. It is strongly affected by the various types of *forced disturbances* generated by the model itself (roughness, vibrations ...) or existing in the free stream (noise, turbulence ...). The first step of the transition process is the boundary layer *receptivity* (Morkovin, [4]) ; receptivity describes the means by which the forced disturbances enter the boundary layer as well as their signature in the disturbed flow. This signature constitutes the initial conditions for the

development of more or less complex mechanisms which ultimately lead to turbulence. Two kinds of transition processes are usually considered :

a - If the amplitude of the forced disturbances is small, one can observe at first exponentially growing instabilities, the development of which is governed by *linear* equations (Tollmien-Schlichting waves, crossflow waves, Görtler vortices ...). Three-dimensional and non linear effects occur subsequently, inducing secondary instabilities and then transition. In these cases of so-called "natural transitions", the transition Reynolds numbers can be very large.

b - If the amplitude of the forced disturbances is not weak (high free stream turbulence level, large isolated roughness elements ...), *non linear* phenomena are immediately observed and transition occurs a short distance downstream of the leading edge of the body. This mechanism is called a "*bypass*" (Morkovin, [5]), in the sense that the linear stages of the transition process are ignored (bypassed).

The fundamental aspects of these mechanisms are described in the previous lecture by Saric [6]. The main goal of the present chapter is to give a review of the different techniques which are available to predict transition on a given body. In the case of a "natural transition", the linear stability theory constitutes a very efficient tool to describe the amplification of the unstable waves which are observed in the boundary layer after the forced disturbances have been internalized through some receptivity mechanism. The main features of the linear theory will be reminded in Section 2, where emphasis is given on incompressible and transonic flows which are of major interest for practical applications such as aircraft (the problem of transition at high speeds will not be discussed in this paper). However, due to the fact that the stability equations are linearized, we can only compute the amplification of the unstable waves, but their amplitude remains unknown. This amplitude is linked to that of the environmental disturbances which are not necessarily the same in flight conditions and in ground facilities, as it will be shown in Section 3. Section 4 explains how it is possible to estimate the streamwise location where the instabilities break down into turbulence. Practical calculation methods include the so-called e^n method, empirical criteria, data base methods and intermittency methods. Even if these techniques do not claim to simulate all the details of the transition phenomena, most of them are able to predict the movement of the transition point when some flow parameters are changed. These parameters are essentially the streamwise pressure gradient, the wall cooling (or heating) and the wall suction. They constitute efficient "transition modifiers" which must be optimized in order to delay transition and to obtain transition Reynolds numbers as large as possible. This problem is discussed in Section 5, in which the theoretical aspects of passive and active boundary layer control are illustrated by wind tunnel measurements or flight tests results.

Section 6 is devoted to a survey of problems linked to the attachment line of a swept body. If the body is attached to a solid surface, the attachment line can be contaminated by the turbulent structures coming from the wall ; this leading edge contamination mechanism is a typical example of bypass, in the sense that it occurs at Reynolds numbers lower than the critical Reynolds number computed from the linear stability theory. The "natural" transition problems along a leading edge are also described in this Section.

In many cases, the surface of a wing is not perfectly smooth, and irregularities such as waviness, gaps, steps or roughness elements (rivets, insects, ice crystals ...) can induce premature transitions. An overview of these problems is given in Section 7. It will be shown that the effect of two-dimensional irregularities (for instance steps normal to the mean flow direction) can be accounted for by the linear theory and the e^n method ; however, as stability computations are time consuming, simple criteria have been developed to estimate the allowable roughness size of the irregularities. For large three-dimensional roughness elements (for instance rivets or insects impacts), transition is often triggered by fully non linear mechanisms (bypass), so that the linear theory no longer applies. In this case, the only way to predict the permissible height of the protuberances is to use empirical correlations.

The objective of Section 8 is to compare flight and wind tunnel results. As the forced disturbances are not necessarily identical in flight conditions and in laboratory conditions (Section 3), it is not obvious that ground facilities are able to properly simulate the transition mechanisms occurring on the wing of an aircraft. These comparisons are focused on the values of the transition Reynolds numbers as well as on the values of the n factor at transition onset. Despite the complexity of the numerous problems associated with laminar-turbulent transition, n factors between 9 and 11 correlate two-dimensional and three-dimensional experimental data obtained during flight tests and in the quietest wind tunnels where the disturbance environment is low. This rather simple (too simple ?) result will be finally discussed.

2. LINEAR STABILITY THEORY

A detailed description of the linear stability theory is given in the previous lecture by Saric [6]. Review papers can also be found in [7] and [8] for example. In the present paragraph, the basic features of this theory are reminded and typical results are presented for low speed and transonic flows. The problem of Görtler vortices will not be discussed, because it does not seem to be of practical importance for aeronautical applications.

2.1. Problem Formulation

Let us recall that the principle is to introduce sinusoidal small disturbances into the linearized Navier-Stokes equations in order to compute the range of unstable frequencies. It is assumed that any fluctuating quantity r' (velocity, pressure, density or temperature) is expressed by :

$$r' = r(y) \exp[i(\alpha x + \beta z - \omega t)] \quad (2.1)$$

x, y, z is an orthogonal coordinate system, which can be either cartesian or curvilinear, y being normal to the surface. The complex amplitude function r depends on y only (parallel flow approximation). In the general case, α, β and ω are complex numbers.

This leads to a system of 6 ordinary differential equations in y for the amplitude functions $r(y)$. Due to the homogeneous boundary conditions (the disturbances must vanish at the wall and in the free stream, except the pressure fluctuations which have a non zero amplitude at the wall), the problem is an eigenvalue one : when the mean flow is specified, non trivial solutions exist only for certain combinations of the parameters α, β, ω and R , where R is the Reynolds number.

In the framework of the *temporal* theory, α and β are real, ω is a complex quantity : $\omega = \omega_r + i\omega_i$. Relation (2.1) then becomes :

$$r' = r(y) \exp(\omega_i t) \exp[i(\alpha x + \beta z - \omega_r t)] \quad (2.2)$$

Depending on the sign of the temporal amplification rate ω_i , the disturbances are damped ($\omega_i < 0$), amplified ($\omega_i > 0$) or neutral ($\omega_i = 0$). ω_r represents a circular frequency ; α and β are the components of the wavenumber vector \vec{k} in the x and z directions, respectively. The angle ψ between the x direction and \vec{k} is given by :

$$\psi = \tan^{-1}(\beta/\alpha) \quad (2.3)$$

When the *spatial* theory is used, ω is real, α and β are complex : $\alpha = \alpha_r + i\alpha_i$ and $\beta = \beta_r + i\beta_i$. r' is now expressed by :

$$r' = r(y) \exp(-\alpha_i x - \beta_i z) \exp[i(\alpha_r x + \beta_r z - \omega t)] \quad (2.4)$$

In this case, we define a wavenumber vector $\vec{k} = (\alpha_r, \beta_r)$ and an amplification vector $\vec{A} = (-\alpha_i, -\beta_i)$, with angles ψ and ψ with respect to the x direction :

$$\psi = \tan^{-1}(\beta_r/\alpha_r) \quad (2.5a)$$

$$\psi = \tan^{-1}(\beta_i/\alpha_i) \quad (2.5b)$$

If β_i is set equal to zero, the waves can be amplified ($\alpha_i < 0$), neutral ($\alpha_i = 0$) or damped ($\alpha_i > 0$) in the x direction.

As a general rule, Gaster's relation [9] makes it possible to convert a temporal to a spatial amplification rate by using the group velocity concept, see paragraph 4.1.

By neglecting the terms of the order $1/R$ in the stability equations (inviscid theory), Lees & Lin [10] showed up the importance of the so-called "generalized inflection point", which corresponds to the altitude y_s where :

$$\frac{d}{dy} \left[\rho \frac{dU}{dy} \right]_{y_s} = 0 \quad (2.6)$$

where ρ and U are the mean density and the mean velocity. It was demonstrated that the presence of such a point is a sufficient condition for the appearance of unstable disturbances at infinite Reynolds numbers (practically at large Reynolds numbers) : it is the *inflectional instability*. The existence of a generalized inflection point is also a necessary and sufficient condition for the appearance of neutral waves.

2.2. Some Results in Two-dimensional Flows

The eigenfunctions which are solutions of the linearized stability equations for two-dimensional basic flows are usually referred to as Tollmien-Schlichting waves (TS waves).

In this paragraph, x represents the mean flow direction. The computations were performed using the spatial theory with a numerical code developed at ONERA/CERT [11]. A basic assumption is that $\beta_i = 0$, i.e. there is no amplification in the spanwise direction.

Figure 2.1 shows stability diagrams computed for flat plate flow on adiabatic wall for $Me = 0$ and $Me = 1.1$, where Me is the Mach number at the boundary layer edge. We consider at first two-dimensional waves ($\psi = 0^\circ$). For the sake of clarity, only some curves of equal amplification rates ($\alpha_i < 0$) are plotted in the (Reynolds number, wavenumber) plane. The Reynolds number $R\delta_1$ is computed from the displacement thickness δ_1 , the free stream velocity U_e and the kinematic viscosity ν_e of the outer flow. α_r and α_i are made dimensionless with δ_1 . For both Mach numbers, there is a critical Reynolds number $R\delta_{1cr}$ below which all disturbances are damped.

It is clear that the shape of the stability diagrams does not change very much from incompressible to transonic flows ; the generalized inflection point, which is at the wall for $Me = 0$, remains very close to it for $Me = 1.1$, so that inflectional instability has practically no effect. In fact, the boundary layer is unstable essentially through the action of viscosity ; this phenomenon, whereby the maximum amplification rate increases with decreasing Reynolds number at a fixed value of α_r , is called *viscous instability*. Another important observation is that the amplification factors of the unstable waves are smaller in the transonic range than in incompressible flow : compressibility has a stabilizing effect.

However, an important aspect of instability for transonic Mach numbers is the effect of the wavenumber direction ψ on the amplification rates. At low speed, only two-dimensional waves need to be considered, because it can be demonstrated that they are the most unstable ones (Squire's theorem). This is no longer the case in compressible flow. Figure 2.2 shows the evolution of the maximum amplification rate at a given Reynolds number, as a function of the wave orientation. Three Mach numbers in the transonic range are considered. Up to $Me = 0.9$, the maximum value of $-\alpha_i$ corresponds to $\psi = 0^\circ$. But at higher Mach numbers, the largest amplification rate is obtained for a non zero value of the ψ angle (oblique waves). This value will be denoted as ψ_M .

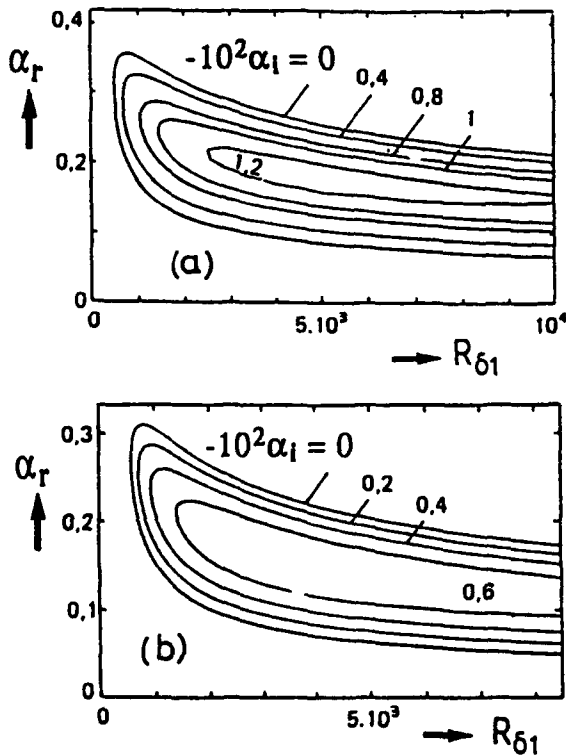


Fig. 2.1. Stability diagrams : flat plate, adiabatic wall, two-dimensional waves
 a) $Me = 0$ b) $Me = 1.1$

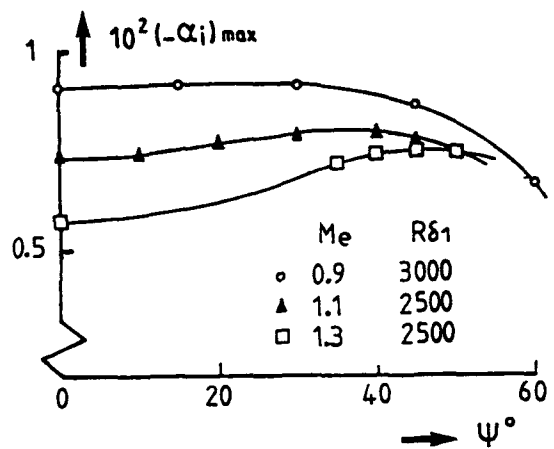


Fig. 2.2. Maximum amplification rates as functions of the wavenumber direction

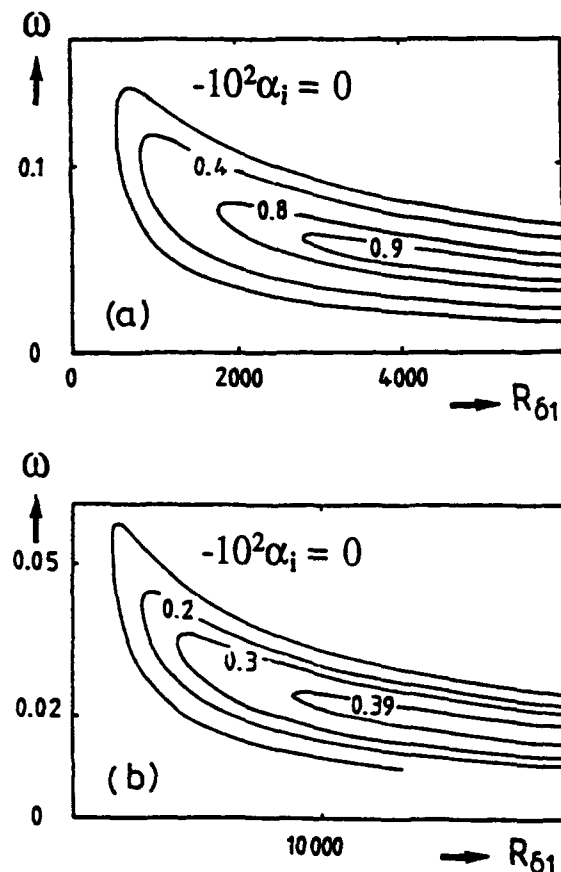


Fig. 2.3. Effect of wall cooling : flat plate, $Me = 0.9$, two-dimensional waves
 a) $T_w/T_{aw} = 1$ b) $T_w/T_{aw} = 0.8$

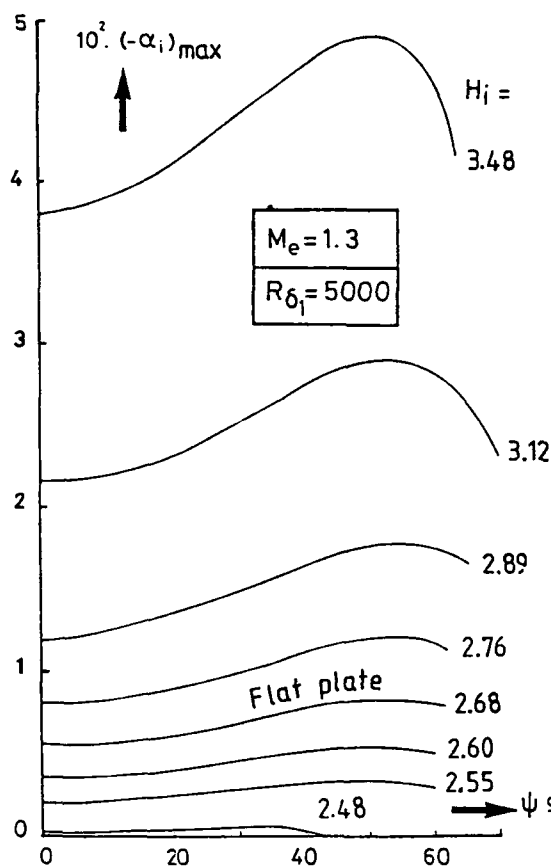


Fig. 2.4. Effect of streamwise pressure gradient on the maximum amplification rates - $M_e = 1.3$, adiabatic wall

The linear stability theory makes it possible to study the effects of some parameters acting on transition. Figure 2.3 illustrates the influence of wall cooling. Two stability diagrams are compared for $Me = 0.9$, $\psi = 0^\circ$, $T_w/T_{aw} = 1$ (adiabatic wall) and 0.8 . T_w is the wall temperature and T_{aw} is the adiabatic wall temperature. It is clear that cooling the wall strongly increases the critical Reynolds number and reduces the amplification rates.

The effect of streamwise pressure gradients is illustrated in figure 2.4, where the maximum values of the amplification rates computed at $R\delta_1 = 5000$ for $Me = 1.3$ are plotted as functions of ψ for several values of the incompressible shape factor Hi , which can be used as a pressure gradient parameter. As for low speed flows, negative pressure gradients ($Hi < 2.68$) are stabilizing, whereas positive pressure gradients ($Hi > 2.68$) have the opposite effect. In the latter case, *inflectional instability* becomes the dominant mechanism. The value of ψ_M does not depend very much on Hi , except for strongly accelerated flows.

2.3. Three-dimensional Flows : Crossflow Instability

Let us consider the flow on a swept wing of constant chord and "infinite" span. ϕ is the sweep angle. The free stream velocity Q_∞ gives a component U_∞ normal to the leading edge, and a component W_∞ parallel to the leading edge, figure 2.5. Two coordinate systems are usually introduced : one (X, Z, y) is linked to the wing, the other (x, z, y) is linked to the external streamline. In both cases, the y -direction is normal to the wall, the other two coordinates being defined on the wing surface. For instance, X represents the curvilinear abscissa measured from the geometrical leading edge, in the direction normal to it.

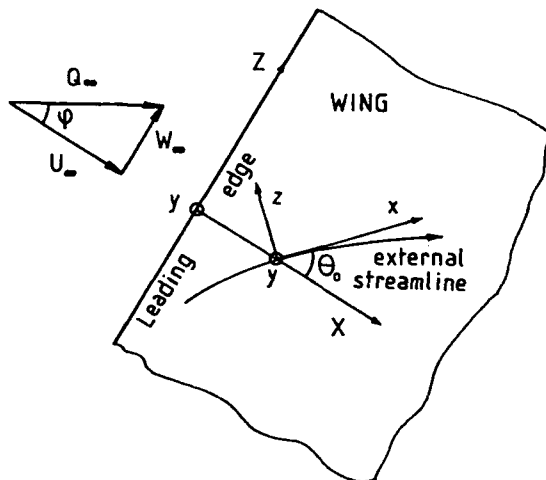


Fig. 2.5. Swept wing flow : notations and coordinate systems

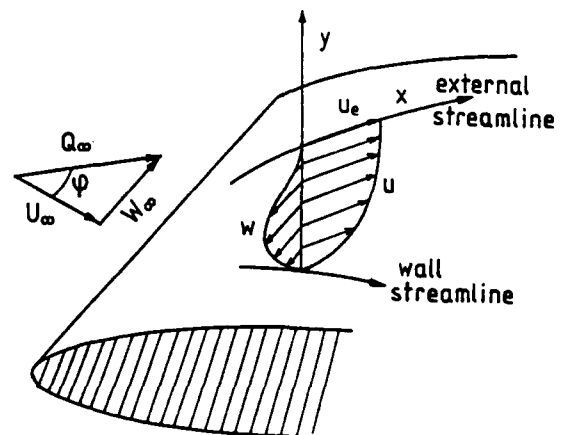


Fig. 2.6. Swept wing flow : streamwise (u) and crossflow (w) mean velocity profiles

As it is illustrated in figure 2.6, the mean velocity profile is now decomposed into a streamwise profile u (in the direction x of the external streamline) and a crossflow profile w (in the direction z normal to this streamline). From the leading edge to the chordwise location X_M where the free stream velocity is maximum, the crossflow is directed towards the concave part of the external streamline (figure 2.7). Its magnitude is zero at the attachment line, then it increases more or less rapidly due to the flow acceleration ; this behaviour will be discussed in some length in subsection 5.1.2.. In

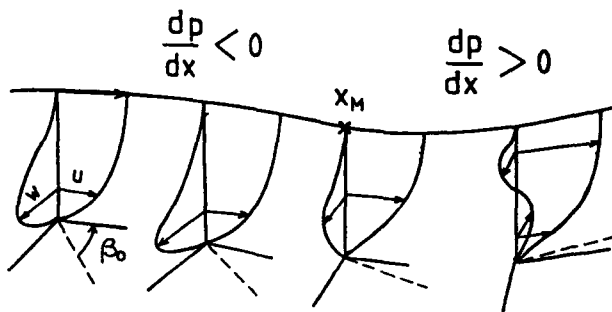


Fig. 2.7. Laminar boundary layer development on a swept wing - X inflection point of the potential streamline ; β_0 is the angle between wall and potential streamlines

the negative pressure gradient region, the maximum value of the crossflow velocity component remains rather weak, about 5 to 10 percent of the free stream velocity ; it will be shown, however, that this is sufficient to create a strong crossflow instability.

As X_M is approached, the pressure gradient intensity decreases, leading to a decrease in the crossflow amplitude. At $X = X_M$, the pressure gradient becomes positive, the curvature of the external streamline changes, and the velocity w close to the wall reverses (S-shaped profiles, see figure 2.7). If the positive pressure gradient is strong enough, the crossflow profile can be completely reversed. In the same region, an inflection point appears on the streamwise profile u .

The mechanisms of three-dimensional transition are now relatively well understood, see review papers by Poll [12], Arnal [13], Saric & Reed [14] and the precedent lecture by Saric [6]. As a first approximation, it can be assumed that transition is triggered either by streamwise instability or by crossflow instability. To illustrate this point, Figure 2.8 shows a free stream velocity distribution on a swept wing with a maximum located at $X = X_M$, as well as typical variations of the temporal amplification rate ω_i of two unstable frequencies as a function of the angle ψ between the external streamline and the wavenumber vector. Two chordwise positions

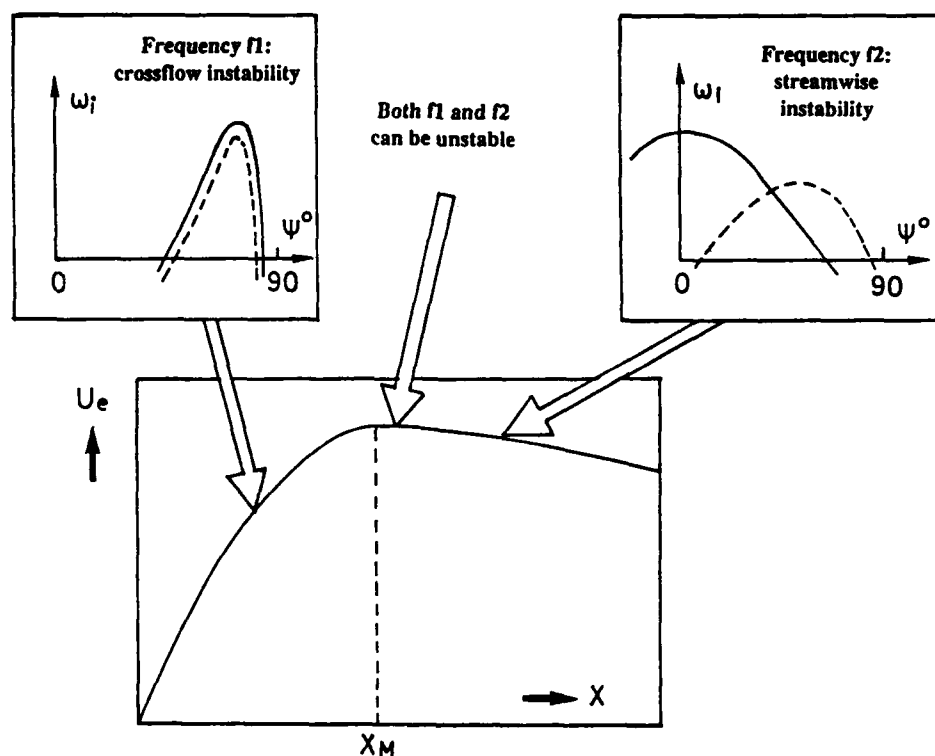


Fig. 2.8 Typical variations of the temporal amplification rates as functions of the wavenumber direction. Full lines : subsonic - Dotted lines : transonic

are studied, one in negative pressure gradient ($X < X_M$), the second in zero or positive pressure gradient ($X \geq X_M$). The full lines correspond to incompressible stability computations, the dotted lines correspond to compressible calculations for typical transonic Mach numbers.

a-Streamwise instability : as the streamwise mean velocity profiles look like classical two-dimensional profiles, they are essentially unstable in decelerated flows (right hand part of figure 2.8). For low speed flows, the most unstable direction ψ_M is close to 0° . When compressibility effects are taken into account, the stability results exhibit the same trends as in two-dimensional flows : the amplification rates are reduced, and ψ_M is shifted towards 40 to 70° . The wavelengths of the streamwise disturbances are about 10 times the boundary layer thickness.

b-Crossflow instability : as an inflection point is always present on the crossflow mean velocity profile, a powerful inflectional instability is expected to occur in regions where the crossflow velocity develops rapidly, i.e. in strong negative pressure gradients (for instance in the vicinity of the leading edge of a swept wing, left hand part of figure 2.8). ψ_M is never exactly equal to 90° , but it lies in a narrow range close to the crossflow direction, say between 85° and 89° . The instability is dominated by the properties of the inflection point (height, local value of the velocity derivative dw/dy ...) which are not very much affected by compressibility effects, so that the most unstable direction and the amplification rates are nearly identical for incompressible and for transonic flows. The wavelengths of the crossflow disturbances are 3 to 4 times the boundary layer thickness.

Let us notice that the most unstable frequencies are usually lower for crossflow instability than for streamwise instability. In particular, linear stability analyses show that crossflow instability can amplify zero frequency disturbances. This leads to the formation of stationary, corotating vortices practically aligned in the streamwise direction. In the experiments, crossflow vortices are observed as regularly spaced streaks.

Immediately downstream of the point of maximum free stream velocity, crossflow instability is decaying, while streamwise disturbances start to be amplified.

Interactions are likely to occur, especially for transonic Mach numbers where both unstable directions are close together. This problem is not yet fully understood.

2.4. Secondary Instability, Non Linearity, Breakdown

The receptivity theories explain how forced disturbances generate unstable waves which exhibit at first an exponential growth in the streamwise direction. When these initially weak instabilities reach a finite amplitude, their development begins to deviate from that predicted by the linear theory. Most of our knowledge about the last stages of the transition process comes from *low speed, two-dimensional* studies. The experiments show that the initially two-dimensional Tollmien-Schlichting waves are distorted into a series of "peaks" and "valleys" ; the origin of this peak-valley system is explained by the secondary instability theories developed by Herbert [15]. Further downstream, three-dimensional and non linear effects become more and more important. The non linear development of the disturbances terminates with the "breakdown" phenomenon : experiments and direct numerical simulations indicate that the peak-valley structures are stretched and form horseshoe vortices which break down into smaller vortices, which again break down into smaller vortices. The fluctuations finally take a random character and form a turbulent "spot". The streamwise location where the first spots appear can be defined as the transition onset. In fact, the distance between the end of the linear region and the breakdown to turbulence is rather short : for flat plate conditions, the streamwise extent of linear amplification covers about 75 to 85 percent of the distance between the leading edge and the beginning of transition. This explains why most of the practical transition prediction methods are based on linear stability only (Section 4). For *three-dimensional flows*, however, the phenomena seem to be different, at least when transition is induced by crossflow instability. In this case, low speed experiments by Müller & Bippes [16] and numerical studies by Meyer & Kleiser [17] demonstrated that the extent of the region where non linearities play a dominant role is much longer than for two-dimensional flows. In *transonic* flow, the last stages of the transition process are not yet well known.

3. FREE STREAM DISTURBANCES : WIND TUNNEL/FLIGHT

Some properties of the laminar boundary layer as a linear oscillator have been briefly discussed. But how are the unstable waves excited by the available disturbance environment? This question is a part of the problem which is usually addressed under the word of "receptivity", introduced by Morkovin [4]. Receptivity was defined in Section 1 as the mechanisms by which forced disturbances (sound, free stream turbulence) enter the laminar boundary layer. It also describes their signature into the disturbed flow. It has been shown that a part of this signature is the development of unstable waves, which constitute the eigenmodes of the boundary layer.

During the last decade, many works have been devoted to the understanding of the receptivity mechanisms ; they are summarized in [18] for example. It has been demonstrated that the receptivity process occurs in regions of the boundary layer where the mean flow exhibits rapid changes in the streamwise direction. This happens near the body leading edge and/or in any region farther downstream where some local feature forces the boundary layer to adjust on a short streamwise length scale (sudden change in the wall slope or in the wall curvature, suction strip for instance). An important feature is that a forced disturbance of frequency f will excite a boundary layer eigenmode having the same frequency but a different wavelength.

Let us assume that the body surface is perfectly smooth and that there is no vibration. The forced disturbances which will excite the boundary layer eigenmodes are the outer flow fluctuations : velocity fluctuations u' , v' and w' in the x , y and z directions (free stream turbulence), pressure fluctuations p' (acoustic disturbances) and temperature fluctuations T' . Intuitively, one can assume that the initial amplitude A_0 of the unstable waves increases with increasing amplitude of the forced disturbances, as it is sketched in figure 3.1. Further downstream, the waves are amplified according to the linear theory. If we assume that transition will occur as soon as the eigenmodes amplitude reaches a "universal" threshold value, then it becomes clear that larger the forced disturbances amplitude is, smaller the transition

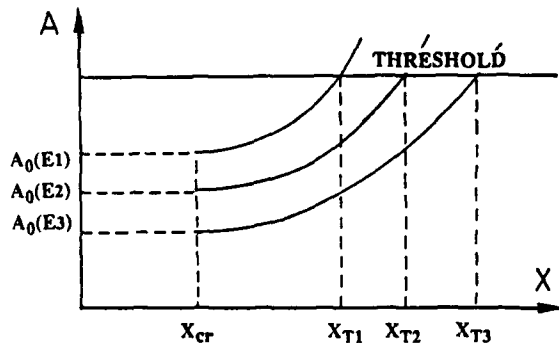


Fig. 3.1. Effect of the amplitude E of the forced disturbances on the transition location X_T . A_0 is the initial amplitude of the unstable waves

Reynolds number will be. For this reason, the knowledge of the free stream disturbances environment is of first importance.

This section is devoted to a survey of available data on environmental disturbances which can be encountered in wind tunnels as well as in flight conditions. The problem is not simple, because the origin, the amplitude and the frequency range of these disturbances depend also on the flow Mach number (Pate [19]). All these parameters will ultimately affect the transition location.

3.1. Wind Tunnel Disturbances

3.1.1. Subsonic wind tunnels

Free stream disturbances in low speed wind tunnels are typically velocity fluctuations and/or pressure fluctuations.

Velocity fluctuations are generated in the settling chamber as a result of flow separated regions and wakes from honeycombs or screens. They are then convected along streamlines over the model in the test section. These disturbances are usually characterized by a single parameter, the free stream turbulence level T_u measured in the test section :

$$Tu = \left(\frac{\tilde{u}^2}{e} + \frac{\tilde{v}^2}{e} + \frac{\tilde{w}^2}{e} \right)^{1/2} / \left(3U_\infty^2 \right)^{1/2} \quad (3.1)$$

where \sim denotes a root mean square (rms) value.

As the v' and w' components of the velocity fluctuations are generally not measured, the definition of T_u often reduces to :

$$Tu = \tilde{U}_e / U_\infty \quad (3.2)$$

Let us observe that this definition does not take into account the spectral distribution of the disturbances. Turbulence generated in the settling chamber generally produces no discrete frequencies. By proper selection of damping screens, the turbulence intensity T_u can be reduced up to 0.1 %.

Acoustic disturbances can be standing waves caused by resonance in the wind tunnel or travelling acoustic waves (acoustical noise) generated by fan noise or other sound generators. Their rms level is low, but the energy is concentrated on discrete frequencies; when an acoustic frequency, or a strong harmonic falls in the range of unstable Tollmien-Schlichting waves, the onset of turbulence may be displaced in the upstream direction.

The effect of velocity and acoustic disturbances on transition location is shown on figures 3.2 and 3.3, where the transition Reynolds number R_{XT} is plotted as a function of T_u . R_{XT} is defined as :

$$R_{XT} = \frac{U_e X_T}{V_e} \quad (3.3)$$

U_e and ν_e are the mean velocity and the kinematic viscosity at the boundary layer edge ; X_T represents the location of transition onset.

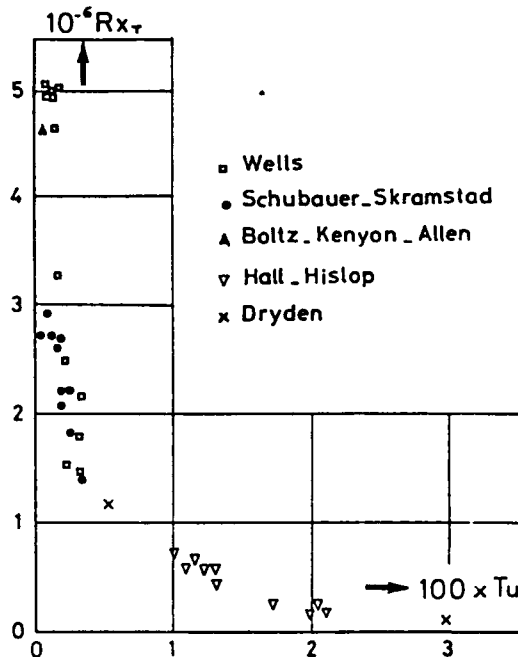


Fig. 3.2. Effect of free stream turbulence level on transition Reynolds number. Flat plate, incompressible flow $0 < Tu < 3 \cdot 10^{-2}$

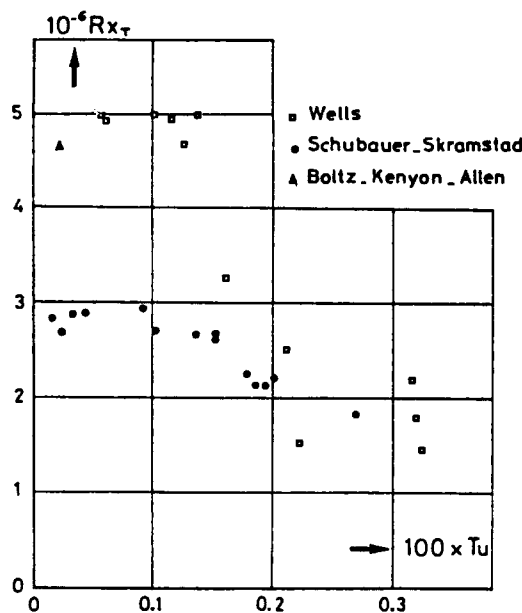


Fig. 3.3. Effect of free stream turbulence level on transition Reynolds number. Flat plate, incompressible flow $0 < Tu < 3 \cdot 10^{-3}$

In fact, a hot wire senses both turbulence and sound, and what is called "turbulence intensity" often consists of a mixing of both types of disturbances. In figure 3.2, Tu is varying from 0 to $3 \cdot 10^{-2}$. It is clear that increasing Tu strongly reduces the transition Reynolds number and that the experimental data seem to collapse onto a single curve. Figure 3.3 presents an enlargement of the previous graph for $Tu < 0.3 \cdot 10^{-2}$. The measurements of Schubauer-Skramstad [20] and those of Wells [21] exhibit the same trend, in the sense that Rx_T reaches a constant value. But this value is about $2.8 \cdot 10^6$ for Schubauer-Skramstad and about $5 \cdot 10^6$ for Wells. The explanation is that acoustical noise controls transition when Tu becomes very low. In the Schubauer-Skramstad experiments, the addition of screens in the settling chamber reduced velocity fluctuations, but had little effect on acoustic disturbances. Wells eliminated the sound sources with a sonic throat and obtained larger transition Reynolds numbers. The conclusion is that the effect of "true" free stream turbulence can be only observed at values of Tu greater than $0.1 \cdot 10^{-2}$.

3.1.2. Transonic wind tunnels

As pointed out by Pate [19], velocity fluctuations could be significant in a transonic wind tunnel, but little information has been published. On the other side, it is now clearly established that pressure fluctuations play a major role. The usual dominant acoustic sources are disturbances associated with hole/slot resonances in porous and/or slotted wall wind tunnels. These facilities are classified as very noisy compared to well-designed solid-wall wind tunnels. Systematic measurements performed on the so-called AEDC cone in 23 US and European wind tunnels confirmed this trend ; typical results will be presented in paragraph 3.2.2. and compared with flight measurements.

A new problem related to the development of cryogenic wind tunnels is the generation of temperature fluctuations at low stagnation temperatures. This problem is not fairly well documented up to now.

3.2. In-flight Disturbances

3.2.1. "Free stream turbulence"

In the atmosphere, the usual sources of stream "turbulence" are instabilities associated with "natural convection", e.g. instabilities in stratified flows. Some values of the "free stream turbulence level" Tu have been reported in the literature for flight conditions. During flight tests performed on a Falcon 50 aircraft by Dassault Aviation (in collaboration with ONERA/CERT), a hot wire probe was fixed on the vertical fin. For Mach numbers from 0.70 to 0.85 and for altitudes around 12 km, the "free stream turbulence level" was found to be very low, i.e. between 0.01 and 0.02 percent. Most of the energy was concentrated below 2 KHz [22]. Otten et al [23] measured similar values of Tu for M_∞ between 0.3 and 0.8 at altitudes between 4 and 12 km. Much higher values were obtained by Zanin [24] who used a hot wire mounted on the nose of a glider (no engine noise). At a flight velocity of 25 ms^{-1}

and for altitudes below 1 200 m, the measurements yielded turbulence intensities in the range of 0.2 percent, with most of the signal at low frequencies below 200 Hz ; a miniature hot wire probe attached to the glider wing showed Tollmien-Schlichting instabilities at a mean frequency of 600 Hz.

In fact, the scales of the atmospheric turbulence are generally much larger than those of the viscous flow developing on an aircraft. This is a fundamental difference with the ground facilities, where the free stream turbulence possesses scales similar to those of the boundary layers which are studied in wind tunnels. Even if there is some residual energy of the atmospheric turbulence at high frequencies (0.1 m Kolmogorov microscale), the transition mechanisms do not seem to be strongly affected by the free stream velocity fluctuations in flight conditions [25]. Pfenninger wrote thirty years ago : "The atmospheric turbulence has much less influence on transition than the microscale turbulence of low-turbulence tunnels" [26].

3.2.2. Pressure fluctuations

It is now recognized that the transition process on an airplane is usually dominated by acoustic fields which are generated by engines and by airframe. These noise sources include separated regions and turbulent boundary layers developing along the fuselage. The laminar flow control systems such as suction pumps can also act as noise generators.

Most of our knowledge about the fluctuating pressure field around an aircraft comes from the AEDC cone experiments [27], [28]. As mentioned earlier, this 10-deg sharp cone was tested in different wind tunnels and in flight. In the latter case, the model was flown mounted from the nose of an F-15 aircraft, as it is shown in figure 3.4. The transition data which were obtained for both subsonic and supersonic conditions will be summarized in paragraph 8.1.1. A measurement of the incident pressure fluctuations \tilde{p}_s on the cone surface was performed using two flush mounted microphones ; in addition, a free stream impact probe contained another microphone to obtain total pressure fluctuations \tilde{p}_t .

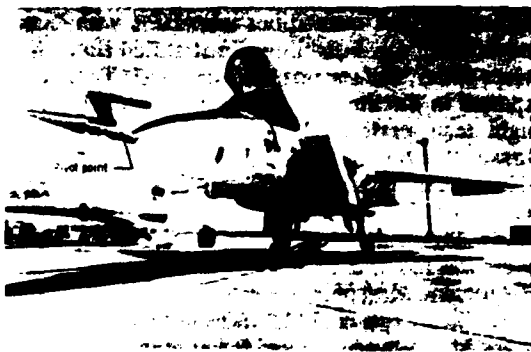


Fig. 3.4. AEDC cone mated to the test aircraft [27], [28]

Figure 3.5 shows the variation of \tilde{p}_t/q_∞ as a function of the free stream Mach number, and the cone microphone data \tilde{p}_s/q_∞ acquired under laminar boundary layer conditions at the sensor location are given in figure 3.6. In both figures, the data collapse into a single curve and exhibit a strong decrease as the Mach number increases. At subsonic speeds, much of the pressure fluctuations are acoustic disturbances (engines, airframe) radiated forward onto the cone. This forward radiation disappears at supersonic speeds, and the fluctuations "must be due either to disturbances convected into the probe face or probe vibrations [25]". An interesting feature is the

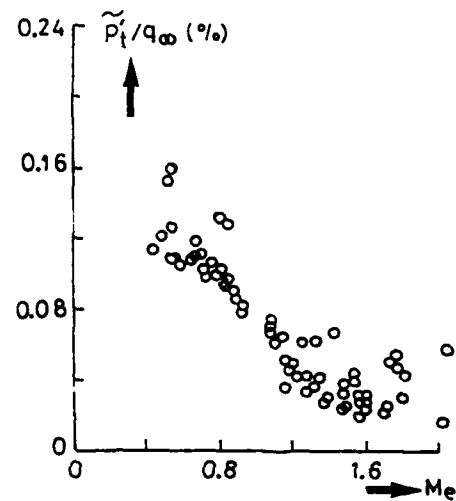


Fig. 3.5. Free stream impact pressure fluctuations as a function of Mach number at boundary layer edge [27], [28]. q_∞ is the free stream dynamic pressure

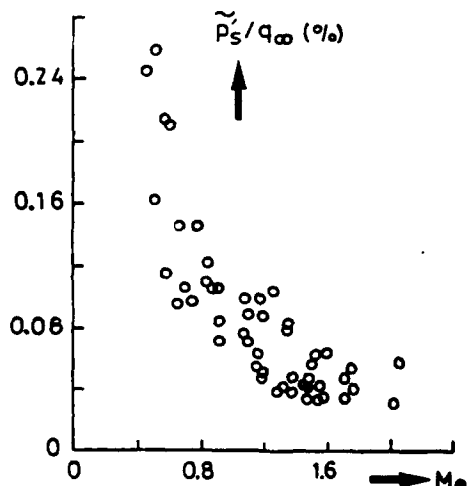


Fig. 3.6. Cone surface pressure fluctuations as a function of Mach number at boundary layer edge [27], [28]

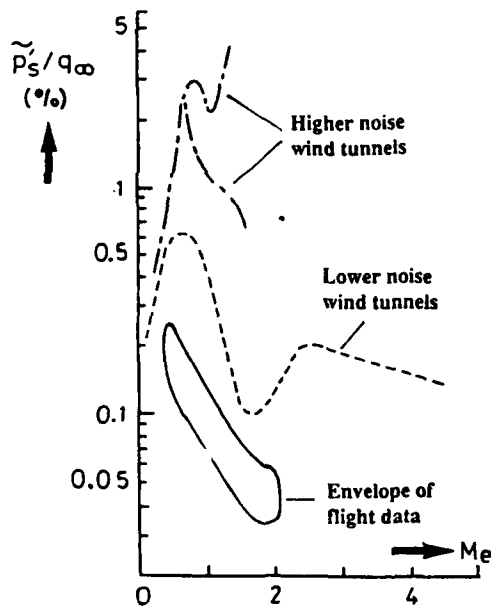


Fig. 3.7. Comparison of disturbance levels measured in wind tunnels with disturbances in-flight [28]

broad band nature of the fluctuations spectra (up to 20 KHz).

Figure 3.7 presents a comparison between the values of \tilde{p}_s measured in flight and in wind tunnel conditions for the same unit Reynolds number ; the values obtained in noisy facilities are obviously larger than those obtained in low disturbance wind tunnels and raise an order of magnitude above the flight data. This will result in strong variations of the transition Reynolds number, paragraph 8.1.1.

The free stream static pressure fluctuations were also recorded during the flight tests on the Falcon 50 aircraft with a probe placed near the fin [22]. At Mach numbers

around 0.8, \tilde{p}_s/q_∞ was found to vary between 0.2 and 0.4 percent. This value is somewhat larger than that measured on the AEDC cone, but the difference can be explained by the fact that the probe was sensitive not only to the engine noise, but also to the pressure fluctuations radiated by the thick boundary layer in the rear part of the fuselage. In addition, it is not obvious that disturbances recorded in the free stream (Falcon 50) and at the wall (AEDC cone) can be compared.

As the pressure fluctuations cover a wide frequency range, they are able to excite the instability waves and to cause early transitions if their amplitude is large enough. Therefore empirical correlations have been developed to estimate the critical sound-pressure levels (critical SPL) which must not be exceeded for maintenance of laminar flow.

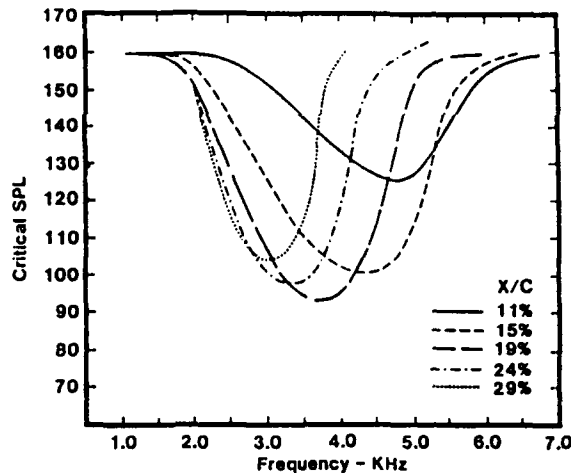


Fig. 3.8. Sensitivity of critical sound-pressure level to noise frequency. $M_\infty = 0.822$, chord Reynolds number = $35.5 \cdot 10^6$, sound directionality = 0° [32]

An important body of experimental data was obtained during the X-21 research and development program [29]. At an altitude of about 7 km, a microphone located at the wing tip of a laminar flow control airplane showed that the engine exhaust noise predominated at low Mach numbers until it was masked at transonic speeds by the sound radiated from the fuselage turbulent boundary layer. The critical SPL were deduced from these measurements, but the criteria were based on spectrally integrated quantities which did not take into account neither the sound directionality nor the frequency sensitivity. These parameters were included later on into improved correlations with the use of the linear stability theory and of semi-empirical methods [30]. An example of result is presented on figure 3.8. The critical SPL spectra are plotted at five chordwise positions on an airfoil flying in the same direction as the incident sound. Each curve has a minimum corresponding to the locally most amplified frequencies computed from the linear stability theory.

Acoustic flight data were recently obtained on a 21-deg swept laminar wing glove on a Boeing 757 airplane (see summary in [31]). The results indicated that the predicted SPL were not accurate at high speeds, but that the engine noise did not affect significantly the growth of crossflow disturbances. Flight tests on the VFW 614/ATTAS research aircraft [140] also showed that under most conditions, no influence of the engine noise could be noticed. However, as pointed out in [32], "for applications where TS wave growth may be significant .. engine noise might limit the extent of laminar flow for configurations with wing-mounted engines."

4. TRANSITION PREDICTION ON A SMOOTH WALL

Sections 2 and 3 emphasized the major shortcomings of our knowledge of the transition mechanisms. The first problem is that the detailed characteristics of the forced disturbances are not very well known in many circumstances ; for instance the free stream turbulence level is usually characterized by the amplitude of the streamwise velocity fluctuations only. Secondly, the receptivity theories cannot be used routinely for practical purposes, because the results are restricted to simple cases. Thirdly, many aspects of the last stages of the transition process are still unclear for three dimensional and/or compressible flows.

A pessimistic conclusion could be that a good prediction of transition constitutes an impossible task. In spite of this negative situation, transition predictions must be made ! This Section describes some of the tools which are available for people who are tasked with the job of making transition prediction. The most popular method is the e^n method, which is based on linear stability computations, but simpler techniques such as criteria or data base methods are often used. Each of them will be discussed below. A possible modelling of the transition region will be also presented.

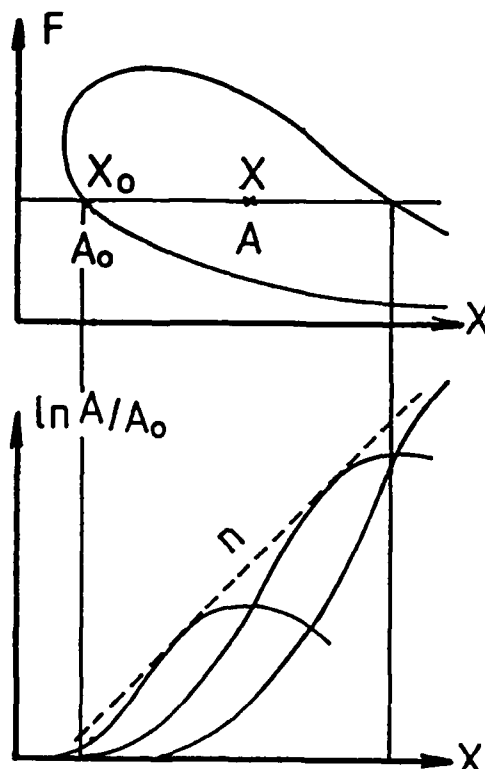


Fig. 4.1. Integrated amplification rates, envelope curve, n factor

4.1. The e^n Method

4.1.1. The e^n method for two-dimensional mean flows

This well known method was primarily developed for two-dimensional, incompressible flows by Smith-Gamberoni [33] and van Ingen [34]. In this simple case, the amplification vector and the wavenumber vector are aligned in the mean flow direction x , i.e. $\beta = 0$ in (2.2). For a given mean flow, it is possible to compute a stability diagram (figure 4.1) showing the range of unstable frequencies f as a function of the streamwise distance. Let us consider now a wave which propagates downstream with a fixed physical frequency f . This wave passes at first through the stable region ; it is damped up to x_0 , then amplified up to x_1 , and it is damped again further downstream.

At a given station x , the total amplification rate computed from the *spatial theory* can be defined as :

$$\ln(A/A_0) = \int_{x_0}^x -\alpha_i dx \quad (4.1)$$

A is a measure of the wave amplitude, for instance its maximum rms value in the boundary layer, and the index 0 refers to the streamwise position where the basic flow becomes unstable.

If the *temporal theory* is used, $-\alpha_i$ is replaced by ω_i/Vg , where $Vg = \frac{\partial \omega_f}{\partial \alpha}$ is the group velocity ; this link between spatial and temporal theories was first derived by Gaster [9].

The envelope of the total amplification curves is (figure 4.1) :

$$n = \max_f [\ln(A/A_0)] \quad (4.2)$$

With a low disturbance environment, it is assumed that transition occurs as soon as the n factor reaches a critical value in the range 7-10, i.e. when a given frequency is amplified by a factor e^7 to e^{10} , i.e. 1 100 to 22 000 ! The value of the n factor at transition onset will be discussed later on.

Up to now, the eigenvalue problem is rather simple ; whatever theory one considers, four real parameters are involved : either $(R, \omega_r, \omega_i, \alpha)$ in the temporal theory or $(R, \omega, \alpha_r, \alpha_i)$ in the spatial theory. Two of them are given (usually the Reynolds number and the frequency), the other two are computed by solving the complex dispersion relation.

When compressibility effects begin to play a role, the problem becomes somewhat more complex ; even by assuming $\psi = 0$ in the spatial theory, an additional parameter appears : the angle ψ between the x direction

and the wavenumber vector. At each streamwise location and for a fixed frequency, the disturbance growth rate is usually maximized with respect to the wavenumber direction, i.e. the total amplification rates are computed with $\alpha_i(\psi_M)$ or $\omega_i(\psi_M)$. Gaster's group velocity transformation is still valid, but the group velocity has a second component $\partial\omega_r/\partial\beta$ in the spanwise direction; in fact, this quantity is usually much smaller than the component $\partial\omega_r/\partial\alpha$ in the streamwise direction, so that it can be neglected.

4.1.2. The e^n method for three-dimensional mean flows [35]

The extension of the e^n method in three-dimensional flow is not straightforward: we now have either five real parameters in temporal theory ($R, \omega_r, \omega_i, \alpha, \psi$) and six in spatial theory ($R, \omega, \alpha_r, \alpha_i, \psi, \psi$) because the assumption $\psi = 0$ is not necessarily correct for three-dimensional flows. The increase in the number of parameters explains why three-dimensional problems are often treated with the temporal theory. Let us observe that the difficulties are the same at low speed and in compressible flow.

a - Temporal theory

When the Reynolds number and the frequency are specified, the values of α and ω_i are not unique, because $\alpha = \alpha(\psi)$ and $\omega_i = \omega_i(\psi)$. The so-called envelope method is similar to the strategy previously described for two-dimensional, compressible flows; it seeks the wavenumber direction ψ_M for which ω_i is maximum, and $\omega_i(\psi_M)$ is then integrated according to a generalized Gaster's transformation:

$$\ln(A/A_0) = \int_{s_0}^s \frac{\omega_i(\psi_M)}{|\vec{Vg}|} ds \quad (4.3)$$

where $\vec{Vg} = (\partial\omega_r/\partial\alpha, \partial\omega_r/\partial\beta)$ is the group velocity vector and s represents the arclength along the group velocity direction, which is most of the time close to the external streamline direction. If the stability equations are solved in the coordinate system linked to this streamline, $\partial\omega_r/\partial\beta$ is very small (as in two-dimensional flows). The n factor is then computed from relation (4.2).

The first code in which this technique was introduced for general use was the incompressible SALLY code of Srokowski & Orszag [36]. This code was later superseded by the COSAL code of Malik [37], which includes the compressibility effects.

Another solution is to use the fixed wavelength and fixed frequency method: for a given frequency and a given wavelength $\lambda = 2\pi/(\alpha^2 + \beta^2)^{1/2}$, the value of

the temporal amplification rate is integrated along the potential flow direction. Srokowski & Orszag [36] and Dagenhart [38] employed this technique for the zero-frequency waves, as well as Hefner & Bushnell [39] for non zero frequency waves. Other optional strategies are included in the COSAL code: fixed frequency and fixed direction method, fixed frequency and fixed spanwise wavelength method ...

In the previous methods, the notions of streamwise and crossflow instabilities do not appear explicitly; an interesting idea is to separate both kinds of instability by computing a crossflow n factor, n_{CF} , and a streamwise (Tollmien-Schlichting) n factor, n_{TS} :

$$n_{CF} = \max_f \int_{s_0}^s \max_{\psi} (\omega_i) \frac{ds}{|\vec{Vg}|} \quad (4.4a)$$

with ψ close to 90° , where ψ is defined in the coordinate system linked to the external streamline. Another possibility is to compute the n_{CF} factor by taking into account the zero frequency disturbances only; the maximization is then performed with respect to the wavelength of the stationary vortices [40].

The n factor for TS waves is defined as:

$$n_{TS} = \max_f \int_{s_0}^s \frac{\omega_{i0}}{|\vec{Vg}|} ds \quad (4.4b)$$

with $\omega_{i0} = \omega_i(\psi = 0^\circ)$.

The criterion for transition onset is not a unique value of n_{CF} and n_{TS} , but a "universal" curve n_{CF} (n_{TS}) which can be established from experimental data. Figure 4.2 [40] shows three possible n_{CF} - n_{TS} diagrams. The

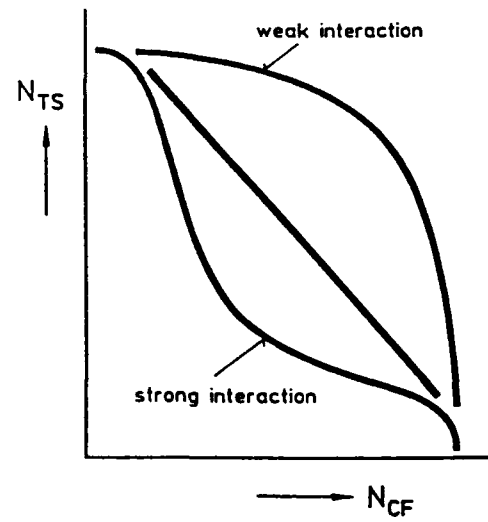


Fig. 4.2. Different types of n_{TS} - n_{CF} curves for transition prediction [40]

region below (respectively above) the curves indicate laminar (respectively turbulent) boundary layers. The concave curve represents the case of a strong interaction between crossflow and streamwise instabilities, which reduces the amplification factors. The straight line $nCF + nTS = \text{constant}$ represents a moderate interaction, and the convex curve indicates that the interaction is weak. It can be guessed that each type of curve is associated with a particular type of pressure distribution. From the ATTAS flight experiments for instance, it was found that the critical curve for transition onset is convex, see paragraph 8.1.2..

b-Spatial theory

As stated before, the problem becomes more intricate, because of the appearance of an additional parameter ; the amplification is not a scalar anymore but a vector $\vec{A} = (-\alpha_i, -\beta_i)$.

To remove the arbitrariness in the definition of the total amplification rate, a possible solution is to use the wave packet theory and to impose that the ratio $(\partial\alpha/\partial\beta)_{\omega,R}$ be real (Nayfeh, [41], Cebeci-Stewartson [42]). This condition comes from an asymptotic evaluation of the integral giving the pressure p for a wave packet :

$$\bar{p}(x, y, z, t) = \int I(y, \beta) \exp[i(\alpha x + \beta z - \omega t)] d\beta \quad (4.5)$$

The saddle point method is then used to evaluate the principal part of the integral. This leads to the relationship :

$$(\partial\alpha/\partial\beta)_{\omega,R} = -z/x \text{ which must be real} \quad (4.6)$$

It follows that the local amplification rate is $\alpha_i - \left[\alpha_i \cdot \left(\frac{\partial\alpha}{\partial\beta} \right)_{\omega,R} \beta_i \right]$ and the disturbance angle ψ is

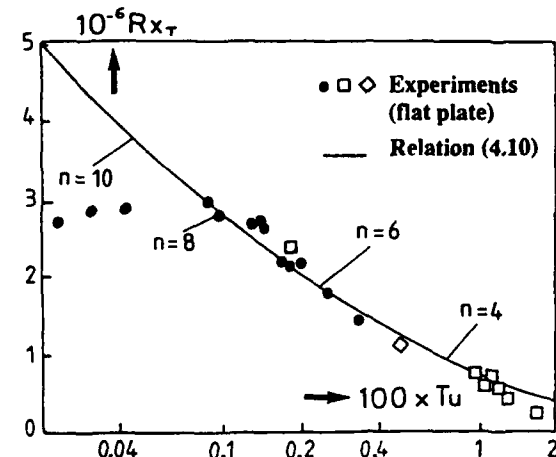


Fig. 4.3. Application of the e^n method with relation (4.10) - Flat plate, incompressible flow [46]

$\tan^{-1}(\partial\alpha/\partial\beta)_{\omega,R}$. At a given location, for a given frequency, the amplification rate is then maximized with respect to the ψ direction. This method was successfully used by Cebeci et al [43], [44].

An alternate approach was proposed by Mack [45]. Let us assume that any disturbance r' is expressed in the wing-fixed coordinate system, figure 2.5 :

$$r' = r(y) \exp[-\alpha_i X - \beta_i Z] \exp[i(\alpha_i X + \beta_i Z - \omega t)] \quad (4.7)$$

The basic assumption is to impose $\beta_i = 0$, i.e. there is no amplification in the spanwise direction. In addition, Mack applied the irrotationality condition to the wavenumber vector ; for an infinite swept wing, this condition reduces to :

$$\beta_i^* = \text{constant} \quad (4.8)$$

where the star denotes a dimensional quantity.

Numerically, the chordwise evolution of α_i is computed for several frequencies and for several β_i^* at each frequency. The maximization is then performed with respect to both parameters. This strategy strongly differs from those where the growth rates are maximized with respect to the wavenumber direction.

A third approach which was developed at ONERA/CERT [35] combines the assumptions which were introduced in the previous strategies. Following Mack's idea, the condition $\beta_i = 0$ is used and the total amplification rate is computed by looking at the most unstable direction of a given frequency, as it is done in the envelope method :

$$n = \max_f \int_{X_0}^X \max_{\psi} (-\alpha_i) dX \quad (4.9)$$

4.1.3. Some comments on the e^n method
What is the value of the n factor at transition onset ? Mack [46] suggested the following relationship :

$$n = -8.43 - 2.4 \ln Tu \quad (4.10)$$

This expression was established to fit two-dimensional, low speed experimental data without pressure gradient, see figure 4.3. For $Tu = 10^{-3}$ (typical low disturbance environment), $n = 8.15$ and $Rx_T = 2.8 \cdot 10^6$. For $Tu = 10^{-2}$ (typical high disturbance environment), $n = 2.62$ and $Rx_T = 0.7 \cdot 10^6$. When Tu is lower than 10^{-3} , sound disturbances may become the factor controlling transition rather than turbulence, and relation (4.10) is no longer adequate. The use of this relation can also give bad results for analyzing flight tests data because free stream turbulence has less effect than pressure fluctuations.

It is interesting to note that relation (4.10) can be interpreted in a way which is coherent with figure 3.1 by taking into account the receptivity of the boundary layer to free stream turbulence. If it is assumed that transition takes place for a constant value A of the Tollmien-Schlichting waves amplitude, then it follows from (4.10) that the initial amplitude A_0 increases like $Tu^{2.4}$.

A shortcoming of the e^n method is that it is based on linear stability only. This does not constitute a crucial problem for two-dimensional flows, because non linearities are observed on a short distance upstream of the breakdown to turbulence. The question remains open, however, for three-dimensional and compressible flows.

Many applications of the e^n method in two-dimensional flows (with and without pressure gradient) showed a good agreement with measurements. There are at least two questions arising in three-dimensional flows :

- Is the n factor identical for transitions triggered by streamwise instability and by crossflow instability ? Streamwise instability is very sensitive to noise and to free stream turbulence, but crossflow instability is also sensitive to leading edge microroughnesses which constitute initial conditions for stationary vortices. In addition, crossflow instability is less sensitive to noise than streamwise instability.
- Is the n factor identical for the different strategies which were reviewed before? As it will be demonstrated in paragraph 4.4, the answer is no.

Let us notice also that the value of the n factor strongly depends on the experimental definition of the transition point. For instance, hot films or hot wires detect the location where the first turbulent spots are created, but infrared images roughly indicate the middle of the transition region, so that the n factor can be significantly lower in the first case. This problem will be discussed in Section 8.

4.2. Transition Criteria

The use of the linear theory and of the e^n method often leads to satisfactory results for predicting transition onset, but it involves time consuming and expensive computations. For this reason, the development of simple transition criteria presents an unquestionable practical interest. The word criterion must be interpreted as a more or less empirical correlation between laminar boundary layer parameters at the transition onset.

4.2.1. Two-dimensional flows

Many empirical correlations have been proposed for two-dimensional, incompressible flows, see review in [47]. Michel, for example (1952, [48]), correlated the values of two Reynolds numbers at transition, $R\theta$ and R_x . Granville (1953, [49]) developed a correlation which takes into account two important parameters, namely the stability properties and the flow history ; the stability is characterized by the difference $R\theta_T - R\theta_{cr}$ in

momentum thickness Reynolds number from the neutral stability point to the transition location ; the flow history is characterized by an averaged Pohlhausen parameter :

$$\bar{\Lambda}_{2T} = \frac{1}{X_T - X_{cr}} \int_{X_{cr}}^{X_T} \frac{\theta^2}{V} \frac{dU_e}{dx} dx \quad (4.11)$$

These correlations were deduced from experimental data collected in low turbulence wind tunnels ; they take into account the pressure gradient effects, for low values of Tu .

More recently, the influence of the free stream turbulence level was introduced in practical criteria. For example, Arnal et al (1984, [50]) extended Granville's correlation on theoretical basis. Curves corresponding to several values of Tu are plotted on figure 4.4. It can be observed that the proposed criterion coincides practically with the Granville's one for $Tu = 0.05 \cdot 10^{-2}$ to $0.1 \cdot 10^{-2}$. An analytical expression is :

$$R\theta_T - R\theta_{cr} = - 206 \exp(25.7 \bar{\Lambda}_{2T}) [\ln(16.8 Tu) - 2.77 \bar{\Lambda}_{2T}] \quad (4.12)$$

To compute the critical Reynolds number, it is assumed that $R\theta_{cr}$ depends on a single parameter, for instance the shape factor H [50]. The curve $R\theta_{cr}(H)$ is an analytical representation of exact stability computations for Falkner-Skan profiles.

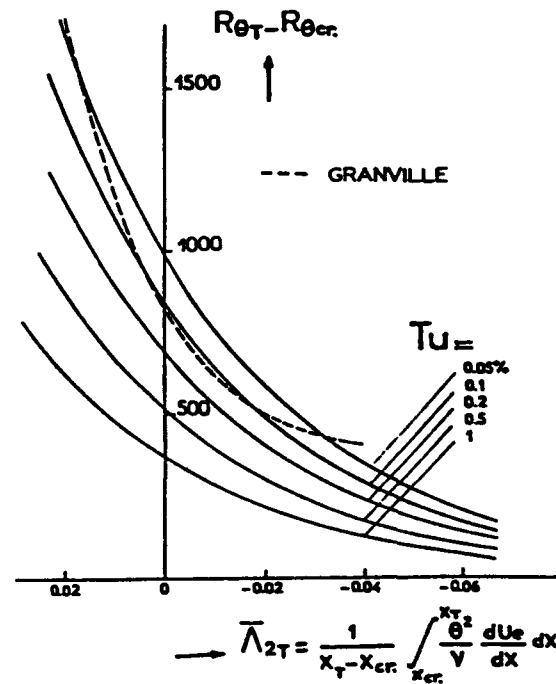


Fig. 4.4. Two-dimensional criterion for incompressible flow [50]

4.2.2. Three-dimensional flows

For three-dimensional flows, the use of empirical criteria is based on the following rule : it is assumed that turbulence will appear either by streamwise instability or by crossflow instability (this implies that there is no leading edge contamination, see paragraph 6.3). Criteria are applied separately for each one of these mechanisms, and it is assumed that the boundary layer will cease to be laminar as soon as one of them is satisfied.

As the streamwise mean velocity profiles look like Falkner-Skan profiles, the *streamwise instability* is similar to that of a two-dimensional flow. It can be predicted by applying simple two-dimensional criteria along the external streamline. For example, if the correlation (4.12) is used, θ will represent the streamwise momentum thickness and the chordwise distance x appearing in (4.12) is replaced by the curvilinear abscissa computed along the potential streamline.

As far as the *crossflow instability* is concerned, specific criteria need to be developed. The first attempt at correlating experimental data on swept wings was conducted by Owen & Randall (1952, [51]) who introduced a Reynolds number χ defined as :

$$\chi = \frac{|w_{\max}| \delta}{v} \quad (4.13)$$

where δ represents the boundary layer thickness.

They proposed a critical value $\chi = 175$ for transition onset. Later studies showed that this value was too low, because the experiments from which the criterion was derived were biased by leading edge contamination.

Treadgold & Beasley (1973, [52]), see also Beasley (1976, [53]) developed a criterion which involved the crossflow Reynolds number $R\delta_2$ given by :

$$R\delta_2 = \frac{1}{v} \int_0^\delta w dy \quad (4.14)$$

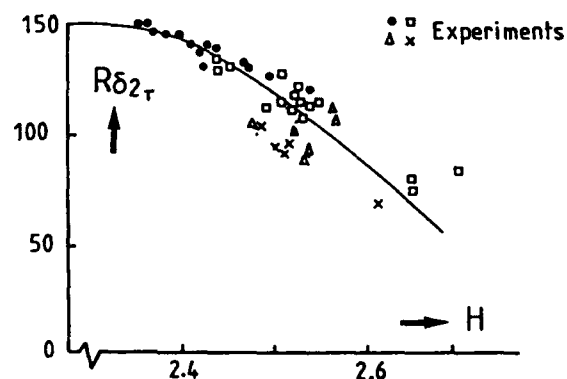


Fig. 4.5. C1 crossflow criterion [50], [54]

It was observed that transition occurred for $R\delta_2$ between 100 and 140. This shows that the use of a constant value of any crossflow parameter cannot give good results in all situations. For this reason, two more elaborate criteria, C1 and C2, have been developed at ONERA/CERT [50], [54].

The C1 criterion is plotted on figure 4.5. It is a correlation between two boundary layer integral parameters taken at the transition location : the crossflow Reynolds number $R\delta_2$ and the streamwise shape factor H . A similar correlation was later proposed by Poll [12] who replaced $R\delta_2$ by χ , relation (4.13).

The C2 criterion is based on the fact that the most unstable direction is not exactly the crossflow one, but makes an angle ϵ_{\min} with this direction. At a given chordwise position, it is assumed that the ϵ_{\min} direction is that which possesses the lowest critical Reynolds number. The C2 criterion is a correlation between a Reynolds number taken in the ϵ_{\min} direction, the streamwise shape factor and the free stream turbulence level T_u .

4.3. Data Base Methods

The criteria which were described in the preceding paragraph were deduced from low speed experiments. The question arises of their validity in compressible, transonic flows.

Exact solutions of the stability equations have shown that compressibility has a rather small effect on *crossflow instability* for the Mach number range under consideration, due to the inflectional nature of the crossflow disturbances (see paragraph 2.3.). In addition, this instability often occurs in the vicinity of the leading edge, where the local Mach number is low. For these reasons, we believe that the incompressible crossflow criteria can be applied at transonic speeds without any modification.

Unlike the crossflow instability, the *streamwise instability* is reduced at transonic speeds, so that incompressible criteria largely underestimate the transition Reynolds numbers. As compressibility effects are difficult to take into account in simple analytical criteria such as those described in paragraph 4.2.1., a possibility is to develop data base methods, the complexity of which is intermediate between empirical correlations and direct numerical solutions of the stability equations. The principle is to compute the stability properties of self similar (or locally similar) basic flows and to interpolate between the tabulated results for any real situation in order to estimate the n factor. Although these methods are generally developed for two-dimensional flows, they can be used to describe the streamwise instability of three-dimensional flows by integrating the amplification rates along the external streamline.

A data base method was proposed by van Ingen [55] for low speed flows, and by Arnal [56] for Mach numbers between 0 and 1.3. In the latter work, analytical

relationships between the eigenvalues of a given basic flow were established in order to reduce the size of the tables containing the data : the numerical coefficients entering these relationships are tabulated functions of the free stream Mach number and of a pressure gradient parameter. By comparison with exact stability calculations, the computing time is reduced by 4 to 5 orders of magnitude.

4.4. First Examples of Application

The objective of this paragraph is neither to discuss the physical aspects of the transition mechanisms, nor to compare the values of the n factor in different disturbance environments ; it is to analyze the advantages, the shortcomings and the limitations of the prediction methods which were described before.

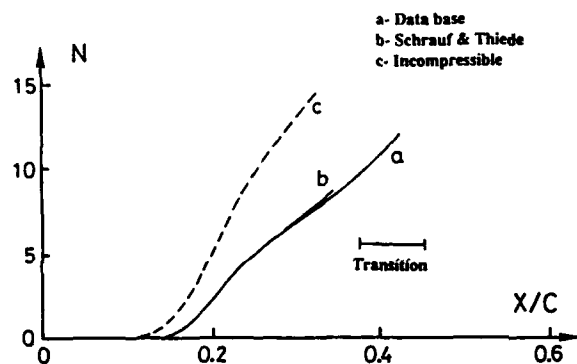
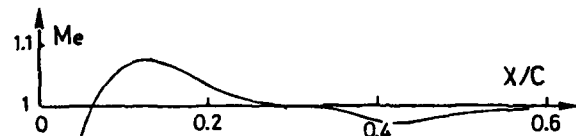


Fig. 4.6. n factors for a two-dimensional, transonic flow : CAST 10 airfoil, $M_{\infty} = 0.73$, angle of attack = 0° , chord Reynolds number = $4 \cdot 10^6$

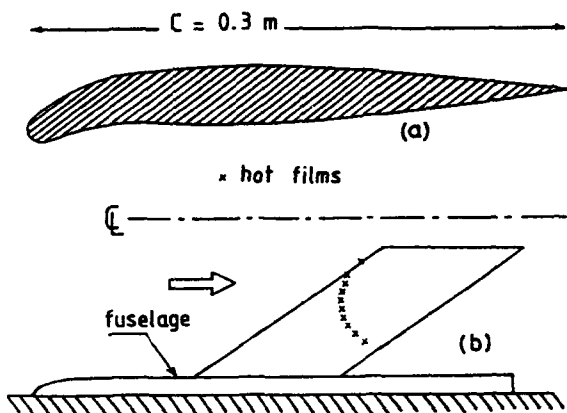


Fig. 4.7. ONERA D airfoil with a cambered leading edge - a) Airfoil b) Experimental arrangement in the F2 wind tunnel

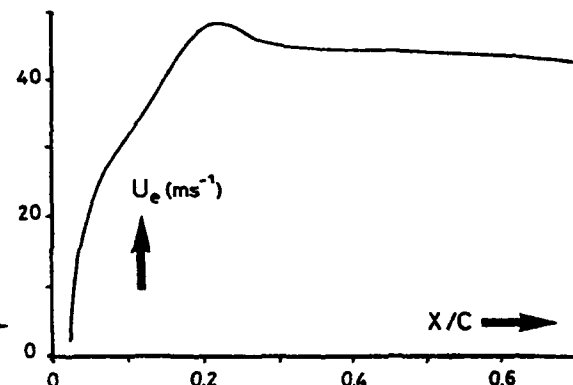


Fig. 4.8. Free stream velocity component normal to the leading edge

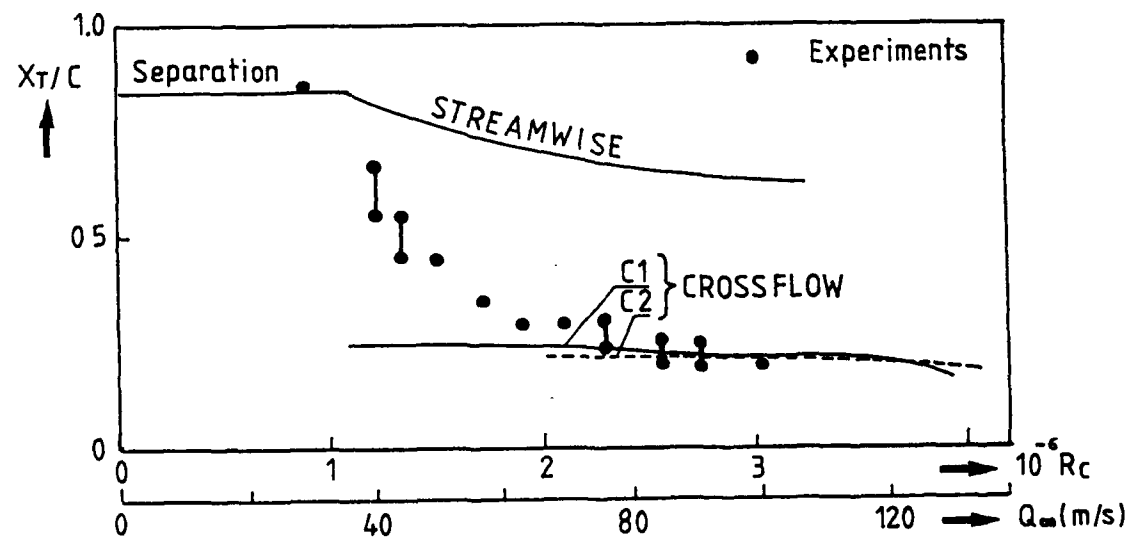


Fig. 4.9 Comparison between measured and predicted transition locations (streamwise and crossflow criteria)

The first example is related to a *two-dimensional* airfoil (CAST 10 airfoil) which was tested in the *transonic* wind tunnel T2 at ONERA/CERT [57]. The upper part of figure 4.6 shows that the local Mach number is close to 1. Three curves of total amplification rate are presented on the lower part of the figure. Curve a was obtained with the compressible data base method [56] ; curve b was computed by Schrauf & Thiede [58] by solving the compressible stability equations. The results are very close together. The n factor is about 9 at the beginning of the measured transition region. Curve c was deduced from incompressible stability computations, i.e. the free stream Mach number was set equal to zero. The stabilizing effect of compressibility is very strong, since it reduces the amplification rates by a factor 2 !

The second example is a *three-dimensional, low speed* configuration. The model is an ONERA D airfoil equipped with a cambered leading edge (figure 4.7a). It is fixed on a half-fuselage with an angle of sweep of 49° . Hot films are used to detect the transition location

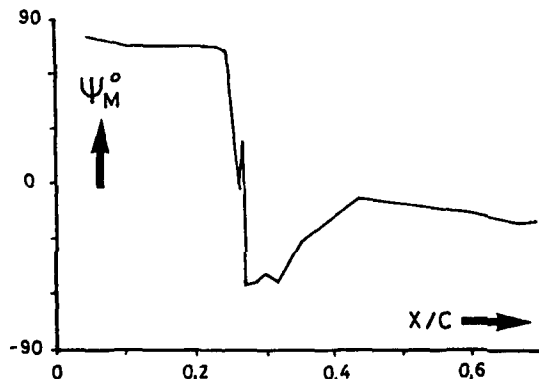


Fig. 4.10 Evolution of the most unstable direction for $f = 3$ KHz

(figure 4.7b). The experiments were carried out in the F2 wind tunnel at Le Fauga-Mauzac Center near Toulouse. Figure 4.8 shows the evolution of the free stream velocity component normal to the leading edge for $Q_\infty = 60 \text{ ms}^{-1}$ and for a geometrical angle of attack of -2° . The peak of minimum pressure is located at $X/C = 0.233$. Further downstream, a strong positive pressure gradient is observed, and the laminar boundary layer becomes nearly separated. For $X/C > 0.3$, the external flow is at first practically uniform and then slightly decelerated towards the trailing edge.

The evolution of the transition location X_T as a function of the wind tunnel speed is plotted in figure 4.9. The experimental data are compared with the predictions given by the transition criteria developed at ONERA/CERT. Near the leading edge, the crossflow criteria C1 and C2 agree rather well with the measurements. However, as soon as the positive pressure gradient is entered, the hot films detect transition points which cannot be predicted by the criteria.

Stability computations were performed by Casalis [59], [60] to understand this behaviour. A typical result is shown in figure 4.10 : for a given wind tunnel speed ($Q_\infty = 60 \text{ ms}^{-1}$) and for a highly amplified frequency ($f = 3$ KHz), the variation of the locally most unstable direction ψ_M is plotted as a function of the chordwise distance. ψ_M remains close to the crossflow direction in the negative pressure gradient (crossflow instability) but, a short distance downstream of the minimum pressure point, there is an abrupt change in ψ_M , which indicates that streamwise instability becomes dominant. The same behaviour was observed for all the other unstable frequencies. If the total amplification rate of a fixed frequency is performed by integrating the local amplification rate taken in the ψ_M direction (relation

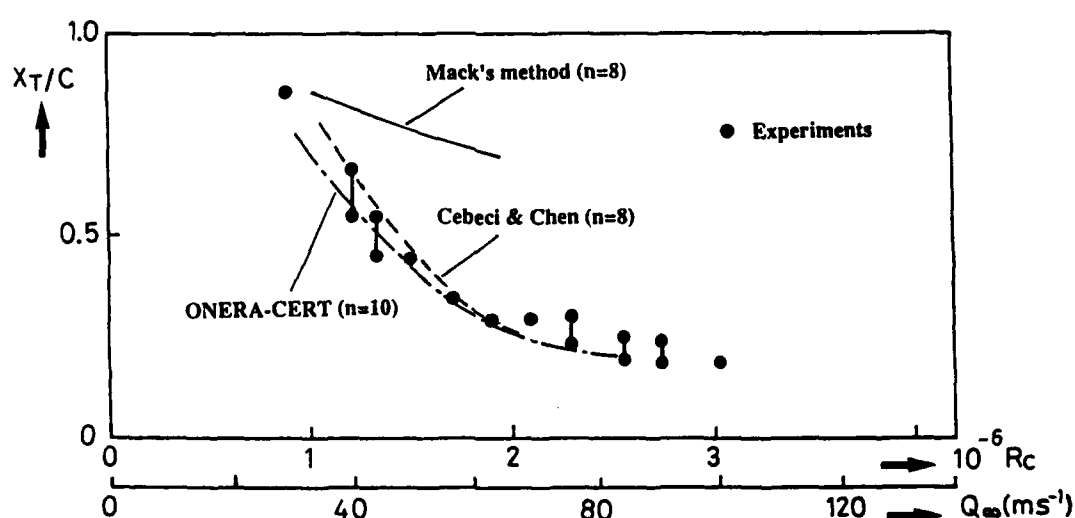


Fig. 4.11 Comparison between measured and predicted transition locations (e^n methods)

(4.3) or relation (4.9)), streamwise and crossflow instabilities will have *additive* effects. The physical meaning of this strategy (envelope method) is not clear. On the contrary, the use of independent streamwise and crossflow criteria assumes that both instabilities act *separately*. In any case, possible interactions are not taken into account.

Applications of the e^n method are presented on figure 4.11, where the experimental and computed transition locations are compared. Three series of calculations are shown ; they correspond to the three strategies described in paragraph 4.1.2. :

- The square symbols represent results obtained by Cebeci et al [44] who used the saddle-point method with $n = 8$. The agreement with the experimental data is fairly good.
- Theoretical results based on Mack's method (constant spanwise wavelength) with $n = 8$ overestimate the transition abscissas ; n factors of the order of 4 to 5 lead to a better agreement with the measurements.
- The method developed at ONERA/CERT gives a satisfactory estimate of the transition location for $n = 10$.

The conclusion is that different strategies often give different n factors. To be meaningful, comparisons between n factors computed for different disturbance environments must be done with the same strategy and with the same experimental definition of the transition onset.

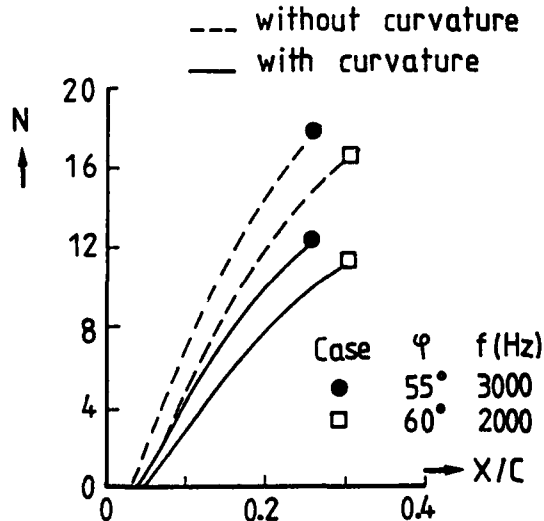


Fig. 4.12 Total amplification rates computed by Malik & Poll [61]. Symbols denote experimental transition locations

The third example illustrates the problem of curvature terms in three-dimensional flow. The COSAL code was used by Malik & Poll [61] to predict transition on the windward face of a long yawed cylinder, for which low speed experimental data were available (Poll [62]). The curvature terms were introduced into the stability equations, and the n factor was computed with the envelope method. The integrated amplification rates of the most unstable frequencies are plotted on figure 4.12 for two experimental cases. At the measured transition locations, the n factors without curvature are of the order of 17-18 ; they are reduced to 11-12 when the curvature terms are accounted for. This shows that body curvature and streamline curvature produce strong damping effects. However, recent computations done by Schrauf et al [63] for the same test case revealed a much weaker influence. It is not clear today if these discrepancies come from theoretical or from numerical problems.

4.5. Transition Region Modelling

Let us assume now that the location of the transition onset is known. The next problem is to model the progressive variations of the boundary layer properties from the laminar state up to the fully turbulent regime. This problem is not necessarily negligible, because the extent of the transition region can represent 10 to 20 percent of the extent of the upstream laminar flow.

The transition region is characterized by the growth of turbulent structures (spots) which originate in a more or less random fashion around a mean "transition point". The spots are swept along with the mean flow, extend laterally and axially, overlap and form a turbulent boundary layer. When sensors such as hot wires or hot films are placed near the wall or at the wall, the fluctuations which are recorded in the transition region show the successive appearance of turbulent spots and of laminar regions : it is the intermittency phenomenon. The intermittency factor γ represents the fraction of the total time that the flow is turbulent ; it increases from 0 at the transition onset to 1 at the completion of transition.

For practical purposes, the intermittency phenomenon is often represented by simple, completely empirical models, see review in [47]. For instance, the method which was developed by Coustols [54], [64] for three-dimensional, incompressible flows assumes that :

$$\begin{aligned}
 -\rho \overline{u'v'} &= \varepsilon \mu_t \frac{\partial U}{\partial y} \\
 \text{and} \\
 -\rho \overline{v'w'} &= \varepsilon \mu_t \frac{\partial W}{\partial y}
 \end{aligned} \tag{4.15}$$

where $-\rho \overline{u'v'}$ and $-\rho \overline{v'w'}$ are the Reynolds shear stresses of the X- and Z-momentum equations. μ_t represents an eddy viscosity coefficient, which is expressed by a classical turbulence model. At first sight, the ε coefficient represents the intermittency factor γ , in the sense that it increases from 0 to 1 in the transition region. Experimental data collected in low speed wind

tunnels showed that ε could be represented as a function of θ/θ_T , where θ is the streamwise momentum thickness ; θ_T represents its value at transition onset. The function $\varepsilon(\theta/\theta_T)$ is plotted in figure 4.13. One of the problems was to model the overshoot in the skin friction coefficient, which exists in the middle of the transition region due to the intermittency phenomenon. This was done by imposing an overshoot to the function ε , which does not represent the physical intermittency factor, but rather an empirical weighting coefficient for the Reynolds shear stresses. This method was extended to high speed flow configurations by introducing a compressibility correction which is negligible for transonic Mach numbers [65].

This method was tested for two and three-dimensional incompressible flows [47], [66]. It was also used in the context of flight experiments performed by Dassault Aviation with the financial support of the French Ministry of Defence. For these tests, the upper part of the fin of a Falcon 50 aircraft was removed and replaced by a swept, slightly tapered model (figure 4.14). This model was designed by Dassault Aviation to have an important part of natural laminar flows, see next Section. Transition was detected by 22 hot films glued on both sides of the model, as well as by two infrared cameras installed on the horizontal tail. The wall pressure distributions were also measured. The flight conditions were chosen in the transonic range, for unit Reynolds numbers between 4 and $7 \cdot 10^6$.

An appropriate calibration of the hot films made it possible to measure the streamwise evolution of the skin friction coefficient. Figure 4.15 gives a typical example of result ($M_\infty = 0.76$, altitude = 12 km, sweep angle = 35°). The experimental data are compared with a theoretical curve ; the transition onset is predicted by the C1 crossflow criterion and the transition region is modelled with the intermittency method. The agreement is as satisfactory as possible.

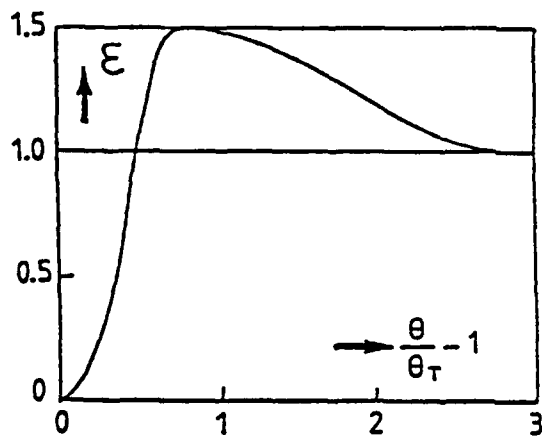


Fig. 4.13 Intermittency function



Fig. 4.14 Falcon 50 aircraft

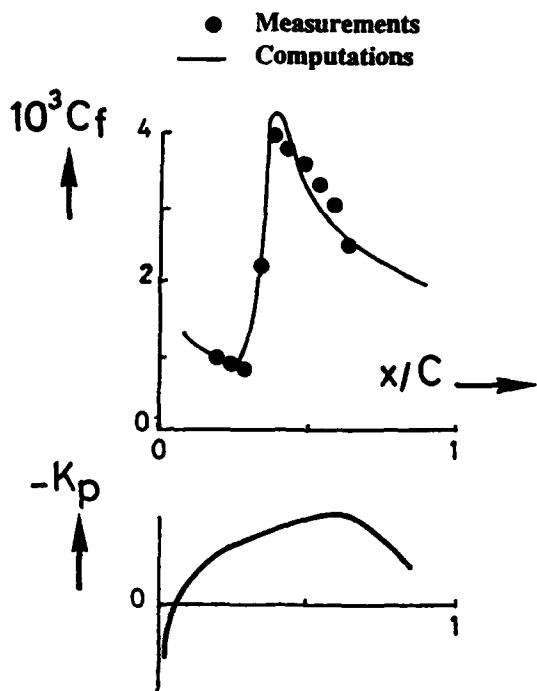


Fig. 4.15 Measured and computed skin friction coefficients, upper side

5. HOW TO DELAY TRANSITION ?

Laminar flow control is essentially a war against the inflection points. As indicated by the inviscid theory, the inflectional mean velocity profiles are highly unstable at infinite Reynolds numbers, but even including viscous effects they are still unstable at finite Reynolds numbers of practical interest. The main objective is to try to eliminate the inflection points or, at least, to reduce their destabilizing effect, for instance by modifying their position into the boundary layer.

Clearly the problem is not easy to solve for crossflow instability, because the crossflow profile always exhibits an inflection point, generally towards the outer edge of the boundary layer. For the streamwise instability (and also for two-dimensional flows), it can be assumed that the possibility of an inflectional instability will be less if the second derivative of the mean velocity near the wall becomes more negative. Thus the transition modifiers can be identified by examining the two-dimensional momentum equation close to the surface (Reshotko, [67]):

$$(\rho V_w - \frac{d\mu}{dT} \frac{\partial T}{\partial y}) \frac{\partial U}{\partial y} + \frac{dP}{dx} = \mu_w \frac{\partial^2 U}{\partial y^2} \quad (5.1)$$

This equation shows that negative pressure gradients, suction ($V_w < 0$), cooling in air ($\frac{\partial T}{\partial y} > 0$) or heating in water ($\frac{\partial T}{\partial y} < 0$)¹ tend to make the second derivative of U more negative.

5.1. Effect of Streamwise Pressure Gradients

Because this stabilization technique requires no "active" system, such as suction, cooling or heating, it is often referred to as "Natural Laminar Flow" (NLF) control. The aim is to delay transition onset by optimizing the pressure distribution along the body, i.e. by "shaping" the surface.

5.1.1. Two-dimensional Flows

In two-dimensional flows, stabilization of the laminar boundary layer is a rather simple problem: as Tollmien-Schlichting waves are damped (or only slightly amplified) in negative pressure gradients, the distance between the stagnation point and the point of minimum pressure must be as extensive as possible. On shaped airfoils or bodies, the flow usually remains laminar up to the streamwise location of minimum pressure (if the Reynolds number is not very large), then it undergoes transition as it enters the positive pressure gradient region where separation can occur. The exploitation of this principle dates back to the 1930's and led to the development of the NACA6-series airfoils. Wind tunnel experiments performed on these airfoils showed transition Reynolds numbers of 14 to 16 million (Braslow & Visconti, [68]). The shaping technique has also been used for low Reynolds number airfoils such as those found on sailplanes.

It is also possible to apply this method for shaping turbofan nacelles, which can be considered, as a first approximation, as two-dimensional axisymmetric bodies. Figure 5.1 (Younghans & Lahti, [69]) shows a conventional nacelle and a reshaped nacelle, together with the corresponding pressure distributions. Wind tunnel tests of the shaped nacelle (with wing and pylon) confirmed the predicted drag reduction.

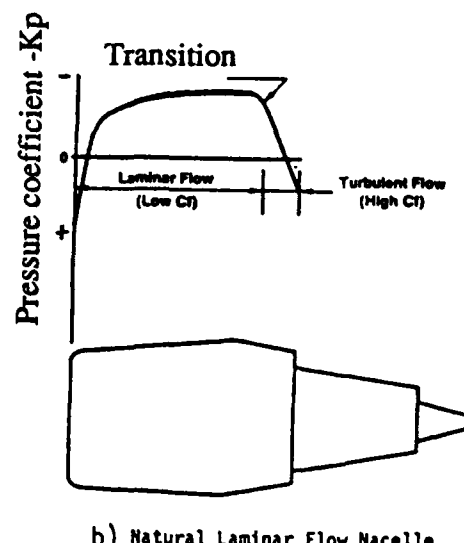
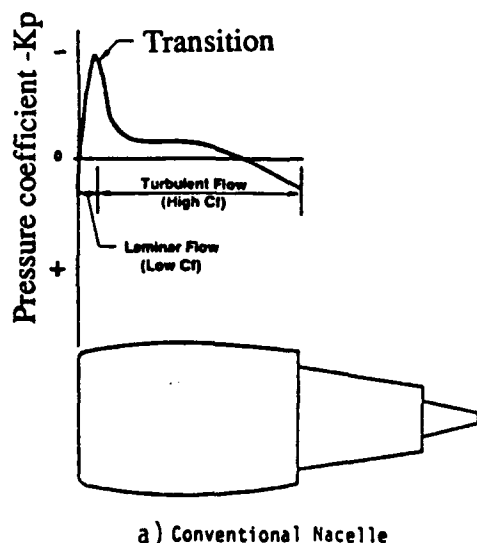


Fig. 5.1 Effect of shaping on transition for a turbofan nacelle [69]

¹ Because $d\mu/dT$ is positive in air and negative in water

5.1.2. Three-dimensional flows

Shaping a swept wing constitutes a much more difficult task than shaping a two-dimensional airfoil, because one has to find a compromise between two opposite effects. Close to the leading edge, a negative pressure gradient damps out the streamwise, Tollmien-Schlichting type instabilities, but it creates a crossflow velocity component which amplifies crossflow disturbances: negative pressure gradients are "favourable" for two-dimensional flows only! Downstream of the location where the free stream velocity reaches its maximum, a positive pressure gradient reduces crossflow instability, but streamwise disturbances start to grow rapidly.

Figure 5.2 shows an example of upper surface pressure distribution that might be used for NLF application to swept transonic wings. Near the leading edge, the pressure falls very rapidly in order to minimize the development of the crossflow velocity component and consequently of the crossflow disturbances. This can be demonstrated by considering a linear distribution of the free stream velocity component U_e normal to the leading edge and by assuming that this distribution corresponds to that of the potential flow around a circular cylinder of radius r , i.e.:

$$U_e = 2 \frac{Q_\infty \cos \varphi}{r} X \quad (\text{see paragraph 6.1}) \quad (5.2)$$

The upper part of figure 5.3 shows two velocity distributions for $\varphi = 30^\circ$, $Q_\infty = 220 \text{ ms}^{-1}$, $v = 4.7 \cdot 10^{-5}$ (typical flight conditions at $M_\infty = 0.75$ and altitude = 12 km) and two values of r , 8 and 16 cm. Let us recall that X is measured along the leading edge surface. It can be established from incompressible self-similar solutions that the crossflow Reynolds number $R\delta_2$ is given by:

$$R\delta_2 = 0.2677 \left[\frac{Q_\infty r}{v} \sin \varphi \operatorname{tg} \varphi \right]^{1/2} \frac{X/r}{[\operatorname{tg}^2 \varphi/4 + (X/r)^2]^{1/2}} \quad (5.3)$$

For small values of X/r , $R\delta_2$ varies like $r^{-1/2}$ but for large values of X/r , $R\delta_2$ tends towards an asymptotic value $R\delta_{2\infty}$ which is proportional to $r^{1/2}$, see lower part of figure 5.3. In this example, $R\delta_2$ is approached very rapidly, since $R\delta_2 = 0.96 R\delta_{2\infty}$ for $X/r = 1$.

Let us assume now that the strong acceleration extends up to the point where $U_e = 210 \text{ ms}^{-1}$. At this location, $R\delta_2$ is close to 80 for $r = 8 \text{ cm}$ and close to 110 for $r = 16 \text{ cm}$. This demonstrates the interest of using small leading edge radii, i.e. large negative pressure gradients to keep $R\delta_2$ below a certain limit. In addition, the strong acceleration helps to eliminate leading edge contamination by reducing the attachment line Reynolds number, paragraph 6.3.

Downstream of the knee of the pressure distribution (figure 5.2), the flow is slightly accelerated in order to avoid the development of streamwise disturbances. In the

same region, $R\delta_2$ remains close to $R\delta_{2\infty}$ or even decreases, so that the n factor remains below the critical level for transition onset.

Reference 70 (Wagner et al, 1989) gives a survey of flight research conducted on NLF control, including early tests performed immediately after World War II. This paper summarizes the main results obtained more recently on the F-111/TACT aircraft and on the F-14 aircraft, both at transonic speeds. In the former flight tests, transition Reynolds numbers of about 15 million were measured on the upper surface of a glove for 9 degrees of sweep; the maximum transition Reynolds number measured on the lower surface was close to 14

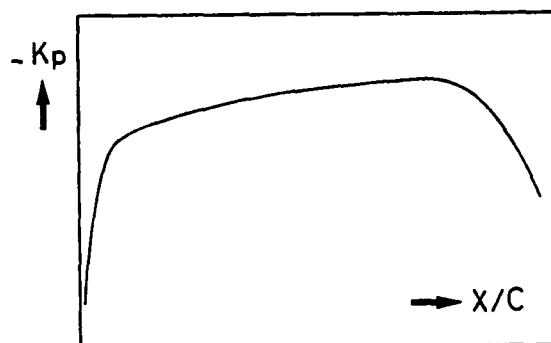


Fig. 5.2. Typical pressure distribution for natural laminar flow

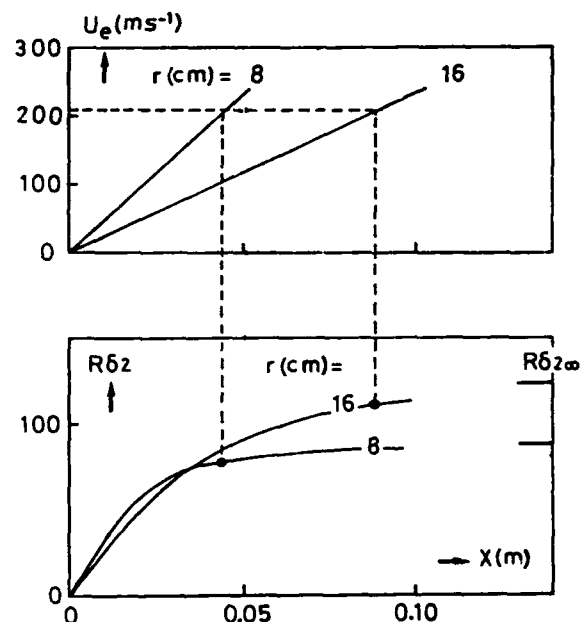


Fig. 5.3. Crossflow Reynolds numbers for linear distributions of the velocity component normal to the leading edge

million for a sweep angle of 15 degrees. The F-14 Variable Sweep Transition Flight Experiments (F-14 VSTFE) program was initiated in 1984 with flight tests completed in 1987. Two gloves were tested, as it is shown on figure 5.4 : one was a "clean-up" of the basic F-14 wing, while the second was designed at NASA Langley to achieve very large values of R_{xT} . A maximum transition Reynolds number of about 17.6 million was obtained for $\phi = 15^\circ$. Figure 5.5 [70] summarizes the main results of these flight experiments (wind tunnel data obtained in the 12-Foot Tunnel at NASA Ames are also shown for comparison). The largest values of the transition Reynolds number based on free stream conditions are plotted as a function of the sweep angle. The average value of the n factor at transition onset for the most amplified disturbances was about 9 when the curvature terms were included in the computations ; calculations without curvature predicted values of the order of 17. The curve labelled "Laminar Flow Achievable" in figure 5.5 gives an estimate of the maximum transition Reynolds number which could be reached before leading edge contamination occurs. From these results, Wagner et al concluded that "even moderately large transports such as the A320, MD80, or even B-757, might be able to use NLF with some modest reduction in leading edge sweep, say 5 to 7 degrees" [4].

NLF flight experiments were conducted in France (1985-1987) by Dassault Aviation with state aid and in cooperation with ONERA/CERT [22]. A wing section was installed on the fin of a Falcon 50 aircraft (figure 4.14) and tested in transonic conditions for two sweep angles. Due to the rather low values of the chord Reynolds number, streamwise instabilities dominated for $\phi = 25^\circ$, while transition was induced by crossflow instabilities for $\phi = 35^\circ$. The results agreed well with theoretical predictions.

A European effort is currently being done to study the laminar flow technology within the so-called ELFIN program (European Laminar Flow INvestigation). This program constitutes a collaborative venture, which brings together the majority of European airframe



Fig. 5.4. F-14 aircraft for the Variable Sweep Transition Flight Experiments [70]

manufacturers, research institutes and universities. The essential goals are to prove the basic concept of laminar flow technology and to prepare the tools, methods and systems required for its application. NLF flight tests are planned at the end of 1991 on a Fokker 100 aircraft.

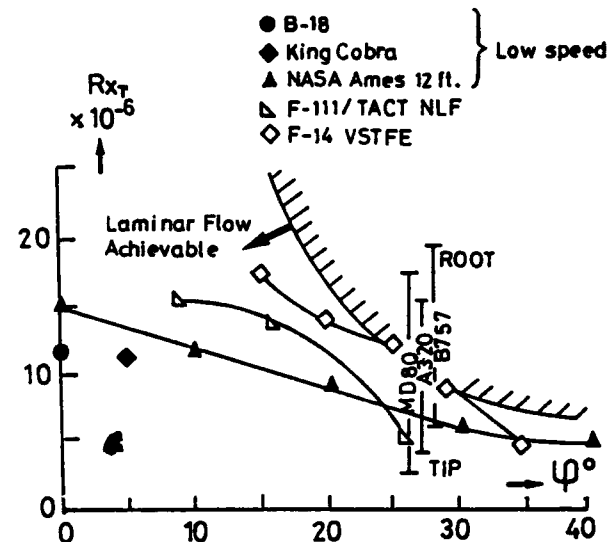


Fig. 5.5 Maximum transition Reynolds numbers for several NLF experiments [70] (The root and tip Reynolds numbers for the MD-80, A-320, B-757 are computed by assuming transition at 50 % of the local chord)

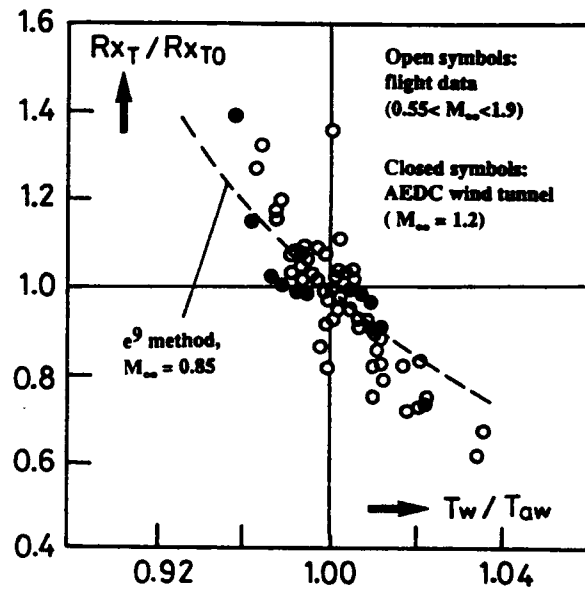


Fig. 5.6 In-flight determined transition Reynolds number as a function of the wall temperature [27]

5.2. Cooling and Heating

The stabilizing effect of wall cooling in air was first demonstrated by Lees (1947, [71]). It has been illustrated by the stability diagrams shown in figure 2.3. These theoretical results were confirmed by the flight experiments performed on the AEDC cone. As previously shown in figure 3.12, this two-dimensional, axisymmetric model was mounted in front of the fuselage of a F-15 aircraft [27]. Transition was detected by displacing a surface pitot tube along a cone ray. Figure 5.6 gives an idea of the effect of wall temperature on the transition Reynolds number: the ratio R_{xT}/R_{xT0} is plotted as a function of T_w/T_{aw} , where T_{aw} is the adiabatic wall temperature and R_{xT0} is the value of R_{xT} for $T_w = T_{aw}$. Some of the data were obtained in the AEDC wind tunnel for $M_\infty = 1.2$ and are in good agreement with the flight results. The strong stabilizing (destabilizing) influence of wall cooling (heating) appears clearly. Theoretical results obtained with the e^9 method for $M_\infty = 0.85$ (reported in [27]) follow the same trend.

In three-dimensional flow, wall cooling is less efficient to reduce the crossflow instability than the streamwise instability; as the inflection point of the crossflow profile is located towards the boundary layer outer edge, it is less sensitive to changes in the wall temperature. Nevertheless, cooling tends to decrease the maximum crossflow velocity, i.e. the crossflow Reynolds number.

The use of cooling in air for drag reduction is a possibility only for an aircraft flying with a cryogenic fuel such as hydrogen. Reshotko [72] showed from a simple, two-dimensional analysis that drag reduction of the order of 20-25 percent can be expected by cooling 75 percent of the wing surface. However, stabilization by cooling cannot be considered as a practical tool for aircraft applications.

In water, the dynamic viscosity decreases with increasing temperature, so that heating the wall can stabilize the laminar boundary layer. This was demonstrated by numerical computations (Wazzan et al [73]) and also by water tunnel experiments. The experiments of Strazisar et al [74] are limited to low overheats, between 0°F and 8°F. Disturbances are introduced into the boundary layer using a vibrating ribbon. The measurements are performed in the vicinity of the critical Reynolds number only.

Barker & Jennings [75] and Barker & Gile [76] described a series of "natural" transition experiments conducted on the inside of a long, electrically heated pipe of constant section. Although the displacement thickness was thin relative to the pipe radius, the flow was accelerated in the streamwise direction, with a mean value of the pressure gradient parameter β close to 0.07⁽²⁾. The

⁽²⁾ $\beta = 2m/(m + 1)$, with $m = \frac{x}{U_e} \frac{dU_e}{dx}$

transition Reynolds number obtained with no heat was $15 \cdot 10^6$, in fairly good agreement with the e^9 method which gives $R_{xT} = 12 \cdot 10^6$ for $n = 9$ and $\beta = 0.07$ (with $\beta = 0$, the theoretical value of R_{xT} is reduced to $4 \cdot 10^6$!). For a wall overheat of 8°C, Barker and Gile measured a transition Reynolds number of $47 \cdot 10^6$. Other experiments were performed by Lauchle & Gunney [77] on an axisymmetric body which supported a favourable pressure gradient along most of its length. The transition Reynolds number was $4.5 \cdot 10^6$ for the body operating with no heat. An overheat of 25°C, corresponding to a total heating power of 93.3 kW, increased R_{xT} up to $36.4 \cdot 10^6$. For large heating levels, however, a degradation in performance was observed in both series of experiments; these limitations were attributed to flow asymmetries and/or to free stream particulates, see paragraph 7.2.2..

5.3. Suction

By contrast with shaping which constitutes a passive method for maintaining Natural Laminar Flow (NLF), stabilization by suction or by cooling is an active method which is referred to as Laminar Flow Control (LFC).

5.3.1. Fundamental aspects

Suction acts in two ways. Firstly, it reduces the boundary layer thickness and the associated Reynolds numbers; however, as the suction rates are usually very small, this effect is weak. The second, and more important effect, is to modify the shape of the mean velocity profile in such a way that its stability is improved. For example, let us consider the asymptotic suction profile in two-dimensional, incompressible flow. This profile is obtained when a continuous suction is applied at the wall of a flat plate. At some distance from the leading edge, the boundary layer becomes independent of the streamwise coordinate, and it is easy to demonstrate that :

$$V(y) = -V_w \quad (V_w \text{ is the absolute value of the suction velocity}) \quad (5.4)$$

$$U(y) = U_e [1 - \exp(V_w y / v)]$$

The displacement thickness and the shape factor are equal to $-v/V_w$ and 2, respectively. Stability computations presented in [78] indicate that the critical Reynolds number $R_{\delta 1cr}$ is about 42 000; other numerical results give higher values, of the order of 50 000 (see discussion in [79]). These values are two orders of magnitude larger than that obtained for the Blasius flow. Stability computations were performed for similar and non similar two dimensional velocity profiles, including the combined effects of pressure gradient and suction [79]. The strong stabilizing influence of suction is explained by the increase of the critical Reynolds number, the decrease in the range of unstable frequencies and the decrease in the amplification rates. A survey of theoretical and fundamental experimental results can be found in [80].

In three-dimensional flows, the inflectional nature of the crossflow mean velocity profile makes stabilization by suction more difficult. Suction is able to suppress the inflection point of a streamwise profile in a mild positive pressure gradient, but it is obviously unable to eliminate the inflection point of the crossflow profile ; its main effect is to reduce the crossflow Reynolds number.

5.3.2. Slots and perforated surfaces

The best way of removing a small portion of the boundary layer flow is to develop a continuous porous-suction surface. But early investigations (1940's and 1950's) failed to yield satisfactory results for both structural and aerodynamic difficulties. At the present time, the best methods to approach a continuous suction are the use of spanwise slots or strips of perforated material. The technological aspects of the problem were discussed by Pfenninger [81], Braslow & Fisher [82] and Braslow et al [32]. The main results are summarized below.

a-Spanwise slots- When slots are used, their spacing is usually much larger than their width, so that the suction distribution is spatially discontinuous. Figure 5.7 shows a slotted LFC wing structural concept, which was studied in [83]. The design is different in the leading edge region and in the wing box region. On the wing box, the load-carrying structure is a thick graphite epoxy skin stiffened with hat section stiffeners which constitute spanwise ducts for the suction air. The spanwise slots are sawed in a thin titanium sheet bonded to the graphite epoxy structure ; small plenums and metering holes are arranged into the main structure between the slots and the hat section ducts. In the leading edge box region, the suction flow is routed through the structure to trunk ducts which collect also the air coming from the wing box slots. Several slots provide a protective fluid for insect protection and anti-icing.

It is obvious that a well-designed slot must avoid to generate disturbances which could reduce the extent of laminar flow. Extensive research performed by Northrop before and during the X-21 program (see paragraph 5.3.4.) yielded the design criteria indicated in figure 5.8 (from [32], [82]). Many parameters must be accounted for : the slot width, the height of the slot lip, the sucked height, the pressure drop, the slot Reynolds number and the spacing between slots. Evaluation of this latter parameter is discussed in [32], [82]. Successful applications of suction through spanwise slots are described in paragraph 5.3.4..

b-Perforated strips- As the spacing between perforated strips is generally smaller than the width of each strip, perforated surfaces represent a closer approach to ideal continuous suction and present a better tolerance to off-design conditions. However, two problems need to be solved :

- Close to the leading edge, the streamwise (negative) pressure gradient may be strong enough to cause inflow

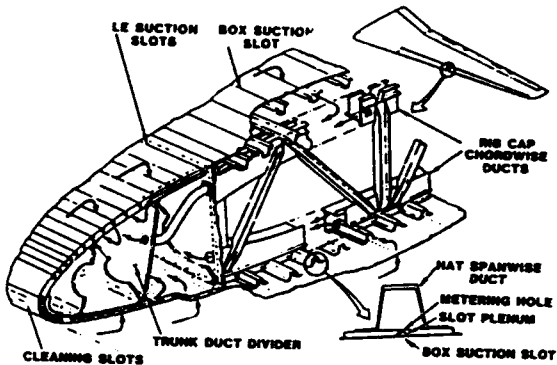


Fig. 5.7 Slotted wing-box design [83]

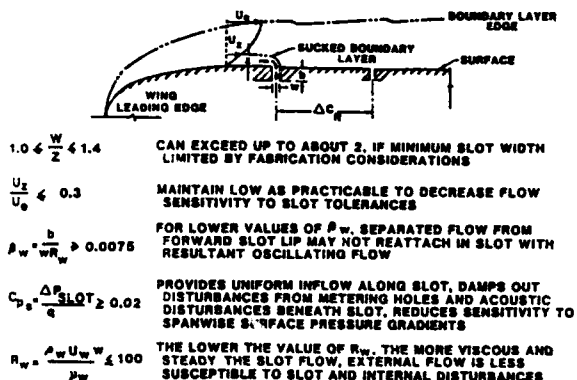


Fig. 5.8 Slotted-surface schematic and design criteria [32], [82]

in the forward region of the strip (as expected) and outflow in the aft region. As blowing is destabilizing, the streamwise extent of the strip must be reduced and/or the pressure drop across the perforated surface must be increased.

- For "large" suction rates, the suction holes generate three-dimensional disturbances which can fix transition on the perforated surface. To avoid this "negative roughness" effect, both the hole diameter and the hole spacing must be small compared to the boundary layer thickness (Gregory, in [84]). Early investigations in the 1950's showed this tripping effect with holes of relatively large diameter ; at that time, the diameter of the smallest holes that could be manufactured practically was of the order of 0.02 in. (0.5 mm). Today, electron and laser beams can drill closely spaced holes as small as 0.001 in. diameter (0.025 mm). As it will be shown in paragraph 5.3.5., such suction panels have established their practicality for aircraft applications.

Figure 7.11 (from [32], [82]) shows an example of perforated-strip approach for the leading edge box. The suction ducts, or flutes, collect the sucked air which is routed to the suction source. A retractable high-lift

device (Krueger flap) is used as an insect-protection device and provides a coating of anti-icing fluid, see paragraph 7.2.1..

A more theoretical problem is the enhancement of receptivity to free stream disturbances at any junction between a perforated strip and the impermeable wall. This is a typical example of localized receptivity which involves abrupt adjustment of the boundary layer to the sudden change of the transverse velocity at the wall. Heinrich et al [18] analyzed this problem by using the triple deck theory.

5.3.3. The e^n method with suction

The estimation of suction quantities for LFC applications can be calculated by imposing that the integrated amplification rates of the unstable waves remain below a prescribed level. To simplify the computations, a continuously applied suction is often assumed ; Nayfeh & El Hady [85] demonstrated that if the same amount of suction is distributed at wide porous strips instead of continuous distribution, the n factors are essentially unchanged. In this case, the basic flow was computed by solving the boundary layer equations ; this procedure is no longer correct for spanwise slots, which exert an upstream influence on the mean flow field, see previous lecture by Saric [6].

An important result is that very small suction rates are sufficient to considerably delay the transition onset : typical values of the ratio $|V_w| / Q_\infty$ range between 10^{-4} to 10^{-3} (Q_∞ is the free stream velocity and V_w represents the mean suction velocity at the wall). It appears that the suction flows required for LFC are weak and have a limited effect on the energy balance. The computations also demonstrate that the best efficiency is obtained when suction is applied as soon as instability starts to develop.

It is not obvious, however, that the n factor remains constant without and with suction. To investigate this problem, wind tunnel experiments were performed on a swept wing equipped with ten independent suction ducts from 13 to 68 percent chord (Arnal et al [86]). The perforated wall was made with a piece of steel drilled by electron beam. Figure 5.9 shows the pressure distribution measured on the upper surface of the wing for $\phi = 60^\circ$ and $\alpha = -8^\circ$. The flow is accelerated all along the wing, except in a short region around $X/C = 0.7$. The bump in the pressure distribution is due to the fact that the shape of the perforated wall is not exactly that of the initial airfoil. Experimental and theoretical results are presented on figure 5.10, where the transition location is plotted as a function of the suction velocity V_w for $Q_\infty = 70 \text{ ms}^{-1}$. Suction is applied to the first three ducts ($0.13 < X/C < 0.35$), and the stability computations are performed with the strategy developed at ONERA/CERT (paragraph 4.1.2) for $n = 7$ and 8. The slope of the theoretical curve is somewhat steeper than that corresponding to the experiments : with $n = 8$, the agreement is excellent for $V_w = 0$, but no transition is detected by the computations for $V_w = -10 \text{ cms}^{-1}$. This discrepancy can be attributed to

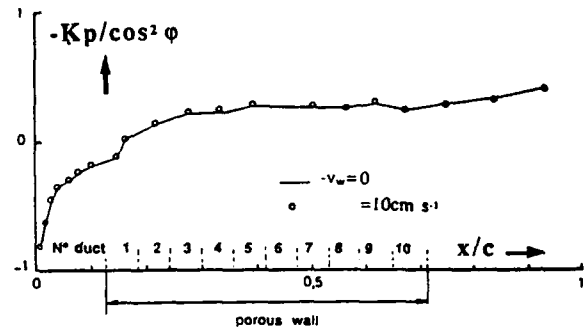


Fig. 5.9 Pressure coefficient distribution

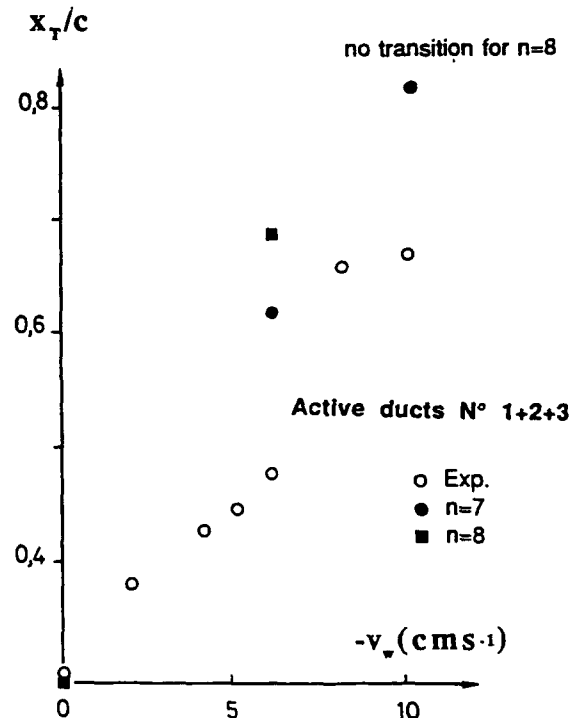


Fig. 5.10 Comparison between measured and predicted transition locations (e^n method with $n = 7$ and 8, $Q_\infty = 70 \text{ ms}^{-1}$)



Fig. 5.11 X-21 aircraft

experimental problems (tripping effect of the suction holes ?) as well as to more fundamental issues (receptivity ? non linear effects ?). Nevertheless the overall trend is fairly well reproduced.

5.3.4. Early experimental work

The pioneering studies in Laminar Flow Control are summarized in the Lachmann volumes (1961, [84]). A few typical examples of LFC applications by suction are briefly discussed in this paragraph.

Laminarization by suction dates back to the late 1930's and early 1940's. Pfenninger (1946, [87]) developed the use of suction slots for laminar flow control and performed experiments on a thick airfoil at the Institute for Aerodynamics in Zürich, Switzerland. He showed that full chord laminarization could be obtained for very small suction rates. During further experiments conducted in 1951 at Langley Field, full chord laminar flow was achieved up to $R_c = 17 \cdot 10^6$, where R_c is the chord Reynolds number. These studies clearly demonstrated that the results were dependent on the turbulence and acoustic disturbance levels of the facilities.

Following studies at NASA Langley of using suction to delay transition on airfoils, the United States Air Force entered into a program with Northrop Corporation to study the feasibility of laminar flow control in flight. An *unswept* suction glove with 69 fine slots located from 40 to 96 percent chord on the upper surface was tested on a F-94 airplane (1957) ; full chord laminar flow was maintained up to $R_c = 36.4 \cdot 10^6$, which was the test limit of the airplane.

The program developed by the USAF and Northrop Corporation culminated in the successful X-21 flight tests (figure 5.11) on a *swept* wing ($\varphi = 30^\circ$) equipped with a large number of suction slots designed by Pfenninger. Approximately 95 percent of the upper surface and 85 percent of the lower surface were slotted. At a chord Reynolds number of $47 \cdot 10^6$, laminarization was nearly complete on the upper surface, whilst the boundary layer was laminar up to 75 percent chord on the lower surface (Whites et al, 1966, [88]). This resulted in a 20 % reduction in airplane drag. Other

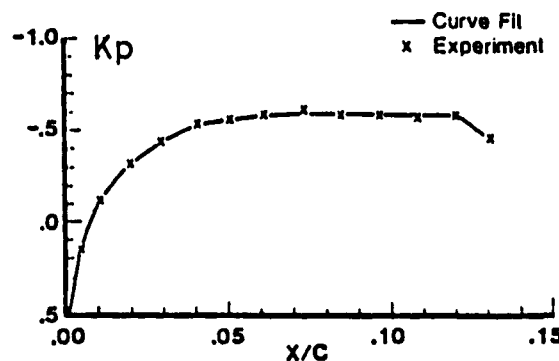


Fig. 5.12 Pressure coefficient distribution at $M_\infty = 0.775$ and 29 000 ft [91]

practical problems, such as leading edge contamination, waviness tolerances, insects impacts ... were also studied ; they will be discussed later on. The issues for laminar flow control by suction on swept wings have been summarized by Pfenninger & Reed (1966, [89]).

5.3.5. Recent flight experiments with suction - HLFC

a-Jet Star - [90], [91] - In 1980, NASA initiated the Leading Edge Flight Test (LEFT) program as a flight validation of LFC systems. This program was the first attempt to use suction control on an aircraft wing since the X-21 program ended in 1965. There are two major differences between the LEFT experiments and the X-21 tests : suction is applied in the leading edge region only (not on the whole wing) through perforated strips (instead of spanwise slots). The leading edge suction panel which was installed in the right wing of a Jet Star aircraft was a titanium sheet perforated with over 1 million holes of 0.0025 in. diameter spaced about 0.035 in. between centers ; it extended from just below the attachment line to $X/C = 0.13$ (chord $C = 9.8$ feet). Fifteen independent perforated strips of 0.62 in. chord were separated by impermeable strips of 0.38 in. chord.

The sweep angle of the test article was 30° . Transition location was detected by near surface pitot tubes on the suction panel only. Figure 5.12 shows the measured pressure distribution for $M_\infty = 0.775$ at an altitude of 29 000 ft : the flow is accelerated up to $X/C = 0.05$, then it is practically uniform.

High initial suction levels were required to control crossflow at the leading edge ; late suction yielded less laminar flow than did earlier suction for the same amount of sucked air. Figure 5.13 presents three typical distributions of the suction coefficient C_q , together with the corresponding boundary layer state on the test model (white = laminar, black = turbulent). Fully laminar flow over the entire perforated area is achieved with the third distribution.

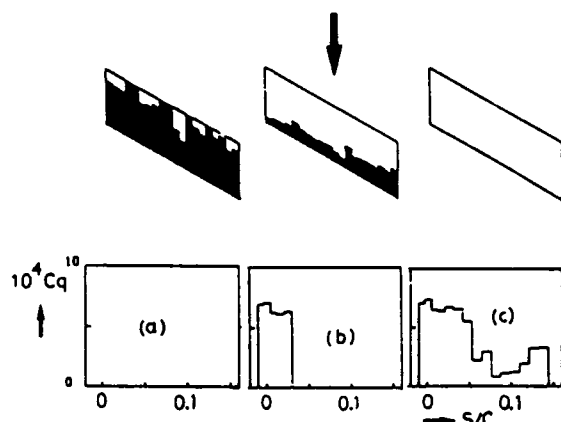


Fig. 5.13 Transition location without and with suction, $M_\infty = 0.77$, altitude = 29 000 ft [91]
 a) No suction b) Suction on flutes 1-5
 c) Suction on flutes 1-15

Linear stability computations were made with the COSAL code (temporal theory, envelope method). By taking into account the surface and streamline curvature effects, the disturbance amplification was reduced by as much as 60 percent. n factors at transition onset varied from about 7.5 to 10.5.

b-Boeing 757- Quite recently, high Reynolds number flight experiments have been performed on a Boeing 757 aircraft (after more than 300 hr of wind tunnel testing on a simulated section of the wing). A 22-ft span section of the left wing was modified for the flight tests. A leading edge Krueger flap was integrated into the high-lift system and designed to be an insect shield. Suction was applied in the leading edge region, i.e. to the front spar, with a structural concept similar to that used for the Jet Star experiments ; the suction surface was a microperforated titanium skin with over $15 \cdot 10^6$ laser-drilled, closely spaced holes of 0.0016 in. diameter. Over the wing box, i.e. downstream of the front spar, the pressure distribution was "tailored" to maintain laminar flow to the wing shock. This combination of an active control system (suction) with a passive control method (shaping) is referred to as Hybrid Laminar Flow Control (HLFC).

Flight test were conducted over a 5-month period to altitudes of 40 000 ft, Mach numbers to 0.82 and chord Reynolds numbers to $30 \cdot 10^6$. In June 1990, the Boeing 757 aircraft achieved laminar boundary layer flow to 65 percent wing chord.

c-Falcon 50- [22]- As described in paragraph 5.1.2., a first phase of flight tests on a Falcon 50 aircraft was aimed at demonstrating the feasibility of the NLF concept on a wing section. The second phase (1987-1990) was much more ambitious since its objective was to use HLFC on the inboard right wing of the same airplane. To perform these tests, Dassault Aviation designed a new wing shape and developed a suction system as well as a leading edge cleaning and anti-icing system. Transition was detected with 36 hot films flush mounted on the wing up to 30 percent chord, downstream of the suction panel (figure 5.14) and a Gaster bump was installed close to the wing-fuselage junction to prevent leading edge contamination. For sweep angles around 30° and weal suction rates, laminar flow was maintained over nearly the whole test surface.

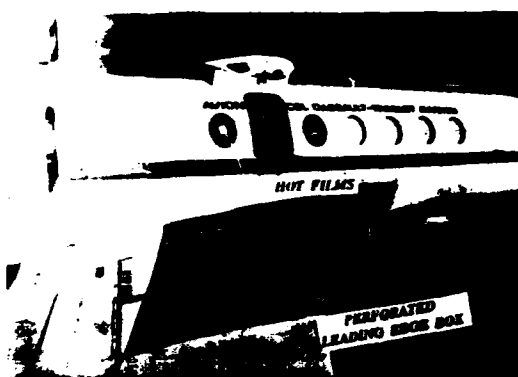


Fig. 5.14 HLFC experiments on the right wing of the Falcon 50 aircraft

6. ATTACHMENT LINE AND LEADING EDGE PROBLEMS

Most of the transition problems which have been discussed so far take place some distance downstream of the attachment line of a swept wing. In this Section, it will be shown that the transition phenomena occurring along this streamline exhibit some peculiar features. For instance, the case of a "natural" transition can be studied by using an appropriate linear stability theory which is somewhat different from that described in Section 2 ; on the other side, the possibility of bypass by leading edge contamination represents a practical problem of first importance, because the flow development on the wing depends on its initial nature along the leading edge.

It is not easy to give an accurate definition of the attachment line, except for simple geometries such as symmetrical bodies of constant chord and infinite span ; it is the line along which the static pressure is maximum. More intuitively, the attachment line represents a particular streamline which separates the flow into one branch following the upper surface and one branch following the lower surface, see figure 6.1.

6.1. The Flow along the Attachment Line

Let us consider first the simple case of a swept cylinder of infinite span (figure 6.1). ϕ is the sweep angle. The free stream velocity Q_∞ has a component $U_\infty = Q_\infty \cos\phi$ normal to the leading edge and a component $W_\infty = Q_\infty \sin\phi$ parallel to the leading edge. Z is the spanwise direction and X the direction normal to it, $X = 0$ corresponding to the attachment line. U and W designate the projections of the mean velocity along X and Z , respectively. Along the attachment line, W represents the streamwise velocity, whilst U is the crossflow component. If it is assumed that the potential flow does not exhibit any spanwise variation, the free stream velocity components U_e and W_e around the attachment line are given by :

$$U_e = kX \quad (6.1a)$$

$$W_e = W_\infty = \text{constant} \quad (6.1b)$$

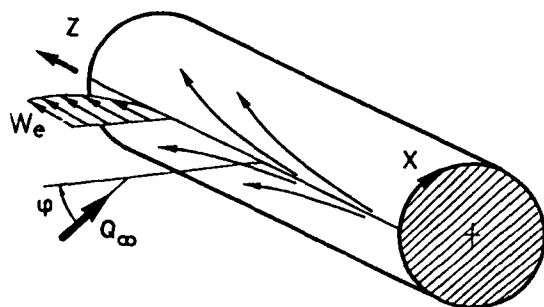


Fig. 6.1 Attachment line flow on a cylinder

To study the leading edge problems, two parameters are introduced :

$$\bullet \text{ the length scale } \eta = (v/k)^{0.5} \quad (6.2)$$

$$\bullet \text{ the Reynolds number } R = W_e \eta / v \quad (6.3)$$

For a circular cylinder of radius r , k and R can be expressed as :

$$k = 2 \frac{Q_\infty \cos\phi}{r} \quad (6.4)$$

$$\text{and } R = \left(\frac{Q_\infty r \sin\phi \tan\phi}{2v} \right)^{1/2}$$

For cylinders of elliptic section at zero angle of attack, it can be shown that :

$$k = 2 \frac{Q_\infty \cos\phi}{r} (1 + \frac{t}{c}) \quad (6.5)$$

$$\text{and } R = \left(\frac{Q_\infty r \sin\phi \tan\phi}{1 + t/c} \right)^{1/2}$$

where r is the leading edge radius and t/c the thickness ratio.

The boundary layer which develops along the attachment line can be either laminar or turbulent. Three possible situations are sketched on figure 6.2. In the first two cases, the swept model is fixed on a solid wall on which the flow is turbulent ; depending on the value of R , the attachment line boundary layer remains laminar (figure 6.2a) or becomes turbulent (figure 6.2b) : it is the leading edge contamination, see paragraph 6.3. If the model is not in contact with a solid surface (figure 6.2c), a laminar boundary layer starts to develop at point A, then possibly becomes turbulent further downstream if

R is large enough : it is a "natural" transition, see paragraph 6.2. When considering the attachment line boundary layer at large distances from its origin, its mean properties no longer depend on the spanwise location, i.e. the shape factor, the skin friction coefficient, the physical and integral thicknesses become constant. As illustrated on figure 6.2, this situation occurs in regions BB' and CC' (laminar boundary layer) or in regions DD' and EE' (turbulent boundary layer). The properties of these "uniform" boundary layers are summarized below.

a-Laminar boundary layer

In the region around the attachment line where (6.1a) and (6.1b) are valid, it is possible to obtain an exact solution of the Navier-Stokes equations which is a generalization of the classical Hiemenz flow [92]. The velocity field can be written :

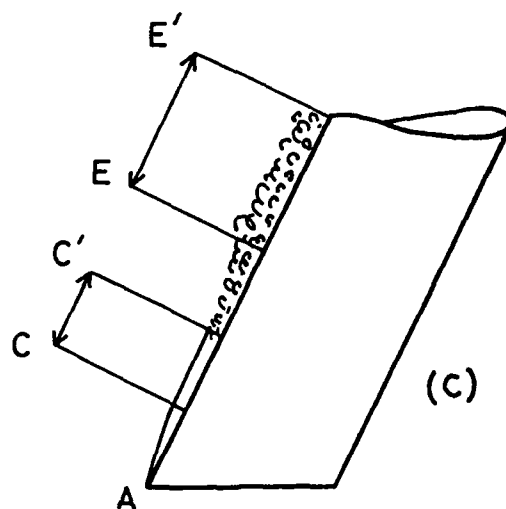
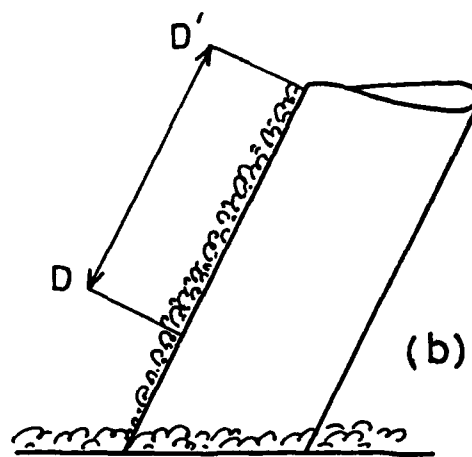
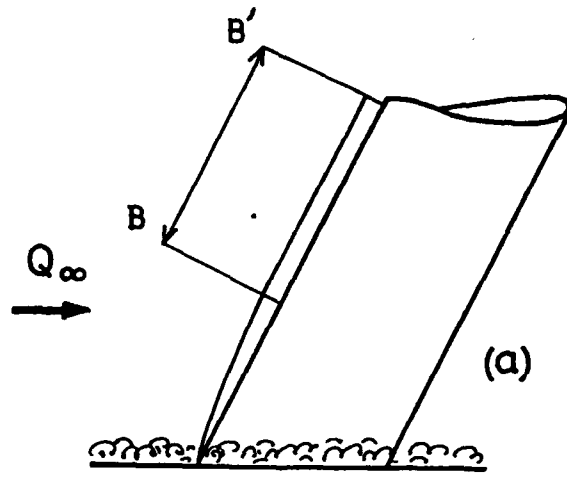


Fig. 6.2 Examples of attachment line flows

$$U = k \bar{X} \bar{U}(\bar{\eta}) ; V = \sqrt{v k} \bar{V}(\bar{\eta}) ;$$

$$W = W_e \bar{W}(\bar{\eta}) \text{ with } \bar{\eta} = y/\bar{\eta} \quad (6.6)$$

By assuming that the spanwise derivatives of velocity and pressure are equal to zero, \bar{U} , \bar{V} and \bar{W} satisfy :

$$\bar{U} + \bar{V}' = 0 \quad (6.7)$$

$$\bar{V}'' + \bar{V}'^2 - \bar{V} \bar{V}' - 1 = 0 \quad (6.8)$$

$$\bar{W}'' - \bar{V} \bar{W}' = 0 \quad (6.9)$$

$$\bar{V}'(0) = 0 \quad \bar{V}(0) = 0 \quad \bar{V}'(\infty) = -1 \quad (6.10)$$

$$\bar{W}(0) = 0 \quad \bar{W}(\infty) = 1$$

where the ' denote derivatives with respect to $\bar{\eta}$. Let us recall that this system is a solution of the full Navier-Stokes equations, not just the boundary layer equations. Along the attachment line ($X = 0$), the ratio U/U_e has non zero values, but $U = 0$ from the wall to the free stream because $U_e = 0$: there is no cross flow component along the attachment line. As it can be seen on figure 6.3, the streamwise mean velocity profile $\bar{W} = W/W_e$ looks like the Blasius solution for two-dimensional flat plate flow. Its main characteristics are :

$$H = 2.54 \text{ (Blasius : 2.59)}$$

$$R_0 = W_e \theta / v = 0.404 \quad R \quad (6.11)$$

$$C_f = 0.461/R_0 \text{ (Blasius : 0.664/R_0)}$$

b-Turbulent boundary layer

Most of our knowledge about the properties of the turbulent flow along the attachment line comes from experimental studies performed by Cumpsty & Head [93], Gaster [94] or Poll [95], [96]. The measurements have shown that the streamwise velocity distribution W/W_e is similar to that of a classical flat plate turbulent

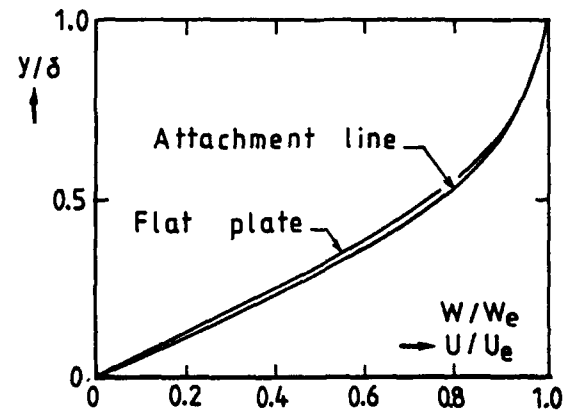


Fig. 6.3. Attachment line and flat plate mean velocity profiles

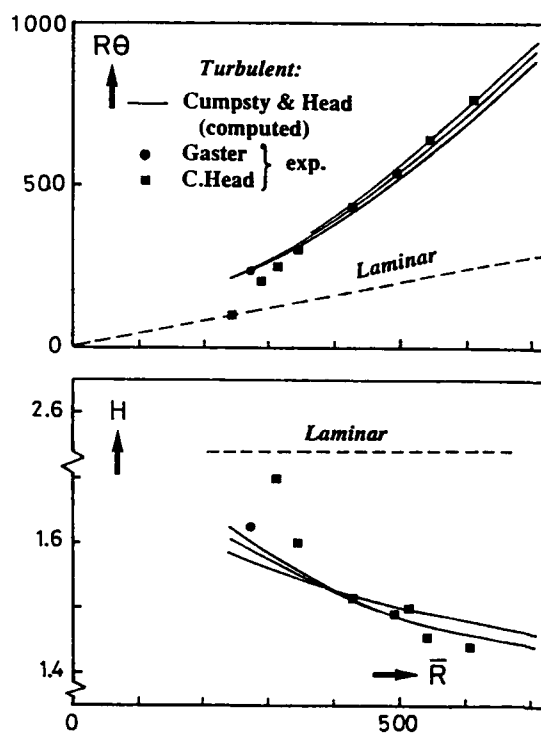


Fig. 6.4. Momentum thickness Reynolds number and shape factor

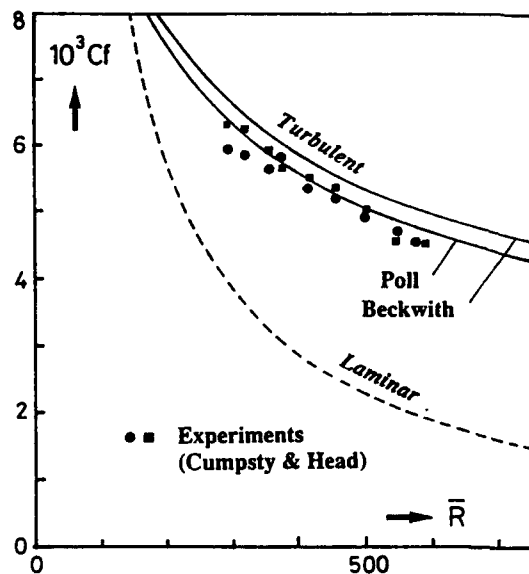


Fig. 6.5 Skin friction coefficient

boundary layer; in particular, a logarithmic law was found to exist. Figure 6.4 shows the evolutions of the momentum thickness Reynolds number $R\theta$ and of the shape factor H as functions of R . The measurements are compared with the laminar values and with three theoretical curves computed by Cumpsty & Head [93]. It is important to keep in mind that R and $R\theta$ have different physical meanings: $R\theta$ is related to the boundary layer properties, R characterizes the potential flow distribution around the leading edge.

The laminar and turbulent skin friction coefficients are plotted in figure 6.5. The measured turbulent values [93] are compared with two empirical relationships proposed by Poll [96] and Beckwith & Gallagher [97]:

$$C_f = \frac{0.0689}{R^{0.42}} \quad (\text{Poll}) \quad (6.12)$$

$$C_f = \frac{0.0646}{R^{0.4}} \quad (\text{Beckwith-Gallagher}) \quad (6.13)$$

For a fixed R , the ratio between the turbulent and laminar values is of the order of 2 to 3 only; this ratio is 3 to 4 times larger for flat plate boundary layers at a given value of the streamwise Reynolds number.

6.2. "Natural" Transition

The process of a "natural" (or "free") transition along the attachment line of a swept body is sketched on figure 6.2c. If there is no source of large disturbances at point A, we can guess that transition will be the result of the amplification of internalized small disturbances which are present, for instance, in the free stream. Pfenninger & Bacon [98] made hot wire measurements along the attachment line of a 45° swept wing. They observed the occurrence of regular, quasi sinusoidal oscillations in the form of modulated wave packets; as these waves packets are convected along the leading edge, their amplitude increases and turbulent spots (breakdown) eventually appear. In this case, a part of the leading edge is laminar, another part is transitional, and a third part is turbulent, figure 6.2c. Similar observations were reported by Poll [95], [99].

It is clear that these mechanisms present strong similarities with those observed in a flat plate boundary layer with a low free stream turbulence level. For this reason, it is possible to develop a linearized stability theory to obtain more quantitative information.

6.2.1. Linear theory

The basic mean flow is computed from the equations (6.7) to (6.10). A special class of small-amplitude disturbances, first introduced by Görtler [100] and Hämmerlin [101], is then superimposed on the laminar flow. These disturbances are of the form:

$$u' \sim Xu(y) \exp(\sigma Z) \exp[i(\alpha Z - \omega t)] \quad (6.14a)$$

$$(v', w', p') \sim (v(y), w(y), p(y)) \exp(\sigma Z) \exp[i(\alpha Z - \omega t)] \quad (6.14b)$$

These expressions represent periodic fluctuations of wavenumber α and frequency ω , growing or decaying in the spanwise direction Z , depending upon the sign of the amplification factor σ . There is no real justification for the X -dependence of the u' fluctuation : Görtler chose it for reasons of "mathematical feasibility" [100], and later investigators (Hall et al [102] for instance) also used this form, with little comment. However, the direct numerical simulations performed by Spalart (1988, [103]) supported this assumption, in the sense that infinitesimal disturbances of the form of equations (6.14a), (6.14b) are the most amplified ones and therefore the most relevant from a stability point of view.

Introducing (6.14a), (6.14b) into the Navier-Stokes equations and linearizing in u , v , w give an eigenvalue problem. By contrast with the Blasius flow problem, homogeneous, ordinary differential equations are obtained without using the parallel flow approximation. The computations performed by Hall et al [102] indicated that the critical Reynolds number $R\theta_{cr}$ is equal

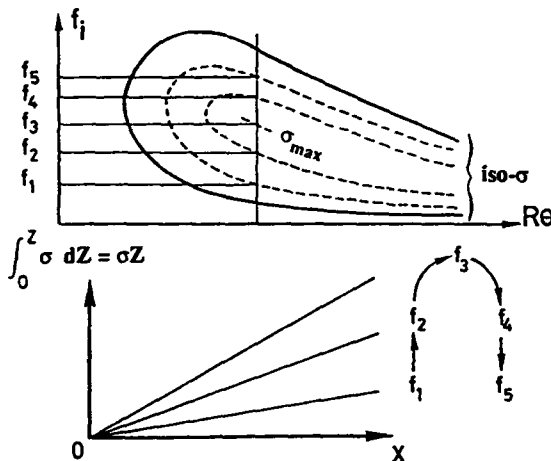


Fig. 6.6 Amplification rates of the attachment line laminar boundary layer

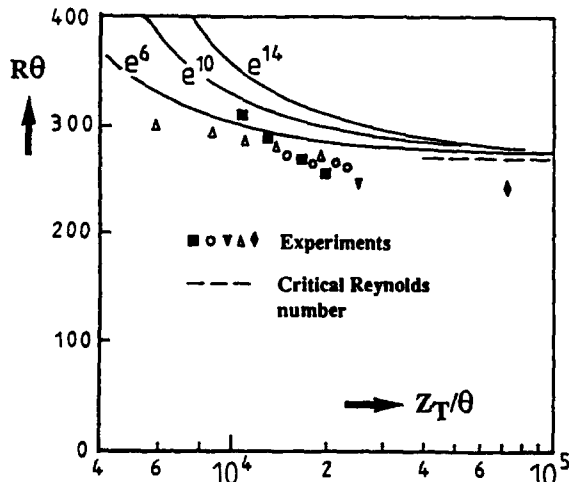


Fig. 6.7 "Free" transition Reynolds number along the attachment line [95]

to 236 ; this corresponds to $R\theta_{cr} = 583$, relation (6.11). The value of $R\theta_{cr}$ is somewhat larger than that of the Blasius flow, which is close to 200 : the attachment line profile is slightly more stable than the two-dimensional flat plate flow. As stated before, Pfenninger & Bacon [98] and Poll [99] observed naturally occurring disturbances along the attachment lines of different swept models. It was found that such disturbances existed above a critical value of $R\theta$ close to 230, in excellent agreement with the linear stability results.

For the sake of simplicity, let us assume now that the laminar boundary layer is uniform from its origin to transition, i.e. $R\theta$ is constant from point A of figure 6.2c to transition. In this case, the calculation of the total amplification rate A/A_0 of a given frequency is very simple. Since $R\theta$ does not depend on Z , A/A_0 is expressed by :

$$A/A_0 = \exp(\sigma Z) \quad (6.15)$$

where $Z = 0$ corresponds to point A. This means that, if we plot $\ln(A/A_0)$ as a function of Z , we obtain a straight line for each value of ω , as it is shown in figure 6.6. The envelope curve is reduced to the line associated with the most unstable frequency (the frequency for which σ is maximum). By applying the e^n rule, the transition location Z_T is :

$$Z_T = n/\sigma_{max} \quad (6.16)$$

Figure 6.7 presents the results of computations performed by Poll [95] for $n = 6, 10, 14$, together with experimental data. Theoretical results with $n = 6$ reflects fairly well the measured evolution. It must be pointed out that the critical Reynolds number $R\theta_{cr}$ computed by Poll is close to 270 (Hall et al [102] obtained $R\theta_{cr} = 236$). This is due to the fact that Poll assumed $U = V = 0$ so that the stability equations simply reduced to the classical Orr-Sommerfeld equation.

6.2.2. Effect of wall suction

It is easy to introduce the effect of wall suction into equations (6.7) to (6.10) by simply changing the boundary condition $V(0) = 0$ by $V(0) = K$, where K is the suction parameter ; it is defined as :

$$K = \frac{V_w}{\sqrt{kv}} = \frac{V_w}{W_e} \frac{R}{R} = \frac{V_w}{Q_{\infty} \sin \varphi} \quad (6.17)$$

where V_w is the transpiration velocity at the wall.

As mentioned in paragraph 5.3.1., suction acts in two ways. First, the viscous layer is thinned with a corresponding reduction in local Reynolds number ; this is shown in the upper part of figure 6.8, which gives the evolution of the ratio $R\theta/R$ as a function of K . The lower part of the same figure presents the variation of

the shape factor H of the streamwise mean velocity profile : H decreases when suction is applied. This explains the second, and more important, effect of surface suction, which is to establish a more stable flow. Hall et al [102] solved the linear stability equations for negative and positive values of K , corresponding to suction and blowing, respectively. Computed neutral curves are plotted in figure 6.9 for $K = -0.1, 0, 0.4$ and 0.8 . The evolution of the critical Reynolds number is given in figure 6.10. The strong stabilizing effect of suction is clear. On the contrary, as blowing creates an inflection point, the neutral curves with $K > 0$ are typical of an inflectional instability : the critical Reynolds number is low and the upper branch of the neutral curves becomes parallel to the horizontal axis.

To our knowledge, the only experimental investigation of the influence of suction on "natural" attachment line transition was conducted by Pfenninger & Bacon [98], who used a 45° swept wing equipped with closely spaced suction slots. However, it is not clear from the results whether the flow was stabilized or destabilized by the suction.

6.2.3. Non linear problems

When TS waves are observed in a two-dimensional flat plate flow, their frequencies usually correspond to those of the most amplified disturbances, i.e. the disturbances associated with the locally largest values of A/A_0 . In the stability diagram, the theoretical location of these frequencies is just below the upper branch of the neutral curve. Such a behaviour is no longer valid for the attachment line flow : the frequencies of natural disturbances measured by Pfenninger & Bacon [98] and by Poll [99] correspond to the lower branch of the

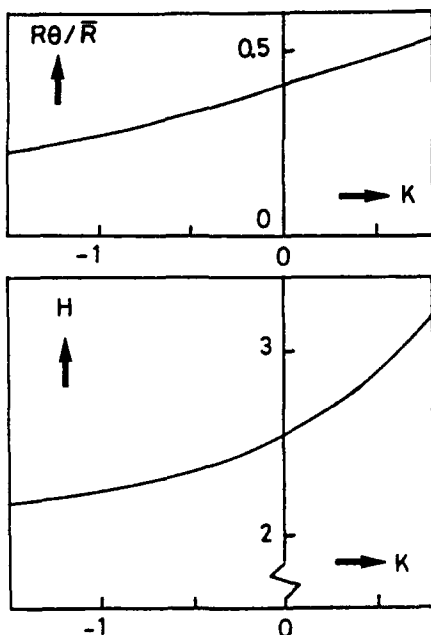


Fig. 6.8 Effect of suction on the momentum thickness Reynolds number and on the shape factor

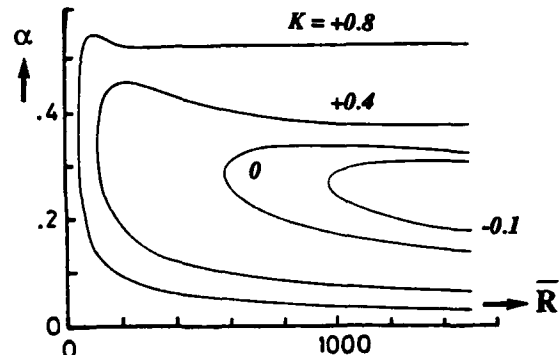


Fig. 6.9 Neutral curves for different values of the suction parameter K [102]

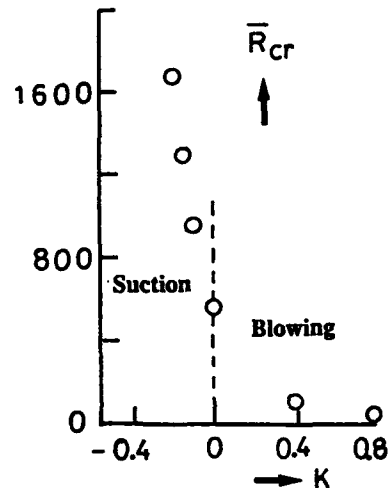


Fig. 6.10 The dependence of the critical Reynolds number on the suction parameter K [102]

neutral curve. Hall & Malik [104] tried to explain why the flow exhibits a preference for lower-branch modes by developing a weakly non linear approach based on the Stuart-Watson expansion procedure. This analysis is applied in the neighbourhood of a point on the neutral curve and it is assumed that the amplitude A of the disturbances depends on a slow time variable $\tau = \varepsilon t$, with $0 < \varepsilon \ll 1$. Keeping the non linear terms in the governing equations leads to a Landau-type equation :

$$\frac{1}{A} \frac{dA}{dt} = \sigma + \ell |A|^2 \quad (6.18)$$

Depending on the values of σ (temporal amplification rate) and ℓ (Landau coefficient), subcritical or supercritical bifurcations can be found. Hall & Malik demonstrated that finite-amplitude solutions bifurcate subcritically from the upper branch. Since these solutions are unstable, they would not correspond to an observable equilibrium state. To confirm this result, Hall & Malik [104] investigated

numerically the full non linear stability equations ; they found that the basic state might be non linearly unstable to sufficiently large finite-amplitude disturbances at wavenumbers that correspond to the upper branch and for Reynolds numbers subcritical to the linear limit. It must be noticed, however, that recent direct numerical simulations by Jimenez et al [105] did not support these results.

Even if the non linear stability of the attachment line flow is not fully understood, many experiments have shown that leading edge transition can occur at Reynolds numbers lower than the critical Reynolds number given by the linear theory. Pfenninger & Bacon [98] for instance placed a small wire 1 m upstream of the attachment line of their swept wing and parallel to it. This wire generated free stream fluctuations which induced large-amplitude disturbances in the boundary layer ; in this case, transition was observed for $R = 385$. Gaster [94] and Poll [95], among others, detected transition at Reynolds numbers significantly below the linear critical point by introducing roughness elements into the attachment line boundary layer. The next question is to know if there is a lower limit to the transition Reynolds number when very large disturbances affect the leading edge region ; in the next paragraph, which is devoted to the leading edge contamination problems, it will be shown that this limit effectively exists and that its value is fairly well known.

6.3. Leading Edge Contamination

Leading edge contamination is likely to occur when a swept wing is in contact with a solid surface (fuselage, wind tunnel wall ...). If the attachment line Reynolds number R is low, the boundary layer developing along the leading edge is laminar, see figure 6.2a ; however, as soon as R exceeds a critical value, the attachment line can be contaminated by the large turbulent structures coming from the wall at which the model is fixed, see figure 6.2b. This phenomenon, which is fully non linear, constitutes a typical example of "bypass" in the sense that the linear mechanisms which control "natural" transition do not play any role.

6.3.1. Historical background (see Poll [95])
 Leading edge contamination was first discovered in 1963 whilst Handley Page Limited (Great Britain) and Northrop Norair (United States) attempted to develop flight scale swept wing with a full chord laminar flow. The two groups observed that at the design conditions the boundary layer was turbulent from the leading edge, except near the wing tip where R was lower due to the wing taper. It was demonstrated that the source of trouble was turbulence propagating from the wing-body junction along the attachment line. As pointed out by Poll [95], "in retrospect there can be little doubt that the existence of leading edge contamination effect was largely responsible for the failure and ultimate cancellation of these early laminar flow projects."

Several series of experiments were then carried out in order to understand the mechanisms of leading edge contamination. Pfenninger (1965, [106]) conducted out flight tests on the 30° swept wing of the Northrop X-21A laminar flow aircraft. He discovered that for $R < 250$ ($R\theta < 100$), almost complete laminar flow could be obtained on the wing surface ; for $R > 250$, leading edge contamination occurred. Wind tunnel tests on swept models confirmed these results.

Gregory & Love (1965, [107]) also performed wind tunnel experiments on a swept airfoil. When large tripping devices were introduced into the attachment line boundary layer, complete turbulence was obtained for R between 235 and 243 ($R\theta$ between 95 and 98). By contaminating the leading edge by a turbulent boundary layer generated on a streamwise flat plate, transition occurred as R increased from 230 to 260 ($R\theta$ increasing from 93 to 105).

Flight experiments were carried out on a fin vertically mounted on the fuselage of a Lancaster aircraft (Gaster, [94]). The first turbulent spots were observed along the leading edge for $R > 218$ ($R\theta > 88$), the fully turbulent state being reached for $R > 240$ ($R\theta > 96$). Gaster undertook some experimental work in a low speed wind tunnel at the College of Aeronautics, Cranfield. He placed large trip wires on the leading edge of a swept model and found that at a fixed distance from the wires, the attachment line flow was "half-way" between laminar and turbulent for $R > 257$ ($R\theta > 104$). Other results obtained by Gaster will be described later on.

The problem was also studied by Cumpsty & Head (1967, [93]) who used a swept model in a subsonic wind tunnel. They measured laminar and turbulent mean velocity profiles on the leading edge and analyzed the effect of large tripping devices along the attachment line : the turbulent spots generated by these devices were damped for $R < 245$ ($R\theta < 99$) and the leading edge was fully turbulent for $R > 280$ ($R\theta > 114$). The same model was used by Poll (1978, [99]) who conducted careful experiments dealing with "natural" transition and with attachment line contamination. His measurements were in agreement with the previous results.

From these experiments, it can be concluded that large roughness elements have the same effect than a turbulent boundary layer developing along the surface on which the wing is fixed ; for $R < 250$ or $R\theta < 100$ (mean values), the turbulent structures generated by these sources of gross disturbances are damped as they are convected along the leading edge. If R is greater than 250, they become self-sustaining ; they develop and the

whole wing can be contaminated. Let us observe that the value $R = 250$ is much lower than that of the critical Reynolds number of the attachment line flow, which is close to 600. This demonstrates that attachment line contamination cannot be described by the linear stability theory.

Since the pioneering studies which were described above, many fundamental work has been devoted to the leading edge contamination problems, see Poll [95], [96], [99], Hardy [108], Arnal & Juillen [109], [110] for instance. This latter work will be described in the next paragraph to give details of the attachment line contamination mechanisms. As these mechanisms are strongly non linear, direct numerical simulations are of great interest ; Spalart [103] solved the full three-dimensional, time-dependent Navier-Stokes equations for decreasing values of R . Starting from a large value of

R for which the attachment line flow was turbulent, he found that the turbulent structures disappeared for R between 250 and 300, in agreement with the simple empirical criterion first proposed by Pfenninger. The validity of this criterion was also checked during flight tests performed on the Jet Star aircraft [91] or the VFW 614/ATTAS aircraft [40] for example.

6.3.2. Examples of experimental results (Arnal & Juillen, [109], [110])

The experiments were carried out in the F1 wind tunnel at Le Fauga-Mauzac Center. The wind tunnel speed can be varied from 0 to about 100 ms^{-1} . The stagnation temperature is the ambient temperature, but the stagnation pressure can be prescribed between 1 and 3 bars. Figure 6.11 shows the shape of the airfoil as well as a sketch of the experimental arrangement.

The model is a RA16SC1 airfoil ; the chord C normal to the leading edge is constant and equal to 0.5 m. The wing is directly mounted on the wind tunnel floor ; the thickness of the floor turbulent boundary layer is around 10 cm at the wing-wall junction. With a 40° sweep

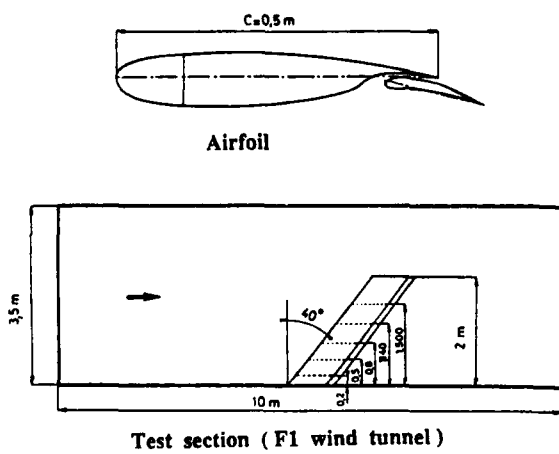


Fig. 6.11 Experimental setup

angle, the tip of the model is 2 m above the floor. Eight rows of static pressure taps are distributed along the span. Figure 6.11 shows the location of the rows n° 2, 4, 5, 6 and 7 which were used during the experiments. Transition was detected with hot films glued on the model.

In this paragraph, we consider a configuration corresponding to $\varphi = 40^\circ$, $\alpha = 10^\circ$, $P_i = 1 \text{ bar}$ and different wind tunnel speeds. Figure 6.12 gives distributions of the pressure coefficient K_p as a function of X/C . Let us recall that X is the curvilinear abscissa measured along the airfoil surface from the geometrical leading edge, in the direction normal to it. The positive and negative values of X refer to the upper side and to the lower side, respectively. The point where K_p is maximum corresponds to the location of the attachment line.

These measurements and the infinite swept wing assumption make it possible to compute the chordwise evolution of the free stream velocity U_e normal to the wing span. The results obtained around the leading edge ($-0.2 < X/C < 0.05$) are plotted in figure 6.13. The velocities on the lower side are multiplied by -1 in order to determine the location of the attachment line ($U_e = 0$). The data obtained at different spanwise positions do not collapse onto a single curve : this means that the abscissa X_p of the attachment line varies slightly along the span direction (hatched area).

The upper part of figure 6.14 shows the location of four hot films labeled A, B, C and D, which were glued on the lower side of the wing, at one or two per cent chord from the attachment line. The wind tunnel speed was progressively increased in order to determine accurately the leading edge contamination onset. The lower part of the same figure presents typical hot film signals recorded for $Q_\infty = 35 \text{ ms}^{-1}$; these signals represent the wall shear stress fluctuations τ_w . The hot film A exhibits

turbulent fluctuations which are generated by the turbulent boundary layer in which the sensor is embedded, but the other three signals are of the laminar type. For $Q_\infty = 61 \text{ ms}^{-1}$ (figure 6.15), turbulent structures are observed on film B. The number of these "spots" decreases from film B to film C, then remains constant. The signals delivered by films C and D are essentially characterized by the spreading of the spots which develop along the leading edge ; it is the beginning of leading edge contamination. When the wind tunnel speed increases from 61 to 64 ms^{-1} , a comparison between figures 6.15 and 6.16 reveals a rapid increase in the number of turbulent spots. For $Q_\infty = 95 \text{ ms}^{-1}$, all signals have a fully turbulent character.

For computing the R parameter at leading edge contamination onset, the main problem lies in the estimate of $k = dU_e/dX$ at $X = X_p$. Figure 6.13 illustrates the difficulty to obtain an accurate

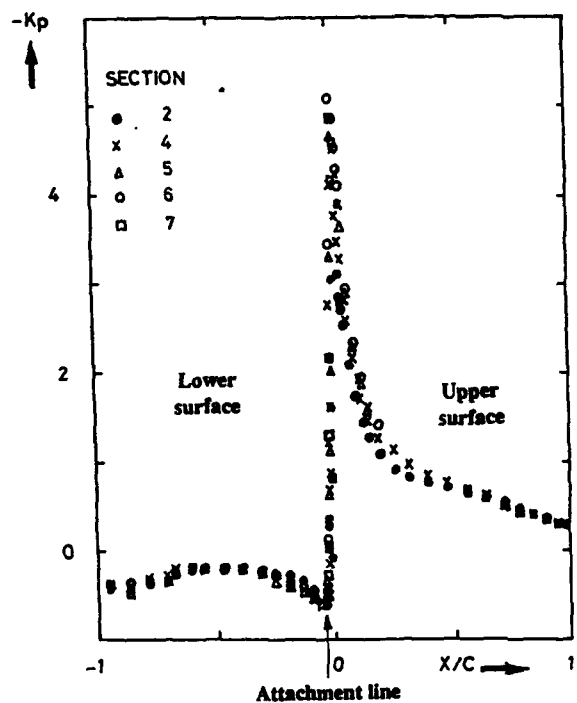


Fig. 6.12 Pressure coefficient distribution, $\phi = 40^\circ$, $\alpha = 10^\circ$, $P_1 = 1$ bar, $Q_\infty = 60 \text{ ms}^{-1}$

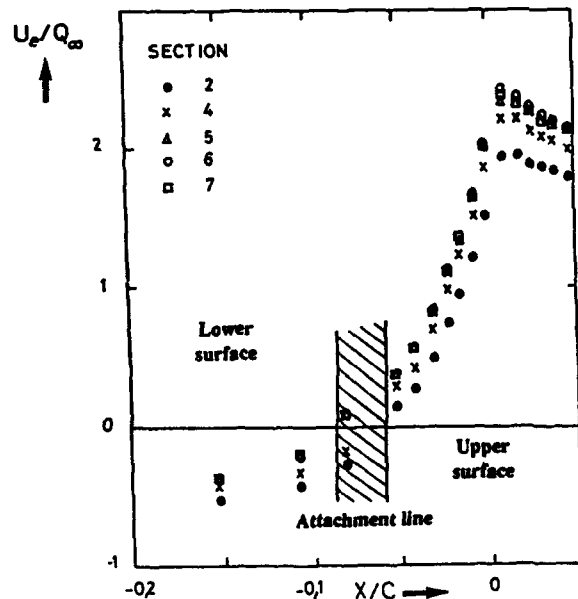


Fig. 6.13 Evolution of the mean velocity component normal to the leading edge. Same conditions as in figure 6.12

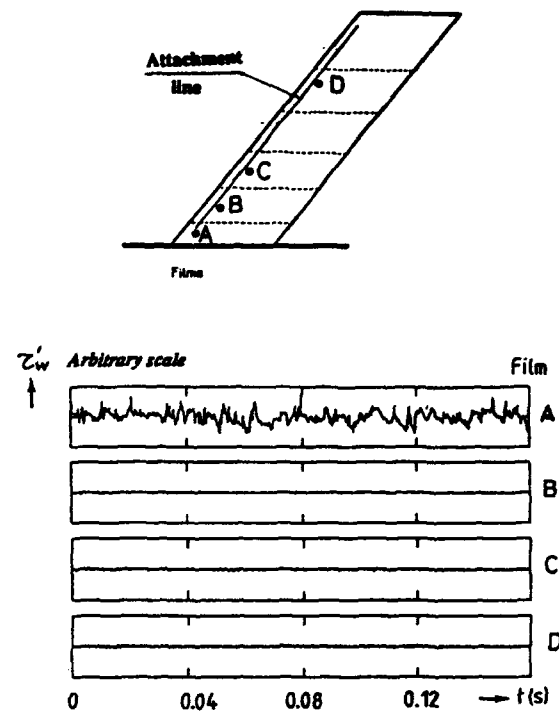


Fig. 6.14 Hot films outputs ($Q_\infty = 35 \text{ ms}^{-1}$)

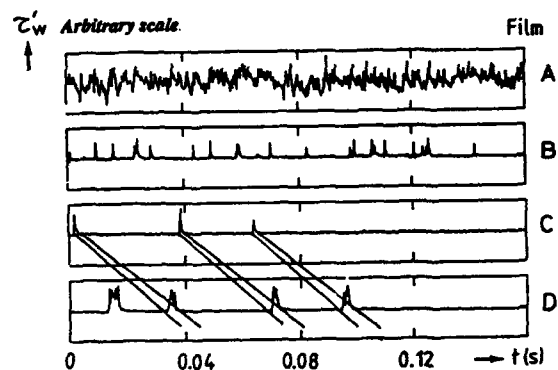


Fig. 6.15 Hot films outputs ($Q_\infty = 61 \text{ ms}^{-1}$)

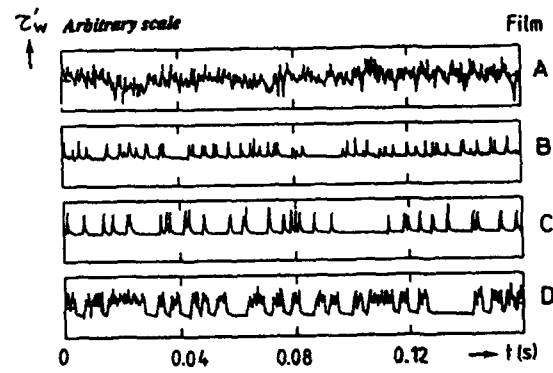


Fig. 6.16 Hot films outputs ($Q_\infty = 64 \text{ ms}^{-1}$)

measurement of the pressure gradient around the leading edge. The experimental data were at first smoothed and the value of k was taken as the arithmetic average of the values corresponding to the five rows of static pressure taps. The result is that leading edge contamination appears for $R = 251 \pm 11$, and that the leading edge is fully turbulent for $R = 318 \pm 22$. These values are in good agreement with those given by other investigators.

When the flow is characterized by the successive appearance of turbulent spots and of laminar regions, an important parameter is the intermittency factor γ , which represents the fraction of the total time where the flow is turbulent. The spanwise evolution of γ was computed for the present experiments at several wind tunnel speeds. The results are plotted on figure 6.17, where $Z = 0$ corresponds to the junction between the wing and the test section floor. At the location of the first hot film, γ is always equal to 1 (turbulent boundary layer of the floor). It decreases at first in the spanwise direction, reaches a minimum, and then increases up to the wing tip. These results reflect the trends observed on the hot film traces. The interpretation is the following: R and $R\theta$ increase from the wing-floor junction up to a certain distance where the infinite swept wing relations can be applied. In the regions where dy/dZ is negative, the local Reynolds number $R\theta$ is lower than the critical value of 100. The intermittency factor starts to increase as soon as this critical value is exceeded.

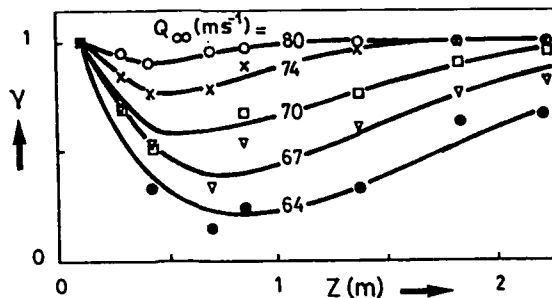


Fig. 6.17 Intermittency factor along the attachment line

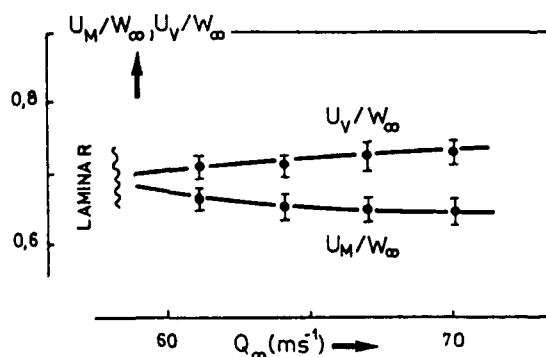


Fig. 6.18 Propagation velocities of the leading and trailing edges of the turbulent spots

In the regions where the size of the turbulent spots increases, it is possible to measure the convection velocities U_M and U_V of their upstream and downstream fronts, respectively (the words "upstream" and "downstream" are defined relative to the direction of increasing values of Z). Figure 6.15 gives examples of such measurements for three spots convected along the attachment line between films C and D. The results are given in figure 6.18: the convection velocities U_M/W_∞ and U_V/W_∞ are plotted as functions of Q_∞ . The streamwise spreading of the turbulent spots is clearly explained by the fact that the downstream fronts propagate faster than the upstream fronts, even if both velocities are not very different. They are close to $0.7 W_\infty$, a value which is in good agreement with previous measurements performed by Gaster [94], who studied the development of artificially created spots along the leading edge of a symmetrical airfoil. Similar results were also obtained by Hardy [108] on tapered wings.

6.3.3. Effect of wing taper

On a tapered wing, the leading edge radius r decreases from the root to the tip. Relations (6.4) and (6.5) indicate that R varies as \sqrt{r} for circular and elliptic cylinders. By assuming that this trend remains roughly the same for any tapered wing, R also decreases as the distance from the wing-fuselage junction increases. Near the root, R is usually larger than 250, so that the attachment line flow is at first turbulent. However, if R becomes low enough, turbulence is no longer self-sustaining and a "reverse transition" is likely to occur. This was verified by Poll & Paisley [111] who conducted wind tunnel experiments on a tapered model. It was found that turbulence completely vanishes when the local value of R becomes lower than 230. This value is nearly identical to that obtained for leading edge contamination on an "infinite" swept wing of constant cross section.

Poll & Paisley performed a theoretical analysis of the attachment line flow on a typical wing, the dimensions

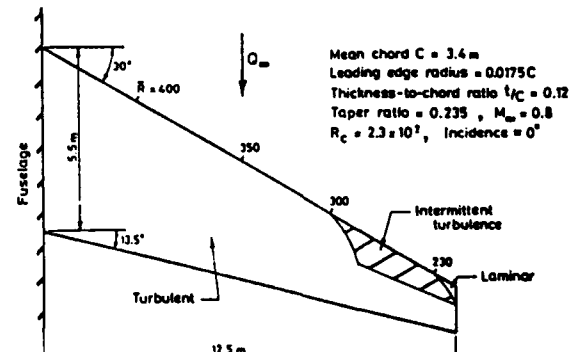


Fig. 6.19 A typical medium sized transport aircraft wing in the cruise condition [111]

of which are broadly similar to those of the McDonnell Douglas DC-9, figure 6.19 (from [111]). In the cruise conditions (Mach number = 0.8, altitude = 10 km), the value of R in the root region is about 435. At a distance of 10 meters from the wing-fuselage junction, the initially turbulent boundary layer is expected to become intermittent as R drops below approximately 300 (this is the minimum value for *fully turbulent* flow on the leading edge of an "infinite" swept wing, see paragraph 6.3.2.). A completely laminar flow is achieved when R drops below 230, and this point is located some 13.6 m from the root. This means that only the last 0.8 m of the 14.4 m attachment line will be laminar. Flight conditions on larger aircrafts, like the A300-B Airbus, the Boeing 727, the McDonnell Douglas DC-10 or the Boeing 747, are expected to produce full-span turbulent attachment flow.

6.3.4. How to prevent leading edge contamination?

Since the effect of taper is not sufficient to produce "reverse transitions" for many practical applications, it is necessary to develop specific tools to delay the onset of leading edge contamination. This is the first problem to solve for maintaining laminar flow on a wing: if the

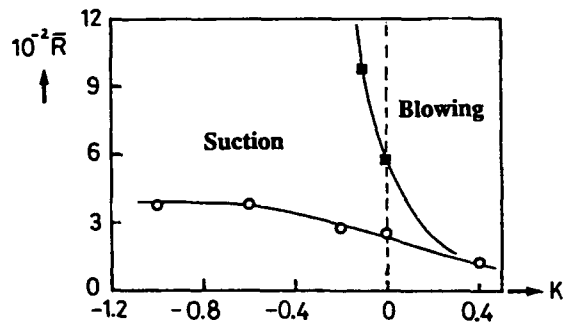


Fig. 6.20 Critical Reynolds number and leading edge contamination Reynolds numbers as functions of the suction parameter [103]

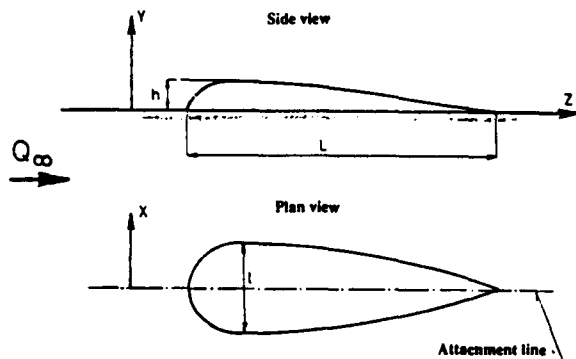


Fig. 6.21 Typical shape of a Gaster bump

attachment line boundary layer is turbulent, turbulence will spread over the whole wing and the benefits of NLF, LFC and HLFC systems will be lost.

As R is proportional to $(r \sin\phi \tan\phi)^{1/2}$, a first idea is to reduce the leading edge radius and/or the sweep angle near the root. Technological problems can make this solution difficult to apply.

Spalart [103] investigated the effects of suction on leading edge contamination by numerically solving the full Navier-Stokes equations. In figure 6.20, the value of R for which leading edge contamination appears is plotted as a function of the suction parameter K (open symbols). When K is lower than approximately -1, the curve seems to reach an asymptotic value close to 400. The critical Reynolds number given by the linear theory is also shown for comparison (full symbols). It is clear that suction has a much weaker effect on non linear phenomena such as leading edge contamination than on the linear stability of the laminar boundary layer. "Given only the linear stability results, one would overestimate the beneficial effects of suction on a contaminated boundary layer" [103]. To our knowledge, the experimental validation of these computations has not yet been done.

A successful device to prevent leading edge contamination is the "Gaster bump" [94]. This consists of a small fairing which is attached to the leading edge close to the wing root; it is shaped in such a way that the contaminated turbulent boundary layer is brought to rest at a stagnation point on the upstream side whilst a "clean" laminar boundary layer is generated on the downstream side (figure 6.21). This device enables to delay the onset of leading edge contamination up to values of R of the order of 350 to 400. Gaster bumps were used during flight experiments, for instance on the Falcon 50 aircraft and on the Jet Star aircraft. In the latter tests, the bump was combined with a leading edge "notch".

Quite recently, Seyfang [112] tested several passive devices aimed at restoring laminar flow on a contaminated attachment line (step-up, step-down, square trips, grooves ...). In all cases, the objective is to create a stagnation point from which a laminar boundary layer starts to develop. The main problem is to optimize the dimensions of these devices in order to avoid boundary layer tripping effects.

6.4. Relaminarisation in a Negative Pressure Gradient

In two-dimensional flows, the reversion of a turbulent boundary layer to a laminar one by the imposition of a large negative pressure gradient is a well established phenomenon, and several relaminarisation criteria have been proposed. For instance, Moretti & Kays [113] and Launder & Jones [114] used the acceleration parameter K defined as :

$$\bar{K} = \frac{v}{U_e^2} \frac{dU_e}{dx} \quad (6.19)$$

The experiments indicate that a reversion from turbulent to laminar flow might begin when \bar{K} exceeds about 10^{-6} , but a value of \bar{K} larger than $5 \cdot 10^{-6}$ is needed for obtaining a complete relaminarisation. Direct numerical simulations by Spalart confirmed these values [115].

In three-dimensional flows, it is assumed that values of K of the same order would be relevant if \bar{K} is evaluated from the velocity and its derivative along the external streamline, i.e. :

$$\bar{K} = \frac{v}{2} \frac{du_e}{dx} \sim \frac{1}{Q_\infty} \text{ for a given wing} \quad (6.20)$$

On a swept wing, the value of \bar{K} tends to reach a maximum very near the attachment line and then decreases rapidly. This means that only turbulence produced by leading edge contamination is likely to be subject to relaminarisation. Poll [95] concluded from analytical computations that relaminarisation cannot be observed on a conventional wing having sections with noses of approximately elliptic form if the angle of attack is low ; under these conditions, K is always

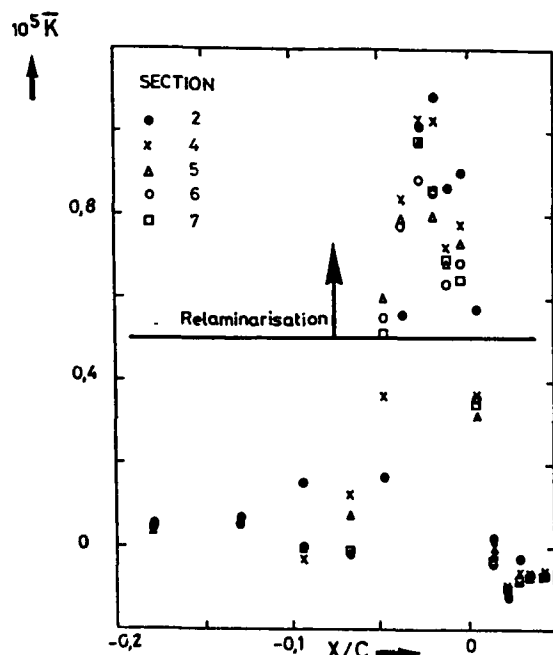


Fig. 6.22 Acceleration parameter \bar{K} - Same conditions as in figure 6.12

much less than $5 \cdot 10^{-6}$ when leading edge contamination occurs.

This conclusion is not necessarily true, however, for large angles of attack ; in this case, a pronounced velocity peak is observed on the suction side close to the leading edge, so that the acceleration parameter attains very large values. For example, the experiments performed in the F1 wind tunnel (paragraph 6.3.2.) showed that a sharp suction peak was present near the attachment line for an angle of attack of 10° , see figure 6.12. Figure 6.13 indicates that the streamwise flow acceleration is stronger in the negative pressure gradient region than at the attachment line location. The corresponding variation of K is plotted in figure 6.22 for a wind tunnel speed of 60 ms^{-1} (this is approximately the velocity for which leading edge contamination appears). The maximum value of K is about 10^{-5} , i.e. two times the minimum value which is required for relaminarisation. Hot films signals recorded in the highly accelerated region [109], [110], showed that the turbulent spots generated by leading edge contamination were damped and practically disappeared ; however, as the hot films were glued on the surface, it was not clear that reversion to laminar flow was also achieved in the outer part of the boundary layer. Wall turbulence was restored in the separation bubble downstream of the suction peak. Similar results were reported by Hardy [108] for wind tunnel experiments and by Bertelrud & Nordstrom [116] for flight tests.

6.5. Concluding Remark : the Minimum Reynolds Number for Turbulence

Some of the results reported in this Section have demonstrated that boundary layers below a certain Reynolds number cannot sustain intrinsic self-energizing turbulent motions on the scale of the local shear layer thickness. This Reynolds number is referred to as the "minimum Reynolds number for turbulence", R_{\min} (Morkovin, 1984 [5]). Two examples were given above :

- turbulence cannot develop along the leading edge of a swept wing as soon as R is below 250 : this is the value of R_{\min} for the attachment line flow ;
- turbulence is damped (at least near the wall) in a highly accelerated flow ; the value of R_{\min} is that which corresponds to $K \sim 5 \cdot 10^{-6}$.

R_{\min} is usually lower than the linear critical Reynolds number R_{cr} . Its value is known for a few types of flows only ; it depends on many parameters, such as pressure gradient, compressibility, three-dimensionality ... It can be considered as the lower limit for bypass-induced transitions ; in other words, the earliest possible transition, important in design, occurs at R_{\min} [5].

7. OTHER FACTORS AFFECTING TRANSITION IN FLIGHT CONDITIONS

Although modern manufacturing techniques can provide smooth surfaces which are compatible with natural laminar flow, many surface imperfections are unavoidable. These imperfections include waviness and bulges, steps and gaps at structural junctions, and three-dimensional roughness elements such as screws or rivets. Other discontinuities arise from leading edge panels or access panels ... In addition, environmental factors such as ice crystals, rain, insects, dirt ... can create localized surface irregularities. Because some of these imperfections cannot be avoided, it is necessary to study their effects on transition and to develop calculation methods or criteria in order to estimate these effects.

From a theoretical point of view, the linear stability theory can be used to analyze the influence of *two-dimensional* irregularities such as bumps, gaps or steps of "infinite" span located normal to the mean flow ; in this case, the surface imperfections do not generate any "new" disturbances, but they amplify existing (or potentially existing) TS waves according to the linear theory. Their main effect is to locally modify the pressure field in such a way that the boundary layer instability is enhanced. By contrast, *three-dimensional* roughness elements such as rivets, insects or ice crystals generate streamwise vortices which trigger transition through essentially non linear mechanisms (bypass). The admissible size of such protuberances can be estimated from empirical correlations only.

7.1. Surface Imperfections and Vibrations

7.1.1. Bulges and hollows (waviness)

A typical example of stability computations around a small two-dimensional bulge is presented in figure 7.1 [117]. These calculations are related to experimental data analyzed by Fage (1943, [118]). The upper part of the figure shows the geometrical shape of the bump, see relation (7.1) below. The mean flow field was at first computed by solving the steady Navier-Stokes equations. The theoretical evolutions of the pressure coefficient K_p and of the skin friction coefficient are plotted in figure 7.1. When the bump is approached, the pressure increases slightly and then exhibits a strong decrease in the forward part of the waviness ; it decreases again in the rear part of the bump, so that the laminar flow is close to separation. The linear stability properties of the mean flow are then computed in order to obtain the total amplification rates of the most unstable frequencies. The lower part of figure 7.1 indicates that the most important effect of the bulge is to amplify TS waves in the decelerated region. The e^n method gives an estimate of the transition location which is in acceptable agreement with the experiments. Similar computations were carried out by Cebeci & Egan [119] and by Nayfeh et al [120].

Because such calculations are rather difficult to handle, empirical criteria have been developed for practical purposes.

Fage [118] analyzed wind tunnel experiments performed by Walker & Greening to determine the effect of two-dimensional bulges and hollows on transition. The bulges and hollows were mounted on a smooth flat plate and could be described by the following relationships :

$$\eta = h' \left[1 - 12 \left(\frac{\xi}{\lambda} \right)^2 - 16 \left(\frac{\xi}{\lambda} \right)^3 \right] \text{ for } -\frac{\lambda}{2} < \xi < 0 \quad (7.1)$$

$$\eta = h' \left[1 - 12 \left(\frac{\xi}{\lambda} \right)^2 + 16 \left(\frac{\xi}{\lambda} \right)^3 \right] \text{ for } 0 < \xi < \frac{\lambda}{2}$$

η and ξ are defined on figure 7.2a. λ is the length of the deformation. The height h' is positive for a bulge and negative for a hollow. The effects of compressibility and sweep were not studied in these experiments.

Fage correlated the experimental data by the following criterion :

$$\frac{h}{\lambda} = 9 \cdot 10^6 \left(\frac{U_e X_T}{v} \right)^{-3/2} \left(\frac{\lambda}{X_T} \right)^{1/2} \quad (7.2)$$

which can be more conveniently written :

$$\frac{h}{\lambda} = 9 \cdot 10^6 \left(\frac{U_e X_T}{v} \right)^{-3/2} \left(\frac{X_T}{\lambda} \right)^{1/2} \quad (7.3)$$

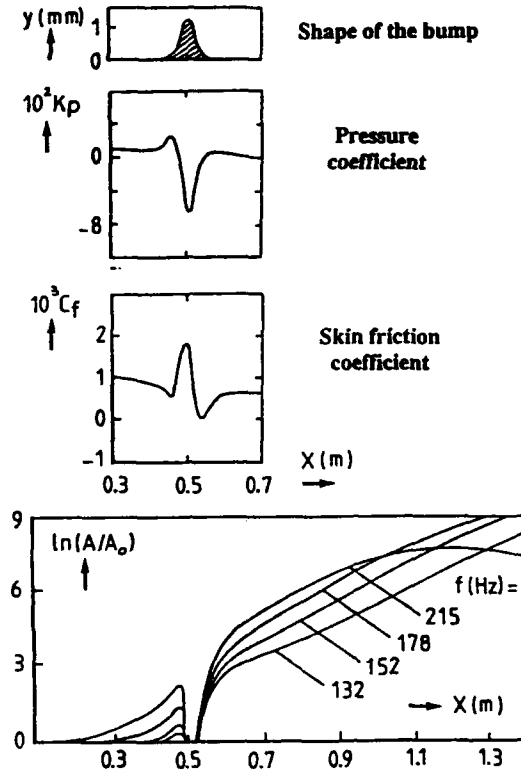


Fig. 7.1 Navier-Stokes and stability computations around a two-dimensional bump on a flat plate - $U_e = 21.15 \text{ ms}^{-1}$

h , B and X_T are given in ft. X_T is the surface length to transition, U_e represents the boundary layer edge velocity (in ft/sec) at the location of the center of the waviness for the undistorted surface.

Another waviness criterion was proposed by Carmichael [121] for sinusoidal bulges, the shape of which is sketched in figure 7.2b. This correlation includes compressibility and sweep angle effects; it is given by :

$$\frac{h}{\lambda} = \left(\frac{59000 C \cos^2 \phi}{\lambda R_c^{1.5}} \right)^{0.5} \quad (7.4)$$

h is the total wave amplitude, which differs from the height h' used by Fage; it is reasonable to assume that $h \approx 2h'$. λ , C , ϕ and R_c represent the wavelength, the streamwise chord, the leading edge sweep angle and the chord Reynolds number, respectively. When the flow parameters and λ are specified, relation (7.4) gives the allowable waviness amplitude h , i.e. the maximum amplitude which does not strongly modify the transition

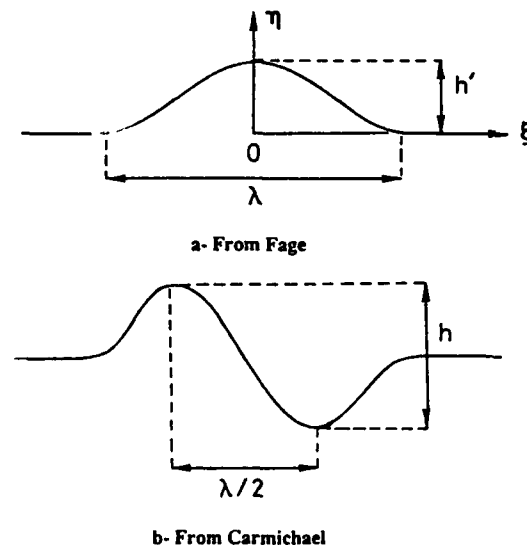


Fig. 7.2 Shapes of the bumps studied by Fage and Carmichael

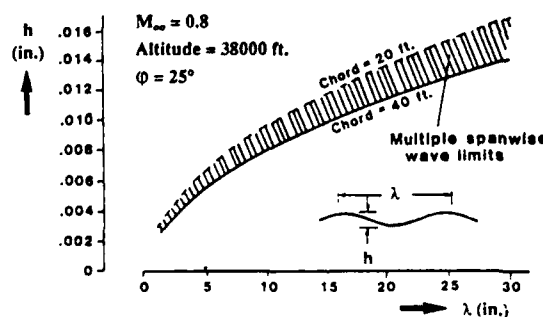


Fig. 7.3 Typical permissible surface waviness [82]

location. This correlation was deduced from experimental results (wind tunnel and flight) for waves located more than 25 percent chord downstream of the leading edge, in regions of flow acceleration. As Fage's criterion is valid for zero pressure gradient flows only, h' is usually much smaller than $h/2$.

Relation (7.4) shows also that the sweep angle is slightly destabilizing. For typical flight conditions, the allowable waviness is reduced by about 10 percent from $\phi = 0^\circ$ to $\phi = 25^\circ$ [122]. On the other side, the permissible amplitude decreases as the wavelength decreases, as it can be seen on figure 7.3 [82].

Carmichael suggested that the values of h/λ from equation (7.4) be multiplied by a factor $\alpha = 1/3$ to estimate tolerances for multiple waves parallel to the wing span. This value is conservative in the sense that the experimental data analyzed by Carmichael covered a range of values between $1/3$ and $3/4$, depending on the spacing of the waves. Holmes et al [122] stated that "most waviness observed on modern airframe surfaces typically consists of only one or two waves, widely spaced, at major structural joints", so that α is certainly close to 1. For chordwise waves, it was suggested to use $\alpha = 2$, i.e. chordwise bulges have less effect than spanwise bulges.

Holmes et al [123] performed extensive flight experiments on several airplanes at chord Reynolds numbers representative of business transport airplanes, for free stream Mach numbers between 0.1 and 0.7. The lifting and non lifting surfaces tested were similar to modern production airframes. The measured wave amplitude was generally smaller than the allowable maximum height computed from relation (7.4).

However, one has to keep in mind that Carmichael's criterion was originally derived for airfoils with a maximum local Mach number of about 1.04. On supercritical airfoils, the supersonic flow region is more extensive; the amplitude of the pressure peak increases but compressibility reduces the growth rates for TS waves. It is not clear which effect dominates [32]. Stability computations associated with the e^n method could provide us with fundamental information for improving the empirical criteria described above.

7.1.2. Steps and gaps

This subsection deals with boundary layer tripping by backward-facing steps, forward-facing steps and gaps, which constitute imperfections of major practical interest for airframe surfaces. The common feature of these imperfections is to produce localized boundary layer separations which strongly increase the growth rates of the unstable waves. The details of the instability mechanisms can be studied by direct numerical simulations, see [124] for instance, and the transition location can be estimated from the e^n method. However, as for two-dimensional bulges or hollows, simple transition criteria are usually used; most of these empirical correlations come from the X-21 experiments [125].

a-Gaps - Let us consider at first two-dimensional rectangular gaps normal to a two-dimensional laminar mean flow, figure 7.4a. h and b denote the depth and the width of the cavity, respectively. Sinha et al [126] studied experimentally the complex recirculating flow inside the cavity. The main feature is that for $h/b > 0.1$, a single elongated eddy can be observed; deeper cavities ($h/b > 1.5$) are characterized by several laminar vortices rolling one above the other.

To estimate the critical value of the width b which moves the transition onset towards the gap, a simple criterion was proposed [125] :

$$R_b = \frac{U_\infty b}{v} = 15000 \quad (7.5)$$

Olive & Blanchard [127] performed low speed wind tunnel experiments for gaps on a flat plate. The results plotted on figure 7.5 show the combinations between h and b (made dimensionless with the local displacement thickness) for which transition is detected immediately downstream of the cavity. As the displacement thickness Reynolds number is close to 860, (7.5) reduces to :

$$b = 17.5 \delta_1 \quad (7.6)$$

for this particular case.

The corresponding vertical line is also shown in figure 7.5. The agreement with the experimental data is reasonably good for $h/\delta_1 > 5$, but for smaller values of

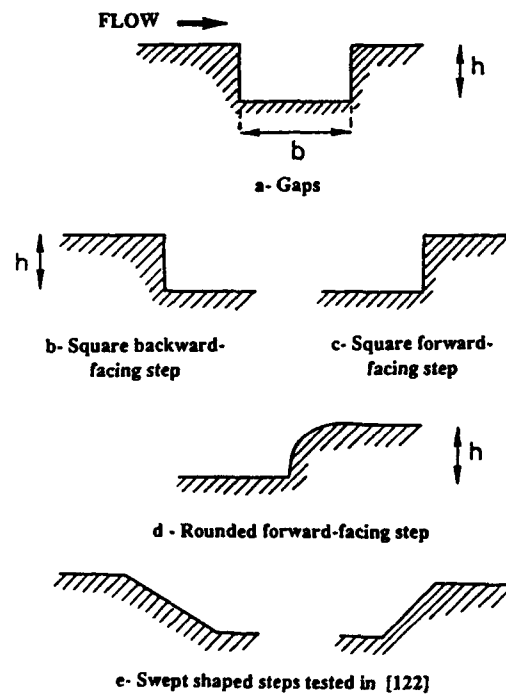


Fig. 7.4 Gaps, backward- and forward facing steps

this ratio, the measurements reveal a rather strong influence of the gap depth, which is not accounted for by relation (7.5).

For gaps aligned with the mean flow, it is recommended to divide the critical width deduced from (7.5) by a factor 7, i.e. streamwise gaps are much more efficient than spanwise gaps for boundary layer tripping and must be avoided. On the other side, a limited amount of experimental data (Juillen & Arnal, [128]) have shown that for gaps parallel to the leading edge of a swept wing, the critical value of R_b is also reduced; in addition to the (possible) role of the crossflow velocity component, this behaviour could be explained by the fact that the external streamline was not perpendicular to the gaps.

b-Backward- and forward-facing steps - If a square step (figures 7.4b, 7.4c) is placed in a two-dimensional mean flow, the allowable height h is given by [10] :

$$R_h = \frac{U_\infty h}{v} = 900 \text{ (backward-facing step)} \quad (7.7)$$

$$R_h = \frac{U_\infty h}{v} = 1800 \text{ (forward-facing step)}$$

This shows that the laminar flow is more sensitive to backward-facing than forward-facing steps, because the extent of the separated flow is larger in the first case. Some experiments [129] have demonstrated that transition caused by a backward-facing step can be delayed if suction is applied in the reattachment region.

Holmes et al [122] reported flight experiments with artificial forward-facing steps located at the 5-percent chord location on the upper surface of an unswept glove, in a slightly favourable pressure gradient. Steps of two different shapes were tested: one was a square step, the other a rounded step (figure 7.4d) with a radius approximately equal to the step height. For $R_h = 2700$, transition occurred at the square step (in agreement with (7.7)) and far downstream from the rounded step, i.e. the tolerances for a rounded step are at least 50 percent larger than for a square step.

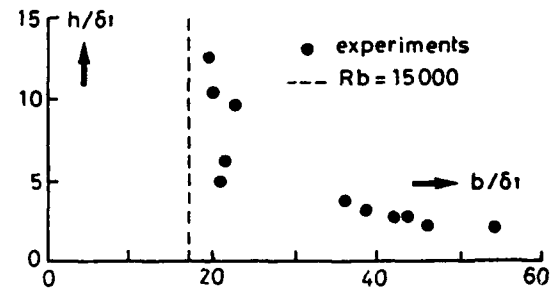


Fig. 7.5 Boundary layer tripping by two-dimensional gaps

Other flight experiments were conducted with steps attached in the glove at several sweep angles. Up to 45° of sweep relative to the free stream in *two-dimensional* mean flows, steps shaped as shown in Figure 7.4e did not cause transition up to $R_h = 4000$ [122]. However, the allowable sizes for steps placed in *three-dimensional* mean flows are not known.

To summarize these results, figure 7.6 gives the variations of permissible step heights and gap widths for a range of cruise altitudes at a free stream Mach number equal to 0.7 (from Holmes et al [122]). When the altitude increases, the unit Reynolds number decreases and the tolerances increase. A shortcoming of the previous criteria is that they do not take into account the chordwise location of the surface imperfection; in fact, these correlations are only valid for rather low Reynolds numbers, for example not too far from the leading edge of a wing.

7.1.3. Three-dimensional irregularities

Incorrectly installed rivets constitute a typical example of three-dimensional irregularities linked to manufacturing tolerances. Other three-dimensional roughness elements can be randomly created on aircraft wings due to environmental factors such as insects or dirt (see paragraph 7.2). The common feature of these protuberances is that their height is of the same order as their spanwise extent. As a consequence, the transition phenomena involved with three-dimensional irregularities are completely different from those involved with two-dimensional roughness elements for which the ratio width/height is very large.

For *isolated* three-dimensional roughness elements of height k , it is usual to consider a characteristic Reynolds number $R_k = U_k k / v_k$, where U_k and v_k denote the mean velocity and the kinematic viscosity at the altitude $y = k$, these values being computed in the undisturbed flow. When a protuberance of increasing size is introduced into a *two-dimensional* laminar boundary layer, the transition location is at first unaffected;

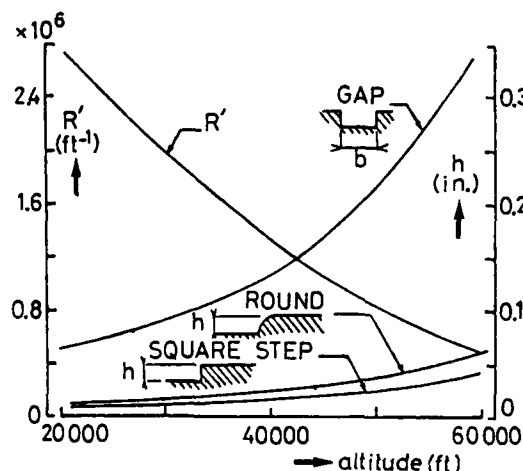


Fig. 7.6 Allowable step heights and gap widths for a range of cruise altitudes at $M_\infty = 0.7$ [122]. R' is the unit Reynolds number

figure 7.7 [130] shows the existence of two sets of streamwise vortices downstream of a cylinder perpendicular to a flat plate; one is a pair of spiral filaments close behind the roughness, the other is a horseshoe vortex wrapped around the cylinder. If R_k is low enough, these vortices are damped and disappear some distance downstream of the roughness element. When R_k increases and exceeds some critical value, transition moves rapidly forward: a turbulence wedge is formed, the vertex of which is located close to the protuberance. The turbulence wedge comprises a fully turbulent core separated from the surrounding laminar flow by edges of intermittent flow. Typical values of the vertex angle range from 10 to 15° . The existence of the turbulence wedge implies that the roughness element is placed at a Reynolds number larger than the minimum Reynolds number for turbulence.

Although no satisfactory explanation has yet been offered for this critical behaviour, it is often assumed that the critical value of R_k for which transition moves up to the roughness element depends essentially on the ratio d/k , where d is a measure of the spanwise or chordwise extent of the protuberance; for circular cylinders normal to the wall, d is the diameter. This criterion is plotted on figure 7.8 (Von Doenhoff & Braslow, [131]). The critical value of R_k is of the order of 500-600 for $d/k = 1$ (spheres). Some typical allowable roughness heights are presented on figure 7.9 for $M_\infty = 0.8$ and several altitudes [32], [82]. To provide some conservatism, a critical value of 200 was used. In this case, the permissible height depends on the distance from leading edge. It increases with increasing altitude.

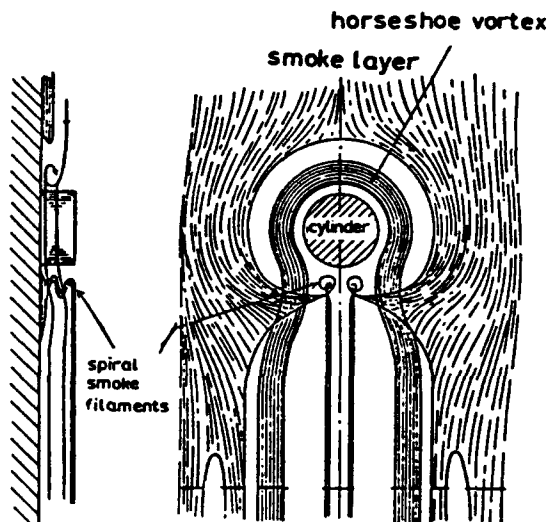


Fig. 7.7 Representation of flow past a cylindrical roughness element on a flat plate [130]

The empirical correlation of figure 7.8 is deduced from zero pressure gradient experiments. In order to simulate the mean flow field in the vicinity of a two-dimensional leading edge, de Bruin [132] studied the effect of isolated roughness elements in a favourable (negative) pressure gradient. These wind tunnel experiments demonstrated that the criterion was still valid for all the values of d/k which were tested.

To our knowledge, the only available information concerning *isolated* roughness elements in *three-dimensional* flow come from wind tunnel experiments performed by Juillen & Arnal [128]. Small pieces of adhesive tape were glued between 3 and 9 percent chord on a swept wing; the ratio d/k was of the order of 5. The apex of the turbulent wedge reached the roughness location for $R_k = 370 \pm 30$, in agreement with the two-dimensional correlation of figure 7.8. These results as well as those reported by de Bruin seem to indicate that three-dimensionality and streamwise pressure gradient have less effect than the large disturbances generated by the protuberances.

7.1.4. Vibrations

Surface vibrations can play a significant role if their spectrum overlaps that of the unstable boundary layer eigenmodes. Wind tunnel experiments performed by Chin & Norton [133] on a flat plate showed that TS waves could be excited by leading edge vibrations. The problem of wing vibrations was studied during the X-21

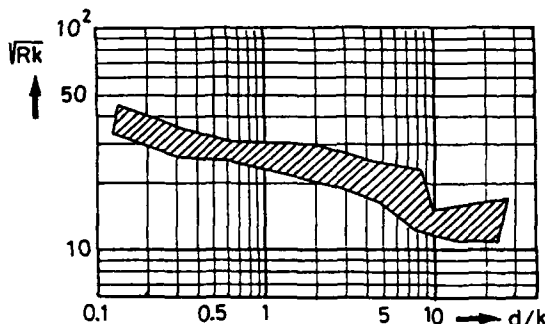


Fig. 7.8 Boundary layer tripping by three-dimensional roughness elements [31]

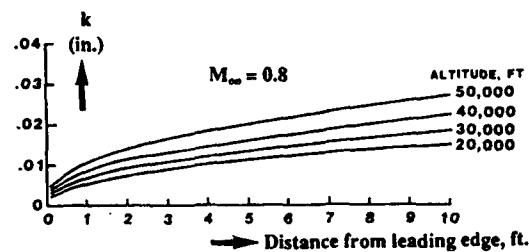


Fig. 7.9 Typical permissible heights of three-dimensional surface protuberances [32], [82]

flight experiments [29] in natural as well as in artificial conditions. In the latter case, two wing panels were driven with internally-mounted electrodynamic shakers. The conclusion was that the panel vibrations did not produce any harmful effect on the maintenance of laminar flow.

7.2. Environmental Factors

7.2.1. Insects

For extensive seasonal periods in many geographic locations, the accumulation of insect debris on wing surfaces can affect aerodynamic performances. Once the insect has ruptured upon impact, the protein content of its body serves as a glue, causing adhesion of the remains to the surface. This creates three-dimensional roughness elements, the final height of which (excrescence) depends on the insect size, normal impact velocity, angle of attack, wing shape and airfoil boundary layer. In the case of laminar flow surfaces, insect debris which exceed a critical roughness height cause boundary layer transition with a resultant rise in drag.

The population density of insects encountered is affected by local terrain vegetation, temperature, moisture, humidity and wind. Insect accretion occurs on aircraft predominantly at low altitudes below 500 ft, mostly on the takeoff roll/initial climb and on final approach/landing. The most critical region of impingement is located around the leading edge, within 15 % of chord on either side of the stagnation point. Although insect populations vary widely, many of them are of similar planform to the fruit fly (*drosophila*) [134].

Figure 7.10 shows the insect accumulation dependence on meteorological conditions. The data were deduced by Croom & Holmes [135] from flight tests on a Cessna 206 airplane. The time to collect approximately 300 insect strikes on the left wing is plotted against ground temperature for three wind speed categories: calm (less than 4 mph), light (4-8 mph) and moderate winds (greater than 8 mph). The maximum rate of accumulation is obtained at 77°F, independently of the wind speed. For any given ground temperature, the fastest insect accumulation rate occurs for winds between 4 and 8 mph. No direct correlation was found to exist between precipitation (rain) and insect accumulation rate. These results are in close agreement with those previously reported by Coleman (1961, referenced in [134] and [135]).

The highest excrescence occurs near the stagnation point where the surface velocities are low. Maresh & Bragg [134] developed a method to predict the performance penalty caused by contamination of an airfoil by insects. The aerodynamics of the fruit flies was modelled, and the impingement on the surface was determined by calculating the trajectories of the insects; the height of the debris was then estimated from experimental data. By using the boundary layer tripping criterion proposed by Von Doenhoff & Braslow (see paragraph 7.1.3.), the

authors found that in many cases a large amount of the insect debris does not cause transition because the local Reynolds numbers are very low in the immediate vicinity of the stagnation point. Holmes et al [123] conducted flight tests on the wing of a Bellanca Skyrocket airplane, and their results confirmed the theoretical trends: only 25 percent of the insect debris triggered transition at sea level; at a typical cruise altitude of 25 000 ft where the unit Reynolds number was close to $2 \cdot 10^6 \text{ ft}^{-1}$, only about 9 percent of the excrescences created turbulent wedges.

Even if the occurrence of serious contamination levels is infrequent, the insect debris can degrade airplane

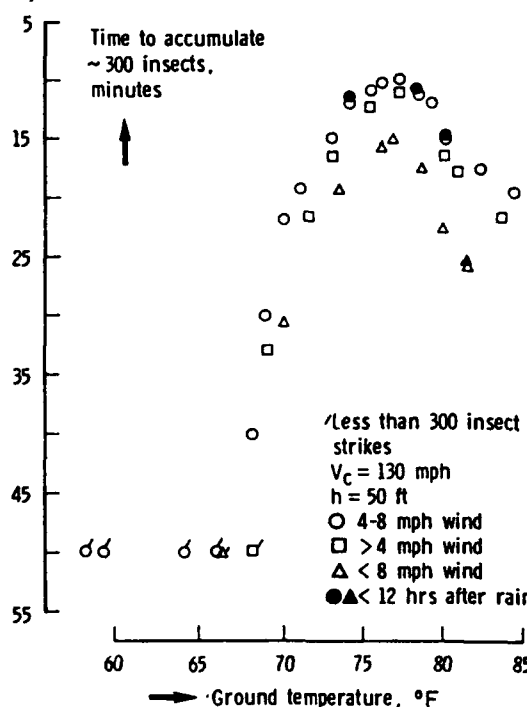


Fig. 7.10 Effect of meteorological conditions on rate of insect accumulation [135]

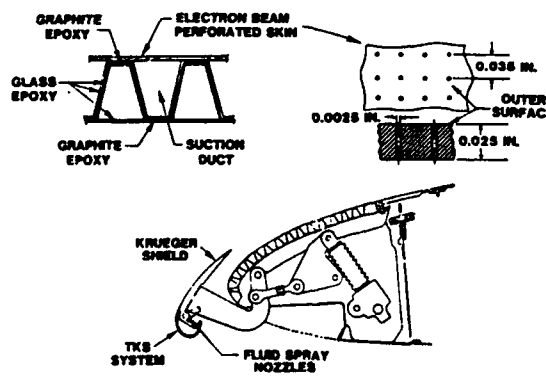


Fig. 7.11 Perforated leading edge box with a Krueger flap [32], [82]

performance [123]. Therefore protection of the wing surface against impacts or a capability to decontaminate the surface is required. A review of the earliest attempts to protect the leading edge region can be found in [135]. At the present time, two solutions are essentially used:

a) The first approach utilizes a Krueger leading edge flap which extends forward and in front of the stagnation line, figure 7.11. This flap acts as an insect shield at low altitudes. In cruise conditions, it is retracted into the wing lower surface and does not interfere with the laminar flow on the upper surface; however laminar flow is difficult to maintain on the lower surface due to the gaps between the flap and the main wing.

b) Another promising solution is the fluid injection. The fluid is discharged on the wing surface either through spanwise slots or through porous metal skins. The porous leading edge concept used by Croom & Holmes [135] during flight experiments was based on the TKS system, which was originally certified for ice protection using monoethylene glycol/water solution. This system acts in two ways: first, the porous skin allows a protective film to continually wet the surface with a minimal amount of fluid; secondly, the fluid is a solvent for insect body protein content. Using very small fluid flow rates, Croom & Holmes observed a 75 percent reduction in the number of insect debris. They pointed out that the TKS system must be activated prior to exposure to insects, because the fluid cannot remove excrescences glued on a dry surface.

Each of these approaches was recently flight-tested on a Jet Star airplane [90] which was flown in different geographical areas, seasons of the year and weather conditions. Both systems proved to be quite practical.

7.2.2. Ice crystals

At cruise altitudes, cirrus clouds contain mainly ice crystals. When ingested into the laminar boundary layer, these crystals are able to trigger turbulent events. Flight tests on the X-21 airplane and, more recently, on the Jet Star airplane clearly showed that, during penetration of cirrus clouds, transition moved forward in the vicinity of the leading edge. Laminar flow was immediately restored upon emergence from the clouds. The number of ice crystals that penetrate the boundary layer and the degree of loss of laminarity depend on the size and on the concentration of the particles, as well as on the airfoil leading edge shape, aircraft speed and altitude. However, flight test and statistical analyses demonstrated that "cloud encounters during cruise of long-range air transports are not frequent enough to invalidate the large improvement in fuel usage attainable through application of LFC. It was estimated that laminar flow might be lost no more than 7 % of the cruise time" [32].

Little is known about the effects of dust or other solid particles in flight conditions. For underwater vehicles, suspended ocean particulates reduce the extent of the laminar flow region, see Lauchle & Gurney [77].

8. TRANSITION REYNOLDS NUMBERS AND n FACTORS : WIND TUNNEL/FLIGHT EXPERIMENTS

The final goal of the theoretical, numerical and experimental studies described in the previous sections is to develop the tools and systems required for practical applications on airplanes. The best way to check the validity of these methods is to perform flight experiments. However, flight tests are very expensive and the measurements are much more difficult to perform than in ground facilities ; for these reasons, many investigations have been conducted in wind tunnels. The question of the ability to properly reproduce the flight conditions arises, because the environmental disturbances are usually different in the atmosphere and in the wind tunnels (see Section 3). The problem is not crucial, of course, if transition is induced by a bypass mechanism (leading edge contamination, large isolated roughness elements ...) ; it is much more important for "natural" transitions where the minute free stream disturbances play a major role.

This Section is devoted to a comparison between free flight results and wind tunnel results. From a practical point of view, the main parameter is the transition Reynolds number R_{xT} . Unfortunately, a direct comparison of this parameter requires to have identical pressure gradients, unit Reynolds numbers, Mach numbers, wall temperatures ... As such similarities are often difficult to achieve simultaneously, the n factor can be used as a useful parameter for comparison between flight and wind tunnel results, because it represents a global measure of the "efficiency" of the environmental disturbances. The implicit assumption is that identical n factors correspond to more or less identical transition mechanisms. Two questions (at least) need to be answered : does a "universal" value of the n factor exist in flight conditions ? If yes, is it possible to obtain the same value in ground facilities ?

8.1. Direct Wind Tunnel / Flight Comparisons

In this paragraph, we describe transition results which were obtained on the same model during flight tests and during wind tunnel experiments. This allows a direct comparison between the transition Reynolds numbers measured in laboratory and in flight conditions. Linear stability computations permit also to compare the n factors at the transition location.

8.1.1. Two-dimensional flows

a-Low speed flows : LFU experiments, [136] to [138]. These flight tests were carried out at DLR Braunschweig with an LFU-205 aircraft, having a small negative leading edge sweep of -4 degree. The general configuration and the main dimensions are given in figure 8.1. The aircraft is equipped with a special laminar glove which contains all flow measurements instrumentation. The transition location is determined by means of an infrared camera installed inside the cabin of the aircraft. The tests were performed in a speed range from 150-330 km/h, at flight levels between 4 000 and

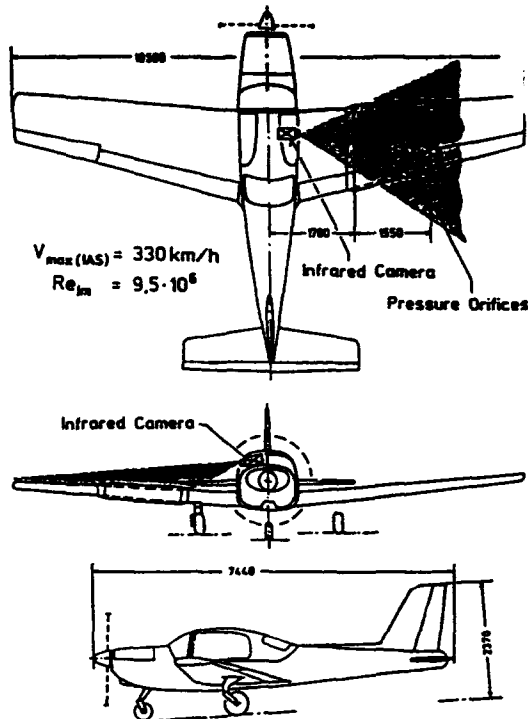


Fig. 8.1 LFU aircraft : installation of the glove and the infrared camera [136], [137], [138]

10 000 ft, resulting in chord length Reynolds numbers from 3 to 10 million.

From the measured pressure distributions, boundary layer stability analysis was carried out with the incompressible SALLY code [36]. The computation of the n factor was unambiguous for these experiments : the mean flow was two-dimensional and the most unstable TS waves were also two-dimensional ($\Psi_M = 0$) due to the low values of the free stream Mach number. The experimental transition locations were fairly well correlated with $n \approx 13.5$. Figure 8.2. gives the theoretical evolution of the integrated amplification rates for a chord Reynolds number of $9.5 \cdot 10^6$ [136], [137]. By using the intermittency method developed at ONERA/CERT (paragraph 4.5), it was found that the extent of the transition region was about 20 percent chord ; if it is assumed that the infrared camera detected the middle of the transition region, then figure 8.2 shows that the n factor at transition onset (minimum of the skin friction coefficient) is reduced to 10. This illustrates the need for an accurate definition of the "transition point".

In a further series of experiments [138], detailed hot wire measurements were performed to characterize the boundary layer instability. The frequency, the wavelength and the amplitude of the TS waves were measured and compared with linear stability results. At

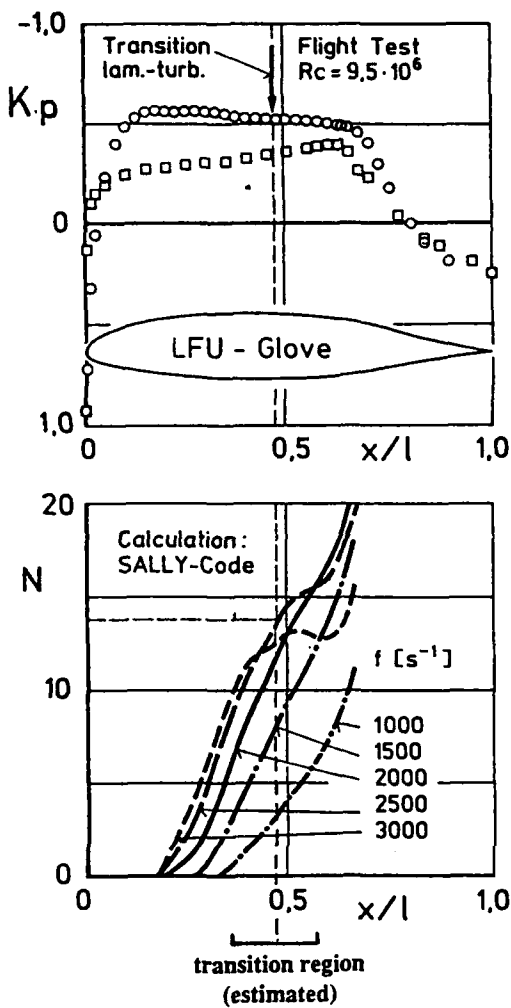


Fig. 8.2 Flight test pressure distribution and growth of n factor on the glove [136], [137]

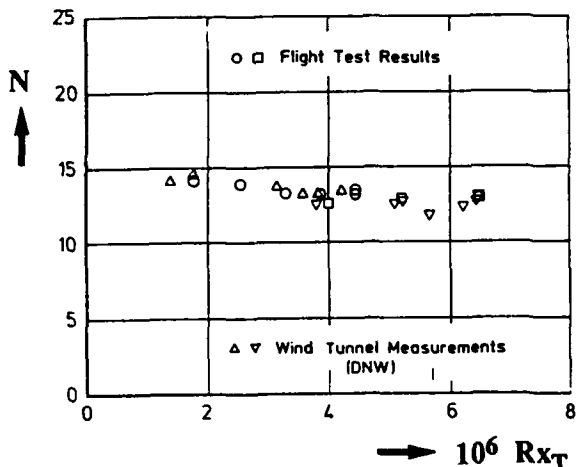


Fig. 8.3 Calculated n factors at transition based on flight and wind tunnel tests [136], [137]

high Reynolds numbers, discrepancies between theory and experiments were attributed to non linear effects.

In order to compare flight and wind tunnel conditions, the real aircraft wing was installed in the $6 \times 8 \text{ m}^2$ test section of the German-Dutch wind tunnel DNW (Deutsch Niederländischer Windkanal) in the Netherlands. Transition was again detected with an infrared camera. Figure 8.3 presents a comparison between n factors of TS waves at transition based on flight and wind tunnel tests. The n values are nearly independent of the transition Reynolds number $R_x T$ in the range $1 \cdot 10^6 < R_x T < 7 \cdot 10^6$. Values around 13.5 were obtained in both series of experiments, demonstrating the excellent flow quality of DNW.

b-Compressible flows : AEDC cone experiments, [27], [28]. This research spanned the period from 1970 to 1978 during which correlative measurements were made in 23 US and European wind tunnels and in flight using a 10-deg sharp cone which became known as the AEDC transition cone. Its length was 44.5 in. for a maximum finished surface length suitable for transition measurements of 36 in. Transition was detected with a surface pivot tube which was displaced along a cone ray. Figure 8.4 shows a typical pressure trace, from which the transition onset X_T and the middle (or end ?) of the transition region, X_M , can be easily defined. Most of the results were correlated by considering the Reynolds number $R_x M$ defined as :

$$R_x M = \frac{U_e X_M}{v_e} \quad (8.1)$$

where U_e and v_e are taken at the boundary layer edge. The experiments revealed that the ratio X_T/X_M had a mean value of 0.86 which does not depend on Mach number. This demonstrates once again that the length of the transition region is not negligible compared with the distance from the stagnation point to the transition onset.

Pressure fluctuations were also measured during these experiments. The results were discussed in paragraph 3.2.2. Some of them are plotted in figure 3.7, which summarizes the differences between flight, "quiet" and "noisy" wind tunnels.

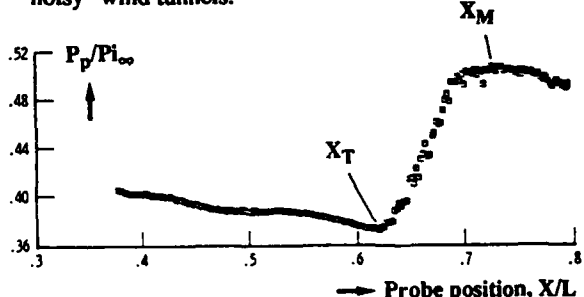


Fig. 8.4 AEDC cone : typical variation of the pilot probe pressure P_p as a function of probe location [27], [28]. P_{∞} is the free stream stagnation pressure

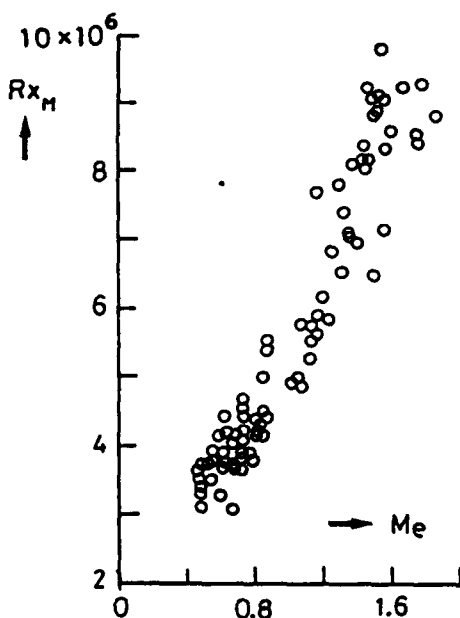


Fig. 8.5 Flight transition Reynolds numbers as a function of Mach number at boundary layer edge [27], [28]

For the flight tests, the AEDC cone was mated to a McDonnell Douglas F-15 aircraft as shown in figure 3.4. The experiments highlighted the strong influence of the wall temperature on transition location, see paragraph 5.2. The results which are presented below were corrected to adiabatic wall conditions.

The Rx_M Reynolds numbers measured in flight are shown as a function of the free stream Mach number Me in figure 8.5. The results range from about $3.5 \cdot 10^6$ at a Mach number of 0.5 to above $9.0 \cdot 10^6$ at Mach numbers above 1.6. The influence of the unit Reynolds number on Rx_M was not clearly established.

Malik [139] computed the n factor for four supersonic cases. He used the compressible COSAL code (temporal theory) and integrated the amplification rates associated with the locally most unstable direction ψ_M . Let us recall that ψ_M is not equal to 0 degree for Mach numbers larger than about 0.6. Malik found that the Reynolds numbers Rx_T at *transition onset* were correlated with n factors between 9 and 11. n factors between 10 and 13 correlated the values of Rx_M measured at the streamwise location where the pitot pressure was maximum. In the experiments, surface pressure fluctuations indicated the formation of TS waves, the frequency band of which was in agreement with linear theory.

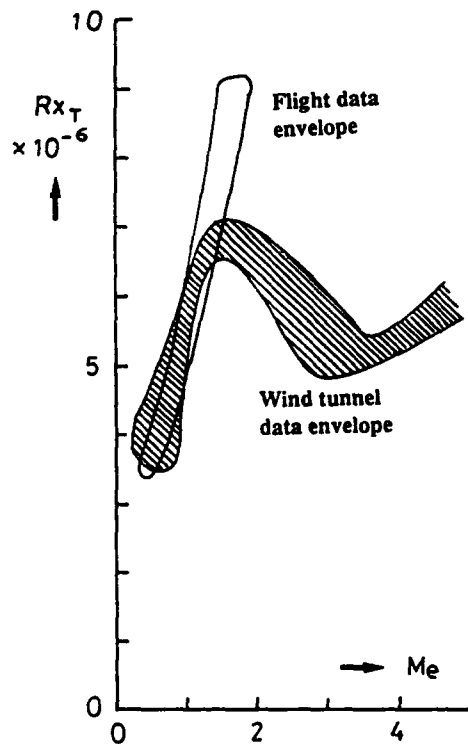


Fig. 8.6 Transition Reynolds numbers in flight and in lower disturbance level wind tunnels [28]

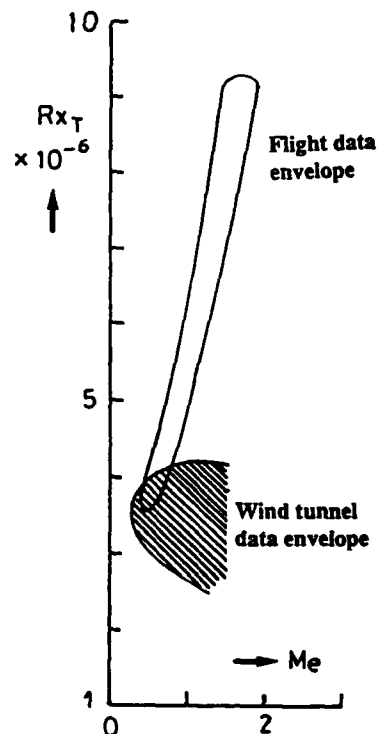


Fig. 8.7 Transition Reynolds numbers in flight and in higher disturbance-level wind tunnels [28]

The wind tunnel data were acquired over a broader Mach number range (M_e up to 5.2). Figures 8.6 and 8.7 give the measured evolution of R_{xM} as a function of M_e for a unit Reynolds number of $3 \cdot 10^6 \text{ m}^{-1}$. We present separately data obtained in the lower-disturbance-level wind tunnels (figure 8.6) and in the higher-disturbance-level wind tunnels (figure 8.7). The flight data envelope is also given for comparison. Transition Reynolds numbers in the quietest wind tunnels are about the same as those obtained in flight for the low subsonic Mach numbers, begin to deviate for $M_e \approx 1.5$ and are 25 percent lower for $M_e \approx 2$. In the noisier facilities, R_{xM} is as much as a factor of two lower than in-flight. TS waves were observed in two of the quietest wind tunnels only.

It is instructive to compare figures 8.6 and 8.7 with figure 3.7 which presents the variations of the rms values of the static pressure fluctuations in flight and in wind tunnels. The transition Reynolds number data exhibit a definable correlation with disturbance levels measured on the cone surface.

8.1.2. Three-dimensional flows : ATTAS experiments [40], [140], [141]

In 1986, a national research program investigating natural laminar flow at transonic speed and high Reynolds number was founded by the German Ministry of Research and Technology. In collaboration between DLR and Deutsche Airbus GmbH, a special glove was designed and installed on the right wing of the DLR research aircraft VFW 614/ATTAS (ATTAS : Advanced Technologies Testing Aircraft System), see figure 8.8. A large number of flight test data were obtained during two test periods in summer 1987.

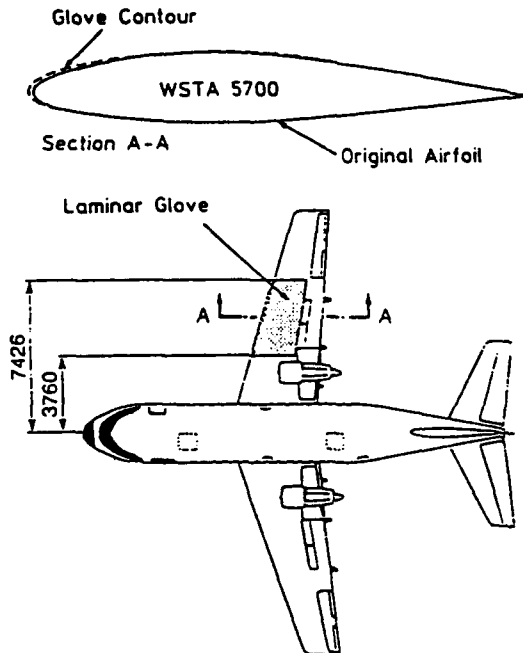


Fig. 8.8 VFW 614/ATTAS with laminar glove [140]

The VFW 614/ATTAS aircraft is a swept wing aircraft with a leading edge sweep angle $\varphi = 18^\circ$. The maximum Mach number for these tests was $M_{\infty} = 0.7$, leading to a Reynolds number based on wing chord close to $30 \cdot 10^6$. The glove covered a spanwise region of 3 m between engine pylon and aileron. The chordwise extension started at $X/C = 0.12$ on the lower surface and reached up to $X/C = 0.55$ on the upper surface. Transition was detected by infrared image technique and by hot films. Changing the yaw angle provided sweep angle variation from $\varphi = 13^\circ$ to $\varphi = 23^\circ$.

By variation of Mach number, flap deflection, yaw angle and flight level, the transition could be induced by streamwise instability, crossflow instability or leading edge contamination. As far as the latter problem is concerned, the flight data showed good agreement with the Pfenninger criterion. In the absence of leading edge contamination, the stability analysis of many flight test points was carried out by means of the incompressible SALLY code. The principle of this analysis was described in paragraph 4.1.2. : the n factor for Tollmien-Schlichting waves (n_{TS}) and the n factor for zero frequency disturbances (n_{CF}) are computed separately. Typical results are plotted on figure 8.9, which shows the theoretical values of n_{TS} and n_{CF} at the measured transition locations. The n_{TS} values do not depend strongly on the n_{CF} values : this means that there is no interaction between streamwise instabilities and crossflow vortices for this kind of airfoil.

Additional experiments showed a weak sensitivity of the laminar flow against engine noise, but a strong sensitivity against single roughness elements in the region between $X/C = 0.05$ and $X/C = 0.20$.

Wind tunnel experiments were also carried out with a 1:2 scale model of the glove in two large facilities : the DNW (Deutsch Niederländischer Windkanal) in the Netherlands and the S1MA (ONERA Soufflerie 1, Modane-Avrieux) in France. Figure 8.9 presents a comparison between the computed values of n_{CF} and n_{TS} for flight conditions and for wind tunnel conditions.

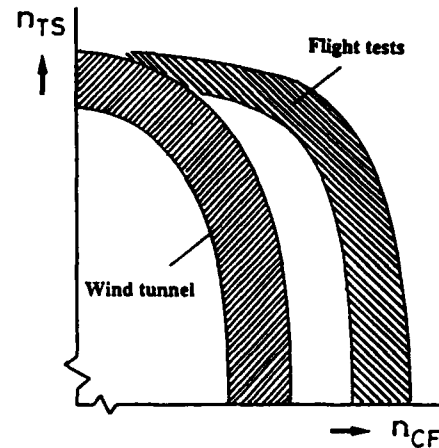


Fig. 8.9 Comparison of n_{TS} and n_{CF} factors from flight tests and wind tunnel tests [141]

The streamwise n_{TS} factors are in good agreement, while transitions induced by crossflow instability occur earlier in wind tunnels. A possible explanation is that crossflow instability is very sensitive to low frequency disturbances which exist in a wind tunnel with a larger amplitude than in flight conditions. It must be also pointed out that the wind tunnel Reynolds numbers were lower than during flight tests. Differences in surface polishing could be another reason for these discrepancies.

8.2. Other Flight Experiments

8.2.1. Two-dimensional, incompressible flows : Phoenix sailplane

Raspet & George-Falvy (1960, [142]) conducted careful flight experiments on a highly smoothed and polished section of a Phoenix sailplane wing. As the wing was unswept, the flow could be considered as two-dimensional. Figure 8.10 shows five pressure distributions obtained at different lift coefficients C_l ; they were measured on the upper surface at low altitude (around 2.2 km) and at low speed (between 16 and 28 ms^{-1}). The chord at the test section was close to 1 m, so that the chord Reynolds number ranged from 1 to $1.6 \cdot 10^6$.

Boundary layer measurements were made using a miniature pitot-rake located at various chordwise positions. The streamwise evolution of the shape factor H is plotted in figure 8.11 for the flight conditions of figure 8.10. If the transition onset is defined as the point where H begins to decrease, it is observed that the breakdown to turbulence always occurs in positive pressure gradient.

The transition results were analyzed by Runyan & George-Falvy (1979, [143]) who computed the n factors of the unstable TS waves. The chordwise locations at which the calculated amplification factors are e^9 and e^{15} are given in figure 8.11. The locations corresponding to $n = 9$ have laminar shape factors, except for $C_l = 1.42$; the locations corresponding to $n = 15$

have turbulent shape factors except for $C_l = 0.92$ (H is still laminar) and 0.76 (H is neither laminar nor turbulent). Because transition occurs in decelerated flows, the integrated amplification rates increase very rapidly, so that the distance between the positions associated with $n = 9$ and $n = 15$ is very short. These results indicate that the *beginning* of transition on the Phoenix sailplane (no engine noise) corresponds to a mean value of the n factor of about 10.

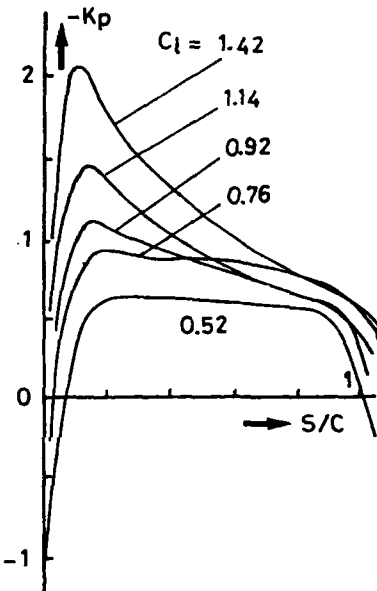


Fig. 8.10 Pressure distributions on the Phoenix sailplane wing [143]

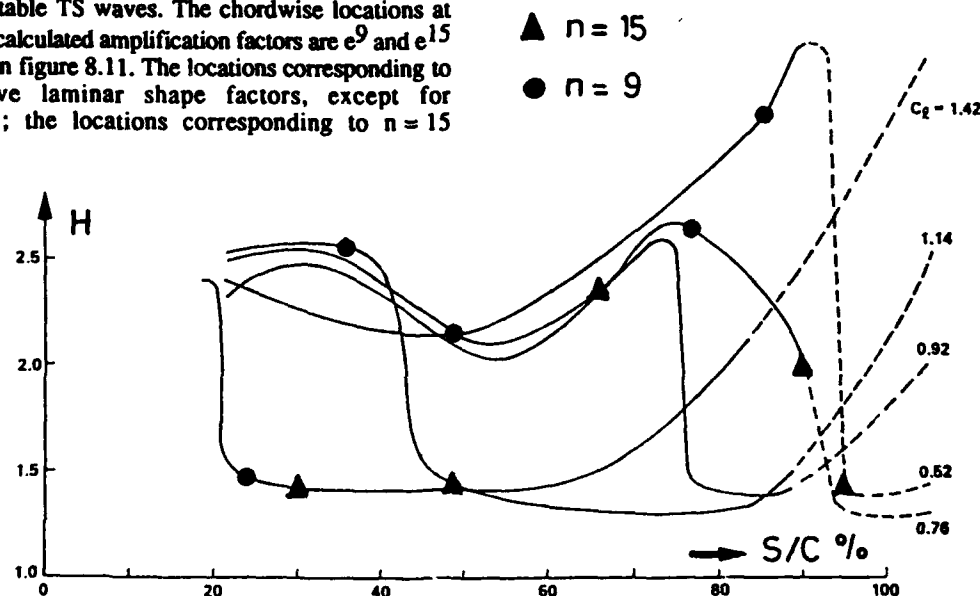


Fig. 8.11 Correlation of amplification factor with shape factor [143]

8.2.2. Three-dimensional, transonic flows
a-F-14 experiments- The flight experiments on the F-14 aircraft have been mentioned in paragraph 5.1.2.. To correlate the experimental data, stability computations were performed with the envelope method option of the COSAL code. A typical result (reported in [70]) is shown in figure 8.12 for $M_\infty = 0.80$, $\phi = 20^\circ$ and a chord Reynolds number of $21 \cdot 10^6$. In this case, transition is triggered by crossflow instability : its location was estimated to be near 45 percent chord, since the hot film output was laminar at $X/C = 0.40$ and turbulent at $X/C = 0.50$. For the sake of clarity, only the n factors for $f = 1500$ Hz (most unstable frequency) and $f = 0$ Hz (stationary disturbances) are given. When the curvature terms are neglected in the stability equations, the n factor at the onset of transition is 20 for $f = 1500$ Hz. This value is reduced to about 9 with the curvature terms included.

Similar computations were performed for a number of F-14 flight conditions for which transition was dominated by crossflow disturbances. The average value of n at transition onset was 9 when curvature effects were taken into account ; it was about 17 without curvature effects.

b-Jet Star experiments- The main results of these flight tests [90], [91], have been summarized in paragraph 5.3.5.. Let us recall that a leading edge suction panel was installed in the right wing of a Jet Star aircraft, from the attachment line to 13 percent chord. The envelope method of the COSAL code was used to compute the n factor with and without suction, for the following conditions : $\phi = 30^\circ$, $M_\infty = 0.775$, altitude = 29 000 ft. The pressure distribution is shown in figure 5.12 : the chordwise pressure gradient is nearly flat beyond $X/C = 0.05$. The general trends are the same

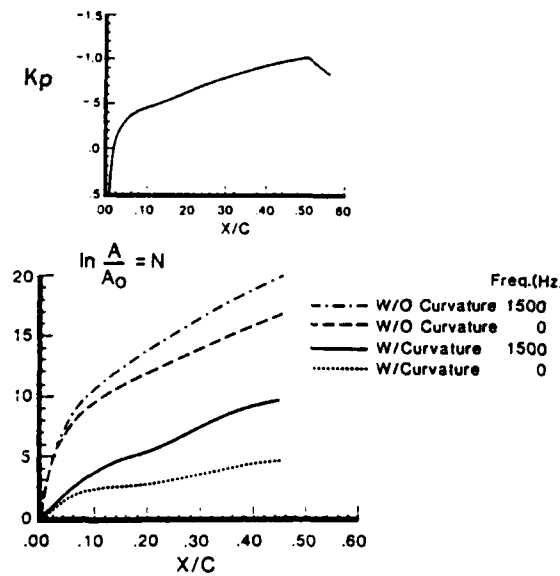


Fig. 8.12 Crossflow n factors for an F-14 "clean-up" glove test point [70]. $M_\infty = 0.80$, angle of sweep = 20° , chord Reynolds number = $21 \cdot 10^6$

as for the calculations related to the F-14 experiments : firstly, travelling disturbances are more amplified than stationary vortices ; secondly, the curvature terms are stabilizing.

When suction is applied near the attachment line in the region of negative pressure gradient (early suction), the values of n at transition are about 8 with curvature terms included. When suction is applied in the region of nearly zero pressure gradient (later suction), the values of n are about 10. The difference between the n factors computed for early suction and for later suction can be explained by the smaller boundary layer thickness in the former case (it becomes more sensitive to the roughness effects of suction holes). Other explanations include uncertainties in the definition of transition onset and possible interactions between TS and crossflow disturbances with early suction. A practical result, however, is that early suction is more efficient to delay transition than later suction for the same rate of sucked air.

8.3. n Factors in Wind Tunnels - Discussion

8.3.1. Two-dimensional flows

The limited number of flight experiments described in sections 8.1. and 8.2. indicate that the n factor at transition onset is close to 10 for two-dimensional flows. This value is valid for low speed experiments (LFU, Phoenix sailplane) as well as for transonic experiments (AEDC cone).

For subsonic flows without pressure gradient, Mack's correlation (4.10) shows that the value $n = 10$ is reached for a free stream turbulence level Tu close to 0.046 percent. Let us recall, however, that so small values of Tu usually include both velocity and pressure fluctuations. The corresponding value of the transition Reynolds number R_{xT} is about $3.7 \cdot 10^6$. As discussed earlier in subsection 3.1.1., similar values were obtained in low disturbance wind tunnels : the limiting values of R_{xT} at low Tu were approximately $2.8 \cdot 10^6$ for the Schubauer-Skramstad experiments ($n = 8$ to 9) and $5 \cdot 10^6$ for the Wells experiments ($n = 11$ to 12).

Other experiments performed in low speed wind tunnels demonstrated that n factors around 10 could be reached for transition occurring in positive or negative pressure gradient. Braslow & Visconti, for example, measured the transition location on an airfoil at very large Reynolds numbers [68]. A practically constant n factor close to 11 correlated all the data, for accelerated and decelerated flows. As reported before, large n values were also obtained in the DNW wind tunnel during the LFU wing experiments.

In transonic flow, flight transition Reynolds numbers were fairly well simulated in the quietest facilities where the AEDC cone was tested, see paragraph 8.11 and figure 8.6. It has been shown in paragraph 4.4. that n factors close to 9 correlated the transition locations measured in the T2 wind tunnel on the CAST10 airfoil.

These examples show that low disturbance facilities can lead to n factors close to those corresponding to flight tests. This does not mean that the disturbance environment is the same for these wind tunnels and for the flight conditions, but it can be estimated that the transition mechanisms are nearly identical for similar values of the n factor.

8.3.2. Three-dimensional flows

It has been shown (paragraph 4.1.2.) that the final value of the n factor was dependent upon the strategy which is adopted to maximize the amplification rates. Three classes of strategies can be distinguished : those in which the amplification rate is maximized at each streamwise position with respect to the wavenumber direction (envelope method of the COSAL code, saddle-point method, ONERA/CERT method), those in which the wavelength, the spanwise wavenumber or the wavenumber direction are kept constant (other options of the COSAL code, Mack's method) and the n_{TS} -versus- n_{CF} correlations. The example of application discussed in paragraph 4.4 (ONERA D airfoil in the F2 wind tunnel at Le Fauga Mauzac Center) illustrated the difficulty to choose the most appropriate strategy.

A survey of the published results indicate that the most commonly used approach is the envelope method. With the curvature terms included into the stability equations, this method gave n factors between 8 and 10 for the flight experiments conducted on the F-14 aircraft and on the Jet Star aircraft, see previous paragraph. Similar values were computed for low speed wind tunnel experiments, for instance those performed by Boltz et al [144] in the NASA Ames 12-foot Low Turbulence Pressure Tunnel or those performed by Poll [61] on a long yawed cylinder, paragraph 4.4. n factors close to 10 were also obtained for the swept wing experiments conducted in the F2 wind tunnel at Le Fauga Mauzac Center ; in this case, the computations were done with the saddle point method and with the strategy developed at ONERA/CERT ; both methods are close to the envelope method in the sense that the amplification rate is maximized with respect to the wavenumber direction.

It is not clear, however, that the n factors must be the same for streamwise instability and for crossflow instability. Two contradictory examples have been given ; in the F2 wind tunnel, the same value of the n factor correlated the low speed results (pure streamwise instability) and the higher speed results (pure crossflow instability). But the limiting values of n_{CF} deduced from the ATTAS experiments were different in flight and in wind tunnel conditions, whilst the limiting values of n_{TS} were identical. As the frequency range of crossflow disturbances strongly differs from that of streamwise disturbances, their receptivity to the forced disturbances (in the free stream or at the wall) is not the same, and there is a priori no reason to observe similar n factors for both instability mechanisms.

Another problem is related to the effect of suction on the n factor. Flight test (Jet Star aircraft, paragraph 8.2.2.)

and wind tunnel experiments (ONERA D swept wing, paragraph 5.3.3.) indicated that this effect is likely to exist, even if it is not very strong. Decreasing the ratio boundary layer thickness/hole diameter, increasing the suction velocity or the extent of the sucked area seem to decrease the n factor at transition onset. It is not necessary to emphasize the importance of this problem for practical applications.

8.3.3. Concluding remarks

As pointed out by Morkovin & Reshotko [145], "(the e^n method) bypasses any need for information on the character and magnitude of disturbances ... and on actual receptivity paths leading to the initial A_0 amplitude. Non linear saturation, secondary and higher instabilities ... are replaced by the continued fictitious linear growth all the way (to the transition onset)". In spite of these shortcomings, n factors of the order of 10 correlate experiments performed in the usual case of atmospheric powered flight and in low turbulence tunnels (Bushnell et al [146]). At first sight, this simple result applies for two and three-dimensional flows at subsonic or transonic speeds. Let us remind, however, some remarks and some issues which were formulated in this Section :

- in three-dimensional flows, n factors around 10 are obtained when using strategies similar to the envelope method ; other methods (fixed wavelength for instance) give lower values ;
- possible interactions between crossflow and streamwise instabilities are not taken into account, except in the n_{TS} -versus- n_{CF} methods ;
- is the n factor identical for streamwise and for crossflow disturbances ?
- influence of the suction on the n factor ?
- when comparing n factors deduced from different experiments, these problems can be of secondary importance if a coherent definition of the "transition point" is not adopted.

9. CONCLUSION

The maintainance of laminar flow needs substantial investigations to understand the transition mechanisms and to develop reliable engineering methods which must be checked by comparison with experimental results.

Our understanding of the flow phenomena has been improved by many experimental, theoretical and numerical studies. It is now recognized that the linear stability theory constitutes a very efficient tool to analyze the fundamental mechanisms leading to transition, and sophisticated experimental studies gradually confirm these theoretical elements. The linear theory can also explain the influence of "transition modifiers" which are currently used to increase the extent of laminar flow. For instance it has been shown that the adverse sweep effects can be significantly reduced if a wing is properly designed (shaping), or if suction is applied in the region where the boundary layer disturbances start to grow. However many questions remain to be solved. The receptivity mechanisms are not completely explained, and the development of the last stages of the transition process needs further investigation. Direct numerical simulations are useful to give a better insight into these problems.

Even if all the transition mechanisms are not completely understood, practical prediction methods need to be developed. In the case of "natural" transitions, the e^n method gives surprisingly good results to "predict" transition onset. Simpler techniques such as criteria or data base methods are also interesting to provide us with a first idea of the transition problems which may be encountered on a wing. The extent of the transition region can be estimated with intermittency methods. If the breakdown to turbulence occurs without resorting to linear mechanisms (bypass), the e^n rule no longer applies, but empirical correlations are available for design purposes. Typical examples are the criterion for leading edge contamination or the criterion for boundary layer tripping by large isolated roughness elements.

As most of these prediction methods were deduced from wind tunnel experiments, their validity has to be tested by comparison with flight results. During the last years, flight investigations have been conducted to get "clean" transition data, and a rather large amount of results is now available. Comparison between flight tests and wind tunnel experiments showed that low disturbances facilities could properly simulate the transition phenomena occurring on an aircraft wing. Provided the "transition point" is defined in a coherent manner, a practically constant value of the n factor correlates flight data and wind tunnel results.

An optimistic conclusion is that many aerodynamic issues seem nearly resolved. On the other hand, modern construction techniques are able to provide aircraft surfaces which are compatible with the maintainance of laminar flow. The manufacturing capabilities have advanced to the point at which the criteria for smooth wing surfaces are a practical production goal. Suction systems were also developed and their efficiency was

demonstrated in flight conditions, so that HLFC appears possible for medium-sized aircraft with moderate sweep.

ACKNOWLEDGEMENTS

The author would like to thank Professor J Cousteix and Mr. J.C. Juillen for their suggestions and useful discussions.

REFERENCES

1. Cousteix, J., "Introduction", AGARD Report n° 786 (Skin friction drag reduction) VKI, Brussels, 1992
2. Robert, J.P., "Drag reduction : an industrial challenge", AGARD Report n° 786 (Skin friction drag reduction) VKI, Brussels, 1992
3. Bushnell, D.M., "Overview on aircraft drag reduction technology", AGARD Report n° 786 (Skin friction drag reduction) VKI, Brussels, 1992
4. Morkovin, M.V., "Critical evaluation of transition from laminar to turbulent shear layers with emphasis on hypersonically travelling bodies", Report AFFDL-TR-68-149, Wright-Patterson Air Force Base, 1968
5. Morkovin, M.V., "Bypass transition to turbulence and research desiderata", Symp. "Transition in Turbines", Cleveland, Ohio, May 1984
6. Saric, W.S., "Laminar-turbulent transition : fundamentals", AGARD Report n° 786 (Skin friction drag reduction) VKI, Brussels, 1992
7. Mack, L.M., "Boundary layer stability theory" (2 volumes), Jet Propulsion Laboratory, California Institute of Technology, Pasadena, California, November 1969
8. Mack, L.M., "Boundary layer linear stability theory", AGARD Report n° 709 (Special Course on Stability and Transition of Laminar Flow), VKI, Brussels, 1984
9. Gaster, M., "A note on the relation between temporally increasing and spatially increasing disturbances in hydrodynamic stability", J. Fluid Mech., Vol. 14, pp. 222-224, 1962
10. Lees, L., Lin, C.C., "Investigation of the stability of the laminar boundary layer in a compressible fluid", NACA TN N° 1115, 1946
11. Arnal, D., "Stabilité et transition des couches limites laminaires bidimensionnelles en écoulement compressible, sur paroi athermante", La Recherche Aérospatiale, N° 1988-4, 1988

12. Poll, D.I.A., "Transition description and prediction in three-dimensional flows", AGARD Report n° 709 (Special Course on Stability and Transition of Laminar Flow), VKI, Brussels, 1984

13. Arnal, D., "Three-dimensional boundary layers : laminar-turbulent transition", AGARD Report N° 741 (Computation of Three-dimensional Boundary Layers including Separation), VKI, Brussels, 1986

14. Saric, W.S., Reed, H.L., "Three-dimensional stability of boundary layers", Perspectives in Turbulence Studies, Springer Verlag, 1987

15. Herbert, T., "Secondary instability of boundary layers", Ann. Rev. Fluid Mech., Vol. 20, pp. 487-526, 1988

16. Müller, B., Bippes, H., "Experimental study of instability modes in a three-dimensional boundary layer", AGARD CP N° 438, 1988

17. Meyer, F., Kleiser, L., "Numerical investigation of transition in 3D boundary layers", AGARD CP N° 438, 1988

18. Heinrich, R.A., Choudhari, M., Kerschen, E.J., "A comparison of boundary layer receptivity mechanisms", AIAA Paper 88-3758 CP, 1988

19. Pate, S.R., "Effects of wind tunnel disturbances on boundary layer transition with emphasis on radiated noise : a review" AIAA Paper 80-0431, 1980

20. Schubauer, G.B., Skramstad, H.K., "Laminar boundary layer oscillations and transition on a flat plate", Rept. 909 NACA, 1948

21. Wells, C.S., "Effects of free stream turbulence on boundary layer transition", AIAA Journal, Vol. 5, N° 1, pp. 172-174, 1967

22. Bulgubure, C., Arnal, D., "Dassault Falcon 50 laminar flow flight demonstrator", First European Forum on Laminar Flow Technology, Hamburg, March 1992

23. Otten, L.J., Pavel, A.L., Finley, W.E., "A survey of recent atmospheric turbulence measurements from a subsonic aircraft", AIAA Paper 81-0298, 1981

24. Zanin, B.Yu., "Transition at natural conditions and comparison with the results of wind tunnel studies", Laminar-Turbulent Transition, Ed. V.V. Kozlov, IUTAM Symp., Novosibirsk, USSR, pp. 541-546, 1984

25. Bushnell, D., "Notes on the initial disturbance fields for the transition problem", Instability and Transition, Vol. 1, Ed. M.Y. Hussaini & R.G. Voigt, Springer Verlag, pp. 217-232, 1990

26. Pfenninger, W., "Recent developments in the field of low drag boundary layer suction research", AGARD Report N° 262, April 1960

27. Fisher, D.F., Dougherty, N.S. Jr., "In-flight transition measurements on a 10° cone at Mach numbers from 0.5 to 2", NASA TP-1971, June 1982

28. Dougherty, N.S. Jr., Fisher, D.F., "Boundary layer transition on a 10-degree cone : wind tunnel/flight data correlation", AIAA Paper 80-0154, 1980

29. Fowell, L.R., Antonatos, P.P., "Some results from the X-21A program, part 2 - Laminar flow control flight test results on the X-21A" Recent Developments in Boundary Layer Research , Part IV, AGARDograph 97, May 1965

30. Swift, G., Munger, P., "A study of the prediction of cruise noise and laminar flow control noise criteria for subsonic air transports", NASA CR-159 104, August 1979

31. Wagner, R.D., Maddalon, D.V., Bartlett, D.W., Collier, F.S. Jr., "Fifty years of laminar flow flight testing", SAE Tech. Paper Series 881393, October 1988

32. Braslow, A.L., Maddalon, D.V., Bartlett, D.W., Collier, F.S. Jr., "Applied aspects of laminar-flow technology", in "Viscous Drag Reduction in Boundary Layers", Ed. Bushnell & Hefner, Progress in Astronautics and Aeronautics, Vol. 123, AIAA Inc. Publishers, 1990

33. Smith, A.M.O., Gamberoni, N., "Transition, pressure gradient and stability theory", Douglas Aircraft Co. Rept. ES 26388, El Segundo, Calif., 1956

34. Van Ingen, J.L., "A suggested semi-empirical method for the calculation of the boundary layer transition region", Univ. of Techn., Dept. of Aero. Eng., Rept UTH-74, Delft, 1956

35. Arnal, D., Casalis, G., Juillen, J.C., "Experimental and theoretical analysis of natural transition on "infinite" swept wing", IUTAM Symp. "Laminar-Turbulent Transition", Toulouse, Ed. Arnal and Michel, Springer Verlag, 1990

36. Srokowski, A., Orszag, S.A., "Mass flow requirements for LFC wing design", AIAA Paper n° 77-1222, 1977

37. Malik, M.R., "COSAL - A black-box compressible stability analysis code for transition prediction in three-dimensional boundary layer", NASA CR-165925, 1982

38.Dagenhart, J.R., "Amplified cross flow disturbances in the laminar boundary layer on swept wings with suction", NASA Technical Paper 1902, 1981

39.Hefner, J.N., Bushnell, D.M., "Status of linear boundary layer stability theory and the e^n method, with emphasis on swept wing applications", NASA Technical Paper 1645, 1980

40.Redeker, G., Horstmann, K.H., Köstler, H., Thiede, P., Szodruch, J., "Design of natural laminar flow glove for a transport aircraft", AIAA Paper n° 90-3043, 1990

41.Nayfeh, A.H., "Stability of three-dimensional boundary layers", AIAA Paper n° 79-0262, 1979

42.Cebeci, T., Stewartson, K., "On stability and transition in three-dimensional flows", AIAA Journal Vol. 18, N° 4, 398-405, 1980

43.Cebeci, T., Chen, H.H., "An evaluation of stability-based methods for transition of three-dimensional flows", IUTAM Symp. "Laminar-Turbulent Transition", Toulouse, Ed. Arnal and Michel, Springer Verlag, 1990

44.Cebeci, T., Chen, H.H., Arnal, D., "A three-dimensional linear stability approach to transition on wings at incidence" AGARD Conference Proceedings N° 438, 1988

45.Mack, L.M., "Stability of three-dimensional boundary layers on swept wings at transonic speeds", IUTAM Symp. "Transsonicum III", Göttingen, Ed. Zierep and Oertel, Springer Verlag, 1988

46.Mack, L.M., "Transition and laminar instability", Jet Propulsion Laboratory Publication 77-15, Pasadena, Calif., 1977

47.Arnal, D., "Description and prediction of transition in two-dimensional, incompressible flow", AGARD Report n° 709 (Special Course on Stability and Transition of Laminar Flow), VKI, Brussels, 1984

48.Michel, R., "Détermination du point de transition et calcul de la traînée des profils d'aile en incompressible", ONERA Publication n° 58, 1952

49.Granville, P.S., "The calculation of the viscous drag of bodies of revolution", David Taylor Model Basin Report 849, 1953

50.Arnal, D., Habiballah, M., Coustols, E., "Laminar instability theory and transition criteria in two- and three-dimensional flows", La Recherche Aérospatiale n° 1984-2, 1984

51.Owen, P.R., Randall, D.G., "Boundary layer transition on a swept back wing", RAE Technical Memorandum 256, 1952

52.Treadgold, D.A., Beasley, J.A., "Some examples of the application of methods for the prediction of boundary layer transition on sheared wings", Aeronautical Research Council, CP n° 1246, 1973

53.Beasley, J.A., "Calculation of the laminar boundary layer and prediction of transition on a sheared wing", Aeronautical Research Council, R&M n° 3787, 1976

54.Coustols, E., "Stabilité et transition en écoulement tridimensionnel : cas des ailes en flèche", Thesis, ENSAE Toulouse, June 1983

55.Van Ingen, J.L., "Transition, pressure gradient, suction, separation and stability theory", AGARD CP 224, 1977

56.Arnal, D., "Transition prediction in transonic flow", IUTAM Symp. "Transsonicum III", Göttingen, Ed. Zierep and Oertel, Springer Verlag, 1988

57.Blanchard, A., Mignosi, A., Dor, J.B., Seraudie, A., "Essais de profils CAST7 et CAST10 dans la soufflerie cryogénique à parois adaptables T2. Etude de l'effet Reynolds en transition naturelle et en transition déclenchée", 22ème Colloque d'Aérodynamique Appliquée, Lille, 1985

58.Schrauf, G., Thiede, P., Private communication

59.Casalis, G., "Instabilités primaire et secondaire dans la couche limite laminaire pour un fluide incompressible", Thesis, Paris 6 University, June 1990

60.Casalis, G., Arnal, D., "Prévision de la transition sur une aile en flèche", La Recherche Aérospatiale n° 1990-1, 1990

61.Malik, M.R., Poll, D.I.A., "Effect of curvature on three-dimensional boundary layer stability", AIAA Journal, Vol. 23, N° 9, 1985

62.Poll, D.I.A., "Some observations of the transition process on the windward face of a long yawed cylinder", J. Fluid Mech., Vol. 150, 1985

63.Schrauf, G., Laburthe, F., Casalis, G., "Stability computations on the long yawed cylinder of Poll : comparison of stability codes, curvature effects", Internal Report ONERA/CERT/DERAT, November 1991

64.Arnal, D., Coustols, E., Juillen, J.C., "Etude expérimentale et théorique de la transition sur une aile en flèche infinie", La Recherche Aérospatiale n° 1984-4, 1984

65.Arnal, D., "Laminar-turbulent transition problems in supersonic and hypersonic flows", AGARD Report

n° 761 (Special Course on Aerothermodynamics of Hypersonic Vehicles), VKI, Brussels, 1988

66. Arnal, D., Juillen, J.C., "Three-dimensional transition studies at ONERA/CERT", AIAA Paper n° 87-1335, 1987

67. Reshotko, E., "Environment and receptivity", AGARD Report n° 709 (Special Course on Stability and Transition of Laminar Flows), VKI, Brussels, 1984

68. Braslow, A.L., Visconti, F., "Investigation of boundary layer Reynolds number for transition on a NACA 65(215)-114 airfoil in the Langley two-dimensional low turbulence pressure tunnel", NACA TN 1704, October 1948

69. Younghans, J.L., Lahti, D.J., "Experimental studies on natural laminar flow nacelles", AIAA Paper 84-0034, 1984

70. Wagner, R.D., Bartlett, D.W., Collier, F.S.Jr., "Laminar flow - The past, present and prospects", AIAA Paper 89-0989, 1989

71. Lees, L., "The stability of the laminar boundary layer in a compressible fluid", NACA Report 876, 1947

72. Reshotko, E., "Drag reduction by cooling in hydrogen-fueled aircraft", J. Aircraft, Vol. 16, N° 9, pp. 584-590, September 1979

73. Wazzan, A.R., Okamura, T.T., Smith, A.M.O., "The stability and transition of heated and cooled incompressible laminar boundary layers", Proc. 4th Int. Heat Transfer Conf., ed. Grigull and Hahne, Vol. 2, FC1.4, Elsevier, 1970

74. Strazisar, A.J., Reshotko, E., Prahl, J.M., "Experimental study of the stability of heated laminar boundary layer in water", J. Fluid Mech., Vol. 83, Part 2, pp. 225-247, 1977

75. Barker, S.J., Jennings, C., "The effect of wall heating upon transition in water boundary layers", AGARD Conference Proceedings n° 224, 1977

76. Barker, S.J., Gile, D., "Experiments on heat-stabilized laminar boundary layers in water", J. Fluid Mech., Vol. 104, pp. 139-158, 1981

77. Lauchle, G.C., Gurney, G.B., "Laminar boundary layer transition on a heated underwater body", J. Fluid Mech., Vol. 144, pp. 79-101, 1984

78. Rosenhead, L., "Laminar boundary layers", Oxford University Press, 1963

79. Saric, W.S., Nayfeh, A.H., "Non parallel stability of boundary layers with pressure gradient and suction", AGARD CP 224, 1977

80. Saric, W.S., "Laminar flow control with suction : theory and experiment", AGARD Report n° 723 (Aircraft Drag Prediction and Reduction), VKI, Brussels, 1985

81. Pfenninger, W., "Laminar flow control : laminarization", AGARD Report n° 654 (Special Course on Concepts for Drag Reduction), VKI, Brussels, 1977

82. Braslow, A.L., Fischer, M.C., "Design considerations for application of laminar flow control systems to transport aircraft", AGARD Report n° 723 (Aircraft Drag Prediction and Reduction), VKI, Brussels, 1985

83. "Evaluation of laminar flow control system concepts for subsonic commercial transport aircraft", NASA CR-159253, September 1980

84. Lachmann, G.V. editor, "Boundary layer and flow control", Vols. I and II, Pergamon Press, 1961

85. Nayfeh, A.H., El Hady, N.M., "An evaluation of suction through strips for laminar flow control", AIAA Paper 79-1484, 1979

86. Arnal, D., Juillen, J.C., Casalis, G., "The effects of wall suction on laminar-turbulent transition in three-dimensional flow", First ASME/JSME Fluids Engineering Conf., Portland, Oregon, June 1991

87. Pfenninger, W., "Untersuchungen über Reibungsverminderungen an Tragflügeln, insbesondere mit Hilfe von Grenzschichtabsaugung", Mitteilung n° 13 des Inst. für Aerodynamic, E.T.H., Zürich, 1946

88. Whites, R.C., Sudderth, R.W., Wheldon, W.G., "Laminar flow control on the X-21", Astronautics and Aeronautics, Vol. 4, N° 7, pp. 38-43, 1966

89. Pfenninger, W., Reed, V.D., "Laminar flow research and experiments", Astronautics and Aeronautics, Vol. 4, N° 7, pp. 44-50, 1966

90. Wagner, R.D., Maddalon, D.V., Fisher, D.F., "Laminar flow control leading edge systems in simulated airline service", ICAS-88.3.7.4., Jerusalem, Israel, 1988

91. Maddalon, D.V., Collier F.S.Jr., Montoya, L.C., Putnam, R.J., "Transition flight experiments on a swept wing with suction", IUTAM Symp. "Laminar-Turbulent Transition", Toulouse, Ed. Arnal and Michel, Springer Verlag, 1990

92. Schlichting, H., "Boundary layer theory", 7th Ed., p. 95, McGraw Hill, 1979

93. Cumpsty, N.A., Head, M.R., "The calculation of the three-dimensional turbulent boundary layer : Part

II : attachment line flow on an infinite swept wing", The Aeron. Quarterly, Vol. XVIII, Part 2, May 1967

"Part III : comparison of attachment line calculations with experiment", The Aeron. Quarterly, Vol. XX, May 1969

94.Gaster, M., "On the flow along leading edges", The Aeron. Quarterly, Vol. XVIII, Part 2, May 1967

95.Poll, D.I.A., "Some aspects of the flow near a swept attachment line with particular reference to boundary layer transition", College of Aeronautics Report 7805, August 1978

96.Poll, D.I.A., "Skin friction and heat transfer at an infinite swept attachment line", The Aeron. Quarterly, Vol. XXXII, November 1981

97.Beachwith, I.E., Gallagher, J.J., "Local heat transfer and recovery temperatures on a yawed cylinder at a Mach number of 4.15 and high Reynolds numbers", NASA TR R-104, 1961

98.Pfenninger, W., Bacon, J.W.Jr., "Amplified laminar boundary layer oscillations and transition at the front attachment line of a 45° swept flat-nosed wing with and without boundary layer suction", Viscous Drag Reduction, C.S.Wells Ed., Plenum Press, 1969

99.Poll, D.I.A., "Some observations of the transition process on the windward face of a long yawed cylinder", J.Fluid Mech., Vol. 150, pp. 329-356, 1985

100.Görtler, H., "Dreidimensionale Instabilität der ebenen Staupunktströmung gegenüber wirbelartigen Störungen", In Fifty Years of Boundary Layer Research (Ed. Görtler & Tollmien), p. 304, Vieweg und Sohn, Braunschweig, 1955

101.Hämmerlin, G., "Zur Instabilitätstheorie der ebenen Staupunktströmung", In Fifty Years of Boundary Layer Research (Ed. Görtler & Tollmien), p. 315, Vieweg und Sohn, Braunschweig, 1955

102.Hall, P., Malik, M.R., Poll, D.I.A., "On the stability of an infinite swept attachment line boundary layer", Proc. R. Soc. Lond. A 395, pp. 229-245, 1984

103.Spalart, P.R., "Direct numerical study of leading edge contamination", AGARD CP N° 438, 1988

104.Hall, P., Malik, M.R., "On the instability of a three-dimensional attachment line boundary layer : weakly non linear theory and a numerical approach", J. Fluid Mech., Vol. 163, pp. 257-282, 1986

105.Jimenez, J., Martel, C., Agui, C.J., Zufiria, J.A., "Direct numerical simulation of transition in the incompressible leading edge boundary layer", Technical Note ETSIA/MF-903, April 1990

106.Pfenninger, W., "Flow phenomena at the leading edge of swept wings", Recent Developments in Boundary Layer Research, Part IV, AGARDograph 97, May 1965

107.Gregory, N., Love, E.M., "Laminar flow on a swept leading edge - Final progress report", NPL Aero. Memo. 26, 1965

108.Hardy, B.C., "Experimental investigation of attachment line transition in low speed, high lift wind tunnel testing", AGARD CP N° 438, 1988

109.Arnal, D., Juillen, J.C., "Etude de la transition et de la contamination de bord d'attaque sur ailes en flèche", AGARD CP N° 438, 1988

110.Arnal, D., Juillen, J.C., "Leading edge contamination and relaminarisation on a swept wing at incidence", 4th Symp. on Numerical and Physical Aspects of Aerodynamic Flows, Cebeci Ed., Springer Verlag, 1989

111.Poll, D.I.A., Paisley, D.J., "On the effect of wing taper and sweep direction on leading edge transition", Aeron. J., pp. 109-117, March 1985

112.Seyfang, G.R., "Turbulence reduction on swept leading edges", Turbulent Drag Reduction by Passive Means, London, September 1987

113.Moretti, P.M., Kays, W.M., "Heat transfer to a turbulent boundary layer with varying free stream velocity and varying surface temperature. An experimental study", Int. J. Heat Mass Transfer, Vol. 8, pp. 1187-1202, 1965

114.Launder, B.E., Jones, W.P., "On the prediction of laminarisation", ARC CP 1036, 1969

115.Spalart, P.R., "Numerical study of sink-flow boundary layers", J. Fluid Mech., Vol. 172, pp. 307-328, 1986

116.Bertelrud, A., Nordstrom, J., "Experimental and computational investigation of the flow in the leading edge region of a swept wing", AIAA Paper n° 83-1762, 1983

117.Ginovart, C., ONERA/CERT Internal Report (unpublished), 1988

118.Fage, A., "The smallest size of spanwise surface corrugation which affects boundary layer transition on an airfoil", R&M N° 2120, A.R.C. Technical Report, January 1943

119.Cebeci, T., Egan, D.A., "The effect of wave-like roughness on transition", AIAA Paper n° 88-0139, 1988

120.Nayfeh, A.H., Ragab, S.A., Al-Maaitah, A., "Effect of roughness on the stability of boundary layers", AIAA Paper 86-1044, 1986 - Also *Phys. Fluids* 31(4), April 1988

121.Carmichael, B.H., "Surface waviness criteria for swept and unswept laminar suction wings", *Norair Rep. n° NOR-59-438 (BLC-123)*, 1959

122.Holmes, B.J., Obara, C.J., Martin, G.L., Domack, C.S., "Manufacturing tolerances for natural laminar flow airframe surfaces", SAE Paper 850863, General Aviation Meeting and Exposition, Wichita, Kansas, April 16-19, 1985

123.Holmes, B.J., Obara, C.J., Yip, L.P., "Natural laminar flow experiments on modern airplane surfaces", NASA Technical Paper 2256, June 1984

124.Fasel, H., Bestek, H., Schefenacker, R., "Numerical simulation studies of transition phenomena in incompressible, two-dimensional flows", AGARD CP n° 224, 1977

125.Nenni, J.P., Gluyas, G.L., "Aerodynamic design and analysis of an LFC surface", *Astronautics and Aeronautics*, July 1966

126.Sinha, S.N., Gupta, A.K., Oberai, M.M., "Laminar separating flow over backsteps and cavities - part I : backsteps", *AIAA Journal*, Vol. 19, N° 12, December 1981 - "Part II : cavities", *AIAA Journal*, Vol. 20, N° 3, March 1982

127.Olive, M., Blanchard, A., "Etude expérimentale du déclenchement de la transition par des cavités en écoulement incompressible", Internal Report ONERA/CERT N° 18/5007 DN, 1982

128.Juillen, J.C., Arnal, D., "Etude expérimentale du déclenchement de la transition par rugosités et par rainures sur le bord d'attaque d'une aile en flèche en écoulement incompressible", Internal Report ONERA/CERT N° 51/5018.35, 1990

129.Hahn, M., Pfenninger, W., "Prevention of transition over a backward step by suction", *J. Aircraft*, Vol. 10, N° 10, October 1973

130.Gregory, N., Walker, W.S., "The effect on transition of isolated surface excrescences in the boundary layer", *ARC C&M n° 2779, Part 1*, 1951

131.Von Doenhoff, A.E., Braslow, A.L., "The effect of distributed surface roughness on laminar flow", *Boundary Layer Control*, Vol. II, Lachmann Ed., Pergamon, New York, 1961

132.De Bruin, A., "The effect of a single cylindrical roughness element on boundary layer transition in a favourable pressure gradient", *Symp. "Laminar-Turbulent Transition"*, Toulouse, Ed. Arnal and Michel, Springer Verlag, 1990

133.Chiu, W.K., Norton, P., "The receptivity of laminar boundary layer flow to leading edge vibrations", *J. of Sound and Vibrations*, 141(1), pp. 143-164, 1990

134.Maresh, J.L., Bragg, M.B., "The role of airfoil geometry in minimizing the effect of insect contamination of laminar flow sections", AIAA Paper 84-2170, 1984

135.Croom, C.C., Holmes, B.J., "Flight evaluation of an insect contamination protection system for laminar flow wings", SAE Paper 850860, General Aviation Meeting and Exposition, Wichita, Kansas, April 16-19, 1985

136.Horstmann, K.H., Quast, A., Redeker, G., "Flight and wind tunnel investigations on boundary layer transition at Reynolds numbers up to 10^7 ", ICAS Congress, Jerusalem, Paper 88-3.7.1., 1988

137.Horstmann, K.H., Quast, A., Redeker, G., "Flight and wind tunnel investigations on boundary layer transition", *J. of Aircraft*, Vol. 27, N° 2, pp. 146-150, February 1990

138.Horstmann, K.H., Redeker, G., Miley, S.J., "Flight investigations of Tollmien-Schlichting waves on an aircraft wing", ICAS Congress, Paper 90-6.1.2., 1990

139.Malik, M.R., "Instability and transition in supersonic boundary layers" in "Laminar Turbulent Boundary Layers", Energy Sources Technology Conference, New Orleans, Louisiana, February 1984

140.Horstmann, K.H., Redeker, G., Quast, A., Dressler, U., Bieler, H., "Flight tests with a natural laminar flow glove on a transport aircraft", AIAA Paper n° 90-3044, 1990

141.Henke, R., Münch, F.X., Quast, A., "Natural laminar flow : a wind tunnel test campaign and comparison with flight test data", AIAA Paper n° 90-3045, 1990

142.Raspot, A., George-Falvy, D., "Boundary layer studies on the Phoenix sailplane", VIII Congress of O.S.T.I.V., Köln, June 1960

143.Runyan, L.J., George-Falvy, D., "Amplification factors at transition on an unswept wing in free flight and on a swept wing in wind tunnel", AIAA Paper n° 79-0267, 1979

144.Boltz, F.W., Kenyon, G.C., Allen, C.Q., "Effects of sweep angle on the boundary layer stability characteristics of an untapered wing at low speeds", NASA TN-D 338, 1960

145. Morkovin, M.V., Reshotko, E., "Dialogue on progress and issues in stability and transition research", IUTAM Symp. "Laminar-Turbulent Transition", Toulouse, Ed. Arnal and Michel, Springer Verlag, 1990

146. Bushnell, D.M., Malik, M.R., Harvey, W.D., "Transition prediction in external flows via linear stability theory", IUTAM Symp. "Transsonicum III", Göttingen, Ed. Zierep and Oertel, Springer Verlag, 1988

AD-P006 969



The Eddy Structures in Bounded Shear Flows

by

Ron F. Blackwelder
 Department of Aerospace Engineering
 University of Southern California
 Los Angeles, CA 90080-1191

92-17811

**Abstract**

The near wall turbulent eddies consist of streamwise vortices, low speed streaks, intense shear layers, inflectional velocity profiles, oscillations and ejections of low speed fluid out into the logarithmic layer. Away from the wall, large scale three dimensional outer structures dominate the flow. A mass of data has been accumulated over the past 25 years concerning these eddies and their interaction. These eddies and events will be discussed as well as their Reynolds number dependence.

Near Wall Eddy Structures

The eddy structure near the wall in bounded shear flows has usually been referred to as the "bursting sequence" or the "bursting phenomenon". This sequence of events is depicted in figure 1 which indicates their order of occurrence. Each of the individual events in the boxes in figure 1 will be discussed separately below. It is also suggested that there is a feed back mechanism between the large scale outer eddies in the shear flow and the wall layer events as seen in the figure. This will be discussed after the large outer eddies are addressed.

Streamwise Vortices

The existence of streamwise vortices in the near wall region has been suggested by many authors. In its simplest hypothetical case, these vortices would appear as vortex tubes aligned with the streamwise direction and appear in counter-rotating pairs as sketched by Blackwelder(1978). They can occur individually but symmetry conditions require that the average ω_x vorticity be zero. Kline et al.(1967)¹ assumed such vortices existed within the flow field but offered no supporting evidence. Kim et al.(1971) showed some hydrogen bubble visualization photographs that had rotation consistent with streamwise vortices. Their

photos also clearly showed that the observed vortices were inclined away from the wall. Handler et al.(1989) found a series of correlations, $R_w(\Delta y, y)$ from direct numerical simulations to be consistent with the presence of streamwise vortices with centers at $y' \approx 20$. Bakewell and Lumley(1967) and more recently Aubry et al(1988) used the proper orthogonal decomposition in the near wall region to determine the eddy structure containing the largest amount of energy and found it to be a pair of counter-rotating streamwise vortices. Lee, et al. measured the velocity gradients on the wall and ascribed their results to alternating regions of streamwise vorticity. Blackwelder and Eckelmann(1979) measured the two stress components on the wall and found that the most probable stress pattern conformed to streamwise vortices of opposite sign; however they estimated that the strength of the streamwise vortices to be an order of magnitude less than the shear at the wall. Smith and Schwartz(1983) photographed hydrogen bubbles in the $y-z^2$ plane and found significant streamwise rotation in the wall region for $y' \leq 10$. They observed frequent counter-rotating structures and suggested that they were associated with the low speed streaks. They concluded that rotating, streamwise structures do occur in the wall region and they often occurred in counter-rotating pairs.

The cumulative evidence from these researchers suggests that streamwise vortices do randomly occur in the wall region. They have diameters that grow from 10 to $40v/u$, and they migrate away from the wall during their lifetime such that their centers range from 10 to $50v/u$, from the wall. These vortices may be a part of a larger vortex structure, such as a hairpin or horseshoe vortex, that extends further into the logarithmic region. In this case, the streamwise vortices would be composed

¹ In the earliest research on the subject, this structure was referred to simply as a "burst" as in Kline et al(1967). In view of our increased knowledge, it is more descriptive to use the term "burst" only as an adjective in describing this sequence of events.

² The usual boundary layer coordinates of x , y and z with the velocity components u , v , and w will be used in the streamwise, normal and spanwise directions respectively.

SEQUENCE OF THE BURSTING PROCESS

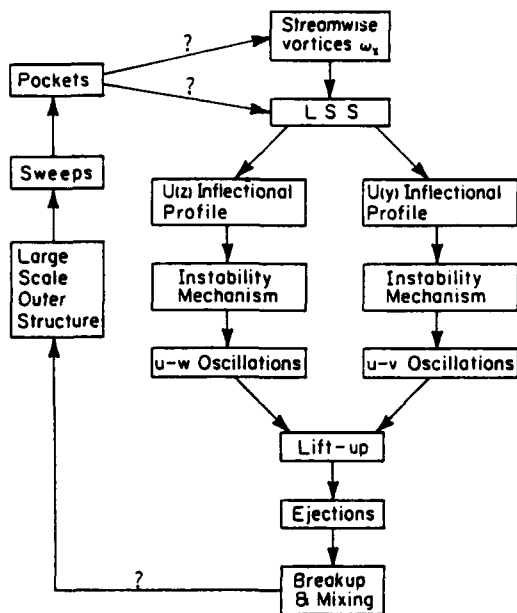


Figure 1. The sequence of events comprising the bursting process.

of some ω_y and ω_z as well as ω_x . Because of the no-slip boundary condition at the wall, the portion of the vortex in the near wall region would be strongly stretched as a result of the strong velocity strain rate there. The length of the vortices has not been ascertained.

The vortices do not necessarily occur in counter-rotating pairs. Homogeneity in the spanwise direction in a two dimensional flow require that the mean ω_z vorticity be zero. Likewise the symmetrical properties of the flow constrain the averaged properties of ω_x about a point to be anti-symmetrical in the spanwise direction (Blackwelder 1988). By using the velocity correlation in the wall region from direct numerical simulations, Moser and Moin (1984) have argued that since $R_{uw}(\Delta z)$ does not have a minimum at $y' > 30$, single vortices must be more predominant than counter-rotating pairs. More recent results have attempted to improve the conditional averages by imposing an additional condition to account for the asymmetries within the instantaneous flow field. Guezenec et al. (1989) used the quadrant detection technique and also determined the location of the stronger vortex. Using reflection, they conditionally averaged with the stronger vortex always on the same side of the centerline. The results indicated that the turbulent producing events identified by the quadrant method were associated primarily with a single vortical structure instead of a pair of equal strength counter-rotating vortices.

It is interesting to note that all of the above evidence has been obtained without a working definition of a vortex. Alternatively, the vorticity is easily defined and can be calculated from the direct numerical simulations. Moin and Kim (1985) found that the predominate fluctuating vorticity component lying in the $x-y$ plane is indeed ω_x for $y' < 30$. At higher elevations, the preferred orientation of the vorticity vector in this plane was at 45°. However when they examined the instantaneous vorticity lines, Kim and Moin (1986) did not find any elongated regions of streamwise vorticity. This results from the fact that the instantaneous vortex lines in the wall region are dominated by the mean vorticity, ω_x . Thus any region that has a vortex line aligned predominately in the x direction will have a stronger ω_x component than ω_z at that location. This must be a rare event, however they do find some vorticity lines satisfying this criteria (viz. figure 20 of Kim and Moin (1986)).

An alternative method to study this problem is to examine a known flow with embedded streamwise vortices, such as the Görtler instability on a concave wall. The perturbation vorticity will be much smaller than the mean vorticity. In addition, the magnitude of the streamwise component of vorticity is an order of magnitude smaller than the other two components of the perturbation vorticity as pointed out by Blackwelder and Swearingen (1989). In spite of this, the streamwise vortices are indeed present and are the principal eddies in the flow. Since they exist in a strong mean shear, their magnitude is not as important as their coherence. From a physical viewpoint, the Görtler streamwise vortices do not make a complete rotation during their life time; i.e. they need to only rotate 30° - 60° to completely redistribute the momentum in the wall region and set up a secondary instability. Hence the existence of vortices do not necessarily imply large amplitude vorticity; rather it is the phase and coherence of the motion that is important.

The origin of the streamwise vortices in the turbulent wall region remains a mystery.

Low Speed Streaks

The low speed streaks (denoted by LSSs) are the most ubiquitous aspect of the bursting process. They were first noted by Hama (see Corrsin 1957) and first studied by Kline et al. (1967). An experimental observation of the low speed streaks is shown in figure 2. The data were taken by a spanwise hot-wire rake at $y' = 15$ in a turbulent boundary layer. The time record from the twelve sensors has been converted to a streamwise spatial distance by Taylor's hypothesis to provide a continuous record over $0 < x' < 4000$. Constant velocity contours for $u(x, z) = k[\bar{U}(y) - u_{rms}(y)]$ are plotted for $k = -1$ and -2 . The lower speed fluid appears inside the elongated regions

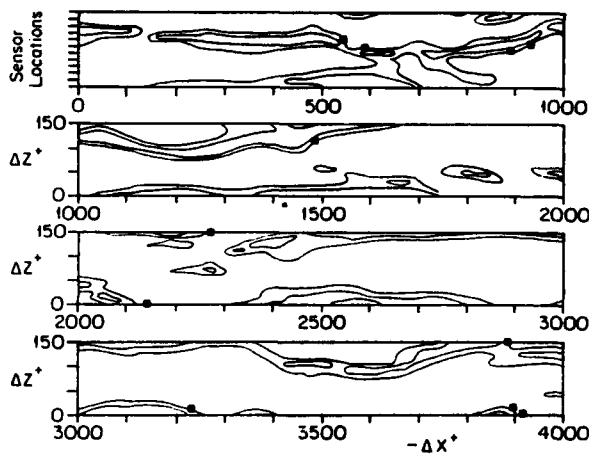


Figure 2. Iso-contours of the streamwise velocity component at $y'=15$ in a turbulent boundary layer. The VITA detection locations are denoted by the solid squares.

which have spanwise scales of typically $20v/u$, and streamwise scales of several hundred viscous scales.

A simplified model of the low speed streaks is found in figure 3. The shape of the streaks is indicated in all three dimensions. The streaks are shown with equal spacing in the spanwise direction but in nature they have a random spanwise distribution. Also the streaks meander during their downstream migration. This motion has deliberately been eliminated to simplify the figure. Lee et al.(1974) found that their most probable spacing is $80v/u$, and their average spacing is $100v/u$, very near the wall. Talmom et al.(1986) showed that their average width is only $20-40v/u$, and that the higher speed fluid lying between them is three to four times as wide. Nakagawa and Nezu(1981) suggested that the spanwise spacing, λ_s , is lognormal and showed that the spacing increased as one approached the logarithmic region. In one of the more comprehensive studies of these eddies, Smith and Metzler(1983) found that the probability distribution of λ_s is indeed lognormal. They also showed that the streaks persisted for $\Delta t' = 500$ on the average but times up to $2500v/u^2$ were observed. Even with a moderate convection velocity of $5u_s$, this observation indicates that the streaks are several thousand viscous scales long. They also showed that the structure of the LSSs is independent of the Reynolds number over the range $700 < Re_s < 5800$ agreeing with the data compiled from different investigators by Hirata et al(1982).

The origin of the streaks is still unknown. Assuming the streamwise vortices exist on the scales indicated above, their induced motion could be sufficient to explain the observation of the streaks. Since the streaks lie in a region of strong velocity gradient, the streamwise vorticity need not be very strong to create the streaks. An alternative suggestion is that the streaks are a manifestation of the strong shear in the wall region. Lee et

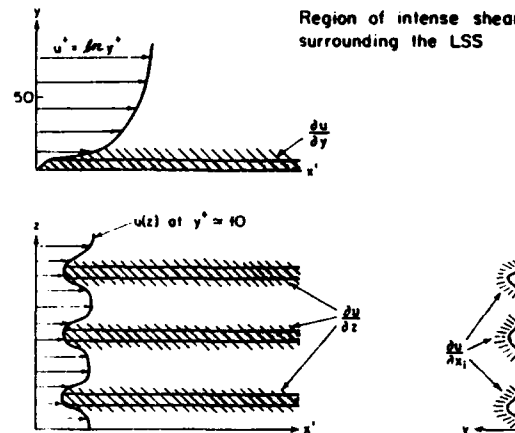


Figure 3. Sketch of a model of the LSSs showing the regions of intense shear and the inflectional surface surrounding the low speed fluid.

al.(1990) studied the effects of a strong uniform shear flow on homogeneous turbulence and found that when the mean shear was comparable to that found in the wall region, low speed streaks resulted, thus suggesting that a solid boundary may not be necessary for their formation. This mechanism would also amplify the existing ϵ , due to stretching and hence the streaky structure may still be associated with ϵ , eddies. It is interesting that only the streamwise velocity component develops the streaky structure. Moin and Kim(1982) showed that neither the v , w , nor the pressure had an elongated streaky structure anywhere in the wall region. However ϵ , should also have an elongated streaky structure primarily due to the strong $\partial u/\partial z$ (discussed below) associated with the LSSs. Streaks have also been observed by Nakagawa and Nezu(1981) and Smith and Metzler(1983) to merge and divide in the wall region, however this happens infrequently and can not be considered as a generation mechanism. Chu and Falco(1988) have suggested that small eddies moving toward the wall may generate the LSSs.

Although the low speed streaks seem to appear in most low Reynolds number bounded flows, there are documented cases where they do not appear, e.g. Grass(1971), and yet the ensuing dynamics seem to be quite similar. That is, ejections etc. seem to appear from the low speed regions(not streaks) that formed behind the roughness elements. This suggests that low speed streaks are not essential to the near-wall layer dynamics, but that sites of low speed fluid are important.

Intense Shear Layers and Inflectional Profiles

Irrespective how the LSSs were created, once they are present they are surrounded by a shear layer and inflectional velocity profiles. Since the streaks are indeed low speed fluid, they have relatively higher speed fluid on both

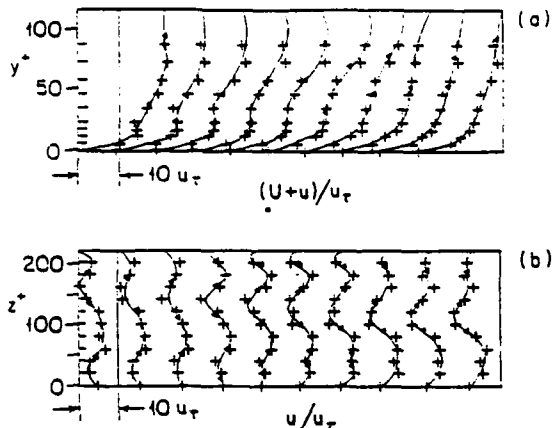


Figure 4. Instantaneous turbulent boundary layer profiles of the streamwise velocity component in the (a) normal and (b) spanwise directions. The data points are indicated by (+) and the inflection points by (x).

sides in the spanwise direction and there is obviously higher speed fluid above them as sketched in figure 3. Since there is no mean gradient in the spanwise direction, the existence of the LSSs implies that there will also be an inflectional velocity profile in that direction as well as seen in the sketch. In the normal direction, inflectional profiles are often seen; however because of the mean gradient in that direction, the LSS can exist without an inflectional $U(y)$ profile.

The frequency of occurrence of the inflectional profiles has been discussed by Blackwelder and Swearingen(1989). They have found that the inflectional profiles in both the spanwise and normal direction are quite ubiquitous within the flow field as seen in figure 4. Surprisingly their results showed that the $U(y)$ profile is also inflectional with approximately the same frequency as the spanwise profile. Thus it is almost impossible to observe an instantaneous velocity profile anywhere in the wall region without it having an inflection point.

It is an interesting exercise to ask where the loci of the inflection points lie. Often the inflectional characteristics are thought of as occurring at a point (i.e. an inflectional point) although that can not be valid in general. In the classical one dimensional textbook case of $U(y) = \tanh(y/4)$, the inflection point is indeed a point. Expanding this concept to a two dimensional flow shows that the inflections lie along a line. In a three dimensional flow as in the wall layer, the inflections are contained within a surface. That is, the loci of the points where the derivative $\partial^2 U / \partial a^2 = 0$ where a is any direction prescribe a surface in the three dimensional space. (Of course one can also examine the inflectional characteristics of the other velocity components as well and find other surfaces.) If the higher speed

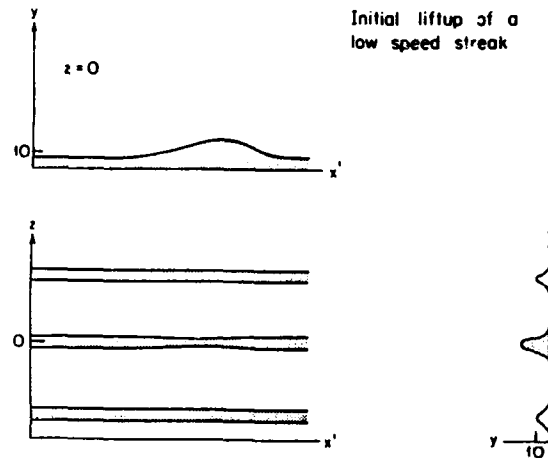


Figure 5. Sketch of the liftup of a portion of the LSS.

fluid above the LSSs has become inflectional, the LSSs will be enveloped by an inflection surface. Thus it is useful to think of this surface as surrounding the low speed regions of fluid. The inflection surfaces are located randomly in space and time and can end at any location in the fluid where the inflectional profiles no longer exist.

The inflectional $U(y)$ profiles have been observed by many investigators. Kim et al.(1971) found that the $U''(y)=0$ was a common feature of all cases of lift up observed and Willmarth and Lu(1972) also found that the bursting phenomenon occurred when the velocity profile first became inflectional. Grass(1971), Kline et al.(1967) and others have concurred.

Lift-up of LSS

At some point in the bursting process, the low speed streaks are lifted up away from the wall as sketched in figure 5. This motion is described by Kline et al.(1967) as a gradual process during which the streaks marked with hydrogen bubbles appear to become thinner as they move away from the wall. Based upon motion pictures of the flow, they suggest that the lift-up is a result of streamwise vorticity. When following a marked streak downstream, it is observed that the slow outward drift suddenly become more rapid and is a precursor to the oscillations discussed below. This lift-up was defined by Kim et al(1971) as the first stage of the dynamical bursting process and that it typically created an inflectional $U(y)$ profile. They also suggested that it leads to an instability such as the inviscid one described below. Bogar and Tiederman(1986) have found that multiple lift-ups occur from the same streak as indicated in figure 6. The oscillations sketched in this figure are discussed in the following section.

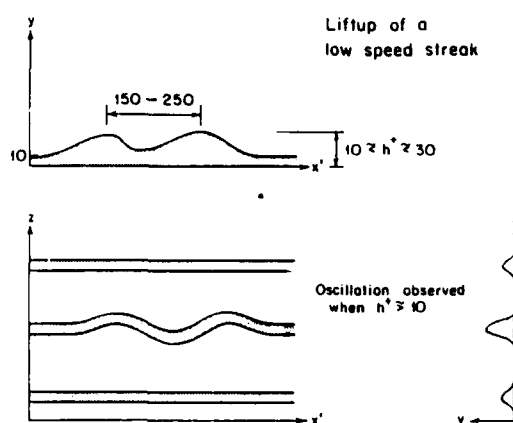


Figure 6. Sketch of the later stages of the lift-up and the oscillations of the streak.

An Instability Mechanism and Oscillations

The importance of the inflectional profiles is that they seem to set up the necessary conditions for an inviscid shear layer instability within the fluid. Michalke(1965) has analyzed this problem in detail for the hyperbolic tangent profile with a spatial scale of Λ . He found that the most rapidly growing disturbance had a wavelength of 14Λ and found the growth rates of the linear instability are extremely large. However Michalke's results apply to a flow field that is parallel, steady and two-dimensional. Gaster et al.(1985) found that the non-parallel effects were minimal and that when the local inflectional profile was used to compute the stability, the theory accurately predicted the measured values even though the flow was nonlinear. Greenspan and Benney(1963) examined a similar flow field as Michalke but with the thickness of the shear layer varying in time with a time scale larger than that of the inherent instability. The unsteadiness increased the growth rates by an order of magnitude more than the steady flow growth rates implying that the unsteadiness made the inherent instability even more unstable.

The two-dimensionality also does not appear to be extremely critical to Michalke's results as long as the spanwise dimension is large compared with Λ . Nishioka et al.(1980) used the two-

dimensional theory to calculate the growth rates of an inflectional profile in a transitional channel flow. The inflectional profile was formed by the latter stages of development of Tollmien-Schlichting waves which was highly three-dimensional when compared with the original Tollmien-Schlichting disturbance. The spanwise extent of the inflectional region was large compared to Λ and the two-dimensional theory accurately predicted the wavelength, eigenfunction and growth rate observed on the centerline of the disturbance.

Another factor that could influence the results from Michalke's theory is the proximity of the wall. Huerre(1983) has shown that Michalke's results are unaffected as long as the wall is more than 1.2Λ away from the wall. The above mentioned results of Nishioka et al.(1980) also support this result.

The inflectional instability will produce a growing disturbance with a wavelength of approximately 14Λ according to Michalke. The difficulty is that if the disturbance grows as fast as Michalke predicts, its amplitude will increase by 36 and its energy by more than 1000 while it travels only one wavelength downstream! Thus in a turbulent flow environment where the background disturbance level is large, it is not evident that one will be able to observe the oscillations over more than one wavelength. Even if it were possible, the nonlinear effects may distort the disturbance to a point of nonrecognition. Kim et al.(1971) did observe an oscillatory disturbance just downstream of the inflectional profile that grew to a relatively large scale in only one or two wave lengths supporting the above hypothesis.

The length scale of the inflectional profiles is roughly $10v/u$, according to Blackwelder and Swearingen(1989) and thus the wavelength of the oscillations should be approximately $150v/u$, for a shear layer instability. This oscillation was first noticed by Kline et al.(1967). Kim et al.(1971) observed that it appeared just downstream of the inflectional profile. The observed wavelengths of other observers is given in the table below.

The oscillations observed by the above investigators is believed to be associated with ejections at a slightly greater distance downstream as discussed below. This oscillation should not be associated with the bursting frequency discussed below.

Table

	R_g	λ^*
Blackwelder and Kaplan(1976)	2550	200
Emmerling(1973)	1800	200
Bogar(multiple ejections)	1700	180
Schewe(1983)	1400	145
Bacher and Smith(1985)	1250	150
Kim, et al.(1971)	660	240
Oldaker and Tiederman(1977)	500	120
Bogar and Tiederman(multiple ejections)	420	225
Blackwelder and Eckelmann	400	160

Ejections

The next stage of the bursting process is a more rapid outward movement of a small low speed parcel of fluid called an ejection by Corino and Brodkey(1969). They stated that the ejections were $20-40v/u$, long in the streamwise direction and were $15-20v/u$, in the spanwise direction and originated at $5 < y' < 15$. The ejections appear to move away from the wall with an angle of approximately 8° and were skewed from the downstream direction an average of 15° in the $x-z$ plane. Since the ejections are low speed fluid moving away from the wall, they contribute significantly to the Reynolds stress in the near wall region. Above $y' \approx 15$, they are the primary contributor to the uv shear stress whereas the sweeps have been found to be the main contributors to the shear stress below $15v/u$.

The ejections originate from a lifted portions of the LSSs and have been studied in detail by Bogard and Tiederman(1986). They define an ejection as an outward movement of a portion of a LSS filament beyond $y' = 15$ with sufficient outward momentum that it continued to move beyond $y' = 35$. They found that single or multiple ejections could occur within a short time interval as reported previously by Corino and Brodkey(1969) and Willmarth and Sharma(1984). A double ejection is shown in figure 7.

The cine films accompanying Oldaker and Tiederman(1978) strongly suggest that the ejections are a later stage of the oscillatory phase of the bursting phenomenon. Their movies and others have shown that when an ejection occurs, it is often preceded by an oscillation upstream. This idea is also suggested by the early work of Kim et al.(1971). The mechanism seems to be that an oscillations begins as a result of the inflectional profile as sketched in figure 3. Since the growth rates are so extremely rapid, the wave train of the oscillations may be quite short; i.e. only one or two crests may be observed. These crests develop from the initial disturbances that had a length scale corresponding to the most amplified wave. The high growth rate of the linear theory suggests that the oscillations increase their energy by 10^3 after traveling one wave length, i.e. $150v/u$, downstream. The movies indicate that part of the wave moves away from the wall more rapidly than the remaining portion, thus forming an ejection as suggested in figure 7. This may be due to non-linear effects, interaction with the wall or other unknown reasons. This idea suggest that when multiple ejections occur, they would originate from the same LSS since it is unlikely that two adjacent streaks would have the same growth rates due to the randomness of the motion in this region. By combining visual and transducer techniques, Bogard and Tiederman found that the multiple ejections do originate from the same streak. Moreover, Bogard(1987) found that when multiple

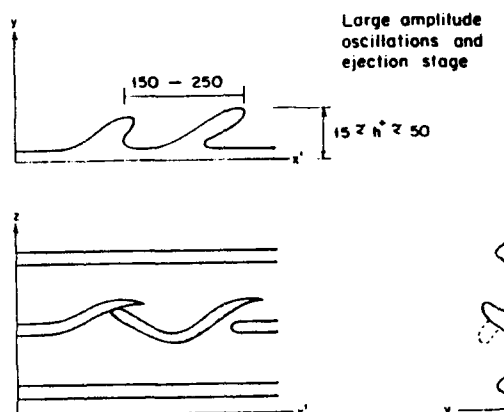


Figure 7. Continuation of the liftup phase of the LSS and the formation of the ejection.

ejections occurred, the mean spacing between them was $225v/u$, consistent with the above argument.

Breakup

'Breakup' is the last phase of the bursting process and terminates the coherent aspect of the phenomenon. A sketch of the mixing associated with the breakup is seen in figure 8. Breakup is often defined from the visualization studies and is described as the loss of the Lagrangian marker in the fluid. Of course this definition just states that it is impossible to follow the motion further and hence does not describe the motion itself. It appears that after the ejection, the mixing is so rapid with the higher speed fluid that all evidence of coherent motion vanishes.

The breakup of the motion is an aspect of the bursting process that occurs in the region $20 < y' < 50$ and is the terminal stage of the ejections. Since more than one ejection may occur from the same streak, breakup includes the termination of multiple ejections. Smith and Metzler(1983) found that the ejections and breakup are not the end of the LSS, but rather a residual amount of low-speed fluid remains near the wall that provides the seed for or grows into a LSS downstream. Hence each streak may have more than one breakup associated with it.

³ This aspect of the motion was originally called the "burst" by Kline et al.(1967) and was renamed the breakup phase by Kim et al.(1971). Present usage prefers to use the term "burst" as an adjective only in describing the near wall turbulence.

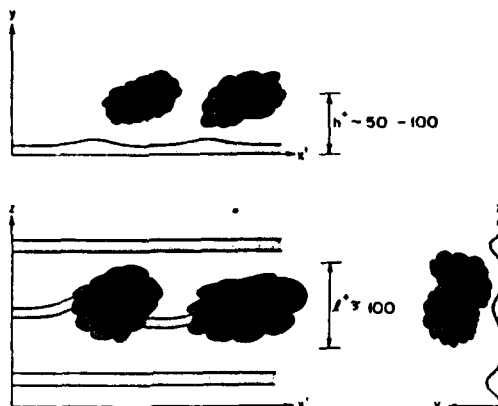


Figure 8. Sketch of the mixing in the near wall region after the breakup of an ejection.

The Eddies in the Outer Region

The Boundary Layer

The outer region of bounded turbulent shear flows has been studied most thoroughly in the turbulent boundary layer primarily because of its technological importance. A visualization of a zero pressure gradient boundary layer at a low Reynolds number is found in figure 9 taken from Falco(1977). The flow is from left to right. The thickness of the boundary layer is δ . Smoke was injected into the boundary layer upstream and fills the turbulent region. Near the wall(i.e. the lower portion of the photo), the flow is completely turbulent and smoke fills the entire region. However for $y > 0.2-0.4\delta$, there are areas without smoke indicating regions of irrotational flow. These irrotational regions are named 'valleys' since they lie between two zones of turbulent regions called 'bulges.' The entire area is called the intermittent region because turbulent and nonturbulent fluid occurs randomly and it extends from $y=0.3\delta$ outwards. The surface that separates these two types of fluid is called the turbulent/nonturbulent interface.

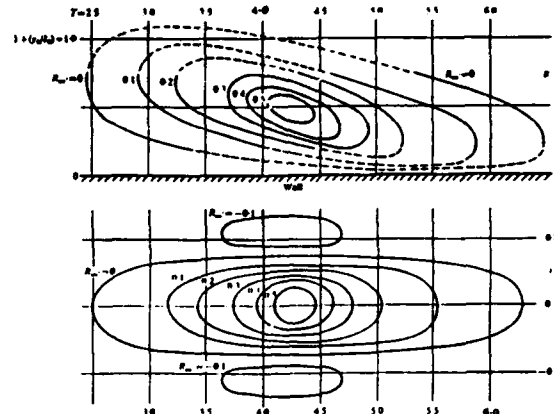


Figure 10. Three dimensional space-time correlation of the streamwise velocity fluctuations, $R_w(Ax_0, Ay, Az, At)$ from Kovasznay et al.(1970). The fixed probe was located at $y/\delta=0.5$ and $Ax_0 = 3.85$.

The early space-time correlations of Favre et al.(1965) in a zero pressure gradient boundary layer indicated that there was considerable structure in this region. Kovasznay, Kibens and Blackwelder(1970) used a streamwise separation between sensors to help filter out the high frequency and uncorrelated fluctuations to provide a more graphical description of these eddies. Their three dimensional correlation of the streamwise velocity component, $R_w(Ax_0, Ay, Az, At)$ is reproduced in figure 10. The fixed spatial separation, $Ax_0 = 3.85$, was sufficient to eliminate uncorrelated structures and only the remaining large scale outer structure(denoted by LSOS) remains. As can be seen, the eddy has characteristic scales of 3δ , δ and δ in the streamwise, normal and spanwise directions respectively. In addition, the eddies are inclined as a result of the mean shear, dU/dy . The earlier work of Klebanoff(1954) and others have shown that the eddies in this region of the flow are much less energetic than those found in the wall region.



Figure 9. Visualization of a turbulent boundary layer with $Re_0 \approx 1000$ taken from Falco(1977)

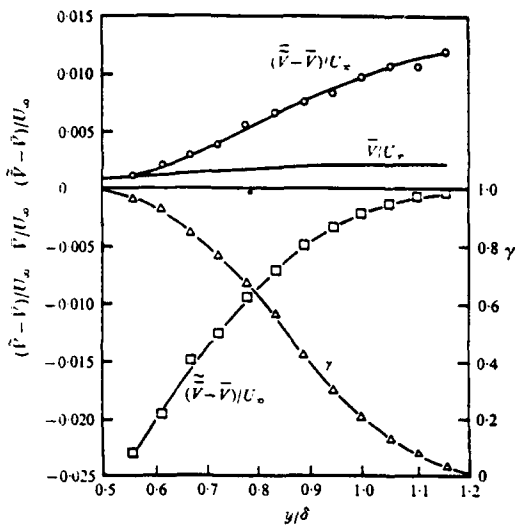


Figure 11. Conditional zone averages of the normal velocity component in the outer region of a turbulent boundary layer from Kovasznay et al.(1970).

In the turbulent boundary layer, the LSOS are associated with the entrainment of irrotational fluid into the turbulent region. This has been studied by using an intermittency function, $\gamma(y)$, which is defined as the fraction of time that the flow is turbulent at the location y . Kovasznay et al.(1970) used a detection scheme to determine when the flow was turbulent and defined conditional zone averages such as shown in figure 11 for the normal velocity component. The intermittency function, $\gamma(y)$, is seen to vary from unity near the wall to zero in the freestream, i.e. $y>1.25$. The mean value of the normal velocity component is shown in the upper portion of the figure along with the zone average for turbulent region, \bar{V} . Since $\bar{V}_t > 0$ everywhere, it indicates that the regions with the turbulence, i.e. the bulges, are generally moving away from the wall. On the other hand, the nonturbulent zone average of the normal velocity component, \bar{V}_{nt} , is always less than zero. Hence this irrotational fluid must be moving toward the wall, i.e into the turbulent region. Note that for $y<0.65$, \bar{V}_{nt} has a magnitude greater than $0.02U_\infty$. Since this is an order of magnitude larger than the maximum value of \bar{V} , the valleys are considered to be the location where most of the entrainment occurs. This strong component towards the wall also suggests that this feature may be important in the wall region as well.

The tangential Reynolds stress, \bar{uv} , is less important in the outer region than near the wall because much less production occurs in the outer region. Blackwelder and Kovasznay(1972) conditionally averaged the Reynolds stress and found that it is carried almost exclusively by the turbulent

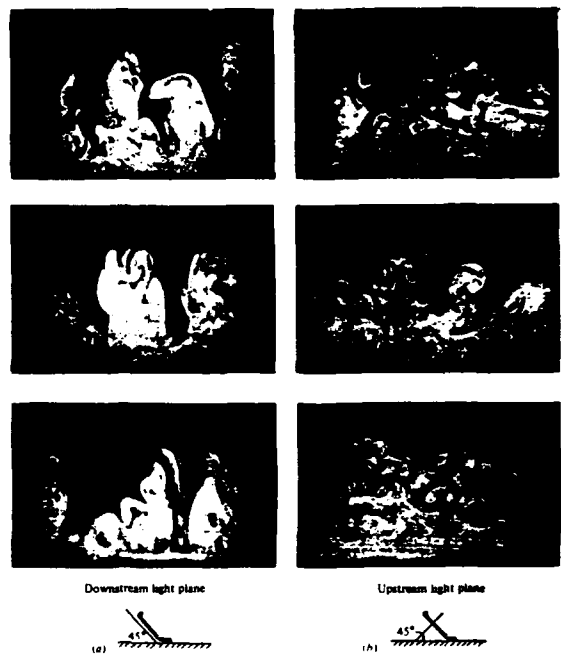


Figure 12. Comparison between views with the transverse light plane inclined at (a) 45° downstream and (b) 45° upstream taken from Head and Bandyopadhyay(1981).

bulges. Antonia(1972) and Hedley and Keffer(1974) measured the distribution of the Reynolds stress within the turbulent bulges and found that the largest portion of it occurs near the upstream interface of the LSOS. This is also the interface where stretching occurs due to the mean shear. Falco(1977) suggest that the Reynolds stress near this interface is associated with smaller 'typical' eddies being carried along with the interface discussed in the next section.

Substructure of the Outer Eddies

Less is known about the substructure of the LSOS than the wall eddies primarily because there is less turbulence production there and hence they are not as interesting. Also it is more difficult to visualize the flow field in the outer region. However as mentioned earlier, Falco(1977), did perform such a visualization study and concluded that the Reynolds stress was borne by smaller scale 'typical' eddies that ride along the upstream interface of the LSOS.

Head and Bandyopadhyay(1981) introduced smoke in a similar manner as Falco. However they orientated their light sheet used for visualization at various angles with respect to the wall. The observed structures appeared to be inclined approximately 45° from the wall in the downstream direction. Their results at $Re=600$ are shown in figure 12 for the two angles $\pm 45^\circ$. The difference between the two angles is striking. The authors interpreted

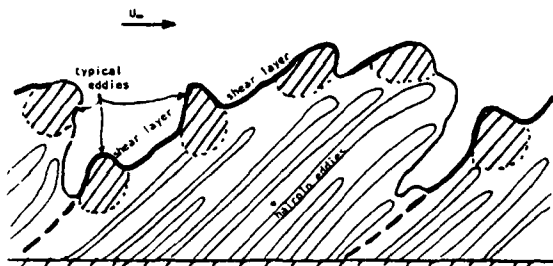


Figure 13. Composite sketch of the large scale outer structure showing the strong shear layers and typical eddies on the upstream interface and the embedded hairpin eddies.

the structures shown in the light plane as hairpin vortices inclined at 45°. Thus the downstream light sheet captures a plan view of the vortices whereas only the cross-section of their legs is captured by the upstream light sheet.

A sketch of their conclusions is shown in figure 13. The hairpin eddies are inclined downstream and are contained within the LSOS. Head and Bandyopadhyay(1981) suggest that the diameter of the vortex legs and other cross-stream dimensions appear to scale with the wall variables, v and u , while their length is limited by the thickness of the layer, δ . A large number of hairpin vortices are contained within each turbulent bulge and this number must increase with Re_θ . Apparently the location of the hairpins are randomly distributed within the turbulent region. Figure 13 also illustrates the location of the typical eddies discussed by Falco(1977). At present there is no known relationship between the typical eddies and the embedded hairpin eddies in spite of the fact that they were both seen under similar experimental circumstances.

In another study of outer region of a TBL, Chen and Blackwelder(1978) slightly heated the wall to use the temperature as a passive contaminant. They utilized a rake of temperature sensors to explore the turbulent structure. An example of their temperature signals is found in figure 14. They discovered sharp shear layers that extended throughout the flow field. One such layer is indicated by the arrows in the figure. In the intermittent region, these shear layers were concomitant with the upstream sides of the turbulent bulges, as indicated in figure 13, but they extended into the fully turbulent region as well. Occasionally a layer was observed to extend into the wall region as seen in the figure leading Chen and Blackwelder to speculate that they may provide a deterministic relationship between these two regions. The shear layers were strongly three-dimensional and usually only a portion of the layer crossed the rake of sensors. Thus they often appeared in short segments as seen.

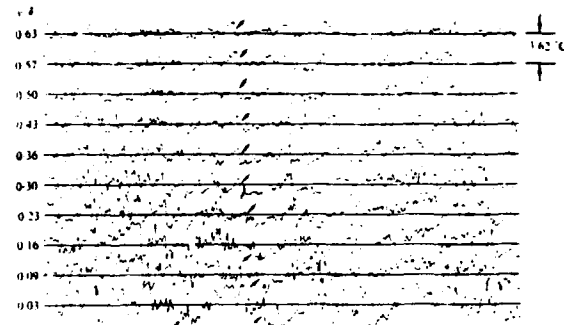


Figure 14. Simultaneous temperature signals at ten locations in the boundary layer denoted on the ordinate. The horizontal time span is $18.64t \cdot U_\infty/6$. Reprinted from Chen and Blackwelder(1978)

Outer Structure in Pipes and Channels

Sabot and Comte-Bellot(1976) used space-time correlations to ascertain the LSOS of a pipe flow at Re_θ of 3250 and 6000. Their results were qualitatively similar to those discussed above for the TBL. For example the $R_{uv}(\Delta x, \Delta y, 0, 0)$ correlations at three locations from Sabot and Comte-Bellot(1972) are shown in figure 15. The correlation at $y/R = 0.1$ is quite similar to that obtained in the boundary layer by Blackwelder and Kovasznay(1972). Comparing the correlation at $y/R=0.5$ with the earlier one in the boundary layer(figure 10) shows that they have the same inclination and scales in both flow fields. However there were some important differences. Since the pipe does not have a nonturbulent region, those effects due to the irrotational fluid are missing in the pipe data. For example, there is no intermittency nor entrainment as the flow is completely turbulent. Consequently the R_{uv} correlation at $y = R$ in figure 15 is circular with not inclination. However in the TBL, the similar correlation is inclined and has an aspect ratio greater than unity aligned in the streamwise direction. In addition Sabot and Comte-Bellot(1976) find that near the pipe centerline, a focusing effect occurs in which structure associated with circular geometry of the wall.

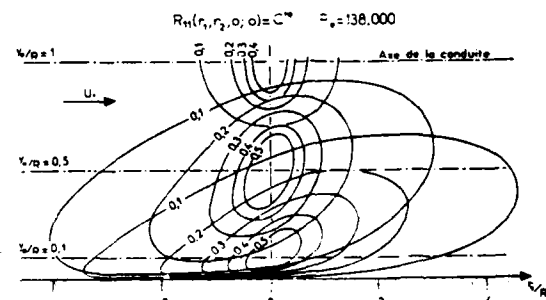


Figure 15. The spatial correlations, $R_{uv}(\Delta x, \Delta y, 0, 0)$, at three locations in a pipe flow at $Re_\theta = 6500$ taken from Sabot and Comte-Bellot(1972).

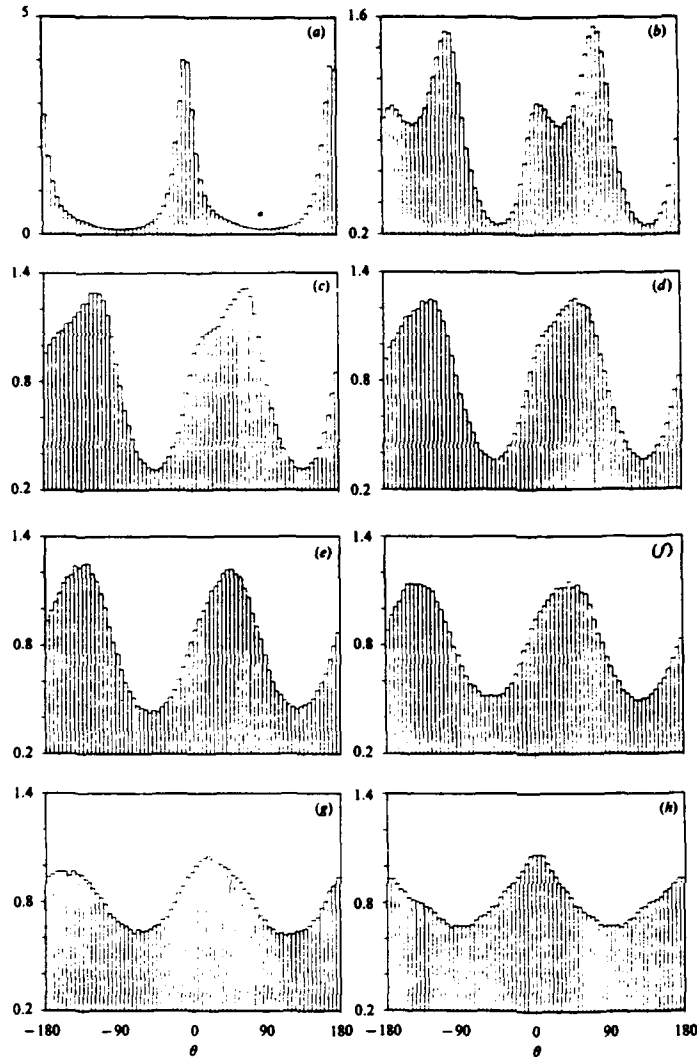


Figure 16. Distribution of the inclination angle of the projection of the vorticity vectors onto x-y planes at $y' =$ (a) 3.9, (b) 31.4, (c) 91, (d) 124, (e) 319, (f) 493, (g) 592, and (h) 642 reprinted from Moin and Kim(1985)

The outer region of fully developed turbulent channel flows have been studied via space-time correlations and higher order statistics by Comte-Bellot(1963) over the range of $330 < h \cdot u/v < 1080$ where h is the half channel height. More recently, Kim, Moin and Moser(1987) used direct numerical simulation with $h' = 180$ to calculate the basis statistics including the vorticity fluctuations. In a similar study, Moin and Kim(1985) used large eddy simulation to study the vorticity field. Statistically they found in the outer region that the vorticity vector has a preferred direction of 45° and -135° to the flow direction as seen in figure 16. This figure was constructed by taking the component of vorticity in the x-y plane and computing the probability distribution of its angle from the wall. Near the wall ω_z must be zero and figure 16a shows that the vorticity has a preferred direction of 0 and 180° and hence consists of ω_x .

Note that the mean vorticity does not contribute directly because figure 16 shows only the vorticity projected onto the x-y plane. At $y' > 30$, the probability distribution peaks at 45° and -135° and remains there until the centerline of the channel is approached. At that point, the vorticity associated with both sides of the channel is felt and symmetry conditions alter the distribution. Moin and Kim interpreted these and their other results as supporting a model of vortical structures inclined at 45° to the wall with the diameter of these structures increasing with distance from the wall. In a further study, Rogers and Moin(1987) found similar vortical structures in a homogeneous shear flow suggesting that they appear in all shear flows away from the boundary.

Interaction between the Wall and Outer Regions

There has been considerable speculation in the literature about possible interactions between the eddies in the wall region and those in the outer flow field. In spite of this, there is very little concrete evidence to support interaction, but there are several possible mechanisms. More importantly, there are several important questions that come to the foreground whenever interaction is discussed. For example, the effect of the Reynolds number on the interactions must be important since the Reynolds number is essentially the ratio of the lengths scale of the outer flow to that of the wall region. These issues are discussed below along with some of the questions that have been debated in the literature.

Any interaction between these two regions must involve the logarithmic region. Millikan(1939) showed by asymptotic matching procedures between the wall(inner) layer and the outer region that the mean velocity profile must be a logarithmic. This form of the velocity profile has been one of the true successes of turbulence theory and is often used as a test to determine if the flow is fully developed.

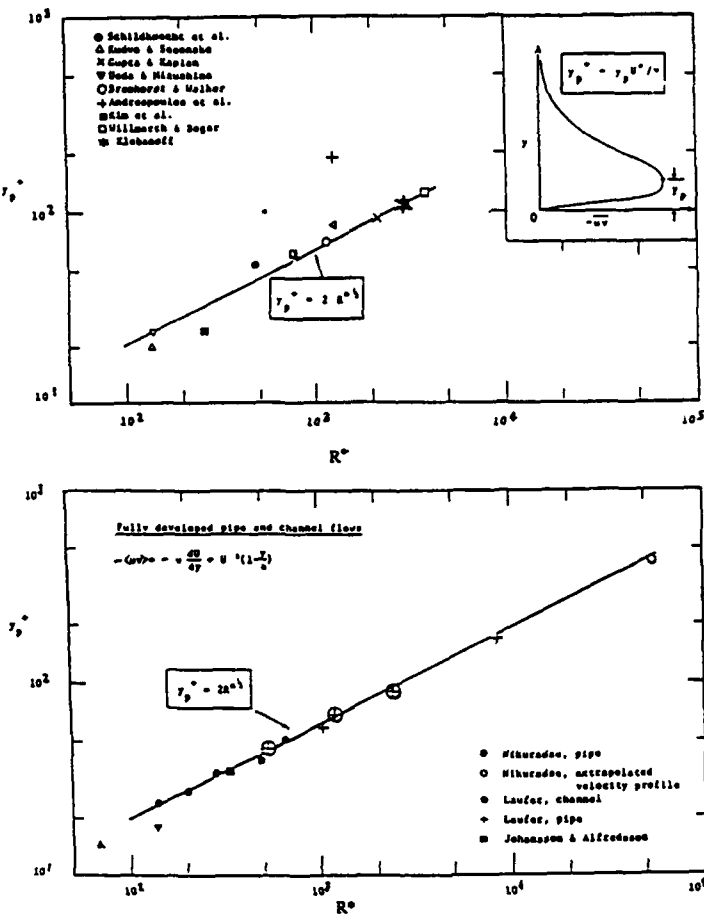


Figure 17. The measured peak Reynolds shear stress location in boundary layer, pipe and channel flows taken from Sreenivasan(1989). $Re^* = \delta^* u_* / v$.

Reynolds Number Effects

One of the more perplexing questions remaining about the bursting phenomenon is the role of the Reynolds number as mentioned earlier. Most all of the measurements and calculations of the structure have been at low Reynolds numbers in order to have sufficient resolution in the wall region. However many applications are typically at much higher Reynolds numbers. The law of the wall is assumed to be independent of the outer layer eddy structure and hence should be independent of the Reynolds number. A similar argument suggests that the wall region of pipes, channel and boundary layers should be similar when scaled with the wall variables. Although these assumptions may be true to first order, as more data become available it appears that there is an influence of the Reynolds number on the wall structure.

Several authors have suggested that asymptotically the Reynolds number will have an influence on the wall region beginning with Afzal and Vajnik(1973). Phillips(1987) shows that even though the mean profile is relatively independent of the Re in the laboratory, the second order statistics in the wall region are not. Furthermore this dependence becomes stronger as Re increases. Sreenivasan(1989) has pointed out that experimental data indicate that

the location of the peak, y_p^* , in the $-uv$ distribution increases as Re increases. Panton(1990) shows that by using the momentum equation for a channel flow with half channel height of h ; namely

$$-\frac{uv}{u_*^2} = -v \frac{du^*}{dy^*} + 1 - \frac{y^*}{h^*}$$

an expression can be obtained for the peak location, y_p^* , by differentiating. This yields

$$\frac{d^2 u^*}{dy^*} (y_p^*) = -\frac{1}{h^*}$$

where h^* is the Reynolds number. Since the maximum occurs in the logarithmic region where $u^* = \kappa^{-1} \log(y^*) + B$, the last equation yields

$$y_p^* = \left(\frac{h^*}{\kappa} \right)^{\frac{1}{2}}$$

in agreement with the experimental results collated by Sreenivasan(1989) shown in figure 17 at the left. This result has been verified more recently in a channel flow by Wei and Willmarth(1989) and in a boundary layer by Spalart (1988). Panton points out that to first order, similar results are obtained for boundary layers. Thus this result indicates that the Reynolds number, and hence the outer length scale δ , have a direct effect upon the wall region.

On the other hand, the peak in the production is not effected by Re . Using the above equation, the production term can be written as

$$-\frac{uv}{u_*^2} \frac{du^*}{dy^*} = -\left(\frac{du^*}{dy^*} \right)^2 + \left(1 - \frac{y^*}{h^*} \right) \frac{du^*}{dy^*}$$

Differentiating this expression shows that the maximum in the production curve, y_p^* , at high Reynolds number occurs when the mean velocity gradient equals half its value at the wall; i.e.

$$\frac{du^*}{dy^*} (y_p^*) = \frac{1}{2}$$

Substituting this into the previous expression indicates that the the maximum production is approximately $\frac{1}{2}$ for high Re . Since the mean velocity profile is not sensitive to the Re , one expects that the peak in the production curve will not be either. Both of these observations are confirmed by

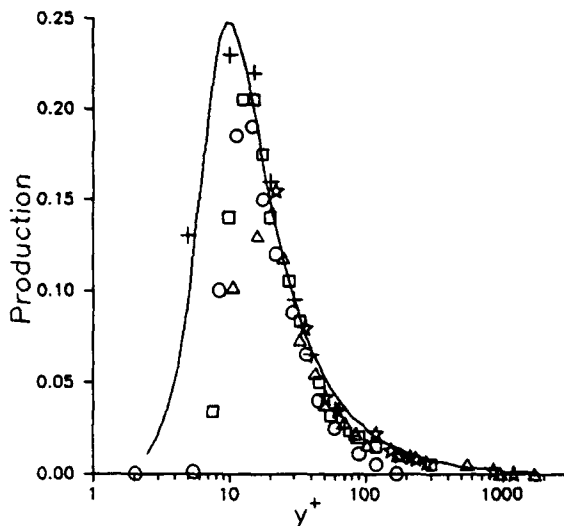


Figure 18. Turbulent production profiles showing the insensitivity to the Reynolds number. Boundary layer data from Spalart(1988) follow the solid line for $300 < Re_e < 1410$. Channel flow data of Wei and Willmarth(1989) at Reynolds number($U_c \cdot h/v$) of; \circ - 1500, \square - 7460, Δ - 11,400, and ∇ - 19,800.

Spalart(1988) in a boundary layer and by Willmarth and Wei(1989) in a channel flow as shown in figure 18. This consequence indicates that the Reynolds number is very selective in its effect upon the wall region.

To study this problem from a different angle, McLean(1990) has analyzed the spanwise correlation structure of the streamwise velocity component. Figure 19 presents the $R_{uu}(\Delta z)$ two point correlations at a constant $y^* = 15$ for $10^3 < Re_e < 10^4$. The data were all taken with hot-wire sensors that had a spatial resolution less than $25v/u$, as indicated in the figure. Two facts are immediately apparent. First, the only evidence of a strong negative region at $\Delta z \approx 50$ is for the lowest Reynolds number. This feature is considered to be a fundamental attribute of the LSSs and its disappearance must denote a change in the turbulent structure. Secondly, the integral scale is not a constant at this location which violates the idea of viscous scaling in the wall region. To check this, the integral scales were computed and are shown in figure 20 versus the Reynolds number along with some similar data taken in an adverse pressure gradient. Also included are some numerical results supplied by Robinson(1988) and Utami et al.(1989). It is obvious that this parameter shows no indication of scaling with Re_e .

Figure 21 presents the same data scaled with the momentum thickness, θ , versus the Reynolds number. This clearly shows that 1) there is a strong Reynolds number effect below $Re_e = 3000$, 2) the

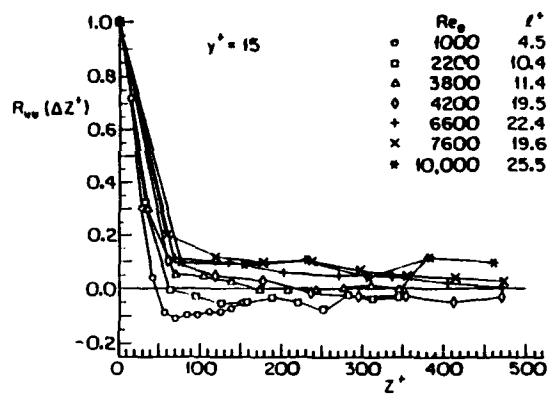


Figure 19. Correlations of the streamwise velocity component in the spanwise direction at different Reynolds numbers. The sensor lengths are indicated.

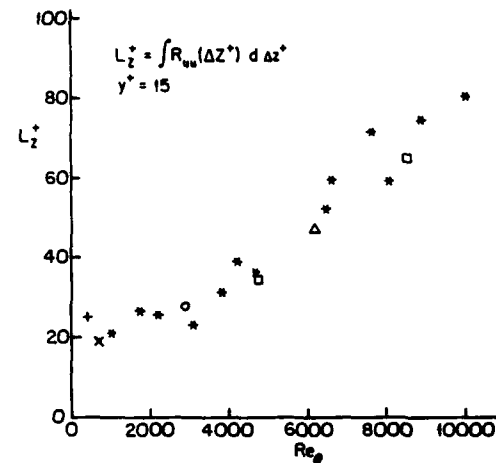


Figure 20. The spanwise integral length scale at $y^* = 15$ normalized with the viscous variables versus the Reynolds number (the symbols are given in Figure 21)

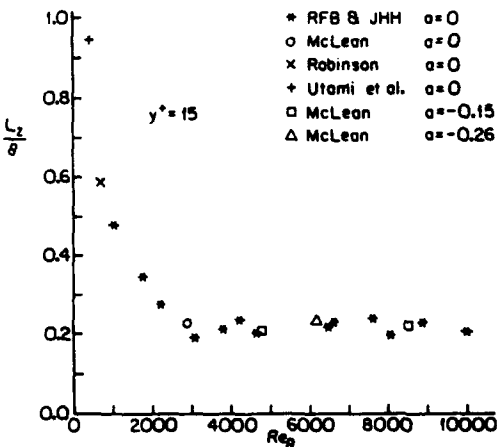


Figure 21. The spanwise integral length scale at $y^* = 15$ normalized with the momentum length scale versus the Reynolds number. The adverse pressure gradients have $U(x) - x^2$.

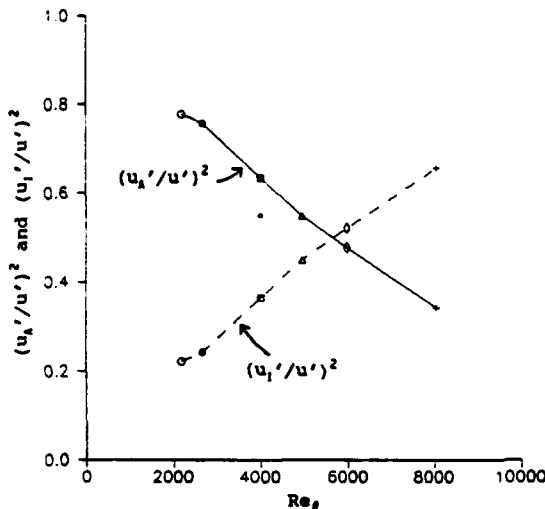


Figure 22. The variation of the 'active' and 'inactive' component of the streamwise velocity component with Reynolds number from McLean(1990).

spanwise integral scale is associated with the outer flow field for $Re_s > 3000$, and 3) the integral scale in the wall region is not altered by the adverse pressure gradients. Wark and Nagib(1991) have reached similar conclusions. Namely they found the spanwise scale, Λ_s , of their conditional averages in the wall region scaled with the momentum thickness over $280 < Re_s < 5200$.

The lack of a negative region in the $R_{u_s}(Az)$ correlations in figure 19 does not suggest that the low speed streaks disappear at the higher Reynolds numbers. It does imply that the underlying eddy structure changes for $Re_s > 3000$. One possible change may be that the streak spacing becomes more random as the Reynolds number increases. Smith and Metzler(1983) have shown that the probability spacing of the streaks is lognormal with an average value of $100v/u$. If the standard deviation of the probability distribution increased as the Reynolds number increased, the streaks would appear more randomly in space. For example, if the standard deviation were very small, the streak spacing would be quite regular and the spanwise correlation would have a strong negative region as well as possibly a secondary positive peak as seen for some low Reynolds number results. (In the limit for a standard deviation of zero, the correlation would be periodic.) Increasing the standard deviation would reduce the secondary peaks and also the negative peak. Another means by which the correlation could be altered as in figure 19 is to add other eddy structures or to have other eddies occur more frequently as the Reynolds number increases. This increase in scales is known to occur as the Reynolds number increases, but it is not clear how it would affect the wall region.

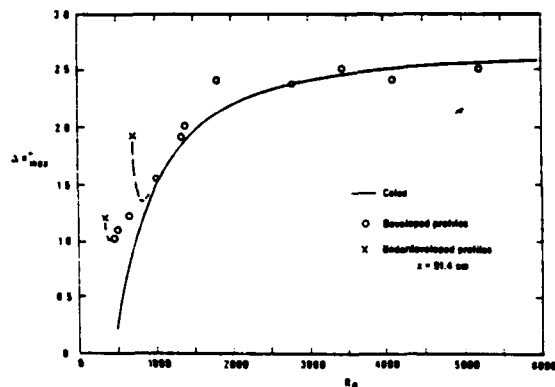


Figure 23. The maximum deviation of the mean velocity profile from the logarithmic law versus the Reynolds number from Purtell et al.(1981).

McLean(1990) suggested that the changes with Reynolds number could possibly be explained if the fluctuations were assumed to be due to 'active' and 'inactive' ones as originally proposed by Townsend(1961). The 'active' component, u_A' , was responsible for the shear stress and scaled with inner variables. The 'inactive' component, u_i' , was assumed to be due to the outer region and Bradshaw(1967) suggests it could be due to irrotational motion as well. McLean devised a detection scheme for these two types of motion and computed the correlations due to each one. By assuming that there was no correlation between the two components, he found that the energy associated with the 'active' component decreased with Reynolds number as shown in figure 22. On the other hand the energy associated with the 'inactive' fluctuations continued to increase over the Reynolds number range explored. His range of Re_s is too limited to determine the asymptotic state, but his results do suggest that the outer region has a more dominate role in the inner region as the Reynolds number increases.

Another parameter that is known to vary strongly with the Reynolds number at low Re_s is Coles wake parameter, Π . Purtell, Klebanoff and Buckley(1981) measured the deviation from the logarithmic law over $600 < Re_s < 6000$ and found the results shown in figure 23. Below Re_s of 3000, a strong dependence is seen suggesting that the LSOS are not fully developed in this region. This conclusion from the outer layer and McLean's results at $y' = 15$ clearly suggests that there is a low Reynolds number effect for $Re_s < 3000$. In addition, there is more subtle (and probably weaker) Reynolds number effect for $Re_s > 3000$ as evidenced by the changes in the 'active' and 'inactive' component above.

Frequency of Occurrence

The frequency of occurrence refers to the average number of occurrences of a specific event per unit time in the near wall region. The specific event is often the breakup in the visualization investigations and is the output of a detection algorithm in the transducer studies. Hence care must be exercised when comparing the frequency of occurrence obtained by different methods since the frequency is dependent upon the measurement method.

Bogard and Tiederman(1986) studied the more popular algorithms and compared their output detections with visualization results. Since the breakups are poorly defined, they found the comparison much easier when individual ejections were studied rather than the breakups. They concluded that the quadrant technique was the best algorithm for detecting the visual ejections. The VITA and U-level methods also had low probabilities of false detections when thresholds near $1.0 \cdot u'$ were used but missed some of the less energetic ejections.

The scaling of the frequency of occurrence has been one of the more controversial topics associated with the bursting process. The earlier work of Kline et al.(1967), Kim et al.(1971) and others indicated that the breakup frequency scaled with the wall variables. However Rao et al.(1971) indicated that the outer scales correlated the detection frequency over a decade of Reynolds numbers for data taken from a fixed length hot-wire. Blackwelder and Haritonidis(1983) showed that as the Reynolds number increased, the nondimensional scale of the probe became large compared with the scale of the ejections. When different hot-wire probes were used such that the nondimensional scale of the sensors remained constant as the Reynolds number increased, the detection frequency scaled with v and u , remained approximately constant as seen in figure 24. This scaling appears to be universal for pipes, channels and TBLs as long as the boundary is sufficiently smooth. This result has been confirmed with transducer techniques by Chambers et al.(1983) in accelerating channel flows, Shemer and Haritonidis(1984) and Sabot and Comte-Bellot(1976) in pipe flows and Willmarth and Sharma(1984) and Guezennec(1985) in TBLs. Kim and Spalart(1987) found similar results with numerical TBL data. Luchik and Tiederman(1987) using hot-film data and Tiederman(1989) with LDA data concluded that inner scaling was correct in channel flows. On the other hand however, Alfredsson and Johansson(1984) have proposed a mixed scaling for detections using a hot-film in a channel flow for Reynolds numbers of $1.3 \cdot 10^4$ to $1.2 \cdot 10^5$ based on the half channel width. Shah and Antonia(1989) have supported this conclusion for higher Reynolds numbers and caution that the inner scaling may be valid only in the range where low Reynolds number effects are known to be important.

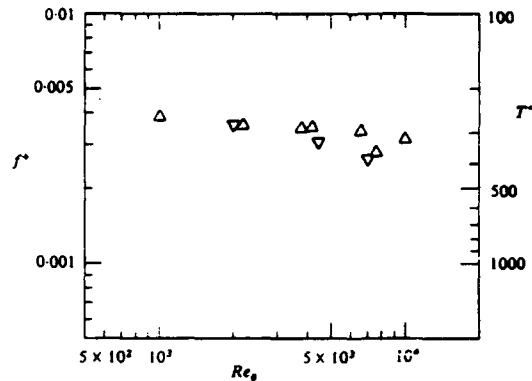


Figure 24. The mean bursting frequency scaled with the wall variables v and u , for sensors having a spatial resolution of less than $20v/u$, from Blackwelder and Haritonidis(1983).

This confusion is not unexpected since the breakup is a fairly nebulous concept in want of a better definition. In addition, Bogard and Tiederman(1986) have shown that none of the popular detection methods used in experiments provide a good correlation with the visualization results. The VITA(and possibly other) techniques used by most investigators, detects the crossing of strong shear layer embedded within the flow. Hence it does not detect a 'bursting event' directly, but only those events associated with strong internal shear layers. Chen and Blackwelder(1978) showed that this shear layer was three dimensional and sometimes extended across the entire boundary layer. In the outer region it was readily identified with the upstream side of the large eddies extending into the irrotational flow as sketched in figure F13. The shear layer often extended from the outer region across the logarithmic region and into the wall area. When this happened, the shear layer was associated with and seemed to stimulate an ejection. In this manner the shear layer was associated with the bursting process and was detected by the VITA technique. From this viewpoint, one would expect the VITA detections to scale with the outer variables. In particular, the scaling of this type of shear layer would be expected to change as the wake region becomes fully developed at $Re_s \approx 3000-5000$.

On the other hand, Chen and Blackwelder found that there were also internal shear layers in the wall region that do not extend over the entire boundary layer. These seemed to be due to ejections that had occurred without any observed stimulus from the outer region of the flow. Because ejections are low speed fluid moving outward into higher momentum flow, they produce sharp velocity gradients. If these ejections occurred as a result of the local dynamics, their frequency should scale with the inner wall variables. Thus the results of Shah and Antonia(1989) would suggest that at lower Reynolds numbers,

these ejections are predominate whereas at higher Re_θ , the shear layers associated with the outer intermittent structure are more prevalent. This important question needs much more clarification.

Pockets, Sweeps and High Speed Regions

It is known that the wall layer eddy structure is often disturbed by the bombardment by regions of higher speed fluid. This high speed fluid parcels originate in the outer area of the shear flow; i.e. in the logarithmic region and the core or wake region, and may be a primary form of interaction between the two regions. These high speed regions were first noticed by Corino and Brodkey(1969) who characterized them as sweeps of high speed fluid moving essentially parallel to the boundary but with a small velocity component inclined toward the wall. This motion often terminated in a breakup and left the flow in a relatively quiescence state. The sweep was a larger scale motion than the ejection in the x-y plane but due to experimental limitations, the extent of the sweep in the spanwise direction could not be ascertained.

The higher speed regions are inherently more difficult to study visually because they originate in the logarithmic and outer regions and it is difficult to place a Lagrangian marker into this region without additional disturbances. Falco(1980) has overcome this handicap by injecting large amounts of marker through the wall. With small amounts of injected smoke, he observed LSSs similar to those of Kline et al.(1967). With higher concentrations, the wall layer was filled with smoke for several hundred viscous scales downstream. Under this condition, the most readily observed features were regions that became devoid of smoke due to strong high speed disturbances hitting the wall region and clearing it of the marker. Falco found these regions were typically $80-100v/u$, in diameter and named them pockets. Since they are high speed disturbance of the wall region, they appear to be related to the sweeps discussed above. In a simulated boundary layer flow, Chu and Falco(1988) found that eddies originating in the outer region of the boundary layer do indeed produce pockets as well as the streaky structure in the wall region.

Other Interaction Mechanisms

There are several means by which the wall layer eddies and the outer eddies can interact that have not been covered here. One of the most obvious is via the pressure. Aubry et al.(1988) have found via a dynamical model of the wall region that the pressure is the main link between the two regions. In particular they found that the pressure signal associated with the outer eddies induced the bursting process nearer the wall. Brown and Thomas(1977) found a strong correlation between the u' fluctuations in the outer region and the shear stress at the wall, τ_w . They suggest that this may be the route to interaction between the two sets of eddies.

There is also evidence that the normal velocity component is related to the interaction between these two different region. Offen and Kline(1974) find that the sweeps associated with negative v' often cause the lift-up of the low speed region. This observation was also echoed by Smith(1978). Brown and Thomas(1977) suggested that a Görtler type of instability may be responsible for the production of w' in the wall region thus leading to the low speed streaks and the ensuing dynamics. Indeed one can show that the random fluctuations in the outer region are sufficient to produce a Görtler instability but it is not obvious that the time scale of the large scale outer motion and the instability are commensurate.

Conclusions

The large amount of data accumulated during the past three decades has increased our understanding of the eddy structure within bounded shear flows immensely. Although much remains to be learned, we have reached a threshold where many applications of the eddy structure can be used, such as in applications to the problem of drag reduction.

Acknowledgements

The research reported here has been supported over the past several years by the Office of Naval Research through contract N00014-82-K-0084 and URI-N00014-86-K-0679 monitored by Mike Reischman and Pat Purtell and the Air Force Office of Scientific Research through contract F49620-85-C-0080 monitored by Jim McMichael.

References

- Afzal, N. and Yajnik, K., 1973, J. Fluid Mech., 61, 23.
- Alfredsson, P.H. and Johansson, A.V., 1984, "Time scales in turbulent channel flow," Phys. Fluids, 27, 1974.
- Antonia, R.A., 1972, "Conditionally sampled measurements near the outer edge of a turbulent boundary layer," 56, 1.
- Aubry, N., Holmes, P., Lumley, J.L., and Stone, E., 1988, "The dynamics of coherent structures in the wall region of a turbulent boundary layer," J. Fluid Mech., 192, 115.
- Bachar, E.V. and Smith, C.R., 1986, "Turbulent boundary layer by surface ripples," AIAA J., 24, 1382.
- Bakewell, P. and Lumley, J.L., 1967, "Viscous sublayer and adjacent wall region in turbulent pipe flow," Phys. Fluids, 10, 1880.
- Blackwelder, R.F., 1978, "The bursting process in turbulent boundary layers," Coherent Structure of turbulent boundary layers, Ed. C.R. Smith and D.E. Abbott, Lehigh Univ., p 211.

Blackwelder, R.F., 1988, "Some symmetrical properties of conditional averages," Transport Phenomena in Turbulent Flows, Ed. M. Hirata and N. Kasagi, Hemisphere Pub. Corp., New York, p89.

Blackwelder, R.F., 1989, "Some ideas on the control of near-wall eddies," AIAA 2nd Shear Flow Conf., AIAA-89-1009, Tempe, AZ.

Blackwelder, R.F. and Eckelmann, H., 1979, "Streamwise vortices associated with the bursting phenomenon," *J. Fluid Mech.*, 94, 577.

Blackwelder, R.F. and Haritonidis, J.H., 1983, "Scaling of the burst frequency in turbulent boundary layers," *J. Fluid Mech.*, 132, 87.

Blackwelder, R.F. and Kaplan, R.E., 1976, "Wall structure of the turbulent boundary layer," *J. Fluid Mech.*, 76, 89.

Blackwelder, R.F. and Kovasznay, L.S.G., 1972, "Time scales and correlations in a turbulent boundary layer," *Phys. Fluids*, 15, 1545.

Blackwelder, R.F. and Swearingen, J.D., 1989, "The role of inflectional velocity profiles in wall bounded flows," Near Wall Turbulence, Ed. S.J.Kline, Hemisphere Pub. Corp.

Bogard, D.G., 1987, private communication.

Bogard, D.G. and Tiederman, W.G., 1986, "Burst detection with single-point velocity measurements," *J. Fluid Mech.*, 162, 389.

Bradshaw, P., 1967, "The turbulence structure of equilibrium boundary layers," *J. Fluid Mech.*, 29, 625.

Brown, G.L. and Thomas, A.S.W., 1977, "Large structure in a turbulent boundary layer," *Phys. Fluids*, 20, S243.

Chambers, F.W., Murphy, H.D. and McEligot, D.M., 1983, "Laterally converging flow. Part 2.," *J. Fluid Mech.*, 127, 403.

Chen, C.-H. P. and Blackwelder, R.F., 1978, "Large-scale motion in a turbulent boundary layer: a study using temperature contamination," *J. Fluid Mech.*, 89, 1.

Chu, C.C. and Falco, R.E., 1988, "Vortex ring/viscous wall layer interaction model of the turbulence production process near walls," *Exp. in Fluids*, 6, 305.

Comte-Bellot, G., 1963, "Contribution a l'étude de la turbulence de conduite," Doctoral thesis, University of Grenoble, France.

Corino, E.R. and Brodkey, R.S., 1969, "A visual study of turbulent shear flow," *J. Fluid Mech.*, 37, 1.

Corrsin, S., 1957, "Some current problems in turbulent shear flows," Symp. on Naval Hydrodyn, Publ. 515, NAS-NRC, 373.

Emmerling, R., 1973, "Die Momentane Struktur des Wanddruckes einer turbulenten Grenzschichtströmung", Mitt. MPI Strömungsforsch u. Aerodyn. Versuchsanst., Göttingen, no. 56.

Falco, R.E., 1977, "Coherent motions in the outer region of turbulent boundary layers," *Phys. Fluids*, 20, S124.

Falco, R.E., 1980, "Structural aspects of turbulence in boundary layer flows," Turbulence in Liquids, Ed. G.K. Patterson and J.L. Zakin, Chem. Eng., U. Missouri, p1.

Favre, A.J., 1965, "Review on space-time correlations in turbulent fluids," *J. Appl. Mech., Series E*, 32, 241.

Gaster, M., Kit, E. and Wygnanski, I., 1985, "Large scale structures in a forced turbulent mixing layer," *J. Fluid Mech.*, 150, 23.

Grass, A.J., 1971, "Structural features of turbulent flow over smooth and rough boundaries," *J. Fluid Mech.*, 50, 233.

Greenspan, H.P. and Benney, D.J., 1963, "On shear layer instability and breakdown," *J. Fluid Mech.*, 15, 133.

Guezennec, Y.G. 1985, "Documentation of large coherent structures associated with wall events in turbulent boundary layers," Ph.D. thesis, Illinois Inst. of Technology.

Guezennec, Y., Piomelli, U., and Kim, J., 1989, "On the shape and dynamics of wall structures in turbulent channel flow," *Phys. Fluids*, A1, 764, 1989.

Handler, R.A., Hendricks, E.W. and Leighton, T.I., 1989, "Low Reynolds Number Calculation of Turbulent Channel Flow," NRL Memorandum Report 6410.

Head, M.R. and Bandyopadhyay, P., 1981, "New aspects of turbulent boundary-layer structure," *J. Fluid Mech.*, 107, 297.

Hedley, T.B. and Keffer, J.F., 1974, "Some turbulent/non-turbulent properties of the outer intermittent region of a boundary layer," *J. Fluid Mech.*, 64, 645.

Hirata, M., Tanaka, H., Kawamura, H., and Kasagi, N., 1982, "Heat transfer in turbulent flows," 7th Int'l Heat Transfer Conf., München.

Huerre, P., 1983, "Finite amplitude evolution of mixing layers in the presence of solid boundaries," *J. de Mecanique Theorique et Appliquee*, Numero Special, p. 121.

Kim, H.T., Kline, S.J., and Reynolds, W.C., 1971, "The production of turbulence near a smooth wall in a turbulent boundary layer," *J. Fluid Mech.*, 50, 133.

Kim, J. and Moin, P., 1986, "The structure of the vorticity field in turbulent channel flow - Part 2," *J. Fluid Mech.*, 162, 339.

Kim, J. and Spalart, P.R., 1987, "Scaling of the frequency of occurrence in turbulent boundary layers at low Reynolds numbers," *Phys. Fluids*, **30**, 3326.

Kim, J., Moin, P. and Moser, R., 1987, "Turbulence statistics in fully developed channel flow at low Reynolds number," *J. Fluid Mech.*, **177**, 133.

Klebanoff, P.S., 1954, "Characteristics of turbulence in a boundary layer with zero pressure gradient," *NACA T.N. 3178*.

Kline, S.J., Reynolds, W.C., Schraub, F.A. and Runstadler, P.W., 1967, "The structure of turbulent boundary layers," *J. Fluid Mech.*, **30**, 741.

Kovasznay, L.S.G., Kibens, V. and Blackwelder, R.F., 1970, "Large-scale motion in the intermittent region of a turbulent boundary layer," *J. Fluid Mech.*, **41**, 283.

Lee, J.L., Kim, J., and Moin, P., 1990, "Turbulence structure at high shear rate," *J. Fluid Mech.*, **216**, 561.

Lee, M.K., Eckelman, L.D. and Hanratty, T.J., 1974, "Identification of turbulent wall eddies . . .," *J. Fluid Mech.*, **66**, 17.

Liepmann, H.W. and Nosenchuck, D.M., 1982, "Active control of laminar-turbulent transition," *J. Fluid Mech.*, **118**, 201.

McLean, Ian, 1990, "The near wall eddy structure in an equilibrium turbulent boundary layer," Ph.D. Thesis, U. Southern California.

Michalke, A., 1965, "On spatially growing disturbances in an inviscid shear layer," *J. Fluid Mech.*, **23**, 521.

Millikan, C.B., 1939, in *Proc. Fifth Cong. Appl. Mech.*, Cambridge, MA, p.386.

Moin, P. and Kim, J., 1982, "Numerical investigation of turbulent channel flow," *J. Fluid Mech.*, **118**, 341.

Moin, P. and Kim, J., 1985, "The structure of the vorticity field in turbulent channel flow - Part 1," *J. Fluid Mech.*, **155**, 441.

Moser, R.D. and Moin, P., 1984, "Direct numerical simulation of curved turbulent channel flow," NASA TM 85974.

Nakagawa, H. and Nezu, I., 1981, "Structure of space-time correlations of bursting phenomena in an open-channel flow," *J. Fluid Mech.*, **104**, 1.

Nishioka, M., Asai, M. and Iida, S., 1980, "An experimental investigation of the secondary instability," *Laminar-Turbulent Transition*, Ed. R. Eppler and H. Fasel, Springer Verlag, Berlin, p37.

Offen, G.R. and Kline, S.J., 1974, "Combined dye-streak and hydrogen bubble visual observations of a turbulent boundary layer," *J. Fluid Mech.*, **62**, 233.

Oldaker, D.K. and Tiederman, W.G., 1977, "Spatial structure of the viscous sublayer in drag reducing channel flows" *Phys. Fluids Supplement*, **20**, S133.

Panton, R.L., 1990, "Scaling Turbulent Wall Layers," *ASME-J. Fluids Engin.*

Phillips, W.R.C., 1987, "The wall region of a turbulent boundary layer," *Phys. Fluids*, **30**, 2354.

Purtell, L.P., Klebanoff, P.S. and Buckley, F.T., 1981, "Turbulent boundary layer at low Reynolds number," *Phys. Fluids*, **24**, 802.

Rao, K.N., Narasimha, R. and Badri Narayanan, M.A., 1971, "The bursting phenomenon in a turbulent boundary layer," *J. Fluid Mech.*, **48**, 339.

Robinson, S., 1988 private communication.

Robinson, S., 1990, "The kinematics of turbulent boundary layer structure," Ph.D. Thesis, Stanford University.

Rogers, M. and Moin, P., 1987, "The structure of the vorticity field in homogeneous turbulent flows," *J. Fluid Mech.*, **176**, 33.

Sabot, J. and Comte-Bellot, G., 1972, "Courbes d'iso-corrélations spatiales et d'iso-corrélations spatio-temporelles relatives aux fluctuations longitudinales de vitesse en conduite lisse circulaire," *Comptes rendus*, **275**, série A, 667.

Sabot, J. and Comte-Bellot, G., 1976, "Intermittency of coherent structures in the core region of fully developed turbulent pipe flow," *J. Fluid Mech.*, **74**, 767.

Shah, D.A. and Antonia, R.A. 1989, "Scaling of the 'bursting' period in turbulent boundary layer and duct flow," *Phys. Fluids*, **A1**, 318.

Shemer, L. and Haritonidis, J., 1984, "The frequency of occurrence in turbulent pipe flow," *Bull. Am. Phy. Soc.*, **29**, 1535.

Schewe, G., 1983, "On the structure and resolution of wall-pressure fluctuations associated with turbulent boundary layer flow," *J. Fluid Mech.*, **134**, 311.

Smith, C.R., 1978, "Visualization of turbulent boundary layer structure using a moving hydrogen bubble wire probe," *Coherent Structure of Turbulent Boundary Layers*, Lehigh U., 48.

Smith, C.R. and Schwartz, S.P., 1983, "Observation of streamwise rotation in the near-wall region of a turbulent boundary layer," *Phys. Fluids*, **26**, 641.

Smith, C.R. and Metzler, S.P., 1983, "The characteristics of low-speed streaks in the near-wall region of a turbulent boundary layer," *J. Fluid Mech.*, **129**, 27.

Spalart, P.R., 1988, "Direct simulation of a turbulent boundary layer up to $R_g = 1410$," *J. Fluid Mech.*, 187, 61.

Sreenivasan, K.R., 1989, "The turbulent boundary layer," Lectures Notes in Engineering, Ed M. Gad-el Hak, Springer-Verlag, vol. 46, p. 159.

Talmon, A.M., Kunem, J.M.G. and Ooms, G., 1986, "Simultaneous flow visualization and Reynolds-stress measurement in a turbulent boundary layer," *J. Fluid Mech.*, 163, 459.

Tiederman, W.G., 1989, "Eulerian detection of turbulent bursts," Int'l Seminar on Near-Wall Turbulence, Ed. S.J. Kline, Hemisphere Pub. Corp.

Townsend, A.A., 1961, *J. Fluid Mech.*, 11, 97.

Utami, T., Blackwelder, R.F. and Ueno, T., 1989, "Flow visualization with image processing of three-dimensional features of coherent structures," New-Wall Turbulence, Ed. S. Kline, Hemisphere Pub. Corp.

Wark, C.E. and Nagib, H.M., "Experimental investigation of coherent structures in turbulent boundary layers," *J. Fluid Mech.*, 230, 183.

Wei, T. and Willmarth, W.W., 1989, "Reynolds-number effects on the structure of a turbulent channel flow," *J. Fluid Mech.*, 204, 57.

Willmarth, W.W. and Lu, S.S., 1972, "Structure of the Reynolds stress near the wall," *J. Fluid Mech.*, 55, 65.

Willmarth, W.W. and Sharma, L.K., 1984, "Study of turbulent structure with hot wires smaller than the viscous length," 142, 121.

AD-P006 970



STUDY OF TURBULENCE STRUCTURE THROUGH NUMERICAL
SIMULATIONS: THE PERSPECTIVE OF DRAG AND REDUCTION

by

J.J. Kim
Turbulence Physics Section
Mail Stop 202A-1
NASA Ames Research Center
Moffett Field, CA 94035-1000
United States

92-17812



Summary

The first part of this note concerns organized structures in the near-wall region of a turbulent boundary layer. A particular emphasis is given to those organized motions believed to be responsible for the turbulence production process in the wall region, and hence, indirectly responsible for the viscous drag. Examples are selected to illustrate how the analyses of numerically generated databases have contributed to improve our understanding of the organized structures in turbulent boundary layers. In the second part, results from an exploratory study based on the direct numerical simulation of the concepts for active control of turbulent boundary layers are presented. A significant drag reduction is achieved when the surface boundary condition is modified such that it could suppress the organized motions in the wall region. This drag reduction is accompanied by a significant reduction in the intensity of the organized structures and in the magnitude of Reynolds stresses throughout the flow.

1 Introduction

The discovery of organized structures in turbulent flows during the past three decades has attracted much attention from turbulence researchers in the hope that this new information will lead us to a better understanding of turbulence. Prior to this discovery, turbulence had been treated largely as a random stochastic process since its existence was first revealed by Osborne Reynolds about a century ago (1883). It is currently anticipated that the knowledge of these organized structures in turbulent flows will be helpful in developing the control strategies for turbulent flows. A large body of knowledge exists in the literature for the organized structures in turbulent flows (Cantwell 1981; Hussain 1986; Robinson 1991a). Although there is little disagreement about the existence of such organized structures and their importance in various turbulent flows, a lack of consensus on the detailed description of the structures still prevails. Robinson (1991a, 1991b) provides an up-to-date review of the organized structures in the

canonical turbulent boundary layer,¹ based on an extensive community-wide survey² as well as his own analyses of a database obtained from direct numerical simulations of a turbulent boundary layer over a flat plate at zero pressure gradient (Spalart 1988). The reader is referred to Robinson (1991a, 1991b) for details on our current understanding of the coherent structures in a turbulent boundary layer. Of particular importance are the points of consensus concerning many of the fundamental structural features for the low-Reynolds number canonical flow which are summarized in the conclusion (Robinson 1991a).

Most of the early works on the organized structures of the turbulent boundary layer was based on flow visualization (Runstadler et al. 1963; Kline et al. 1967; Corino & Brodkey 1969; Kim et al. 1971; Offen & Kline 1974, 1975; Head & Bandyopadhyay 1981). Although flow visualization experiments have been very successful in providing the evidence of their existence and in providing qualitative information, they do not provide the necessary quantitative information. In addition to the limitation that most visualization techniques are only effective at low Reynolds-number flows, they are invariably susceptible to various known effects (high Schmidt number, streaklines vs streamlines or pathlines, etc.). Probe measurements on these structures, on the other hand, provide some "hard" data, but they are very limited owing to the finite number of probes employed in the experiments (Wallace et al. 1972; Willmarth & Lu 1972; Blackwelder & Kaplan 1976; Blackwelder & Eckelmann 1979). A few investigators have tried to map spatial structures of the organized motions by probe measurements (Johansson et al. 1987; Wark 1988; Gueennec & Choi 1989), but only the relatively modern experimental techniques involving digitizing pictures and image processing have started to provide much needed simultaneous information. The information you can get with such modern experimental techniques, how-

¹ A "canonical" flow is defined as a flat-plate, smooth-wall boundary layer with a two-dimensional mean flow in the absence of pressure gradient, large free-stream fluctuations, wall heating, force fields, or compressibility effects.

² A unique survey conducted by Kline and Robinson which included personal interviews with researchers in addition to the usual literature survey.

ever, is still limited to two-dimensional planes, and it will be a while before these techniques start to produce fully three-dimensional information. The numerous controversies on the nature of the organized motions in turbulent flows that exist today (1991) are indeed largely due to the limitation of the experimental techniques employed in the investigation. The organized structures in turbulent flows have many different facets, and different experimental techniques tend to emphasize different characteristics associated with the same organized structures under scrutiny. As a result, different investigators were often led to draw different conclusions based on their limited observations, resulting in confusion and contradictions. For instance, Kim, Moin & Moser (1987) showed how one can possibly draw different conclusions from the same flow field, depending on the visualization techniques employed. It was shown that one could observe either the streaky structures (Runstadler et al. 1963 and others) or the near-wall pockets of swept fluids (Falco 1980), depending on how passive markers were introduced in the same flow field.

With the advent of large and fast computers and the development of accurate numerical algorithms in recent years, numerical simulations of turbulent flows have revolutionized the way we study the basic physics of turbulence. Numerical solutions for turbulent flows at low Reynolds numbers can be obtained by directly integrating the three-dimensional (3D), unsteady Navier-Stokes equations. The databases generated by such computations contain 3D velocity and pressure fields, and provide valuable information to complement the experimental data. The physical realism of these computer-generated databases has been validated by comparing with the existing experimental results in terms of time-averaged statistics as well as instantaneous turbulence structures. The availability of a full, 3D velocity, vorticity and pressure field provides a unique opportunity to probe the organized structures. These databases have indeed played a key role in resolving many existing controversies, and in putting together bits of information collected by different experimental techniques. Also, they have been extremely useful in validating various hypotheses put forward based on limited information obtained from laboratory experiments. Although the current capability of numerical simulation of turbulence is limited to the low-Reynolds number canonical flows because of the excessive computer-time requirements for more complex cases, numerical simulation of turbulence will continue to play a key role in advancing our capability in predicting and controlling turbulent flows. In fact it is most likely that numerical simulation will replace the need for experimental investigations of the low-Reynolds number canonical flows, if it has not done so already. Future experimental efforts should be reoriented towards noncanonical flows in-

volving complex geometries and high-Reynolds number cases, those areas beyond the current capability of numerical simulation. The large-eddy simulations of turbulent flows, in which only the large energy-containing eddies are directly computed from filtered Navier-Stokes equations while the small-scale motions are modeled through a subgrid-scale model, are expected to play an important role in unraveling the physics of noncanonical flows in coming years.

There are several different known organized structures in a turbulent boundary layer, and each structure is associated with its own characteristics. It is not my intention to review all of these structures here, which is beyond the scope of this note; the interested reader is referred to Robinson (1991a, 1991b). Instead I shall focus on the organized structures in the near-wall region, which are believed to play the dominant role in the turbulence production process, and hence, indirectly related to the viscous drag. In doing so, I shall present a number of examples in which physical understanding of the turbulent flows was achieved through computer simulations rather than laboratory experiments. The purpose of these examples is to illustrate that it is now possible to use computer simulations of fluid flows to complement and/or supplement laboratory experiments in studying the physics of turbulent flows. In the second part of this note, the results from an exploratory study based on the direct numerical simulation of the concepts for active control of turbulent boundary layers will be presented. A significant drag reduction is achieved when the surface boundary condition is modified such that it could suppress the organized motions discussed in the first part of this note. The drag reduction is accompanied by a significant reduction in the intensity of the organized structures and in the magnitude of Reynolds stresses throughout the flow.

This note is organized as follows. A brief description of the original references from which I draw most of the conclusions is given in section 2. The fundamental features associated with the organized motions relevant to the viscous drag are reviewed in section 3. In section 4, results from an exploratory numerical experiment in search of an efficient scheme for active turbulence control are presented, followed by concluding remarks in section 5.

In this note x, y, z denote the streamwise, wall-normal (or vertical), and the spanwise directions, respectively. The velocities are u, v , and w in x, y , and z directions, respectively. The subscript w indicates the value at the wall, and the superscript $+$ indicates a non-dimensional quantity scaled by the wall variables: e.g. $y^+ = yu_r/\nu$, where ν is the kinematic viscosity and $u_r = (\tau_w/\rho)^{1/2}$ is the wall-shear velocity.

2 Numerical Simulations and Databases

Most of the results included in this note are obtained from analyses of two databases, the channel flow by Kim et al. (1987) and the boundary layer flow by Spalart (1988). Both cases can be regarded as low-Reynolds number canonical flows, although the fully-developed channel flow is under a favorable pressure gradient. The grid resolution in both simulations is sufficiently fine to resolve all the essential turbulent scales, and hence, no subgrid-scale model is used. The spatial truncation errors are minimized by using spectral methods, and the time advancements are made by the low-storage third-order Runge-Kutta (Wray, unpublished work). In addition to the above two references, a large amount of results from these simulations are reported in the literature (Kim & Spalart 1987; Kim 1989; Robinson 1991b; Johansson et al. 1991; Antonia et al. 1991a, to name a few), and the interested reader is referred to these references for further details. It is worth to note here that in spite of the apparent differences in the outer region of the two flows, near-wall turbulence structures as well as near-wall turbulence statistics are found to be almost identical for the channel and boundary layer flows. Since the major concern of this note is related to the near-wall structures, no effort is made to differentiate the two flows throughout the note. Antonia et al. (1991b) reported the subtle differences between the two flows, to which the interested reader is referred to.

3 Near-Wall Turbulence Structures in Turbulent Boundary Layer

3.1 Streaks and Streamwise Vortices

Many flow visualization experiments (Runstadler et al. 1963; Kline et al. 1967 and many others since then) have shown that the viscous sublayer consists of alternating array of high- and low-speed streaks. The array has a well-defined and repeatable mean spacing in the spanwise direction (about $100\nu/u_*$, or $\lambda_z^+ \simeq 100$). The streamwise extent of the streaks are over $1000\nu/u_*$. The streaky structures have been observed in almost every kind of wall-bounded turbulent shear flows (including noncanonical boundary layers with pressure gradients) at a wide range of Reynolds numbers, suggesting its strength and universality. In fact their presence is so consistent that Kline (1978) suggested to consider the presence of wall-layer streaks as a critical diagnostic for whether a given zone or patch of the layer is turbulent.

From flow visualization data, Kline et al. (1967)

pointed out that the production of turbulence in boundary layers is largely due to the bursting process,³ which consists of lift-up, oscillation, and violent breakup of the streaks. The sweep event which is described as the inrush of high-speed fluid towards the wall (Corino & Brodkey 1969) is also believed to be a major contributor to the turbulence production. Johansson et al. (1991) also reported that much of the turbulence production takes place within the internal shear-layer structure associated with the asymmetric streaky structures. The work by Jimenez & Moin (1991) further punctuates the significance of the streaks. They observed in their numerical experiments that when the spanwise length of their computational domain was reduced below $100\nu/u_*$, and hence, the largest spanwise scale in the flow was smaller than the naturally observed streak spacing, the flow did not remain turbulent at the Reynolds numbers where the same flow would be turbulent with a larger spanwise domain: i.e., *no streaks* (at the proper scale), *no turbulence*. Waleffe & Kim (1991) recognized that the same constraint would lead to a critical Reynolds number close to the commonly regarded nonlinear critical Reynolds number (about 1000 for the channel based on the centerline velocity and the channel half-width), and suggested that the streaks and the instability associated with them should be the essential elements of a self-sustaining mechanism for turbulence. In their numerical experiments, they observed that a quasi-periodic formation and break-down of the streaks were the key elements for sustenance of turbulence.

In spite of the large amount of efforts spent and the large body of knowledge on the streaks, the exact mechanism for the streak formation is not yet well understood; we know a lot of kinematics associated with them but we know very little about their dynamics. A number of investigators proposed earlier an eddy structure that consists of a pair of counter-rotating vortices that are elongated in the streamwise direction and are parallel to the wall (Bakewell & Lumley 1967; Lee et al. 1974; Blackwelder 1978; Blackwelder & Eckelmann 1979). According to this earlier model, the streaks of low-speed fluid are postulated to be lying between the long counter-rotating vortices (figure 1). Moin & Kim (1985) disputed this model based on the results obtained from their simulation, and pointed out that the elongated-vortex model was not a necessary condition for the existence of long persistent streaks. They suggested that a relatively short streamwise vortex (a single vortex instead a pair of counter-rotating vortices would be sufficient) travel-

³Different authors have used different definitions for this widely used term. Its precise definition is not our concern here. The reader is referred to Robinson (1991a, 1991b) for the definition of this and other commonly used terms describing organized motions in a turbulent boundary layer.

ing with a convection velocity higher than the local mean velocity in the sublayer could leave a wake of low-speed streamwise velocity. A concrete evidence supporting the above notion will be described below in conjunction with streamwise vortices.

The answer to the fundamental question associated with the determination of the characteristic streak spacing has been quite elusive and still requires further investigations. Jang et al. (1986) suggested that the nonlinear self-interaction of the large vertical vorticity amplified by the direct resonance (Gustavsson 1981; Benny & Gustavsson 1981) produced streamwise vortices which in turn created streaks. The observed streak spacing was therefore a consequence of the direct resonance. They reported that a pair of wave numbers indeed satisfied the direct resonance condition, and the nonlinear interaction of the corresponding vertical vorticity modes produced a streak with the proper spanwise scale. Waleffe & Kim (1991), however, disputed this claim by showing that the largest vorticity amplitudes obtained in their analysis were not related to the direct resonance, and the linear process that produced the largest amplitudes did not yield a significant scale selection. They suggested that the scale selection must come from a complete self-sustaining nonlinear mechanism which consists of the creation, destruction and regeneration of the streaks. The observed characteristic scale of about $100\nu/u_r$, then corresponds to a critical Reynolds number for that process, below which it would not be self-sustaining. This establishes a link between the streak spacing and critical Reynolds numbers below which turbulent flows can not be maintained. Further study is required to draw any definite conclusion on this very fundamental question.

The central element of the formation and evolution of streaks is quasi-streamwise vortices.⁴ Streamwise vortices have been observed early in the experimental study of turbulence structures (Kim et al. 1971; Grass 1971; Smith & Schwartz 1983); analyses of databases from numerical simulations have confirmed these observation (Kim 1983; Kim & Moin 1986a; Moin 1987; Robinson 1991b). The quasi-streamwise vortices are mostly observed in the buffer layer with centers occurring between $y^+ = 20$ to 70 and average diameters about 15 to $50\nu/u_r$ (Robinson 1991b). A near-wall vortex model by Kim et al. (1987) consisting of streamwise vortices with the center of the vortex at $y^+ \approx 20$ with radius $r^+ \approx 15$ gives a good agreement with the peculiar behavior of the computed root-mean-square value of streamwise vorticity in the wall region, indicating that the near-wall region is so

dominated by such vortices that even the long time-averaged statistics are influenced by their presence.

Early descriptions regarding the nature of the streamwise vortices have been modified over the years since investigators started to examine extensively the databases from numerical simulations for studying turbulence structures. The streamwise vortices are now known to have a relatively long life time. They persist over $100\nu/u_r^2$, during which they travel over $1000\nu/u_r$ in the streamwise direction, and their convection velocity in the wall region ($10-12u_r$) is significantly higher than the local mean velocity (Hussain & Kim 1987; Guezenec et al. 1989; Johansson et al. 1991). As mentioned above, the early investigators considered a long pair of counter-rotating vortices as their conceptual model, but it is now believed that these vortices are relatively short compared to streaks (Kim & Moin 1986a, 1986b; Robinson 1991b). Kim & Moin (1986b) contended that these vortices convecting downstream without losing their coherence for such long distance had given the false impression that the streamwise extent of these vortices was rather long. It is also believed that a single vortex (rather than a pair of counter-rotating vortices) is more likely (Moser & Moin 1984; Kim & Moin 1986a; Guezenec et al. 1989; Robinson 1991b), and the early picture of a symmetric pair is an artifact of the averaging process (Johansson et al. 1991; Guezenec et al. 1989). A single vortex also has been observed to be responsible for both sweep and ejection events associated with the bursting process (Kim & Moin 1986b; Robinson 1991b).

Several physical processes by which a streamwise vortex is formed have been presented in the literature: the splatting motion of vortices, which creates wall vorticity of opposite sign because of the no-slip condition (Kim 1983; Jimenez & Orlandi 1991); the reorientation of the rolled-up spanwise vortices (Jimenez & Moin 1991); the interaction of a ring-vortex eddy (Falco 1982, 1983); the Görtler instability (Brown & Thomas 1977); the roll-ups of horseshoe vortices over a streak (Acalan & Smith 1987); the inherent instability associated with streaks (Waleffe & Kim 1991); the formation of a vortical arch on a streak followed by extension of a leg into the lower buffer layer where the leg is extended because of the high mean shear present (Robinson 1991b). All of the above processes can cause the formation of streamwise vortices; however, the key issue is determining which one of these mechanisms is a dominant one(s). There is no sufficient evidence to favor any particular process at the present time. The self-sustaining mechanism proposed by Waleffe & Kim (1991), in which the streamwise vortices (streamwise rolls according to their terminology) are formed from the instability associated with the streaks, directly relates "streaks and the streamwise vortices — the two dominant structures

⁴Lee, Kim & Moin (1990) showed that the streaky structures were also formed in the absence of vortices in a homogeneous shear flow as long as the imposed mean shear was strong enough, suggesting that the presence of vortices were not the necessary condition.

in the near-wall region where turbulence production is maximum — to the very existence of turbulence.

Some of the event-oriented descriptions of the bursting process have also been changed because of numerical simulations. For example, the original description of the bursting process, which included a violent break-up stage of the lifted streaks as an essential part of the process (Kline et al. 1967), has been disputed by several investigators (Kim & Moin 1986b; Guezenec et al. 1989; Johansson et al. 1991). They contended that it was the spatial intermittency associated with vortical structures that gave the wrong impression to an observer fixed in a laboratory frame. When a spatially intermittent structure, be it a streamwise vortex or a patch of high Reynolds stress region associated with the vortex, passes a fixed probe, the signature from the fixed probe will appear as if a sudden temporal eruption took place. The flow visualizations by dye or hydrogen bubbles can be equally misleading since they can give the same false impression when these passive markers get wrapped around by the passing spatially intermittent structures. Examinations of the computed flow field revealed, for example, that the high Reynolds stress contributions occurred intermittently in space (i.e., the spatial distribution was spotty); however, the persistence of these regions in the Lagrangian frame of reference indicated that there was no apparent violent break-up process during the evolution of these spotty patches of high Reynolds stress regions.

3.2 Near-Wall Shear Layers

Another commonly observed and dynamically significant turbulence structures in the wall region are the near-wall shear layers.⁵ The existence of intense shear layers in the wall region have been known from flow the visualization experiments (Kline et al. 1967; Corino & Brodkey 1969) as well as from the probe measurements (Brown & Thomas 1977; Johansson et al. 1987). Details on the nature of these shear layers including their dynamical significance, however, were not understood well until recently. In the following a brief account of the characteristics of these shear layers is provided based on two recent studies by Johansson et al. (1991) and Robinson (1991b).

Johansson et al. (1991) investigated the near-wall shear layer by using the VISA technique (Kim 1985), which is a spatial counterpart of the VITA technique (Blackwelder & Kaplan 1976). Several modifications of the previously used VISA technique, such as spanwise centering of individual structures, phase jitter removal through the use of correlations, retention of spanwise asymmetric features of the detected structures, were introduced to improve the ensemble-

averaging process. The retention of the asymmetry in the procedure brought out new information on the formation and evolution of the shear layers. The spanwise centering of the individual structures was also found to be essential to obtain correct quantitative estimates of the conditionally-averaged Reynolds stresses. Without such centering, for example, the resulting maximum $\langle uv \rangle$ is drastically reduced (by roughly 50%) on the ejection side. They noted that all previous results, experimental as well as numerical, presented in the literature had been obtained without the proper centering.

Johansson et al. (1991) examined the conditionally averaged production of turbulent kinetic energy to investigate the importance of the near-wall shear layer in the turbulence production process. In addition to the usual Reynolds-shear-stress-associated production, $-\langle uv \rangle dU/dy$, there were additional terms significantly contributing to the total production due to the presence of strong gradients in the x - and y -directions of the conditionally averaged streamwise velocity. The conditionally averaged production integrated over a volume surrounding the near-wall shear layer indicated that the production per unit volume within the regions of shear-layer activity was about three times larger than that of the rest.

Temporal evolutions of the near-wall shear layers were also investigated by following all detected events in time. The average propagation velocity was found to be $10.6u$, and the shear layers retained their coherence over $1000v/u$, in the streamwise direction. Individual near-wall shear layers often developed a strong asymmetry as they propagated downstream. In fact, the near-wall shear layers were most commonly formed at the spanwise kink between the low- and high-speed fluid, and the strength of the shear layers were intensified as the high-speed fluids caught up with the low-speed fluids (see figure 2 and related discussions in section 3.3). As the high-speed fluids passed by the low-speed streaks, the strength of the shear layers slowly decreased. There was no evidence of a violent break-up stage through the formation, intensification, and decay of the shear layer. The asymmetry was found to be the essential element of the shear-layer evolution, which is usually lost in conventional averaging process.

Some of the near-wall shear layers were observed to roll up into transverse vortices, mainly in the region between $30 \leq y^+ \leq 80$, which roughly corresponded with the logarithmic layer of the simulated boundary layer under the study (Robinson 1991b). He concluded that all shear layers may be dynamically significant due to their potential for rolling up into vortices which in turn generated strong ejections. According to Robinson (1991b), the near-wall shear layers were not the major producers of $-uv$ in the buffer zone, where turbulence production peaked, but

⁵ Also known as internal shear layers.

that the shear-layer instability leading to the vortex formation contributed significantly to $-uv$ in the log region. Robinson (1991b) also suggested a method by which a streamwise vortex can give rise to transverse vortices. A streamwise vortex created high vorticity at the wall due to the no-slip boundary condition. These newly-formed shear layers rolled up into transverse vortices, which in turn created streamwise vortices as they evolved into arch or hairpin shapes.

3.3 Conceptual Model for Near-Wall Structure

I have discussed wall-layer streaks, streamwise vortices, and near-wall shear layers with an implication that these are the most important elements for organized motions in the wall region, especially from the perspective of the drag reduction. Each of these organized structures plays an important role in the overall production process, and it is essential to understand how these structural elements are related to each other. Since each realization of a turbulent flow in the boundary layer varies significantly, no single model can represent perfectly all realizations. Nevertheless, it is useful to have a conceptual model containing most common characteristics for all realizations. The following is one of such models that appears to be consistent with many experimental and numerical observations.

Stretch et al. (1990) proposed a conceptual model, in which the streaks, streamwise vortices, near-wall shear layers and pockets of high-wall stress are spatially related. These various structural elements are viewed as part of a basic organized structure (figure 2). The conceptual model was obtained by applying a pattern recognition procedure to the channel data. Near the wall, the streamwise velocity field comprises low- and high-speed streaks over which two attached eddies (or vortices) with opposite sense of rotation are arranged one above another. There is a lateral asymmetry (spanwise kinking) associated with streaks, and this in turn is associated with the near-wall shear-layer structure. The attached eddies, which near the wall are quasi-streamwise vortices, have a characteristic stress signature at the wall comprising a small-scale region of high stress embedded within the more elongated high-speed streaks. Note that the vortices are stacked in the vertical direction rather than in the spanwise direction, and their configuration is more likely to be asymmetric. Note also that the second- and fourth-quadrant events can take place either side by side (in the spanwise direction) along a vortex, back to back (in the streamwise direction) across a single vortex at an oblique angle, or back to back (in the streamwise direction) in-between two vortices.

A possible scenario for the physical process that can maintain such structure in a cyclic manner is

as follows. Streamwise vortices create streaks as explained before (Moin & Kim 1985). Instabilities associated with the streaks induce spanwise oscillations and kinks (Waleffe & Kim 1991), from which the near-wall shear layer develops (Johansson et al. 1991). Interactions of the near-wall shear layer and the streamwise vortices with the wall create new shear layers in the vicinity of the wall (Robinson 1991b), which in turn create streamwise vortices, and the process repeats. There is a minimum spanwise scale that can sustain such cyclic process, and the universal streak spacing is a result of such critical scale, below which the streaks do not become unstable (Waleffe & Kim 1991). The interaction of streamwise vortices with the wall (the splatting motion) is believed to be the main source of high wall-shear stress in the turbulent boundary layer. The closer streamwise vortices are allowed to move toward the wall, the stronger the splatting motion, resulting in a higher surface stress. In the following section, results from a numerical experiment where such interactions are suppressed through an active control are presented.

4 Numerical Experiment of Active Turbulence Control⁶

Most turbulence control strategies for wall-bounded turbulent flows to date have used passive approaches. For example, a flow device, such as riblet or LEBU (Large-Eddy-Break-Up device), is placed in the boundary layer in an attempt to suppress the formation (or interaction) of the organized structures. Such a device plays a passive role in the sense that there exists no feedback loop as the flow structures are modified. The present study is aimed at active control of dynamically significant coherent structures to achieve skin-friction reduction. The control strategy will respond instantly through a feedback loop as instantaneous flow structures are being modified.

4.1 Numerical Procedures

As evident from the previous section, the streamwise vortices are playing a key role in the turbulence production process. Therefore we seek physical algorithms that can suppress the strength of streamwise vortices with subsequent net skin-friction reduction. We use the direct numerical simulation technique to achieve this goal. Owing to availability of all flow variables at many spatial locations, and the ability to readily alter flow boundary conditions, numerical simulation technique provides a unique laboratory for

⁶The major portion of this section is reproduced from Kim et al. (1990) for the benefit of the participants of the lecture series for whom this note is prepared.

testing and design of turbulence control concepts. Although some of the concepts may not turn out to be feasible for implementation, the simulations can provide data on what may be possible to achieve just from fluid dynamical considerations.

The numerical technique used in this study is identical to that of Kim et al. (1987). The boundary condition for the normal component of the velocity is modified according to the particular control strategy, which resulted in a pentadiagonal system compared to a tridiagonal system for the no-slip boundary condition of the unperturbed channel.

The base flow is the fully-developed channel flow. Preliminary experiments were performed using $32 \times 65 \times 32$ spectral modes (streamwise, normal to the wall, and spanwise, respectively) at Reynolds number, $Re = 1800$ based on the centerline velocity and the channel half-width. Starting with the same initial field several different boundary conditions were tried to achieve an optimum result. The final computation was made using $128 \times 129 \times 128$ spectral modes at $Re = 3300$, from which most of results presented in this note were obtained. The particular Reynolds number was chosen to compare with the results of the unperturbed channel.

4.2 Results

Our aim was to examine whether we can reduce the wall-skin friction by suppressing the sweep and ejection events associated with the streamwise vortices. We applied suction or injection on the channel walls exactly opposite to the normal component of velocity at a given y -location in an attempt to suppress the organized motions. At each instant the boundary condition for v at $(x, y = 0, z)$ was prescribed to be $-v(x, y_r, z)$, where y_r is the location of detection. Thus, when fluid was detected at y_r to move towards the wall (sweep) an equally strong blowing velocity was imposed at the wall to "cancel" the sweep event. Similarly, when fluid was detected at y_r moving away from the wall (ejection), an equally strong suction was applied. The initial condition for the calculations was an instantaneous velocity field from fully-developed channel flow. The mass flux was kept constant by adjusting the mean pressure gradient. Thus, any skin-friction reduction would be manifested in the mean pressure gradient necessary to drive the flow with the same mass flow rate. Several computations were performed with the coarse mesh ($32 \times 65 \times 32$) for several different y_r to examine the effect of the location of detection. Using the same initial velocity field, the calculations were continued with the new boundary conditions until a new statistically steady state was obtained or until it became apparent that the drag would increase substantially.

Time histories of the pressure gradient required to

drive the same mass flow rate for an unperturbed fully-developed channel flow and perturbed channel flows are shown in figure 3. Indeed, substantial skin-friction reduction was obtained ($\approx 20\%$ on each wall) with $y_r^+ \approx 10$. For other y_r -locations, either the drag was substantially increased ($y_r^+ \approx 25$) or the reduction is from negligible to small ($y_r^+ \approx 2, 5$).

After the optimum y_r -location was identified with the coarse mesh, a final computation was performed for detail analysis of the modified flow field for the case of $y_r^+ \approx 10$, using $128 \times 129 \times 128$ spectral modes for $Re = 3300$. The mean velocity gradient in the unperturbed fully-developed channel and the perturbed channels are shown in figure 4(a). The reduction in the velocity derivative in the vicinity of the wall is apparent whereas away from the wall there is a slight increase. The mean velocity profile in a semi-log plot is shown in figure 4(b). The shift in the profile in the logarithmic layer is due to the reduction in the wall shear velocity, u_τ , in the perturbed channel.

Turbulent intensities and Reynolds shear stress profiles are shown in figures 5 and 6. Here the velocities are normalized with the shear velocity of the unperturbed channel flow. There is a significant reduction in the intensities throughout the channel. This is in contrast to the experiments with unsteady high-amplitude wavy (but passive) wall motion where the effect of the wall movement was confined to a thin (Stokes-like) layer near the wall (Kuhn et al. 1984). In these latter computations the moving wavy wall was approximated by sinusoidal wall-blowing and suction. Apparently, with the "active" boundary conditions the energy production and transport mechanisms have been significantly altered.

The instantaneous fields have been examined in detail. In an unperturbed channel flow the high-vorticity regions created by the splatting motions induced by the streamwise vortices normally exist right on the surface. It is apparent that the out-of-phase blowing prevents the formation of such high-vorticity regions on the surface (figure 7). In the controlled channel flow, these regions are now located not only off the surface but also the strength of the vorticity is reduced, resulting in a reduction on the surface viscous drag. We have not investigated in detail the role of the out-of-phase suction (the out-of-phase blowing alone does not provide the same amount of drag reduction for the combined), but it is most likely that it tends to stabilize the flow field by suppressing the ejection events and hence reducing the inflection profiles associated with the ejection events.

Other flow structures also have been affected. Contours of constant streamwise velocity fluctuations are shown in figure 8. It is clear that the structure of the wall-layer streaks has been changed. Their strength has been reduced considerably. Two-point correlations of the streamwise velocity component in the

spanwise direction

$$R_{11}(r_z) = \langle u_1(x, y, z)u_1(x, y, z + r_z) \rangle$$

show a significant change in the near-wall region (figure 9). It is well known that the auto-correlation of the streamwise component crosses the r_z axis, and the location of the (negative) minimum is the mean spacing between low- and high-speed streaks. In the perturbed channel, $R_{11}(r_z)$ only has a weak negative region consistent with the observation that the strengths of the streaks have been reduced. The physical streak-spacing has been increased, whereas their mean-spacing in the wall units has remained approximately the same.

4.3 Summary and Future Prospects

The control algorithm just described is probably not optimum. For example, a shift in the streamwise location of the imposed wall velocity relative to the velocity at $y_*^+ \approx 10$ may be more effective in "canceling" local structures or events. Also, one can vary the strength of the blowing and suction at the surface instead of using the same magnitude of v at y_r . One can also add the spanwise velocity component (w) to the normal blowing and suction (v) to cancel the spanwise motions associated with the streamwise vortices. Some of these parametric studies have been performed to yield slightly better results. Detailed results from these numerical experiments will be reported in the future. When the normal component of the velocity at the wall was forced in phase with the normal velocity at the sensor location, the required pressure gradient to drive the same mass flow rate increased dramatically, indicating that one can also augment turbulence generation and heat transfer from the wall.

Although the control algorithm described above was successful in reducing skin-friction and suppression of turbulence, it is clearly not feasible for practical implementation. Among other things, it is difficult to place sensors within the flow field away from boundaries. Several control strategies using the flow variables at the wall for detection of structures above the wall have been tried to yield significantly less drag reduction. Investigation of control strategies implementable at practical situations is under progress. We are also trying to apply an optimal control theory (Abergel & Temam 1990) to the solution of the Navier-Stokes equations.

The same control strategy was applied to a transitional flow to examine the effectiveness of the present algorithm in delaying (or suppressing) transition to turbulence. It was found that one could delay (or completely suppress) all small disturbances at super-critical Reynolds numbers in the plane Poiseuille flow. The change in the boundary condition modified the

original eigensystem of the linearized Orr-Sommerfeld equation such that with a proper choice of y_r , the most unstable mode (a 2D Tollmien-Schlichting wave) became stable. This was true for a wide range of Reynolds numbers tested including $Re \approx 50000$, at which a linear disturbance attains its maximum growth rate for the plane Poiseuille flow. The implication of this result for turbulent flows is not completely clear at this point. It does, however, indirectly suggest that in turbulent channel flow, in which about 20% drag reduction was achieved, the present control strategy probably modified the flow instabilities.

5 Concluding Remarks

The discovery of the organized motions in turbulent flows has generated much excitement in the turbulence research field over the past three decades. Despite such excitement, progress in understanding the organized motion has been painfully slow with many confusing and contradicting claims, largely due to the limitation in the available experimental techniques. Numerical simulations thus far have played a key role in unraveling many mysteries associated with the organized motions, by integrating many of the incomplete information produced over the years. A number of examples in which physical understanding of a turbulent flow was achieved through the computer simulations were given in this note. The purpose of these examples was to illustrate that it is now possible to use the computer simulations of fluid flows to complement and/or supplement the laboratory experiments in studying the physics of turbulent flows, although the simulations are limited to the canonical flows at low Reynolds numbers.

The streamwise vortex motions responsible for the formation of the streaks and the subsequent development of the near-wall shear layer from spanwise kinks of the streaks play the key role in the turbulence production process. The interaction of these vortices with a wall was conjectured to be the main reason for the high wall-shear stress for turbulent flows. A control strategy to suppress the strength of these vortices through modified boundary conditions at the wall not only weakened the strength of the vortices, but also prevented the direct interaction of the vortices with the wall, thus preventing the formation of the high vorticity regions at the wall. As a result, the skin-friction at the wall was substantially reduced. Although not reported in this note, a recent direct numerical simulation of a turbulent flow over riblets (surface mounted longitudinal grooves) also suggested that the key mechanism by which a certain size riblet surface was able to reduce the viscous drag was the prevention of the interactions between the near-wall streamwise vortices and the surface (Choi et al. 1991).

This note is prepared for the two lectures I gave as a part of AGARD FDP/VKI Special Course on "Skin Friction Drag Reduction," March 2-6, 1992, VKI, Brussels, Belgium.

REFERENCES

ABERGEL, F. & TEMAM, R. 1990 On some control problem in fluid mechanics. *Theor. and Comp. Fluid Dynamics.* 1, 303.

ACALAR, M. S. & SMITH, C. R. 1987 A study of hairpin vortices in a laminar boundary layer. Part II: hairpin vortices generated by fluid injection. *J. Fluid Mech.* 175, 43.

ANTONIA, R. A., KIM, J. KIM & BROWNE, L. W. B. 1991a Some characteristics of small scale turbulence in a turbulent duct flow. *J. Fluid Mech.*, *in press*.

ANTONIA, R. A., TEITEL, M., KIM, J. & BROWNE, L. W. B. 1991b Low Reynolds number effects in a fully developed turbulent channel flow. *J. Fluid Mech.*, *in press*.

BAKEWELL, H. P. & LUMLEY, J. L. 1967 Viscous sublayer and adjacent wall region in turbulent pipe flow. *Phys. Fluids.* 10, 1880.

BENNEY, D.J. & GUSTAVSSON, L.H. 1981 A New Mechanism for Linear and Nonlinear Hydrodynamic Stability. *Studies in Appl. Math.* 64, 185.

BLACKWELDER, R. F. 1978 The bursting process in turbulent boundary layers. In *Coherent Structure of Turbulent Boundary Layers*, C. R. Smith & D. E. Abbott (Eds.), AFOSR/Lehigh University Workshop, Dept. Mech. Engng & Mech., Bethlehem, PA.

BLACKWELDER, R. F. & KAPLAN, R. E. 1976 On the wall structure of the turbulent boundary layer. *J. Fluid Mech.* 76, 89.

BLACKWELDER, R. F. & ECKELMANN, H. 1979 Streamwise vortices associated with the bursting phenomenon. *J. Fluid Mech.* 94, 577.

BROWN, G. L. & THOMAS, A. S. W. 1977 Large structure in a turbulent boundary layer. *Phys. Fluids.* 20, S243.

CANTWELL, B. J. 1981 Organized motion in turbulent flow. *Annu. Rev. Fluid Mech.* 13, 437.

CHOI, H., MOIN, P. & KIM, J. 1991 Direct numerical simulation of turbulent flow over ripples, *in preparation*.

CORINO, E. R. & BRODKEY, R. S. 1969 A visual investigation of the wall region in turbulent flow. *J. Fluid Mech.* 37, 1.

FALCO, R. E. 1980 The production of turbulence near a wall. *AIAA Paper 80-1956*.

FALCO, R. E. 1982 A synthesis and model of wall region turbulence structure, *Structure of Turbulence, Heat, and Mass Transfer*, Hemisphere.

FALCO, R. E. 1983 New results, a review and synthesis of the mechanism of turbulence modification. *AIAA Pap. No 83-0377*.

GRASS, A. J. 1971 Structural features of turbulent flow over smooth and rough boundaries. *J. Fluid Mech.* 50, 233.

GUEZENNEC, Y. G., PIOMELLI, P. & KIM, J. 1989 On the shape and dynamics of wall structures in turbulent channel flow. *Phys. Fluids A.* 1, 764.

GUEZENNEC, Y. G. & CHOI, W. C. 1989 Stochastic estimation of coherent structures in turbulent boundary layers. In *Proc. Zoran Zanic Memorial Intl Seminar on Near-Wall Turbulence, May 1988 Dubrovnik*. Hemisphere.

GUSTAVSSON, L. H. 1981 Resonant growth of three dimensional disturbances in plane Poiseuille flow. *J. Fluid Mech.* 112, 253-264.

HEAD, M. R. & BANDYOPADHYAY, P. 1981 New aspects of turbulent boundary layer structure. *J. Fluid Mech.* 107, 297.

HUSSAIN, F. 1986 Coherent structures and turbulence. *J. Fluid Mech.* 173, 303.

HUSSAIN, F. & KIM, J. 1987 Structure of turbulent shear flows, Proceedings of the 1987 Summer Program of the NASA-Stanford Center for Turbulence Research, CTR-S87, December 1987.

JANG, P.S., BENNEY, D.J. & GRAN, R.L. 1986 On the origin of streamwise vortices in a turbulent boundary layer. *J. Fluid Mech.* 169, 109-123.

JIMENEZ, J. & MOIN, P. 1991 The minimum flow unit in near-wall turbulence. *J. Fluid Mech.* 225, 213-240.

JIMENEZ, J. & ORLANDI, P. 1991 The rollup of a vortex layer near a wall, *CTR Manuscript 129*, Center for Turbulent Research, December 1991.

JOHANSSON, A. V., ALFREDSSON, P. H., & ECKELMANN, H. 1987 On the evolution of shear-layer structures in near-wall turbulence. In *Advances in Turbulence, Proc. First European Turbulence Conference, Lyon, July 1986* (ed. G. Comte-Bellot & J. Mathieu), Springer.

JOHANSSON, A. V., ALFREDSSON, P. H. & KIM, J. 1991 Evolution and dynamics of shear-layer structures in near-wall turbulence. *J. Fluid Mech.* 224, 579.

KIM, J. 1983 On the structure of wall-bounded turbulent flows. *Phys. Fluids.* 26, 2088.

KIM, J. 1985 Turbulence structures associated with the bursting event. *Phys. Fluids.* 28, 52.

KIM, J. 1989 On the structure of pressure fluctuations in a simulated turbulent channel flow. *J. Fluid Mech.* **205**, 421.

KIM, H.T., KLINE, S.J. & REYNOLDS, W.C. 1971 The production of turbulence near a smooth wall in a turbulent boundary layer. *J. Fluid Mech.* **50**, 133-160.

KIM, J. & MOIN, P. 1986a The structure of the vorticity field in turbulent channel flow. Part 2. Study of ensemble-averaged fields. *J. Fluid Mech.* **162**, 339.

KIM, J. & MOIN, P. 1986b Flow structures responsible for the bursting process. *Bull. APS* **31**, no 10.

KIM, J., MOIN, P. & MOSER, R.D. 1987 Turbulence statistics in fully developed channel flow at low Reynolds number. *J. Fluid Mech.* **162**, 339-363.

KIM, J. & SPALART, P. R. 1987 Scaling of the bursting frequency in turbulent boundary layers at low Reynolds numbers. *Phys. Fluids* **30**, 3326.

KIM, J., MOIN, P. & CHOI, H. 1990 Active turbulence control in a wall-bounded flow using direct numerical simulations. In *Structure of Turbulence and Drag Reduction*, A. Gyr (ed.), IUTAM Symposium Zürich, Switzerland, July 25-28, 1989, Springer-Verlag.

KLINE, S. J. 1978 The role of visualization in the study of the structure of the turbulent boundary layer. In *Coherent Structure of Turbulent Boundary Layers*, C. R. Smith & D. E. Abbott (Eds.), AFOSR/Lehigh University Workshop, Dept. Mech. Engng & Mech., Bethlehem, PA.

KLINE, S.J., REYNOLDS, W.C., SCHRAUB, F.A. & RUNSTADLER, P. 1967 The structure of turbulent boundary layers. *J. Fluid Mech.* **30**, 741-773.

KUHN, G. D., MOIN, P. KIM, J. & FERZIGER, J. H. 1984 Turbulent flow in a channel with a wall with progressive waves. Proc. of *ASME Symposium on Laminar Turbulent Boundary Layers: Control, Modification and Marine Applications*; New Orleans, 61.

LEE, M. K., ECKELMAN, L. D. & HANRATTY, T. J. 1974 Identification of turbulent wall eddies through the phase relation of the components of the fluctuating velocity gradient. *J. Fluid Mech.* **66**, 17.

LEE, M.J., KIM, J. & MOIN, P. 1990 Structure of turbulence at high shear rate. *J. Fluid Mech.* **216**, 561-583.

MOIN, P. 1987 Analysis of turbulence data generated by numerical simulations. *AIAA Pap. No.* 87-0194

MOSER, R. D. & MOIN, P. 1984 Direct numerical simulation of curved turbulent channel flow. *NASA TM 85974*. See also, "The effects of curvature in wall-bounded turbulent flows," *J. Fluid Mech.* **175**, 479.

MOIN, P. & KIM, J. 1985 The structure of the vorticity field in turbulent channel flow. Part 1. Analysis of instantaneous fields and statistical correlations. *J. Fluid Mech.* **155**, 441.

OFFEN, G. R. & KLINE, S. J. 1974 Combined dye-streak and hydrogen-bubble visual observations of a turbulent layer. *J. Fluid Mech.* **62**, 223.

OFFEN, G. R. & KLINE, S. J. 1975 A proposed model of the bursting process in turbulent boundary layers. *J. Fluid Mech.* **70**, 209.

ROBINSON, S. K. 1991a Coherent motions in the turbulent boundary layer. *Annu. Rev. Fluid Mech.* **16**, 99.

ROBINSON, S. K. 1991b The kinematics of turbulent boundary layer structure. *NASA TM 109859*.

RUNSTADLER, P. G., KLINE, S. J., REYNOLDS, W. C. 1963 An experimental investigation of flow structure of the turbulent boundary layer. *Rep. No. MD-8*, Dept. Mech. Eng., Stanford Univ., Stanford, Calif.

SMITH, C. R. & SCHWARTZ, S. P. 1983 Observation of streamwise rotation in the near-wall region of a turbulent boundary layer. *Phys. Fluids* **26**, 641.

SPALART, P. R. 1988 Direct simulation of a turbulent boundary layer up to $Re_\theta = 1410$. *J. Fluid Mech.* **187**, 61.

STRETCH, D., KIM, J. & BRITTER, R. 1990 A conceptual model for the structure of turbulent channel flow. *Boundary-Layer Structure Workshop*, August 28-30, 1990, NASA Langley Research Center, Hampton, Virginia.

WALEFFE, F. & KIM, J. 1991 On the origin of streaks in turbulent shear flows, *Proceedings of the Eighth Symposium on Turbulent Shear Flows*, Technical University of Munich, September 9-11, 1991.

WALLACE, J. M., ECKELMANN, H & BRODKEY, R. S. 1972 The wall region in turbulent shear flow. *J. Fluid Mech.* **54**, 39.

WARK, C. E. 1988 Experimental investigation of coherent structures in turbulent boundary layers. *Ph.D. thesis, Illinois Institute of Technology*.

WILLMARTH, W. W. & LU, S. S. 1972 Structure of the Reynolds stress near the wall. *J. Fluid Mech.* **55**, 65.

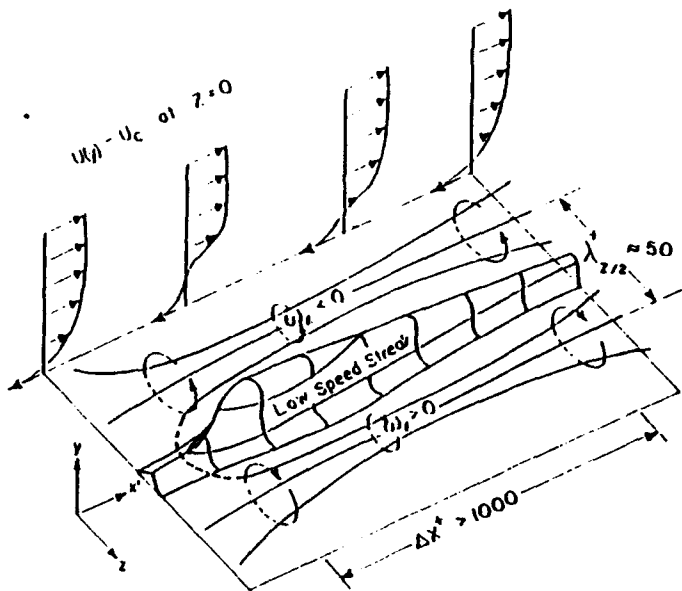


FIGURE 1. Model of the counter-rotating streamwise vortices with the resulting low-speed streak (from Blackwelder 1978).

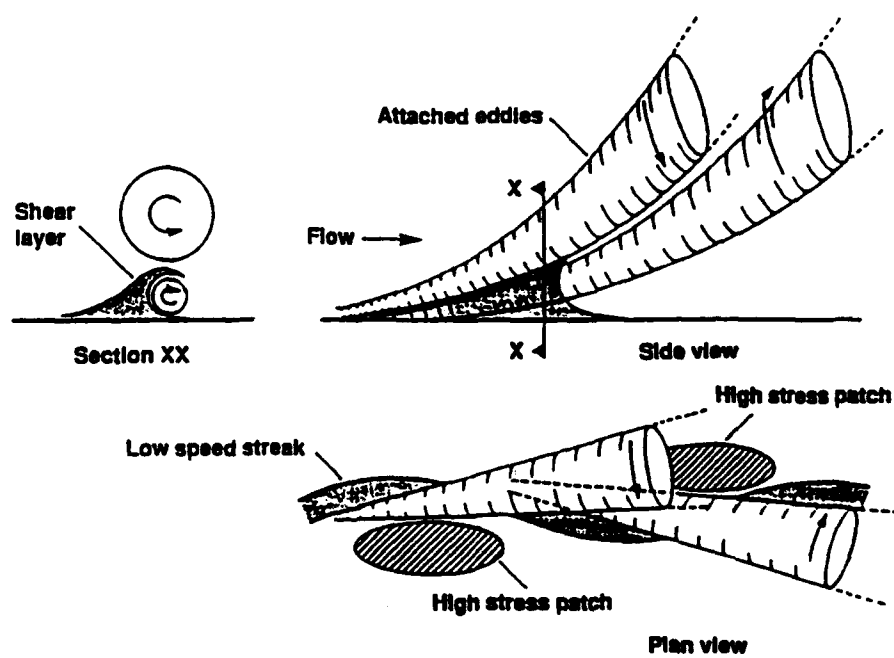


FIGURE 2. A conceptual model for near-wall structures in a boundary layer.

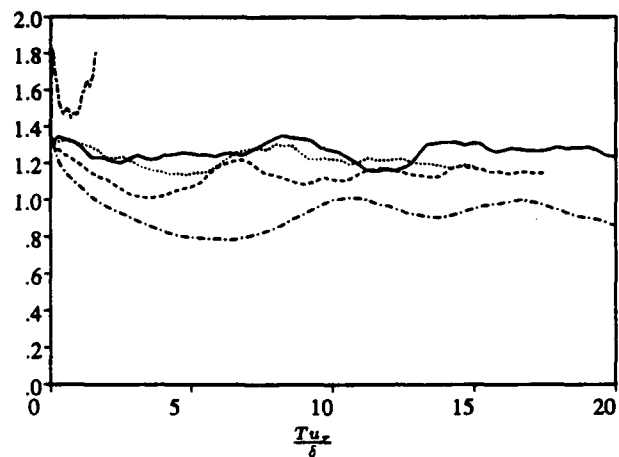


FIGURE 3. Time history of the required pressure gradient to drive the same mass flow rate: —, unperturbed channel; ·····, perturbed channel with sensor at $y_r^+ \approx 2$; - - - - , $y_r^+ \approx 5$; - - - , $y_r^+ \approx 10$; - - - , $y_r^+ \approx 25$.

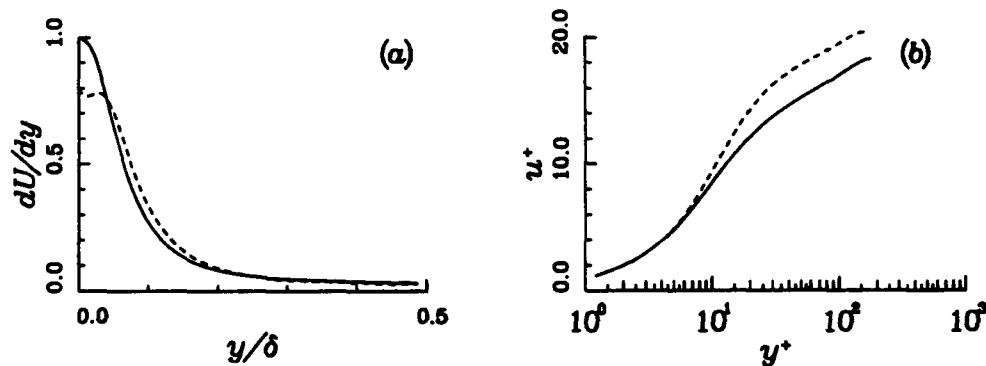


FIGURE 4. Profiles of (a) mean velocity gradient and (b) mean velocity profile normalized by wall variables: —, unperturbed channel; - - - - , perturbed channel.

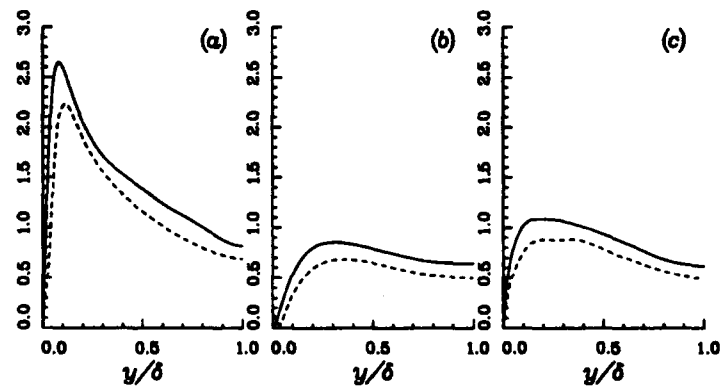


FIGURE 5. Profiles of r.m.s. fluctuations of turbulence intensities: —, unperturbed channel; ·····, perturbed channel. (a) $\langle u^2 \rangle^{1/2}$, (b) $\langle v^2 \rangle^{1/2}$, and (c) $\langle w^2 \rangle^{1/2}$. All intensities are normalized with the wall-shear velocity of the unperturbed channel.

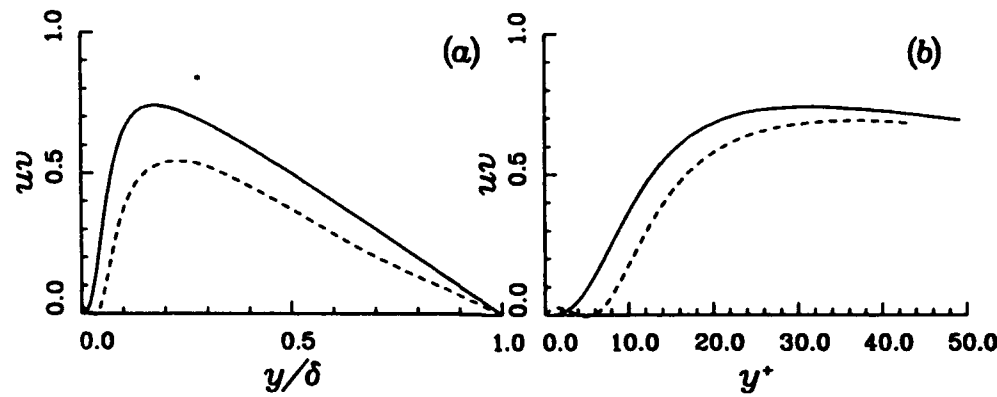


FIGURE 6. Profiles of Reynolds shear stress: —, unperturbed channel; - - - , perturbed channel. (a) The shear stress is normalized by the wall-shear velocity of the unperturbed channel; (b) The shear stress and the y -coordinate are normalized by the corresponding wall-shear velocity.

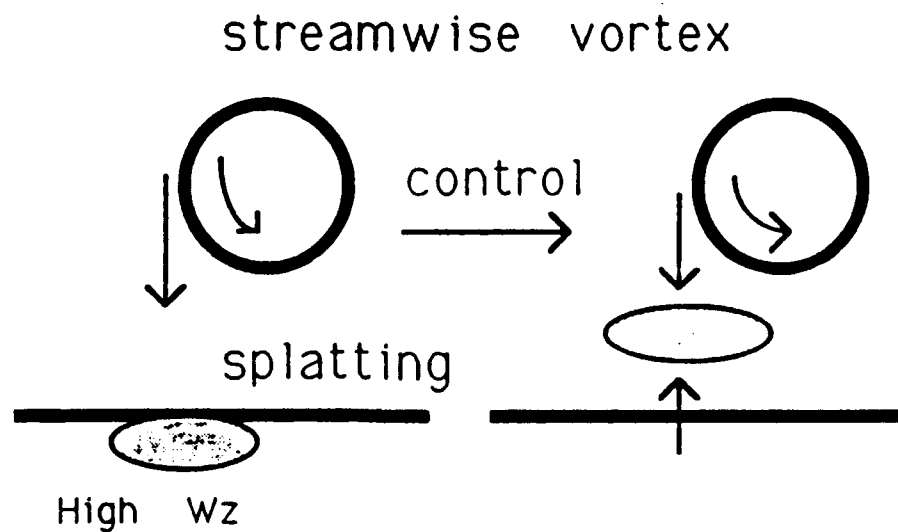


FIGURE 7. Interaction of a streamwise vortex with the no-slip wall. The active control prevents the formation of high vorticity at the wall.

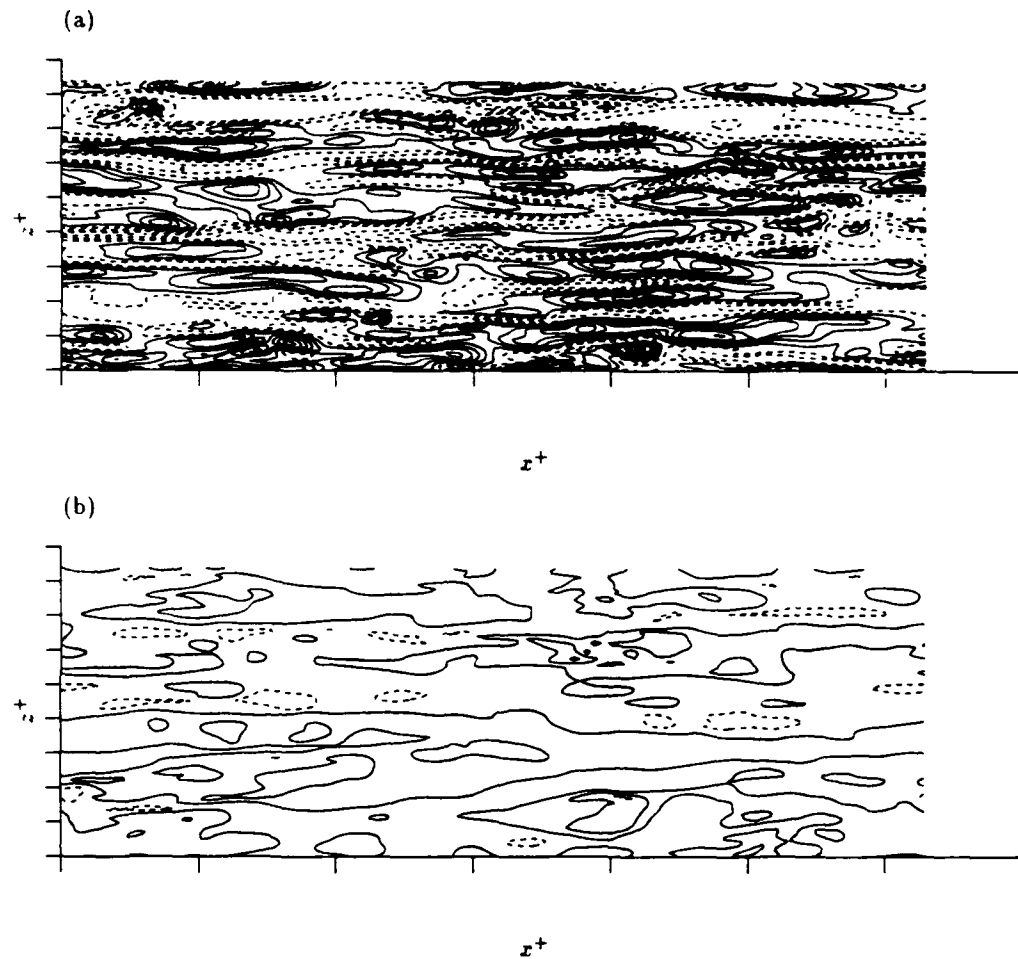


FIGURE 8. Contours of streamwise velocity fluctuations, u , in an (x, z) -plane at $y^+ \approx 5$: (a) unperturbed channel, $u_{\max}=6.5$ and $u_{\min}=-3.6$; (b) perturbed channel, $u_{\max}=2.1$ and $u_{\min}=-1.5$. The contour levels range from -4 to 7 by increments of 1, and negative contours are dashed. The plot domain extends 2300 wall units in x and 800 units in z .

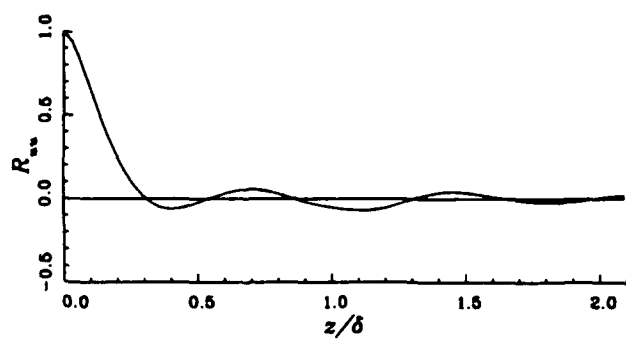


FIGURE 9. Two-point correlation of the streamwise velocity in the spanwise direction, $R_{uu}(r_z)$.



TURBULENT SKIN-FRICTION DRAG REDUCTION BY ACTIVE AND PASSIVE MEANS: Part 1

"Everything you wanted to know about riblets, LEBUs and other devices..."

by

E. Coustols ¹ & A. M. Savill ²

¹ ONERA/CERT, Aerothermodynamics Department, Toulouse. FRANCE

² Engineering Department, University of Cambridge, UNITED KINGDOM

92-17813



Summary

The purpose of this paper is to provide a current overview of turbulent skin friction drag reduction concepts which have potential for reducing aircraft fuel consumption. Then, this review lectures will be organized around four main topics. First, after briefly reviewing what is known about the structure of the turbulent boundary layer, possible mechanisms for both active and passive devices will be discussed ; concentrating on techniques offering nett drag benefits, either through inner or outer layer manipulation. Indeed, both experimental and numerical results will be presented for these boundary layer manipulators. Available data and computer model predictions for low and high subsonic speeds, transonic conditions, and supersonic flow (including flight tests) will be reviewed. Although the emphasis will be on turbulent external flow findings, laminar, transitional and fully developed internal flow results will also be discussed together with those obtained when applying similar control techniques to wall-jets. The aim of these lectures will be to outline the most important results obtained in terms of drag reduction, and to emphasize most recent developments. Finally the combination of passive devices with polymers, suction, blowing, microbubbles, or acoustic forcing - all of which are known to be additive or more than additive - will be discussed ; together with studies of alternative drag reducing surfaces, such as "sparse" (or "Tani") d-type and certain random "sphere" roughnesses, which have also been shown to produce nett drag reductions at certain Reynolds numbers (and combine at least additively with passive devices). Some comments will also be made regarding likely future developments.

1 Introduction

The classical theory of aircraft range performance clearly shows up how propulsion, structural and aerodynamical efficiencies interact to affect aircraft per-

formance. These points should be covered by Bushnell [1]. Nevertheless, particular means of improving aircraft propulsion efficiency are through the development of higher fan efficiency, advanced compressor design, improved seals and bearings. As regards aircraft structural improvements : advanced composite structures, having high strength-to-weight and stiffness-to-weight ratios, should be considered. Aerodynamic efficiency of aircraft configurations can also be improved by ensuring that drag forces generated during any motion are as small as possible. (Since this may also be a prime consideration for hydrodynamic or ground vehicles, much of the discussion presented here is equally relevant to these).

The search for practical means of achieving significant drag reductions has occupied designers for a long time as such reductions translate directly into increased range, speed and manoeuvrability or into decreased fuel consumption. Interest in reducing the latter is strictly related to the impact on the "Direct Operational Cost", as will be mentioned by Robert [2]. In most cases, aircraft performance could be improved through increases in lift characteristics and/or decreases in total drag.

The major sources of drag for climb and cruise conditions, which account for almost 90% of the fuel consumption for subsonic civil transport aircraft, are : skin friction drag, induced drag (or drag due to lift), afterbody (or separation) drag, wave drag, interference drag, and roughness (or excrescence) drag. It is reasonable to assume that drag reductions may be achieved by focusing research on the two major sources, i.e. friction drag due to development of boundary layers, and lift-induced-drag associated with wing-tip vortices. These two drags account for respectively 48% and 37% of the total drag of a modern subsonic transport aircraft, [3]. However, as noted by Thomas, [4], "it is not always worthwhile to address only the more significant drag contributions, since it is very often easier to obtain much greater percentage reductions in the smaller drag sources than in the larger contributions". For instance, a 25% reduc-

tion in afterbody drag is feasible and this might represent rather more than 1% total drag reduction ; the achievement of such a reduction through induced drag control alone could be a very difficult task. Although there would seem to be a tremendous potential for reducing the large amount of drag due to lift this particular drag component varies in proportion to the square of the lift coefficient, and since the latter has to be relatively high, real opportunities for decreases in drag are somewhat restricted. It should be noted, however, that some Airbus & Boeing transport aircraft are already flying with wing tip fences designed for just this purpose - see [2].

The reduction of skin friction drag, has stimulated aerodynamicists imagination for almost half a century. In a book published in 1961, the reader could already find ideas which are at the origin of actual developments today, [5]. Since that time, a growing research effort has been mounted, in a large number of countries, to investigate both novel ideas and ideas which have been looked at in the past but not pursued to the point of application (simply because "the economic facts of life were rather different from now", as pointed out by Young in the Preface to a previous Lecture Series, [6]).

Considering civil transport aircraft, one way of reducing the friction drag is to find control methods for stretching out the laminar flow over as large a part of the boundary layer as possible. This could be done by controlling the stability properties of the laminar boundary layer with either an active device such as wall suction ("Laminar Flow Control" - LFC) or passive control via favourable pressure distributions or shaping ("Natural Laminar Flow" - NLF) or indeed a combination of the two ("Hybrid Laminar Flow Control" - HLFC). These aspects of flow control will be discussed in separate lectures by Saric [7] and Arnal [8]. A commercial aircraft travelling at a speed of 300m/s, would have a unit Reynolds number of $2 \cdot 10^7$ /m at sea level and $1 \cdot 10^7$ /m at an altitude of 33,000ft. Thus, transition delay is feasible on the wing and other appendages of an aircraft (nacelle, horizontal and vertical tails), but not on the much longer fuselage, where half of the skin friction drag takes place. Here, some alteration of the turbulence structure is required.

(It should be noted that for an underwater vehicle, moving at a modest speed of 20m/s, the unit Reynolds number is also close to $1 \cdot 10^7$ and hence as indicated Gad-el-Hak, [9], "short underwater bodies such as torpedoes, are ideal targets for applying transition delay methods" ; whereas, for submarines or most surface vessels turbulent drag reduction or re-laminarization would have to be examined in more detail. Similar length Reynolds numbers are also found on high speed trains.

In fact some drag reduction methods have first been applied in competitive water and motor sports ; for instance the application, apparently successfully, of riblets to the Oxford eight in the 1987 University Boat Race and to the 1987 America's Cup Winning Yacht, Stars and Stripes. Attempts have

also been made to develop laminar keels for 12m class racing boats. Although riblets have also been tested on Formule 1 or Prototype Sports vehicles, as well as on smaller racing boats and windsurfer boards , it would seem that three-dimensional effects as well as the rather small percentage of turbulent friction drag versus total drag, must have restricted any advantages to purely cosmetic ones. However applications to surface marine vessels or high speed trains - such as the French TGV - could reasonably be anticipated to be of practical commercial value).

When considering current aircraft, either civil transport or smaller business ones, it is noticeable that most of the boundary layers are turbulent over almost 100% of their development. Apart from manufacturing technological difficulties, this is due to several reasons such as Reynolds number, angle of sweep, surface finish and so forth. Hence, during the last two decades, there has been considerable worldwide interest in studying specifically turbulent skin-friction drag reduction.

The purpose of this paper is to provide a current overview of turbulent skin friction drag reduction concepts which have potential for reducing aircraft fuel consumption. It should be noted, however, that techniques developed for turbulent skin friction drag reduction could, in many instances, be employed also for other purposes such as self-noise reduction, cavitation inhibition, or controlling heat transfer and mixing and some comments will be made regarding these other uses. Emphasis will be placed upon passive techniques, i.e methods which do not require any external power although some mention will be made of active techniques, when relevant. Among such passive methods, the two most well known techniques involve using either external manipulators - commonly referred to as Large Eddy Break-Up devices (LEBs), Outer Layer Devices (OLDs), Tandem Arrayed Parallel Plate Manipulator (TAPPMs), Boundary Layer DEvices (BLADEs), RIBBONS or other acronyms - embedded within the outer part of a turbulent boundary layer, or internal devices termed RIBLETS or RIBs, which involve an alteration of the wall geometry in the form of small streamwise striations. Other various methods with considerable promise for drag reduction are still at a relatively early stage of investigation, but some details concerning these new ideas will be presented, and the possibilities of achieving larger drag reductions by refining present techniques or by using these in combination with other control methods will also be discussed.

The actual presentation of the review lectures will be organized around four main topics. First, after briefly reviewing what is known about the structure of the turbulent boundary layer, possible mechanisms for both active and passive devices will be discussed ; concentrating on techniques offering nett drag benefits, either through inner or outer layer manipulation. Then experimental and numerical results will be presented for both LEBs and riblets. Available data and computer model predictions for low and high subsonic speeds, transonic conditions, and supersonic flow (in-

cluding flight tests) will be reviewed. Although the emphasis will be on turbulent external flow findings, laminar, transitional and fully developed internal flow results will also be discussed together with those obtained when applying similar control techniques to wall-jets. Since, a number of other review publications have already appeared on a similar subject, the aim will be to outline the most important results obtained in terms of drag reduction, and to emphasize most recent developments. Finally the combination of passive devices, such as riblets and/or LEBUs with polymers, suction, blowing, microbubbles, or acoustic forcing - all of which are known to be additive or more than additive - will be discussed ; together with studies of alternative drag reducing surfaces, such as "sparse" (or "Tani") d-type and certain random "sphere" roughnesses, which have also been shown to produce nett drag reductions at certain Reynolds numbers (and combine at least additively with riblets and LEBUs). Some comments will also be made regarding likely future developments.

It should of course be recognized that in addition to the drag reduction techniques surveyed here, several others have been proposed and in some cases investigated and possibly rejected. The interested reader is invited to refer also to other review articles written by Bushnell [10], Bandyopadhyay [11], Wilkinson et al [12], Bushnell and McGinley [13], Gad-el-Hak [9], and more recently by Savill [14], Walsh [15], and Anders [16]. Most of these earlier review papers covered research first initiated at NASA Langley, and then conducted both in the United States and in Europe. In fact, turbulent drag reduction research has now developed into a worldwide turbulence-control effort encompassing Australia, Canada, China, Hong Kong, India, Japan and Singapore. The most recent European work in this field is well represented by the conference reports of References [17]- [25].

2 Some Ideas and Mechanisms For Turbulent Drag Reduction

The various hypotheses which have been advanced to explain how turbulence manipulators act on friction drag depend upon considerations of the turbulent boundary layer. Both this and the turbulence production cycle could be favourably altered, stabilised or reduced in intensity, by the presence of either outer or inner layer manipulators within the flow.

As reported by Westphal, [26], the possibility of controlling turbulence has excited researchers, at least since the observation made by Liepmann that : "Probably, the most important aspect of the existence of deterministic structures in turbulent flows is the possibility of turbulence control by direct interference with these large structures. Such control could lead to very significant technological advances". Control in this case means interfering with one or more of the eddy structures in order to achieve a desired purpose, [27].

Blackwelder gives some ideas about the philosophy of control and the availability of "selective" control, in the sense that the control device is designed specifically to operate selectively on one or more aspects of the bursting phenomenon, [27].

Before trying to manipulate the turbulent boundary layer, it may be useful to briefly recall the main features related to the structure of the latter. A detailed description of turbulent boundary layer structure can be found, for instance, here in the lecture given by Blackwelder, [28]. The aim is not to detail the kinematics and/or dynamics of the turbulent structure - as has been recently performed by Robinson, [29] or [30] - but to elucidate some particular points which could help in the understanding of how polymers, grooved surfaces, outer layer manipulators, and other devices, might act upon the turbulence. Hence, the following paragraph provides simply a quick description of the turbulence boundary layer structure, which is prerequisite in order to begin any discussion of the drag reduction mechanisms. Indeed, alteration and/or control of turbulence by mechanical, physical or chemical means can be regarded as a subset of the field of turbulent boundary layer structure research.

It should also be appreciated that a better understanding of the mechanisms of drag reduction may perhaps lead not only to the development of more effective drag reducing devices, but also to improved aware news of the structural, spectral and energetic behaviour of the non-manipulated or "natural" boundary layer. Hence, into any experimental investigation of drag-reducing devices, measurements made within the turbulent flow included comparisons without any device. These complement the tremendous amount of data, already available, and, tend to confirm or weaken various proposals, as regards the link between various identified structures.

2.1 Structure of Turbulent Boundary Layer

Turbulent flow is the center of phenomena of production, transport and dissipation of turbulent kinetic energy. Its structure is strongly related to the local equilibrium between these three phenomena which operate to the prejudice of the mean flow and give birth to viscous drag forces. Kinetic energy from the mean flow is converted into turbulent fluctuations and then dissipated into internal energy by viscous action ; this process appears to be part of a continual regeneration cycle.

It is well known that a specific set of features in the turbulent boundary layer are identified with the production of turbulence, which results from dynamically significant motions found in two very distinct regions : the inner region and the outer one.

- the inner region may be subdivided into a viscous sublayer, a buffer layer and a logarithmic layer, in the very near vicinity of the wall ($y/\delta < 0.1$). That region is characterised through viscous shear stresses as large as turbulent ones. In

the innermost region, the correct scaling parameter is the viscous length scale ν_w/U_τ , where ν_w denotes the kinematic viscosity at the wall and U_τ the friction velocity.

$$U_\tau = \sqrt{\frac{\tau_w}{\rho_w}} \quad (1)$$

τ_w is the wall shear stress and ρ_w is the density taken at the wall. The mean velocity obeys to the law of the wall :

$$U^+ = \frac{U}{U_\tau} = f(y^+) = f(y \frac{U_\tau}{\nu_w}) \quad (2)$$

This law of the wall tends to a logarithmic behaviour when $y^+ > 50$, the outer edge of the buffer layer.

- Beyond this, the outer region corresponds to the area with the classic defect velocity form used for representing the mean velocity profile :

$$\frac{U_e - U}{U_\tau} = g\left(\frac{y}{\delta}\right) \quad (3)$$

where U_e represents the mean velocity at the outer edge of the boundary layer. This outer region extends over a greater distance from the wall ; in that region, the flow is fully turbulent. Although the viscous strain is negligible, viscosity plays an important role because of the dissipation process. In the outer region, the scaling parameter is the physical boundary layer thickness, δ .

- Between the inner and outer regions, there exists an intermediate layer which belongs to both regions. This is the overlap region, where both law of the wall and velocity defect forms are valid. This corresponds to the logarithmic law, which could read for incompressible flows :

$$U^+ = \frac{U}{U_\tau} = A \ln y^+ + B \quad (4)$$

The spreading of the logarithmic region depends upon few parameters. The lower limit corresponds usually to $y^+ = 50$; however, the upper limit increases with Reynolds number but decreases with positive pressure gradients. According to the 1968's Stanford Conference on turbulent boundary layers, the generally accepted values for A and B are :

$$A = 2.45 ; B = 5.00 \quad (5)$$

Generally speaking, at high enough Reynolds numbers, the turbulent flow is such that the production and dissipation of the turbulence are large in the inner layer, whereas, in the outer flow, the turbulence is sustained by the excess turbulent energy produced in the inner region and conveyed outward by turbulent motion. By measuring mean and fluctuating quantities, or performing flow visualizations (injection of dye

markers, generation of cathode-wire hydrogen bubble, oil-vapour smoke, etc), it has been possible to detail certain turbulence structures closely associated with the production of turbulent energy. The boundary layer is made up of myriad of such structures, the scale of which varies from one point to another in the boundary layer, but generally increases with distance from the wall.

A great amount of experimental studies, accompanied by flow visualization, have tried to determine the mechanisms which give birth to and/or regenerate turbulence, and are responsible for the energetic transfers between the inner and outer regions. The hydrogen-bubble technique used by the Stanford group, in particular, made it possible to continuously observe the formation of various structures in the flow. More recently, the great power of new super computer "has created a modern renaissance in turbulence knowledge" as mentioned by Robinson, [29]. Most of the experimentally known aspects of wall-layer turbulent structure have been confirmed through such numerical simulations. This "numerical turbulence", the starting point of which is the time-dependent 3D Navier-Stokes equations, deals with either Large Eddy Simulation (LES) - the small scale motions are modelled, for instance, through an eddy viscosity model or a turbulence model - or Direct Numerical Simulation (DNS) - where all the turbulent motions of any scale are computed, classically through a spectral method. One might argue that most of the numerical investigations, in particular, have been carried out at low values of Reynolds number, for which the range of turbulence length scale is limited ; nevertheless, flow visualisations and fine-scale experimental probing are possible. The use of low-speed water channels of large dimensions, and of the Göttingen and Berlin oil channels, made it possible to reach fairly large viscous lengthscales, which in turn made observations in the viscous sublayer possible. However, for higher or "flight" Reynolds numbers, the exact nature of the turbulent boundary layer structure might be subject to uncertainty, but innovative visualisations and qualitative techniques developed by several workers suggest essentially same basic structural form.

Although for almost three decades, a great effort has been expanded in order to try to explain the mechanisms involved in the cycle of wall events, the birth of vortices, the relationship between structures, so far there is still no accepted theory which really details the structural behaviour of turbulent external flows. Emerging results include the identification of the various quasi-coherent structures which make up the boundary layer. However, the picture of the interaction between all of these structures is not really complete as yet. Such boundary layer studies constitute an extensive literature spread over the last twenty years, which we would not attempt to resume since it would be out of the scope of the present paper on turbulent drag reduction. The reader could additionally refer to the two lectures given by Blackwelder, [28] and Kim, [31], and to recent papers, chronologically written by Kline, [32], Robinson et al, [33], Falco et

al, [34], Lyons et al, [35], Kline and Robinson, [36], Robinson, [37], Smith et al, [38], Falco, [39], Robinson, [29] & [30].

As will be seen, a large number of studies have been reported on this subject : dealing with coherent motions, inner-region production cycle, bursting process, appropriate scalings in outer and inner regions, and so forth. From time to time, some authors try to impose their own conceptual model - a definition of which could be "the idealized description of the physical processes underlying the observed behaviour of the turbulent boundary layer". A large number of such conceptual models have been proposed. They are best summarized in the review of Robinson, [30], and by the descriptions provided by the various model originators themselves in the Proceedings of the 1991 NASA Langley Conference on Turbulent Boundary Layer Structure, which he organized, [40]. Alternatively, others try to explain energetic transport of momentum through different simpler mechanisms.

Following an International Collaborative Re-assessment of Boundary Layer Structure, the following classification of quasi-coherent structures was proposed by Kline, [32], in agreement with Robinson et al's analysis of numerical simulations for a turbulent boundary layer, [33]. This "taxonomy" of structures, devised by the Stanford group, considers the following eight features of the turbulent boundary layer which most researchers seem to accept exist :

- 1) Low-speed streaks in the region $0 < y^+ < 10$;
- 2) Ejections of low-speed fluid outward from the wall ;
- 3) Sweeps of high-speed fluid towards the wall ;
- 4) Near-wall vortical structures of several proposed forms ;
- 5) Strong internal shear layers in the wall zone ($y^+ < 80$) ;
- 6) Near wall pockets ;
- 7) Large (δ -scale) discontinuities in streamwise velocity ;
- 8) Large scale motions in the outer layers.

More recently, Kline & Robinson have been trying to classify those structures with respect to creation of Turbulent Reynolds Stress, and creation and dissipation of Turbulent Kinetic Energy. Thus, the aforementioned authors separated the structural features into three groups : the most energetic and apparently the most active (feature 4), those which play an important role (features 2, 3 and 5) and those which play some lesser role (other features). As we shall see, only features 4 & 8 are actually related to causal studies - all of the remaining features are effects of the action of various scale vortical motions. However, accepting this view of structural events, one must then think about various hypothesis relating coherent motions in the wall region to motions in the outer region. Numerous experiments have shown that there

is no preponderance of inner or outer region against the other one, [41]. Instead, it would appear that any perturbations introduced in the outer region (or inner region) using outer layer manipulators (or inner layer manipulators or roughness elements) will have influence upon the inner region (or outer region) respectively. However, this is not to say both regions are of equal importance in the structural regeneration cycle.

The principal problem with wall bounded turbulence, as opposed to free flow, is the determination of how turbulence is generated and sustained. The focus of experimental as well as computational work has been to relate turbulence structure to turbulence production. Both measurements and numerical simulation have shown that both the production and dissipation of turbulence energy are quite large and of the same order in the viscous wall region.

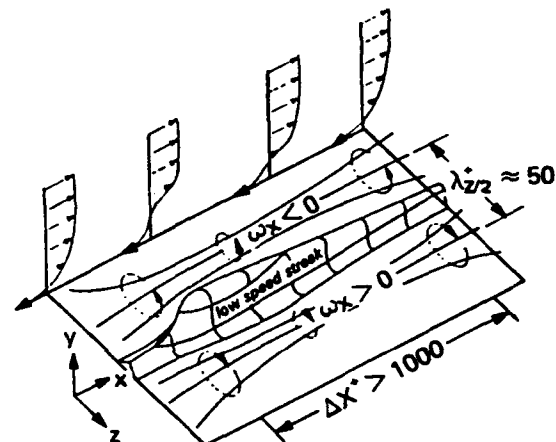


Figure 1: Alternative low and high-speed bands in the near-wall region, from Blackwelder [42].

In that region, within the inner and buffer layer, the flow is always very active and turbulent ; moreover, it is well organised in a streaky structure formed from alternative narrow streaks of high- and low-speed fluid. The low-speed streaks (feature 1) have an average spanwise dimension of about $40-50 \nu/u_r$; they are elongated in the streamwise flow direction and extend up to about a thousand viscous lengths. Very near the wall, around $y^+ \approx 15$, the average spacing of these streaks is 100 wall units, i.e. about twenty times the thickness of the viscous sublayer. Both streamwise and spanwise length scales have been measured by several authors over the range of momentum thickness Reynolds number, $600 < R_\theta < 5000$. However, the mechanism of long-streak formation is not fully understood. A schematic picture of such well-organised movements in the near-wall region is illustrated by Figure 1, taken from [42]. Kline et al, [43], were the first to identify these low-speed streaks in 1967 ; using hydrogen bubbles which grouped together in strips - the low-speed "streaks" - moving less quickly than in the surrounding fluid.

Interaction of these low- and high-speed bands and the effect of large velocity fluctuations imposed, create counter-rotating vortices that wrap their "legs" around the low-speed streak, thus trapping part of the fluid. Visualizations have shown that such streaks gradually rise away from the wall, then oscillate violently, before breaking down. This is the starting point of the turbulent kinetic energy production cycle, referred to as "bursting process" by Kim et al, [44]. This term is commonly used throughout the literature, but it should be noted that this is one of the most controversial issue of the turbulence structure field ; indeed, the bursting process has had several meanings ever since the earlier work performed by Runstadler, Kline and Reynolds in 1963, [45].

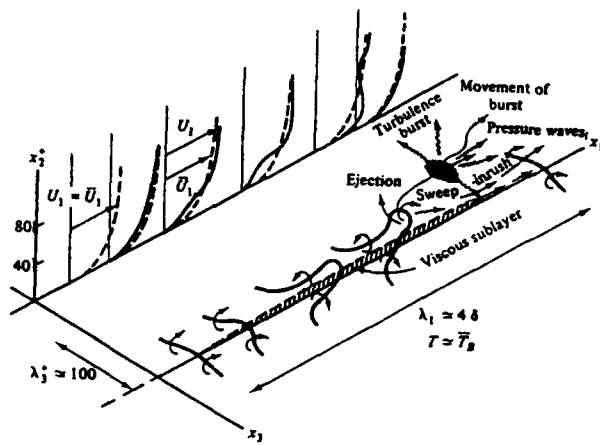


Figure 2: Model of the turbulence near the wall during a cyclic process, from Hinze [49].

The bursting cycle must in fact be considered as a near-wall turbulence production cycle, the main characteristics of which are the intermittency and the quasi-cyclic sequence. Mainly, ejections of low-speed fluid outward from the wall (feature 2) and sweeps of high-speed fluid towards the wall (feature 3) are at the heart of such a process. It should be noted that ejections and sweeps refer to events in respectively the second quadrant ($-u', +v'$) and the fourth quadrant ($+u', -v'$) within the u', v' plane, where u' and v' are respectively the turbulence fluctuations about the mean velocity components in the streamwise direction and the direction normal to the wall. Pratuli and Brodkey, [46], as well as other workers have estimated that almost 70% of the total production of turbulence in a boundary layer occurs during this bursting process. Furthermore, from DNS of a turbulent channel flow, Kim et al, [47] have shown up that, at the maximum of turbulence kinetic energy production, i.e $y^+ \simeq 10-15$, ejections and sweeps together account for about 120% of $-u'v'$; the other quadrants (first and third) account for -20%. At $y^+ \simeq 50$, where the ejections events are dominating, about 80% of the total shear stress is due to ejections, which is in agreement with experiments performed by Alfredsson and Johansson, [48]. A picture of all the wall events appearing during a

cyclic process can be gathered from the conceptual model, suggested by Hinze in 1975, [49], even before the "taxonomy of structures" given by Kline, [32]. This is shown on figure 2 and rather clearly illustrates how sweeps and ejections and streaks are related kinematically (if not yet dynamically) to idealised symmetrical vortex loop structures.

Very often, the formation of low-speed streaks as well as regions of high speed fluid (sweep) has been attributed to the action of vortical structures of various forms (feature 4). It is well known that different embedded vortices, with a variety of strengths, have been clearly identified in the boundary layer. Several forms have been suggested : streamwise vortices, horseshoes, hairpins, tornado-loop like vortices, etc. Some of these geometries have been deduced from flow visualisations, turbulence and/or correlations measurements, statistical studies and, at last, numerical studies. Apparently, according to some authors, vortical structures of a wide variety of shapes exist but, "the evidence for the prevalence of particular forms is not yet conclusive", [29]. It should be pointed out that direct numerical simulations, although performed at low values of the Reynolds number, allow to identify most of these vortical structures, and a major contribution of DNS has been to show that they are predominantly assymmetrical.

Visualisations techniques based upon markers revealed the existence of pockets (feature 6), in the neighbourhood of the wall. Repeated experiments have always verified these events and they are widely believed to be the sublayer "foot prints" of larger outer vortical structures ; however, their exact origin and their interpretation remain unclear.

The portions of fluid ejected away from the wall give rise to considerable mixing in the boundary layer and cause strong turbulence fluctuations. Although the paths followed by the intermittent ejections in the outer part of the boundary layer have not as yet been fully identified, it is thought that the large-scale motions (feature 8) are associated with these.

In fact, in the outer region of the turbulent boundary layer, there appear to be two important scales of motions, each of them having its own contribution to the turbulence production, although that latter is minimum in that region. The first are the large-scale motions (feature 8) and the second are much more compact regions of vorticity concentration which form on the upstream side of the large-scale structures ; a region marked by a sharp spatial discontinuity in the streamwise velocity (feature 7). These smaller motions are called "Typical Eddies" or "Falco Eddies", [50]. The length scale of the large scale motion is of the order of the boundary layer width. On average, their "back side" is inclined at a preferential angle (12° to 30°) to the direction of the flow. In fact, Head and Bandyopadhyay, [51], have shown that the outer region of the boundary layer and hence the large scale motions are made up almost entirely of smaller scales vortices, ideally in the form of symmetrical hairpins but in reality mainly assymetric and highly convoluted. Indeed, as the upper part of these

structures has a rather large transverse vortex intensity, and as the hairpin vortices stretch out during the production cycle, it may be that only their tops exist and are active in the outer region; then, their transverse section may correspond to the "typical eddies". These structures also scale with outer variables in the spanwise direction. According to Falco, [39], the typical eddies scales ranges from $O(\delta)$ at low Reynolds numbers to small fractions of δ , as the Reynolds number increases. Thus, at low values of the Reynolds numbers, the large-scale motions appear to be significantly influenced by the large discontinuities in the streamwise velocity.

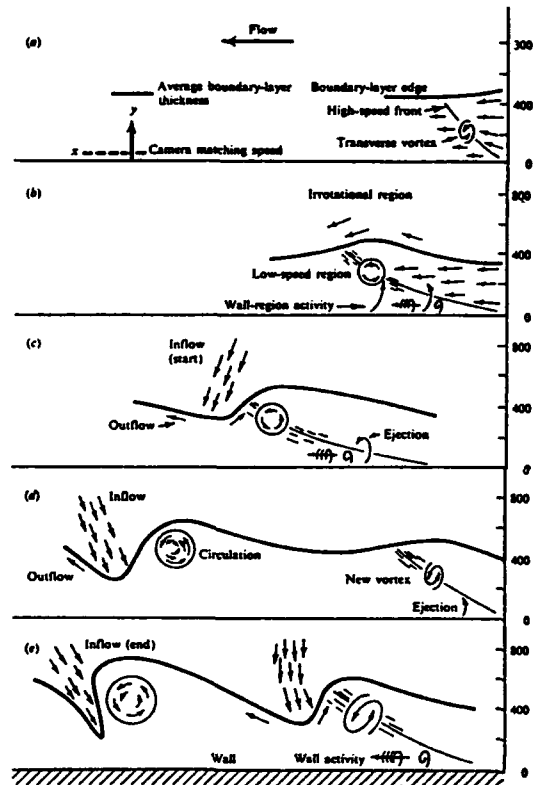


Figure 3: Interactions of outer-flow motions with the wall region, as seen from a downstream-conveying frame of reference, from Pratuli et al [46].

These events happening along the upstream side of the large-scale motions also contain high shear areas; but, these should not be compared with the near-wall shear layers (feature 5) which exist generally in the buffer layer and which, on the other hand, scaled with the inner wall variables (ν and u_r). Through both visualisations and probe surveys, such intense shear-layers have been identified in turbulent channels as well as boundary layer flows. From measurements and dye-flow visualisations, Bogard and Tiederman, [52], confirmed these near-wall shear layers with a high streamwise velocity gradient. They result from the impingement of the high-speed fluid on the back of the low-speed element, due to near-wall vortex inter-

actions. More recently, using direct numerical simulation of turbulent channel flow, Johansson et al, [53] have shown that shear-layer structures are the most persistent features of the near-wall region. Indeed, they also found that the development of asymmetry in the spanwise direction seemed to be a major element in the evolution of near-wall vortical structures and also in showing the clear cause-effect relationship between these shear shear-layer structures.

The large-scale eddies in the outer region of the turbulent boundary layer govern the entrainment of irrotational fluid into the layer. In the boundary layer, this is predominantly "quiescent" by small scale mixing due to typical eddies/hairpin tops along the face of the large collective motions rather than by "active" large scale engulfment at their fronts, as in the turbulent wake (e.g. see Townsend, [51]). The interface between that latter and the irrotational flow is rather irregular, justifying the intermittent character of the outer boundary. Thus, these penetrations complete all the processes occurring as a turbulent boundary layer develops.

Only at low values of the Reynolds number, where there is a very small range of scales present, is the picture as simple as that suggested by Pratuli and Brodkey, [46], to relate wall events with entrainment of large structures in the outer region (cf figure 3). It should be kept in mind that the relationship between the inner region of intense turbulence production and the outer region of weak turbulence production is not firmly established. As discussed by Robinson, [29], or Blackwelder, [27], the correct scaling parameters for the near-wall length scales and/or bursting frequency has been one of the most controversial topics. Thus, while some authors scaled the bursting frequency with the outer variables, mainly the boundary layer thickness, others suggest correlations with wall variables since most of the reduction is generated in the inner region. The generally accepted position now is that some form of mixed scaling, varying throughout the boundary layer, is allowed.

In order to conclude this discussion, different models of the turbulence structure could be constructed in a way that they represent all the structures evidenced throughout the literature. However, ideas on the structure of a turbulent boundary layer are always in a state of evolution and there is as yet no general consensus on several points. For the inner, buffer, logarithmic or wake regions, specific set of features have been revealed and clearly there must exist a cyclic sequence related to the production of turbulence which tightly links the inner and outer regions of the turbulent boundary layer. However, one of the main conclusion from the analysis must be that one has to respect not only the existing duality of scales that exist between these two regions, recognizing that the scaling laws overlap in the logarithmic region, but also the plurality of structures, their causes and effects. Furthermore, spectral analysis is one of the most useful tool that allows to identify the range of different scales involved in energetic transfers, but a group of scales is not enough to characterize the whole spectrum. The

spectral behaviour has to be analysed throughout two separate regions which include :

- large wave numbers and small structures of length scale $(\nu^3/\epsilon)^{1/4}$ and velocity scale $(\nu\epsilon)^{1/4}$, where ϵ denotes the dissipation rate ;
- small wave numbers or large structures of length scale, (δ) , and velocity scale (the mean local velocity).

2.2 Some Ideas for Turbulence Control Methods

As we have just seen, a lot of experimental as well as computational work - which most of the time complement each other - has been performed to aid understanding of production of turbulence, near-wall events, large scale motions, ... and so forth, at low values of the Reynolds number and for uniform flows. Future investigation will be required at higher Reynolds numbers, and in more complex situations including not only effects of surface roughness, surface curvature or pressure gradients but also manipulation of turbulent boundary layers. The involved mechanisms of these cases are not always firmly understood. So, the aim of the present paragraph is to enumerate the principal ideas which have been developed in order to understand such viscous drag reducing techniques. In chapters 3 and 4, more detailed and up to date analysis will be presented particularly for inner and outer layer manipulations.

Furthermore, so as for the studies involved with production of turbulence, a great deal of work, as regards turbulent drag reduction has been performed in flat plate boundary layer cases, at zero pressure gradient. In that case, minimizing turbulent drag means reduction of turbulent skin friction using either active or passive techniques, as it will be discussed below. However, for flows around bodies, with eventually adverse pressure gradient areas, minimum skin friction does not necessarily imply minimum drag. Indeed, in adverse pressure gradient regions, Van den Berg, [55], showed that to minimize the drag, the momentum thickness growth must be minimized at each position along the body and in the wake. Then, minimizing $d\theta/dx$ leads to a dual objective : a low skin friction as well as a small shape factor should be pursued, and this point will be borne in mind in the subsequent discussions.

There exist several approaches for skin friction drag reduction. Indeed, the total wall friction drag force reads :

$$F = \int C_f \cdot q_\infty \cdot dA \quad (6)$$

where q_∞ refers to the free-stream dynamic pressure and dA the portion of wetted area on which applied the local shear stress. Considering a transport aircraft, at a given flight altitude and flight velocity (i.e. given q_∞), reduction in drag forces is obviously achieved through :

- decrease of the local skin-friction ;
- alteration of the area distribution so that the skin-friction is lower over a larger portion of the

area ;

- reduction of the absolute magnitude of the area.

Considering the last two points, Hefner and Bushnell, [56], have given an example of an application dealing with the case of a horizontal empennage. Increasing sweep angle with a smaller chord wing, for the same lift coefficient, would reduce both wetted area and skin friction since more of the area is at higher local Reynolds number. It should be noted that in the following parts of this review paper, the first point listed above will be greatly detailed. Indeed, the rule we considered has been :

For a given wall surface, what are the various methods used for reducing locally the turbulent C_f ?

In some cases, although we could deal with tremendous increases of wetted areas (cases of grooved surfaces, for instance), decreases of local skin friction would balance that increase in such a way that the friction drag force would be less.

As shown in paragraph 2.1, turbulence which could *a priori* appear as a random phenomenon, is made up of structures and suggested mechanisms ; some of them are rather well known, others not. Even if the link between those mechanisms is not firmly understood, it should appear that production of turbulence results from a cyclic process. Then, the goal sought after is to disrupt this cycle and, thereby, modify the energetic transfers between the inner and outer boundary layer regions whether reduction in viscous drag, heat transfer mixing or self-noise is looked for.

Blackwelder, [27], suggested some philosophy of control for turbulent boundary layers, by applying selectively external conditions (suction, surface modifications, ...), i.e. "locally with respect to the eddy structure that one is attempting to control". At first sight, such a selective control might be reached through :

- inserting rectangular or aerofoil section devices in the outer region of the turbulent boundary layer, which selectively operate directly on the large eddies and, only indirectly, alter the wall shear stress ;
- applying surface modification in the vicinity of the low-speed streaks, with dimensions of the order of viscous lengths, in order to alter those streaks ;
- adding another external structure, which interacts with, destroys or replaces the existing eddies under favourable circumstances (cf "eddy substitution" as named by Wilkinson et al, [12] ;
- adding some amounts of polymer near the wall in order to increase the length scale in the wall region and to inhibit the turbulent mixing ;
- ...etc

From all the world-wide studies, it looks like turbulent skin friction drag could be reduced through either addition of several foreign substances such as long-chain molecules, microbubbles in liquid flows and fibers in gas flows or surface modifications such as outer and/or inner manipulators, compliant surfaces, wavy walls and other surface modifications. Different classifications of these techniques have been given by several authors, depending upon the chosen criterion, i.e mainly skin friction reduction or net friction drag reduction. These two comments are obviously linked, but the relationships are not always reversible. Moreover, some methods which reduce skin friction but not overall drag, could also act favourably upon noise disturbance environment, heat transfer control, and others.

In 1977, in the Lecture Series *Special Course on Concepts for Drag Reduction*, [6], Hefner and Bushnell enumerate the viscous drag reduction methods as follows, [56], :

- alteration of turbulence structure : additives, reduction of near-wall momentum, moving walls, convex curvature ;
- reduction/alteration in wetted area for drag minimization ;
- alternative approaches : corrugated surfaces, ...

A few years later, in 1985, in a previous VKI Lecture Series on *Aircraft Drag Prediction and Reduction*, Thomas, [4], referred only to a few efforts in the turbulent skin friction reduction field, through : riblets, large eddy breakup devices or manipulators (LEBU), other surface geometry effects and synthetic boundary layer. However, in the same lecture Series, Bushnell provided the reader with the most complete catalogue ever seen, as regards turbulent drag reduction for external flows, [10], including :

- approaches based upon reducing the near wall longitudinal momentum : adverse pressure gradient, wall mass transfer, ion wind, boundary layer thickeners ;
- approaches based upon altering conditions within the boundary layer : large eddy breakup devices, local suction within the boundary layer, modification of Emmons spot formation, large eddy substitution ;
- approaches based upon alteration of the wall boundary condition : riblets, bubbles, compliant walls, relaminarization using massive wall suction, non-interactive wall motion, micro air bearings ;
- approaches based upon use of a stabilizing body force : longitudinal convex curvature, fibers and other particles, wall cooling ;
- approaches which evidently may not provide net drag reduction : passive porous

walls, oscillatory longitudinal curvature and pressure gradients (wavy walls), wall turbulence "Sieves" and "Furry" surfaces.

A year later still, Bandyopadhyay wrote a review paper on "Mean flow in turbulent boundary layers disturbed to alter skin friction". The author gave a brief description of drag reduction techniques and mechanisms for some of them, [11]. The techniques considered were : polymer addition, compliant wall, coatings, microbubbles, spot forcing, bursting, riblets, outer layer devices and, at last, convex curvature.

Looking back to this literature, it should be noticeable that, during that decade (1977-1986), some techniques disappeared for various reason while others had undergone extensive development. Thus, Wilkinson et al, [12], considered another type of classification, based upon their personal research activity at NASA/Langley, i.e :

- approaches which work : riblets, Langley thin-element study, riblet flight tests, other riblet applications, LEBUs ;
- approaches which may work : two-stage control, compound and three-dimensional riblets, standby separation control for Stratford closure, eddy substitution, relaxation from wall curvature effects ;
- approaches which do not work : wall waviness, injection, direct wall region momentum reduction, turbulence control.

Again, the interested reader could find from a resume of the review papers cited above, a useful list of what has been tried, concerning the reduction of skin friction in turbulent boundary layers. The aim of the present paper is not, of course, to recall each of these methods (which would simply duplicate the work that had been performed by the mentioned research scientists), but, above, to try to present the most recent and/or significant results obtained during the last few years, for specific techniques. The reader must not forget that the present article deals more specifically with passive drag reduction techniques, focusing upon outer and inner layer manipulators (cf sections 3 and 4).

Moreover, most of the methods listed below have already been described from an experimental point of view and some of the active as well as passive manipulation methods have also been studied, through either boundary layer computations using turbulence models (usually low-Reynolds number models) or numerical simulations. Regarding the latter, although some details will be given later on, one might mention here :

- active turbulence control in wall bounded flows using Direct Numerical Simulation (DNS) ; suction or injection are applied on the channel walls exactly at the opposite to the wall-normal velocity at a given distance from the wall (e.g. see Kim et al, [57]) ;

- passive turbulence control through infinitely thin outer layer manipulators in a fully developed channel flow, using Large Eddy Simulation (LES) (e.g. see Friedrich et al, [58] or Klein et al, [59]).

The advantage of such simulations is of course that they allow such study of idealized control devices.

2.3 Some Fruitful Methods as regards Net Turbulent Drag Reductions

Although the emphasis is upon aircraft applications, this review chapter will include several approaches currently available for turbulent skin friction drag reduction. In general, some of these approaches are applicable only to hydrodynamic flows, or require additives or equipment which are obviously out of the question for aircraft. Nevertheless, some of these will be discussed since they could be used successfully in combination with other drag reducing methods.

Thus, there exists several ways to control (in the sense suggested by Blackwelder, [27]) the turbulent boundary layer : destroying one or more type of coherent structures, introducing new ones or trying to re-organize the existing energetic structures. Modifying the transfers between the inner and outer regions, i.e altering the production cycle, will be essentially looked for. However, nobody might, *a priori*, foresee how this cycle of production of turbulence will be modified. Thus, the approach should be more empirical and more exploratory than perhaps for reducing other components of the drag balance. Some techniques involved an external addition of energy or mass and, could be more specific to liquid flows. On the other hand, passive devices could work in either liquid or gaseous boundary layers and provide improvements of a few percents, whereas the injectants (polymers, surfactants, bubbles, ...) for the most part, apply only to liquid flows but offer considerably larger overall reductions in skin friction.

2.3.1 Active Methods for Liquid Boundary Layers

Turbulent skin friction drag can be reduced by the addition of several foreign substances. By looking to literature, it should be noted that three types of additives have been generally used in order to reduce the level of turbulent skin friction drag : polymers, bubbles and particles. Some of this research could be of considerable interest for the turbulent drag reduction of surfaces such as ship hulls. There seems to be no counter-part in aerodynamics, except maybe for particle addition, if one considers the flow of dusty air.

As mentioned in the introduction, there has been quite a lot of excellent review papers on this Turbulent Drag Reduction Field. Nevertheless, the aim of the present paper is to provide the reader with a fresh point of view to the topic, by emphasising, most of the time, the most recent available literature.

2.3.1.1 Polymers and Surfactant Additives

The discovery of the drag reduction phenomenon in turbulent pipe flow, by addition of a small quantity of polymer to a solvent like water, was first published by B.A. Toms in 1949. He discovered that in the turbulent regime and at constant pressure, the rate of flow through a pipe increased with an increase in polymer concentration. Indeed, the results indicated a lowering of the wall shear stress. After this discovery, this effect was discussed in more than one thousand publications as mentioned, for instance by Bandyopadhyay, [11], or Durst et al, [60]. Indeed, the fact that very small quantities of polymer are needed to produce large changes in the flow has generated great interest in these phenomena. Thus, spectacular levels of drag reduction up to 80% could be achieved in pipe flows if a few parts per million (p.p.m.) of soluble polymers were added to the solvents. Nevertheless, additives must be introduced in the wall region in order to reduce the wall shear stress.

Rather recent summaries of this drag-reducing effect could be found in Lumley and Kubo, [61], Hoyt, [62] or Pollert and Sellin, [63].

It has been found that very small concentrations, of the order of a few parts per million by weight, of dissolved high-polymer substance can reduce the frictional resistance in turbulent flows. For instance, concentrations of about 10 to 100 p.p.m. would provide us with maximum effectiveness. The amount of the additive required is so small that there is negligible effect on the density of the baseline fluid. In contrast, when dealing with Particle Addition Field, the amounts required are sufficient "to change the gross density of the mixture so that one speaks of a mixture transport rather than of a solvent transport" as written by Kane, [64].

There are different types of drag reductions additives, resulting from different ways of applications :

- dissolving the polymer in the fluid before the experiment leads to an "homogeneous drag reduction" ;
- injecting relatively high concentrations of polymer solutions into turbulent pipe flows provides with "heterogeneous drag reduction". Injections could be performed through small tubes ; the injected polymer threads are broken into much finer strings by the turbulent flow, but the strings do not dissolve in the solvent phase. The turbulent mixing process as well as the interaction of the polymer solution with the flow, downstream of the injection point, determines the drag reduction effectiveness. Another aspect consists in injecting threads into premixed homogeneous polymer solutions. Injected solutions do not mix very quickly with the mean flow, which means that heterogeneous flow conditions are maintained over a considerably long distance, from the injection station ;
- or, at last, simply considering surfactant solutions. Surfactant is an abbreviation of "surface-active agent". Although the first publication as

regards drag reduction by surfactant solutions was made in 1949 by K.J. Mysels, this type of additives received less attention than polymers, but also impart drag reductions. A very recent review, the title of which is "Drag Reduction in Surfactant Solutions", was made by Bewersdorff, [65].

The mechanisms involved with surfactant solutions is similar to that occurring in both polymer-type solutions, [62]. For practical applications, the advantage of using surfactants instead of polymers is that no degradation occurs over long-time periods. Surfactant molecules consist of a hydrophobic and hydrophilic part; although, these substances have a low-molecular weight, they seem to form long-chain agglomerates or micelles and to assemble to aggregates. Generally speaking, in the concentration range for drag reduction, they are characterized by the presence of rod-like micelles, the length of which is about 25-200nm, whereas the diameter is about 2-5nm, [65].

For heterogeneous drag-reducing solutions, Fruman and Tullin, [66], showed that the best drag reduction results were achieved when the polymer solutions were injected through slots with small angles with respect to the main flow direction, and with slot widths of the order of the thickness of the viscous sublayer. Few researchers pointed out, however, that drag reduction, for such solutions, was a weak function of the injection slot geometry, while being a strong function of polymer flow rate and concentration.

Extensive data and measurements, with all sorts of instrumentation (hot-wire or hot-film anemometers, laser doppler anemometry LDA and flow visualisations) have been made of mean and fluctuating quantities in flows with drag reducing polymer-type solutions since the mid-sixties. The accuracy of some measurements has been questioned when those were performed through Pitot tube, hotwire or hot-film anemometers. Lumley and Kubo, [61], recommend to retain, most of the time, measurements by LDA and flow measurements.

Effect on mean quantities

A lot of experiments have been carried out in pipe flows. Pressure drop measurements provide a direct measure of the wall shear stress, when the flow is fully developed. The fully developed assumption was not strictly applicable when additives were being injected. However, the pressure drop still yielded the best available estimate of viscous drag, [67]. Consequently, the drag reduction in a channel flow will be provided from the difference of pressure drops along a given streamwise length, between the solvent and the polymer solution for a constant flow rate of liquid. Such a definition will be valid whatever polymer solution is concerned: homogeneous, heterogeneous or surfactant solutions.

Measurements of the mean velocity profiles were the first to be made by numerous researchers. It has been observed that, in coordinates normalized with wall variables, any profile has the same behaviour at the wall. Several workers found that the buffer layer

was extended in drag reducing flows, yielding to a thicker wall layer. Moreover, some pointed out that the slope of the logarithmic part was identical as in the non-manipulated case, and spoke about "negative roughness". Indeed, when dealing with surface roughness, it is usual to refer to as a change in the velocity profile which includes a negative ΔB term, which corresponds to the roughness contribution. Thus, working with wall variables, the logarithmic law reads :

$$U^+ = \frac{U}{U_\tau} = A \ln y^+ + B + \Delta B \quad (7)$$

With polymer-type drag reduction, the extra term ΔB is positive; such an effect is similar to a thickening of the viscous sub-layer. This ΔB concept which becomes an important part of the literature, could be looked as a negative roughness as mentioned by Hoyt, [68]; however, this scale-up technique has had only limited success. Indeed, ΔB varies with the Reynolds number, the polymer type, the concentration part, ... Nevertheless, it appeared that not only the intercept of the logarithmic equation changes, but also the slope of the logarithmic region for higher levels of drag reduction, [69]. If equation (7) had been valid, it would have helped for scaling results not only, from one pipe or channel flow to another, but also from internal to external flows. Then, maximum drag reduction asymptote has been defined by Virk, [70], :

$$U^+ = 11.7 \ln y^+ - 17 \quad (8)$$

At the condition of maximum drag reduction, it is

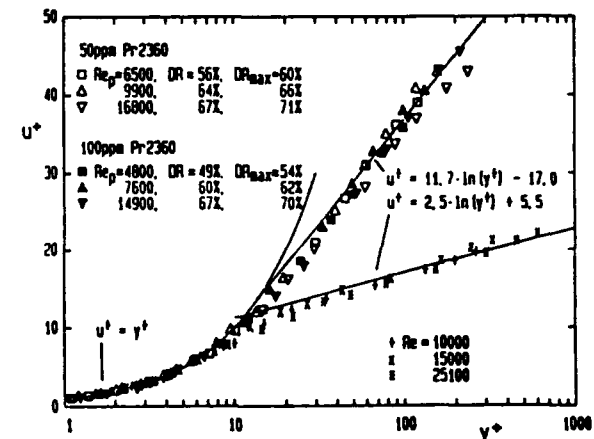


Figure 4: Mean streamwise velocity profile for homogeneous polymer-type drag reduction, from Gampert et al [71].

known both from equation (8) and some measurements that the boundary layer of a polymer flow is not laminar (e.g. see [11]). Then, depending upon the level of drag reduction, experimental points lie between the two lines, given by equations (4) and (8). An example of results is plotted on figure 4, from [71]; two polymers have been solved in deionized water for two concentrations (50 and 100p.m) at different values

of the Reynolds number, $U_m d / \nu$, where U_m is the axial channel velocity, d the channel width and ν the viscosity of the solution.

As regards "heterogeneous polymer drag reduction", results reported, for instance by Usui et al, [72], show a similar trend to that observed for "homogeneous drag-reducing" pipe flow experiments; indeed, when plotting the time averaged velocity distributions in a (u^+, y^+) diagram, one ended up with figure 5, given in Ref. [72].

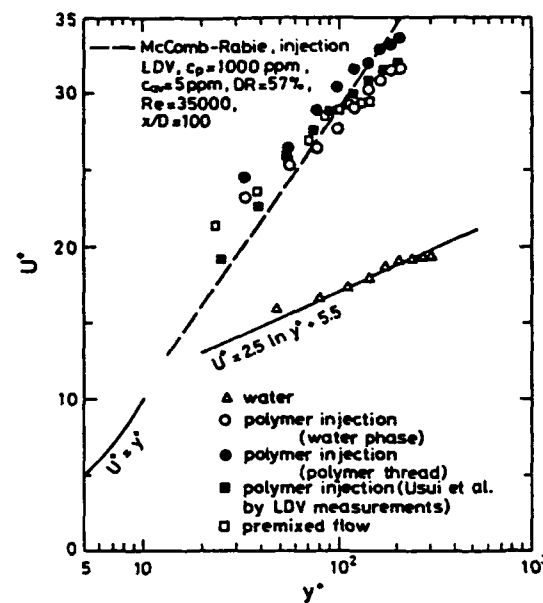


Figure 5: Mean streamwise velocity profile during the centerline injection of polymer solutions, from Usui et al [72].

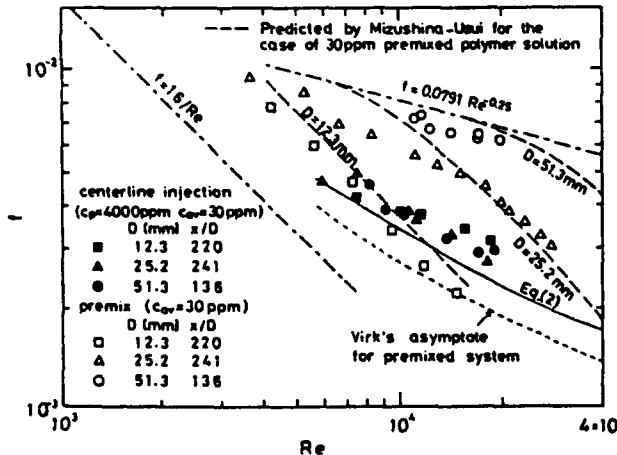


Figure 6: Pipe diameter effect on "heterogeneous polymer drag reduction", from Usui et al [72].

Considering either a pipe or an immersed body, one can relate the friction factor (or the drag coefficient) to some Reynolds number, based on either the inner pipe diameter or the length of the body. Then, results

could be given in a (f, Re) diagram, by the means of the Prandtl-Karman coordinates. Then, the friction factor is defined as $f = 2U_r^2/U_m^2$, where U_m refers to as the flow velocity averaged over the cross-section of the pipe, for instance. Results for different pipe diameters, at different downstream distances to the injection point - to which correspond drag reductions up to 58% - are plotted on figure 6, for given polymer concentration of injected solution (4000 p.p.m) and a bulk averaged polymer concentration (30 p.p.m.). On that figure, the solid line corresponds to the maximum drag reduction asymptote for heterogeneous drag reduction with centerline polymer injection, [72]. This line is given by the following relationship :

$$\frac{1}{\sqrt{f}} = 16.2 \log (Re \cdot \sqrt{f}) - 26.7 \quad (9)$$

It slightly differs from the empirical law of maximum drag reduction for homogeneous drag reduction, deduced from Virk's maximum asymptote (cf. equation (8)) :

$$\frac{1}{\sqrt{f}} = 19.0 \log (Re \cdot \sqrt{f}) - 32.4 \quad (10)$$

Effect on turbulence

Measurements of turbulence intensity (mainly streamwise component rather than transverse one), frequency spectra, correlations, burst frequencies have been carried out by numerous researchers. The mechanisms of drag reduction are usually associated with various mechanisms of rheological nature. In dilute polymer solutions, the large scale structures could be significantly influenced. It should be emphasized that it is clear that the polymer additive does reduce the production of turbulence and that this effect occurs in the near-wall region. There is a dramatic difference between the polymer solution and the Newtonian solvent, because the polymer solution has a higher resistance to axisymmetric strains than it does to rotational strains. Thus, the viscosity of the polymer solution in such strains could be couple of orders of magnitude larger than the viscosity in rotational strains. However, when considering injection of concentrated polymer threads, since "the thread occupies a very small fraction of the fluid volume and all the rest of it is essentially a Newtonian fluid, it seems that the drag reduction is not due to rheological effects", as quoted by Tsinober, [73]. In that case, the experimental results obtained thus far, indicated that the configuration of the polymer threads and the manner of interaction with the turbulent eddies are quite dependent upon the polymer concentration, the injection process and the Reynolds number, which is an agreement with earlier findings of Fruman and Tullin, [68].

For homogeneous drag-reducing solutions, mechanisms are not as simple as one could imagine : many anomalous phenomena have been reported some time ago by Hunston and Zakin, [74], and more recently by Usui, [75]. Some of those have been attributed to what

is called the "elongational viscosity" due to a one-dimensional stretching motion. The interaction between turbulent eddies and polymer additives remains still an open question. There seems to be a qualitative difference between the dilute polymer drag reduction and the heterogeneous one in the fact that the former primarily acts and modifies directly the small scale structures of the flow while the latter mostly the large scale ones. However, the average spacing between low-speed streaks increases linearly with increasing drag reduction ; this correlation is valid for homogeneous as well as inhomogeneous drag reducing flows, [76]. Some experiments showed that the spanwise vortex stretching could be inhibited, which in turns lowers turbulence production and, hence, drag.

Some measurements have shown a thickening of the buffer region as well as an increase in the peak value of the RMS of the streamwise velocity component ; this peak is located further away from the wall. Luchik et al, [76], reported through three beams two-colour Laser Doppler Anemometry measurements that profiles of the mean and root-mean-square velocities as well as the shear product, confirmed that additives mainly modify the buffer region of the flow. Indeed, the major influence occurred through damping of the fluctuation of the normal velocity component. Furthermore, using different burst detection methods, they found that the average time between bursts increased the same amount as the streak spacing.

Concerning surfactant solutions, several authors reported investigations of the physico-chemical properties of those solutions at the beginning of the 1980's. Interactions caused by electrostatical forces between the rod-like micelles are thought to be the source of the visco-elastic behaviour of these surfactant solutions, [77]. The advantage of using surfactants instead of polymers in practical applications is that no degradation occurs over long-time periods.

Modelling

Although some mechanisms have been suggested to explain the observed features, most of them have been highly speculative. Couple of approaches have received interest. The first one, from Lumley, is statistical and does not require a detailed mathematical theory for turbulent boundary layers, [78]. Polymer molecules are expanded in the flow outside the viscous sublayer due to the fluctuating strain rate, and cause an increase in the effective viscosity, which in turn damps small dissipative eddies. According to Lumley and Kubo, [61], the mechanism just described above is consistent with essentially all of the existing experimental evidence which has been evaluated.

Secondly, Landhal's approach is mechanistic, and is based upon the so-called two-scale model, [79], where turbulence consists of a coupled motion at two disparate scales. The velocity field is then subdivided into a large-scale (primary) and small-scale (secondary) fields. The mechanisms of drag reduction due to the additives is that the elongation of added polymer molecules stabilizes the small-scale field, and thereby inhibits turbulence production. Both authors,

Lumley and Landhal, agree that "it is the change in the stress-deformation relation for the solution due to molecular stretching, that is responsible for damping smaller disturbances in the buffer region. A more sophisticated model, the "flat-eddy model" developed by Landhal and Henningson, [80], showed up that "the key effect is the inhibition of vortex stretching associated with spanwise motion". In this model, the development of a flat eddy, initiated because of a local inflectional instability, is looked for in an inviscid flow ; the eddy is flat in the sense that its horizontal dimension is much greater than its vertical one.

More recent interpretations of polymer drag reduction have been investigated by Hanratty et al, [81]. Those are based upon dimensionless analysis and scaling of viscous sublayer. Using the experimental evidence of increase in the streak spacing close to the wall, their conclusions lead to the fact that drag reduction could be associated with an increase of the dimensionless dissipation of turbulence energy, which corresponds to a larger production of turbulent eddies close to the wall.

Gyr and Bewersdorff, [82], showed, through Navier-Stokes equations, that size and vorticity of the streamwise near-wall vortices (feature 4 of the taxonomy of structures, cf §2.1) were changed in flows of drag-reducing polymer solutions. In such flows, the observed deficit could be interpreted as an increase of the local effective viscosity, which is in agreement with earlier findings, such as Lumley's approach.

Applications

Different proposals for the technical application of drag reducing polymeric additives have been published in literature. Industrial applications involve more or less internal flows, with either re-circulation of the flow or flow in very long pipes.

An especially important application is the saving of pumping energy in hydraulic transport system, which would induce considerable economic advantages. However, the first commercial applications of polymers were in crude oil pipelines, i.e. The Trans Alaska Pipeline System (1288, 1km of 1,194m inner diameter pipeline) and the Iraq-Turkey pipeline, [83], [84]. In the Alaska pipeline, the pressure drop resulting from cooling of the crude oil during winter was underestimated, so that the power of the pumping stations was insufficient. This was "cheaply" rectified by polymer additives to reduce the drag, [61]. Nevertheless, as mentioned by Motier and Carrier, [83], "shear degradation presents an interesting dilemma for pipeline Drag Reducing Addition's". Indeed, the polymer must obviously survive along a significant portion of the pipeline in order to provide drag reduction. In all these techniques, referring to as polymer additives, the term degradation indicates a loss of drag reducing effectiveness during utilisation.

Most of the forms of degradation are due to an input of either mechanical energy (due to severe elongational strain and, for instance, due to passing through pumps) or thermal energy (due to heating) into the polymer solutions ; a review of degradation of drag re-

ducing polymers and surfactant additives is given by Pollert and Sellin, [63]. Both laboratory and pipeline experiments have been performed ; the latter under control with laboratory measurements. It appeared that pipe diameter, polymer concentration and wall shear stress intensities are crucial parameters acting on mechanical degradation. According to Durst et al, [60], the degradation is enhanced at higher temperatures ; however, this effect could be avoided with some stabilizing additives. As mentioned above, interest in considering surfactant solutions in practical applications is that no degradation occurs along long-time periods ; indeed, such an interest is maintained because of surfactant potential in re-circulating systems such as central heating schemes. Viscoelastic surfactant formulations could provide with a better response under favourable flow system conditions.

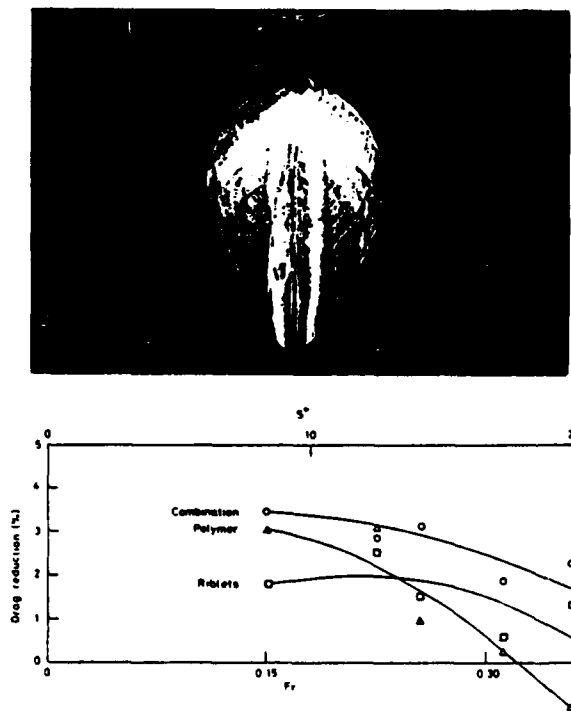


Figure 7: One-third scale model of Australia II hull. Total drag variations for each of the case tested : \square : riblets, \triangle : polymer and \circ : combination, from Choi et al [86].

Most of the work mentioned in this subsection deals essentially with liquid internal flows. Some work has been recently evoked as regards applications of such drag reducing polymer solutions to external flows, [85]. Experiments were performed using injection of polymers into the near-wall region through an inclined narrow slot. The turbulent diffusion of the injected polymer away from the wall as it convects downstream diminishes both the polymer concentration near the wall and the local drag reduction levels. In 1989, experiments were just under investigation ; more detailed information might be available by

now.

A couple of years ago, experiments were carried out at BMT (U.K) on a one-third scale model of the 1983 America's Cup winning yacht, Australia II, [86]. Polymer coating as well as U-type groove riblets had been set upon the yacht hull ; total drag variations were estimated by measuring the hydrodynamic resistance of the model when it was towed through the tank. An example of results is given on figure 7, taken from [86]. For the polymer test, a solution of long-chain polymer had been sprayed onto the hull. The polymer swelled to approximately $5\mu\text{m}$ thick as it absorbed water in tank, and gradually leached out to the surrounding boundary layer during the experiment. When combining polymer solution with riblet film, the polymer solution was also sprayed onto the vinyl riblet film. Experimental results are plotted on figure 7 in a diagram : percentage of total drag variation versus either the Froude number or the dimensionless riblet spacing (s^+). Maximum overall drag reduction of 3.1% had been recorded with polymer coating, at lower values of the Froude number. Therefore, a small increase of drag had been noticeable at the largest Froude number, reached during the runs at highest towing speeds. The authors wrote that "this increase in drag is believed to be attributable to the orange peel type roughness developed on the polymer coated surface", [86]. Furthermore, results indicated that the polymer/riblet combination offered an overall improvement in drag reduction characteristics.

It should be noted that one of the major oil Company made a careful calculation of the economic advantages of ejecting polymers in the boundary layer of a super-tanker in order to reduce the drag. Taking into account a lot of factors, see [61], their conclusions were that the Company would just break even ; they, then, decided not to pursue the matter.

2.3.1.2 Microbubbles

Compared to aforementioned studies (homogeneous and non-homogeneous polymer solutions or surfactant solutions), there has been a very limited research effort on the use of microbubbles to reduce viscous drag in liquid flows. Besides the fact that the level of skin friction reduction could be comparable in magnitude to those recorded for polymer additions, one of the advantages of such an active methods, compared to others, is that it could be considered for external flow applications.

Injection of bubbles is an ancient concept, with patents dating back to the last century. Indeed, the idea was to reduce drag by placing or fixing a thin layer of air between a ship and its turbulent boundary layer. Thus, many possibilities have been considered : among others, the use of a gas film in water has always looked very attractive. Such a concept was at first developed through injection of very small bubbles into the boundary layer ; rather recent studies evoked the possibility of dealing with lubricating film, lying close to the wall, [87]. Historically, the major problem has been the instability of this air film, because not only of the size of the bubbles, but also

of buoyancy since the air/water interface is very unstable, [61]. As a matter of fact, the bubbles must be very small in order to stabilize the gas-liquid interface. On the other hand, very small bubbles could induce roughness effects if the surface coverage is not really uniform, [10] ; so, a compromise has to be looked for.

At first, the microbubble technique involved the injection of bubbles into the boundary layer ; then, further improvements have been made by Soviet researchers through microporous surfaces, with a very high quality in terms of uniformity. It should be noted that, earlier on, another method of producing bubbles had been developed using electrolysis of water (H_2 gas bubble generation) ; nevertheless, such a development would provide, for sure, an increase of the total drag balance, when taking into account the energy for making up the electrolysis, [10].

Although the first experimental success with bubble injection was reported in the United States, by McCormick and Bhattacharya in 1973, [88], most of the research has been conducted later on in Soviet Union and, then, in the United States (mostly at the Pennsylvania State University). So, this active technique has been developed for nearly two decades, but has not been included in most reviews to date. A very recent review paper has been given by Merkle and Deutsch, [87] ; it should be noted that those authors provided the reader with a summary of all the known Soviet work, which could be very interesting since it is often very difficult to get (and to read...) these publications written essentially in Russian. Nevertheless, as mentioned by Merkle and Deutsch, [87], the work performed at the Pennsylvania State University and the Soviet work "complement rather than contradict each other".

Effect on mean quantities

Redundant drag experiments using different techniques for measuring the shear stress at the wall, have been performed by the team from the Pennsylvania State University and the Soviet engineers, and have allowed to demonstrate the trustworthiness of the measurements. Several microbubbles experiments witnessed decreases in drag ranging from about 40% up to almost 90% downstream the region of injection, when compared with non-bubble flows. However, very little is known as regards skin friction relaxation, bubble sizes or trajectories, optimum bubble concentrations, and so forth.

Thus, the first experimental work was reported by McCormick and Bhattacharyya, [88], almost 25 years after the first experiment carried out by Toms with long-chain polymer solutions. These authors introduced hydrogen bubbles into their towed-body boundary layer, using water electrolysis. Drag reductions as high as 30% were recorded ; however, those authors experienced difficulties because of flow separation and boundary layer transition on the body, due to flow disturbance effects.

Few years later on, Soviet researchers forced air through a porous flat plate at the bottom of the turbulent boundary layer, instead of using electrolysis

to generate bubbles. All the recent experiments, up to now, have used that technique. At Pennsylvania State University, most of the experiments reported by Madavan et al, [89] or [87], have been carried out over flat plates, for Reynolds numbers based upon the momentum thickness, $R\theta$ between about 3,400 and 11,000. Maximum skin friction reductions, measured from floating-element force balance, of about 80% were observed for maximum airflow rate close to $5 \cdot 10^{-3} m^3/sec$. Changing the orientation of the plate (plate set on either the top or the bottom of the tunnel test-section) allowed then to point out the influence of gravity. Considering another set of experimental results, Madavan et al, [90], were able to show that substantial drag reductions persisted for as much as 50 boundary layer thicknesses downstream of the injection porous area.

When dealing with microbubble injection, one has to be aware that it is quite difficult to represent results in terms of ratio of local skin friction. Indeed, if the skin friction without bubble is well defined, it is not the case when considering the friction with bubbles, because the density of the gas-liquid mixture varies considerably within the boundary layer. So, authors used very often the same wall density to define both local skin frictions, which means that the ratio of the two corresponds straightly to the ratio of the shear stress forces.

The ratio of the integrated skin friction coefficient in the presence of microbubbles to that without microbubble has been plotted versus the parameter Q/SU_∞ , where Q is the gas flow rate, U_∞ the tunnel speed and S a reference surface, usually chosen as the wetted surface of the porous section. This representation allows to gather all the results onto a single curve, as shown on figure 8, taken from [89].

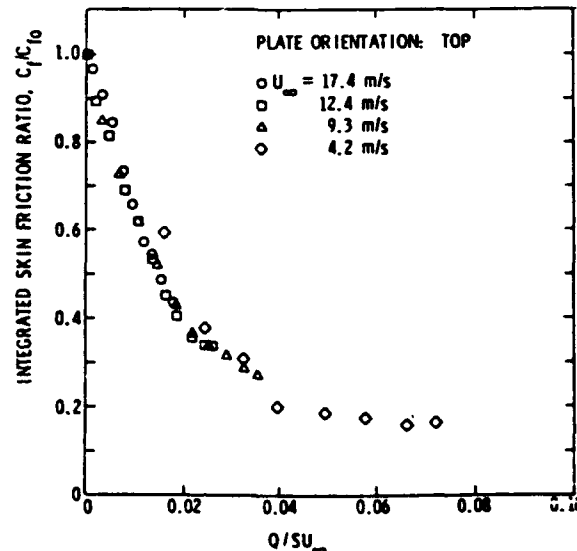


Figure 8: Average skin friction ratio as a function of dimensionless injection rate, from Madavan et al [89].

Skin friction drag measurements have been extended, later on, by Deutsch and Castano, [91], to an axisymmetric body. They found that the amount of drag reduction was a function of the gas type. Indeed, injection of helium or air produced large skin friction drag reductions, measured through force balance displacement, of roughly 80% and 40%, respectively. Experiments were conducted for a somewhat larger Reynolds number range, $R\theta : 2,600-14,200$. Helium seemed to be somewhat more effective in reducing drag than was air, for the highest free-stream velocities. Furthermore, as for the flat plate cases, the persistence of the phenomenon was found to last some 30 to 50 boundary layer thicknesses. Results are given on Figure 9, taken from [87], in a diagram integrated skin friction ratio as a function of Q/b , where b denotes the injector width.

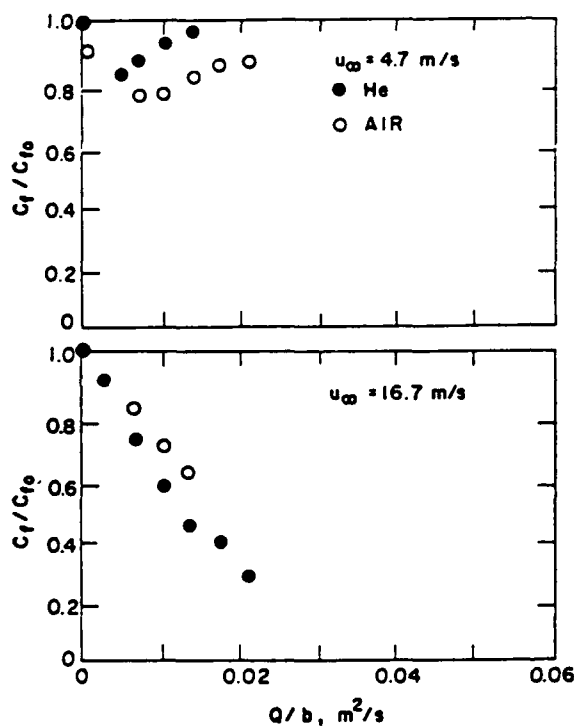


Figure 9: Average skin friction ratio as a function of the gas flow rate, from Merkle et al [87].

So far, all the reported experiments had been conducted in zero-pressure gradient conditions. Rather recently, Clark and Deutsch, [92], examined the influence of both a favourable and an adverse applied axial pressure gradient on microbubble-induced skin friction reduction on an axisymmetric body. Integrated skin friction drag was measured using a force balance. The strength of the pressure gradient has been judged from the following parameter :

$$K_u = \frac{\nu}{U_{\infty}^2} \cdot \frac{dU_{\infty}}{dx} \quad (11)$$

Considering the favourable pressure gradient, the values of K_u are very much smaller than those required

for re-laminarization of the flow ; in fact, K_u varies from $2.8 \cdot 10^{-8}$ to $1.1 \cdot 10^{-7}$. For the adverse gradient, K_u ranged from $-1.8 \cdot 10^{-8}$ to $-9 \cdot 10^{-8}$. These applied gradients are relatively weak. Nevertheless, these gradients have a strong influence on the microbubble drag reduction phenomenon as shown on figure 10, for the considered air flow rates, up to $12 \cdot 10^{-3} \text{ m}^3 \text{s}^{-1}$. The presence of a favourable pressure gradient inhibits the drag reduction mechanism, while separation of the boundary layer is induced at low levels of gas injection, approximately $5 \cdot 10^{-3} \text{ m}^3 \text{s}^{-1}$, for an applied adverse gradient. It should be noted that the apparition of separation was controlled visually by looking at the bubble motion, and that gas injection did not alter the intensity of the pressure gradient and that the flow remains axisymmetric.

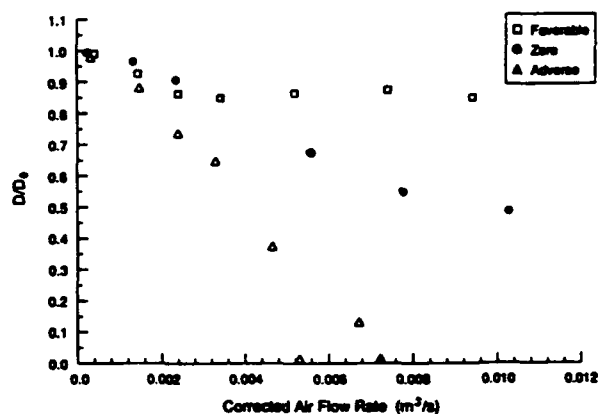


Figure 10: Influence of pressure gradient on drag ratio as a function of the air flow rate (\square : favourable, \bullet : zero \triangle : adverse), from Clark et al [92].

According to several authors the size of the bubbles, generated by the porous wall, as well as the bubble concentration appeared to be two essential features for boundary layer control experiments. Unfortunately, very little is known about their specific actions. Furthermore, contrary to either polymer solutions or surfactant solutions, it did not come into view, from all the aforescribed experiments, any asymptotic maximum drag reduction regime. Nevertheless, Bandyopadhyay, [11], reported that in injection of microbubbles in water, in a flat plate boundary layer, the work of Soviet researchers indicated that the limit is described by the laminar flow of a homogeneous mixture, at the same value of the local Reynolds number. Thus, for the maximum altered boundary layer, the skin friction coefficient will be given by the following relationship :

$$C_f = \frac{0.664}{\sqrt{Re_x}} \quad (12)$$

It might be suggested that the limiting drag reduction situation could correspond to the limiting bubble package, [11]. The most recent experimental programmes in turbulent microbubble drag reduction are under way ; they reported, anyway, general trends

which are similar to those related in the previous observations, [87].

Maximum local skin friction reductions were observed to occur near the porous section, while further downstream the boundary layer relaxed back toward its undisturbed condition, [90]. The parameters which control the characteristic length that describes this relaxation had not been determined, but would have to be attributed to the migration of microbubbles outside the boundary layer. Such a migration could be explained throughout different phenomena such as buoyancy, diffusion or interaction with the local mean velocity gradient, [89].

Effect on turbulence

The specific mechanisms by which microbubbles affect the skin friction are a matter of conjecture ; indeed, a possible mechanism, similar to that acting in polymer solutions begins to suggest itself, while another one, dealing with separation, could be ruled out. On the other hand, some authors had suggested, in the past, that the responsible mechanism would probably be similar to that responsible for the reduction with particle addition.

As translated by Merkle and Deutsch, measurements made by Soviet researchers indicated that bubbles were not present in the sublayer, [87]. Moreover, the region adjacent to the wall, extending over several viscous sublayer thicknesses, remains free of bubbles. This apparent lack of bubbles in the very near wall region is important. Indeed, the bubbles may stay in the turbulent field only, and not in the sublayer or migrate out of it. So, this would come into the same sort of mechanism which has been evidenced for polymers : an increase in the viscosity in the turbulent part of the flow, which will damp small scale motions. The buffer layer will thicken, the large eddies will scale up and the mean velocity will increase, at the same shear velocity, hence resulting in drag reduction, see [61]. Furthermore, there appears to be a consensus that the high frequency parts of the wall pressure spectra as well as the shear stress fluctuations spectra are damped when the drag is reduced, [90]. So, that would confirm the damping of the small scale motions.

Concerning turbulence intensity fluctuations, experiments performed by Madavan et al, [89], using Laser Doppler Anemometry revealed that turbulence profiles in the outer region of the boundary layer showed no real different character when bubbles are present compared to when they are absent. More detailed experimental data are needed if one plans not only to understand the specific mechanisms by which microbubbles affect the turbulent boundary layer, but also to apply it under best conditions as regards net drag reductions.

Modelling

Looking back to literature, only two computational studies have been conducted in this microbubble injection field. According to the possible mechanisms, briefly discussed in the preceding paragraph, assumptions had been made that microbubbles modify at first

the physical fluid properties near the wall (viscosity and density of the fluid). As a consequence, the local turbulent Reynolds number would be changed and the turbulence altered indirectly.

Thus, simple mixing length eddy viscosity formulations - the functional form of which is unchanged when dealing with bubbles - have been developed chronologically by Legner, [93], and then by Madavan et al, [94]. In both studies, the impact of bubbles on the boundary layer characteristics are reflected back on the density and viscosity which are strongly dependent upon the bubble concentration. However, specifications on these concentration profiles are somewhat different : either constant through the near wall region - approximated to the constant maximum concentration since bubbles are injected into the bottom of the boundary layer - and equal to zero everywhere else, [93], or as a function of the dimensionless distance to the wall, y^+ , [94].

More sophisticated models could be certainly developed, but the advantages of these two simple ones are that global effects, due to the presence of bubbles could be evidenced ; indeed, predictions indicate that the level of skin friction reduction depends upon the bubble concentration and upon their location and distribution within the boundary layer, [94]. Legner, [93], even showed up that the maximum skin friction reduction was obtained when the gas volume fraction approaches the bubble packing limit, which confirm earlier findings from Bandyopadhyay, [11].

Applications

It is apparent from all the experiments done to date that large reductions in skin friction and total drag maybe obtained by using gas injection in a turbulent boundary layer, provided that a sufficient concentration of bubbles can be maintained in the near wall region. According to Deutsch and Castano, [91], the extrapolation of these results to practical geometries at practical Reynolds numbers, is very much dependent on the dynamics of the bubbles in these situations. So, although the results are very encouraging, one does not know at the moment if such a technique will have engineering benefits.

The application of this technology to surface ships could appear quite straightforward. However, one has to keep in mind that such a method would require onto fit on the wall an external porous skin, through which air will be continuously injected. As quoted by Bushnell, [10], "the amount of drag reduction must be large enough to circumvent the need of injected gas and the research tools for designing such a surface skin".

An alternative method would be to introduce gas in such a way that the gas volume forms a very thin gas lubricating film staying close to the wall. Then, a "slip layer" would be generated between the surface and the gas. Although this method has not been detailed in almost all the last recent review papers, it has been studied for couple of decades in Soviet Union, but not for the purpose of drag reduction... Moreover, developing of such lubricating films had been consid-

ered to vehicles moving at very small speeds, such as river barges. It should be noted that microbubble injection has been shown to be effective at much higher speeds, but then, it could go against gas-flow requirements, [87].

One could wonder whether a reverse operation, i.e either injection of a liquid layer (liquid droplets, for instance) or liquid film-lubrification into a gaseous boundary layer, would work... In that case, gravity and/or buoyancy problems as well as instabilities of liquid gas interfaces would certainly act against such an operation. On the other hand, lubrication of liquid flows by other liquids could be reasonably speculated.

2.3.1.3 Particle Addition

It is the purpose of this subchapter to consider some of the research devoted to the field of "Particle Addition", with emphasis set on a very quick review of updated experimental work. It is obvious that applications of such mechanisms to drag reduction, for either internal or external flows, will be discussed if necessary. *A priori*, the phenomenon of adding particles to a flow in order to decrease the turbulent shear stress could appear very surprising, since it would be expected that a denser fluid develop a greater friction on the wall along which it creeps... However, the large number of very reliable reports published throughout literature, as regards the mechanism of drag reduction using particles or fibers in various fluids, confirm that this effect is real and should be expected when carrying out careful minutious experiments.

For sure, examples of drag reduction data by addition of foreign substances has been developed, precedingly with long-chain polymers. In such situations, the concentration of polymers in the solvent is very small, which means that there is a negligible effect on the physical properties of the baseline fluid (density, for instance). On the other hand, non-negligible amounts of external particles have to be added to the fluid, so that, for instance, the density of the resulting mixture is really changed, leading then to an heterogeneous fluid.

Most of the experiments reported in literature dealt with gas (air)-particle suspensions or liquid (water)-particle suspensions for internal flows. Nevertheless, it should be mentioned that reports for external flows applications are very rare. On one of the most recent review paper on Particle Addition, from Kane, [64], listed the different encountered situations from the number of published articles in literature :

- gas-particle suspensions ;
- liquid-fiber suspensions ;
- liquid-particle (non-fiber) suspensions ;
- some combinations of particle suspensions with mainly polymer solutions or surfactant solutions.

Herein, Particle Addition in liquid flows will be only considered. Applications to gaseous flows will be

given in §2.3.3.1. The mechanisms of drag reduction in gas-solid and liquid-solid flows may be different, so that no straight relationship between one fluid to the other would be definitive.

When dealing with drag reduction, the main point is to be sure of appropriate measurements. For internal flows, drag reduction data have more or less been reported from pressure drop measurements. However, Kane reported that it is possible and, frequently the case, that pressure drop increases, although skin friction drag has occurred, [64]. Indeed, in order to be consistent, one would have to measure the shear stress, between the base fluid and the wall, before and after the addition of particles or fibers. Thus, if one would like to evaluate as precisely as possible the pressure drop term, seven contributors would have to be looked for (e.g. see [64]). The weight of some of these drag forces to the others, depend upon several parameters, such as : type of internal flows (horizontal or vertical), type of fluid (liquid or gas), type and size of fibrous or non-fibrous particles, concentration, ... and so forth. Furthermore, for gas-particle suspensions flows, an additional variable known to be important is the electrostatic or magnetic charging. The exact relationship between the latter, the relative humidity and the pressure drop has been the subject of some debate, especially for drag-reducing system, in the last decades, [95]. Of course, the use of electric and magnetic fields for the management of particles is of general interest, even if further applications might be for experiments or process control, where particles will be involved naturally, [96]. Thus, Kane recommends that "viscous drag reduction is said to have occurred in a practical sense if the sum of the shearing forces between the fluid and the wall, between the particles and the wall, the drag forces between the particles and the fluid, and any electrostatically based forces are less than the value of the shear force between the fluid and the wall at the same mass flow rate and acceleration conditions ... of the fluid without any particles in the flow" [64].

So, based upon such considerations, drag reductions in flows of liquid-solid suspensions have been reported for water suspensions of ground wood and wood pulp, nylon, rayon or asbestos fibers, derived products and clay minerals. There has been some controversy about the data from different authors since the amount of drag reduction, if any, was rather different, depending upon not only the level of concentration of particles in the flows, but also particle shape. For liquid-solid suspensions, particles have been classified either as being fibrous or non-fibrous. In the latter, the low aspect ratio (length/diameter particle) allows to define an equivalent spherical diameter for the particle. On the other hand, for fiber particles, such an approach is not possible.

Liquid-Fiber Suspensions

As mentioned just above, the main difference between non-fibrous and fibrous solid cases is, for sure, the shape and size of particles : the fibers are non-spherical and their aspect ratio might vary over several orders

of magnitude (between 50 and 50,000, for instance). In that sense, such fibrous suspensions could be compared to long-chain polymers. For achieving drag reductions, experimental review revealed that very low concentrations of fibers (in weight percentage, which could be referred to as loading ratio) are needed.

Indeed, as reported in Ref. [95], nylon fibers with an aspect ratio of the order of 100 caused a 10% drag reduction in water at a loading ratio, η , (kg flowing solid/kg flowing water) of about 0.01. At almost the same operating Reynolds numbers, asbestos fibers with a greater aspect ratio of 10,000 provided 70% drag reduction at $\eta=0.005$. Furthermore, experiments carried out with nylon and rayon fibers, with aspect ratio less than 105, revealed drag reductions up to 25%, for $0.002 < \eta < 0.04$ (reference given in [95]).

Liquid-Particle (non-fiber) Suspensions

Most of the experimental work deals with water open-channel and pipe flows. A brief summary of some reported or suggested cases of drag reduction for liquid-nonfibrous suspensions could be found in Kane, [64]. Some years after Toms' first experiments with polymer solutions, turbulent flows with suspensions have been investigated for engineering purposes. The occurrence of turbulent drag reduction by suspended clay minerals was suggested by Zandi in 1967. Then, some hydrodynamic and/or geophysical engineers have looked at the behaviour of two-phase systems consisting of cohesive sediments suspended in fresh water or in seawater.

Rather recent hot-wire anemometer measurements have been made by Gust, [97], in a dilute seawater/mineral-clay suspension, in an open channel. The dimensions of clay particles were varying between $20\mu\text{m}$ and $150\mu\text{m}$, with a loading ratio, η , varying between 0.001 and 0.01. Measurements indicated that turbulent drag reduction occurred for all the investigated water-tunnel velocities, corresponding to Reynolds numbers, Re_U varying between 5,400 and 27,800 ($Re_U=UD/\nu$, where U is the mean channel

flow velocity and D the water depth). According to the author, these Reynolds numbers correspond to eroding and non-eroding flow rates. The friction velocity, deduced from the typical gradient method, was reduced between 20 and 40%, depending upon the Reynolds number, but for the same experimental flow conditions. In contrast to the reference case (fresh water), the velocity profiles did not fit the universal law of the wall (equations (4) and (5)), but produced a system of curves with different thickened viscous sublayers and an invariant slope of the logarithmic part. For sure, the ΔB terms, which appears in equation (7), changes with the Reynolds number, but there is no clearly dependence. It appears that an additional new layer seems to be inserted within the region : $5 < y^+ < 30$, i.e. approximately the buffer layer. Dimensionless velocity profiles, for the clay-mineral suspensions, are plotted on figure 11 and compared with some velocity profiles measured in the case of drag reducing polymer flows, [70]. The similarity of the flow structures clearly demonstrate the occurrence of drag reduction for such a liquid-nonfibrous suspension.

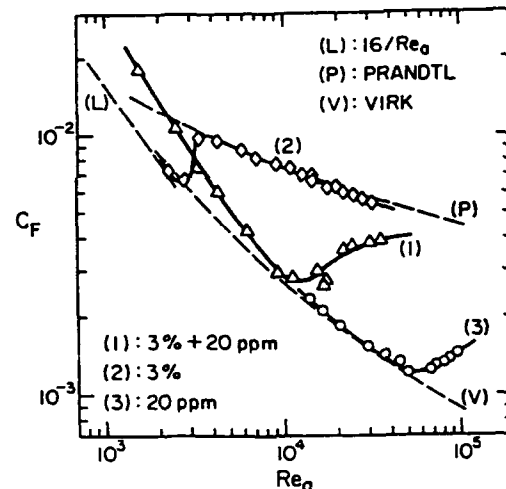


Figure 12: Friction results for solutions of polymers (20 p.p.m.), particles (3%), and combination of the two additives, from Matthys et al [98].

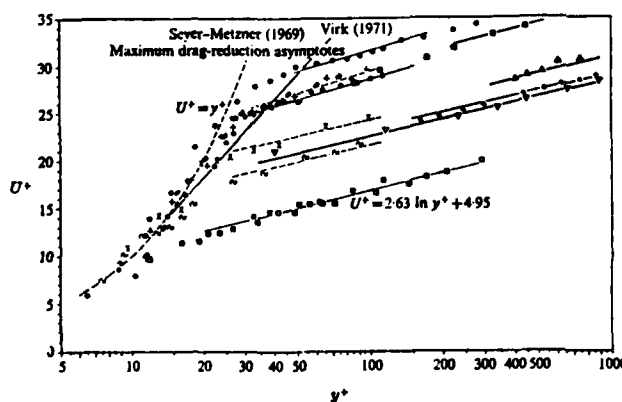


Figure 11: Drag-reduction data for experimental clay-mineral suspensions from Gust [96], (for symbols, see that same reference).

It has been observed that clay suspensions might sometimes induce unexpectedly large reductions in drag with respect to Newtonian fluids. An experimental study has been conducted by Matthys et al, [98], on the heat transfer, friction and rheology characteristics of both suspensions of pure bentonite and suspensions of bentonite to which polymer solutions had been added. The pressure drop along the test tube was measured at various streamwise locations; from these measurements, the wall shear stress could be computed from classic formulae, valid for internal flows applications. Both the entrance and fully-developed regions were examined, since both laminar and turbulent regimes could be obtained. A viscosity model, based upon rheological measurements (such as mea-

surements of the effective suspension viscosity, of concentrations, of density, ...) was suggested ; it allows to represent the results obtained for the clay suspensions with Newtonian relationships, whatever flow regime is concerned, using this particular choice of an appropriate non-Newtonian viscosity (cf. figure 12). The resulting "apparent Reynolds number" (based upon the effective suspension viscosity) is thus "capable of satisfactorily absorbing the reduction in friction" due to purely viscous non-newtonian fluids, as quoted by Matthys et al, [98]. Then, the viscoelastic drag reduction is well evidenced by a marked decrease of the friction coefficient below the newtonian values. Thus, in this specific set of experiments, considering polymer solutions, the friction results verify Virk's drag reduction asymptote at low values of the "apparent" Reynolds number, but exhibit thereafter an abrupt increase due to degradation (curve (3) on Fig. (10)). However, when combining clay suspension and polymer addition, the degradation effects appeared at lower Reynolds numbers, but the level of drag reduction is greater. It looks like with clay suspension, the polymer becomes more sensitive to mechanical degradation. Because of this sensitivity, the heat transfer results showed large variations with downstream distances.

Concerning this liquid-nonfibrous suspensions, maximum reductions up to 50% have been recorded, cf. [64]. However, in some cases, combination of additives could be very fruitful in terms of drag decreases. In fact, Kane reported that experiments with an addition of $350\mu\text{m}$ sand provided maximum reductions up to 30% in water and a bit less in a double phase oil-water flow. When combining sand with polymer solutions, 95-98% drag reductions were recorded.

Inertial Interaction - Particles Orientation

The flow of concentrated suspensions of slender particles could be encountered in a variety of practical applications such as hydraulic transport, for instance. The efficiency of the process could be related to the volume fraction of the disperse material. Then, the prediction and the control of the "suspension viscosity" - by analogy with the elongational viscosity for polymer solutions - could be crucial for drag reduction. So, one could wonder whether the orientations of the particles do play or do not an important role.

Krol undertook recently such an investigation, [99]. In a pipe water flow, at a Reynolds number of approximately 40,000, he considered a suspension of glass spheres, the mean diameter of which was about $50\mu\text{m}$. Krol showed that the components of the relative velocities of the spherical particles are independant of the particle orientation. On the other hand, when dealing with non-spherical particles, the relative particle-fluid velocities are determined by the inertial and orientational effects ; these latter are even stronger for rod-like particles. Using a very sophisticated measurement arrangement, he was able to measure the orientation of nearly cylindrical glass particles (aspect ratio close to 21) in turbulent pipe flows, for various particle volume fractions. Preliminary results seemed to indicate the

existence of a preferential fibre-orientation ; however, for very low particle volume fractions, these orientations seem to be random, [99].

Modelling

Calculations of the velocity field influenced by a multitude of spherical and/or non-spherical particles represent still a challenging theoretical and computational problem. Durlofsky and Brady, [100], presented recently a powerful method for studying the suspension of non-fiber like particles (identical spheres), immersed between two infinite plane boundaries. Using a simulation method, they were able to compute the "suspension viscosity" for different volume fractions of spheres. According to the authors, the method could be extended to dynamically simulate particle suspensions immersed in a pressure driven flow between two walls or through a tube.

As mentioned by Kane, [64], the number of analytical and theoretical studies on drag-reducing particle flows is quite limited in number and scope. Coughran even added that "one notable aspect of the many published studies on liquid-fiber drag reduction is the absence of any analytical work". The fact that the mechanisms of drag reduction by particle addition remains an open question, explains why the lack of knowledge limits the development of theoretical studies.

Applications

When dealing with Particle Addition for internal flows, some experimental work revealed that the orientation of the pipe had quite a lot of effect. Indeed, this has to be connected with the process of sedimentation of particles. Thus, when thinking of applying such a mechanism, one has to deal with means to keep particles in suspension in the liquid, which is not so evident with clay, sand, stone, agglomerates... Moreover, combining such mechanism with polymer solutions will add the extra degradation agent. Though all these restrictions, some scientists believe possible, the application of such methods for reducing turbulent viscous drag to naval vessels, as it will be evoked in §2.3.3.1.

2.3.2 Passive Methods for Liquid Boundary Layers

These passive methods are not specific to liquid boundary layers rather than gaseous boundary layers, which means that a lot of devices are commonly used for both layers. Thus, some of those "common" devices will be examined in detail in the following sub-chapter (cf. §2.3.4). This is the reason why coating applications will be the only ones discussed hereafter.

In either liquid or gas flows, the compliant wall motion has attracted a lot of researchers ; indeed, a lot of theoretical as well as experimental work have been done on that topic for nearly 20 years. From time to time, compliant wall terminology has been improperly used. In fact, such a sentence must be kept for referring to as passive flexible surfaces, and not to other wall surfaces.

The use of compliant surfaces to alter fluid flow phenomena was initially based upon anecdotal observations from the Pacific bottle-nosed Dolphins ; these latter used to swim at very high speed when they go by passenger ships. Without any doubt, the dolphin was the original inspiration as regards the use of compliant walls for a lower viscous drag and for the delay of laminar/turbulent transition. Calculations performed, at that time, by Gray in 1936, indicated that the apparent speed required a power output greater than mammalian muscle could produce : this is known as Gray's paradox. As quoted by Lumley and Kubo, [61], "it was concluded that dolphins must be exercising some form of drag reduction". Some scientist community, to which belong Kramer, attempted to examine several sections of dolphins skins in order to try to exploit their technological secret. In fact, the skin reveals a very complex structure ; that observation gave birth to the compliant boundary drag reduction research.

The pioneering compliant surfaces were based closely upon the dolphin's epidermis. Experimental studies had been undertaken with surface coatings, similar to the sea-animal one, set on axisymmetric bodies, the drag of which were measured from towing in water tunnels. Furthermore, tests performed on a trained dolphin did not indicate any trend versus drag reduction. Then, other experimental studies did not support Kramer's prediction, maybe simply because it was not possible to reproduce the fact that dolphins were scrutinizing the bow waves of the naval vessels...

From an experimental point of view, irreproducibility of results has been the most crucial point. It has not been conclusively demonstrated that a compliant wall motion could lead to drag reductions in turbulent flows. It seems likely that the whole compliant surface drag reduction research effort was based on a misapprehension, [61]. These results might explain why there has been a general disaffection in the scientific and engineering community for a couple of decades. Thus, unfortunately, most of the last years history of compliant surfaces research has been fraught with experimental irreproducibility and misinterpretation.

Although all these difficulties, a recrudescence of interest has again grown up, in the eighties', as regards the application of compliant walls for transition delay. The purpose of the reviews given recently by Carpenter, [101], and Carpenter et al, [102], were to focus on progresses towards such an application, using today's technology. Recent theoretical work was in good agreement with experimental findings, since it showed that significant transition delay was possible, [101]. The first ideas for applying compliant walls for turbulent flows came from the work performed by Benjamin in 1964 ; he suggested that a skin friction reduction in turbulent boundary layers might be achieved even if the same coating did not succeed in transition delay. He observed that although the turbulent kinetic energy was distributed rather uniformly over the boundary layer, the production and dissipation of this energy are concentrated very close to the

wall (cf §2.1) ; then, a flexible boundary layer might change the balance between these energetic processes and exert some influence upon turbulence as a whole, which would lead to turbulence reduction.

It should be mentioned that the case of active compliant cases - where the motion of the surface is prescribed - has been also investigated through numerical simulations. Using a numerical simulation of a turbulent boundary layer flow, Moin et al [103], found that 20% of drag reduction had been recorded over a "smart" wall ; in such cases, the normal component of the velocity at the wall had been prescribed to be 180° out of phase with the normal component of the velocity, slightly above the wall. Furthermore, this reduction was associated with a decrease in the intensity of the wall-layer structures and in the magnitude of the Reynolds stresses.

Attempts have been made to develop surface coatings for use in liquid flows, which consider both compliant wall technology and polymer solutions. According to older experiments, soluble coatings of polymer have shown either a weak turbulent drag reduction or a drag increase. The idea of a joint use of additives and viscoelastic coatings is based upon the fact that these two techniques altered different structures and, then different scales of turbulence, [104]. Indeed, dilute polymer solutions act not only upon the spacing of the near-wall low-speed streaks, but also on the small scale structures of the flow (cf. §2.3.1.1), i.e structures the length of which could be less than 100 viscous lengths. On the other hand, compliant boundaries act on the long-wave disturbances, the scale of which could be important of the order of 1000 or more viscous lengths. It seems that there is a positive action of compliant walls on polymer additives : recent experiments showed that it was possible for instance to decrease considerably the polymer consumption, [105].

It should be mentioned that a lot of recent numerical and experimental studies have been performed by Soviet researchers in order to correctly select the viscoelastic properties of coatings for drag reduction ; information could be found in references [106], [107]. Work involves study of the vibrational properties of the coating surface. The studies dealt essentially with passive coatings rather than active ones ; thus, the surface deflection of the coatings results from the action of the pressure fluctuations of the turbulent flow field. As mentioned by the Soviet authors, experimentators have been using in the past all possible materials in order to obtain any drag reduction. Moreover, most of the work did not refer to as membrane coating. Then, unsuccessful attempts to reproduce successful data obtained in other laboratories, could be explained by the differences in visco-elastic properties of coatings which were not measured in the great majority of the studies. Soviet engineers took special care for technology simplicity, using industrial materials, ...

This simple and attractive concept of using a compliant material to delay transition or to achieve skin friction reduction has proven to be a strong motivation for theoretical, numerical and experimental works. If it is possible for a compliant wall surface to reduce the

skin friction in a turbulent boundary layer, it now appears likely that the material will have to be carefully chosen to produce a small amplitude, stable response and to avoid some instabilities due to pressure fluctuations, mean shear stress, vortex sheets, ...

2.3.3 Active Methods for Gazeous Boundary Layers

As for liquid boundary layers, introduction of extra particles, such as solid particles or fibers could be used in either gases or liquids. However, techniques involving modification of near-wall momentum using blowing or suction are more advisable.

2.3.3.1 Particle Addition

The purpose of this subchapter is to consider applications of particle addition to gas flows ; it should be recalled that adding fibrous or unfibrous particles to liquid flows has been developed in a preceding section (cf. §2.3.1.3). Moreover, the mechanisms of drag reduction in gas-particles and liquid-particles flows may be very different, since electrostatic or magnetic charging could have a greater relative importance in gas-solid flows than in liquid-solid ones, [95].

Drag data

In 1961, Sproull observed that adding dust to air flowing in turbulent motion through a pipe appreciably reduces the resistance coefficient. A summary of reported work as regards experimental evidence of gas-solids drag reduction has been tabulated in Kane, [64]. It should be noticed that particles have generally been spherical and been made of glass and convected through air ; some solids are made of alumina, magnesia and even zinc. Maximum drag reduction data have been obtained with vertical flow cases, which allows to get rid of any problem of deposition. However, this latter is of most concern in horizontal flows.

Looking back to the table given by Kane, [64], the maximum amount of drag reduction has been 75%, for fine spherical glass particles, the diameter of which is $34\mu\text{m}$, for a turbulent pipe flow at a Reynolds number of about 22,000. These data were recorded with loading ratios, η (kg flowing solid/kg flowing air), varying between approximately 0.5 and 2.5 for glass particles. Other experimentors reported equally rather important levels of drag reductions with higher particles loading ratios : 75% with zinc particles (η up to 7.0 at a Reynolds number of about 50,000) or 50% with alumina particles (η close to 6.0 at a Reynolds number of about 140,000).

On the other hand, 6% of drag reduction was only recorded when adding wood pulp fibers in an air flow, for a Reynolds number range : 150,000 - 300,000 at a loading ratio close to 0.2, (e.g see [95]). More recently, Coughran looked at the effect of particle shape on pressure drop in turbulent pipe flow of a gas-solid suspension, [95]. The pressure drop was measured for suspensions of both spherical particles (made of silica glass) and two types of fibers (made from nylon), all having mean diameters between $8.4\mu\text{m}$ and

$21.0\mu\text{m}$. The fibers differ from the mean aspect ratio, either 31 or 75. A Reynolds number range of 61,000 to 114,000 and loading ratio range of 0.06 to 0.30 were investigated. The friction factor, f , was computed from the measured pressure drop at different pipe Reynolds numbers. The gas-solid pressure drop was evaluated by the ratio f_{s+g} / f_g , where f_g and f_{s+g} denote the friction factors measured respectively in clean air and in gas-solid suspension, but at the same air Reynolds number. An example of results is given on figure 13, from [95] ; the friction ratio is plotted as a function of the loading ratio, at $Re=114,000$ and for the three types of particles. It should be observed that the spherical particles gave 8% drag reduction, while the drag increase is close to 12% for fiber-type particles. Similar trends were reported for lower values of the Reynolds numbers. Thus, air-sphere suspensions demonstrated drag reductions abilities, in agreement with previous published results). On the other hand, fairly uniform fibers gave either no drag variations or drag increases, depending upon the value of the aspect ratio and of the loading ratio, which is contrary to water-fiber results. Coughran attributed these observations to the existence of a relative humidity effect, which is probably related to electrostatic charging, [95]. Once again, as mentioned earlier, the exact relationship between electrostatic charging, relative humidity, pressure drop and drag variation is still subject to some debate, especially in view of drag-reducing methods.

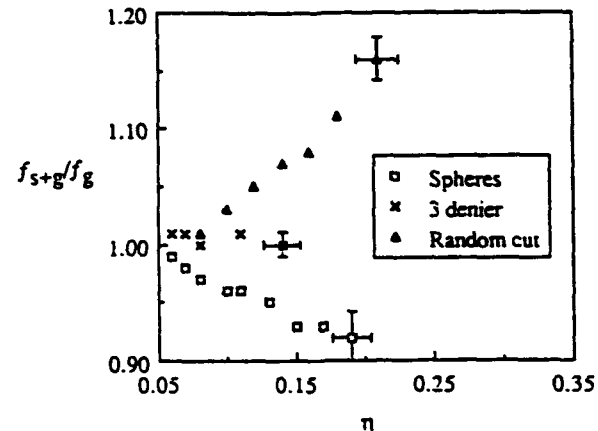


Figure 13: Particle shape effect at $Re=114,000$, from Coughran [95] ; cross : uncertainty bars.

Mechanisms

The mechanisms by which drag reduction occurs in the gas-solid suspensions has not been proven, yet. Theoretical explanations vary although it appears to be generally accepted that, because of particle addition, the turbulence structure is altered. As it was the case with clay suspension in water (cf. Fig. 9), the sublayer thickness increases in gas-solid suspensions. This thickening seems to be common to most of the skin-friction reduction methods which alter the turbulence structure. As reported by Hefner and Bushnell, [56], although the addition of particles causes a drag decrease, turbulence intensities might increase in

the region close to the wall. These authors suggested three possible mechanisms : either turbulence dissipation increase due to particle wakes, or modulation in the near-wall flow due to changes in particle velocities or, at last, anisotropic viscosity which increases the velocity profile stability. The problem, in fact, is to be able to perform reliable measurements, on mean and fluctuating quantities, just after particles have been added to the "clean" flow. Such an approach will be necessary in order to understand the mechanisms of action and, possibly, to improve the percentage of drag reduction.

Modelling

Some of the reported models show promise for predicting velocity profiles or particle orientations, for the simple kinds of suspension flows. However, important features such as, for instance, particle shape and size, have not been incorporated, yet. Sophisticated models cannot presently be extended to correctly predict pressure drop, which is a crucial criterion for any of fluid-particle combination.

Some researchers investigated the properties of dusty gases either under laminar conditions or for parallel flows. The advantage of dust particles is that besides internal flow applications, it could also be applied with success for external flows. Chakrabarti, [108], developed a boundary layer theory for a dusty gas past an infinite flat plate, in the primary stages of the motion. He assumed that the dust is uniformly distributed in the gas and that the density of the dust material is allowed to be large compared with the gas density, which are reasonable assumptions. The expression for local skin friction coefficient due to dusty gas has been deduced and compared with that for the case of a clean gas. The calculations showed how the velocities of the dust particles differ with the potential velocity of the fluid in the main stream. It appears from the calculations that the effect of dust reduces the local skin friction ; this reduction diminishes as the time increases. However, such an analysis is only valid in the initial development of motion, but could be encouraging for practical purposes.

Applications

Thus, particles injected into a turbulent boundary layer can alter the turbulence, the normal velocity gradients and, as a consequence, the drag. To utilize such an effect for external flows, high efficiency means must be provided for both the confinement of particles to a subregion of the boundary layer and their collection. Configurations that exploit electric and/or magnetic charging have been exemplified earlier on by Davey and Melcher, [96].

If one assumes that applying particle injection to external flows is not utopic, any scheme which did not involve particle collection, would have to be prohibited. Indeed, because of weight problems and pollution environment, carrying suitable particles on an aircraft does not appear feasible. In some way, confinement of the particles to some region close to the wall

would eventually help for a subsequent collection. The two afore-mentioned authors suggest possible magnetic migrations of particles in turbulent flows, [96]. For the moment, such an extrapolation to aircraft applications, seems out of scope.

In one of his review paper, Bushnell, [10], believed that the application of fiber drag reduction to external flows is not straightforward. The idea would be to inject particles or fibers, just downstream the nose of the fuselage and to recover maximum of them, in the neighbourhood of the tail of the fuselage, in order to send them back again at the nose and so forth. This simple approach, though easy to formulate, would be rather hard to design in the future. Bushnell even followed his findings by writing that "a possible (but still improbable) approach would be to form fibers from the fuel, use them for drag reduction... and then collect fuel plus boundary layer into an engine at the tail for subsequent consumption". Various investigations must be needed before thinking of applying this concept of particle addition to external air flows, and more precisely to commercial aircraft.

2.3.3.2 Synthetic Boundary Layer

Such a terminology refers to as turbulent boundary layer, which has been constructed by generating systematic moving patterns of turbulent spots in a laminar flow. The general idea is to "force" transition to occur by closely spaced Emmons' spots, generated by external forcing in the area where, otherwise, transition would take place naturally. This apparently produces smaller scales of turbulence.

The point of departure from such an application was the fact that natural transition from laminar to turbulent flow in a boundary layer is characterized by the appearance of turbulent spots, [7] or [8]. The turbulent spot which was discovered, at first, by Emmons in 1951 and, then, was documented experimentally by Schubauer and Klebanoff in 1955, is an arrowhead-shaped region of turbulence that appears in a laminar boundary layer. A spot grows approximately linearly in all directions and is convected within the laminar boundary layer.

Thus, a local reduction of turbulent skin friction could be obtained, if the birth and the formation of these turbulent spots are artificially modified and if their growth is restrained. To this purpose, an array of turbulent spot generators was judiciously set in the laminar part of the boundary layer. The aim was to promote transition at the streamwise abscissa corresponding to the occurrence of the first natural Emmons spot ; then, experiments would consist of inducing the spots to form simultaneously at the same longitudinal location and quite close together, thereby eliminating "islands of laminar sea" in the transition area (e.g. see Bushnell [10]). This drag reduction technique deals in fact with a form of controlled transition and has been suggested as a possible means of creating stable turbulent flow of reduced skin friction.

Savas and Coles, [109], produced turbulent spot generators by displacing small cylindrical nylon pins into the laminar boundary layer, through a rotating

cam. Intermittency had been the primary measured variable in that research programme. The question which could arise in such a "manipulation" would be : what is the degree of equivalence that can be expected between a synthetic boundary layer and a natural boundary layer, other things being equal? In other words, will it be possible, for instance, to directly compare the altered skin friction to the unaltered one... The study performed by Savas and Coles revealed that the downstream large eddy pattern develops directly from the original disturbance pattern, with an explicit correspondence between spots and large eddies. The original large eddies were replaced by new eddies at new positions, intermediate to the original ones. It has also been observed smaller turbulence scales in the initial streamwise growth of the turbulent boundary layer.

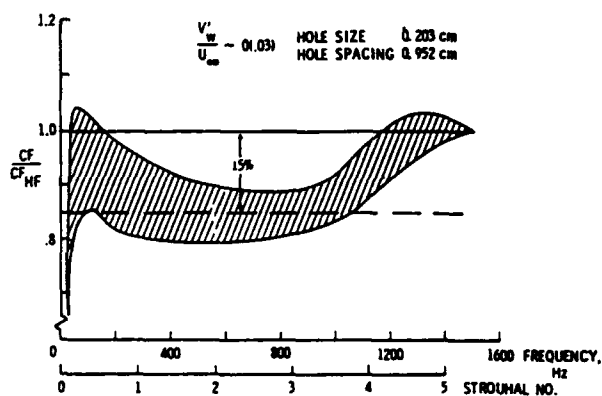
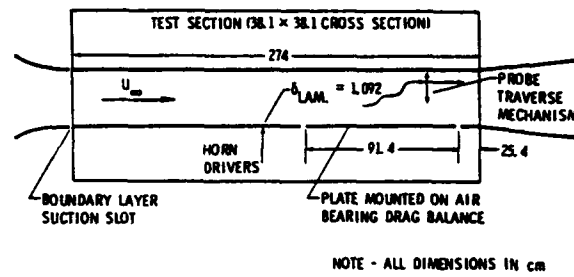


Figure 14: Influence of acoustic frequency on local skin friction, from Goodman [110] (shaded area : data scatter from repeated runs).

Such a method had been under examination at Lockheed-Georgia, some time ago, [4]. However, experiments carried out by Goodman at NASA Langley showed local skin friction reductions, [110]. In order to generate artificial spots, Goodman considered a spanwise row of small holes with acoustic horn drivers mounted underneath. Experiments were undertaken in the low-turbulence wind tunnel of NASA Langley, where u_{∞}/U_{∞} is of the order of 0.03%. The necessary acoustic velocity perturbation, in order to generate Emmons spots, is equal to 20% of the free-stream velocity. The variations in friction forces had been

measured through a drag balance. Local skin friction reductions of the order of 15% were recorded, [110]. The evolutions of the measured skin friction coefficient are plotted on figure 14, versus the physical frequency, f , and/or the Strouhal number ($f \cdot \delta / v$), knowing that $\delta = 1.09\text{cm}$ for $U_{\infty} = 3.65\text{ms}^{-1}$. According to smoke wire pictures interpretation and momentum thickness measurements, the author suggested that the averaged drag reductions were most probably the result of the production of smaller turbulence scales than a shift in the transition region. Of course, the skin friction will relax back to some uncontrolled values, as these decreases are only local. The balance taking into account the acoustic horn driver trigger did not allow to obtain positive reductions.

Although the concept is dynamic in character, it could conceivably be implemented by a purely passive means. Then, other maybe passive trigger devices (such as small pin heads, as suggested by Thomas, [4]) with very low device drag penalty might allow to approach such net drag reductions.

Though the efficiency of such a method dealing with the generation of artificial turbulent spots might be questionable, further research could be justified through the use of small passive devices to insert in the laminar part of the boundary layer. If then skin friction reduction occurs, turbulence measurements will be also needed in order to compare the turbulence of the synthetic boundary layer to the uncontrolled natural boundary layer.

2.3.3.3 Suction

The shape of the mean velocity profile and, consequently, the skin friction at the wall is affected not only by the pressure gradient in the ambient flow or by the viscous gradient at the wall (due to heating, cooling or particle addition) but also by the boundary conditions, i.e. transpiration (suction or injection). These different means of boundary layer alteration are clearly evidenced from the following equations.

As the wall is approached ($y \rightarrow 0$), the time-averaged streamwise momentum equation could be read :

$$\rho v_0 \frac{\partial U}{\partial y} \Big|_{y=0} = - \frac{dP}{dx} + \frac{\partial}{\partial y} \left(\mu \frac{\partial U}{\partial y} - \rho \bar{u} \bar{v} \right) \Big|_{y=0} \quad (13)$$

Assuming the flow is incompressible, that equation becomes after rearranging :

$$\begin{aligned} \rho v_0 \frac{\partial U}{\partial y} \Big|_{y=0} = & - \frac{dP}{dx} - \rho \frac{\partial \bar{u} \bar{v}}{\partial y} \Big|_{y=0} + \mu \frac{\partial^2 U}{\partial y^2} \Big|_{y=0} \\ & + \frac{d\mu}{dT} \left[\frac{\partial T}{\partial y} \frac{\partial U}{\partial y} \right]_{y=0} \end{aligned} \quad (14)$$

where U and T are the mean streamwise velocity and mean temperature field respectively, v_0 the transpiration velocity (positive value for injection and negative value for suction). Therefore, the integrations of the continuity and streamwise momentum equations, for steady incompressible flows, yields to the extended

von Karman equation, valid for both laminar and turbulent flows :

$$\frac{Cf}{2} = \frac{d\theta}{dx} + \theta \left(\frac{H + 2}{U_e} \frac{dU_e}{dx} + \frac{1}{\rho_e} \frac{d\rho_e}{dx} + \frac{1}{R} \frac{dR}{dx} \right) - \frac{v_0}{U_\infty} \quad (15)$$

These equations allow to point out the important role played by the wall transpiration on both the velocity profile and, consequently, the local shear stress.

Therefore, couple of studies have suggested that control of the normal to the wall component of the fluctuation field could be probably one of the most efficiency tools for altering the outer turbulent flow. Thus, this could be achieved by wall conditions alterations through transpiration and more precisely suction (injection technique would be developed in the subsection below).

Besides drag reduction goals, suction has been used in order to delay laminar to turbulent transition (form of transition control), postpone separation, achieve an asymptotic boundary layer, re-laminarize an already turbulent flow. It has already been pointed out (cf. for instance, Arnal [8]) that the application of suction to a laminar boundary layer is an effective means for reducing drag. The effect of suction is to stabilize the boundary layer and the reduction in drag is achieved by preventing transition from laminar to turbulent flow. It should be mentioned that a recent joined study between ONERA/CERT and IMST has just been carried out in order to analyse the effects of suction through slots upon the turbulent boundary layer and to look at the relaxation distance downstream the suction area, [111]. The aim is to alter the fuselage turbulent boundary layer just ahead of the wing-body junction, in order to get rid of swept wing contamination. This would involve a new application for skin friction drag reduction.

For turbulent boundary layers, suction has of course been applied onto aerofoils in order to prevent separation. The needed suction rate coefficient was relatively low, typically in the range of 0.002 to 0.004, [112]. The suction rate coefficient, currently referred to as C_q , is defined as :

$$C_q = \frac{\rho_w |v_0|}{\rho_\infty U_\infty} \quad (16)$$

Couple of authors would rather characterize suction through the A^+ parameter which involves inner layer parameters :

$$A^+ = \frac{\rho_w |v_0|}{\rho_e U_\tau} \quad (17)$$

Influence on turbulence characteristics

Therefore, suction has an important effect on the turbulence structure. Indeed, experiments revealed that suction, through a porous surface, increases the stability of the viscous sublayer by decreasing the amplitude of both the longitudinal and spanwise oscillations ; this has been consistent with flow visualisations performed by Anselmet et al, [113]. Linked to that observation, suction causes an appreciable stabilization of the low-speed streaks in the near-wall region

(cf. Antonia et al [114]) : the low-speed streaks tend to oscillate less in the spanwise direction while their streamwise persistence is increased. Experiments performed in the water-tunnel at IMST indicated that suction reduced the average frequency of dye ejections into the outer layer, [113], enhanced the stabilization of near-wall flow and reduced the root mean square spanwise and longitudinal velocity fluctuations as plotted on figure 15, [114]. On that figure, the velocity fluctuations are non-dimensionalised by the friction velocity ; therefore, the open and closed symbols refer to as $A^+ = 0$ and 0.055 respectively, which corresponds to $C_q = 0$ and 0.003.

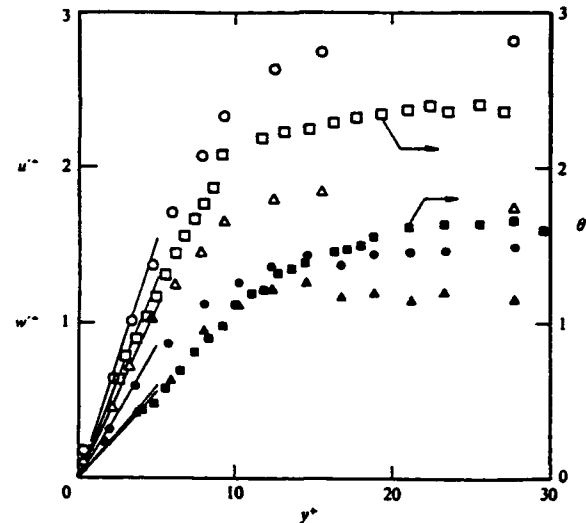


Figure 15: Distributions of the r.m.s longitudinal and spanwise velocity fluctuations as well as the r.m.s temperature fluctuation, (\circ : u^+ , \triangle : w^+ and \square : θ^+), from Antonia et al [114].

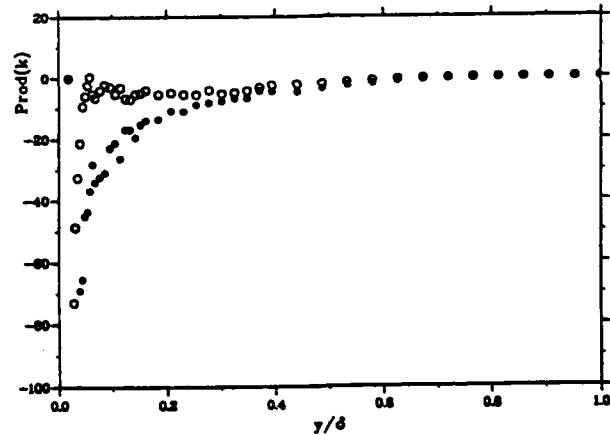


Figure 16: Production of turbulent kinetic energy, at one boundary layer thickness downstream the suction area (\bullet : $A^+ = 0$, \circ : $A^+ = 0.055$, three slots), from Pailhas et al [111].

In agreement with those results, Elena [115], reported earlier measurements of the instantaneous velocity and temperature signals with and without suction. His results were consistent with the idea that suction primarily affects the low-speed streaks by reducing their magnitude and thus inhibiting their ability to participate in the production of turbulent energy.

Most of the afore-mentioned results concern suction through porous surfaces. Rather recent experiments, [111], revealed that with slot suction, the standard deviations of longitudinal and transverse velocity fluctuations are mainly modified in a region close to the wall ; however, in the region close to the wall, the effects are not as important as those relative to a porous wall, where suction is continuously applied.

Therefore, the streamwise shear stress component is strongly affected in the inner wall region ; when moving downstream, such alteration propagates to the whole boundary layer thickness. When plotting the production of either turbulent kinetic energy or shear stress similar results are obtained : at one boundary layer thickness, δ , downstream three slots, the spacing of which is close to 1.76, production is mainly reduced in the buffer layer and at the beginning of the logarithmic law (cf. figure 18). Results seemed also to indicate that recovery on the Reynolds stress components is very rapid downstream the suction area (made of three slots) : a couple of boundary layer thicknesses.

Asymptotic suction

The suction rate necessary for establishing an asymptotic turbulent boundary layer is much lower than the rate required for re-laminarization ($C_s = 0.01$) as reported by Gad-el-Hak, [112]. As regards the asymptotic behaviour, the solution is particularly simple for the case of a flat plate at zero incidence with uniform suction. In that case, it should be recalled that the velocity profile as well as the integral thicknesses, become independent of the streamwise co-ordinate, from a certain distance from the leading-edge onwards. Thus, equation (15) becomes :

$$\frac{C_f}{2} = \frac{d\theta}{dx} - \frac{v_0}{U_\infty} = C_s \quad (18)$$

Generally speaking, suction increases the local skin friction and decreases the streamwise turbulence intensity, in the near wall region. According to various authors, the asymptotic suction rate coefficient C_s is close to 0.003, which means that the asymptotic friction coefficient is close to $6 \cdot 10^{-3}$. That latter is in fact higher than "classic" turbulent values, one will have to consider when dealing with typical wings or fuselage Reynolds numbers. For instance, for a Reynolds number close to 50 millions, the resulting incompressible skin friction coefficient in flat plate case is, only $1.7 \cdot 10^{-3}$. Furthermore, this asymptotic turbulent suction rate is much higher than the equivalent one, obtained for laminar boundary layers : $1.4 \cdot 10^{-5}$, for which the critical Reynolds number ($U_\infty \delta_1 / \nu$) and the displacement thickness of the asymptotic suction profile are equal to 70,000 and to ν / v_0 respectively, [116].

From an experimental point of view, the value of C_s , to which the momentum thickness ceased to growth is defined as the zero-growth suction rate and could be used in order to compare performances of different suction surfaces. This specific value of suction coefficient rate is somewhat restricted, because according to equation (18), the value of C_s at which $d\theta/dx = 0$ should be dependent of the Reynolds number. Indeed, looking back to literature, the zero-growth rate suction coefficients - determined experimentally - vary from 0.0025 up to 0.0076 depending not only upon the type of suction surface (discrete slots, porous surface) but also slightly with the local Reynolds number (exploratory range : $0.2 \cdot 10^6$ - $3.7 \cdot 10^6$).

It is interesting to notice the dependence of skin friction on both Reynolds number and suction rate coefficient, C_s . Therefore, at a constant local Reynolds number, numerous authors found that the local skin friction coefficient (as well as the average one) has increased with the value of C_s . One might also add that the behaviour of such suction surfaces could induce different friction values depending upon whether new turbulence is generated in the turbulent boundary layer.

Applications - Selective suction

An extensive number of studies, involving either large discrete holes or small uniformly distributed holes, have been used to apply suction through a surface for turbulent boundary layer control. Available literature indicates that porous surfaces are capable of providing nearly uniform suction, with smaller drag increases at a given suction rate, than the more abrupt, discrete holes or slots. Nevertheless, in a more general way, porous surfaces are more difficult to fabricate and require a larger pressure drop. Wilkinson et al, [117], even developed what is called an *hybrid suction surface* for turbulent flows. It is in fact a slotted suction surface which consists of an array of closely spaced slots aligned in the direction of the mean streamwise flow. They performed experiments and compared that surface to other ones such as porous surfaces or isolated suction surfaces. As a result, this type of surface could be successfully used since, as mentioned by the authors, "it has nominally the same suction characteristics as a uniformly porous surface".

Gad-el-Hak and Blackwelder, [118], suggested an approach which is called *selective suction*, in which small amounts of suction are applied below the low-speed streaks in order to reduce the intensity of the ejections of low-speed streaks outward from the wall (item 2 from the taxonomy of structures). The goal sought after is to slow or disrupt the bursting process. Thus, if these events could be inhibited, the Reynolds stress would be decreased and the turbulence production cycle be interrupted. This idea of selective suction found birth with the earlier research due to Wilkinson et al, [117], who applied suction along the troughs of the afore-mentioned slotted surface. In this last study, Wilkinson et al achieved zero boundary layer growth rate with suction rate coefficients, C_s , close to 0.003, which agrees with results reported by other authors

through porous surfaces, for instance. However, the total drag, resulting from the integrated skin friction and the momentum loss due to suction, increased with C_s .

The feasibility of selective suction has been first demonstrated by altering the low-speed streaks artificially generated in a laminar boundary layer. Indeed, suction was applied through a single streamwise slot, one viscous length unit wide and 1,500 units long; this slot was located between the burst generators. The burst-like events, and consequently, the low-speed streaks are produced by withdrawing near-wall fluid from two minute holes separated in the spanwise direction, [119]. Gad-el-Hak and Blackwelder found that values of C_s as low as 0.0006 to 0.0015 eliminated the artificially generated streaks and the accompanying hairpin vortices, [118]. This rate is 2-5 times smaller than the one reported in other experimental work, when looking at the rate necessary to yield zero-growth rate of the boundary layer's momentum thickness.

If this result is sustained in naturally developing turbulent boundary layer, a skin friction decrease close to 60% would be achieved, [112]. That technique had been applied to turbulent flows with considering suction from the single streamwise slot, [118]. Since ejections are intermittent, suction needs to be continuous. The main difficulty, when applying selective suction in a turbulent flow, is that one must at first fix in space the low-speed streaks, i.e. eliminate or decrease their spatial randomness. This is the reason why this selective suction could be incorporated with other drag reduction methods, the aim of which would be to fix the low-speed streaks.

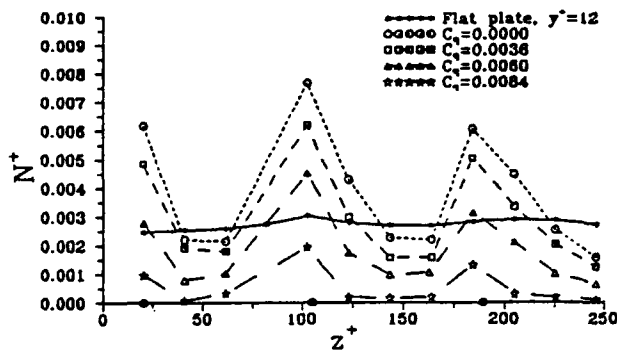


Figure 17: Frequency of occurrence of low-speed streaks ; (● : Large Roughness Elements locations) from Roon et al [120].

To our knowledge, Roon and Blackwelder, [120] and Wilkinson et al, [12], have tried to combine transpiration technique and surface modifications. In their series of experiments, Roon et al introduced longitudinal roughness elements. Though those had been found to be successful in reducing the spatial randomness inherent in low-speed streaks, ejections of fluid still occur randomly in the streamwise direction; however, the frequency of occurrence of the low-

speed streaks generally decreased, as it is shown on figure 17. On that figure, if N denotes such a frequency, $N^+ = N\nu/U_\tau^2$ is plotted versus the spanwise abscissa, z^+ non-dimensionalised with the kinematic viscosity and the friction velocity. Increasing suction tremendously reduced the number of streaks detected through the use of the VITA technique. An example of the root mean square velocity distribution is given on figure 18, for different suction rate coefficients. According to the authors, large suction rates are needed ($C_s > 0.005$) in order to get significant structural changes: this is maybe due to the fact that selective suction was applied under the roughness elements for a small streamwise extent ($\Delta x^+ \approx 400$).

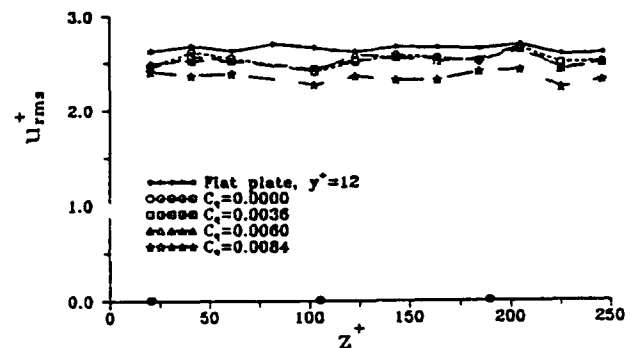


Figure 18: Root mean square velocity distributions across the span ; (● : Large Roughness Elements locations) from Roon et al [120].

A couple of years before Roon and Blackwelder's experiment, Wilkinson et al considered a simple aspirated grooved surface in which continuous suction was applied to the peak of widely spaced riblets, [12]. The riblet spacing was close to 100 wall units while the height was approximately 15 wall units. According to riblet studies (cf. §4), this non-dimensionalised spacing is too important in order to get any net drag reduction, but is necessary to fix a vortex pair within the riblet channel. There is no obvious evidence that suction had only affected riblet vortex bursting in order to act properly on turbulence production. All these invoked reasons might explain why no drag reduction was achieved.

It must be emphasized that selective control is a rather new concept which needs further developments. The interesting key point of this technique is that less energy expenditure would be required than continuous or uniform suction, thus decreasing the momentum loss due to suction. This latter has to enter into account when dealing with total drag balance.

Applications to aircraft

Selective suction appears to be in such an early stage that improvements must be suggested before trying to apply it on a commercial aircraft. Nevertheless, combining such types of suction with other passive devices would be, for sure, very profitable.

A few years ago, in a VKI Lecture Series, Bushnell pointed out the notion of re-laminarization using

massive wall suction, [10]. The basic idea was then to try to re-laminarise the boundary layer downstream the cockpit, since the flow would become quickly turbulent in this area because of a lot of excesses, Pitot probes or angle of attack meters. In order to achieve such a goal, important values of the suction rate coefficient would be necessary ; furthermore, control of this laminar part all along the fuselage length would be needed. One of the main difficulty remains in the location of this suction area, so that laminar flow begins to develop in a stabilizing pressure gradient area. Right now, it does not seem that such an application could be considered more especially as the massive volume of air, eventually sucked from the fuselage, combined with the air sucked through the wings would have to be re-used or injected somewhere... (cf. Bushnell [10].)

On the other hand, suction of the fuselage turbulent boundary layer ahead of the wing-body junction, horizontal tail-body or fin-body junctions could perhaps be more profitable since it would be a pity to work on transition control on such appendices, without keeping in mind the possible appearance of leading edge contamination. Therefore, suction could be perhaps used along the wing leading edge, in order to help flow re-laminarization.

2.3.3.4 Injection

According to Gad-el-Hak and Blackwelder, [118], an alternative technique that conceivably could reduce the Reynolds stress and, consequently, reduce the drag is to inject selectively fluid under the high-speed regions, as opposite to selective suction where fluid is sucked just below the low-speed streaks. The immediate effect would be to decrease the viscous shear at the wall resulting in less drag (cf. equation (15) or (18)). In addition, the two authors believe that the velocity profiles would have a smaller $\partial U / \partial x$ since injection would provide a more uniform flow in the spanwise direction.

Wiedemann and Gersten, [121], experimented the use of injection, or more exactly blowing, near the stagnation point of a porous circular cylinder. They observed that turbulent boundary layers with relatively strong blowing (v_0/U_∞ up to 0.18) still have a two layer structure, with a wall layer and a defect layer. However, the characteristic velocity is still the "classic" friction velocity, U_τ as defined by the equation (1), but based on the maximum shear stress, the location of which within the boundary layer depends upon the blowing rate, instead of the wall shear stress. Furthermore, the boundary layer thickness is growing with the blowing velocity. The combination of boundary layer control by blowing and suction has been applied to a circular cylinder in incompressible flow. The arrangement is shown on figure 19 : the front quarter of the cylinder is used for blowing, whereas the rest of the periphery is used for suction (that ensures a net volume rate equal to zero). The interest of suction in the rear part of the cylinder is that it acts on boundary layer separation and, consequently, reduces the pressure drag. For a Reynolds number of $9 \cdot 10^4$, using a

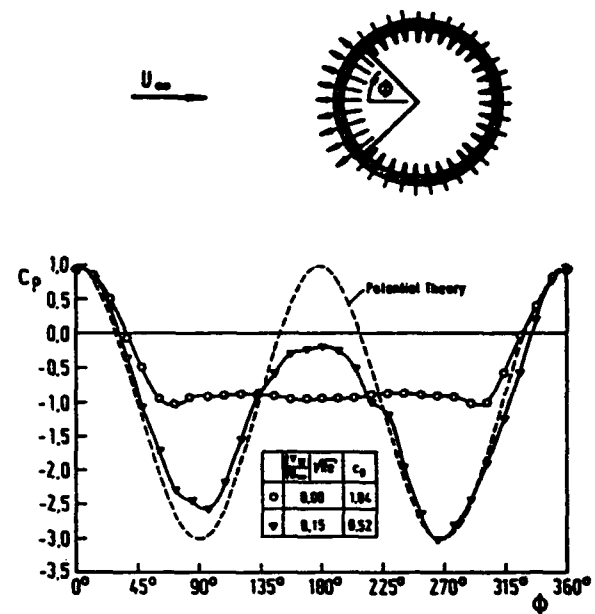


Figure 19: System of combined blowing and suction on a circular cylinder. Azimuthal pressure distribution ($v_0 \text{ blow.} = 3v_0 \text{ suc.}$), from Wiedman et al [121].

suction rate coefficient, C_s , close 0.03, these two authors were able to reduce the pressure drag from 1.04 to 0.052!.

Another approach for reducing near wall momentum is to consider tangential slot injection, as developed by Hefner and Bushnell, [56], Bushnell, [10]. A recent review has been provided, again, by Hefner and Bushnell, [122]. Tangential slot injection had been mainly used, during the last decades, for separation control by a lot of aerodynamicists ; the aim sought after was to energize the boundary layer by increasing the local streamwise velocities near the wall. The injection velocity was close to the free-stream velocity and, very often, higher.

However, in order to achieve local skin friction reduction, the injection velocity, v_0 , must be much smaller than U_∞ . At the interface of the slot and boundary layer flow, a mixing layer develops, begins to spray as it evolves downstream, and then reaches the wall. Between the mixing region and the wall, turbulent skin friction decreases, and then relaxes back to its undisturbed value once the mixing region has been in contact with the wall. The rate of mixing between the slot and boundary layer flows determines the exact distribution of skin friction. The control of the mixing region in the turbulent flow could be performed through different techniques, e.g. reference [123] : it should be recalled that the further the mixing region reaches the wall, the more important the decrease of the skin friction drag is. An illustration of such a tangential injection approach is given on figure 20, for both transonic and hypersonic Mach numbers, but for the same injection rate coefficient, $v_0/U_\infty = 0.3$.

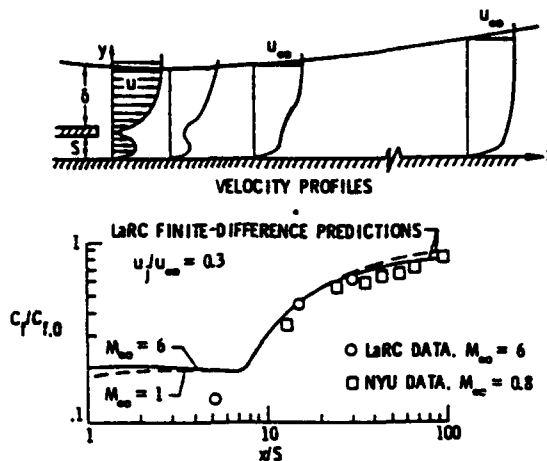


Figure 20: Typical measured and predicted flows downstream tangential slot injection, from Hefner et al [56].

Just downstream of the slot, the reduction in skin friction is a function of the injection rate coefficient ; other parameters are of importance such as injection angle, slot-lip thickness, pressure gradients, ... However, there is not too much literature available for describing slot efficiency. The last paper from Hefner and Bushnell, [122], is very complete since it deals with slot injection in low-speed flow, in high-speed flow. Furthermore, a discussion of aircraft applications, as well as possibilities for future improvements of slot-drag reduction capability are really detailed. So, the authors would advice the readers to refer to as this review paper.

As a summary, it would be reasonable to say that large amounts of local skin friction reductions could be achieved with slot injection. Moreover, such amounts seem to be predictable with present-day numerical technology. However, when thinking to apply such a method to commercial airplane, positive aspects (skin friction drag reduction and thrust due to injection) could be completely counter-balanced by negative aspects (losses associated with collecting, ducting and distributing the slot air, slot base drag penalty). In fact, the main penalty remains the cost of collecting slot air and might explain why "slot-injection has not historically been considered an attractive drag-reduction system", from [122].

2.3.4 Passive Methods for Gazeous Boundary Layers

The most recent researched techniques to reduce the turbulent skin friction drag deal with geometric modifications. These include outer layer and inner layer manipulators, compliant and wavy walls, roughnesses, curvature and some other surface modifications.

2.3.4.1 Manipulators

A concentrated research programme at NASA Langley and many other laboratories in the United States,

India and Japon, together with an increasingly collaborative effort between research groups in Europe and Canada, has established that turbulent skin friction drag could be reduced by suitable scaled devices, depicted on figure 21, such as :

- thin plates or aerofoil outer layer devices (with various acronyms, cf §1) introduced into the external part of the flow itself and commonly referred, in the following lines, to as "outer layer manipulators".

For this type of devices, the classic nomenclature usually involves : α : angle of attack, c : chord length of aerofoil device, l : chord length of flat plate device, h : height within the boundary layer, s : spacing (leading edge to leading edge) of tandem configuration, g : gap (trailing edge to leading edge) of tandem configuration, t : thickness of flat plate device and δ_0 : boundary layer thickness at the leading edge of the upstream device.

- longitudinal grooves or "riblets", which directly modify the wall geometry and, so, the boundary conditions, which will be called "inner layer manipulators".

On the other hand, as regards this passive device, s will denote the spacing of riblet, and h their height : L refers to as the streamwise length of the riblet model.

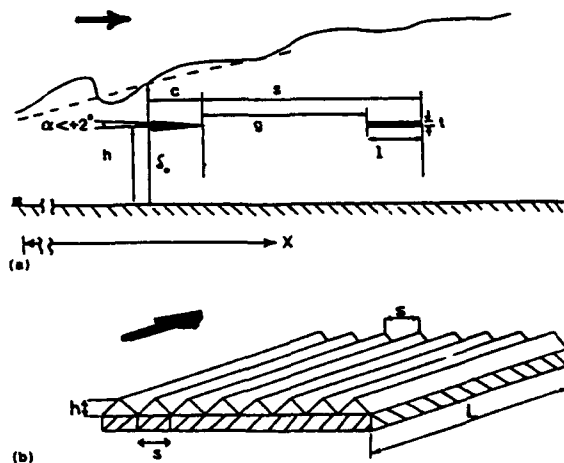


Figure 21: Definition of configurational parameters for : a) outer layer manipulators & b) inner layer manipulators, from Savill [14].

These two passive devices will be examined in detail in the subchapters 3 and 4. Since a number of other review publications have already appeared on this subject of drag reduction (for instance [15] and [16]), the scope of this paper will be to outline the most important results obtained in terms of drag reduction, and to emphasize most recent developments.

Since quite a lot of work (both experimental and theoretical) have been performed either at Cambridge University or at ONERA/CERT or in collaboration with other research groups, these studies will be put forward, without neglecting of course the updated experimental and numerical work.

2.3.4.2 Roughness

For viscous drag reduction, a necessary condition is a provision of a smooth surface. Roughness can affect drag not only locally, but also globally through increased displacement thickness/form drag and as a transition trip. Some viscous drag reduction techniques for turbulent flows can still provide reasonable benefits, even in the presence of such roughness, but others cannot, which justifies why roughness could be successfully combined with other drag reduction means.

The practical importance of determining the amount of admissible roughness for a given set of circumstances is very great, because it determines the amount of labour which is worth spending in manufacturing a given surface. Of course, the answers to such a question will depend on whether the flow under consideration is laminar or turbulent. In the case of turbulent boundary layers, roughness has no effect, and the wall is hydraulic smooth, if all protuberances are contained within the laminar sublayer. In connection with pipe flow it has been found that the condition for a wall to be hydraulically smooth - condition on the dimensionless roughness Reynolds number - is given by the following relationship :

$$\frac{U_\tau \cdot k}{\nu} < 5 \quad (19)$$

It should be noted that this relation could be considered also valid for flat plate cases. In the case of aircraft surfaces, admissible roughness dimensions lie between 0.01 and 0.1 mm ; however, in the case of ships' hulls, admissible roughnesses are of the order of several hundredths of one millimeter, [116]. That latter is a very severe constraint, since it cannot be attained in practice ; in fact, it is always necessary to allow for a considerable increase in drag due to roughness.

Some studies have been developed as regards drag reduction in the marine environment. Within a few hours of a clean surface being immersed in coastal waters colonization by micro-organisms begins, [124]. A slime coating is formed which may grow up to a few millimetres in thickness, which is much more than the afore-mentioned admissible roughness. Thus, drag reduction means inhibiting fouling and reducing paint surface roughness. Hence, underwater surfaces are generally painted with a toxic paint film, leaving aside any question of fouling. In that marine environment, in order to achieve low roughness drag, one has, at first, to ensure that fouling organisms cannot survive on the hull and that antifouling coating would be applied carefully. The next point which is, of course, of some interest will be to be able to maintain such smooth surfaces. Overspray or any polishing polymer could help to some extent. On the other hand,

Townsin, [124], reported that full scale drag reduction has been achieved on a fregate by injecting polymer into the boundary layer, but the mass to be carried for a long lasting effect outweighed the gains in performance. This example would confirm some of the performances of polymer, as regards drag reduction as active devices (cf. 2.3.1.1).

Tani, [125], and Abe et al, [126], considered the case of uniformly distributed roughness in a two-dimensional boundary layer, for instance, sand-grain roughness, which has first been investigated by Nikuradse (1933) in pipe flow. For a two-dimensional turbulent boundary layer, the complete velocity profile could be expressed, outside the viscous sublayer ($y > 50\nu/U_\tau$) by the law of the wake :

$$\frac{U}{U_\tau} = \frac{1}{k} \ln \frac{U_\tau y}{\nu} + B - F + \frac{\Pi}{k} w \quad (20)$$

where U is the mean local streamwise velocity and k the Karman constant equal to $1/A$ (A and B are the constants defined by equation (5), according to the 1968's Stanford Conference). Therefore, F is the constant shift due to wall modification (grooves, roughness, ...) ; it has been sometimes referred not only to as the extra ΔB term in equation (7), for polymers and surfactant solutions when dealing with negative roughness, but also to the roughness function $\Delta U/U_\tau$. Π is the wake parameter and w is the universal wake function of y/δ , if δ denotes the boundary layer thickness. Of course, for smooth wall turbulent boundary layers, the constant shift is equal to zero.

As suggested by Coles, equation (20) could be used for evaluating the friction velocity and the wake parameter, by fitting this expression to the experimentally measured velocity profiles. The initial form of the function $w(y/\delta)$, proposed by Coles, has been :

$$w\left(\frac{y}{\delta}\right) = 1 - \cos\left(\pi \frac{y}{\delta}\right) \quad (21)$$

That latter was then extended in order to take into account several parameters. Integral versions have even been proposed. Coles proposed also an empirical formulation for the wake parameter, valid only for flat plate boundary layer, given in the following equation :

$$\Pi = 0.55 \left[1 - \exp(-0.243\sqrt{\xi} - 0.298\xi) \right] \quad (22)$$

where $\xi = R\theta/425 - 1$. Therefore, if equation (20) is written at the outer edge of the boundary layer, where $U = U_\tau$ and $w = 2$ at $y = \delta$, one ended up with a formulation for the skin friction coefficient, for incompressible flows :

$$\sqrt{\left(\frac{2}{C_f}\right)} \exp\left(k \frac{2}{C_f}\right) = \frac{U_\tau \delta}{\nu} \exp(2\Pi + kB - kF) \quad (23)$$

For a given value of the Reynolds number $U_\tau \delta / \nu$, one could obtain by simple differentiation the correlation between the skin friction coefficient and the constant shift, F , i.e. :

$$\frac{dC_f}{C_f} = \frac{2kdF - 4d\Pi}{1 + k\sqrt{\left(\frac{2}{C_f}\right)}} \quad (24)$$

Thus, a skin friction reduction is obtained when the numerator is less than zero ; for instance, for a given wake parameter, the decrease of C_f is straightly related to the decrease in the shift value.

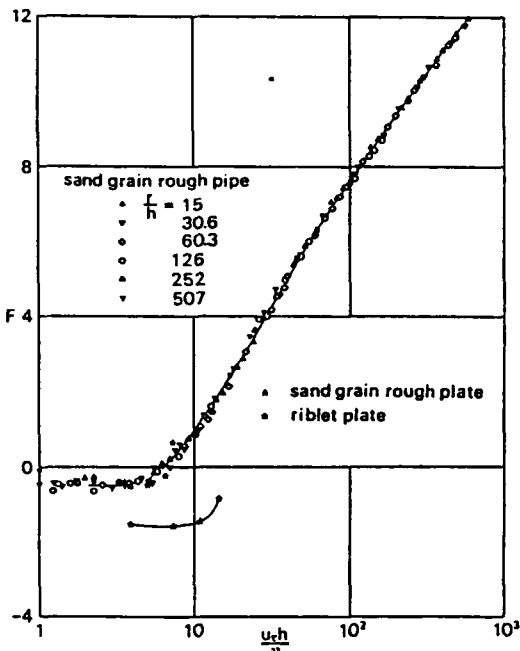


Figure 22: Roughness shift plotted against roughness Reynolds number, for turbulent flows in sand grain rough pipe, over sand grain flat plate and over riblet surfaces, from Abe et al [126].

This approach has at first been applied by Tani, or Tani and his colleagues to Nikuradse's experimental data for sand grain rough pipes, (see [125], for instance). Results have been plotted on figure 22, taken from [126], in a diagram : roughness shift F versus the non-dimensional roughness height $h^+ (=hU_\tau/\nu)$. Then, it should be noted that results recorded for different roughness heights, covering different ranges of h^+ , collapse roughly onto a single curve. These authors found that F was negative for a limited range of the roughness Reynolds number ($h^+ < 6$), but became positive with an increase of h^+ .

These observations pointed out in rough pipes have been confirmed for turbulent boundary layers developing over flat plates roughened with sand grains, [126], for almost the same range of r/h and/or δ/h , if r denotes the pipe radius and δ the physical boundary layer thickness. In their experiments, Abe et al, [126], considered two sizes of sand grain, $h=0.2\text{mm}$ and 0.4mm for unit Reynolds number, ranging approximately between 450 and 850 per mm. For values of U_0h/ν less than 170, skin friction reductions up to 7% were recorded. Therefore, values of F for sand grain rough plates are in good agreement with rough pipe data. However, according to the authors, the main difference between the two sets of data is that the wake parameter, Π , is increasing for rough plates but decreasing for rough pipes.

In addition to the main experiment, Abbe et al performed similar measurements with a plate coated with riblet film, manufactured by the 3M-Company, having a symmetric V-shape such as $h=s=0.152\text{mm}$. Data are also plotted on figure 22. The shift F is negative for the explored values of h^+ , for which net drag reductions have been achieved. When F will become positive, the riblet acts then as a drag-increasing roughness. It should be observed that the change of sign for F , in the riblet plate case, appears to be a little bit smaller than the observed experimental values. It is interesting to note that a distributed roughness, such as sand grain or those tested by Nikuradse, follows what is called the k -scaling. Indeed, the main difference between k - and d -type groove roughness consists in the scaling of the shift or roughness function with kU_τ/ν or dU_τ/ν respectively ; k usually is equal to the roughness height, while d refers to as the boundary layer thickness.

With reference to the results reported by Tani and his colleagues, it might be said that the sand grain roughness behave somewhat similarly to that of a riblet surface, though the amount of drag reduction is much smaller. Nevertheless, as mentioned by Tani, [125], "the sand-grain roughness has the advantage of insensitiveness to flow direction, escaping from such penalties as for riblet non-misalignment".

It has long been known that the drag of d -type surfaces is anomalously low compared to similar scale k -type roughness and recently Japanese researchers have shown that sparsely spaced d -type transverse cavities, with spacings 10 and preferably 20 times their width or depth may also offer drag savings over certain low Reynolds number ranges. Following a joined Rolls-Royce/British Maritime Technology sponsored project in Cambridge University, high speed video records of low Reynolds number flow, as well as measurements of the mean and fluctuating quantities, over sparse d -type cavity roughness had confirmed earlier suggestions regarding possible drag reduction mechanisms (see [22]), and lent some support to the Japanese findings. Furthermore, extra observations also indicated that there might be possible additional benefits to be gained by combining such surfaces with aerofoil manipulators, since the initial effect of these latter was to stabilise the flow within such cavities in its immediate downstream vicinity ; furthermore, when the aerofoil wake reaches the wall fewer disturbances were observed (see [22]).

More recently, experiments were performed by Fanourakis and Savill, [127], in order to try to measure the drag of sparse d -type roughness, thanks to a special floating element balance. Experiments were conducted in a low-speed blower tunnel facility for Reynolds numbers, based upon cavity depth, lying between 600 and 3,200. The results obtained represented the first set of direct drag balance data for such surfaces and confirmed previous momentum balance measurements made at low-speed by Tani and co-workers and at high subsonic Mach numbers by those same authors. These latter mentioned also the study of future configurations involving other existing

control techniques, such as incorporating vinyl riblet films with a *d*-type surface, which had already been developed by Osaka and Mochisiki, [128]. Within the explored Reynolds number range ($R\theta$: 750-1, 200), Osaka et al observed that the local skin-friction of the *d*-type rough surface, modified by the presence of longitudinal ribs, is definitely small compared to that of the smooth surface at the same value of the Reynolds number.

Bandyopadhyay, [129], suggested also to look at the effect of outer layer manipulators in rough wall turbulent boundary layers. The examined passive devices consisted of thin flat plates set in a tandem configuration. The considered wall conditions are *d*-*k*-type transverse grooves and also sandgrain roughnesses. His conclusions were that the absolute reductions in the local wall shear stress are similar in both the rough and smooth walls. The efficiency of outer layer devices is not increased in a rough-wall boundary layer compared to their performances in a smooth wall boundary layer. The author believed that this might come from the fact that the manipulators are not as effective on the pressure component of the rough wall drag.

2.3.4.3 Curvature

It is known from Prandtl's early works that a streamwise convex surface curvature has a stabilizing effect on boundary layers. Indeed, he attempted to quantify curvature effects through the introduction of a curvature parameter into a mixing length model. A possible application of this on turbulent boundary layers is to lower skin friction coefficient below what would occur in a flat surface at the same Reynolds number.

Bradshaw, [130], provided an excellent historical review of these initial studies, as well as further insights into the effects of curvature. In fact, he parameterized the curvature effects through appropriately chosen ratios of the extra source terms to the production terms appearing in the Reynolds stress transport equations in both two- and three-dimensional flows. Extra strain rates are "extra" in the sense that they are additional to the usual shear $\partial U / \partial y$, and they are generally introduced by changing the flow geometry. It is widely known that extra strain rates can have significant and long-lasting effects on the behaviour of turbulent boundary layers. The nature of the response depends upon the strength of the perturbation as well as the distance over which it is applied, [131]. The response depends also on the sign of the extra strain rate. For example, concave curvature is destabilizing and tends to increase turbulence length scales and enhance turbulent activity, whereas convex curvature is stabilizing and reduces the length scales and suppresses turbulence mixing.

Experimental results have shown that the effects of convex and concave curvature on boundary layers are completely different, even qualitatively. Indeed, convex curvature tends to attenuate the pre-existing turbulence apparently without producing large changes in statistical average eddy shape, while concave curvature resulted in the quasi-inviscid generation of longi-

tudinal vortices ("Taylor-Görtler" vortices), with significant changes in the turbulence structure, [131]. An example of strong convex curvature is given in the experiments conducted by Gillis and Johnston, [132]. The flow passed from a flat surface with 90° of turning and then onto a flat recovery surface. They observed that the disappearance of the curvature effects was an extremely slow process. Indeed, the streamwise evolution of the skin friction is plotted on figure 23 : the sudden removal of strong convex curvature is followed by a very slow recovery of the boundary layer.

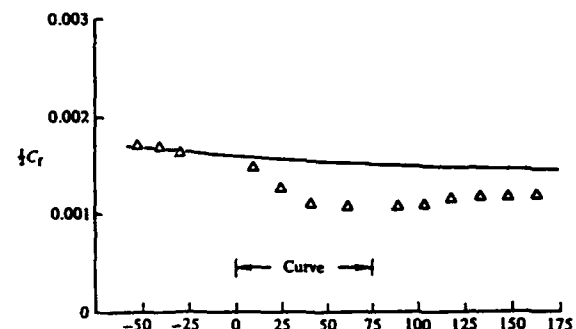


Figure 23: Streamwise evolution of the local skin friction coefficient, Δ : data, - : numerical flat wall prediction for $\delta/R \approx 0.1$, from Gillis et al [132].

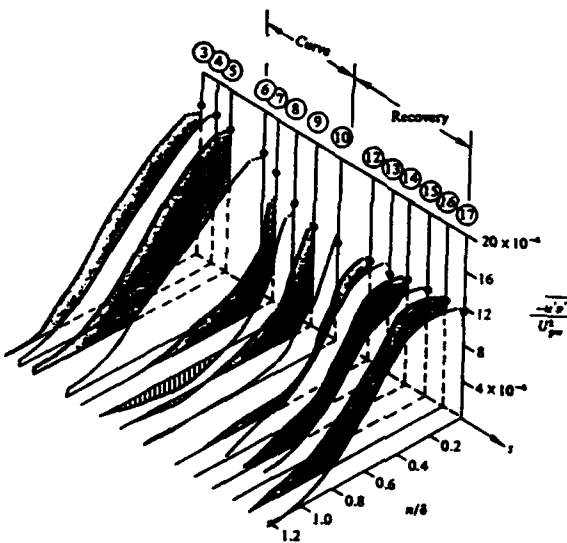


Figure 24: Streamwise evolution of the shear stress profiles, from Gillis et al [132].

For this same set of experiments, figure 24 is an example of isometric plot of the measured shear stress profiles at different streamwise abscissa, for $\delta/R \approx 0.1$. On that figure, the closed circles correspond to wall shear values calculated from Clauser's plot ; the agreement with the recorded values is rather good. Therefore, the shear stress has been non-dimensionalised by $U_p w$, the potential velocity taken at the wall.

It should be noted important variations of the profiles, especially in the curved area, where large regions of negative shear stress could be pointed out. As mentioned by the authors, for a curved wall boundary layer, the total production is positive in the inner layer, whereas in the outer layer the positive and negative production terms are about equal, justifying why negative shear stress values could be obtained. So, the absence of shear stress in the outer layer (in the outer 70% of the boundary layer) means there is no production mechanism, and consequently the turbulence there decays as it moves downstream. Consequently, the outward turbulent diffusion could be almost totally eliminated.

For the purpose of drag reduction, the stabilizing influence of convex curvature appears to be the most interesting case. Moreover, quite small curvature inputs (i.e. $\delta/R \approx 0(0.1)$, if R denotes the radius of curvature) produced tremendous effects, not only on some of the fluctuating quantities but also on the mean local skin friction coefficient. Although more experimental work is needed before one could correctly understand the effect of curvature, practical applications have already undergone. Some practical drag-reducing configurations had been suggested by Bushnell, [10], as regards the nose regions of axisymmetric bodies. Moreover, Smits, [131], showed that, in a body of revolution, the drag-reducing behaviour of a convex curvature could be enhanced by combining it with streamline divergence over the nose. Thus, the effect of combining strain rates appeared to be favourable, although streamline divergence alone is known to be destabilizing. Therefore, one has to be aware that the application of convex curvature requires the introduction of short regions of concave curvature ahead of each region of convex surface as well, [129].

Besides experimental studies, a lot of numerical work has been performed in parallel ; even though a plethora of turbulence models have been proposed, "none seems to do a good job over a range of flows", as quoted by Gatski and Savill, [133]. For some cases, the models tend to deteriorate as the curvature is increased. Bandyopadhyay, [134], claimed that modelling of curved flows is difficult because the physics of the flow is not well understood. Nevertheless, Bandyopadhyay suggested a mixing-length model to be applied in turbulent boundary layers over curved surfaces. He concluded that the convex curvature concept could be applied to an axisymmetric nose-body, without causing any separation, if application is made in several stages of short regions of curvature. Then, the "three-stage nose-body" had been put forward (cf. figure 25 taken from [134]). Therefore, on that same figure, the C_f distribution for a usual half-elliptic nose-body is also included for comparison. Above the main cylinder, the skin friction coefficient does not relax back to the undisturbed value. Taking into account the variations of the pressure drag (by considering the equivalent-area half elliptic nose) and of the pure friction drag, and above all trying to estimate as precisely as possible the drag variations, Bandyopadhyay concluded that the three-stage nose-body yields a net

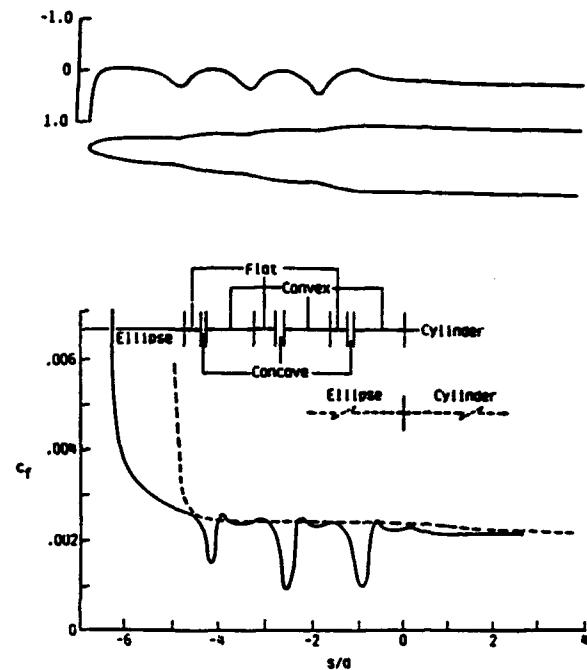


Figure 25: Three-stage nose-body ; computed surface pressure and skin friction distributions, from Bandyopadhyay [134].

drag reduction of almost 5%.

2.3.4.4 Miscellaneous

As reported by Bandyopadhyay, [11], attempts have been carried out in the past to develop surface wall coatings for use in air. When applied to some wing section, viscous drag had been reduced. It appeared that such a decrease had been recorded during flight tests, because the surface was smoother ; in other words, the drag reduction did not result from a positive alteration of the turbulent boundary layer.

2.3.5 Combined methods

Some combinations of methods will be detailed in Chapter 5, but others will not ; this is the reason why some references have been added for some topics which will not be detailed herein, so that any interested reader could refer back to them. Nevertheless, it should be mentioned :

- Combination of Passive Devices :

- inner and outer layers manipulators (riblets and LEBUs) : Walsh and Linde-mann, [135], Coustols and Cousteix, [136], Savill et al, [137], Nguyen et al, [138] ;
- outer layer manipulators and roughness : Bandyopadhyay, [129], Fanourakis and Savill, [127] ;

- inner layer manipulators and roughness : Osaka and Mochizuki, [128], Fanourakis and Savill, [127] ;
- ...etc
- Combination of Active Devices :
 - polymer solutions and particle additives ;
 - selective suction and injection : Gad-el-Hak and Blackwelder, [118] ;
 - ...etc
- Combination of Passive and Active Devices :
 - polymer solutions and inner layer manipulators ; Choi et al, al, [86], Reidy and Anderson, [139], Rohr et al, [140] ;
 - surfactant and inner layer manipulators : Reed and Weinstein, [141] ;
 - polymer solutions and outer layer manipulators ;
 - polymer solutions and coatings : Semenov, [104], Kulik, [105] ;
 - polymer solutions and roughness : Thiel, [142], Bewersdorff and Thiel, [143] ;
 - injection with either inner or outer layer manipulators ;
 - suction with surface modification involving either slotted surfaces surfaces : Hybrid suction : Wilkinson et al, [117], or grooved surfaces : Wilkinson et al, [12] ;
 - suction with outer layer manipulators ;
 - suction with roughness elements : Roon and Blackwelder, [120], Wilkinson et al, [12] ;
 - acoustic forcing and outer layer manipulators : Bardakhanov et al, [144] ; Zurich ;
 - ...etc

3 Inner Layer Manipulators : Riblets

For a long time, it has been believed that the smoother and the cleaner the wall, upon which the turbulent boundary layer developed, was, the smaller the turbulent skin friction drag would be. It would seem rather obvious that the viscous drag is less than upon a rough surface, but one has to be aware that, now, it is recognised that some non planar geometry-type surfaces could be very useful under some circumstances. This is, of course, true for grooved surfaces or riblets, but also for some other "rough" surfaces, now.

As described by Walsh in his rather recent review paper, [15], there have been a couple of distinct directions, which lead to turbulent drag reduction through surface modification. Indeed, the first appearance of such an idea is in a 1937 German patent application,

from Kramer (that reference could be found in [15], for instance). In this application, it was suggested that suspended streamwise wires could be used to reduce skin friction by shielding the wall from turbulent fluctuations. In 1956, people from Douglas Aircraft Company (reference found in [145]) attempted unsuccessfully to delay transition thanks to a riblet-like structure ; their findings were that fluctuations leading to transition would be damped.

In fact, Liu et al, [146] are the first authors to have looked at the behaviour of a wall surface modification. They considered thin flow-aligned rectangular fins about the same size as the low streaks ; in fact, the height and the spacing expressed in wall units covered the ranges $h^+ : 45-111$ and $s^+ : 180-373$, respectively. Compared to a smooth wall, they recorded 3 to 4% nett drag reduction and 20-25% decrease in the bursting frequency. Since these first experiments, a lot of research has been undertaken in the world with different surface geometries.

Since a number of other review publications have already appeared on this subject of drag reduction by inner layer manipulators, [12], [14], [15] or [147], the scope of this section has been restricted to consider primarily research conducted at ONERA/CERT or in collaboration with other research groups. However, all the following developments are being reviewed with the emphasis being placed on the latest results obtained for riblets in Europe and worldwide (at least, to our knowledge).

3.1 Global Performances

It has been now widely demonstrated that turbulent skin friction drag could be reduced with a modified wall geometry. Besides the tremendous enhancement of wetted area, the percentage of which depends upon the groove cross-section (L-, U- or V-shaped grooves), maximum nett friction drag reductions of almost 10% have been recorded. Whatever groove cross-section is concerned, all the examined models, the length of which is L , would allow to evaluate the effect of rib spacing (s), rib height (h) and also aspect ratio (s/h).

The measurements of the skin-friction reductions require, therefore, a great accuracy. Discrepancies between various data sets had been attributed not only to experimental uncertainties in measuring small effects, but also to apparent sensitivity of riblet performance to fine details of their geometry possibly amplified by machining or moulding processes. The latter problem has largely been overcome by the development of adhesive-backed vinyl riblets, supplied for most of them by the 3M Company and for some of them by the Hoechst Company. Availability of those has led to far more consistent results.

Extensive experimental studies from Walsh [154], Walsh et al [135], Squire et al [148], Sawyer et al [149], Enyutin et al [151], Coustols [152] and Coustols et al [150], [153], for instance, have been concerned with drag estimates from either local or global measurements in order to determine the most effective riblet geometry and dimensions, for subsonic as well as trans-

sonic and supersonic flow conditions.

3.1.1 Low-speed data

3.1.1.1 Zero-pressure gradient flows

At NASA Langley Research Center, a complete experimental investigation of such passive drag-reducing devices was performed by Walsh [154], and Walsh and colleagues [135], [147], [155].

They have tested many different groove geometries (cf. figure 26) and found that the optimum shapes for drag reduction have a sharp peak protruding into the flow and have a height and spanwise spacing of the order of the viscous sublayer thickness. Nett drag reductions up to 8% have been recorded on the most popular symmetric V-shaped riblet, for which the aspect ratio (s/h) is equal to one.

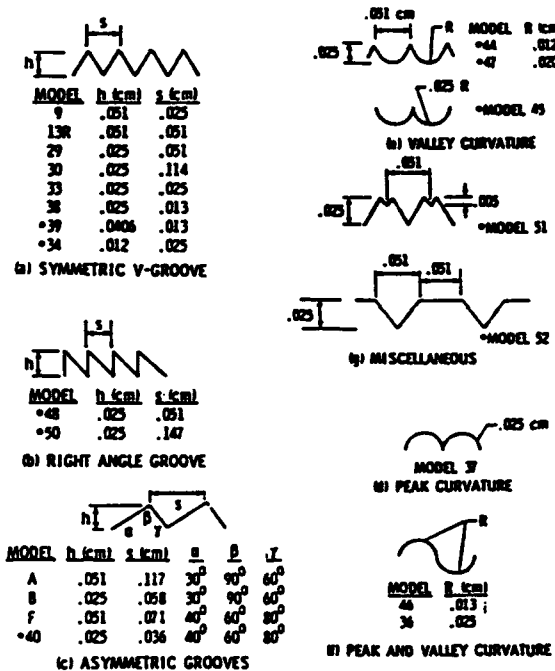


Figure 26: Examples of grooved surfaces tested at NASA Langley, from Walsh [154].

In the experiments carried out at NASA Langley, the drag reduction performances of riblets has typically been measured using both velocity profiles and drag balances. However, in a few experiments, where the groove size was relatively large, the velocity gradient at the wall was used in order to determine the local skin friction. Examples of drag data, for several symmetric V-shaped vinyl riblet films, the height of which varied from 0.0013- to 0.0060-in., are given on figure 27, taken from [147]. The data band labeled "low-speed film data" represents a 4% band that fits all the symmetric riblet film data except for the data of Coustols, [152]. Comparisons are made with other set of data, which unfortunately have not been

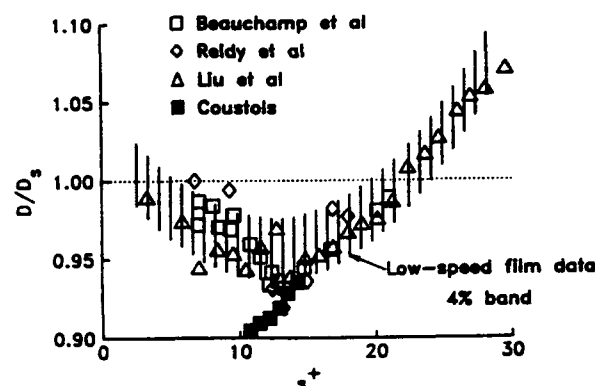


Figure 27: Examples of low-velocity drag data for riblets, from Walsh and Anders Jr. [147].

recorded using the same measurement technique. Indeed, Beauchamp et al., [156], determined the riblet performance by measurements of the terminal velocity of a body in drop tests in a water tank ; Liu et al., [173] from pressure drop in a pipe flow ; Reidy et al., [139] and Coustols, [152] evaluated grooved surfaces efficiency through changes in momentum thickness. It should be noted that data from Reference [152] do not follow the dominant trend of the other data.

At ONERA/CERT, Coustols, [152], and Cousteix, [150] carried out experiments in a wind-tunnel at low subsonic free-stream speeds with nominally two-dimensional flows developing on the lower floor of the test section, under zero-pressure gradient conditions. So, the influence of thin longitudinal striations has been considered : several machined aluminium surfaces as well as vinyl models having an adhesive backing have been tested. The performances of these devices have been judged from differences between momentum thicknesses obtained through hot-wire surveys and evaluated just behind the trailing edge of the ribbed surface. Since the variations of θ along L have to be as large as possible to avoid too much scattering on data, $L=0.64m$ has been scrutinized for estimating variations of the friction drag coefficient, C_d . One has to be aware that the amount of drag reduction or increase might be subject to discussion since the momentum balance technique is very depending upon a lot of parameters, which might not be completely controlled. Thus, the results have to be discussed in terms of "tendency", and have to be analysed from a comparative point of view.

For instance, for symmetric V-shaped models, nett drag reductions were achieved when $h^+ < 13$, where h^+ denotes the rib height scaled with the inner variables of the turbulent boundary layer : ν and U_τ , the friction velocity. The effect of varying the aspect ratio (s/h) has been studied with machined models (figure 28). Data from the different models collapse better when plotted versus h^+ than s^+ ; h^+ appears to be some "crucial" parameter. Therefore, it appears that the zero drag reduction cross-over point is smaller when s/h increases from 1 to 3, [152]. It should be

recalled that the greater the ratio s/h is, the smaller the increase of wetted area is. However, one does not have to forget the extreme sensitivity of results to the quality of the machined surface... Considering a vinyl model having the same triangular shape ($s/h=1$), a maximum of net drag reductions was recorded for $h^+ \sim 7 - 8$; the zero drag reduction cross-over point was h^+ close to 17, which agreed with the machined model and with experiments performed by Walsh and Lindemann, [135], on the same type of riblet film.

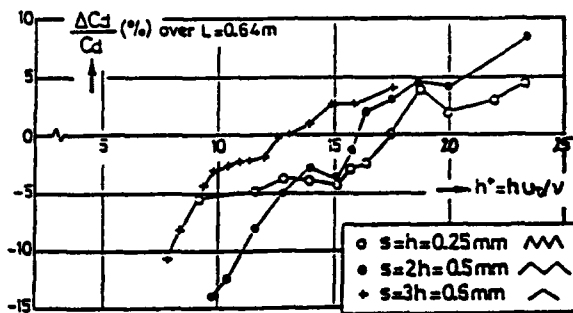


Figure 28: Synthesis of drag data from machined aluminium models ; influence of aspect ratio, from Coustols and Cousteix [150].

Influence of angle of yaw

It was obtained that grooved models keep a beneficial effect for angles of yaw up to 20° ; in that case, the ribs are aligned at a given angle to the direction of the mean external flow. The average skin-friction reductions are lower than those recorded without any angle of yaw, and the zero drag reduction cross-over point is smaller in terms of h^+ [150], [152]. These results are consistent with those obtained by Walsh and Lindemann, [135], for angles of yaw slightly different : 15° and 30° ; for the explored range of $s^+ : 10-50$, smaller reductions were recorded at 15° , while drag increases were obtained at 30° .

Influence of curvature

Drag data from a vinyl model ($s/h \approx 3.5$), the cross-section of which is sine-shaped, have been compared to a symmetric V-shaped machined aluminium model, [150]. Only couple of percents of drag reduction have been recorded; furthermore, the zero drag reduction cross-over point was close to 6, instead of 13 (cf. figure 28). These results are consistent with those obtained at NASA Langley, [154], and [135], and showed up that curvature has some negative effect on drag reduction performance. Unfortunately, it has not been possible to dissociate the influence of peak or valley curvature. However, one could believe that increasing the radius of peak curvature made larger the area exposed to maximum shear stress and, consequently, would diminish the possible average skin friction reduction. Then, it was suggested that a slight additional benefit might be achieved by rounding the grooves and reducing the included angle of the peaks to less than 25° , according to Bechert et al's results, [158]. In fact, the use of such U-profile

grooves had emerged almost independently from a different line of research pursued by researchers in Germany, where interest in these was initially stimulated by the suggestion that shark scales, which have a similar cross-section profile, non-dimensional size and flow aligned, might also act in a similar manner.

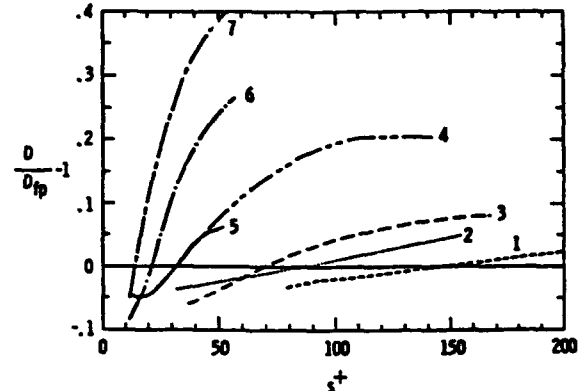
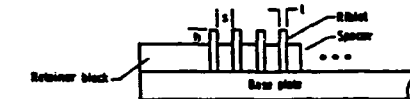


Figure 29: Low-speed drag data for thin-element riblet models ; Model 1: ($s/h=14.2$), 2 (8.5), 3 (6.2), 4 (3.2), 5 (2.6), 6 (1.25), 7 (1.0), from [12].

Thin-element or L-shaped riblet models

Initial drag reduction success was with triangularly shaped riblets and most research, today, is performed with this type of riblet. However, Wilkinson et al, [12] and/or Lasos and Wilkinson, [157] have reported equal magnitudes of drag reduction with very thin, rectangular type riblets, called thin-element riblets. Direct drag data were acquired for several series of thin-element models, as shown on figure 29, taken from [12].

Drag reductions might persist over $s^+ = 140$! Nevertheless, that figure clearly revealed the influence of the riblet aspect ratio (s/h) on drag. On that figure, the models are numbered in order of decreasing aspect ratio. However, if one had plotted results versus h^+ , there would be much less discrepancies between curves and, for instance, the zero drag reduction cross-over point would not vary so much.

3.1.1.2 Non zero-pressure gradient flows

It is rather difficult to measure skin friction variations under pressure gradient conditions, since drag estimates based either on drag balance measurements (errors due to Δp on the floating element) or on changes in momentum thickness are not sufficiently accurate. This is the reason, why Coustols, [152] and Coustols and Cousteix, [138] controlled the behaviour of couple of internal devices, set upon the upper side of an aerofoil, through wake surveys. Then, total drag variations (pressure and friction drags) would be recorded ; skin

friction drag reductions or increases would then be deduced, knowing the percentage of pressure drag in the total drag balance, through computations, for instance. It is believed that such a method is sufficiently accurate to measure small changes in the wake momentum thickness.

The considered aerofoil was a LC100D one operating at two chord Reynolds numbers, R_c , close to $5.30 \cdot 10^5$ and $7.95 \cdot 10^5$ ($c=0.4m$). The transition was tripped on the upper side at $x/c \approx 2.5\%$ from the leading edge. Two riblet models, having an adhesive backed film and a symmetric V-shaped ($s/h=1$), have been applied between $x/c=0.20$ and 0.95 : $h=0.152mm$ and $0.076mm$. On the other hand, upwards to the leading edge as well as downwards to the trailing edge, a smooth vinyl sheet has been used. Thus, the reference configuration consisted of an aerofoil the upper side of which is entirely covered with smooth vinyl film from the tripping wire down to the trailing edge. Let us mention that the thicknesses of the ribbed and smooth films were almost identical; the former depending in fact upon the ribs height, [152], [136].

On the upper side of the aerofoil, the higher the angle of attack, α , was, the stronger the adverse pressure gradient was. Replacing smooth film by ribbed one did not bring noticeable modification on the pressure field. The parameter :

$$\beta = -\frac{\delta}{U_r} \cdot \frac{dU_e}{dx} \quad (25)$$

where δ denotes the physical boundary layer thickness, has been computed through a boundary layer code when introducing the experimental pressure distribution; its average value along the manipulated length varied between 0.018 (at $\alpha = 0^\circ$), and 0.255 (6°), [136].

The effect of grooved surfaces has been determined through Pitot tube surveys performed at $x/c=1.5$. Boundary layer computations have shown that the h^+ parameter had a smooth evolution with x , except along the rear part of the aerofoil because of the camber; moreover, its average value along the manipulated length was independent of α at least up to 4° . For the lowest angles of attack, significant nett drag reductions (2 - 2.5%) have been recorded. At $\alpha=2^\circ$ and for $R_c=5.30 \cdot 10^5$, by integrating the computed local skin-friction coefficient one could estimate the contribution of the friction drag from the upper side: 40% of the total drag. Then, since 75% of the suction side is covered with riblet, a 2.1% reduction of the total drag at $h^+ \sim 10$ corresponds to a 7% reduction of the friction drag over the manipulated length. This is consistent with the usual recorded values for zero-pressure gradient flows. For higher angles of attack, there is no more drag reduction; the interpretation of the results is very difficult since a separation bubble occurs close to the leading edge and, moreover, flow visualisations have shown that the boundary layer separated along the rear part of the aerofoil.

So far, in non-zero-pressure gradient flows, the influence of ribbed surfaces has raised up very little interest. Let us point out that experimental results have

been obtained by Pulvin, [159], in a subsonic diffuser ring have shown that "riblets" keep a beneficial effect as long as β^* is rather small. This pressure gradient parameter, β^* is the Clauser parameter defined as :

$$\beta^* = \frac{\delta_1}{\tau_w} \cdot \frac{dp}{dx} \quad (26)$$

where δ_1 is the displacement thickness. Maximum skin-friction reductions of the order of 5 - 6% for $\beta^* < 0.2$ at $h^+ \sim 13$. Drag reductions decreased to 3-4% for $\beta^* = 0.2$ and to 0% for $\beta^* > 0.6$.

In very recent experiments, Nieuwstadt et al, [160], examined the influence of adverse pressure gradients. Turbulent wall shear stress had been measured directly by means of a floating element; the accuracy of the measurements was a bit less than 1%. Maximum skin friction decreases, up to 6%, were recorded when considering sawtooth riblets ($s/h=1$), for values of β^* smaller than 1.5.

3.1.1.3 Three-dimensional flows

In order to go closer to flight applications, the effect of small streamwise grooves on a slender body, was considered by CERT in the F2-ONERA/Fauga wind-tunnel, [161]. The model was a 1/38th scale Airbus-type fuselage. The Reynolds number range, based upon fuselage length ($l=1.34m$), was $:R_l : 2.8 \cdot 10^6 - 8.0 \cdot 10^6$. Transition was tripped with a carbon-dum band at 0.165m from the body nose. The cross-section of the vinyl riblet model, was triangular such that $s=2h=0.12mm$. The adhesive backed film overlays the cylindrical part of the model with a constant circular section; then, 48% of wetted area was covered with riblet film. The variations of the drag coefficient have been given through an internal one-component drag balance.

Nett total drag reductions were recorded over the h^+ range : 5 - 12. Boundary layer computations, performed using flat plate approximations, revealed that the contribution of the pressure drag was close to 20%, for the considered R_l range. Then, a maximum of 3.5% reduction on the friction drag coefficient was recorded for the lowest values of h^+ . This first application to slender bodies gave cheerful results since substantial skin-friction reductions were obtained, with a maximum for a rib height of approximately $5 \nu/U_r$. Nevertheless, the drag reductions have been underestimated because of the boundary layer tripping just ahead of the leading edge of the riblet model, the fac-ing step effect (the reference configuration would have been fuselage covered with a smooth vinyl film over the same manipulated length), the rather small percentage of ribbed surface compared to the total wetted area and, at last, the low values of the tests Reynolds numbers. Indeed, the pressure drag is rather important, due to separation on the rear part of the fuselage, and consequently the recorded drag benefit is under-rated facing flight applications, [161].

These experiments pointed out the extreme sensitivity of riblet drag performances to a lot of parameters, although in this specific experiment drag variations were carefully measured...

However, in case of future applications of such internal passive devices to subsonic transport aircraft onto, not only the fuselage, but also the wings, fin and horizontal tail, it is necessary to analyse the behaviour of "riblets" in three-dimensional boundary layers. To our knowledge, very little experimental work has been completed as regards turbulent manipulation of three-dimensional boundary layers, at low speeds. Indeed, "riblets" have been applied to the hull of a one-third scale model of an Americas cup yacht, [86], and the "MOBY-D" high-speed buoyancy propelled vehicle, [163].

Thus, an experimental study has been undertaken at ONERA/CERT ; "riblets" have been applied on both sides of an ONERA D section aerofoil, set at an angle of sweep of 22.5° , for two chord Reynolds numbers : $2.65 \cdot 10^5$ and $4.25 \cdot 10^5$, [162]. The performance of riblet models have been determined through total drag variations estimated from Pitot tubes surveys in the aerofoil wake, one chord length behind the trailing edge. Grooved surfaces have been applied between $x/c=0.15$ and 1.00 , on the upper as well as lower sides of the aerofoil. Therefore, grooves have been aligned with the free-stream flow direction.

In order to estimate as carefully as possible the effect of streamwise grooves not only on the total drag coefficient but also on the skin-friction drag coefficient, a couple of features have to be mentioned : the contribution of the friction part in the total drag balance represents almost 50% and corrections due to the afterbody drag penalty (the grooved surface was applied onto the trailing edge) have been taken into account.

Drag reductions were recorded for each of the three tested models over the range, $h^+ : 2.5-13.5$. Maximum decreases up to 5-6% have been obtained ; these maxima are somewhat weaker than those generally recalled when manipulating two-dimensional turbulent boundary layers. That could be attributed not only to three-dimensional effects, but also to the fact that grooves were applied on the last 10% chord length of the aerofoil where strong adverse pressure gradients induced important wall streamlines deviations since the layer is close to separation. Nevertheless, the "riblet" data have been recorded when the grooves are approximately aligned with the infinite free-stream flow direction. It is likely that if the crests had been set in a direction normal to the leading edge of the aerofoil, either small decreases or even increases would have been measured, since the deviation to the wall streamlines and *a fortiori* to the external streamlines be too important.

Experiments with drag reducing riblet film on a 1:4.2 model of a DORNIER Do 328 commuter aircraft have been carried out in the large German-Dutch Wind Tunnel (DNW), by Van der Hoeven and Bechert [164]. Drag variations were determined through a six-component strain gauge balance located inside the model. Measurements were performed for both natural and tripped transition on wings, fuselage and nacelles. 82% of the aircraft model, including large parts of the wings and nacelles, were covered with the vinyl riblet film, although the considered ri-

blet film did not seem to be of the optimum size for the wing, [164]. In this set of experiments, besides the measurements discrepancies due to the lack of reliability of the wind tunnel balance, data revealed drag reductions by 1-6% with riblet film (reduction on the conventional drag coefficient minus the induced drag contribution from the wings). The upper value did not seem realistic, but as quoted by the authors "the data did confirm previous estimations of 2 -3% total drag reductions". An important result is that grooved surfaces did not cause premature separation. Therefore, it is interesting to note that both lift gradient and maximum lift coefficient were marginally increased by the riblet film, but only by 1 and 1.5% respectively.

3.1.2 Transonic data

The following step was to continue the evaluation of such inner layer manipulators at transonic speeds in order to provide data on riblet performance applicable to transport aircraft fuselage and wings.

3.1.2.1 Zero-pressure gradient flows

Experiments were conducted in the T2-transonic cryogenic wind tunnel of ONERA/CERT. That wind tunnel is a closed circuit pressurised (up to 4 bar) facility. Operational runs can be carried out in cryogenic runs, with self-adaptive walls. The flow is driven by an injector system (air) and can be cooled down to 110 K by a liquid nitrogen injection. The aim of upper and lower adaptive walls is to create an unconfined flow around the model, in a limited section, by controlling boundary conditions. The dimensions of the test section are : 1320mm length, 390mm width and 370mm height.

So, the efficiency of grooved surfaces has been checked on an axisymmetric body. The turbulent boundary layer, which is going to be manipulated by altering the wall geometry, develops along a cylinder-type body, under zero-pressure gradient conditions. For transport aircraft applications, this arrangement deals with a rather important part of the fuselage. The model is a cylindrical body of 600mm length, 80mm diameter, with an upstream elliptical nose of 150mm length. The model axis has been aligned with the external free-stream flow direction. The boundary layer which develops along that ogive has been tripped with a carborundum band (average height close to 0.06mm) at 30mm from the ogive nose ; this location is far away upstream so that the turbulent boundary layer will be fully turbulent when it reaches the leading edge of the riblet model. In order to judge of ribs performances, the diameter of the cylinders has been reduced to 79.8mm ; then, whatever riblet model is considered, the ribs trough plane is approximately mounted flush with the adjacent upstream smooth part, [152], [153]. So, this arrangement allows to avoid the facing step effect. Four symmetric V-groove riblets, manufactured by the 3M Company in an adhesive backed film, with an aspect ratio (s/h) of one, have been tested : $h = 0.023, 0.033, 0.051$ and

0.076mm. The turbulent boundary layer length, manipulated by such models, is then : $L=550\text{mm}$, which means that the percentage of manipulated wetted area is close to 77%.

Drag measurements have been completed using an internal five-component balance. The observed accuracy on the drag coefficient is equal to $5 \cdot 10^{-4}$ for $C_d=0.1$. That accuracy became twice larger when taking into account the measurement uncertainties (variations of free-stream Mach number, stagnation pressure, ...) but is small enough to define, precisely, drag reductions or increases due to grooved surfaces.

The tests have been performed at ambient stagnation temperature ; the Reynolds number R_L , based on the manipulated length L , varies from $3.8 \cdot 10^6$ up to $18.7 \cdot 10^6$, for a free-stream Mach number range, $M_\infty : 0.3-0.815$ and a stagnation pressure range : $1.1-3.0$ bar. At low-speed tests, it has been more difficult to reproduce faithfully the drag measurements. However, at $M_\infty \simeq 0.7$ (resp. 0.4) the data scatter corresponds to $\Delta C_d/C_d \simeq 1.3\%$ (resp. 3.5%), which is quite acceptable, [152].

Whatever the value of M_∞ is, the local Mach number is practically constant all along the manipulated length ; this could be achieved because of the existence of adaptive walls in the T2 tunnel. Knowing these distributions, boundary layer computations were performed and revealed that the contribution of the pressure drag was rather weak ($\simeq 3-5\%$) and almost independent of the Reynolds number, [152].

The results for the four riblet models collapse best when non-dimensionalised by \bar{h}_w^+ , where the rib height is scaled with respect to the inner variables of the turbulent boundary layer taken at the wall : $\bar{h}_w^+ = (h/\nu_w) \cdot \sqrt{\tau_w/\rho_w}$. Of course, \bar{h}_w^+ decreases with respect to the streamwise coordinate, because of the "Reynolds effect". However, its streamwise variation is smooth so that it is possible to define an average value, \bar{h}_w^+ , integrated all along the riblet model length. Then, that value is representative of the rib geometry for given test conditions.

Nevertheless, maximum turbulent skin-friction reductions close to 7-8% have been recorded for \bar{h}_w^+ close to 10-15 ; however, when $\bar{h}_w^+ \leq 20$ (resp. ≥ 30) drag reductions (resp. increases) exist whatever riblet model is concerned. Some authors argue that the upper limit of the reduction domain (the zero-drag reduction crossover point, as quoted by Walsh et al, [147]) be slightly higher in the transonic regime. However, one has to be aware that for transonic conditions, the rib height could be scaled with either the wall variables :

$$\bar{h}_w^+ = \frac{h}{\nu_w} \cdot \sqrt{\frac{\tau_w}{\rho_w}} \quad (27)$$

or the free-stream ones :

$$\bar{h}_e^+ = \frac{h}{\nu_e} \cdot \sqrt{\frac{\tau_e}{\rho_e}} \quad (28)$$

This latter corresponds to the incompressible value and is used by some authors, for instance Squire et

al, [148]. Depending upon the Reynolds and Mach numbers, the difference between \bar{h}_w^+ and \bar{h}_e^+ can be more or less important. Thus, considering this cylinder-type body, when $R_L \simeq 13 \cdot 10^6$ that ratio is close to 7.2% (resp. 12.2%) for a free-stream Mach number of 0.6 (resp. 0.82). So, the differences between high and low subsonic data could come from that observation since it is not always obvious to guess what variable is used on different plots...

Similar tests have been performed in the Cambridge facility, for two infinite Mach numbers of 0.50 and 0.88, [148] and [14]. The drag variations have been deduced from momentum thickness measurements from traverses onto the downstream end of the various lengths of riblet material, to which corresponded Reynolds number lying between $1.6 \cdot 10^7$ and $3.0 \cdot 10^7$. When plotted versus \bar{h}_w^+ , the agreement between the two sets of data is excellent, with a maximum 6% reduction. Analogous results have also been obtained by Gaudet, [165], for free-stream Mach numbers of 0.53 and 0.87, using a drag balance set into the wall of the RAE Bedford 8' tunnel.

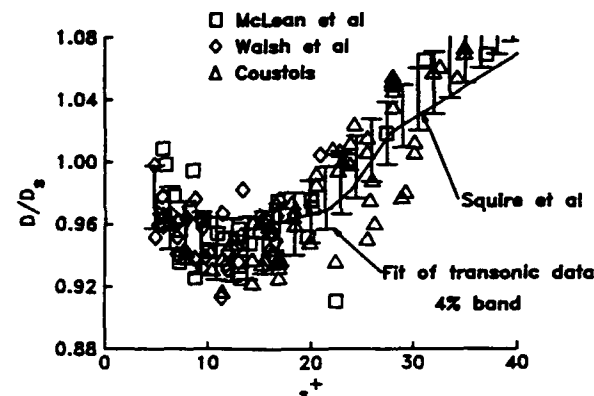


Figure 30: Examples of transonic drag data for riblets, from Walsh and Anders Jr. [147].

The available riblet film data have been summarized and correlated by Walsh and Anders Jr. [147]. It appears that "significant riblet data are now available to firmly establish their drag reduction performance". Collecting data from Coustols, [152], McLean et al, [166], Squire et al, [148] and Walsh et al, [155], Walsh and Anders Jr. found that all the transonic data, as for the low speed data, are essentially contained in a 4-percent data band as shown on figure 30. One has to be aware that the riblet performances have been obtained through different techniques for estimating the drag variations (changes in momentum thickness, direct drag measurements, ...). There is some scatter on that figure ; besides the fact that drag decrease is very sensitive to cross-section uniformity, surface finition, ... it could be noticed that the biggest rib size ($h=76\mu\text{m}$) constitutes the lower branch of the data band. For this specific groove height, the lower the value of M_∞ is, the smaller the non-dimensionalised height is, but also the weaker the con-

sistency of results is, according to the afore-mentioned explanations (non adapted lower and upper walls of the test section, for low values of M_∞).

Influence of angle of yaw

In this present experiment, the model axis was maintained aligned with the direction of the external free-stream flow ; on the other hand, the streamwise grooves were at a given angle, ϕ , to the cylinder symmetry line. It has been assumed that there was no induced three-dimensional or helicoidal effect. Data are showed that the grooves keep a beneficial effect, even at 20° of angle of yaw. However, the recorded drag reductions are less important than at zero angle of yaw, and the higher ϕ is, the smaller the zero drag reduction crossover point is, [152], [153]. Thus, this effect is quite comparable to that evidenced at low speeds, for flat plate-type experiments. During their flight test experiments, McLean et al, [166], found that a deliberate yaw angle of 15° decreased the riblet drag reduction of about 50%. This is a stronger effect of misalignment than those observed either in this set of experiments or in others ; that could be explained by the additive effect of pressure gradient and angle of yaw, or by the difficulty to achieve a good measurement accuracy in flight, using changes in momentum thickness for evaluating riblet performances.

3.1.2.2 Non zero-pressure gradient flows

With a view of a possible application of this type of passive devices, not only to the fuselage of a transport aircraft but also to the wings, fin and horizontal tail, it is necessary to analyse the behaviour of riblet models under adverse and/or favourable pressure gradients. Then in the T2-transonic wind tunnel of CERT, experiments have been carried out with the CAST7 aerofoil, the chord length of which is 200mm ; it is steadily held within the two lateral walls of the test section, at an angle of attack of 0° , and an angle of sweep of 0° . The boundary layer is tripped at 5% chord length from the leading edge, on the suction and pressure sides, [153].

Four symmetric V-groove riblets, manufactured by the 3M Company in an adhesive backed film, with an aspect ratio (s/h) of one, have been tested : $h = 0.017, 0.023, 0.033$ and 0.051mm . The grooved surfaces have been applied between 15% and 100% chord length ; in front of the leading edge of the ribs, a smooth vinyl sheet has been stuck, in order to avoid the facing step effect. The reference configuration, i.e the "smooth" aerofoil, will consist of the upper and lower sides covered completely with the smooth vinyl sheet ; of course, the carborundum band will lay upon the smooth surface.

The tests have been performed at ambient stagnation temperature, for a stagnation pressure close to 1.6 bar, and for a free-stream Mach number range, $M_\infty : 0.65-0.76$. The performances of these four riblet models, under different pressure gradients, have been determined through drag variations estimated from Pitot tube surveys in the aerofoil wake at $x/c=1.5$. Special care has been taken in order to lay hold of measurement accuracy : the data scatter on the wake

momentum thickness or on the total drag coefficient is $\Delta Cd/Cd \simeq 0.7\%$; for greater values of the Mach number, the scatter is greater mainly because the experiments are carried out very close to the divergence Mach number, from which the total drag coefficient rapidly increases.

On the pressure side, whatever the value of M_∞ is, the flow is decelerating from $x/c=35\%$ to 90%, then accelerating towards the trailing edge. On the other hand, on the suction side, all along the distance subject to future manipulation ($0.15 \leq x/c \leq 1.00$), the data exhibit a flat plate-type evolution for $M_\infty \leq 0.74$; above that value, a shock appears at about 40% chord length. The friction contribution to the total measured drag slightly decreases as the free-stream Mach number increases : 58% at $M_\infty=0.65$ down to 48% at $M_\infty=0.76$.

Thus, when grooved surfaces cover about 85% of the aerofoil wetted area, friction drag reductions have been recorded for $h_w^+ \leq 20$. Maximum total drag decrease of about 3.5% was obtained for the smaller rib heights, which corresponds to maximum skin-friction reduction of almost 7.5-8% at h_w^+ close to 12 - 16. This result is obtained by assuming that grooves do not modify the pressure drag but act only on the friction drag. For free-stream Mach numbers less than the divergence Mach number, the average pressure gradient parameter estimated along the manipulated area, β -Clauser parameter - for instance, is weak on the suction side since the local Mach number is almost constant over 35-40% chord length ; on the pressure side, this parameter is stronger but still moderate.

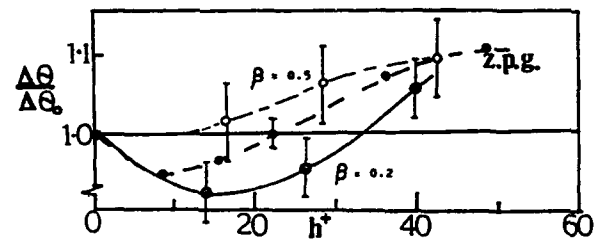


Figure 31: Effect of increasing adverse pressure gradient on riblet performance, from Savill [14].

The effect of adverse pressure gradients on riblets has been investigated at Cambridge University by inclining the top liner of the tunnel test section, [14]. In this way, it was possible to generate two relatively uniform adverse gradients along the lower liner test surface. The local Mach number dropped from approximately 0.88 at a position near the leading edge of the riblet model to 0.72 or 0.62 respectively at the traverse location ; that provided pressure gradient parameter, β , of 0.2 or 0.5 respectively. The results are compared with those recorded in zero-pressure gradient on figure 31, taken from [14]. The evidence is that similar levels of drag reduction can be obtained in mild pressure gradients up to $\beta=0.2$ (over a somewhat larger range of h^+) and possibly $\beta=0.5$, but there might be some loss of efficiency in more severe gradients.

Thus, comparing wind tunnel experiments, Squire and Savill, [148] or Coustols and Schmitt, [153] but also measurements in flight by McLean et al, [165], the data seemed to be consistent, though the drag variations were estimated through different measurement techniques. In summary, significant riblet data are available, for flows subject to adverse and/or favourable pressure gradients, to suggest their drag reduction efficiencies as much as the pressure gradient is moderate, which is the case for most of the wing surface, where grooved surfaces might be applied, in the future.

3.1.2.3 Three-dimensional flows

Very little work had been devoted towards manipulation of three-dimensional boundary layers. Following the successful tests, as regards the efficiency of grooved surfaces, either on an axisymmetric body or on an aerofoil, in transonic regime, further experiments were undertaken by CERT at the ONERA/Modane S1-wind tunnel in collaboration with the Aerodynamics Branch of ONERA/Chatillon and Aérospatiale, [153].

The model is a 1/11th scale Airbus A320 model, mounted on a straight sting, which is maintained through a tripod set-up. The considered model configuration has no vertical as well as no horizontal tail. The fuselage length, l , is 3.416m and the mean aerodynamic chord length is 0.381m.

The experiments have been performed at ambient stagnation temperature and at a stagnation pressure of 0.9 bar. The unit Reynolds number range is : $5.5-11.8 \cdot 10^6$. The free-stream Mach number varied between 0.3 up to 0.82 ; this latter value corresponded to the configuration "Fuselage alone", for which the maximum Reynolds number based on the fuselage length is approximately equal to $40 \cdot 10^6$. The angle of attack of the model has been varying between -2° and $+3^\circ$. Boundary layers were tripped on the fuselage and on the wings, using carborundum bands. Only one symmetric V-groove riblet ($s/h=1$), manufactured by the 3M Company in an adhesive backed film has been tested onto the fuselage and wings.

From boundary layer calculations, it appeared that h_w^+ was not varying too much with either the streamwise abscissa or the peripheral co-ordinate ; so, a mean value would be representative of the riblet scale, for given stagnation conditions. Thus, considering a groove depth of 0.023mm, for the riblet material set on the fuselage, ended up with an optimized h_w^+ value close to 8-9, at $M_\infty=0.7$.

Measurements have been performed for fuselage and wing-body type arrangements. Several configurations have been considered : Fuselage alone without riblets ; Fuselage covered with riblets ; Wing-body configuration without riblets ; Wing-body configuration with riblets set only on the fuselage ; Wing-body configuration covered with riblets.

Along the wings, the grooves were approximately aligned with the external free-stream flow direction. No grooved surface was set in areas subject either to high geometric curvature (nose or tail cone) or to

important streamline curvature (more than 15° from the ribs direction). The corresponding percentage of wetted areas covered with longitudinal grooves is approximately : fuselage alone : 73% ; wing-body configuration (fuselage, wings and fairings covered with riblets) : 66%.

The total forces, especially drag and moments, were measured through an internal six-component balance. An excellent repeatability on C_d measurements has been achieved, [153]. So, it was with confidence that the efficiency of grooved surfaces has been checked under very good conditions. A dozen of pressure taps, inserted within the fuselage (sting cavity), allowed to check the homogeneity of these pressures as well as their constancy during all the drag measurements.

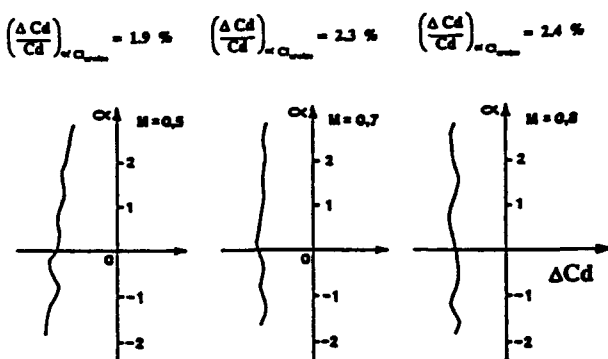


Figure 32: Synthesis of drag data (Fuselage configuration), from Coustols and Schmitt [153].

For the fuselage configuration, the variations of the total drag coefficient are plotted, on figure 32, versus the model angle of attack for three values of M_∞ : 0.5, 0.7 and 0.8. Thus, a very positive effect in terms of drag reduction has been evidenced, whatever the value of the angle of attack is, especially for large values of M_∞ . Indeed, at $M_\infty=0.7$ and 0.8, the total drag coefficient decrease is almost constant when the angle of attack, α , varies, [153]. For α corresponding to the C_l cruise value ($C_l=0.5$), nett drag reductions of 1.9%, 2.3% and 2.4% were recorded respectively for $M_\infty=0.5, 0.7$ and 0.8. The angle of attack corresponding to $C_l = 0.5$ varies, of course, with the free-stream Mach number.

When considering the complete wing-body configuration with riblets set only on the fuselage, nett drag reductions were also obtained at $M_\infty=0.5$ and 0.7, for different C_l values lying between 0.1 and 0.6. Furthermore, adding riblets on the wings and fairings allowed to get lower C_d values, than the ones corresponding to the preceding configuration. The nett reduction in C_d was 1.6% at $M_\infty=0.7$ and at cruise level, with negligible changes in ΔC_d over the C_l range : 0.1-0.6 (figure 33).

Whatever configuration is concerned, it is rather difficult to guess a correct estimate of the skin friction reduction mainly because the sting induced pressure field modification and, consequently, drag inter-

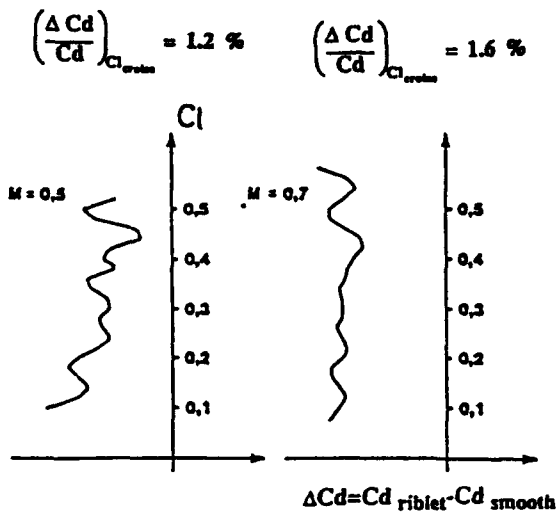


Figure 33: Synthesis of drag data (Wing-body configuration), from Coustols and Schmitt [153].

ferences. Anyway, at $M_\infty=0.7$ and at cruise level, if one assumes that friction represents about 50% of the total drag, the average nett skin-friction drag reduction, estimated over the 66% manipulated wetted area, is close to 4.85%.

This benefit is not certainly the highest one, because the percentage of wetted areas covered with ribbed surfaces was rather small (especially on the wings due to boundary layer tripping) and also because the grooves size had not been optimised on the wings (same depth and geometry as the ones used on the fuselage were considered, mainly because of material availability).

In spite of these observations, substantial drag gains have been recorded on the wing-body configuration. Furthermore, these results agree rather well with the predictions made from measurements under laboratory conditions, for instance with data obtained on either the cylinder or the CAST 7 aerofoil. Since the fuselage length Reynolds number reaches around $4 \cdot 10^7$, it was expected that these results would translate pretty easily to practical flight test conditions where the Reynolds number is only increased by a factor 5.

3.1.3 Supersonic data

Up to now, at least to our knowledge, only few studies had only been performed under supersonic conditions. At first, S.K. Robinson, [167], analysed the effects of riblets (V-shaped grooves, $s/h=1$, $h^+=17$) on turbulence structure at a Mach number of 2.97. The experiments suggested that the wall modification did not alter the fundamental mechanisms of near-wall turbulence production, but simply attenuated its intensity (reduction of turbulence intensity for $y/\delta < 0.1$). No measurement of drag variations was made, but the author believed that riblets could be effective for reducing friction drag at supersonic as well as subsonic

speeds.

Later on, L. Gaudet looked up at the properties of a riblet surface at a Mach number of 1.25, [168]. Skin-friction measurements had been made through a balance mounted beneath the side wall of the wind tunnel. Maximum reduction of 7% was observed at optimum flow conditions. The results of a detailed study of the variation of skin friction with misalignment of the flow with respect to the riblet is given on figure 34, from [168]. These results were recorded for a unit Reynolds number of $8 \cdot 10^6$ per metre, from a considerable amount of data for angular increments of about 5° . On that figure, the ordinate is the ratio of the skin friction to its minimum value, i.e. that at $\phi=0^\circ$ with the flow conditions close to optimum for maximum drag reduction. These results clearly indicated the loss in benefit due to misalignment ; at $\phi=20^\circ$, the benefits are halved while at 30° all benefits are lost. This trend recorded by Gaudet, [168] is similar to that found at low-speed by Walsh and Lindemann [135], or in transonic conditions by Squire and Savill [148] or Coustols [152].

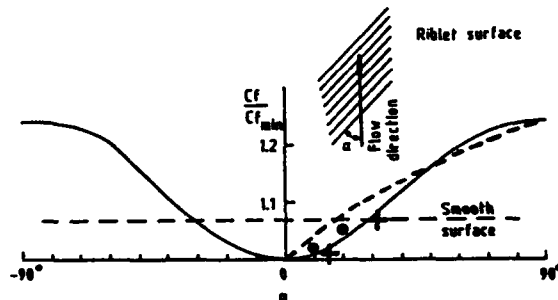


Figure 34: Influence of flow direction on riblet performance ; + : Walsh et al [135], • : Coustols [152], - - : Squire et al [148] ; from Gaudet [168].

A preliminary study had been undertaken at CERT, on a flat plate at a Mach number of 1.90. Drag variations were estimated through wake surveys at $x/c=1.20$, [169]. Nett drag reductions had been recorded, with maximum close to 9-10% when the dimensionless groove depth, h^+ , was less than 10. However, the results had to be analysed from a qualitative point of view because the size of the flat plate was rather important compared to the dimensions of the test section of the wind tunnel, and shock wave reflections and interferences were acting on the flat plate and more precisely on the grooved surfaces.

Another experimental study had been more recently conducted in the ONERA/Modane S2 wind tunnel, [170]. The model is 2m long : a cylindrical centerbody, the diameter of which is 90mm, was mounted along the axis of the tunnel. The nose of the centerbody, the length of which is close to 0.44m, was defined in order to minimise shock wave generation : a conical nose with a half tip angle of 6° . Experiments were performed for three values of the infinite Mach number, M_∞ , of approximately 1.6, 2.0 and 2.5, at a range of stagnation pressures lying be-

tween 0.55b and 1.55b. The stagnation temperature was kept constant at 300K ; as a consequence unit Reynolds numbers between 5 and 20 millions could be reached. Transition was tripped at 20mm downstream the nose tip, through a carborundum band (average height : 203 μ m).

Three riblet models, supplied by the 3M Company, have been applied along the constant-radius part of the body. Their aspect ratio is constant and equal to 1 ; three depths have been considered : $h_w^+ = 76\mu$ m, 51 μ m and 33 μ m. The grooves are aligned with the infinite free-stream flow direction. The explored h_w^+ range is : 1.5-35.0.

The reference smooth centerbody was equipped with 20 pressure taps along the upper symmetry line. As regards the conical nose, 4 pressure taps, set at right angles, were inserted at two streamwise sections. Couple of pressure taps were also placed upon the base-line of the body in order to correct the total drag force given by the balance from the afterbody drag. All the measurements have been performed for angles of attack and yaw of 0°. Measurements of the local Mach number on the conical nose allowed us to compare the experimental value to the theoretical one and, so, to take into account small disturbances on M_∞ .

Drag variations were measured through an internal one-component drag balance, which provided us with an excellent repeatability on C_d measurements. The greatest scatter was observed at $M_\infty = 1.6$ and Re/m of about $7 \cdot 10^6$; it did not exceed 2%, yet.

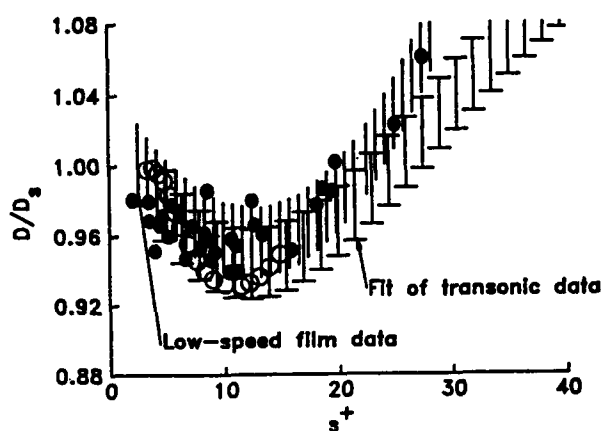


Figure 35: Supersonic drag data.

For $M_\infty = 2.0$ and 2.5, nett total drag variations have been recorded over the whole Reynolds number range for the three riblet models. However, at $M_\infty = 1.6$, drag increases were observed for unit Reynolds numbers greater than 15 millions, which corresponds to h_w^+ greater than 20. Maximum total drag reductions of 4-4.5% have been completed. When taking into account the percentage of friction drag manipulated with the riblet models, one ended up with a trend similar to the transonic and subsonic ones, with a maximum of reduction for h_w^+ close to 9-13, [170]. Results are plotted on figure 35 and com-

pared with Gaudet's data, [168], and both the "low-speed film data" band and the "fit of transonic data" band. Then, it should be noted that supersonic data fit perfectly with subsonic and transonic ones, when scaled with variables taken at the wall.

Moreover, it should be mentioned that the first investigation of riblets in supersonic flow (on shock/boundary layer interaction) had also been conducted at Cambridge University, [14]. The vinyl riblet material had been stuck along the whole length of the lower nozzle surface. Spark shadowgraphs photographs were taken with the riblet material attached in the free-stream direction for different values of h_w^+ , up to 60, or at 45° or 90° to the free-stream direction. For h_w^+ less than 20, there appeared to be very little change in the nature or scale of the interaction. However, the scale of the interaction increased significantly for larger values of h_w^+ , and for other angles of yaw, [14].

3.1.4 Internal flows

To date, there has been much less work investigating the effect of riblets in fully developed internal flows than in external flows. In addition to providing an opportunity for comparisons between drag reducing effects in developing (flat plate) and fully developed (pipe) flows, and addressing a need for reducing turbulent frictional losses in piping systems, pipe flow experiments offered a simple method for measuring wall shear stress. Indeed, that latter can be directly calculated from the pressure drop.

Nitschke, [171], studied air flow in a pipe with streamwise grooves with rounded peaks and flat valleys machined into its interior surface. Drag reductions up to 3% were measured through pressure drops over a length of 120 pipe diameters. Drag reductions were obtained when the spacing, s^+ was between 8 and 23, with the maximum in the neighbourhood of 11-15, for riblets with an aspect ratio s/h close to 1.1.

Rohr et al, [140], reported between 6 and 8% maximum drag reductions for symmetric "3M" V-groove shaped riblets ($s/h=1$), when h^+ is between 11 and 15. A specially constructed split pipe has provided convenient internal access for application of riblets. In that same set of experiments riblets have been combined with dilute polymer solutions ; in dilute polymer solutions, there is no significant difference in drag reduction with the addition of riblets.

It should be noted that Lowson et al, [172], looked at the behaviour of riblets in fully developed turbulent flow, in a two-dimensional duct, by measurement of the pressure gradient. The experiments are not conclusive and needed further developments, since conflicting results were recorded.

More recently, Liu et al, [173], reported experiments in fully developed turbulent flows of water through couple of diameter pipes. Maximum drag reductions of 5-7% have been recorded when considering aligned film of grooved equilateral triangles ($s=0.11\text{mm}$). The maximum drag reduction occurred for $s^+ \approx 11-13$.

At last, Nakao, [174], investigated a few months ago the performances of riblets for drag reduction in pipe flows, at Reynolds numbers between $5 \cdot 10^3$ and $4 \cdot 10^4$. Riblet pipes were made by the extrusion process ; the aspect ratio, s/h , varied from 3.7 to almost 1.0, depending of the groove depth, h , the range of variation is : 0.40-0.86mm. The grooved surface, with $h=0.55$ mm and $s/h=2.1$ showed the maximum drag reduction of 8% and worked over the widest range of Reynolds number. Those data indicated that the value of the aspect ratio is important for overall drag performances. Nakao wrote that the value of s^+ , which provided the maximum drag reduction was not the same in pipe flows as in flat plate boundary layers. However, if the results had been plotted versus h^+ , $s^+=23$ with s/h close to 2 would provide h^+ close to 12, which is in perfect agreement with $s^+=12-13$ for the world-wide symmetric V-shaped model, with an aspect ratio of 1... that might confirm that s^+ is the more appropriate parameter for collapsing data from different experiments or for various riblet sizes...

So, according to those experiments, the results of drag reduction in turbulent pipe flows are in good agreement with previous and numerous investigations for turbulent boundary layer flows, as regards zero drag reduction cross-over point, for instance ; however, the level of drag reduction appeared to be somewhat smaller.

3.1.5 Conclusions

All the reported experiments carried out under either subsonic or transonic or supersonic conditions have allowed to verify the efficiency of internal manipulators, riblets or grooved surfaces, in the aim of reducing turbulent skin-friction drag. Thus, from different research groups, significant riblet data are now available to firmly establish the potential of such devices for drag reduction performances. It appears that maximum drag reduction are found for grooves geometries, such as the height or the spanwise spacing is typically of the order of $10-15 \nu/U$.

It should be mentioned that most of the studies dealing with riblet have been performed in turbulent boundary layers. Therefore, a great amount of experimental as well as numerical work, in laminar boundary layers, has been undergone at IMST (see [187], [190], for instance). However, very detailed measurements above and within the grooves were made, but without looking at riblet performances in terms of nett drag reduction.

Furthermore, experiments performed on a complete A320 model, in the S1-wind tunnel, showed up that important total drag coefficient reductions could be achieved, at cruise conditions. Since the fuselage Reynolds number reaches around $40 \cdot 10^6$, it is expected that these results could be rather easily applied to practical flight test conditions where the Reynolds number is only increased by a factor 5.

Although the mechanisms involved in such a drag reducing process have not still been understood, a couple of flight tests have already been performed

with fuselage, wings, fin, horizontal tail and nacelles equipped with riblets. Some information concerning the flight tests, carried out by Airbus Industrie and its partners - in collaboration with the Aerodynamics Branch of ONERA/Chatillon and the Aerothermodynamics Department of ONERA/CERT - on the Airbus A320 N°1 in October 1989, is given by Robert in his lecture [2].



Figure 36: Riblet flight tests on Airbus A320 N°1.

With approximately 75% of the wetted surface covered with riblets, the size of which had been optimised for cruise conditions, results indicated an average saving of 1.5% on the total drag force. This number is in good agreement with the prediction made up from the promising ONERA S1-wind tunnel riblet tests.

3.2 Effect of inner layer manipulators on turbulent flow

Thus, as mentioned in the preceding section, numerous experimental studies have investigated the potential of riblet for reducing friction drag. These micro-grooves surfaces are one of the most effective and relatively easy to manufacture drag reducing surface modifications. All the data have allowed to verify with laboratory measurements that the optimum shapes had a sharp peak protruding into the flow and had a height and spacing of typically $15\nu/U$. The way they produced friction drag alteration is not exactly defined, yet. Although the tremendous amount of data, the important question, which is still open, is whether skin-friction reductions are due to wall geometry arrangement (because of tremendous C_f decreases above the valleys) or to some re-organisation of turbulence structure.

The mechanisms involved in such a drag reducing process are still under investigation in some laboratories. Indeed, one could think that those ribs might increase the spanwise streak spacing and then decrease the burst intensity [178], restrict the spanwise motion of the longitudinal vortices [186], "act as a nucleation site causing a focusing of low-speed streaks over their peaks" as quoted by Gad-el-Hak and Blackwelder [118], increase the viscous sublayer thickness [179], ...etc. Nevertheless, the optimum spacing in terms of nett drag reduction did not correspond to

the average spacing of the low speed streaks ; hence, the ribs are apparently not locking these streaks into a fixed spanwise location, [27]. On the other hand, many researchers still feel that the correspondance between the near wall turbulence microscales and the size in wall units, at which riblets reduce drag, is too close to be coincidental, [145]. As a matter of fact, several experimental studies have been undertaken, because grooved surfaces were believed to reduce drag by weakening the near-wall vortical structures of the turbulent boundary layer.

It has been surmised that the effect of grooves is to retard the flow in the valley, thus creating a viscosity dominated region where the local skin friction is greatly reduced. Then, viscous effects might play the leading part in this near-wall flow manipulation and the resulting outcome on the Reynolds stress components be a consequence. Nevertheless, in order to look at the response of the boundary layer to such a manipulation, detailed hot-wire measurements performed by several researchers, either very close to the trailing edge of some models or upon some vinyl ones, would be referred to ; the main scope would be not only to investigate whether skin-friction reductions are due to some re-organisation of the turbulence structure, but also to try to provide some possible mechanisms of action. The general consensus of opinion seems to be that riblets act primarily to increase the sub-layer thickness but, at the same time influence the near wall turbulent structure and production directly by inhibiting spanwise motions.

3.2.1 Mean quantities

Because of the micro-geometry of these grooves, measurements just above or inside the ribs are very difficult. Nevertheless, few data showed that the mean velocity profile, as well as the turbulence intensity profiles were rather altered by the surface modification.

Boundary layer measurements made by Sawyer and Winter, [149], confirmed earlier findings evidenced by Hooshmand et al, [177], and showed that the mean velocity profiles plotted logarithmically were shifted upwards, suggesting an increase of viscous-sublayer thickness, similar to drag reducing polymers. However, the slope of the log law remained the same as that of a smooth surface ; just, the intercept of the law was increased. It should be recalled that an upward shift of the log region is associated with decreased values of friction velocity or skin friction, while a downward shift indicated skin friction increases. Such a downward shift has been previously seen in sand-grain roughness studies. This is the reason why riblets act as a kind of negative roughness in the sense that the roughness shift, F , to the constant B of the logarithmic law (cf. equation (20)), is negative within the drag reducing range and only changes sign when there is drag increase. Values of F for two V- and two U-groove riblets are plotted versus h^+ , on figure 37 taken from [125]. It could be seen that F is negative for a limited range of h^+ , the upper limit of which varies with the shape of the groove as well as with the

aspect ratio, s/h . Results obtained from sand-grain roughnesses (cf. §2.3.4.2) are also drawn.

It should be mentioned that an upward shift can be considered as an adjustment of the balance between the turbulence energy production and the viscous dissipation, which is reflected by a change in the viscous sublayer thickness or the smallest size of turbulent eddies in the boundary layer, [78]. Therefore, the turbulence energy production is less with an upward shift, resulting in the reduction of turbulent drag.

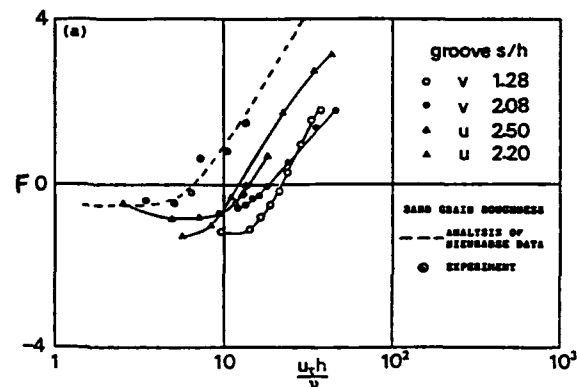


Figure 37: Shift due to riblets plotted versus h^+ ; evaluated by Gaudet [165] from experimental data of Sawyer and Winter [149] ; figure taken from Tani [125].

When performing boundary layer traverses above grooved surfaces, one of the main difficulty for analysing and plotting results is to define the location of the origin! This notion is crucial, for instance, when trying to deduce a value of the span-average local skin friction, since as it has been mentioned just above, the slope of the log law remained the same as that of a smooth surface. From an entirely viscous analysis, Bechert and Bartenwerfer, [182], defined the "apparent origin", i.e. the elevation where the boundary layer "sees" an equivalent smooth wall. Another way to interpret the apparent origin is to consider it as the centre of gravity of the shear stress distribution on the riblet surface.

Sublayer velocity traverses performed by Hooshmand et al [177], have suggested that the outer flow saw this apparent origin raised to an effective height of $0.75s$, so that only $0.25s$ of the riblet protruded above that origin. The estimates of "protusion height", h_p , derived by Bechert et al [182], for U-, L- and V-groove riblets are plotted on figure 38. Considering saw-tooth, blade-like or scalloped riblet cross section, a clear limit of the protusion height has become visible : $h_p/s = \ln 2/\pi \sim 0.22$. It seems likeley, therefore, that about three quarters of the riblet effect is due simply to the response of the flow to the change in wall condition. It has been mentioned by Savill, [14], that close-packed hemispherical roughness of diameter D provided a protusion height of about $0.2D$, close to this protusion height limit.

It is likely that riblets act mainly upon the viscous

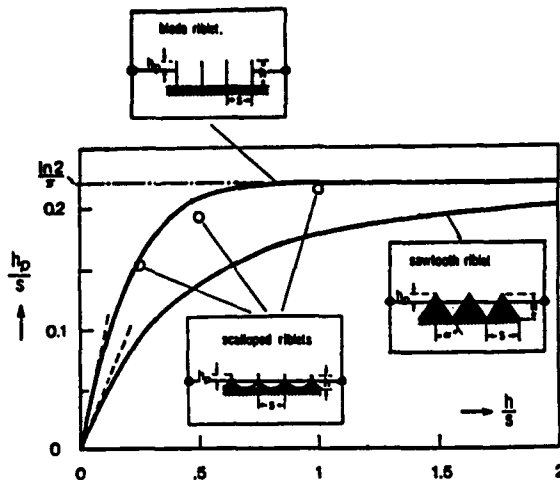


Figure 38: Protusion height as a function of groove height for different types of riblets, from Bechert and Bartenwerfer [182].

sublayer. Consequently, in the downstream of a length of grooved surfaces, the drag-reducing effect would not subsist beyond several sublayer thicknesses, [11]. This has been confirmed by Bacher and Smith [178], Cousteix et al [41] and Coustols et al [161]. Indeed, skin friction relaxation was very quick ; skin friction was obtained with hot-element skin friction gauges and a floating element drag balance, manufactured at Laval University, Canada (see [138] for instance).

To our knowledge, the only attempts to measure turbulent quantities within triangular grooves have been performed earlier on by Vukoslavcevic et al [183], and more recently by Benhalilou et al [175], while Hooshmand et al [177], or Coustols et al [161], looked at the flow modification in the close vicinity above the crests plane. Those latter revealed that the wall shear is increased near the peak of the riblet but substantially reduced within the valley, so that a nett drag reduction ensues.

Vukoslavcevic et al, [183], measured the mean and fluctuating streamwise velocities, using hot-wire anemometry. However, no information was provided as regards the mean and fluctuating spanwise velocities, which seemed, both, to be of some prime importance. Rather recently, Benhalilou et al, [175], reported a very detailed experimental study of a turbulent boundary layer within V-groove riblets. It must be recalled that behaviour of riblets in laminar flows has been extensively examined at IMST for the last few years [187], [190].

So, experiments were carried out in the IMST water tunnel at an external free-stream velocity of about 9 cm s^{-1} . Large triangular V-shape grooves have been considered ($s=2h=7 \text{ mm}$, $h^+=15$) in order to be able to perform velocity measurements inside the riblet. Results, obtained with a one-component laser Doppler velocimeter, have been dealing with both mean and fluctuating streamwise and spanwise velocity components, as well as the $u'w'$ correlation, [175].

Measurements showed that the mean velocity at a constant altitude y (taking $y=0$ at the valley, for instance) and along the span is like a sine function. This trend is clearly visible on figure 39 for two positions within the boundary layer $y/\delta=0.04$ and 0.05 , respectively. It should be noted that $z/s=0$ or 1 refers to as the groove peak, and $z/s=0.5$ the groove bottom.

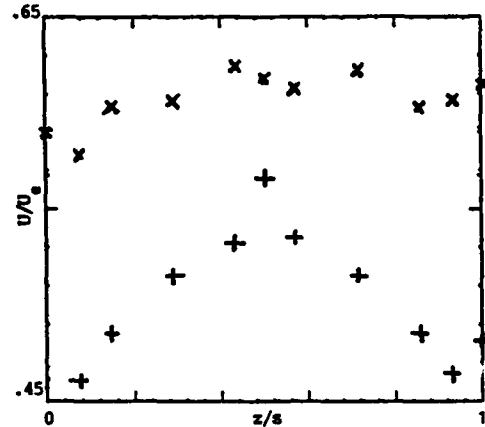


Figure 39: Spanwise evolution of mean streamwise velocity over riblets ($s=2h=7 \text{ mm}$, $h^+=15$), $+$: $y/\delta=0.04$, x : $y/\delta=0.05$, from Benhalilou et al [175].

It could be equally observed that the difference between the mean velocity at a fixed y or y/δ , over the peaks and valleys, decreases when moving away from the wall. This observation is in agreement with Hooshmand et al's results ; indeed, from their hot-wire measurements, those researchers showed that the spanwise periodicity of the mean velocity almost disappeared at $y^+=13$, and that the damping of the spanwise variations was very rapid when moving away from the wall, [177]. Moreover, Bacher and Smith, [178], observed visually that the riblets appeared also to have the greatest effect for $y^+ < 15$.

3.2.2 Fluctuating quantities

For the same experiments, as the ones mentioned just above (Benhalilou et al [175]), the streamwise and spanwise turbulence intensity profiles have been plotted on figures 40 and 41, respectively. Indeed, u'/U_e and w'/U_e are given as a function of y_1/δ , where y_1 represented the distance normal to the wall, measured straight over either the peak or the trough, extending within the groove ; at the measurement location, the value of h/δ is close to 0.11.

It should be noted important turbulence decrease in the trough vicinity and significant increase close to the peak. However, these profiles were non-dimensionalised by the external free-stream velocity ; when taking into account the local components of the mean velocity, U and W , it could then be recorded that u'/U and w'/W are almost identical over either groove peak or groove trough. As quoted by the au-

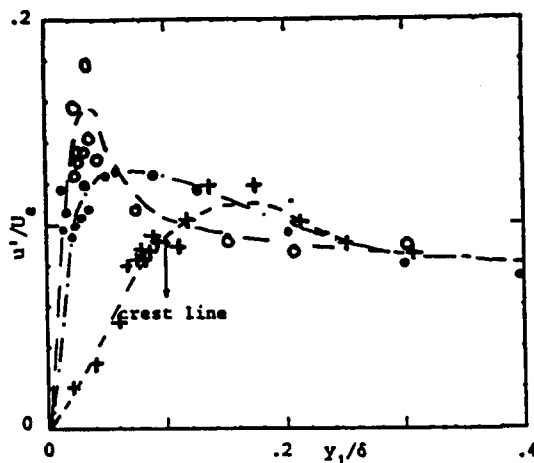


Figure 40: Streamwise turbulence intensity profiles ; o : peak, + : trough, • : smooth plate ; from Benhalilou et al [175].

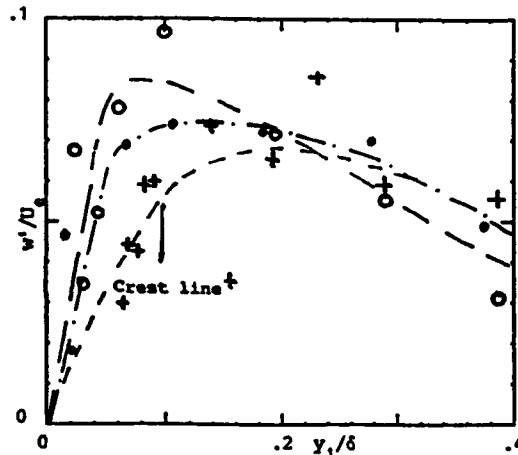


Figure 41: Spanwise turbulence intensity profiles ; o : peak, + : trough, • : smooth plate ; from Benhalilou et al [175].

thors, "this result supports the concept of flow stabilisation by riblets and strengthens the argument relative to the relevance of viscous effects in the mechanism of turbulent drag reduction by riblets", [175].

Considering small L-type ribs, Wilkinson et al [12], have shown that the amplitude and the position within the boundary layer of the maximum turbulence intensity varied with the spacing of the thin-element riblet model (cf. figure 42). In fact, for streamwise spacings less than $50\nu/U_\tau$, the location of that u_{rms} maximum increased to $y^+ \sim 35$ instead of 15 for the smooth case, suggesting that the turbulent eddies were displaced away from the wall, at a distance equal approximately to the riblet height. On the other hand, for spacings greater than $65\nu/U_\tau$, that maximum occurred at about the same location as that for the flat plate case. Wilkinson and Lazos indicated that the afore-mentioned shift was associated with a decrease

in the rate of drag increase, e.g. see [15].

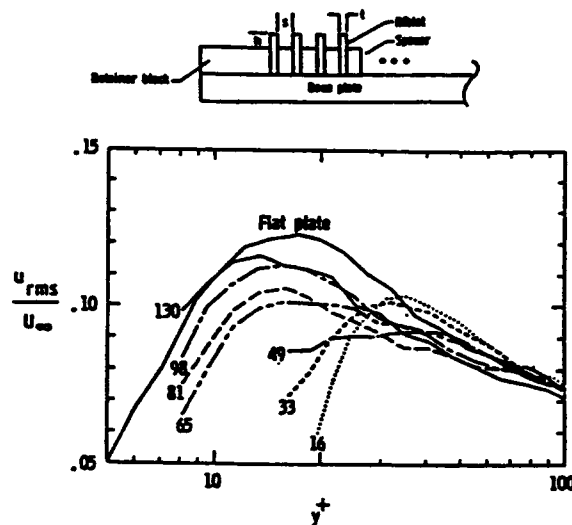


Figure 42: Streamwise turbulence intensity profiles above valleys of thin-element riblet models (same legend as figure 29) ; from Wilkinson et al [12].

Using the technique of spatial cross-correlation between a fixed shear-stress sensor and a movable hot-wire, Wilkinson and Lazos (in Proc. IUTAM Symp. Bangalore) recorded that the thin-element array data showed a greatly diminished correlation, although the trend of the observed structures was similar. Then, these thin-element models have a first order effect on turbulence. Nevertheless, it has never been demonstrated that this turbulence modification induced turbulent skin friction reduction, since that latter could be simply attributed to the "corner effect" at the array-wall junction, [41]. Moreover, in this specific set of experiments, no conclusion could be drawn whether thin-element arrays reduced the intensity or frequency of turbulent bursting.

However, it would appear that both bursts and sweeps are modified on riblet surfaces and the remarkable similarity and regularity of burst signatures that has been recorded in a number of cases [178], [186], points to the existence of a more stable and more ordered streaky structure. Some work dealing with the periods of ejections and sweeps above smooth and grooved surfaces have been going on at the Eindhoven Institute of Technology, [180]. Results were obtained using a quadrant analysis method.

An example of results concerning bursting and structure of turbulence, when an internal flow is manipulated by riblets is given on figure 43 by Tardu and Truong [184]. The profiles of the ejection and bursting frequencies are determined and compared using three single point detection schemes. The effect of riblets on the bursting mechanism is found confined in a localized region $y^+ < 12$, for a riblet such as $h^+ = s^+ = 9$. The skewness and flatness factors are larger in the manipulated layer than in the standard boundary layer

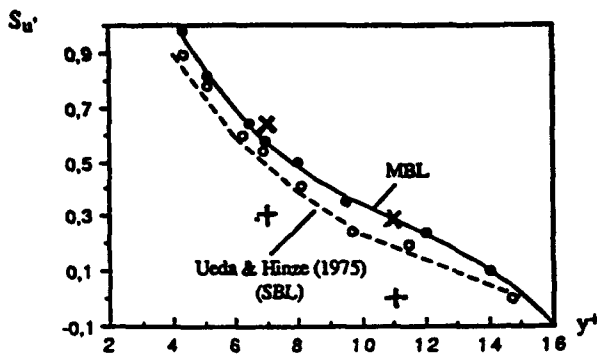


Figure 43: Distribution of the Skewness factor in manipulated (MBL) and standard (SBL) boundary layers (\circ : SBL ; \bullet : MBL ; $+$: Choi SBL ; \times : Choi MBL) from Tardu and Truong [184].

(cf. figure 43) and are consistent with those reported earlier on by Choi, [176].

Coustols and Cousteix [181], performed experiments over a V-shape riblet model ($s=h=0.152\text{mm}$, $h^+ \sim 6.5$), using a classic straight wire probe. On the other hand, they observed that the flatness and skewness factors were reduced for the lowest values of y^+ , over the grooves, compared to the smooth case. However, above $y^+=20$ these factors are not altered anymore. That would confirm other measurements, recorded just downstream of the trailing edge of some riblet model ($s=2h=0.5\text{mm}$, $h^+ \sim 12$) ; using a miniature X-wire probe, surveys did not reveal any modification in the outer part of the turbulent profiles, [150]. Unfortunately, the probe size did not allow to go closer to the wall, below $y^+=20$. If it is believed that riblets act straightly upon the inner region, as it was pointed out by Wilkinson et al. [12], because of the energetic transfers within the layer, some modification of the external part should appear, later on, along the streamwise direction and might perhaps depend upon the manipulated length.

Besides "classic" hot-wire measurements, a spectral analysis has been undertaken by Coustols et al, [150] and [181], since it would allow to define more precisely the structure of a turbulent boundary layer from either an energetic purpose or a dimensional one (small or large scale structures). Thus, information could be obtained about the energy density distribution depending on wave numbers or frequencies, to which correspond length scales or time scales.

Downstream the model : $s=3h=0.6\text{mm}$, for $h^+ \sim 8$, there was no noticeable difference on the u^2 spectra behind smooth and ribbed plates, at the two scaled altitudes $y^+=21$ and 210. Consequently, the spectrum integrals were almost constant, which meant that the r.m.s value remained unaltered. This was consistent with previous X-wire surveys above-mentioned, showing no difference on the five components of the Reynolds stress tensor, at least in the outer part of the turbulent boundary layer, [150], [181].

The preceding results are in agreement with

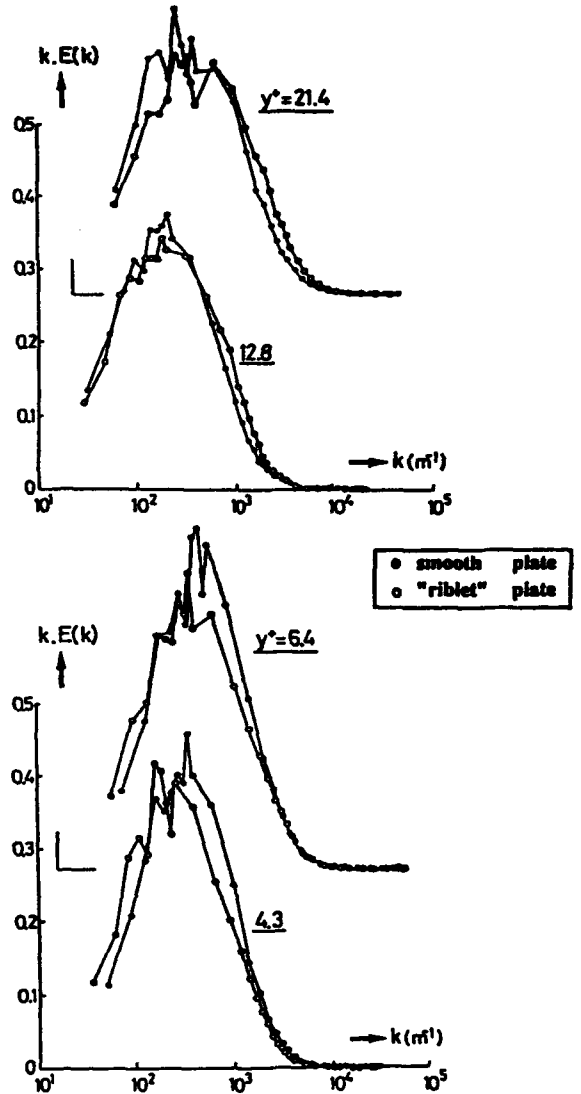


Figure 44: Streamwise fluctuations spectra upon riblet model ($s=h=0.152\text{mm}$, $h^+ \sim 6.5$) from Coustols and Cousteix [181].

the suggestion, generally mentioned, that grooves might mainly affect the inner layer by increasing the thickness of the viscous sub-layer. Measurements were carried out upon the V-shaped vinyl model $s=h=0.152\text{mm}$, at $h^+ \sim 6.5$ using a straight wire probe (wire length : 1.25mm), which means that measurements will correspond to an average value in the crosswise direction. Figure 44 reports the u^2 spectra for four altitudes lying within either the viscous sub-layer or the buffer layer, at a streamwise abscissa located 0.75L downstream the leading edge of the riblet model, the length of which is L(0.64m). Let us mention that $y=0$ corresponds to the crests plane. When comparing to the smooth case, several modifications existed : at the upper part of the viscous sub-layer ($y^+=4.3$ and 6.4), the grooves would induce a deficit of small scale structures, and on the other hand, an

excess in the high frequency range in the middle of the buffer layer. Thus, this spectral analysis would suggest that ribs would bring about smaller structures in the region of intense production ($y^+ \sim 10 - 15$).

From the spectral analysis, it was possible to compute the dissipation length, $\lambda_u = U/(2\pi N)$, where U is the local streamwise velocity. If k denotes the wave number, the reduced frequency N is defined as :

$$N^2 = \int_0^\infty k^2 E(k) dk \quad (29)$$

In homogeneous and isotropic turbulence, this length scale would correspond to Taylor's dissipation length. Over the smooth plate, λ_u increased with y ; the turbulence Reynolds numbers $\lambda_u \cdot \sqrt{u'^2}/\nu$ developed from 45 up to 120 for $y/\delta \leq 0.2$, and remained rather small. One could observe that behind the riblet model, that length was slightly greater than the one obtained behind a smooth wall. However, upon the grooves, λ_u was reduced. As the value of that dissipation length allows to evaluate the dissipation rate ϵ ($\epsilon = 15\nu u'^2/\lambda_u^3$), and consequently the Kolmogoroff scale $\eta = \nu^{3/4}\epsilon^{-1/4}$, these measurements might indicate that the characteristic scale of the wall structures is smaller, which is consistent with the aforementioned explanation, i.e. that smaller scale structures exist very close to the wall.

Choi has combined flow visualisations and instantaneous wall-shear stress measurements for tapered L-shaped riblets, at $h^+ = 12$ and $s^+ = 30$, respectively, [186]. That size had been chosen, since it allowed to set a hot-film sensor, mounted flush with the bottom surface. That same author observed that the fluctuating component of the wall skin friction was significantly reduced. The reduction was considered to result from a quiescent period for the turbulence observed in the flow. The energy spectrum showed that the reduction was mainly contained in the lower part of the frequency range. A similar reduction, although small in magnitude was found in the spectrum of wall pressure fluctuation (4% reduction in the r.m.s value), suggesting that noise could perhaps be reduced by the manipulation of turbulent boundary layer through inner layer manipulators.

Pressure fluctuations have been carried out downstream some vinyl riblet model ($s = 3.5h = 0.46\text{mm}$, $h^+ \sim 3.5$) by Coustols and Cousteix, [150]. Whatever the location of the microphone was, there was no perturbation on the p'^2 spectrum on the explored frequency range : 50Hz-20kHz. This result might be attributed to the important downstream distance between the microphone location and the trailing edge of the riblet model, or because the diameter of the microphone was not appropriate for such measurements (d^+ was close to hundreds of wall units) or simply because the relaxation is very quick downstream the riblet model.

3.2.3 Effect on heat transfer

Compared to the tremendous amount of data as regards riblet performances, in terms of friction drag

reduction, only couple of studies, dealing with the effect of riblets on heat transfer have been recorded (see references given in [15], for instance). For such studies, one of the important parameter is the Reynolds analogy factor, which relates the heat transfer and the skin friction. It is defined as the ratio of the Stanton number to half the coefficient of friction, while the Stanton number is :

$$St = \frac{q_w}{\rho_e U_e^2 C_p (T_w - T_e)} \quad (30)$$

where ρ_e is the density taken at the wall, q_w if the wall heat flux, C_p the specific heat, T_w and T_e the wall and free-stream temperatures, respectively.

According to Stone et al, [145], the previous studies did not clearly established whether riblets produced a nett reduction in heat transfer. In the last couple of years, two studies have been undertaken on that subject.

Choi and Hamid, [185] examined the heat transfer characteristics of V-shape grooves having an aspect ratio of 1, but two different spacings 0.73 and 1.83mm. Heat transfer measurements have been performed at local Reynolds numbers varying between $2.8 \cdot 10^5$ and $11.3 \cdot 10^5$, for riblet spacings, s^+ of 6 to 60. Heat transfer coefficient could be divided in two parts : one from the forced convection and the other one from radiation. Therefore, the radiative heat transfer coefficient was extrapolated from the measured total heat transfer coefficient to zero speed. Experiments revealed that riblets could enhance the convective heat transfer by as much as 30% compared with the smooth surface without providing any penalty of increasing drag.

Stone et al, [145], considered the influence of riblets on the convective heat transfer in a turbulent boundary layer, which developed along a flat plate. Data were recorded at Reynolds numbers from $4.5 \cdot 10^5$ to $11.0 \cdot 10^5$, i.e. approximately for the same conditions as Choi and Hamid, [185]. However, thin-element riblet models were chosen, allowing riblet spacing from 15 to 50 wall units. Heat transfer variations were determined from direct measurements of heated power to the test areas at approximately constant wall temperature. An example of results is given on figure 45, where the Reynolds analogy factor is plotted as a function of the spacing s^+ .

The variations for the flat and grooved test sections were calculated from least square curves of the Stanton coefficient data as a function of the Reynolds number. For the flat plate case, results for the Reynolds analogy factor agreed pretty well with the empirical formulation. For low values of the spacing s^+ less than 15, heat transfer reductions, down to 5%, were observed, while increases up to 35% were obtained for higher values of s^+ . Moreover, estimates from skin friction variations showed that heat transfer reductions corresponded roughly to drag decreases, since reductions, with a maximum of 7% at $s^+ = 15$, had been obtained for riblet spacings less than 30 wall units.

Thus, from these two recent studies, performed for different cross-section grooves, it might be reasonable to say that riblets might have heat-transfer

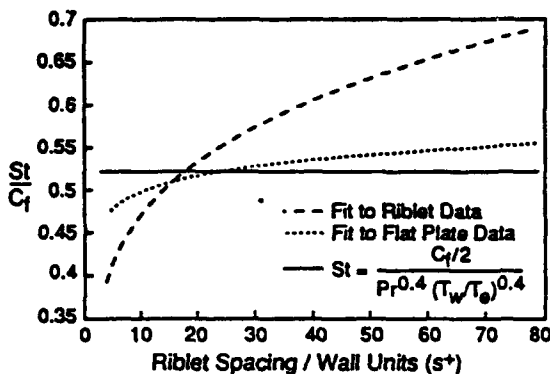


Figure 45: Reynolds analogy factor versus s^+ , from Stone et al [145].

applications. Low heat transfer reductions have been recorded compared to large heat transfer increases, to which corresponded friction drag increases. It would be very interesting to confirm through other experimental studies the afore-mentioned observations, since, first of all these types of measurements are very difficult and secondly, riblets could find use in some applications as a heat transfer- as well as drag-reducing agent.

3.3 Modelling

A general consensus has now been reached that V-shaped groove riblets might produce as much as 8% in skin friction drag reduction. Although a great number of detailed experimental investigations have been undertaken for turbulent boundary layers, the drag reduction mechanisms are not really known. Viscous dominated low-speed fluid inside the riblet valleys might be one reason for the drag reduction. Indeed, it appears from several studies that viscous effects may play the main role in the drag reduction due to riblets ; the wall shear is increased near the peak, but substantially reduced within the valley, so that a nett drag reduction could ensue. It is therefore reasonable to think that a purely viscous mechanism may be involved and that this either partly or entirely counteracts the wetted area increase.

Since the shape the grooves can have is unlimited it is impossible to carry out experiments for every conceivable configuration, so there are two main reasons why numerical studies have been undertaken: They may provide a better understanding of the possible drag reduction mechanisms, but also they can be used to help define the optimum shapes of the grooves.

Before going on to apply models to turbulent riblet flows, laminar regimes have been first been considered by several researcher. Their purpose was to investigate whether the skin friction reduction in the riblet valley is sufficient to overcome the increase in the peak region in order to end up with a nett drag reduction in laminar flows. Some early investigators concentrated on fully developed laminar channel flows, in order to get rid of streamwise evolution of the flow, [188], [195].

and [196].

- An early computational study, which seems to have been the first one on this topic, was carried out by Khan [189] who used a very much simplified algebraic stress relationships in considering manipulation of laminar as well as turbulent boundary layers over the usual V-shaped groove riblet. Khan reported a 1% reduction in laminar flow conditions over a groove, the aspect ratio of which (s/h) was equal to 2 : furthermore, when increasing a little bit the Reynolds number to get a higher h^+ , from 14 up to almost 21, a 33% drag increase was reported. (Note: h^+ can still be calculated for laminar flows, though its meaning is different). Although the results for turbulent flows agreed with experimental observations (maximum drag reduction for $h^+ \sim 8$), it is fair to say that this study was incomplete and, indeed, there must be some concern regarding the low mesh resolution employed.

- A collaborative programme, between IMST Marseille and ONERA/CERT, was subsequently set up in order to look in more detail at laminar boundary layer manipulation with V- and L-shaped grooves, respectively, [190]. The code, originally developed for a cartesian mesh by de Saint Victor (1987) at ONERA/CERT, solved the Parabolized Navier Stokes equations with either a semi-elliptic or parabolic approach, depending on whether the streamwise gradient is unknown or given. Using a SIMPLE method, one of the most significant results obtained by de Saint Victor was that, when calculating the three-dimensional laminar boundary layer over a V-shaped groove ($s/h=2$), the transverse velocity component was negligible in all the computational domain ie. the calculations revealed the absence of secondary flows within the groove, [190].

Hence later results have been reported by Djenidi et al, [187], based upon a forward marching method and a finite volume approach in order to solve the system of parabolic equations assuming $W=0$. Djenidi et al considered computations of laminar smooth wall flow, stepping down onto V-groove riblets, in order to be able to compare the numerical results with their own experiments carried out in the IMST water tunnel, [187]. Measured and computed streamwise velocity profiles within the V-groove are plotted on figure 46 as a function of η , where $\eta = y/(U_e/\nu x)^{1/2}$. The velocity component has been measured using LDA backscatter technique, for which the effective probe volume is rather small compared to the groove size : the height and width were 4.3mm and 5.0mm, respectively. A remarkable agreement is observed between the experimental profiles and the predicted ones; particularly since $W=0$. At the same time, undertaking a parametric study of V-groove, Djenidi et al, [187], showed that it would be possible to obtain a slight drag reduction, for laminar boundary layers over riblets, or more exactly that despite the large wetted area increase, riblets did not have practically any effect on friction. However, as will be discussed later on questions remained as to the sensity of this small amount of drag reduction (close to 2%)

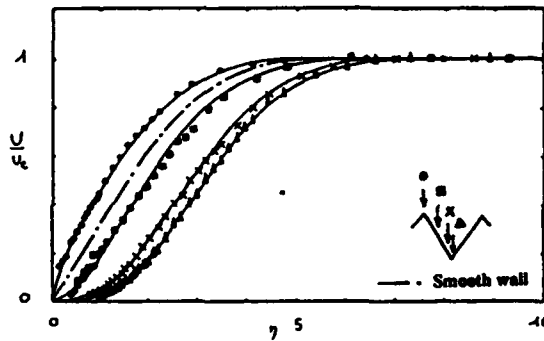


Figure 46: Computed and measured streamwise velocity profiles at selected spanwise locations (•, □, + and ▲ : measurements, — Computations), from Djenidi et al [187].

to further grid refinement, especially in the vicinity of the peak and trough.

Coustols reported that computations for L-grooves, deduced from the same numerical code, indicated a similar drag reduction. One of the advantages in dealing with zero-thickness L-shaped riblets is that the rectangular grid is always orthogonal to the walls, but the increase of wetted area is very important, especially for L-shaped grooves : 400% and 200% for $s/h=0.5$ and 1.0, respectively. A very detailed study of grid refinement has been reported in reference [190] ; of course, grids were refined in regions of large velocity gradients, i.e close to groove crest. Nevertheless, similar results to those from V-shaped grooves have been reported (cf. figure 47).

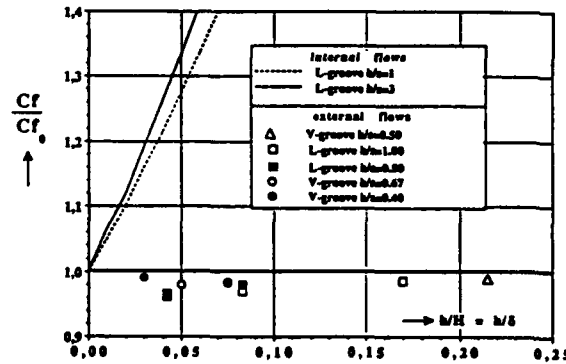


Figure 47: Variations of relative skin friction drag with groove shape for internal and external flows, from Liandrat et al [190].

In fact, results collected for V- and L-shaped grooves in external flows are collected on figure 47 and compared to those obtained by Launder and Li, [188], for L-shaped groove in internal flows. However, the different nature of external and internal flows prevents any direct comparison being made between the amount of drag reduction or increased recorded. Thus the laminar flow computations, performed by Launder and Li in a fully developed duct flow, have shown

a significant skin friction variation (about 30% drag increase, for an aspect ratio of 1 and for $h/H=0.05$, where H refers to as the channel half-width). These authors concluded that the minimum drag, determined from mass flow rate, occurred in limit of h tending to zero. It should be mentioned, however, that no grid refinement study in the regions of high velocity gradients has been performed by Launder and Li, which could explain why results might be subject to caution.

Pulvin, [159] carried out turbulent flow computations for riblets in diffuser flow, by considering a modified mixing length scheme. In order to calculate the inner region of the turbulent boundary layer, without going onto the grooves, they used a "negative roughness" function, developed by McLean et al, [166], following their flight tests. The model had to be extended to include the pressure gradient term. Those computations have proved to be in remarkably good agreement with experiments, [159] and see in [21].

Chu and Em Karniadakis, [195], investigated the flow developing in a channel, the lower wall of which was covered with riblets, while the upper part was smooth. This configuration is different from the ones generally considered throughout literature ; according to the authors, "it is more manageable numerically and allows for tests of accuracy via momentum balances". The chosen riblets were symmetric V-shaped ones, with an aspect ratio of 1. The range of investigated Reynolds numbers was 500 to 3500, which covered the laminar to transitional regime. The grid used for the computations is given on figure 48. Simulations have been performed by integrating the full Navier Stokes equations in the entire domain. Spatial discretisation of the equations is obtained using the spectral element methodology ; the details of this methodology could be found in [195]. The simulations were performed at a constant flow rate, while Reynolds number variations were obtained through the kinematic viscosity. Results are plotted on figure 48.

In the laminar regime no drag reduction has been reported although they observed a re-distribution of time-averaged skin friction within the groove. However, in the transitional regime, for Reynolds numbers close to 3,000, 10% reduction were recorded. Further work would be needed, for higher computational domains or for smaller grid spacings, since for instance the minimum spacing along the normal and transverse directions is close to 16.5% of the height and 4.2% of the groove width, respectively.

Choi and al, [196], considered the effect of riblets in fully developed laminar channel flows. The upper and lower walls of the channel are triangular grooves, the spacing of which could vary with respect to the height and the width of the computational domain ; moreover, different ridge angles have been taken into account. The Poisson equation has been solved, through Direct Simulations by using a multi-grid method in generalized coordinates. The mean pressure gradient as well as the cross-sectional area have been kept constant for the whole riblet calculations. Thus, variations of the mass flow rate would

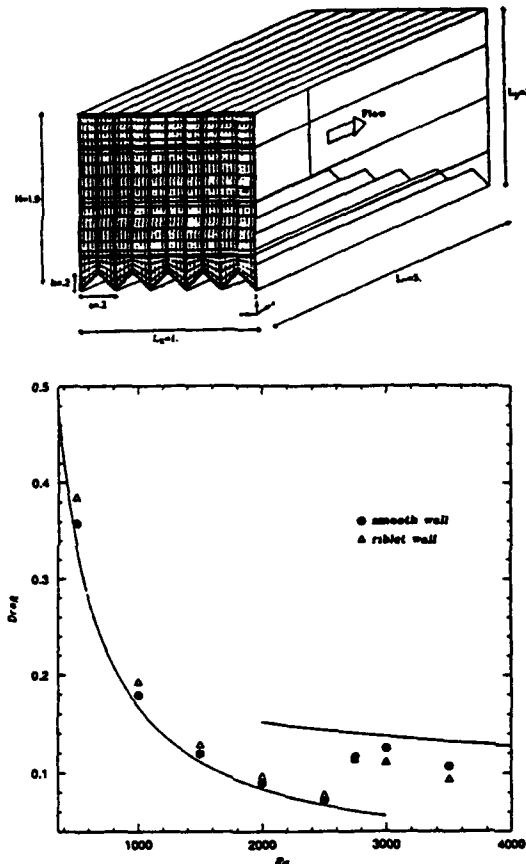


Figure 48: Variations of drag versus the Reynolds number, from Chu and Em Karniadakis [195].

determine the effects of riblets on drag.

Special care has been taken when considering at the size of the computational mesh, [196]. For instance, doubling the number of mesh points in the direction normal to the wall induced only 0.1% variation on the mass flow ratio. All calculations showed a mass flow decrease, implying that the drag increased for the same mass flow rate. Furthermore, as the groove spacing became smaller, the mass flow rate approached that of the smooth plane channel, which seemed to be in agreement with earlier results from Launder and Li as regards behaviour of riblets in internal flows, [188].

• More recently, Launder and Li, [193], explored the effectiveness of L-, V- and U-shaped riblets in fully turbulent developed flows. Depending upon the shape of the groove, either Cartesian code or generalised orthogonal version were considered. Launder and Li used a local model : the Launder-Sharma low-Reynolds number $k-\epsilon$ model. Results obtained from the V-groove riblet model are given on figure 49.

It should be noted that the amount of drag reduction achieved is quite comparable to that obtained from experiments. However the maximum drag decreases occurred at values of h^+ still too large by a factor of 3, and also drag increases have been obtained for

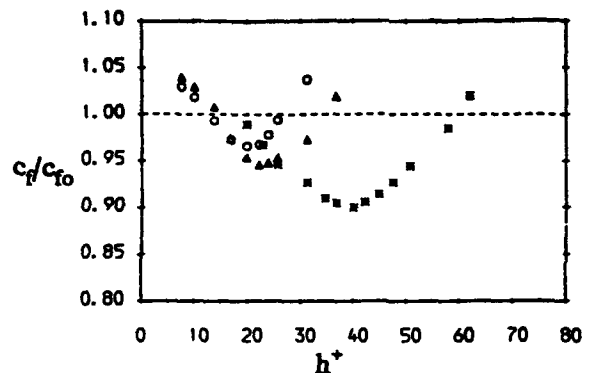


Figure 49: Variation of relative skin friction drag for V-groove riblet models (\circ : $s/h=2.0$, Δ : 1.6, $*$: 1.0) from Launder and Li [193].

h^+ less than 10. Despite these deficiencies the results are very encouraging ; the main difficulty is, of course, the modelling of the flow within the groove, especially when the flow seems to be essentially laminarized in this area.

• Djenidi et al, [191], have also recently continued their numerical studies by considering orthogonal curvilinear meshes, which allowed them to calculate flow behaviour inside more groove shapes, without being limited to V- or L-shaped riblet models. As mentioned by the authors, such an approach has the advantage of increasing the grid resolution in regions where velocity gradients are often highest (i.e. crest vicinity). Extensions of the IMST and CERT numerical code, originally developed for laminar boundary layers, were made for turbulent flow by using a conformally transformed mixing length, [191]. Work is now in progress in order to introduce within the code a low Reynolds number $k-\epsilon$ model, [192].

Although very few experiments have been reported with detailed measurements within the grooves in turbulent flows, comparisons have been made with studies of Vukoslavcevic et al [183] and those from IMST, which have been reported recently by Benhalilou et al [175]. An example of comparison is given on figure 50, in a $U^+(y^+)$ diagram ; the experimental conditions are : $s=2h=7\text{mm}$, $U_\infty=9\text{cm}^{-1}$, $h^+=15$.

It is fair to say that the predicted velocity profiles are quite comparable with the experimental ones, especially in the near wall region. Discrepancies seemed to appear in the outer edge of the buffer layer, where the experimental profiles over the peak and the valley collapse onto a single curve. It should be noted that even for the smooth case the wake law is not very well satisfied ; one has to be aware that experiments have been performed at low Reynolds number ($Re \sim 300$), for which transition had to be tripped, justifying the differences in the outer part of the turbulent boundary layer.

• Such developments of turbulent codes, accounting for the effects of riblets, should be pursued, but the models must be compared to several sets of experiments in order to determine which parts of the

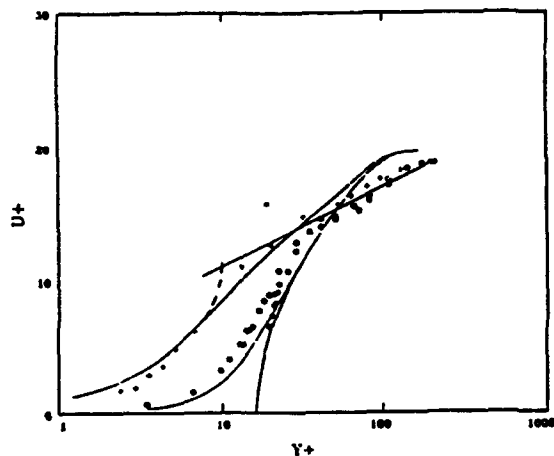


Figure 50: Computed and measured streamwise velocity profiles in turbulent flows (+ : smooth wall, o : trough, • : peak) from Djenidi et al [191].

considered low Reynolds number models need further refinement.

Finally a recent study carried out by Tullis and Pollard, [194], from Queen's University, Kingston Canada must be mentioned. They developed a fairly new control volume finite element method which provides triangular elements which fit exactly the cross-section of the V-shaped riblet; allowing computations to be made over several riblets and thereby accounting for significant interactions between the grooves.



TURBULENT SKIN FRICTION DRAG REDUCTION BY ACTIVE AND PASSIVE MEANS: Part 2

by

E. Coustols & A.M. Savill

92-17814



4 Outer Layer Manipulators: LEBUS

The use of in-flow manipulator devices, such as LEBU's originated from research into the optimum use of screens and honeycombs for controlling (reducing) free-stream turbulence in wind tunnels [197]. Such 'flow management' techniques were first applied to boundary layers by researchers at NAL Bangalore about 15 years ago [198], and a rapid succession of further studies (conducted first at IIT [199], NASA [200] in the USA, then at the FFA in Sweden [201] and the Cavendish Laboratory of the University of Cambridge, England [202]) led to the identification of single or preferably tandem (in-line) thin element devices as the best means of achieving any nett drag reduction. Early studies were restricted to nominally zero pressure gradient low Reynolds number external boundary layers, and subsequent more detailed parametric surveys [201] - [152] indicated the following optimum manipulator parameters for such flows (in terms of the boundary layer thickness, δ , at the device leading edge) of: chord length: $1 \leq l \leq 2$; height: $0.5 \leq h \leq 0.75$; spacing for tandem arrangements: $s \sim 10 - 12$ and thickness $t \leq 0.1\text{mm}$ - see figure.

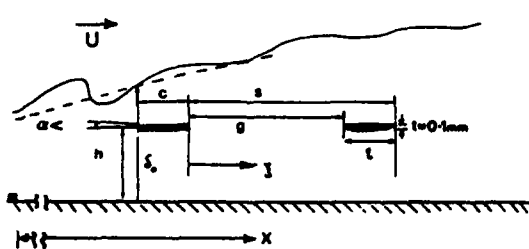


Figure 51: Configurational parameters for typical LEBU geometry

In order to minimize device drag it also quickly became evident that the devices must be sufficiently tensioned to avoid vibration, have sufficiently smooth surfaces and rounded leading edges to reduce device drag to essentially just laminar skin friction, and have a sharp trailing edge to avoid any separation. With such devices it would appear that nett drag reductions in the range 0 - 2% (for single elements) and 0 - 5 or 7% (for tandem devices) might be attained under very carefully controlled laboratory conditions (especially avoiding any 3D flow effects and possible amplification or modification of these by the device).

The uncertainty in the above estimates is a reflection of the wide range of estimates provided by different researchers due to the difficulties of measuring either the device drag or performance (and particularly their difference) with sufficient accuracy. In fact all of the optimum parameters result from a compromise between the additional drag due to the introduction of the devices into the flow and the reduction in skin friction drag they produce downstream. This is particularly true of the chord length, since both the device drag and the integrated C_f reduction downstream increase with l , but at different rates, but there is a notable advantage in employing plates with $l > \delta$ largely due to the fact that this is the scale of the largest eddy structures in the flow. The optimum height is determined primarily by the influence it has on the shape of the C_f distribution produced behind the device since placing this nearer the wall, where the mean velocity and hence (in absence of any ground effect) device drag is lower, results in a larger maximum C_f reduction (exceeding 33%), but a much more rapid recovery ($\sim 50\delta$) and thus a smaller integrated effect. However mounting the manipulator nearer the outer edge of the layer reduces their effect and increases their drag penalty - see figure.

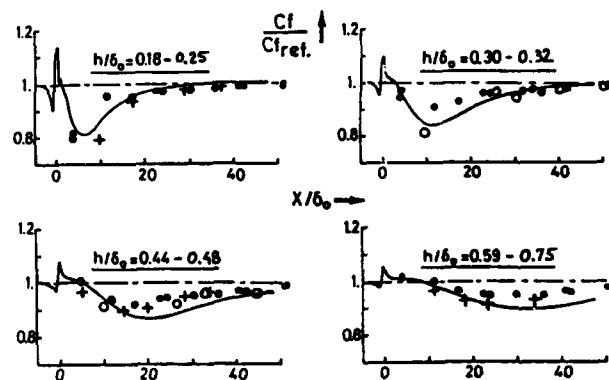


Figure 52: Effect on C_f of varying LEBU height for an optimised tandem device (o : DATA Laval, • : DATA CERT and + : DATA Cambridge).

By comparison the device thickness does not appear to have a very large effect on its performance [207], at least for $t \sim 0 - 0.3\text{mm}$, although thicker devices may generate a much larger wake (mainstream deficit) and hence have more effect and this should be kept to less than 0.1mm to minimize form drag. The spacing s (from leading or trailing edge of the first manipulator element to the leading or trailing edge of

the second) again has rather less influence on either the skin friction reduction or device drag - it is also not obvious that this is the most relevant dimension since the gap g between the two elements (from the trailing edge of the first to the leading edge of the second) may be of greater significance. A close spacing (or gap) ensures that the drag of the second device is reduced because of the 'shielding' influence of the first, but a wider spacing extends the region of maximum C_f reduction thus producing a larger integrated effect. It might therefore be expected that the apparent optimum value for s which has been confirmed by a number of independent studies, also represents a simple compromise between these two rather weak effects. However it would appear from other research that the optimum s (or g) also depends on l - see figure. In particular for plates with a shorter than

optimum chord length $l < \delta$ there is evidence that it is more advantageous to have a gap $g < 2\delta$, and indeed a nett drag reduction has been reported for $g < \delta$ [201]. However for plates with a chord length greater than the optimum, $2\delta < l < 3\delta$, it would seem the optimum g varies such that $s \sim 10\delta$ once more [206]. A possible influence from these observations is that for small tandem plates the main effect of a small gap may be to simply increase their combined effective length to that of an equivalent single device with $l > s$ (particularly if they are connected by a laminar wake). Clearly for plates which are already larger than optimum such an effect would be of no added benefit. However it has been noted that the performance (whether defined in terms of the nett drag reduction, integrated C_f reduction or local maximum C_f reduction they produce) of such larger, and more widely spaced tandem, plates in fact varies in a weakly periodic manner with s/δ [205] or g/l [208] (the scaling used for galloping instabilities between tandem obstacles in a free-stream) with the optimum value being merely the best of several subsidiary optima. This suggests that the spacing may also influence a beneficial 'beating' interaction between the turbulent vortex wakes produced behind the two devices. Such an interpretation implies that there should be some advantage in replacing each of the elements of an optimised tandem device by a close pair of lower drag (or larger wake generating) plates. This type of 'quadruplet' arrangement has in fact been tested [209] and found to produce a larger integrated C_f reduction than an equivalent tandem configuration with the same device drag. It has been suggested that the principal advantage of multiple plates over a single (larger) element plate is that the device drag and hence momentum deficit is introduced in smaller stages [209], [210], but in fact three independent studies [14], [211], [212] of 'triplet' devices with l , s_1 and s_2 similar to that of the optimum tandem manipulator have failed to find any additional benefit from such a configuration once the extra device drag is accounted for. However larger drag reductions have been achieved with serrated trailing edge devices which may introduce more resistant longitudinal vortices into the manipulator wake [14] - see figure.

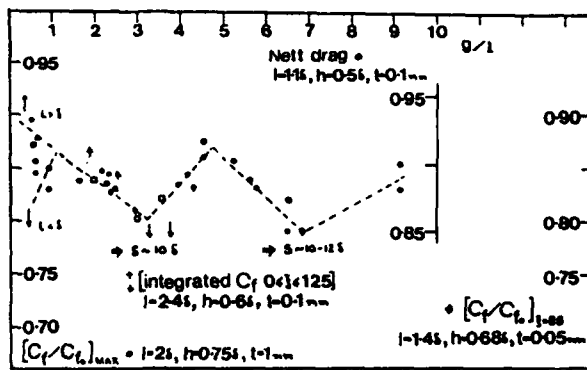


Figure 53: Effect of varying tandem LEBU spacing on drag reduction performance

optimum chord length $l < \delta$ there is evidence that it is more advantageous to have a gap $g < 2\delta$, and indeed a nett drag reduction has been reported for $g < \delta$ [201]. However for plates with a chord length greater than the optimum, $2\delta < l < 3\delta$, it would seem the optimum g varies such that $s \sim 10\delta$ once more [206]. A possible influence from these observations is that for small tandem plates the main effect of a small gap may be to simply increase their combined effective length to that of an equivalent single device with $l > s$ (particularly if they are connected by a laminar wake). Clearly for plates which are already larger than optimum such an effect would be of no added benefit. However it has been noted that the performance (whether defined in terms of the nett drag reduction, integrated C_f reduction or local maximum C_f reduction they produce) of such larger, and more widely spaced tandem, plates in fact varies in a weakly periodic manner with s/δ [205] or g/l [208] (the scaling used for galloping instabilities between tandem obstacles in a free-stream) with the optimum value being merely the best of several subsidiary optima. This suggests that the spacing may also influence a beneficial 'beating' interaction between the turbulent vortex wakes produced behind the two devices. Such an interpretation implies that there should be some advantage

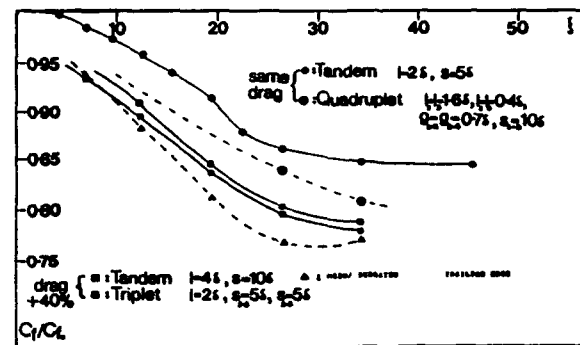


Figure 54: Effect of varying LEBU configuration on C_f reduction

If extended C_f reduction is required, it may be desirable to 're-manipulate' the boundary layer prior to its eventual recovery (at around 150δ downstream) by introducing a second tandem device into the relaxing flow. The maximum local C_f reduction location might seem the best position to attempt re-manipulation, but in general this will be too close ($\sim 30 - 40\delta$) behind the first manipulator for any nett drag reduction to be realised and so re-manipulation later in recovery (at about 100δ) should be envisaged. In principle this procedure could be repeated ad infinitum, although it may be that the additional manipulators require re-optimisation other than just rescaling their dimensions on the local δ . Surprisingly no examination of this possibility has yet been reported.

Equally, very little research has been conducted into the effect of LEBUs on laminar or transitional, as opposed to fully turbulent flows. This is presumably largely due to the expectation that other control techniques are more effective in such flows, however the only two experimental studies which have been carried out have shown that LEBUs may both delay the development of Tollmein-Schlichting waves [144] and have a similar average effect on turbulent spots as on a fully developed turbulent boundary layer, but a

larger influence on the region of a spot which is dominated by large structures [213]. The latter is perhaps to be expected of a Large Eddy Breaking device and could also explain the larger nett reductions reported in some very low Re turbulent boundary layer flows which may not have been fully turbulent with a 'transitional' structure closely resembling collections of turbulent spots.

Until recently little attention had also been directed to possible internal flow applications of LEBUs despite obvious interest in this and the ease of making direct drag measurements from pressure drop. However over the last 5 years a number of experimental investigations have been made of manipulated developing [214] and fully developed [215] - [220] pipe flows as well as fully developed channel flows [221]- [222] and the latter have been complemented by a number of Large Eddy Simulations for both laminar [223] and turbulent channel flows [54], [55], [224], [225]. None of these studies have in fact revealed any nett drag reduction and it would appear that there is insufficient development length for this to be achieved in developing internal flows even with ring devices optimised for axisymmetric external flow [226] and scaled on the developing layer thickness - see figure.

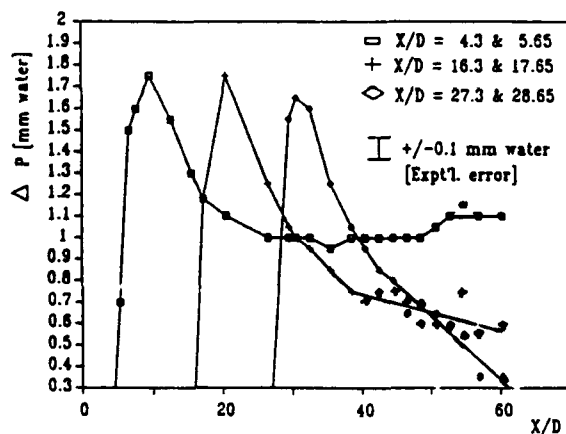


Figure 55: Performance of various ring manipulator configurations in pipe flow

However only a very limited range of single and tandem manipulator configurations has so far been evaluated compared to the very extensive parametric surveys that have been conducted for external flows; the flow development length downstream of the manipulator (s) has not always been sufficient for complete recovery to occur; and there is still some uncertainty what the optimum device parameters should be once the flow is fully developed and the pipe radius R or half channel width ($D/2$) replaces δ as the reference length scale. Certainly it is too early to rule out the possibility of any nett drag reduction in such flows particularly as in some cases [216], [220] the device drag has virtually been recovered and an analysis [227] of pipe flow in comparison to annulus flow (equivalent to

a pipe flow containing very long chord length manipulator rings) has indicated that a nett drag reduction may theoretically be possible given sufficient flow development length.

From a study of the limited available data it would appear that thus far the optimum manipulator configuration determined for fully developed pipe flow is $l \sim 0.4R$, $h \sim 0.2R$, $s \sim 3R$ and $t \leq 0.15mm$, although devices with larger chord $l \sim 1.2R$ have yet to be tested experimentally. [Note that ... alternative values of $l \sim R$, $h \sim 0.75R$, $s \sim 9.5R$, equivalent to those found to be optimum in both external and developing internal flows, have been indicated in some cases where the manipulator was mounted at only $40D$ from the pipe inlet, but this may be sufficient only to ensure that the developing wall layer has merged (at $\sim 30D$) and not for the flow to be fully developed (requiring perhaps $75D$) as ensured in other cases].

For fully developed channel flows the LES studies suggest that such devices would also have the strongest influence on the near wall eddy structure [228]. However direct drag measurements suggest ($l \sim 1.2(D/2)$, $k \sim (D/2)$, $s \sim 10(D/2)$) is then preferable. This rather unexpected difference between pipe and channel flows may reflect an important difference in flow dynamics, for although there is no entrainment to be influenced in either case (one reason advanced to explain why nett reductions should not be expected in such internal flows [229]). Analysis of the LES results [228] clearly show that there is 'encroachment' of each of the two halves of a plane unmanipulated channel flow on the other and that this is most strongly damped by the introduction of manipulator plates at the centre line - a control option which has not parallel in the pipe flow case. However the pipe flow structure is now known to be even more highly correlated around its circumference [230] and attention should perhaps be directed to interrupting this as well or even instead. Since pipe flow manipulator devices inevitably take the form of rings these will be self-tensioning, but must be supported in some way from the walls. These supports may therefore already be contributing to the device performance as well as device drag so the manner in which the number and arrangement varies from case to case needs to be considered in greater detail. It is reasonable to expect that further studies would enable a better understanding of the drag reduction mechanisms of LEBUs generally and the influence on these of different flow and boundary conditions even if no nett reduction is attainable.

Of course for high speed flow and most possible practical applications more robust and more rigid manipulators are required. Thus the attention of external flow researchers in recent years has shifted to aerofoil devices. The replacement of thin (albeit shaped) flat plate manipulators by aerofoil section devices introduces two other significant configurational parameters: profile shape and angle of attack. Initial studies were still restricted to relatively thin symmetrical shapes, such as NACA 0009 aerofoils, in low speed flow ($M < 0.2$, $Re < 10,000$) at chord Reynolds numbers

Re_c less than 100,000 [231]-[150]. However subsequent investigations have assessed the performance of both various asymmetrical profile manipulators under similar low speed conditions [14], [232] as well as single and tandem devices at much higher velocities [14], [233] ($M \sim 0.5 - 0.9$; $Re_c > 10,000$) and Re_c greater than 10^5 (although this is still rather low for aerofoil applications).

The low speed studies have revealed that essentially the same values of l , h and s are required to optimise the performance of aerofoil devices and similar nett drag reductions (of up to $\sim 7\%$) have been estimated for optimised tandem NACA 0009 devices at nominally zero angle of attack from indirect drag measurements in some carefully controlled 2D laboratory flows. Other direct drag balance measurements, however, have not indicated any such nett benefit although it would appear that the device drag can at least be recovered. There is also some evidence that larger benefits may be achieved by placing the devices at a small angle of attack (of under 1° - see [210]) or by replacing symmetrical profile elements by similar drag inverted asymmetric devices such as NACA 4409 profile manipulators - possibly because these act as a kind of one-sided vortex generator [234] - see figure. In addition it has been suggested that larger drag re-

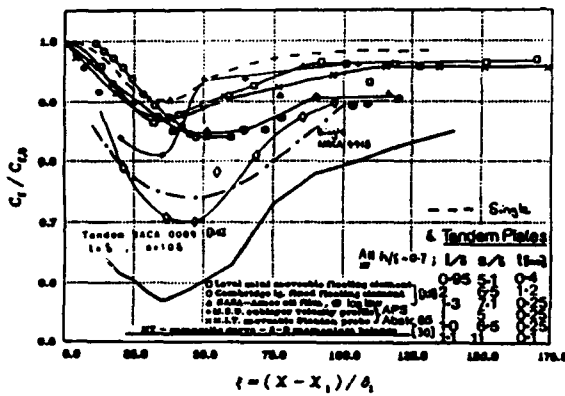


Figure 56: Typical variation of skin friction data for various tandem devices

ductions might be realised at chord Reynolds numbers exceeding 300,000 [235], when trailing edge separation might be avoided, or if the flow leaving the device is laminar and transition occurs within the wake of the manipulator rather than on its surface [236]. (In fact much of the scatter observed between different sets of data for both thin plate and aerofoil manipulators has been attributed to the great sensitivity and to the exact nature (laminar, transitional or turbulent/vertical structure) of the flow over the manipulator and within its wake).

The evidence from the latest high subsonic tests of single and tandem NACA 0009 aerofoil manipulators, as performed for Airbus Industrie [209] is that similar levels of performance are maintained, with the same optimum configuration as for low speed, pro-

vided vibration and shock/pressure losses are avoided. This finding is contrary to other results reported from studies of ring manipulators on an axisymmetric body in water at similarly high Re_θ , but much lower free stream velocities [237]. The conclusion from these other studies was that LEBUs might be less effective at higher Re because they only directly influence the larger outer scale motions and rely on communication of effects across the layer through even smaller scales of motion to indirectly effect the wall (shear) properties - the argument being that at higher Re their indirect influence was weakened due to the much larger hierarchy eddies of scales. It now appears that this is not the case, at least at higher M , perhaps because it has recently been shown [238] that the large structure is stronger in transonic flows and this may compensate any cross-spectral damping of the manipulator influence. In fact at $M = 0.8$ close to the typical Airbus aircraft cruise condition (which varies from 0.78 to 0.82 depending on aircraft type) the integrated C_f reduction behind an optimum single NACA 0009 manipulator was found to approximately balance the device drag despite the fact that C_D was approximately twice the value found in the free-stream (both being measured with direct floating element) although conveniently C_D was found to be a minimum at $h/\delta \sim 0.67$. However this result was very sensitive to the fine details of the device leading and trailing edge geometry. Indeed at $M = 0.7$ with a different device, having nominally the same profile shape, only half device drag was recovered and vibration resulted in no C_f reduction at all - see figure.

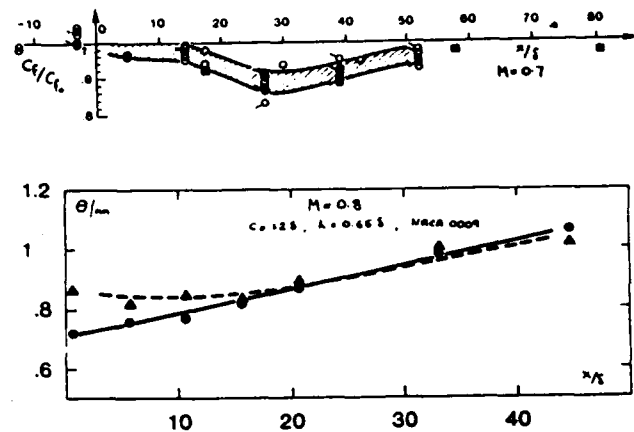


Figure 57: Comparison of Cambridge and CEAT data for a single NACA 0009 LEBU (legend : top : open symbols CEAT Data, filled symbols : Cambridge Data).

In addition at $M = 0.8$ Schlieren photography revealed the existence of an expansion fan and associated pressure waves emanating possibly from a small sonic bubble on the upper surface near maximum thickness. Oil flow liquid crystal visualisation indicated transient separation on the pressure surface

which became more sharply defined at M nearer 0.9 when a normal shock was generated at the top of the device. To avoid deleterious effects the use of a flat-topped aerofoil (eg. an inverted NACA 4409) has again been recommended. Although no such asymmetrical profile device has yet been tested under such flight representative conditions it is interesting to note that similar devices, although with a rather cruder shape, were employed in the only flight tests which have been concluded of LEBUs [201] and gave similar C_f reductions. However the main reason for using devices with this type of negative lift-generating profile was to ensure that they put their supports into compression rather than tension when aerodynamically loaded; in order to both maintain them on the aircraft and to minimise vibration. It seems likely from other studies in water that vibrational effects may have contributed to the generally poor results obtained in this medium whether at high or low Re . It is also clear that a wide aerofoil parameter range remains to be explored.

Most research to date has considered only the manipulation of undisturbed 2-D flows in zero pressure gradient, but any practical application of LEBUs to real engineering flows, such as the external surfaces of aircraft or the internal passages of aero engines, would need to take into account several additional disturbing influences. Fortunately a number of studies have already been made which suggest that similar manipulator performance can be maintained under a variety of relevant flow conditions. Thus investigations into the use of manipulators for flow over various (drag increasing) rough [11]-[240], or longitudinally (convex) curved [241] surfaces and in mild adverse pressure gradients ($\beta \sim 0.2$) [201], [206] has revealed little change in the absolute C_f reduction compared to that found in undisturbed flow using similar optimised devices. The same is approximately true for manipulated layers subjected to the effects of free-stream turbulence (low intensity $T_u \leq 3\%$, and length scale $l_u < \delta$) [242] and stronger adverse pressure gradients ($\beta \sim 0.5$) [208], [243]. There is also some evidence that larger reductions might actually be achieved for larger free-stream intensities and length scales, due to an enhanced influence of the 'blocking effect' of the manipulator and its wake [244], but the benefits attainable in a sustained positive pressure gradient are limited by the fact that manipulator advances separation, due to the simultaneous reduction in C_f and increase in H that it produces. Similar levels of performance can however be anticipated in favourable pressure gradient flows and those subjected to 3D (in-plane) curvature, since such additional effects appear to have had little influence on the flight tests [201], where they were inevitably present. It would also seem likely that LEBUs should be at least as effective in concave wall flows due to the increased larger (longitudinal) eddy content of such flows.

It has to be accepted, however, that any practical application of LEBUs to aircraft solely for the purpose of reducing skin friction drag seems rather unlikely. Even if a nett reduction of under 10% could

be achieved using (say) some form of tandem inverted supercritical aerofoil manipulators (which would have to have been optimised for a high turbulence environment at transonic speed in ground effect), additional penalties associated with supports, repeated re-manipulation, vibration (etc.) would almost certainly reduce any practical benefit below a cost effective threshold. Nevertheless it is clear that manipulators can be very low (essentially zero) drag penalty control devices and that the LEBU concept is better suited to, and therefore likely to be more effective in, flows containing much stronger large eddy/vortical structures than near-equilibrium attached flows. There are thus a number of areas on aircraft where LEBUs still might find application for other purposes e.g. in wing/body junctions (for controlling longitudinal trailing vortices); on the rear part of the fuselage (for controlling separation); and wing tips (for both purposes).

Although no detailed studies have yet been made of the possible benefits of using LEBUs for such purposes it is known that both surface parallel LEBUs and perpendicular fins/supports are effective in suppressing longitudinal vortices [213], [245], while it would appear LEBUs are also at least as effective for controlling a reattaching boundary layer [246]. It has also been shown that boundary layer manipulation prior to separation at a trailing edge can reduce mixing between the separated flow and a much lower speed blown wall flow [247]. In addition, although direct manipulation of separated mixing layers, has not been attempted LEBU-type devices have been successfully applied to other free shear flows [248]. [Note that a cylindrical rod manipulator has been applied to a wall jet [249] with similar results to those obtained using such a device in a boundary layer [202]].

It has also been demonstrated that LEBUs can reduce flow separation due to shock boundary layer interactions if they are positioned at the shock location so as to prevent it impinging on the wall [250]. They should thus be able to influence form drag, induced drag and wave drag.

LEBUs might also be used to control other properties of the flow such as heat transfer and noise since it has already been demonstrated, both experimentally and computationally that they can reduce heat transfer to or from aerodynamic surfaces [251]- [254], as well as surface pressure fluctuations, and hence flow noise [255], [256]; although in the latter case it appears desirable to revert to the use of drag-increasing, multi-component, honeycomb-like devices [257], [258] to maximise the benefits. For subsonic aircraft any advantages of LEBU heat transfer reduction may be restricted to possible engine application, but for a future HST there might be scope of external flow control. The use of LEBUs for noise-reducing could be considered for the boundary layers on the fuselage of any future aircraft fitted with unducted fans, or those on present prop-fan nacelles.

It is therefore likely that at least some interest will be maintained in LEBU research not only with a view to the possibly more varied practical applications en-

visaged above, but also because such studies afford us a better appreciation of the response of turbulence to imposed in-flow distortions and thus allow a better appreciation of the flow dynamics as well as the means or mechanisms by which it may be controlled.

4.1 Modelling the effects of outer layer manipulators

From a computational standpoint manipulated flows are of equal interest because they represent a more challenging test of current methods than the simpler undisturbed, near-equilibrium shear layers subjected to additional straining considered at the 1980-81 Stanford Conference and other more recent ER-COFTAC and other workshops. In particular LEBU manipulated flows highlight weaknesses in the single length/single time scale, equilibrium flow assumptions which form the foundation of most present modelling, and emphasise deficiencies in the pressure-strain. Diffusion and Dissipation closure approximations employed in even state-of-the-art full Reynolds stress transport (RST) schemes, while the need to resolve the flow over the manipulator and wall surface in great detail provides a useful examination of the wide variety of near wall modelling approaches in current use (though the modelling of non-planar riblet surfaces represents an even more severe test).

At the same time interest in the possibility of predicting the effects of manipulation has been stimulated by the desire to avoid having to repeat the expensive experimental parametric optimisation studies which have been carried out for low-speed turbulent boundary layer flows when considering the possible application of (perhaps aerofoil) manipulators to laminar, transitional, transonic or supersonic external flows or internal flows under a variety of (disturbed) flow conditions. It is not surprising therefore to find that a large number of attempts have already been made to model such flows with some notable successes.

The earliest attempts to compute manipulated flows were restricted to consideration of the effects of imposed momentum deficits, and/or changes in length scale, on boundary layer development using simple mixing length [259] and $K-\epsilon$ models [200]. However, over the last 5 years more realistic manipulated turbulent boundary layer computations have been performed using a wide range of models at an ever-increasing level of closure starting with integral [260] and one [261] or two [262] mixing length methods as well as an alternative prescribed eddy viscosity approach [263]; a one-equation (τ -l) scheme using the method of characteristics; further high- Re [264] and low Re (Chien [265] Launder-Sharma [266] $K-\epsilon$ models); an Algebraic Stress Model (ASM) treatment [205], [208], [241], [243]; a 3-equation $K-\epsilon-uv$ scheme [267], [268]; and a 5-equation or full RST $K-\epsilon-uv-u-u^3-v^3$ transport closure [152], [244], [267] - all within the framework of the Reynolds averaged Navier-Stokes equations. In addition Rapid Distortion Theory (RDT) [269]- [271] discrete point vortex [272] and vortex core [258] modelling, as well

as a vorticity/stream function approach [273], have been applied to manipulated boundary layers. Large Eddy Simulations (LES) have also been performed for manipulated boundary layers [224]- [226], and fully spectral Direct Numerical Formulations (DNS), based on patching techniques, have been used to study the effect of LEBUs on subcritical synthetic wall flows containing known vortical structures [274].

A first series of parametric computations have also been performed (in the absence of any turbulence model) for the case of a laminar boundary layer manipulated by both single and tandem manipulators [268], and similar parameterised results have been obtained (using a Lam and Bremhorst low- Re $K-\epsilon$ model) for developing pipe flow [214], [215], [217]. In addition LES have been performed for manipulated laminar and turbulent channel flows [222]- [224] as well as a laminar boundary layer [222].

The simulations have provided useful 'data' to complement the very detailed mean and turbulence field experimental data which has now been acquired from a large number of independent studies - most notably those carried out at Cambridge University [202], [205], [207], [208], CEAT Poitiers [207], [275]- [278], EPFL [206], and ONERA CERT [152], [150], [279], [280]. The availability of such data has allowed an almost complete specification of initial conditions, and a detailed comparison of output, for all of the various numerical schemes which have been tested thus far.

Although some instructive results have been obtained from simpler models it would appear that (at least within the framework of a parabolic Reynolds averaged scheme) an ASM closure is the minimum required to post-dict the development of a manipulated boundary layer (particularly the C_f distribution) downstream of the device to sufficient accuracy for engineering purposes. This is perhaps not surprising since this level of closure provided quite reasonable predictions for a wide range of the Stanford test cases including flows subjected to pressure gradients, streamline curvature and free-stream turbulence models. (Indeed considerably better than $K-\epsilon$ models and generally equivalent to full or reduced RST schemes). In addition the same 'standard' ASM scheme was subsequently found to be capable of modelling a range of confluent wake/boundary layer interaction flows [281], including ones exhibiting strong negative-production regions [282], and a manipulated boundary layer might be regarded as a category of the same class of flows where the wake merges internally rather than externally with the boundary layer.

The main deficiency of such an ASM approach (and indeed of all the other turbulence models tested to date) is that because of its near-equilibrium matrix it tends to indicate too rapid a recovery following manipulation and it is rather sensitive to the initial dissipation profile behind the device. (The dissipation is one of the hardest qualities to measure or extract from formulations - generally only being obtained from a balance of other terms which are themselves subject to some uncertainty - and this has only attempted in a few cases). Nevertheless very reason-

able agreement has been obtained with experiment for turbulent boundary layers manipulated by optimised single and tandem devices in nominally undisturbed zero pressure gradient conditions, by introducing some allowance for non-equilibrium effects through RDT modifications to the model constants [241] and by evaluating the initial dissipation profile from a modified mixing length expression [244]. The same approach has also been used to post-dict the effects of a strong adverse pressure gradient ($\beta \leq 0.5$ representative of wing applications) [243] as well as small free stream turbulence intensity (< 3%) and length scale (< 1.56) [244] on a manipulated layer; and subsequently to predict the effect of convex or concave curvature [241] and larger free-stream turbulence intensities/length scales [244] likely to be encountered in manipulating external aircraft and internal aerodynamic flows - see figures.

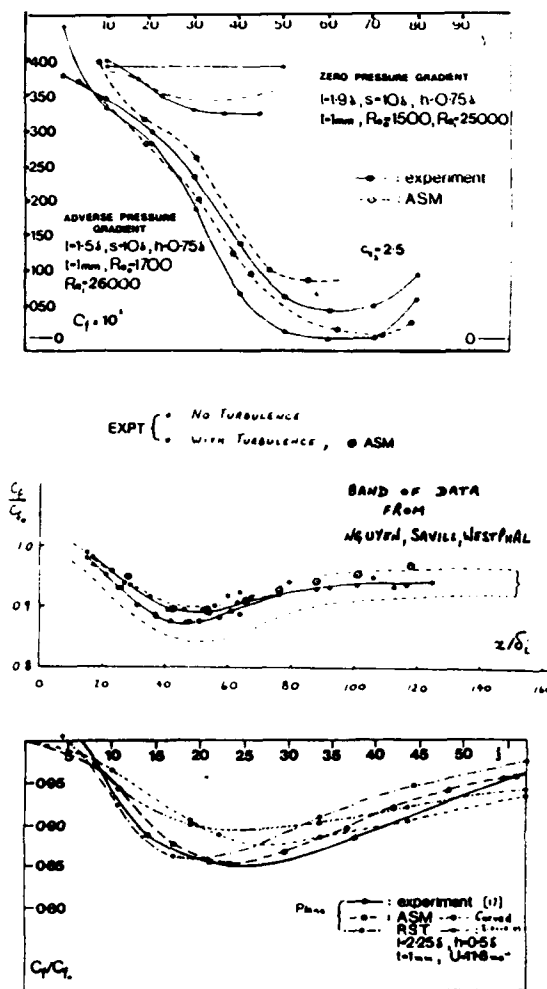


Figure 58: ASM postdiction of a manipulated layer subjected to strong adverse pressure gradient and freestream turbulence and ASM & RST predictions for effect of curvature on a manipulated layer

To perform computational parametric optimisation of LEBUs themselves, however, elliptic computations starting upstream of the device(s) are required. These largely avoid the problems caused by any inexact specification of initial conditions since 'standard' profile forms for the initial unmanipulated layer can be either assumed or generated from a pre-cursor computation starting from upstream. However the ASM formulation is not well suited to an elliptic numerical scheme. For the case of developing and fully developed pipe flows controlled by single [214] and tandem ring [215] where only a few manipulator configurations have been studied experimentally, a low Re (Lam and Bremhorst) $K - \epsilon$ has been employed in an effort to first fairly successfully post-direct some of these and then in an attempt to predict a more optimum configuration [217] for future experimental validation. The computations tend to confirm conclusions first arrived at on the basis of the more limited experimental evidence that nett drag reduction is unlikely to be achieved in developing flow, but could still be possible in fully developed flows. In the latter case the optimum manipulator spacing is predicted to be $S \sim 4R$ (larger and smaller spacings being less effective) for rings with $h/R \sim 0.25$ and $I/R \sim 1$ and $t \sim 0.15-0.3mm$. further computations are now being performed for thinner devices which it is hoped may reveal any nett drag reduction capability - see figure.

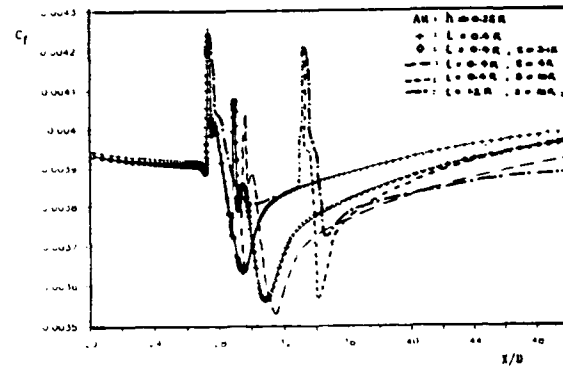


Figure 59: Parametric optimisation for pipe ring manipulator spacing with $k-e$ model

However it would appear from comparisons with high and low Re (Lauder-Sharma) model computations made at ONERA-CERT that some form of Differential Stress Model (DST) is required for elliptic turbulent boundary layer computations. A 5-equation RST model has been found to produce predictions for both single and tandem flat plate manipulators in excellent agreement with the experimental data from Cambridge, CERT, EPFL, and the ER-COFTAC Database test case for a flat plate manipulated boundary layer, compiled from very extensive data collected at CEAT [278]. However, since the re-

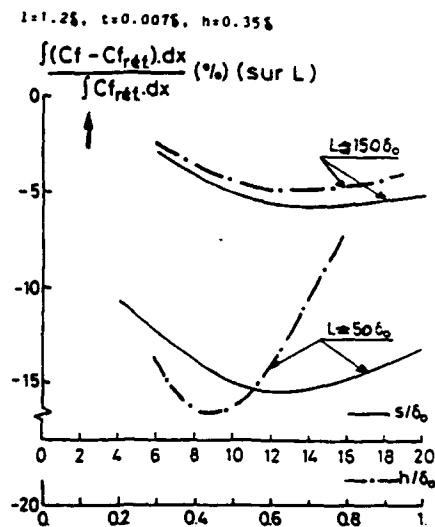


Figure 60: Parametric optimisation predictions obtained from a 3-equation model

sults obtained from a simpler 3-equation $K - \epsilon - \bar{u}\bar{v}$ model were not very dissimilar this was adopted for subsequent parametric computations which successfully predicted both the optimum spacing and height of tandem manipulators (as determined experimentally for maximum integrated C_f reduction) of $s \sim 128$ and $h \sim 0.3 - 0.656$ depending on the integration length - see figure.

The same code has now been employed in general curvilinear co-ordinates with conformal meshes to model the flow around and downstream of single and tandem aerofoil manipulators. Initially computations were restricted to symmetrical ONERA-D [279] or NACA 0009 [268] devices in first laminar and then low-speed turbulent flows. The parametric series of results which have been obtained for laminar flow again represent true predictions since no similar experimental investigations have yet been undertaken. However results for single flat plate manipulators have proved to be in good agreement with LES results for laminar boundary layer and channel flows, and the aerofoil predictions are sufficiently interesting to warrant further experimental verification. In particular they indicate that for similar configuration devices approximately the same maximum local C_f reduction is generated in laminar flow as in turbulent and the optimum $l \sim 1.36$ and $s \sim 6 - 128$ are therefore also similar. However, although the distance from the device where this maximum reduction occurs again seems to be closely related to the rate at which the device wake spreads to the wall (and varies in a similar manner with h). It increases far more rapidly with h than in turbulent flow (so that the optimum $h/\delta \sim 0.4$) and recovery may take more than six times longer! This unexpected result seems to be connected with an observed greater persistence of the LEBU wake deficit and an equally delayed recovery of the wall static pressure - presumably due to the absence of turbulent mixing - see fig-

ure.

Since very similar results were obtained from both ONERA-D and NACA 0009 devices only the latter have been considered in subsequent turbulent computations. Comparison of parametric predictions with the further ERCOFATAC Database test case for single and tandem NACA 0009 manipulated boundary layers, based on data compiled at ONERA CERT [280], has revealed that these are in good agreement regarding the location, magnitude, and variation with h/δ of the maximum C_f reduction both behind and between the devices (at least within experimental error), but recovery is always predicted to be too rapid.

It has very recently been found that a larger maximum reduction is predicted for an inverted asymmetrical profile device, and also that the recovery is delayed (and thus the nett performance again improved as anticipated) if the device boundary layers and its wake are kept laminar. (Since the model normally assumes a simple mixing length description near surfaces it is relatively easy to impose laminar conditions around the device and to extend these into its wake). However it is quite clear that the present modelling is insufficient to take proper account of near wall/transitional low- Re [283] and thin element wake [284] effects.

Accordingly future RST modelling will incorporate the latest low- Re and '2D-2C limit' extensions [284] which can account for these and should thus improve further present predictive capabilities. At the same time it is recognised that because manipulation introduces very small scale wake vortices into a boundary layer flow dominated by much larger scale energetic eddies (hereby promoting a rapid beneficial energy cascade) such flows may represent an ideal case for the implementation of multi-scale models where large and small scales are modelled by separate transport equations, particularly as spectral range data can be provided by the CEAT group and the problem of a continually shifting frequency cut off may now be overcome by multi-filtering [285]. It is expected that this will be attempted shortly.

Other modelling is now underway, aimed at predicting the effect of manipulators on heat transfer and preliminary ASM and $K-\epsilon$ results for both heated devices and heated walls are encouraging - see figure.

The same 3-equation model code used for the aerofoil device predictions has also been extended to include weak compressibility effects and is currently being used to predict the effect of tandem NACA 0009 manipulators at $M \sim 0.8$, in advance of further experimental studies. At the same time a modified Lam and Bremhorst low- Re $K-\epsilon$ model is being employed in an adaptive unstructured Navier-Stokes code in an effort to predict the effect of a single NACA 0009 device at similar and higher Mach numbers [286] - see figure. Work had also been underway at ONERA/Chatillon aimed at optimising the shape of aerofoil LEBUs for use under flight representative conditions, [287]. However it has to be accepted that the achievement of sufficiently accurate parametric computations of complex profile but small chord Reynolds number aerofoils

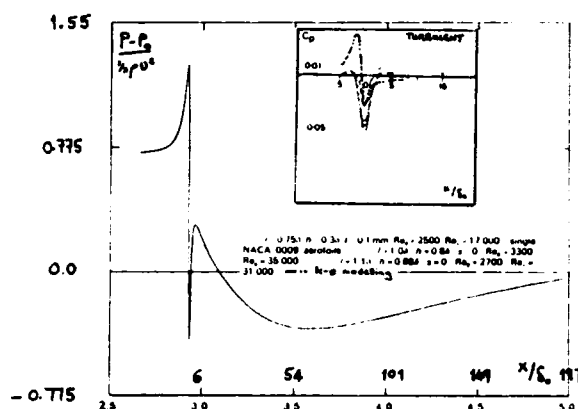
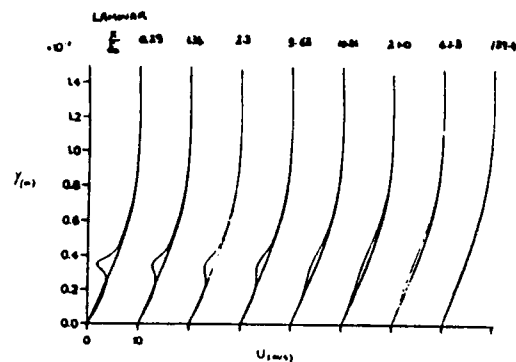
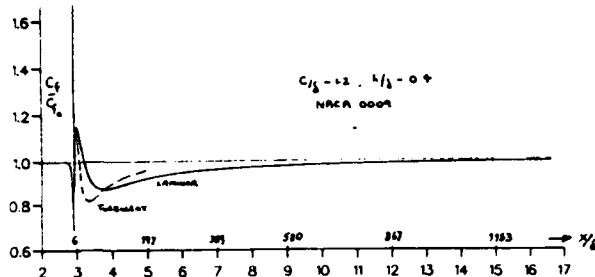


Figure 61: Comparison of laminar and turbulent flow predictions for NACA 0009 LEBU (a) C_f , (b) mean velocity profile & (c) pressure

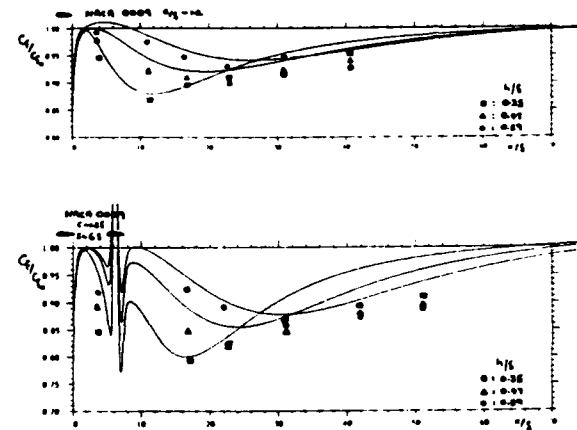


Figure 62: Comparison of model predictions with data for single and tandem NACA 0009 LEBU manipulators

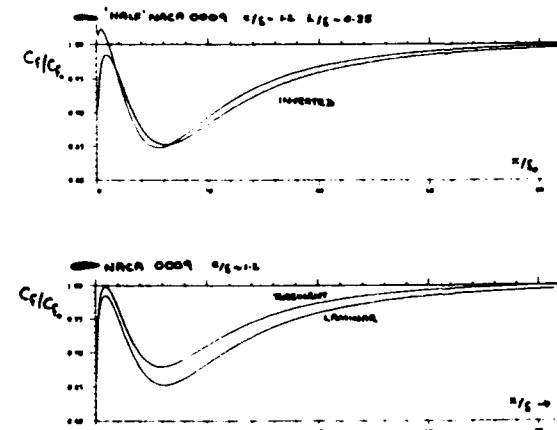


Figure 63: Comparison of model predictions for 'half-NACA 0009' & NACA 0009 devices and for a NACA 0009 device with laminar or turbulent wake

operating at transonic speeds - in a high turbulence environment close to a wall is, at best, right at the very limit of current computing capabilities.

In fact the RDT computations have already provided some evidence that LEBUs could be more efficient at high subsonic Mach numbers ($M \sim 0.8$) if a way could be found of broadening the range of turbulence scales which they suppress. RDT also correctly predicts that the plate chord l should be greater than δ and that close gaps tend to increase the 'effective' manipulator length as far as the flow is concerned, but that $S > 10\delta$ is to be preferred as the second device then has a multiplicative effect.

None of the other computational approaches has so far produced any quantitative parametric results, but they have provided support for some of the various proposed drag reduction mechanisms. Thus the

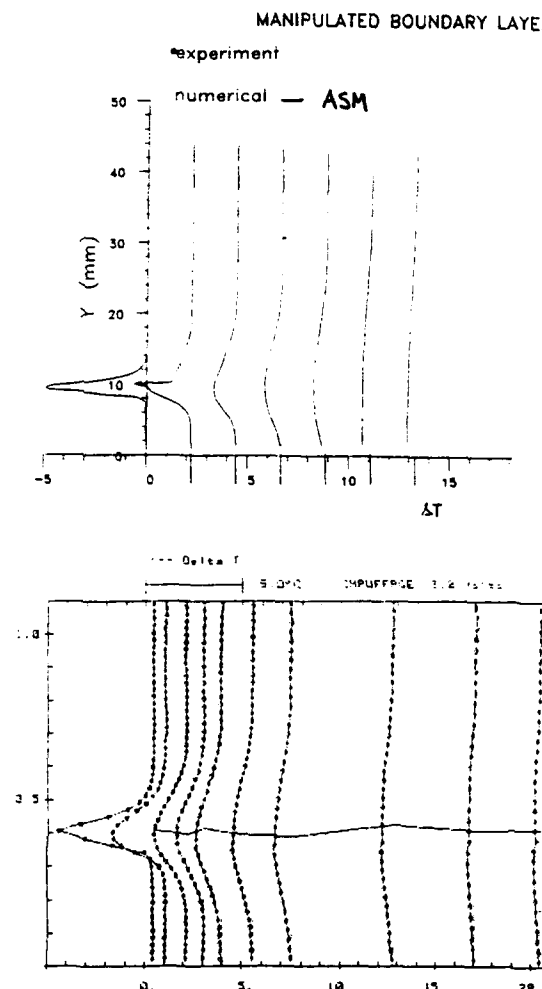


Figure 64: Comparison of ASM predictions with data for a heated LEBU/wake

discrete and distributed vortex modelling has emphasised the immediate influence of the device itself, and particularly the possibility of 'vortex-unwinding' (although this process has never actually been observed), while the vorticity/stream function approach has emphasised the persistent 'blocking' effect of the device wake.

[RDT in fact tends to confirm the suggestion that the coherent cortices shed into the wake of the device partially cancel the remaining boundary layer vorticity. However the important role played by the device wake is actually best illustrated by the method of characteristics approach which tracks the \bar{uv} minimum behind a manipulator to the wall at a point coincident with the maximum C_f reduction and then also captures the subsequent overshoot in \bar{uv} and \bar{v}^2 seen moving away from the wall in the relaxing layer - see figure].

The patched spectral direct simulations indicate that it is only transverse large vortical structures

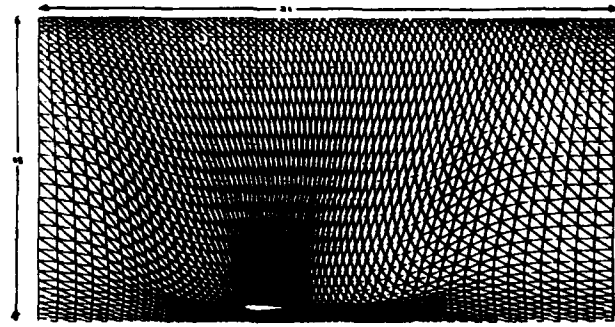


Figure 65: Unstructured mesh for optimised single NACA 0009 LEBU configuration

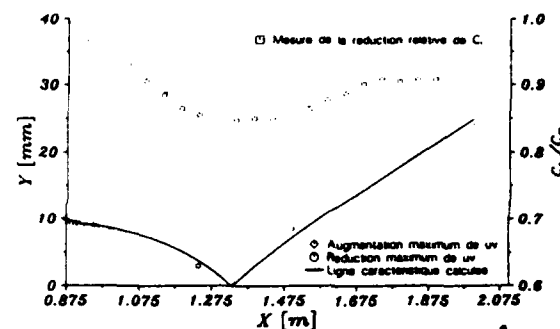


Figure 66: Method-of-characteristics predictions of the flow development behind a manipulator

which are suppressed (reduced in size) due to the restriction placed on vertical velocity fluctuations by the imposition of the manipulator while predominantly longitudinal and elliptical vortices suffer similar scale reductions due to a severe damping of the vertical vorticity component and confirm that recovery then occurs over a much larger relaxation length.

The LES 'data' has yet to be subjected to detailed analysis, but it is already clear that these have produced more comprehensive, higher resolution (both spatial and temporal), multi-point information than has been gathered even from 8, 12 and 16 hot-wire rakes in the case of manipulated boundary layers (including 'data' on quantities which cannot easily be measured) and certainly by far the most detailed results for manipulated channel flows. Recently the possibility of applying Pattern Recognition Analysis (PRA) techniques to such LES output has been considered and it has been found that patterns can be identified in the velocity fluctuations which are similar to ensemble averaged patterns derived from PRA

of multi-probe data for a manipulated boundary layer [288]. The latter have revealed that the immediate effect of the plate and its near wake is simply to cut through the predominantly asymmetric (part hairpin-loop) structures which stretch across the oncoming boundary layer, with the outer and inner regions (although not entrainment and near-wall production) initially remaining correlated to a lesser degree; while the more persistent influence of the wake is seen near the maximum local C_f reduction, where it's 'footprint' on the wall can clearly be identified, and in recovery, where its continued 'blocking' of external disturbances seems to be responsible for the establishment of a more organised and quiescent near-wall structure.

It would also appear from the LES that when manipulators (and their wakes) are introduced into fully-developed channel flow they act in a similar manner on the squatter horse-shoe vortex structures found there. In addition, the presence of such larger, stronger structures in both halves of the flow seem to be associated with cross-flow from the opposite wall region (just as the similar vortices found in the far wake are linked to stronger entrainment) so that although there is no entrainment the manipulators act in the same manner to damp such cross-flow influences. Furthermore although the streamlines remain parallel with the walls, and so there is no beneficial 'downwashing' (as seen in external flows due to the effective angle of attack imposed by the boundary layer growth) at least for devices aligned with these, the minimum C_f location is still found to be co-incident with the point at which the device wake reaches the wall. The LES thus confirm that there is rather more similarity between channel and boundary layer flow manipulation than had previously been suspected.

5 Alternative Passive Drag Reduction Techniques

Once it had clearly been established that nett drag reductions could be achieved by passive as well as active means the search began for devices, other than riblets or LEBUs, which might offer larger practical benefits. Because of the problems encountered in achieving repeatable nett reductions with in-flow manipulators researchers have concentrated their attentions on other surface modifications, and within the last few years it has been demonstrated that drag reductions (again essentially per unit area treated) similar to those produced by the now standard V , U and L groove riblets can also be achieved with so-called 'compound riblets' (exhibiting larger range spanwise variations in height and spacing [2], [235]), and with 3D patterns of similarly scaled short fin-like ribs [287], intended to be more representative of shark skin. Although these findings would at first sight appear disappointing, since in both cases such surfaces might have been expected to generate larger nett drag benefits, they have indicated that a wide range of surface geometries have drag reducing properties. In particular consideration of 3D deterministic arrangements of surface-

mounted elements has opened up a far wider parameter space than that previously explored for continuous 2D repeating patterns of riblets [eg. see [15]], and it is too early to say whether we have actually found the optimum form for even these. Research is therefore continuing on potentially better forms based on an ever improving understanding of the turbulent flow structure of attached flows and their influence on this. In this context even flexible or 'hairy' riblet surfaces are being considered (based on an early patented idea of Kramer involving thin wires stretched longitudinally above the wall surface). Viscous flow analyses have suggested [289], [290] these should offer some advantages over riblets (at least as measured by Δh , the difference between their effective protusion heights for longitudinal and transverse flow - see figure), but such computations do not take into account any turbulence interaction (losses?) or mounting difficulties - see figure.

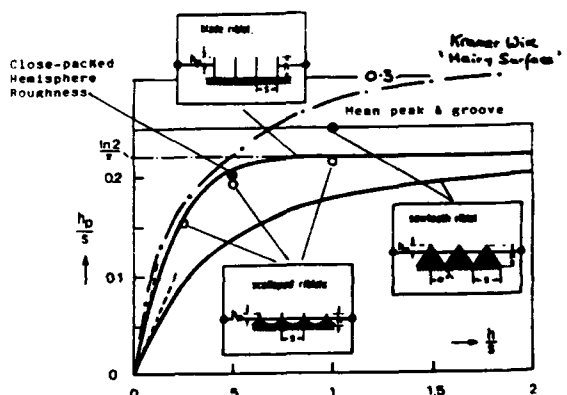


Figure 67: Comparison of protrusion heights for riblets and other alternative surfaces

Studies of other possibly drag reducing 'roughnesses' are no longer being restricted to surface geometries which may be regarded as riblet-type. Indeed it has been known for a long time (certainly since well before the discovery of any advantage yielded by very small longitudinal grooves) that the drag of certain much larger, but especially close spaced transverse grooves - in the form of 'd-type' roughnesses - may be anomalously low for particular ranges of Reynolds numbers. More recently it has been found that so-called 'sparse' - or (perhaps more appropriately) Tani-d-type surfaces [291], [292], which have streamwise groove spacings (L) on order of magnitude larger than their depth (d) and width (w) dimensions, may actually produce drag reduction of order 2-3% at least in low- Re turbulent flows ($Re_x \sim 0.8 - 2.6 \times 10^6$, $Re_d = O(5000)$) providing they are suitably scaled with $d = w$, $d/\delta = O(0.1)$, $Rd^+ = O(200)$ and later parametric studies [293] indicated an optimum $L = 20d$ - see figure.

Independent flow visualisation studies [294] and comparative and quantitative measurements for a single cavity [295] have suggested that any drag reduc-

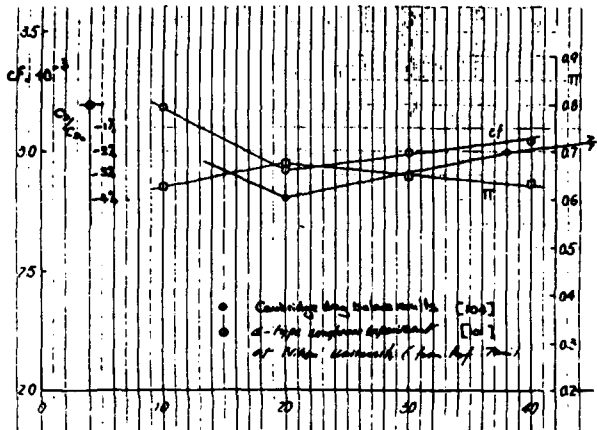


Figure 68: Skin friction distribution over 2 wave-lengths of a sparse-d-type surface $L=20w$ at $M=0.8$

tion is partly due to the establishment of a single stable 'stress relieving' vortices in each of the cavities themselves (which occurs for values of Re_d , d^+ and d close to the observed optima) and partly due to a consequent beneficial modification to sublayer structure over the wall surface between these. In particular it would appear that, in the absence of any significant cavity 'bursting' (associated with additional pressure drag), flapping of the cavity/boundary layer interface and partial 'clipping' of the cavity vortex on the downstream lip of the cavity lead to the release of small vortices into the sublayer. However both are clearly rather weak effects since C_f is reduced by only 4-5% over the cavities and just 1-2% between these. In addition it would appear from the isolated cavity studies that the standard flat plate logarithmic profile is maintained over the cavities provided the virtual origin is adjusted to coincide with the of the cavity vortex at its centre-plane, however there is some indication of a compensating increase in wake component at the rear of the cavity.

A number of further experiments on such sparse cavity arrangements have now been carried out at both very low speeds [296] and at high subsonic Mach numbers [297] ($M \sim 0.8$) again representative of civil transport conditions. The low speed parametric studies using a direct floating element drag balance have tended to confirm the optimum groove spacing of $L \sim 20w$; indicating a 2% nett drag reduction at the lower end of the Reynolds number range for near optimum values of the other configurational parameters - see figure.

Complimentary velocity profile measurements have also confirmed the existence of a near standard log layer, but without any detrimental increase in the wake component π . Surprisingly similar results were obtained from velocity traverses carried out as part of the high speed tests (despite the larger than optimum Reynolds number conditions considered in that case), and the local skin friction and integrated momentum

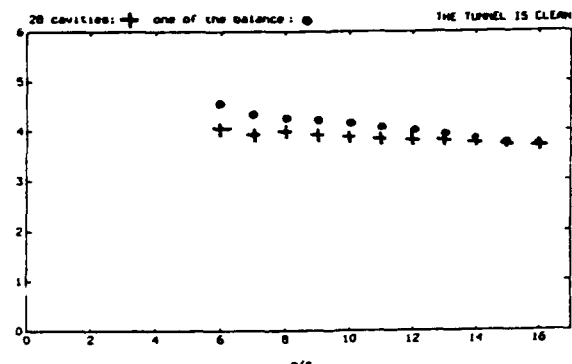


Figure 69: Drag performance of one wave-length of a continuous sparse-d-type surface ($L=20w$) compared to an equivalent single cavity surface element

balance estimates derived from these were again consistent with the low speed studies; revealing average C_f reductions of $\sim 4\%$ over and 2% between the cavities, with an overall nett benefit of $\sim 1\%$ - see figure.

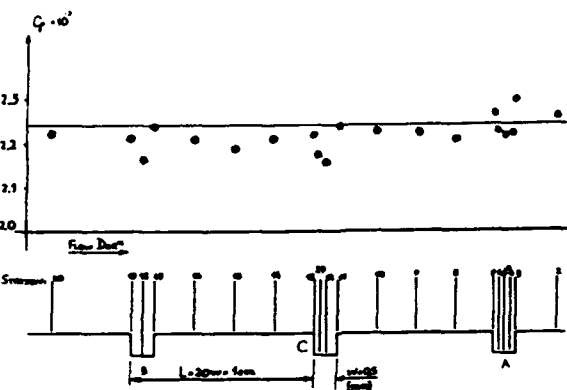


Figure 70: Skin friction distribution over a sparse-d-type surface ($L=20w$) at $M=0.8$

Although these levels of drag reduction are considerably smaller than those obtained from riblets it has to be noted that such grooves are more easily manufactured and that they may be amenable to further optimisation and/or additional control techniques. No attempt has yet been made to optimise the groove profile. Although sharp upper corners would appear to be necessary, rounding of the base would be one obvious way to reduce any cavity flow losses, and sparse grooves of this shape have apparently already been investigated for channel flow control [298]. It is expected that the very detailed studies which have now been made of closer spaced d-type grooves [299] - [302] will assist further refinement of such drag-reducing deterministic 'roughnesses'.

At the same time a re-analysis of Nikuradse's original pipe flow data [303] has suggested that some

random 'said gain' roughnesses may also exhibit drag reductions (and a corresponding negative roughness shift of the log law) for sufficiently small $K^+ < 7$ (a maximum reduction of 2-3% being indicated at about $K^+ = 3$). This finding has however, been questioned on the grounds that the skin friction was determined from the measured velocity profiles using a different log law constant than that assumed by Nikuradse himself, and indeed when his value was adopted the drag maximum reduction was reduced to 1 - 2% [304], possibly within the experimental uncertainty. [It has to be accepted that there is now some general concern amongst the research community regarding the details and accuracy of Nikuradse's results]. Nevertheless a subsequent boundary layer experiment [126], in which an attempt was made to reproduce Nikuradse's $\sim 80\%$ coverage roughness from his original photos (but using rounded steel shot sitting on top of a thin layer of adhesive rather than sharp or partially rounded sand grains embedded in a lacquer), appeared to confirm a drag reduction for $K^+ < 7$ (reaching $\sim 4\%$ at $K^+ \sim 4$). (In fact the same analysis technique as initially applied to the Nikuradse data indicated a drag reduction as high as 7%, but this was subsequently found to overestimate riblet drag reductions by a similar amount). Drag increases were observed for larger sized roughness and also for random roughness distributions having much greater open area (only 28% coverage) over the whole K^+ range [305] - see figure.

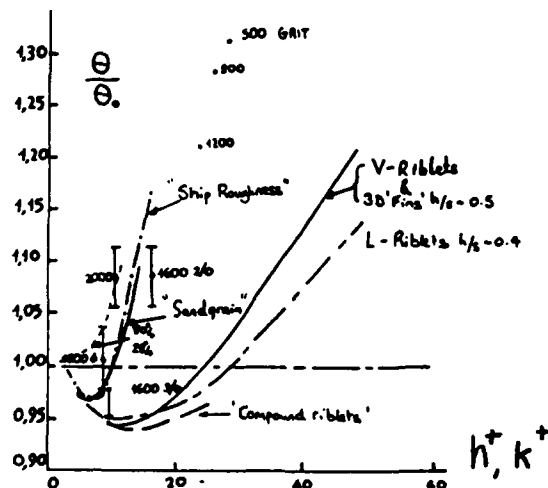


Figure 71: Drag performance of various 'roughness' distributions compared to riblets

In fact a very similar drag (reduction) behaviour versus K^+ had also been observed in earlier studies of ship roughness [306], but, until this was pointed out [14], the drag reduction had been regarded as simply an artifact of experimental uncertainties.

In an effort to establish the reality of any nett benefits from such random 'roughnesses' a number of further studies have recently been undertaken of a variety of 'sandpaper' [307] and 3M 'lapping' film rough-

nesses [308], in addition to similar spherical roughness distributions [297] at both very low and high subsonic speeds. Studies at $M \sim 0.8$ have indicated that drag reductions of the order of a few percent might be achieved under flight representative conditions provided the surface geometries consist of sufficiently close packed 'sand grains', are hole-dominated' rather than 'peak-dominated', and based on the mean peak to valley height $K^+ \leq 5$ - see figure. Although the possible benefits are again small compared to riblets such surfaces do have the same potential advantage as hairy surfaces in that their performance should be independent of local flow angle.

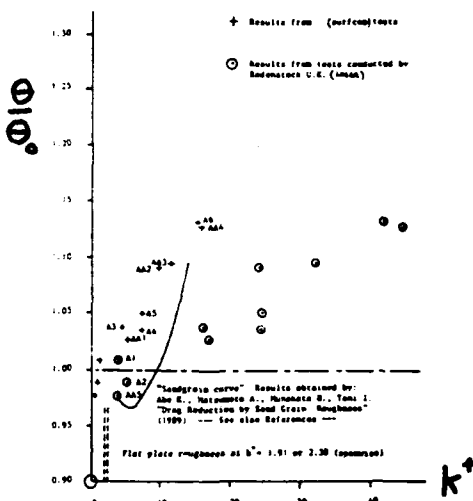


Figure 72: Drag versus metrology measurements for a range of commercially available abrasive films

Unfortunately very precise measurements conducted of close replicas of the surfaces studied in reference [126], using a large floating element drag balance in the Berlin oil channel [297], have not confirmed the reported drag reduction for 'spherical' particle roughnesses. However the data have indicated that the drag of such surfaces is at worst very nearly equivalent to that of a perfectly smooth surface for $K^+ \leq 7$ - a finding which has important practical implications for those attempting to minimise excessiveness drag or improve surface definition by costly machining/polishing - see figure. Studies of spherical roughnesses have in fact also already been made in turbine rotor boundary layers [309], and also in wall jets [310], [311]. In the former case the roughness apparently increased drag, but in the latter a reduction in turbulence intensity and a thickening of the viscous sublayer were observed; both of which would be expected to lead to drag reduction.

It would therefore appear that the drag performance of random roughnesses is very sensitive to the exact detail of their surface profile including the exact shape, orientation and spacing of the individual roughness elements, as well as the degree of variability of all of these. Certainly it is unrealistic to expect that the performance of such surfaces can be qual-

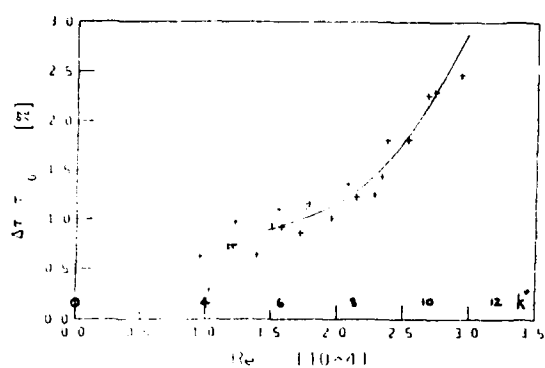


Figure 73: Drag performance of closely packed spherical 'roughness'

fied simply in terms of K^+ or an effective equivalent sand grain roughness (however defined), as is usually assumed. Instead some form of overall statistical description is required which can be used to distinguish between drag reducing and drag increasing forms and this is now being sought [297] following a similar approach to that used for correlating ship roughnesses [312] or for deterministic surfaces - eg. see figure.

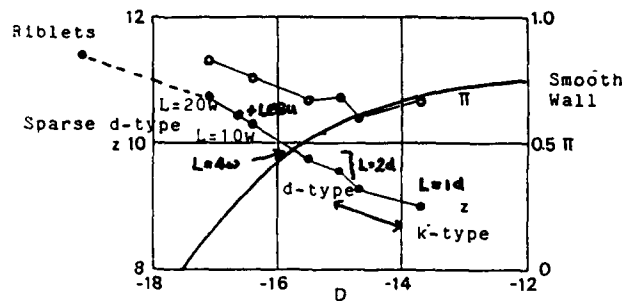


Figure 74: Correlation of d-type surfaces with riblets as function of wake component and roughness shift log law constant D

Clearly, just as will '3D riblets' the parameter space to be explored is very large and it is unlikely that any computational technique could be devised which could help in optimisation. However some unrelated studies of water flow over erodible sand beds [313] may surprisingly offer some guidance for those attempting to ascertain likely optimum surface geometries. Since certain self-stabilised bed formations of sand particles appear to be drag reducing, it may be worthwhile replicating these transient 'minimum drag' surfaces for more detailed static testing in air or water. It should also be noted that some low drag random roughnesses have already been found to offer significant heat transfer benefits [314].

Before leaving such alternative approaches some mention must also be made regarding the possibility

use of another kind of non-planar surface for passive drag reduction; namely smooth walls with imposed longitudinal and/or in-plane curvature. The so-called 'curvature-concept' for drag reduction [10] relies on the observation that the turbulent shear stress and C_f are reduced much more by convex curvature than they are increased by a similar degree of concave curvature. In addition it is known that the combination of in plane curvature (particularly the influence of lateral divergence) with convex curvature produces a surprisingly larger beneficial effect and can also suppress the detrimental formation of Taylor-Gortler vortices in concave wall flows. It has been demonstrated that these effects can to an extent be predicted by RST models. More recent parametric computations [315] have suggested that the reductions in convex curved flow depend on turning angle alone while the corresponding increases in concave flow are a function of the ratio of total rotation to total shear. Further computer optimisation may therefore be possible and this is now being attempted for the practical situation of concave curvature followed by convex using a more refined RST treatment [316] - see figure.

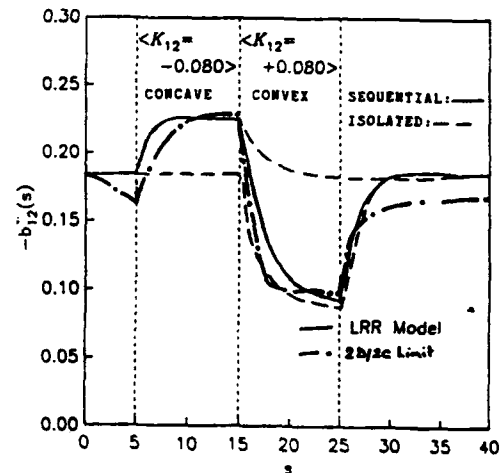


Figure 75: Second moment closure predictions of benefit of curvature drag reduction concept

6 Combinations of drag reduction techniques

One way in which it is already known that larger drag reductions may be achieved is by applying passive techniques in combination either with one another or with additional active control methods. Indeed a very large number of such combinations have now been studied and in nearly all cases it has been found that the resulting benefits are at least additive. Since riblets scale on wall variables and act directly on the very near wall flow while LEBU's scale on the thickness of the whole shear layer and act directly on the main part of the flow, it is not at all surprising to find that the two devices can be combined con-

structively [135]-[318] at least at low-speed (Tests at around $M \sim 0.8$ for Airbus applications have so far proved rather less conclusive). Flow visualisation studies [319] have suggested that the riblets complement both the immediate effects of an outer layer manipulator and the beneficial persistent influence of its wake by imposing additional stability onto the wall sublayer regions, and have indicated that improved performance might be realised if the devices were then re-optimised to ensure an appropriate matching of scales - as suggested also by some parametric studies [137]. In particular it would appear that a reduction in the chord (to $l \sim 0.8\delta$) and spacing ($s \ll 12\delta$) may then be possible, thereby reducing the LEBU device drag, while maintaining the same LEBU effectiveness - see figure.

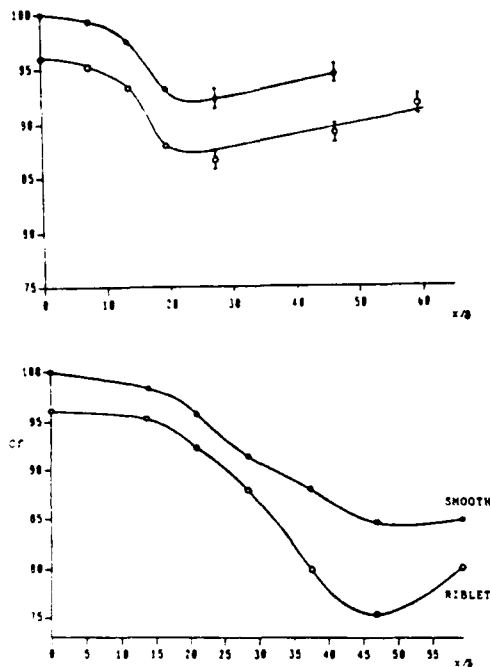


Figure 76: Performance of manipulators and riblets in combination, (Upper part : manipulator plate $l=0.8\delta$; Lower part : tandem manipulator : $s=5\delta$, $l=1.6\delta$, $h=0.75\delta$, $R\Theta=3000$ and $Rl=45,000$).

Both riblets and manipulators have also been tested in conjunction with various transverse grooved surfaces. Such studies were prompted by the realisation that equilibrium flow development could be maintained even in zero pressure gradient on *d*-type roughness [320] [Note that such equilibrium flow is also possible for flows on smooth or *k*-type walls, but only in favourable pressure gradients or if K increases linearly with x [321]]. Since C_f is maintained constant there is then the possibility that passively induced drag reductions might be maintained over a larger downstream extent; although eventually the C_f may exceed that on a smooth plate because this varies inversely with x . In fact it has been found that when such flows are perturbed by either cylindrical rods or

thin element LEBUs they appear to recover to a new equilibrium condition with a lower constant C_f [239], [320] and it has been suggested that riblets introduced onto the surface between adjacent grooves may offer similar benefits [322]. Since it equilibrium flow can also be established on drag reducing sparse - *d*-type surfaces [291], [292], even at high subsonic conditions [297], the combination of LEBUs with these would appear particularly worthwhile, and indeed some initial studies have revealed additive effects at $M \sim 0.8$ for combinations of such sparse-*d*-type surfaces with both optimised NACA 0009 aerofoil manipulators and 3M v-groove riblets.

It is perhaps worth noting that some studies are presently being undertaken of symmetrical LEBU/isolated cavity configurations with a view to improving the (pressure) drag of gaps between carriages of the French TGV [322]. The possibility of mounting ribs within the cavities themselves has also been considered for both close-spaced (drag increasing) [323] and sparse-spaced (drag reducing) [297] *d*-type surfaces. In both cases the effect of the ribs was beneficial, but a nett reduction (of 3%) was only recorded in the first case (possibly because the main effect of the ribs was to minimise the detrimental effects of cavity interactions). However the spanwise spacing of the ribs ($s = w$ and $s^+ \geq 30$) was almost certainly not optimal - see figure.

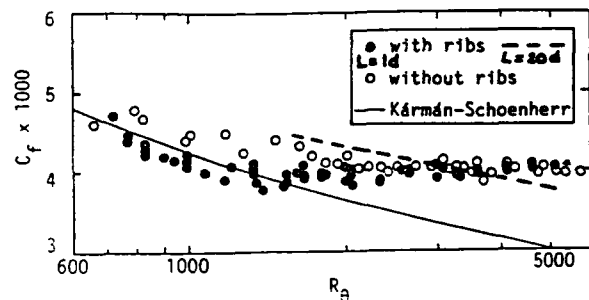


Figure 77: Comparison of drag measurements for close and sparse *d*-type grooves containing riblets

LEBUs, riblets and close *d*-type (as well as *k*-type, but not yet sparse *d*-type) surfaces have also been tested in conjunction with polymers, both injected through the wall surface (heterogeneous drag reduction) or dispersed in the flow (homogeneous). Heterogeneous [324] and homogeneous [325] rough pipe flow studies have shown that for $K^+ < 12$ the drag reduction is equal to that found in a smooth walled pipe and indicated that larger drag reductions might be possible for the combination of a sparse *d*-type surface with polymer solutions.

Similar heterogeneous [326] and homogeneous [327]-[328] studies have conducted of polymers and riblets. In the first of these the polymer was coated onto riblets on the hull of 1/3 scale Americas cup yacht [326], and towing tank tests showed that the two effects combined almost additively at the optimum s^+

for riblets alone of $s^+ \sim 12$. the overall effect was actually rather more than additive at higher 'wave-making' speeds; this synergistic effect being attributed to the riblet reducing the wall shear and so delaying any polymer degradation as well as helping to retain polymer near the surface in the same manner as roughness - a view supported by homogeneous pipe flow studies [327] - and/or preventing the development of so-called 'orange peel' roughness in the polymer coating on smooth surfaces. However the combined effect was rather less than additive at lower speeds and s^+ .

It has been suggested that this might have been because the shear stress was reduced sufficiently to inhibit the action of the polymer. However other homogeneous studies of an axisymmetric body in a drop tank [156] have suggested that riblets may instead lower the threshold for polymer activity. The same study also indicated that riblets may act as a nucleation site for beneficial (passive?) micro bubble drag reduction [328]. Subsequent independent investigations of riblets in conjunction with both surfactants and microbubble injection in water [141] have shown that in some cases the riblets act via surface tension forces to trap the bubbles as a tube of air attached to the wall thereby reducing the required bubble injection by an order of magnitude for the same reduction in skin friction drag.

L profile riblets have also been tested in combination with normal [235] and tangential blowing [332] at their peaks in both air and water, so far without success although the latter study has indicated an optimum $L/s \sim 0.6$ for further studies. Very much better results have been obtained for the combination of riblets with selective suction [118], [333] in turbulent flow (even with non-optimal riblet and suction methods), and it seems likely that even larger benefits may be possible in both transitional and transonic flows.

A similar series of studies have been conducted for thin element [329] or aerofoil [330] LEBUs. In homogeneous polymer solutions additive effects have again been observed, but heterogeneous injection from the manipulator trailing edge [330] has so far failed to produce any larger benefits. This is surprising in view of the fact that very significant drag reductions have been achieved from the injection of 'polymer threads' along the centre-line of a pipe [331] (which may after all offer a parallel to the optimal use of LEBUs on the centre line of a channel flow), and one would expect some additional advantage from increased stabilisation, persistence, and hence influence, of the device wake. Certainly theoretical studies have clearly indicated that better performance should be achieved if the wake turbulence is sufficiently damped [236].

The advantages of combining LEBUs with tangential slot injection (where the downstream effectiveness of the latter may be doubled) [247] has already been mentioned, but it would also appear beneficial, in order to avoid possible transient separation on the device itself, to employ mild suction in conjunction with negative camber aerofoils [334]. Microbubble injection through the trailing edge might also be used to destroy the large scale wake turbulence [335]. Al-

ternatively, however, there may be considerable advantages in stabilising the coherent vortex structure of the wake either by deliberately inducing a more persistent longitudinal vortex structure [338] - [339] or by utilising some kind of additional forcing to amplify and strengthen the existing predominantly transverse near-wake vortices. Both mechanical [340] and acoustic excitation [341]- [342] have in fact already been investigated experimentally and in each case a larger drag reduction has indeed been obtained for a particular frequency range related to the shedding frequency of the device - see figure; although a theoretical analysis for flexible LEBUs [343] has confirmed the experimental finding that LEBU performance can be reduced very significantly if flutter is induced at other frequencies. Acoustic forcing or free-stream oscillation may also provide advantageous additional control benefits in the case of *d*-type roughnesses [344]- [345], but this possibility has yet to be fully explored or exploited.

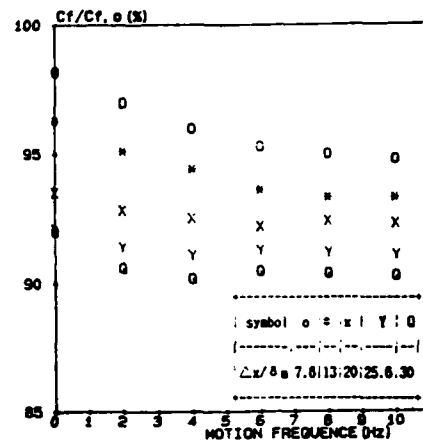


Figure 78: Effect of forcing on the performance of a single flat plate LEBU

7 Concluding Remarks

In conclusion it has to be said that the prospects for passive skin friction drag reduction on present and future civil transport aircraft have never been brighter. Riblets are a mature technology and only questions regarding application and safety aspects are delaying their regular use 'in service'. Certainly the current $\sim 2\%$ saving in total aircraft drag that they offer is worth having providing it is not traded off against costly 'down time'. However this estimate is based only on the turbulent flow performance of standard (uniform height spacing and profile) 2D *u* or *v* groove riblets optimised on average for the various parts of the aircraft to which they are applied. It does not take account of the possibility that larger benefits might be achieved in turbulent flow using locally optimised variable height/spacing and/or profile 3D riblet configurations, or of the now recognised additional advantages of using riblets in laminar/transitional flow

regions as well. From initial rather limited parametric studies of other possibly drag reducing surface geometries already some other deterministic and even random 'roughnesses' would appear to exhibit similar characteristics to riblets. Even though these appear at present to offer only at best equivalent performance to riblets they open up new possibilities for at least minimising drag increases if not maximising drag reductions. In addition surfaces presently offering similar or even less benefit than riblets may have other advantages in terms of improved yaw response or greater heat transfer efficiencies and/or may be more amenable to combination with additional control techniques. Certain combinations look particularly attractive for transition and shock-boundary layer control but further research is needed on these. In addition the possible use of riblet type devices for more than one purpose e.g. perhaps for skin friction, heat transfer and separation control on Concorde or future HSTs deserves consideration. The same is also true of manipulators. Although it is unlikely these will ever produce nett C_f reductions in practice their use as very low drag penalty devices for controlling shocks/separation, heat transfer and/or noise, possibly also in combination with other control techniques, cannot be ruled out.

Acknowledgements

The authors are grateful to all those who have assisted in the preparation of these Lecture Notes through the provision of results and information, often in the form of private communications of as yet unpublished work, and thereby assured that these form as up to date a review as possible of the subject. The authors have benefitted greatly from collaboration with colleagues at CEAT Poitiers, EPFL Lausanne, IMST Marseille, and UMIST in Manchester; within the ERCOFTAC Special Interest Group on Drag Reduction.

EC wishes to acknowledge the support of Airbus Industrie and the "Service Technique des Programmes Aéronautiques" for supporting all the riblet studies developed at ONERA/CERT. He is also very grateful to colleagues and students, who have joined him for a while, during part of these studies. He would also like to thank Prof. J. Cousteix for comments upon his contribution and Dr. D. Arnal for providing encouragements during the writing.

Much of the work discussed by the second author has been funded by Rolls-Royce plc and AMS gratefully acknowledges their continuing support under University Research Brochure PVA3-120D. Further support has been provided by Airbus Industrie, Aerospatiale & BAe as well as BAC, BMT and the UK SERC (Grants GR/E/0682.4 and 7703.9) and British Council. Special thanks are also due to EPFL for the additional support they have provided through the Swiss ERCOFTAC Pilot Centre in Lausanne.

References

- [1] Bushnell D.M. : AGARD Report No. 786, March 1992, Paper 3.
- [2] Robert J.P. : AGARD Report No. 786, March 1992, Paper 2.
- [3] Schmitt V. : 24ème Colloque AAAF, Poitiers, France, October 1987, Paper 15.
- [4] Thomas A.S. : AGARD Report No. 723, May 1985, Paper 1.
- [5] Lachmann G.V. : "Boundary Layer and Flow Control", Oxford, UK, Pergamon Press, 1961.
- [6] AGARD Report No. 654, April 1977.
- [7] Saric W.S. : AGARD Report No. 786, March 1992, Paper 4.
- [8] Arnal D. : AGARD Report No. 786, March 1992, Paper 5.
- [9] Gad-el-Hak M. : in Drag Reduction in Fluid Flows (eds. R.H.J. Sellin & R.T. Moses, Ellis Horwood Publishers) pp. 9-20, 1989.
- [10] Bushnell D.M. : AGARD Report No. 723, May 1985, Paper 5.
- [11] Bandyopadhyay P.R. : J. Fluid Eng., Vol 108, pp. 127-140, 1986.
- [12] Wilkinson S.P., Anders Jr. J.B., Lazos B.S. and Bushnell D.M. : Int. J. Heat and Fluid Flow, Vol. 9, No. 3, pp. 266-277, 1988.
- [13] Bushnell D.M. and McGinley C.B. : Ann. Review Fluid Mech., Vol. 21, pp. 1-20, 1989.
- [14] Savill A.M. : in Structure of Turbulence and Drag Reduction (edited by A. Gyr, Springer-Verlag) pp. 429-465, 1990.
- [15] Walsh M.J. : in Viscous Drag Reduction in Boundary Layers (edited by D.M. Bushnell & J.N. Hefner, Progress in Astronautics and Aeronautics Vol. 123, AIAA Inc. publishers), pp. 203-261, 1990.
- [16] Anders Jr. J.B. : in Viscous Drag Reduction in Boundary Layers (edited by D.M. Bushnell & J.N. Hefner, Progress in Astronautics and Aeronautics Vol. 123, AIAA Inc. publishers), pp. 263-284, 1990.
- [17] Berteirud A., Drouge G. and Landahl M.T. : a Report on Euromech 181, Rept. FFA TN 1984-60, 1985.
- [18] Savill A.M., Truong T.V. and Ryhming I.L. : a Review and Report on the First European Drag Reduction Meeting, J. of Theoretical and Applied Mech., Vol. 7, No. 4, pp. 353-378, 1988.
- [19] Proceedings of Turbulent Drag Reduction by Passive Means Conference, The Royal Aeronautical Society, London, 1987.
- [20] Coustols E., Savill A.M. : Resume of Important Results Presented at the 3rd Turbulent Drag Reduction Meeting, Applied Scientific Research, Vol. 46, No. 3, pp. 183-196, 1989.
- [21] Applied Scientific Research, Vol. 46, No. 3, Special Issue on Drag Reduction Applications of Riblets and Manipulators, edited by A.M. Savill, Kluwer Academic Publishers, July 1989.

- [22] Coustols E., Savill A.M. and Truong T.V. : a Report on the 4th European Drag Reduction Working Party Meeting, ERCOFTAC Bulletin, No. 4, December 1989.
- [23] Turbulence Control by Passive Means, Fluid Mechanics and its Applications, Vol. 4, edited by E. Coustols, Kluwer Academic Publishers, 1990.
- [24] Recent Developments in Turbulence Management, Fluid Mechanics and its Applications, Vol. 6, edited by K-S. Choi, Kluwer Academic Publishers, 1991.
- [25] Proceedings of the 6th European Drag Reduction Working Meeting, Eindhoven, November 1991.
- [26] Westphal R.V. : AIAA Paper 86-0283, 1986.
- [27] Blackwelder R.F. : AIAA Paper 89-1009, 1989.
- [28] Blackwelder R.F. : AGARD Report No. 786, March 1992, Paper 6.
- [29] Robinson S.K. : PhD dissertation, Stanford, 1990, or NASA-TM-103859, April 1991.
- [30] Robinson S.K. : Ann. Review Fluid Mech., Vol. 23, pp. 603-639, 1991.
- [31] Kim J. : AGARD Report No. 786, March 1992, Paper 7.
- [32] Kline S.J. : Zoran P. Zaric Memorial International Seminar on Near-Wall Turbulence, Dubrovnik, May 1988.
- [33] Robinson S.K., Kline S.J., Spalart P.R. : Zoran P. Zaric Memorial International Seminar on Near-Wall Turbulence, Dubrovnik, May 1988.
- [34] Falco R.E., Klewicki J.C., Pan K. and Gendrich C.P. : 7th Symposium on Turbulent Shear Flows, Stanford, August 1989, Paper 2-5.
- [35] Lyons S.L., Hanratty T.J. and McLaughlin J.B. : 7th Symposium on Turbulent Shear Flows, Stanford, August 1989, Paper 2-1.
- [36] Kline S.J. and Robinson S.K. : in Structure of Turbulence and Drag Reduction (edited by A. Gyr, Springer-Verlag) pp. 3-22, 1990.
- [37] Robinson S.K. : in Structure of Turbulence and Drag Reduction (edited by A. Gyr, Springer-Verlag) pp. 23-50, 1990.
- [38] Smith C.R., Walker J.D.A., Haidari A.H. and Taylor B.K. : in Structure of Turbulence and Drag Reduction (edited by A. Gyr, Springer-Verlag) pp. 51-58, 1990.
- [39] Falco R.E. : Phil. Trans. R. Soc. Lond. A, Vol. 336, pp. 103-129, 1991.
- [40] Proceedings of the NASA Langley Conference on Turbulent Boundary Layer Structure, 1991.
- [41] Cousteix J., Coustols E. and Arnal D. : AGARD Conference Proceedings No. 438, Cesme, 1988.
- [42] Blackwelder R.F. : AGARD Conference Proceedings, September 1979, Paper 24.
- [43] Kline S.J., Reynolds W.C., Schraub F.A. and Runstadler P.W. : J. Fluid Mech., Vol. 30, pp. 741-773, 1967.
- [44] Kim H.T., Kline S.J. and Reynolds W.C. : J. Fluid Mech., Vol. 50, pp. 133-160, 1971.
- [45] Runstadler P.W., Kline S.J. and Reynolds W.C. : Report No. MD-8, Stanford Univ., Stanford, Calif., 1963.
- [46] Praturi A.K. and Brodkey R.S. : J. Fluid Mech.. Vol. 89, pp. 251-272, 1978.
- [47] Kim J., Moin P. and Moser R. : J. Fluid Mech.. Vol. 177, pp. 133-166, 1987.
- [48] Alfredsson P.H. and Johanson A.V. : J. Fluid Mech., Vol. 139, pp. 325-345, 1984.
- [49] Hinze J.O. : Turbulence, ed. McGraw Hill, New York, 1975.
- [50] Falco R.E. : Phys. Fluids, Vol. 20, No. 10, Part II, pp. S124-S132, 1977.
- [51] Head M.R. and Bandyopadhyay P. : AGARD Report No. 271, September 1979, Paper 25.
- [52] Bogard D.G. and Tiederman W.G. : J. Fluid Mech., Vol. 179, pp. 1-19, 1987.
- [53] Johansson A.V., Alfredsson P.H. and Kim J. : J. Fluid Mech., Vol. 224, pp. 579-599, 1991.
- [54] Townsend A.A. : J. Fluid Mech., Vol. 41, pp. 13-46, 1970.
- [55] Van den Berg B. : NLR Report MP 86060, European Meeting on Turbulent Drag Reduction. Lausanne, 1986.
- [56] Hefner J.N. and Bushnell D.M. : AGARD Report No. 654, April 1977, Paper 1.
- [57] Kim J., Moin P. and Choi H. : in Structure of Turbulence and Drag Reduction (edited by A. Gyr, Springer-Verlag) pp. 417-425, 1990.
- [58] Friedrich R. and Klein H. : in Structure of Turbulence and Drag Reduction (edited by A. Gyr, Springer-Verlag) pp. 483-493, 1990.
- [59] Klein H. and Friedrich R. : in Turbulence Control by Passive Means (edited by E. Coustols, Kluwer Academic Publishers, Fluid Mechanics and its applications) pp. 41-65, 1990.
- [60] Durst F., Schmitt K. and Brunn P.O. : in Drag Reduction in Fluid Flows (eds. R.H.J. Sellin & R.T. Moses, Ellis Horwood Publishers) pp. 171-178, 1989.
- [61] Lumley J.L. and Kubo I. : in The Influence of Polymer Additives on Velocity and Temperature Fields (edited by B. Gampert, Springer) pp. 3-21, 1985.
- [62] Hoyt J.W. : in Viscous Drag Reduction in Boundary Layers (edited by D.M. Bushnell & J.N. Hefner, Progress in Astronautics and Aeronautics Vol. 123, AIAA Inc. publishers), pp. 413-432, 1990.
- [63] Pollert J. and Sellin R.H.J. : in Drag Reduction in Fluid Flows (eds. R.H.J. Sellin & R.T. Moses, Ellis Horwood Publishers) pp. 179-188, 1989.
- [64] Kane R.S. : in Viscous Drag Reduction in Boundary Layers (edited by D.M. Bushnell & J.N. Hefner, Progress in Astronautics and Aeronautics Vol. 123, AIAA Inc. publishers), pp. 433-456, 1990.

[65] Bewersdorff H-W. : in *Structure of Turbulence and Drag Reduction* (edited by A. Gyr, Springer-Verlag) pp. 293-312, 1990.

[66] Fruman D.H. and Tullin M.P. : *J. of Ship Research*, Vol. 20, No. 3, pp. 171-180, 1976.

[67] Walker D.T., Tiederman W.G. and Luchik T.S. : *Experiments in Fluids*, Vol. 4, No. 2, pp. 114-120, 1986.

[68] Hoyt J.W. : *Experiments in Fluids*, Vol. 11, No. 3, pp. 142-146, 1991.

[69] Tiederman W.G. : in *Structure of Turbulence and Drag Reduction* (edited by A. Gyr, Springer-Verlag) pp. 187-200, 1990.

[70] Virk P.S. : *American Institute of Chem. Eng. Journal*, Vol. 21, No. 4, pp. 625-656, 1975.

[71] Gampert B. and Yong C.K. : in *Structure of Turbulence and Drag Reduction* (edited by A. Gyr, Springer-Verlag) pp. 223-232, 1990.

[72] Usui H., Maeguchi K. and Sano Y. : *Phys. Fluids*, Vol. 31, No. 9, pp. 2518-2523, 1988.

[73] Tsinober A. : in *Structure of Turbulence and Drag Reduction* (edited by A. Gyr, Springer-Verlag) pp. 313-340, 1990.

[74] Hunston D.L. and Zakin J.L. : in *Viscous Flow Drag Reduction* (edited by G. R. Hough, *Progress in Astronautics and Aeronautics*, Vol. 72, AIAA Inc. publishers), pp. 373-385, 1979.

[75] Usui H. : in *Structure of Turbulence and Drag Reduction* (edited by A. Gyr, Springer-Verlag) pp. 257-274, 1990.

[76] Luchik T.B., Walker D.T. and Tiederman W.G. : *Office of Naval Research, Technical Report PME-FM-85-1*, 1985.

[77] Schmitt K., F. Durst and Brunn P.O. : in *Drag Reduction in Fluid Flows* (eds. R.H.J. Sellin & R.T. Moses, Ellis Horwood Publishers) pp. 205-213, 1989.

[78] Lumley J.L. : *Phys. Fluids*, Vol. 20, No. 10, Part II, pp. S64, 1977.

[79] Landhal M.T. : *Phys. Fluids*, Vol. 20, No. 10, Part II, pp. S55, 1977.

[80] Landhal M.T. and Henningson D.S. : *AIAA Paper 85-0560*, 1985.

[81] Hanratty T.J., Lyons S.L. and McLaughlin J. : in *Structure of Turbulence and Drag Reduction* (edited by A. Gyr, Springer-Verlag) pp. 407-415, 1990.

[82] Gyr A. and Bewersdorff H-W. : in *Structure of Turbulence and Drag Reduction* (edited by A. Gyr, Springer-Verlag) pp. 215-222, 1990.

[83] Motier J.F and Carrier A.M. : in *Drag Reduction in Fluid Flows* (eds. R.H.J. Sellin & R.T. Moses, Ellis Horwood Publishers) pp. 197-204, 1989.

[84] Motier J.F : in *Proceedings of the 6th European Drag Reduction Working Meeting*, Eindhoven, November 1991.

[85] Brungart T.A., Harbison W.L., Petrie H.L. and Merkle C.L. : in *Drag Reduction in Fluid Flows* (eds. R.H.J. Sellin & R.T. Moses, Ellis Horwood Publishers) pp. 149-153, 1989.

[86] Choi K-S, Gadd G.E., Pearcey H.H., Savill A.M. and Svensson S. : *Appl. Sci. Res.*, Vol. 46, No. 3, pp. 209-216, 1989.

[87] Merkle C.L. and Deutsch S. : in *Viscous Drag Reduction in Boundary Layers* (edited by D.M. Bushnell & J.N. Hefner, *Progress in Astronautics and Aeronautics* Vol. 123, AIAA Inc. publishers), pp. 351-412, 1990.

[88] McCormick M.E. and Bhattacharya R. : *Naval Eng. J.*, Vol. 85, pp. 11-16, 1973.

[89] Madavan N.K., Deutsch S. and Merkle C.L. : *Phys. Fluids*, Vol. 27, No. 2, pp. 356-363, 1984.

[90] Madavan N.K., Deutsch S. and Merkle S. : *J. Fluid Mech.*, Vol. 156, pp. 237-256, 1985.

[91] Deutsch S. and Castano J. : *Phys. Fluids*, Vol. 29, No. 11, pp. 3590-3597, 1986.

[92] Clark III H. and Deutsch S. : *Phys. Fluids A*, Vol. 3, No. 12, pp. 2948-2954, December 1991.

[93] Legner H.H. : *Phys. Fluids*, Vol. 27, No. 12, pp. 2788-2790, 1984.

[94] Madavan N.K., Merkle C.L. and Deutsch S. : *J. Fluid Eng., Trans. of the ASME*, Vol. 107, pp. 370-377, 1985.

[95] Coughran M.T. : *J. Fluid Eng., Transactions of the ASME*, Vol. 110, pp. 222-225, 1988.

[96] Davey K.R. and Melcher J.R. : in *Viscous Flow Drag Reduction* (edited by G. R. Hough, *Progress in Astronautics and Aeronautics*, Vol. 72, AIAA Inc. publishers), pp. 90-107, 1979.

[97] Gust G. : *J. Fluid Mech.*, Vol. 75, Part 1, pp. 29-47, 1976.

[98] Matthys E.F., Ahn H. and Sabersky R.H. : *J. Fluid Eng., Transactions of the ASME*, Vol. 109, pp. 307-312, 1987.

[99] Krol M. : in *Structure of Turbulence and Drag Reduction* (edited by A. Gyr, Springer-Verlag) pp. 361-368, 1990.

[100] Durlofsky L.J. and Brady J.F. : *J. Fluid Mech.*, Vol. 200, pp. 39-67, 1989.

[101] Carpenter P.W. : in *Viscous Drag Reduction in Boundary Layers* (edited by D.M. Bushnell & J.N. Hefner, *Progress in Astronautics and Aeronautics* Vol. 123, AIAA Inc. publishers), pp. 79-113, 1990.

[102] Carpenter P.W., Lucey A.D. and Dixon A.E. : in *Recent Developments in Turbulence Management, Fluid Mechanics and its Applications*, Vol. 6, edited by K-S. Choi, Kluwer Academic Publishers, pp. 195-221, 1991.

[103] Moin P., Kim J. and Choi H. : *AIAA Paper 89-0960*, 1989.

[104] Semenov B.N. : in *Proceedings of the 6th European Drag Reduction Working Meeting*, Eindhoven, November 1991.

[105] Kulik V.M. : in *Proceedings of the 6th European Drag Reduction Working Meeting*, Eindhoven, November 1991.

- [106] Kulik V.M., Poguda I.S. and Semenov B.N. : in *Recent Developments in Turbulence Management, Fluid Mechanics and its Applications*, Vol. 6, edited by K-S. Choi, Kluwer Academic Publishers, pp. 263-289, 1991.
- [107] Semenov B.N. : in *Recent Developments in Turbulence Management, Fluid Mechanics and its Applications*, Vol. 6, edited by K-S. Choi, Kluwer Academic Publishers, pp. 241-262, 1991.
- [108] Chakrabarti K.M. : *AIAA Jour.*, Vol. 12, No. 8, pp. 1136-1137, 1974.
- [109] Savas O. and Coled D. : *J. Fluid Mech.*, Vol. 160, pp. 421-446, 1985.
- [110] Goodman W.L. : *AIAA Jour.*, Vol. 23, No. 1, 1985.
- [111] Pailhas G., Cousteix J., Anselmet F. and Fu-lachier L. : 8th Symposium on Turbulent Shear Flows, München, September 1991, Paper 18-4.
- [112] Gad-el-Hak M. : in *Structure of Turbulence and Drag Reduction* (edited by A. Gyr, Springer-Verlag) pp. 357-360, 1990.
- [113] Anselmet F., Antonia R.A., Benabid T. and Fu-lachier L. : in *Structure of Turbulence and Drag Reduction* (edited by A. Gyr, Springer-Verlag) pp. 349-356, 1990.
- [114] Antonia R.A., Fulachier L., Krishnamoorthy L.V., Benabid T. and Anselmet F. : *J. Fluid Mech.*, Vol. 190, pp. 217-240, 1988.
- [115] Elena M. : *Thèse de Doctorat ès Sciences*, Université d'Aix Marseille, Marseille, France 1975.
- [116] Schlichting H. : *Boundary Layer Theory*, Mc Graw Hill, 1968.
- [117] Wilkinson S.P., Ash R.L. and Weinstein L.M. : in *Viscous Flow Drag Reduction* (edited by G. R. Hough, *Progress in Astronautics and Aeronautics*, Vol. 72, AIAA Inc. publishers), pp. 233-248, 1979.
- [118] Gad-el-Hak M. and Blackwelder R.F. : *AIAA Jour.*, Vol. 27, No. 3, pp. 308-314, 1989.
- [119] Gad-el-Hak M. and Fazle Hussain A.K.M. : *Phys. Fluids*, Vol. 29, No. 7, pp. 2124-2139, 1986.
- [120] Roon J.B. and Blackwelder R.F. : in *Structure of Turbulence and Drag Reduction* (edited by A. Gyr, Springer-Verlag) pp. 517-524, 1990.
- [121] Wiedemann J. and Gersten K. : AGARD-CP-365, Paper No. 14, May 1984.
- [122] Hefner J.N. and Bushnell D.M. : in *Viscous Drag Reduction in Boundary Layers* (edited by D.M. Bushnell & J.N. Hefner, *Progress in Astronautics and Aeronautics* Vol. 123, AIAA Inc. publishers), pp. 457-478, 1990.
- [123] Bushnell D.M., Anders Jr. J.B., Walsh M. and McInville R.V. : AGARD-CP-365, Paper No. 17, May 1984.
- [124] Townsin R.L. : in *Recent Developments in Turbulence Management, Fluid Mechanics and its Applications*, Vol. 6, edited by K-S. Choi, Kluwer Academic Publishers pp. 181-191, 1991.
- [125] Tani I. : in *Proc. of the Japan Academy*, Vol. 64, Ser. B, No. 2, pp. 21-24, 1988.
- [126] Abe K., Matsumoto A., Munakata H. and Tani I. : in *Structure of Turbulence and Drag Reduction* (edited by A. Gyr, Springer-Verlag) pp. 517-524, 1990.
- [127] Fanourakis P. and Savill A.M. : in *Proceedings of the 6th European Drag Reduction Working Meeting*, Eindhoven, November 1991.
- [128] Osaka H. and Mochizuki S. : in *Recent Developments in Turbulence Management, Fluid Mechanics and its Applications*, Vol. 6, edited by K-S. Choi, Kluwer Academic Publishers, pp. 163-180, 1991.
- [129] Bandyopadhyay P.R. : *Experiments in Fluids*, Vol. 4, No. 5, pp. 247-256, 1986.
- [130] Bradshaw P. : AGARD Report AGARD-AG-169, August 1973.
- [131] Smits A.J. : *AIAA Paper85-0538*, 1985.
- [132] Gillis J.C. and Johnston J.P. : *J. Fluid Mech.*, Vol. 135, pp. 123-153, 1983.
- [133] Gatski T.B. and Savill A.M. : *AIAA Paper89-1014*, 1989.
- [134] Bandyopadhyay P.R. : *AIAA Paper88-0135*, 1988.
- [135] Walsh M.J. and Lindemann A.M. : *AIAA Paper 84-0347*, 1984.
- [136] Coustols E. and Cousteix J. : in *Structure of Turbulence and Drag Reduction* (edited by A. Gyr, Springer-Verlag) pp. 577-584, 1990.
- [137] Savill A.M., Koury E., Sebastian W. and Squire L.C. : in *Drag Reduction in Fluid Flows* (eds. R.H.J. Sellin & R.T. Moses, Ellis Horwood Publishers) pp. 43-52, 1989.
- [138] Nguyen V.D., Dickinson J., Jean Y., Chalifour Y., Smaili A., Pagé A. and Paquet F. : in *Turbulence Control by Passive Means* (edited by E. Coustols, Kluwer Academic Publishers, *Fluid Mechanics and its applications*) pp. 159-172, 1990.
- [139] Reidy L.W. and Anderson G.W. : *AIAA Paper 88-0138*, 1988.
- [140] Rohr J., Anderson G.W. and Reidy L.W. : in *Drag Reduction in Fluid Flows* (eds. R.H.J. Sellin & R.T. Moses, Ellis Horwood Publishers) pp. 263-270, 1989.
- [141] Reed J.C. and Weinstein L.M. : *AIAA Paper 89-0962*, 1989.
- [142] Thiel H. : in *Drag Reduction in Fluid Flows* (eds. R.H.J. Sellin & R.T. Moses, Ellis Horwood Publishers) pp. 43-52, 1989.
- [143] Bewersdorff H-W. and Thiel H. : in *Proceedings of the 6th European Drag Reduction Working Meeting*, Eindhoven, November 1991.
- [144] Bardakhanov S.P., Koslov V.V. and Larichkin V.V. : in *Structure of Turbulence and Drag Reduction* (edited by A. Gyr, Springer-Verlag) pp. 503-506, 1990.

- [145] Stone T.D., Guenette G.R. and Epstein A.H. : AIAA Paper 92-0063, (1992).
- [146] Liu C.-K., Kline S.J. and Johnston J.P. : Report MD-15, Stanford University, Dept. Mech. Eng., 1966.
- [147] Walsh M.J. and Anders Jr. B.J. : Appl. Sci. Res., Vol. 46, No. 3, pp. 255-262, 1989.
- [148] Squire L.C. and Savill A.M. : Int. Conf. on Turbulent Drag Reduction by Passive Means, London 1987.
- [149] Sawyer W.G. and Winter K.G. : Int. Conf. on Turbulent Drag Reduction by Passive Means, London 1987.
- [150] Coustols E., Cousteix J. : 16th ICAS Congress, Jerusalem, Vol. 2, ICAS 88-3.7.3, pp. 999-1013 1988.
- [151] Enyutin G.V., Lashkov Y.A., Samoilova N.V., Fadeev I.V. and Shumilkin E.A. : Translated from Izvestiya Akademii Nauk. SSSR (March-April 1987).
- [152] Coustols E. : AIAA Paper 89-0963 1989.
- [153] Coustols E. and Schmitt V. : in Turbulence Control by Passive Means (edited by E. Coustols, Kluwer Academic Publishers, Fluid Mechanics and its applications) pp. 123-140, 1990.
- [154] Walsh M.J. : AIAA Paper 82-0169 1982.
- [155] Walsh M.J., Sellers III W.L., McGinley C.B. : AIAA Paper 88-2554, 1988.
- [156] Beauchamp C.H. and Philips R.B. : in Proceedings of the Symp. on Hydrodynamic Performance Enhancement for Marine Applications, Rhode Island, 1988.
- [157] Lazos B.S. and Wilkinson S.P. : AIAA Jour., Vol. 26, No. 4, pp. 496-498, 1987.
- [158] Bechert D.W., Hoppe G. and Reif W-E. : AIAA Paper 85-0546, 1985.
- [159] Pulvin P. : Ph.D dissertation No. 809, EPFL Lausanne, 1989.
- [160] Nieuwstadt F.T.M., Wolthers W. and Leijdens H. : in Proceedings of the 6th European Drag Reduction Working Meeting, Eindhoven, November 1991.
- [161] Coustols E., Gleyzes C., Schmitt V. and Berrue P. : 24ième Colloque AAAF, Poitiers 1987.
- [162] Coustols E. : in Recent Developments in Turbulence Management, Fluid Mechanics and its Applications, Vol. 6, edited by K-S. Choi, Kluwer Academic Publishers, pp. 43-64, 1991.
- [163] Choi K.S. : Aeronautical Journal, Vol. 94, No. 933, pp. 79-85, March 1990.
- [164] Van der Hoeven J.G. Th and Bechert D.W. : in Recent Developments in Turbulence Management, Fluid Mechanics and its Applications, Vol. 6, edited by K-S. Choi, Kluwer Academic Publishers, pp. 3-24, 1991.
- [165] Gaudet L. : Int. Conf. on Turbulent Drag Reduction by Passive Means. London 1987.
- [166] McLean J.D., George-Falvy D.N., Sullivan P.P. : Int. Conf. on Turbulent Drag Reduction by Passive Means, London 1987.
- [167] Robinson S.K. : AIAA Paper 88-2526, 1988.
- [168] Gaudet L. : Appl. Sci. Res., Vol. 46, No. 3, pp. 245-254, 1989.
- [169] Coustols E. and de Zotti A. : in Proceedings of the 5th European Drag Reduction Working Meeting, Teddington, November 1990.
- [170] Coustols E. : in Proceedings of the 6th European Drag Reduction Working Meeting, Eindhoven, November 1991.
- [171] Nitschke P. : Ph D Dissertation, Göttingen, FRG, 1983.
- [172] Lawson M.V., Bates J.H.T. and Jewson A.R. : in Drag Reduction in Fluid Flows (eds. R.H.J. Sellin & R.T. Moses, Ellis Horwood Publishers) pp. 77-83, 1989.
- [173] Liu K.N., Christodoulou C., Riccius O. and Joseph D.D. : AIAA Journal, Vol. 28, No. 10, pp. 1697-1698, 1990.
- [174] Nakao S-I : Journal of Fluid Eng., Trans. of the ASME, Vol. 113, pp. 587-590, December 1991.
- [175] Benhalilou M., Anselmet F., Liandrat J. and Fuchquier L. : 8th Symposium on Turbulent Shear Flows, München, September 1991, Paper 18-5.
- [176] Choi K-S. : in Turbulence Control by Passive Means (edited by E. Coustols, Kluwer Academic Publishers, Fluid Mechanics and its applications) pp. 109-121, 1990.
- [177] Hooshmand D., Youngs R. and Wallace J.M. : AIAA Paper 83-0230, 1983.
- [178] Bacher E.V. and Smith C.R. : AIAA Journal, Vol. 24, No. 8, pp. 1382-1385, 1986.
- [179] Clark D.G. : in Turbulence Control by Passive Means (edited by E. Coustols, Kluwer Academic Publishers, Fluid Mechanics and its applications) pp. 79-96, 1990.
- [180] Schwarz-van Manen A.D., Hoogsteen R., Stouthart J.C., Krishna Prasad K. and Nieuwstadt F.T.M. : in Recent Developments in Turbulence Management, Fluid Mechanics and its Applications, Vol. 6, edited by K-S. Choi, Kluwer Academic Publishers, pp. 93-112, 1991.
- [181] Coustols E. and Cousteix J. : 7th Symposium on Turbulent Shear flows, Stanford, September 1989, Paper 25-3.
- [182] Bechert D.W. and Bartenwerfer M. : J. Fluid Mech., Vol. 206, pp. 105-130, 1989.
- [183] Vukoslavcevic P., Wallace J.M. and Balint J-L : Int. Conf. on Turbulent Drag Reduction by Passive Means, London 1987.
- [184] Tardu S. and Truong T.V. : in Proceedings of the 6th European Drag Reduction Meeting, Eindhoven, November 1991.
- [185] Choi K-S. and Hamid S. : in Recent Developments in Turbulence Management, Fluid Mechanics and its Applications, Vol. 6, edited by K-S. Choi, Kluwer Academic Publishers, pp. 25-41, 1991.

- [186] Choi K-S. : J. Fluid Mech., Vol. 208, pp. 417-458, 1989.
- [187] Djenidi L., Liandrat J., Anselmet F. and Fulachier L. : Appl. Sci. Res., Vol. 46, No. 3, pp. 263-270, 1989.
- [188] Launder B.E. and Li S. : Appl. Sci. Res., Vol. 46, No. 3, pp. 271-279, 1989.
- [189] Khan M.M.S. : AIAA Paper 86-1127, 1986.
- [190] Liandrat J., Coustols E., Djenidi L., Anselmet F., de Saint-Victor X., Fioc F. and Fulachier L. : in Turbulence Control by Passive Means (edited by E. Coustols, Kluwer Academic Publishers, Fluid Mechanics and its applications) pp. 141-157, 1990.
- [191] Djenidi L., Squire L.C. and Savill A.M. : in Recent Developments in Turbulence Management, Fluid Mechanics and its Applications, Vol. 6, edited by K-S. Choi, Kluwer Academic Publishers, pp. 65-92, 1991.
- [192] Djenidi L. : in Proceedings of the 6th European Drag Reduction Meeting, Eindhoven, November 1991.
- [193] Launder B.E. and Li S. : in Proceedings of the 6th European Drag Reduction Meeting, Eindhoven, November 1991.
- [194] Tullis S. and Pollard A. : (private communication).
- [195] Chu D. and Em Karniadakis G. : AIAA Paper 91-0518, 1991.
- [196] Choi H., Moin P. and Kim J. : Phys. Fluids A, Vol. 3, No. 8, pp. 1892-1896.
- [197] Loerke, R.I. & Nagib, H.M.: AGARD Rep 598 (1972)
- [198] Yajnik, K.S. & Acharya, M.: Lecture Notes in Physics 76, p.249 (1977)
- [199] Corke, T.C., Nagib, H.M. & Guezennec, Y.: NASA CR 165861 (1982)
- [200] Hefner, J.N., Anders, J.B. & Bushnell, D.M.: Prog Aero & Astro 72, p.110 (1979)
- [201] Bertelrud, A., Truong, T.V. & Avellan, F.: AIAA-82-1370 (1982)
- [202] Savill, A.M. & Mumford, J.C.: ASME Fluids Eng. Div. 11, p.41 & JFM 191, p.389 (1988)
- [203] Hefner, J.N., Anders, J.B. & Bushnell, D.M.: AIAA-84-0345 (1984).
- [204] Lemay, J., Provencal, D., Gourdeau, R., Nguyen, V.D. & Dickinson, J.: AIAA-85-0521, (1985).
- [205] Savill, A.M.: Advances in Turbulence, p.533, Springer (1986).
- [206] Veuve, M. Ph.D. thesis No. 768, EPFL, Switzerland, (1988).
- [207] Lemay, J., Savill, A.M., Bonnet, J.-P. and Delville, J.: TSF6, Springer (1987).
- [208] Savill, A.M. (1987) IUTAM Symp. Turbulence Management and Relaminarisation, Bangalore Springer p.89 (1987).
- [209] Narasimha, R. & Sreenivasan, K.R.: AIAA-85-0517 & IIS FM 4 (1986)
- [210] Narasimha, R. & Sreenivasan, K.R.: Flat plate drag reduction by turbulence manipulation. Sadhana 12 (1& 2) p.15 (1988).
- [211] Nguyen, V.D.: unpublished Laval University Results (1988)
- [212] Blackwelder, R.F.: Private communication (1989)
- [213] Taylor, S.: The effects of large-eddy manipulator devices on the turbulent spot and turbulent boundary layer. Ph.D. thesis Caltech (1986).
- [214] Pollard A., Thomann, H. & Savill, A.M. Appl. Sci. Res. Special Volume 46, No.3 (1989).
- [215] Pollard, A., Savill, A.M. & Thomann, H.: Turbulent pipe flow manipulation: some experimental and computational results for tandem manipulator rings. Proc. 10th Australasian Fluid Mechanics Conference, Vol., p.9.31 (1989).
- [216] Nguyen, V.D. & Dickinson, J.: Some observations of the static pressure distributions in pipe flow perturbed by a LEBU ring. See ERCOFTAC Bulletin 4 p.8(1989)
- [217] Pollard, A., Thomann, H. & Savill, A.M.: In Turbulence Control by Passive Means (Ed. E. Coustols, Kluwer Academic Publishers) p.23 (1990)
- [218] Mah, Y.A., Chew, Y.T. & Khoo, B.C.: Blade manipulators in fully developed turbulent pipe flow. Proc. Joint ASME/JSME Conf., Portland (1991).
- [219] Mah, Y.A., Khoo, B.C. & Chew, Y.T.: The effect of blade manipulator in fully developed pipe flow. Submitted to JFM (1991).
- [220] Mah, Y.A., Khoo, B.C. & Chew, Y.T.: Measurements of skin friction behind BLADE manipulators in a turbulent pipe flow. Submitted to AIAA J. (1992).
- [221] Prabhu, A., Kailas Nath, P., Kulkarni, R.S. & Narasimha, R., "Blade manipulators in channel flows", Proc. IUTAM Symp. turbulence Management and Relaminarisation, Bangalore, Springer, p.97 (1087).
- [222] Narasimha, R: Unpublished NAC Bangalore results (1990).
- [223] Freidrich, R. & Klein, H.: Manipulating large-scale turbulence in a channel. Abstr. TSF7 (1989).
- [224] Klein, H. & Freidrich, R.: Manipulating large-scale turbulence in a channel and a boundary layer. Proc. 7th Turbulent Shear Flows Symp. Abstr (1989).
- [225] Klein, H.: Numerische Simulation Manipulierter Turbulenter Scherstromungen. Ph.D. thesis T.U. Munchen (1990).
- [226] Poddar, K. & van Atta, C.W.: TSF5, Springer (1985).
- [227] Shengxi, S.: A comparison of pipe flows with annulus flows. Unpublished report Nanjing Aeronautical Institute (1990).

[228] Savill, A.M., Klein, H. & Freidrich, R.: Pattern Recognition Analysis of structure in manipulated channel flow simulations. Submitted to Journal of Turbulence 1 (1) (1992).

[229] Chang, S.I.: Ph.D thesis Uinversity of southern California (1988)

[230] Dinkelacker, A., Bauman, C. & Otto, W.: On flow processes related to wall pressure fluctuations in turbulent pipe flow. Proc. 10th AFMC, Melbourne Vol 1.1. p. 2.43 (1989).

[231] Anders, J.B. & Watson, R.D.: AIAA-85-0520 (1985).

[232] Anders, J.B.: SAE Tech paper 8661769 (1986).

[233] Bonnet, J.P., Delville, J. & Lemay, J.: Experimental study of the behaviour of NACA 0009 profile in a transonic LEBU configuration. Proc. TSF7 (1989).

[234] Goodman, W.L.: AIAA-85-0550 (1985).

[235] Wilkinson, S.P., Anders, J.B., Lazos, B.S. and Bushnell, D.M.: Proc. Roy. Aero. Soc. Int. Conf. on Turbulent Drag Reduction by Passive Means Vol.1. p.1 (1987).

[236] Bertelrud, A. & Liandrat, M.P.: The importance of LEBU device shape for turbulent drag reduction. In turbulence control by passive means (Ed. E. Coustols; Kluwer Acad. Publis.) p.67 (1989) - see also AIAA-91-1601

[237] Anders, J.B.: LEBU drag reduction in high Reynolds number boundary Layers. AIAA-89-1011.

[238] Smits, A. & colleagues: Viscous papers on the structure of high Re boundary layers as revealed by new experimental techniques. Princeton University (1990-1992).

[239] Sakamoto, M., & Osaka, H.: see [1] (1987)

[240] Pineau, F., Nguyen, V.D., Dickinson, J. & Belanger, J.: AIAA-87-0357 (1987).

[241] Savill, A.M.: Proc. 3rd Int. Symp. Refined Flow Modelling and Turbulence Measurements, Tokyo, Universal Academy Press Inc. (1988).

[242] Roach, P.E. & Brierley, D.H.: Submitted to Appl. Sci. Res. (1989).

[243] Savill, A.M.: Int. J. Heat & Fluid Flow, June (1989).

[244] Savill, A.M.: Proc. Roy Aero. Soc. Int. conf. Trubulent Drag Reduction by Passive Means, London, Vol. 1 p.89 RAeS (1987).

[245] McGinley, C & Bushnell, D.M.: Proc. 2nd AIAA Shear Flow Control Conference. Boulder, Colorado (1985).

[246] H.H. Fernholz: Private communication (1987).

[247] McInville, R.M. & Hassan, H.A.: AIAA-85-0541 (1985).

[248] Grinstein, F.F., Boris, J.P. & Griffin, O.M.: Passive pressure-drag control in a plane wake. AIAA J. 29 (9) p.1436 (1991).

[249] Nakamura, I., Osaka, H. & Yamada, H.: Re- sponse of a plane turbulent wall jet to the perturbation by a cylinder. Proc. 3rd Turbulent Shear Flows Symp. Davis (1981).

[250] Goodman, W.L., Morissette, E.L., Hiussaini, M.Y. & Bushnell, D.M.: Control plate for shock boundary-layer interactions. AIAA-85-0523 (1985).

[251] Trigui & Guezennec: Heat transfer reduction in a manipulated turbulent boundary layer. Int.J. Heat & Fluid flow 11 (3) p.214 (1990).

[252] Bonnet, J.P., Alem, D & Handouni, A.: Effect of external manipulator (LEBU) on the heat transfer of a flat plate boundary layer. Abstr. EDRM 6 Eindhoven (1991).

[253] Savill, A.M. & Djenidi, L.: Some studies of the effect of manipulation on heat transfer. Abstr. EDRM 6 (1991).

[254] Suzuki, K., Suzuki, H., Inaoka, K. & Kigawa, H.: Heat transfer in a turbulent boundary layer with insertion of a LEBU plate. Proc. TSF8, Munich p.24-5-1 (1991).

[255] Moller, J.C. & Leehey, P.: Measurements of wall shear and wall pressure downstream of a honeycomb boundary layer manipulator. MIT Rep. No. 97457-3 (1989).

[256] Dowling, A.: The effect of large-eddy breakup devices on flow noise. Unpublished Cambridge University Engineering Dept. Report (1990).

[257] Roth, K.W. & Leehey, P.: Velocity profile and wall shear stress measurements for a large-eddy breakup device (LEBU). MIT Rep. No. 71435-1 (1989).

[258] Camelio, F.J.: Variation of wall shear stress and Reynolds stress over a flat plate downstream of a boundary layer manipulator. M.S. thesis MIT (1990).

[259] van den Berg, B.: AGARD CP 365 (1985).

[260] van den Berg, B.: Abstr. EUROMECH 181. Saltsjobaden (1984)

[261] Nagib, H.M. & Westphal, R.V.: Unpublished IIT results (1985).

[262] Veuve, M: Unpublished EPFL results (1987).

[263] Dhanak, M: Unpublished Topexpress results (1987).

[264] Johnston, L.J.: Private communication (1987).

[265] Shengzi, S. & Zhou, M.D.: The influence of plate manipulator wake on skin friction. Nanjing Aeronautical Institute Report (1989).

[266] Tenaud, C.: Unpublished ONERA/CERT results (1988).

[267] Tenaud, C., Coustols, E. & Cousteix, J.: Proc. roy. Aero. Soc. Int. conf. on Turbulent Drag Reduction by Passive Means Vol.1 (1987).

[268] Djenidi, L., Ioualalen, M., Squire, L.C. & Savill, A.M.: SERC Report on Maximising Drag Reduction by LEBUs and Riblets (1992).

[269] Gerbert, G. & Atassi, H.: AIAA-89-0212 (1989).

[270] Balakumar, P. & Widnall, S.E.: Phys. Fluids 29, p.1779 (1986).

- [271] Augier, E., Atassi, H.M., Alcarez, E., Ladhari, F., Morel, R.: Analytical and experimental study of energy density spectra of the outer region of a manipulated turbulent boundary layer. In *Recent developments in turbulence management* (Ed. K.S. Choi, Kluwer) p.127 (1991).
- [272] Dowling, A.P.: *JFM* 160, p.447 (1985).
- [273] Kinney, R.B., Taslim, M.E. & Hung, S.C. Univ. Arizona Coll. Eng. Rep. NAG-1-141 (1984).
- [274] Balasubramanian, R. & Bandyopadhyay, R.: Vortex-LEBU interactions in subcritical synthetic flows. *AIAA-89-1012*.
- [275] Delville, J. & Lemay, J.: *Etude expérimentale du comportement de la turbulence dans une couche limite incompressible en présence d'un manipulateur externe*. Ph.D. thesis Université Laval, Québec (1989).
- [276] Lemay, J., Delville, J. & Bonnet, J.P.: Turbulent kinetic energy balance in a LEBU modified turbulent boundary layer. *Proc. 11th Turbulence Symp. Missouri-Rolla* (1988) & *Experiments in Fluids* 9 p.301 (1990).
- [277] Lemay, J., Bonnet, J.P. & Delville, J.: Experimental analysis of second order closure models in a LEBU modified turbulent boundary layer. *Proc. 7th Turbulent Shear Flows Symp.* (1989).
- [278] Bonnet, J.P.: Turbulent boundary layer modification by flat plate manipulation. *ERCOFTAC data base* (1991).
- [279] Tenaud, C.: Ph.D. thesis, ENSAE Toulouse (1987).
- [280] Coustols, E., Cousteix, J. & Belanger, J.: *Proc. RAeS Int. Conf. on Turbulent Drag Reduction by Passive Means* Vol.2 p.250 (1987).
- [281] Savill, A.M.: *Proc. IMA-SMAI Conf. Computational Methods in Aeronautical Fluid Dynamics*, OUP (1987).
- [282] Savill, A.M. & Zhou, M.D.: *5th Asian Congr. Fluid Mech.*, Hong Kong (1989).
- [283] Savill, A.M.: *ERCOFTAC Special Interest Group on Transition/Retransition Report* ERCOFTAC Bulletin 11 p.20 (1991).
- [284] Launder, B.E. & Tselepidakis, D.P.: directions in Second-Moment modelling of near-wall turbulence. *AIAA-91-0219* - see also - El Baz, A., Launder, B.E. & Nemouchi, A.: On the prediction of memory effects in plane turbulent wakes. *Proc. 7th Turbulent shear Flows Symp.* (1989).
- [285] Germano, M.: *Proc. TSF8*, Munich Vol.2 p.19-1.1 (1991).
- [286] Hustad, C., Dawes, W. & Savill, A.M.: Unpublished results (1992).
- [287] Schmitt, V.: Private communication (1990).
- [288] Savill, A.M. & Ferre, J.A.: Extension of Pattern Recognition Analysis Techniques to distorted and manipulated flows. *Proc. 10th Australian Fluid Mechanics Conference*, Vol.1, p.6.1 (1989).
- [289] Luchini, P.: *Viscous sublayer analysis of ripples*. *Abstr. EDRM6*, Eindhoven (1991).
- [290] Bartenwerfer, M. & Beckett, D.W.: *The viscous flow on hairy surfaces*. *Abstr. EDRM6*, Eindhoven (1991).
- [291] Tani, I.: In *Perspectives in Turbulence Studies* (Ed. H. Meir & P. Bradshaw; Springer Verlag) p.223 (1987).
- [292] Tani, I., Munakata, A., Matsumoto, A. & Abe, K.: *Nihon University Research Report* (1987).
- [293] Tani, I.: Unpublished Nihon University results (1988).
- [294] Savill, A.M.: *Proc. FLUCOME 88*, Sheffield, p.436, H.S. Stephens & Associates (1988)
- [295] Choi, K.-S., Fujisawa, N. & Savill, A.M.: *Proc. 5th Int. Symp. Flow Visualisation*, Prague (1989).
- [296] Fanourakis, P. & Savill, A.M.: *Drag reducing d-type roughness*. *Abstr. EDRM 5*, BMT, London (1990) - also video presented at EDRM4 Lausanne (1989).
- [297] Fanourakis, P.: *Possibly drag reducing rough surfaces in turbulent flow*. Ph.D. thesis University of Cambridge (in preparation 1992).
- [298] Demenok, S.: Priv. communication (1991).
- [299] Osaka H., & Mochizuki S.: *Proc. TSF 6*, Toulouse (1987).
- [300] Osaka H., & Mochizuki S.: *Proc. 1st KSME-JSME thermal & Fluids Eng. Conf.* Seoul (1988).
- [301] Osaka, H., & Mochizuki, S.: *Proc. 1st Int. Conf. on Fluid Dynamic Measurement and its Applications* Beijing (1989).
- [302] Osaka, H., & Mochizuki, S.: *Proc. 2nd KSME-JSME Fluids Engineering Conf.* Seoul (1990).
- [303] Tani, I.: *Tokyo University Research Report* (1989).
- [304] Tani, I.: *Proc. 2nd European Turbulence Conf.*, Berlin, Springer (1988).
- [305] Tani, I., Abe, K. & Matsumoto, A.: Unpublished Nihon University results (1989).
- [306] Karlsson, R.I.: *ASME Conf. Paper 81-FE-35* (1981).
- [307] Fanourakis, P.: *Studies of drag reducing d-type and sandgrain roughness at high subsonic mach numbers*. Cambridge University Eng. Dept. Report (1990).
- [308] Fanourakis, P.: *Further studies of surfaces with drag reducing properties at high sub-sonic mach numbers*. Cambridge University Eng. Dept. Report (1991).
- [309] Munakata, M., Kimura, S., Iuchi, M. & Abe, K.: *Wind tunnel tests of rotor aerodynamics with various surface roughness*. Nihon University Report (1990).
- [310] Scilliba, M.F., Leboucher, P. & Michaelides, E.E.: *Velocity and turbulence profiles in a wall jet with embedded particles*. *Abstr. 1st European Fluid Mechanics Conf.* Cambridge (1991).

- [311] Scilliba, M.F. & Bleboucher, P.: Turbulence Modification in a Wall Jet Due to Embedded Particles. FED Vol. 110 Turbulence Modification in Multiphase Flows. ASME (1991).
- [312] Towsin, R.L.: Private communication of Newcastle University research results (1991).
- [313] Gyr, A.: Initial interaction of a turbulent channel flow with a smooth, erodible sand bed. Abstr. 1st European fluid Mechanics Conf. Cambridge (1991) - see also - Gyr, A. & Schmid, A.: Fine sand as a tracer to study turbulent flows close to a flat, smooth and rigid wall. Unpublished ETUZ Institut fur Hydromechanik und Wasserwirtschaft Report (1991).
- [314] Coney, M.H., Ferreira, J. & Harrogate, I.: Observations regarding the influence of surface finish on the overall performance of a thermal barrier coat deposited by plasma arc. Proc. 10th ISABE, Nottingham p.15.5 (1991).
- [315] Tselepidakis, D.P., Gatski, T.B. & Savill, A.M.: A comparison of turbulence models for homogeneous shear flows with longitudinal curvature. Proc. NASA Langley Transition and Turbulence Conf. (1991).
- [316] Gatski, T.B., Savill, A.M. & Tselepidakis, D.P.: Unpublished work (1991).
- [317] Walsh, M.J. & Anders Jr., J.B. Abstr ONR-NSSC-AFOSR-NASA Symp. Drag Reduction and Boundary layer Control, Washington (1985)
- [318] Dickinson, J., Nguyen, V.D., Chalifour, Y., Smaili, A., Page, A. & Paquet, F.: Boundary layer over a ribbed surface using tandem turbulence manipulators. Proc. 1st Canadian Symp. on Aerodynamics, Ottawa (1989) - see also ERCOF-TAC Bulletin 8 p.18 (1991).
- [319] Savill, A.M.: Flow Visualisation IV, Hemisphere Publishing Corporation, Washington, p.303 (1986).
- [320] Tani, I. & Motohashi, T.: Proc. Japan Acad. 61. Ser.B p.333 (1985) see also Proc. 16th Turbulence Symposium, Tokyo (1984).
- [321] Tani, I.: Proc. Japan Acad. Sci. 63 Ser. B (3) p.96 (1987).
- [322] Girard, H.: Industrial applications of drag reduction to the French high speed train (TGV). Abstr. EDRM6, Eindhoven (1991)
- [323] Osaka, H. & Mochizuki, S.: In Recent Developments in Turbulence Management (Ed. K.-S. Choi; Kluwer) p.163 (1991) - see also Khalid. M.: NAE Canada Aero Note NAE-AN-39, NRS No.26163, (1986)
- [324] Thiel, H.: In Drag Reduction in Fluid Flows (Ed. RJH Sellin & R.T. Moses, Ellis Horwood p.287 (1989).
- [325] Bewersdorf, H-W. & Thiel, H.: Priv. communication (1991).
- [326] Choi, K.-S., Gadd, G.E., Pearcey, H.H. & Savill, A.M., Svenson, S.: In Drag Reduction in Fluid Flows (Ed. RJH Sellin & R.T. Moses. Ellis Horwood p.287 (1989)
- [327] Rohr, J.J., Reidy, L.W. & Anderson, G.W. AIAA-88-0138 (1989).
- [328] Merkle, C.L. & Deutch, S.: NASA Star Abstracts (1985).
- [329] Park, J.T. & Johnson, J.E.: Abstr. ONR-NASA-AFOSR-NSSC Drag Reduction Conference, Washington, (1985).
- [330] Pollard, A.: Unpublished Queens University Mechanical Engineering Department results (1990)
- [331] Smith, R.E. & Tiedemann, W.G.: Investigation into the mechanism of polymer thread drag reduction. Purdue Univ. School of Mech. Eng. Rep (1990).
- [332] Buse, M. & Bechert, D.W.: Experiments with adjustable surfaces. Abstr. EDRM 6 Eindhoven (1991).
- [333] Roon, J.B. & Blackwelder, R.F.: The effects of longitudinal roughness elements and local suction upon the turbulent boundary layer. AIAA CP (1989)
- [334] Falco, R.: Correlation of outer and passive wall region manipulation with boundary layer coherent structure dynamics and suggestions for improved devices. AIAA-89-1026, (1989).
- [335] Hunt, J.C.R.: Priv. communication (1991)
- [336] Osaka, H. & Fukushima, C.: Effect of controlled longitudinal vortex arrays on the development of turbulent boundary layer. In engineering Turbulence Modelling & Experiments (eds. Rodi & Ganic; Elsevier 1990)
- [337] Fukushima, C. & Osaka, H.: Interaction of a turbulent boundary layer with a row of longitudinal vortices. Proc. JSME Spring Annual Meeting (1990).
- [338] Fukushima, C. & Osaka, H.: Interaction of a turbulent boundary layer with a row of longitudinal vortices - Turbulence quantities Proc. Fluids Engineering Conf. Tokyo (1990).
- [339] Osaka, H. & Fukushima, C.: Boundary layer turbulence structure interacting with controlled longitudinal vortex arrays. Proc. 2nd KSME/JSME Fluids engineering Conf. 1 p.189 (1990).
- [340] Zhou, M.D.: Private communication (1990).
- [341] Papathanasiou, A.G. & Nagel, R.T.: AIAA-86-1954 (1986).
- [342] Nagel, R.T.: Enhanced viscous flow drag reduction using acoustic excitation. NASA-CR-182734 (1988).
- [343] Mengle, V. & Hsiao, C.: Analysis of a flexible large eddy break-up device in a turbulent boundary layer. AIAA-89-0211 (1989).
- [344] Bandyopadhyay, P.R.: Resonant flow in small cavities submerged in a boundary layer. Proc. Roy. Soc. London A 420 p.219 (1988).

[345] Bandyopadhyay, P.R.: Turbulent flow over a transversely grooved surface - a distinct low Reynolds number behaviour and an approach to its control. Abst. IUTAM Conf. on Turbulence Management & Relaminarisation (1987).

“... but were afraid to ask”

REPORT DOCUMENTATION PAGE			
1. Recipient's Reference	2. Originator's Reference	3. Further Reference	4. Security Classification of Document
	AGARD-R-786	ISBN 92-835-0661-8	UNCLASSIFIED
5. Originator	Advisory Group for Aerospace Research and Development North Atlantic Treaty Organization 7 rue Ancelle, 92200 Neuilly sur Seine, France		
6. Title	SPECIAL COURSE ON SKIN FRICTION DRAG REDUCTION		
7. Presented in	an AGARD-FDP-VKI Special Course at the VKI, Rhode-Saint-Genèse, Belgium, 2nd–6th March 1992.		
8. Author(s)/Editor(s)	Various		9. Date March 1992
10. Author's/Editor's Address	Various		11. Pages 286
12. Distribution Statement	This document is distributed in accordance with AGARD policies and regulations, which are outlined on the back covers of all AGARD publications.		
13. Keywords/Descriptors	Aerodynamic drag Skin friction Transport aircraft Drag reducing agents Laminar flow Boundary layer control		
14. Abstract	<p>Lecture notes for the AGARD Fluid Dynamics Panel (FDP) Special Course on "Skin Friction Drag Reduction" have been assembled in this report. The aim and scope of this Course was to provide an overview of the state of the art of current technology programmes focused on reducing aircraft drag caused by skin friction. This Course is complementary and provides an update to topics reported in two previous FDP Special Courses held in 1977 and 1985.</p> <p>This report provides a review of recent progress in the field of skin friction drag reduction for transport aircraft. It provides a general introduction to the technology and then focuses on two specific aspects of drag reduction: maintaining laminar flow by controlling transition and manipulating the turbulence structure in boundary layers to help reduce skin friction. Technology associated with the use of riblets, LEBU, polymers, additives, etc., is also reviewed.</p> <p>The material assembled in this report was prepared under the combined sponsorship of the AGARD Fluid Dynamics Panel, the Consultant and Exchange Programme of AGARD, and the von Kármán Institute (VKI) for Fluid Dynamics.</p>		

<p>AGARD Report 786 Advisory Group for Aerospace Research and Development, NATO SKIN FRICTION DRAG REDUCTION Published March 1992 286 pages</p>	<p>AGARD Report 786 Advisory Group for Aerospace Research and Development, NATO SKIN FRICTION DRAG REDUCTION Published March 1992 286 pages</p> <p>Lecture notes for the AGARD Fluid Dynamics Panel (FDP) Special Course on "Skin Friction Drag Reduction" have been assembled in this report. The aim and scope of this Course was to provide an overview of the state of the art of current technology programmes focused on reducing aircraft drag caused by skin friction. This Course is complementary and provides an update to topics reported in two previous FDP Special Courses held in 1977 and 1985.</p> <p>P.T.O.</p>	<p>AGARD Report 786 Advisory Group for Aerospace Research and Development, NATO SKIN FRICTION DRAG REDUCTION Published March 1992 286 pages</p> <p>Lecture notes for the AGARD Fluid Dynamics Panel (FDP) Special Course on "Skin Friction Drag Reduction" have been assembled in this report. The aim and scope of this Course was to provide an overview of the state of the art of current technology programmes focused on reducing aircraft drag caused by skin friction. This Course is complementary and provides an update to topics reported in two previous FDP Special Courses held in 1977 and 1985.</p> <p>P.T.O.</p>
<p>AGARD Report 786 Advisory Group for Aerospace Research and Development, NATO SKIN FRICTION DRAG REDUCTION Published March 1992 286 pages</p>	<p>AGARD Report 786 Advisory Group for Aerospace Research and Development, NATO SKIN FRICTION DRAG REDUCTION Published March 1992 286 pages</p> <p>Lecture notes for the AGARD Fluid Dynamics Panel (FDP) Special Course on "Skin Friction Drag Reduction" have been assembled in this report. The aim and scope of this Course was to provide an overview of the state of the art of current technology programmes focused on reducing aircraft drag caused by skin friction. This Course is complementary and provides an update to topics reported in two previous FDP Special Courses held in 1977 and 1985.</p> <p>P.T.O.</p>	<p>AGARD Report 786 Advisory Group for Aerospace Research and Development, NATO SKIN FRICTION DRAG REDUCTION Published March 1992 286 pages</p> <p>Lecture notes for the AGARD Fluid Dynamics Panel (FDP) Special Course on "Skin Friction Drag Reduction" have been assembled in this report. The aim and scope of this Course was to provide an overview of the state of the art of current technology programmes focused on reducing aircraft drag caused by skin friction. This Course is complementary and provides an update to topics reported in two previous FDP Special Courses held in 1977 and 1985.</p> <p>P.T.O.</p>

<p>This report provides a review of recent progress in the field of skin friction drag reduction for transport aircraft. It provides a general introduction to the technology and then focuses on two specific aspects of drag reduction: maintaining laminar flow by controlling transition and manipulating the turbulence structure in boundary layers to help reduce skin friction. Technology associated with the use of riblets, LEBU, polymers, additives, etc., is also reviewed.</p> <p>The material assembled in this report was prepared under the combined sponsorship of the AGARD Fluid Dynamics Panel, the Consultant and Exchange Programme of AGARD, and the von Kármán Institute (VKI) for Fluid Dynamics. It was presented in an AGARD-FDP-VKI Special Course at the VKI, Rhode-Saint-Genèse, Belgium, 2nd–6th March 1992.</p>	<p>ISBN 92-835-0661-8</p>	<p>This report provides a review of recent progress in the field of skin friction drag reduction for transport aircraft. It provides a general introduction to the technology and then focuses on two specific aspects of drag reduction: maintaining laminar flow by controlling transition and manipulating the turbulence structure in boundary layers to help reduce skin friction. Technology associated with the use of riblets, LEBU, polymers, additives, etc., is also reviewed.</p> <p>The material assembled in this report was prepared under the combined sponsorship of the AGARD Fluid Dynamics Panel, the Consultant and Exchange Programme of AGARD, and the von Kármán Institute (VKI) for Fluid Dynamics. It was presented in an AGARD-FDP-VKI Special Course at the VKI, Rhode-Saint-Genèse, Belgium, 2nd–6th March 1992.</p>
<p>ISBN 92-835-0661-8</p>	<p>ISBN 92-835-0661-8</p>	<p>ISBN 92-835-0661-8</p>

AGARD
 NATO  OTAN
 7 RUE ANCELLE · 92200 NEUILLY-SUR-SEINE
 FRANCE
 Téléphone (1)47.38.57.00 · Télex 610 176
 Télécopie (1)47.38.57.99

DIFFUSION DES PUBLICATIONS
AGARD NON CLASSIFIEES

L'AGARD ne détient pas de stocks de ses publications, dans un but de distribution générale à l'adresse ci-dessus. La diffusion initiale des publications de l'AGARD est effectuée auprès des pays membres de cette organisation par l'intermédiaire des Centres Nationaux de Distribution suivants. A l'exception des Etats-Unis, ces centres disposent parfois d'exemplaires additionnels; dans les cas contraire, on peut se procurer ces exemplaires sous forme de microfiches ou de microcopies auprès des Agences de Vente dont la liste suite.

CENTRES DE DIFFUSION NATIONAUX

ALLEMAGNE Fachinformationszentrum, Karlsruhe D-7514 Eggenstein-Leopoldshafen 2	ISLANDE Director of Aviation c/o Flugrad Reykjavik
BELGIQUE Coordonnateur AGARD-VSL Etat-Major de la Force Aérienne Quartier Reine Elisabeth Rue d'Evere, 1140 Bruxelles	ITALIE - Aeronautica Militare Ufficio del Delegato Nazionale all'AGARD Aeroporto Pratica di Mare 00040 Pomezia (Roma)
CANADA Directeur du Service des Renseignements Scientifiques Ministère de la Défense Nationale Ottawa, Ontario K1A 0K2	LUXEMBOURG <i>Voir Belgique</i>
DANEMARK Danish Defence Research Board Ved Idrætsparken 4 2100 Copenhagen Ø	NORVEGE Norwegian Defence Research Establishment Attn: Biblioteket P.O. Box 25 N-2007 Kjeller
ESPAGNE INTA (AGARD Publications) Pintor Rosales 34 28008 Madrid	PAYS-BAS Netherlands Delegation to AGARD National Aerospace Laboratory NLR Kluiverweg 1 2629 HS Delft
ETATS-UNIS National Aeronautics and Space Administration Langley Research Center M/S 180 Hampton, Virginia 23665	PORTUGAL Portuguese National Coordinator to AGARD Gabinete de Estudos e Programas CLAFA Base de Alfragide Alfragide 2700 Amadora
FRANCE O.N.E.R.A. (Direction) 29, Avenue de la Division Leclerc 92320, Châtillon sous Bagneux	ROYAUME UNI Defence Research Information Centre Kentigern House 65 Brown Street Glasgow G2 8EX
GRECE Hellenic Air Force Air War College Scientific and Technical Library Dekelia Air Force Base Dekelia, Athens TGA 1010	TURQUIE Milli Savunma Başkanlığı (MSB) - ARGE Daire Başkanlığı (ARGE) Ankara

**LE CENTRE NATIONAL DE DISTRIBUTION DES ETATS-UNIS (NASA) NE DETIENT PAS DE STOCKS
DES PUBLICATIONS AGARD ET LES DEMANDES D'EXEMPLAIRES DOIVENT ETRE ADRESSEES DIRECTEMENT
AU SERVICE NATIONAL TECHNIQUE DE L'INFORMATION (NTIS) DONT L'ADRESSE SUIT.**

AGENCES DE VENTE

National Technical Information Service (NTIS) 5285 Port Royal Road Springfield, Virginia 22161 Etats-Unis	ESA/Information Retrieval Service European Space Agency 10, rue Mario Nikis 75015 Paris France	The British Library Document Supply Division Boston Spa, Wetherby West Yorkshire LS23 7BQ Royaume Uni
---	--	---

Les demandes de microfiches ou de photocopies de documents AGARD (y compris les demandes faites auprès du NTIS) doivent comporter la dénomination AGARD, ainsi que le numéro de série de l'AGARD (par exemple AGARD-AG-315). Des informations analogues, telles que le titre et la date de publication sont souhaitables. Veuillez noter qu'il y a lieu de spécifier AGARD-R-nnn et AGARD-AR-nnn lors de la commande de rapports AGARD et des rapports consultatifs AGARD respectivement. Des références bibliographiques complètes ainsi que des résumés des publications AGARD figurent dans les journaux suivants:

Scientific and Technical Aerospace Reports (STAR)
publié par la NASA Scientific and Technical
Information Division
NASA Headquarters (NTT)
Washington D.C. 20546
Etats-Unis

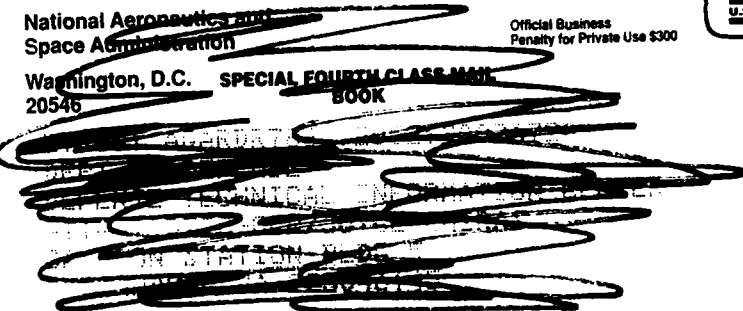
Government Reports Announcements and Index (GRA&I)
publié par le National Technical Information Service
Springfield
Virginia 22161
Etats-Unis
(accessible également en mode interactif dans la base de données bibliographiques en ligne du NTIS, et sur CD-ROM)



AGARD
 NATO OTAN
 7 RUE ANCELLE · 92200 NEUILLY-SUR-SEINE
 FRANCE
 Telephone (1)47.38.57.00 · Telex 610 176
 Telefax (1)47.38.57.99

**DISTRIBUTION OF UNCLASSIFIED
AGARD PUBLICATIONS**

AGARD does NOT hold stocks of AGARD publications at the above address for general distribution. Initial distribution of AGARD publications is made to AGARD Member Nations through the following National Distribution Centres. Further copies are sometimes available from these Centres (except in the United States), but if not may be purchased in Microfiche or Photocopy form from the Sales Agencies listed below.

<u>NATIONAL DISTRIBUTION CENTRES</u>	
BELGIUM Coordonnateur AGARD — VSL Etat-Major de la Force Aérienne Quartier Reine Elisabeth Rue d'Evere, 1140 Bruxelles	LUXEMBOURG See Belgium
CANADA Director Scientific Information Services Dept of National Defence Ottawa, Ontario K1A 0K2	NETHERLANDS Netherlands Delegation to AGARD National Aerospace Laboratory, NLR Kluiverweg 1 2629 HS Delft
DENMARK Danish Defence Ved Idrætsplads 2100 Copenhagen	NORWAY
FRANCE O.N.E.R.A. (Dir) 29 Avenue de la 92320 Châtillon	<p style="text-align: center;">  National Aeronautics and Space Administration Washington, D.C. SPECIAL FOURTH CLASS MAIL 20546 BOOK </p> 
GERMANY Fachinformation Karlsruhe D-7514 Eggenstein	<p style="text-align: center;"> Postage and Fees Paid National Aeronautics and Space Administration NASA-451 </p> <p style="text-align: center;"> Official Business Penalty for Private Use \$300 </p> 
GREECE Hellenic Air Force Air War College Scientific and Technical Dekelia Air Force Dekelia, Athens	
ICELAND Director of Aviation c/o Flugrad Reykjavik	SCIENCE RESEARCH INFORMATION CENTRE Kentigern House 65 Brown Street Glasgow G2 8EX
ITALY Aeronautica Militare Ufficio del Delegato Nazionale all'AGARD Aeroporto Pratica di Mare 00040 Pomezia (Roma)	UNITED STATES National Aeronautics and Space Administration (NASA) Langley Research Center M/S 180 Hampton, Virginia 23665

**THE UNITED STATES NATIONAL DISTRIBUTION CENTRE (NASA) DOES NOT HOLD
STOCKS OF AGARD PUBLICATIONS, AND APPLICATIONS FOR COPIES SHOULD BE MADE
DIRECT TO THE NATIONAL TECHNICAL INFORMATION SERVICE (NTIS) AT THE ADDRESS BELOW.**

SALES AGENCIES

National Technical Information Service (NTIS) 5285 Port Royal Road Springfield, Virginia 22161 United States	ESA/Information Retrieval Service European Space Agency 10, rue Mario Nikis 75015 Paris France	The British Library Document Supply Centre Boston Spa, Wetherby West Yorkshire LS23 7BQ United Kingdom
--	--	--

Requests for microfiches or photocopies of AGARD documents (including requests to NTIS) should include the word 'AGARD' and the AGARD serial number (for example AGARD-AG-315). Collateral information such as title and publication date is desirable. Note that AGARD Reports and Advisory Reports should be specified as AGARD-R-nnn and AGARD-AR-nnn, respectively. Full bibliographical references and abstracts of AGARD publications are given in the following journals:

Scientific and Technical Aerospace Reports (STAR) published by NASA Scientific and Technical Information Division NASA Headquarters (NTT) Washington D.C. 20546 United States	Government Reports Announcements and Index (GRA&I) published by the National Technical Information Service Springfield Virginia 22161 United States (also available online in the NTIS Bibliographic Database or on CD-ROM)
--	---



Printed by Specialised Printing Services Limited
40 Chigwell Lane, Loughton, Essex IG10 3TZ